



ISSN 1983-4195

IBRACON Structures and Materials Journal
Revista IBRACON de Estruturas e Materiais

Special Edition: Shear and Punching Shear

Editors: Leandro Trautwein, Mauro Real, Mario Pimentel

Volume 16, Number 3

June 2023





Special Edition – Shear and Punching – Editorial

The design of structural concrete elements under bending and shear is a subject of research, and intense debate since the pioneering works of Ritter and Morsch in the early 1900s. In recent decades, significant developments in shear and punching shear design of reinforced concrete beams and slabs have been achieved, with the emergence of new theories that received wide acceptance amongst the scientific and technical community. This effort and interest are motivated by the fact that shear and punching shear are among the most known sources of brittle failures in structural concrete elements. Structural engineers and researchers must find innovative ways and methods to design against brittle failures safely and economically. Strengthening the existing infrastructure to ensure safety, resilience, and sustainability under more severe loading conditions is also necessary. The main objective of this Shear and Punching Special Edition of the IBRACON Structures and Materials Journal is to bring together some of the most recent research advances on the analysis and design of reinforced concrete beams and slabs subjected to shear and punching, as well as in masonry structures under in-plane shear forces. This special edition contains two keynote articles and ten original research papers focusing on these subjects.

The Critical Shear Crack Theory (CSCT) is being developed since 1985 to assess the shear resistance of members without shear reinforcement and the punching shear resistance of reinforced concrete slabs in a rational manner. In this special edition, the article by Muttoni and Simões provides the historical framework of the development of the theory, followed by a presentation of its most up-to-date refined models.

Although masonry structures have long been built, work is yet to be developed to fully understand the behavior of a masonry wall subjected to in-plane shear, particularly in the case partially grouted concrete masonry. The factors that are known to affect the strength of this type of masonry are discussed in the article by Zhu and Shrive.

Experimental studies are most often the basis for the development of new design calculation methods. The study by Debella et al. evaluates the contribution of aggregate interlock throughout the critical crack formation process up to the ultimate load by performing bending tests on small-scale rectangular RC and SFRC beams without considering the effect of transverse reinforcement. A novel type of stud for punching shear reinforcement, containing an additional element designated as anti-cracking pin, is investigated through experimental tests in the paper by Ferreira et al. The main objective of the research is to find the optimal spacing between these pins so as to achieve a failure mode and a failure load similar to the reference slabs with conventional studs.

The finite element method (FEM) can be used to provide accurate simulations of the behavior of reinforced concrete structural elements once the models are properly calibrated and validated. Using FEM, it is possible to extrapolate laboratory data and simulate realistic geometric arrangements, boundary and loading conditions without the costs and limitations of experimental investigations. The use of construction waste as aggregate in concrete production is becoming a more frequent alternative due to the advantages associated with sustainability. The work by Siqueira et al. proposes a numerical approach to predict and understand the structural



behavior and failure patterns of reinforced recycled aggregate concrete slabs with and without steel fibers. The paper by Soares et al. demonstrates the viability of computational simulation for reproducing the behavior of reinforced concrete beams shear strengthened with CFRP. Finally, the study by Araújo et al. presents computational models that represent the shear behavior of concrete beams without transverse reinforcement described in the literature, with or without steel fibers. Smearred and discrete crack models are compared, and their performance is discussed.

A good design standard must have safe, economical, and simple design recommendations. The design requirements of the Brazilian standard NBR-6118 are the object of study of many articles of this edition. The paper by Araujo de Sá et al. evaluates the behavior of the combined bending and shear loads in reinforced concrete beams. The verification presented in ABNT NBR 6118 was used and compared to the more detailed Modified Compression Field Theory (MCFT). Size effects are known to be relevant in the behaviour of quasi-brittle materials like concrete whenever failure is governed by localized fracture. In Brazil, recent publications identified non-conservative trends in predictions of ABNT NBR 6118:2014 for larger beam depths. The Brazilian code never considered size effects because they are suppressed by transverse reinforcement. Considering this background, the paper by Ribeiro et al. presents a comprehensive analysis of NBR 6118:2014 shear strength predictions using data from the ACI-ASCE DatStb 445-D database as a reference. The study by Sousa et al. describes a set of recommendations to improve the accuracy of shear and punching shear capacity predictions for one-way slabs under concentrated loads, regardless of the governing failure mechanism, using the ABNT NBR 6118:2014 code provisions. The paper by Souza et al. proposes a numerical procedure for determining the asymmetrical plastic shear diagrams in punching control perimeters. Asymmetrical diagrams occur for edge, corner, and internal columns with unbalanced biaxial moments. The procedure intends to support the use of the NBR 6118, which covers asymmetrical shear distributions due to internal moments of edge and corner columns. Finally, the possibility of the occurrence of a second punching shear failure and of a Progressive Collapse after a punching shear failure had occurred in one flat slab column connection is investigated by Galdino and Melo in two building structures, using numerical analyses, the Yield Line Method, and the American, European, and Brazilian codes.

This Special Edition will interest designers often faced with shear and punching-related design requirements that fall outside of traditional research areas and existing code provisions, as well as researchers performing research in related areas.

Editors Dr. Leandro Mouta Trautwein, Dr. Mario Pimentel, and Dr. Mauro de Vasconcellos Real are grateful for the contributions of the authors and sincerely value the time and effort of the authors in preparing the papers in this Special Edition. Acknowledgment is also due to the reviewers of the manuscripts.

Leandro Trautwein, Mario Pimentel, and Mauro Real
Special Edition Invited Editor-in-Chief,
IBRACON Structures and Materials Journal

IBRACON Structures and Materials Journal

Revista IBRACON de Estruturas e Materiais

Contents

Partially grouted concrete masonry shear walls subject to in-plane shear load: a critical review..... 16301
J. ZHUA and N. SHRIVE

Shear and punching shear according to the Critical Shear Crack Theory: background, recent developments and integration in codes..... 16302
A. MUTTONI and J.T. SIMÕES

Investigation of aggregate interlock contribution to shear strength of reinforced concrete and steel fiber reinforced concrete beams..... 16303
L.C. DEBELLA, L.A. MONTOYA-CORONADO, T.L. RESENDE and R. PIERALISI

Identification of the failure modes of CFRP shear-strengthened reinforced concrete beams by the finite element method..... 16304
P.B. SOARES, P.M. LAZZARI, A. CAMPOS FILHO, B.M. LAZZARI and A.R. PACHECO

Experimental analysis of concrete flat slabs with internal stud-type shear reinforcement..... 16305
D.B. FERREIRA, L.M. TRAUTWEIN, J.P. VIRGENS, R.B. GOMES and L.C. ALMEIDA

Analysis of size effect in shear transfer mechanisms and size effect suppression by transversal reinforcement – contributions to NBR 6118 16306
I.J.S. RIBEIRO, J.R.C. PESSOA, T.N. BITTENCOURT and A.T. BECK

Punching shear design with control perimeters subjected to asymmetrical bending 16307
M.N. SOUZA, M.S.P.L. PERLINGEIRO and M. SCHULZ

Recommendations to assess the shear and punching capacity of one-way slabs under concentrated loads according to the ABNT NBR 6118:2014..... 16308
A.M.D. SOUSA, E.O.L. LANTSOGHT, D.L. ARAÚJO, L.P. PRADO and M.K. EL DEBS

Evaluation of shear design criteria of beams according to NBR6118 applying the modified compression field theory..... 16309
M.A. SA, S.H.C. SANTOS and J.J.H. SILVA FILHO

Numerical simulation of punching shear failure in recycled aggregate concrete slabs with steel fiber reinforcement 16310
A.H.C. SIQUEIRA, M. GIMENES, O.L. MANZOLI and E.A. RODRIGUES

Computational modeling of plain and steel fiber-reinforced concrete beams without transverse reinforcement 16311
D.L. ARAÚJO, C.R. SIQUEIRA FILHO and F.A. LOBO

Post punching shear pattern and progressive collapse of flat slab building 16312
B.C.P. GALDINO and G.S. MELO



Cover: Parametric Tower

Courtesy: Marcela Noronha P. de O. e Sousa



IBRACON

IBRACON Structures and Materials Journal is published bimonthly (February, April, June, August, October, and December) by IBRACON.

IBRACON

Instituto Brasileiro do Concreto Founded in 1972

Av. Queiroz Filho, nº 1700 — sala 407/408
Torre D — Villa Lobos Office Park
CEP 05319-000 — São Paulo, SP — Brazil
Phone: +55 11 3735-0202
Fax: +55 11 3733-2190
E-mail: riem@ibracon.org.br
Website: <http://www.ibracon.org.br>

Cover design & Layout: Editora Cubo
www.editoracubo.com.br

Support: Wallison Angelim Medeiros

Aims and Scope

Aims and Scope

The IBRACON Structures and Materials Journal (in Portuguese: Revista IBRACON de Estruturas e Materiais) is a technical and scientific divulgation vehicle of IBRACON (Brazilian Concrete Institute), published every two months. Each issue has 12 to 15 articles and, possibly, a technical note and/or a technical discussion regarding a previously published paper. All contributions are reviewed and approved by professionals with recognized scientific competence in the area. The IBRACON Structures and Materials Journal is an open access Journal, free of charges for authors and readers.

Objectives

The IBRACON Structures and Materials Journal's main objectives are:

- Present current developments and advances in concrete structures and materials.
- Make possible the better understanding of structural concrete behavior, supplying subsidies for a continuous interaction among researchers, producers, and users.
- Stimulate the development of scientific and technological research in the areas of concrete structures and materials, through papers peer-reviewed by a qualified Editorial Board.
- Promote the interaction among researchers, constructors and users of concrete structures and materials and the development of Civil Construction.
- Provide a vehicle of communication of high technical level for researchers and designers in the areas of concrete structures and materials.

Submission Procedure

The procedure to submit and revise the contributions, as well as the formats, are detailed in the Journal Website (ismj.org).

The papers and the technical notes are revised by at least two reviewers indicated by the editors. Discussions and replies are accepted for publication after a review by the editors and at least one member of the Editorial Board. In case of disagreement between the reviewer and the authors, the contribution will be sent to a specialist in the area, not necessarily linked to the Editorial Board. Conflict of interests is carefully handled by the Editors.

Contribution Types

The Journal will publish original papers, short technical notes, and paper discussions. Original papers will be accepted if they are in accordance with the objectives of the Journal and present quality of information and presentation. A technical note is a brief manuscript. It may present a new feature of research, development, or technological application in the areas of Concrete Structures and Materials, and Civil Construction. This is an opportunity to be used by industries, companies, universities, institutions of research, researchers, and professionals willing to promote their works and products under development.

A discussion is received no later than 3 months after the publication of the paper or technical note. The discussion must be limited to the topic addressed in the published paper and must not be offensive. The right of reply is granted to the Authors. The discussions and the replies are published in the subsequent issues of the Journal.

The submission file should be in accordance with the paper template available at the Journal Website. It is recommended that the length of the papers does not exceed 25 pages. Where available, URLs for the references should be provided.

The IBRACON Structures and Materials Journal will conduct the review process for manuscripts submitted in English. Titles, abstracts, and keywords are presented in English, and in Portuguese or Spanish. Articles and technical notes are peer-reviewed and only published after approval of the reviewers and the Editorial Board.

Once accepted, an article is typeset according to the journal layout. The author will be required to review and approve the galleys before publishing. At this stage only typesetting errors will be considered.

Internet Access

The IBRACON Structures and Materials Journal Webpage is available at <http://ismj.org>.

Sponsors

The funds for the maintenance of the Journal are currently obtained from the IBRACON. The Journal is not supposed to be maintained with funds from private sponsorship, which could diminish the credit of the publications.

Photocopying

Photocopying in Brazil. Brazilian Copyright Law is applicable to users in Brazil. IBRACON holds the copyright of contributions in the journal unless stated otherwise at the bottom of the first page of any contribution. Where IBRACON holds the copyright, authorization to photocopy items for internal or personal use, or the internal or personal use of specific clients, is granted for libraries and other users registered at IBRACON.

Copyright

All rights, including translation, reserved. Under the Brazilian Copyright Law N^o. 9610 of 19th February 1998, apart from any fair dealing for the purpose of research or private study, or criticism or review, no part of this publication may be reproduced, stored in a retrieval system, or transmitted in any form or by any means, electronic, mechanical, photocopying, recording or otherwise, without the prior written permission of IBRACON. Requests should be directed to IBRACON:

IBRACON

Av. Queiroz Filho, 1700 – sala 407/408 – Torre D
Villa Lobos Office Park
05319-000 – Vila Hamburguesa
São Paulo – SP
Phone: +55 (11) 3735-0202
E-mail: riem@ibracon.org.br

Disclaimer

Papers and other contributions and the statements made, or opinions expressed therein are published on the understanding that the authors of the contribution are the only responsible for the opinions expressed in them and that their publication does not necessarily reflect the views of IBRACON or of the Journal Editorial Board.

Editorial Board

Editor-in-chief emeritus (*in memoriam*)

José Luiz Antunes de Oliveira e Sousa, Universidade Estadual de Campinas - UNICAMP, Campinas, SP, Brazil.
<https://orcid.org/0000-0002-1108-4356>

Editor-in-chief

Guilherme Aris Parsekian, Universidade Federal de São Carlos - UFSCar, São Carlos, SP, Brazil, parsekian@ufscar.br
<https://orcid.org/0000-0002-5939-2032>

Associate Editors

Antônio Carlos dos Santos, Universidade Federal de Uberlândia - UFU, Uberlândia, MG, Brazil, acds@ufu.br
<https://orcid.org/0000-0001-9019-4571>

Bernardo Horowitz, Universidade Federal de Pernambuco - UFPE, Recife, PE, Brazil, bernardo.horowitz@ufpe.br
<https://orcid.org/0000-0001-7763-7112>

Bernardo Tutikian, Universidade do Vale do Rio dos Sinos - UNISINOS, São Leopoldo, RS, Brazil, bftutikian@unisinos.br
<https://orcid.org/0000-0003-1319-0547>

Bruno Briseghella, Fuzhou University, Fujian, China, bruno@fzu.edu.cn
<https://orcid.org/0000-0002-8002-2298>

Carmen Andrade, Universidad Politécnica de Catalunya, Spain, candrade@cimne.upc.edu
<https://orcid.org/0000-0003-2374-0928>

Diogo Rodrigo Ribeiro, Universidade do Porto - FEUP, Portugal, drr@isep.ipp.pt
<https://orcid.org/0000-0001-8624-9904>

Edna Possan, Universidade Federal da Integração Latino Americana - UNILA, Foz do Iguaçu, PR, Brazil, edna.possan@unila.edu.br
<https://orcid.org/0000-0002-3022-7420>

Fernando Pelisser, Universidade Federal de Santa Catarina - UFSC, Florianópolis, SC, Brazil, f.pelisser@ufsc.br
<https://orcid.org/0000-0002-6113-5473>

José Marcio Fonseca Calixto, Universidade Federal de Minas Gerais - UFMG, Belo Horizonte, MG, Brazil, calixto@dees.ufmg.br
<https://orcid.org/0000-0003-2828-0967>

José Tadeu Balbo Universidade de São Paulo - USP, São Paulo, SP, Brazil, jotbalbo@usp.br
<https://orcid.org/0000-0001-9235-1331>

Leandro Mouta Trautwein, Universidade Estadual de Campinas - UNICAMP, Campinas, SP, Brazil, leandromt@fec.unicamp.br
<https://orcid.org/0000-0002-4631-9290>

Lia Lorena Pimentel, Pontifícia Universidade Católica de Campinas - PUCCAMP, Campinas, SP, Brazil, lialp@puc-campinas.edu.br
<https://orcid.org/0000-0001-5146-0451>

Luís Oliveira Santos, Laboratório Nacional de Engenharia Civil, Lisboa, Portugal, luis.osantos@lnec.pt
<https://orcid.org/0000-0003-2591-2842>

Mark G Alexander, University of Cape Town, Cape Town, South Africa, mark.alexander@uct.ac.za
<https://orcid.org/0000-0002-0986-3529>

María Josefina Positieri, Universidad Tecnológica Nacional, Argentina, mpositieri@gmail.com
<https://orcid.org/0000-0001-6897-9946>

Mário Jorge de Seixas Pimentel, Universidade do Porto - FEUP, Porto, Portugal, mjps@fe.up.pt
<https://orcid.org/0000-0001-8626-6018>

Maurício de Pina Ferreira, Universidade Federal do Pará - UFPA, Belém, PA, Brazil, mpina@ufpa.br
<https://orcid.org/0000-0001-8905-9479>

Mauro de Vasconcellos Real, Universidade Federal do Rio Grande - FURG, Rio Grande, RS, Brazil, mauroreal@furg.br
<https://orcid.org/0000-0003-4916-9133>

Nigel G. Shrive, University of Calgary, Calgary, Canada, ngshrive@ucalgary.ca
<https://orcid.org/0000-0003-3263-5644>

Oswaldo Luís Manzoli, Universidade Estadual Paulista “Júlio de Mesquita Filho” - UNESP, Bauru, SP, Brazil, osvaldo.l.manzoli@unesp.br
<https://orcid.org/0000-0001-9004-7985>

Pedro Castro Borges, CINVESTAV, Mérida, Mexico, castro@cinvestav.mx
<https://orcid.org/0000-0001-6983-0545>

Rebecca Gravina, RMIT University, Melbourne, Australia, rebecca.gravina@rmit.edu.au
<https://orcid.org/0000-0002-8681-5045>

Editorial Board

Ricardo Carrazedo, Universidade de São Paulo - USP, São Carlos, SP, Brazil, carrazedo@sc.usp.br
<https://orcid.org/0000-0002-9830-7777>

Samir Maghous, Universidade Federal do Rio Grande do Sul - UFRGS, Porto Alegre, RS, Brazil, samir.maghous@ufrgs.br
<https://orcid.org/0000-0002-1123-3411>

Sérgio Hampshire de C. Santos, Universidade Federal do Rio de Janeiro - UFRJ, Rio de Janeiro, RJ, Brazil, sergiohampshire@gmail.com
<https://orcid.org/0000-0002-2930-9314>

Túlio Nogueira Bittencourt, Universidade de São Paulo - USP, São Paulo, SP, Brazil, tbitten@usp.br
<https://orcid.org/0000-0001-6523-2687>

Vladimir Guilherme Haach, Universidade de São Paulo - USP, São Carlos, SP, Brazil, vghaach@sc.usp.br
<https://orcid.org/0000-0002-9501-4450>

Yury Villagrán Zaccardi, Universidad Tecnológica Nacional Facultad Regional La Plata, Buenos Aires, Argentina, yuryvillagran@gmail.com
<https://orcid.org/0000-0002-0259-7213>

Former Editors

Américo Campos Filho, Universidade Federal do Rio Grande do Sul - UFRGS, Porto Alegre, RS, Brazil

Denise C. C. Dal Molin Universidade Federal do Rio Grande do Sul - UFRGS, Porto Alegre, RS, Brazil

Eduardo Nuno Brito Santos Júlio, Instituto Superior Técnico - IST, Lisboa, Portugal

Emil de Souza Sánchez Filho, Universidade Federal Fluminense - UFF, Rio de Janeiro, RJ, Brazil

Fernando Soares Fonseca, Brigham Young University – BYU, Provo, UT, USA

Geraldo Cechella Isaia, Universidade Federal de Santa Maria - UFSM, Santa Maria, RS, Brazil

Gonzalo Ruiz, Universidad de Castilla-La Mancha - UCLM, Ciudad Real, Spain

Guilherme Sales Melo, Universidade de Brasília - UnB, Brasília, DF, Brazil

Leandro Francisco Moretti Sanchez, University of Ottawa, Ottawa, ON, Canada

Luiz Carlos Pinto da Silva Filho, Universidade Federal do Rio Grande do Sul - UFRGS, Porto Alegre, RS, Brazil

Mounir Khalil El Debs, Universidade de São Paulo - USP, São Carlos, SP, Brazil

Nicole Pagan Hasparyk, Eletrobras Furnas, Aparecida de Goiânia, GO, Brazil

Paulo Helene, Universidade de São Paulo - USP, São Paulo, SP, Brazil

Paulo Monteiro, University of California Berkeley, Berkeley, CA, USA

Roberto Caldas de Andrade Pinto, Universidade Federal de Santa Catarina - UFSC, Florianópolis, SC, Brazil

Ronaldo Barros Gomes, Universidade Federal de Goiás - UFG, Goiânia, GO, Brazil

Romilde Almeida de Oliveira, Universidade Católica de Pernambuco - UNICAP, Recife, PE, Brazil

Romildo Dias Toledo Filho, Universidade Federal do Rio de Janeiro - UFRJ, Rio de Janeiro, RJ, Brazil

Rubens Machado Bittencourt, Eletrobras Furnas, Aparecida de Goiânia, GO, Brazil

Vladimir Antonio Paulon, Universidade Estadual de Campinas - UNICAMP, Campinas, SP, Brazil



Direction

Board of Direction 2021/2023

Biennium

President

Paulo Helene

1st Vice-President Director

Júlio Timerman

2nd Vice-President Director

Enio José Pazini Figueiredo

Presidency Advisors

Arnaldo Forti Battagin

Eduardo Antonio Serrano

Gilberto Antonio Giuzio

Iria Lícia Oliva Doniak

Jaques Pinto

João Luis Casagrande

Jorge Batlouni Neto

José Marques Filho

Mario William Esper

Ronaldo Tartuce

Rubens Machado Bittencourt

Selmo Chapira Kuperman

Simão Prizskulnik

Túlio Nogueira Bittencourt

Wagner Roberto Lopes

1st Director-Secretary

Cláudio Sbrighi Neto

2nd Director-Secretary

Carlos José Massucato

1st Treasurer Director

Júlio Timerman

2nd Treasurer Director

Hugo S. Armelin

Marketing Director

Alexandre Brites

Marketing Director Advisor

Guilherme Covas

Publications Director

Guilherme Parsekian

Publications Director Advisor

Túlio Nogueira Bittencourt

Event Director

Rafael Timerman

Event Director Advisor

Luis César De Luca

Technical Director

Carlos Brites

Technical Director Advisor

Emílio Takagi

Institutional Relations Director

César Henrique Daher

Institutional Relations Director Advisor

José Vanderley de Abreu

Course Director

Jéssica Pacheco

Course Director Advisor

André Mendes

Student Activities Director

Jéssica Andrade Dantas

Student Activities Director Advisor

Patrícia Bauer

Personnel Certification Director

Adriano Damásio Soterio

Personnel Certification Director Advisor

Paula Baillot

Research and Development Director

Bernardo Tutikian

Research and Development Director Advisor

Roberto Christ

Council 2021/2023 Biennium

Individual Members

Alio Ernesto Kimura

Antônio Carlos dos Santos

Antônio Domingues de Figueiredo

Arnaldo Forti Battagin

Bernardo Fonseca Tutikian

Carlos José Massucato

César Henrique Sato Daher

Claudio Sbrighi Neto

Enio José Pazini Figueiredo

Geraldo Cechella Isaia

Iberê Martins da Silva

Inês Laranjeira da Silva Battagin

Iria Lícia Oliva Doniak

Jéssica Mariana Pacheco Misko

José Tadeu Balbo

Leandro Mouta Trautwein

Luiz Prado Vieira Júnior (*in memoriam*)

Mário William Esper

Rafael Timerman

Rubens Curti

Vladimir Antonio Paulon

Past President Members

Eduardo Antônio Serrano

José Marques Filho

Júlio Timerman

Paulo Roberto do Lago Helene

Ronaldo Tartuce

Rubens Machado Bittencourt

Selmo Chapira Kuperman

Simão Prizskulnik

Túlio Nogueira Bittencourt

Corporate Members

ABCIC - Associação Brasileira da Construção Industrializada de Concreto – Iria Lícia Oliva Doniak

ABCP - Associação Brasileira de Cimento Portland – Paulo Camilo Penna

ABECE - Associação Brasileira de Engenharia e Consultoria Estrutural – João Alberto de Abreu Vendramini

ABESC - Associação Brasileira das Empresas de Serviços de Concretagem – Wagner Roberto Lopes

EPUSP - Escola Politécnica da Universidade de São Paulo – Túlio Nogueira Bittencourt

IPT - Instituto de Pesquisas Tecnológicas do Estado de São Paulo – José Maria de Camargo Barros

MC-BAUCHEMIE BRASIL INDÚSTRIA E COMÉRCIO LTDA – Jaques Pinto

PhD Engenharia Ltda – Douglas de Andreza Couto

TQS Informática Ltda – Nelson Covas

VOTORANTIM Cimentos S/A – Mauricio Bianchi

Reviewers List 2021-2022

Abdalla Filho, João Elias
Adriano Rossignolo, João
Aguiar, Cássio
Aguilar, Maria Teresa
Albuquerque, Arthur
Almeida Filho, Fernando
Almeida, Luiz
Almeida, Saulo José de Castro
Alva, Gerson Moacyr Sisniegas
Alves, Antônio
Alves, Elcio
Andrade, Daniel
Andrade, Jairo José de Oliveira
Ângulo, Sérgio
Araújo, Daniel
Araújo, Francisco Celio de
Araújo, Tereza
Asche, Harry
Azevedo, Afonso
Azevedo, Crysthian Purcino
Balbo, José
Barboza, Aline
Barros, Rodrigo
Beck, André
Bernardin, Adriano
Bernardo, Luís
Bezerra, John
Bittencourt Junior, Luis
Bittencourt, Eduardo
Bolina, Fabrício
Botte, Wouter
Bounassar Filho, Jorge
Brito, José
Buttignol, Thomaz
Caldas, Rodrigo Barreto
Caldentey, Alejandro Perez
Calixto, José Marcio
Campelo, Henrique
Campos Filho, Américo
Campos, Heloisa
Capuzzo, Valdirene Maria Silva
Cardoso, Daniel Carlos Taissum
Carrazedo, Ricardo
Carrazedo, Rogério
Carvalho, Hermes
Carvalho, Roberto Chust
Castro, Alessandra Lorenzetti de
Cervenka, Jan
Cheung, Andrés
Christ, Roberto
Christoforo, André
Cincotto, Maria
Ciriades, Jean Pierre
Cordeiro, Luciana
Costa, Carla Neves
Costa, Fernanda Bianchi Pereira da
Couto, Douglas
Dalfré, Gláucia
De Nardim, Silvana
Delalibera, Rodrigo
Diniz, Sofia Carrato
Dominguez, Joel
Durand, Raúl
Fairbairn, Eduardo
Fakury, Ricardo
Feldmann, Markus
Ferreira, Fernanda
Ferreira, Gisleiva Cristina dos Santos
Ferreira, Luiz Eduardo Teixeira
Figueiredo, Antônio Domingues de
Flórez-López, Júlio
Folino, Paula
Fonseca, Ana
Formagini, Sidiclei
Frizon, Tiago
Futai, Marcos
Gachet, Luisa
Garcez, Mônica Regina
Garcia, Maria da Luz
Gaspar, Cássio
Gavilan, Sergio
Genikomsou, Aikaterini S.
Giuseppe, Guimarães
Golaszewski, Jacek
Gomes, Carlos Marmorato
Gomes, Francisco Augusto Aparecido
Gomes, Ronaldo
Gonçalves, Paulo J. P.
Greco, Marcelo
Gumieri, Adriana
Gusmão, Alexandre
Haach, Vladimir
Haselbach, Liv
Horowitz, Bernardo
Hosen, Akter
Hotza, Dachamir
Irassar, Edgardo F.
Iskander, Mina
Isoldi, Liércio André
Isufi, Brisid
Jacintho, Ana
Jacinto, Luciano
Joshaghani, Alireza
Justino Filho, Manoel Rodrigues
Kadhim, Majid M. A.
Karayannis, Chris G.
Kazmi, Syed
Kazmierczak, Cláudio
Kempka, Mariane
Kenai, S.
Khazanovich, Lev
Khoshnazar, Rahil
Kowalski, Robert
Krahl, Pablo Augusto
Kripka, Moacir
Kroetz, Henrique Machado
Lameiras, Rodrigo
Lantsoght, Eva O. L.
Lazzari, Bruna
Lazzari, Paula
Leite, Mônica Batista
Lemes, Igor
Li, Hui
Liang, Qing Quan
Liberati, Elyson
Lima, Flávio
Lima, Silvio Souza
Liu, Yi
Loredo-Souza, Acir
Lübeck, André
Ludvig, Péter
Luz, Caroline Angulski da
Machado, Roberto
Maciel, Geraldo
Maedo, Michael
Magalhães, Aldo de
Magalhães, Fábio
Mansur, Alexandra
Manzoli, Osvaldo
Mappa, Paulo César
Marques Filho, José
Marques, Marília
Marques, Severino
Mata, Rodrigo da
Matos, Ana Mafalda
Matos, Paulo de
Medeiros, Arthur
Medeiros, Marcelo
Medeiros, Ronaldo
Melges, José Luiz Pinheiro
Melo, Antônio
Mendes, Júlia Castro
Meneghetti, Leila Cristina
Menendez, E.
Menezes, Ruy
Mennucci, Marina Martins
Mesquita, Esequiel
Miguel, Leandro Fleck Fadel
Moahmed, Hoda
Modolo, Regina
Monte, Renata
Montes-Garcia, Pedro
Moraes, Poliana Dias de
Morsch, Inácio
Mota, Neusa
Munaiar Neto, Jorge
Muñoz-Rojas, Pablo
Neves Junior, Alex
Nóbrega, Petrus
Nogueira, Caio
Nogueira, Fernando
Nunes, David
Oliveira, Cristina
Oliveira, Dênio
Oliveira, Leonardo Henrique
Oliveira, Luciane Marcela Filizola de
Oliveira, Mateus Antônio Nogueira
Oliveira, Romilde
Paccola, Rodrigo
Pachêco, Alexandre
Pachêco, Fernanda
Paes, José Luiz
Palermo Junior, Leandro
Pantoja, João
Parente Junior, Evandro
Parsekian, Guilherme A.
Patil, Chetan
Pedroso, Cynthia
Peixoto, Ricardo André Fiorotti
Pelisser, Fernando
Pereira, Eduardo
Pereira, Sebastião Salvador Real

Reviewers List 2021-2022

Perlingeiro, Mayra
Pfeil, Michèle
Picelli, Renato
Pileggi, Rafael
Pimenta, Roberval
Pimentel, Lia Lorena
Pinto, Roberto Caldas de Andrade
Pinto, Silas
Pires, Tiago
Pituba, José Júlio de Cerqueira
Pontes, Helder
Possan, Edna
Pravia, Z. M. C
Punhagui, Katia
Quaranta, Giuseppe
Quinino, Uziel
Rashad, Alaa
Real, Mauro
Rêgo, João da Silva
Resende, Thomás Lima de
Ribeiro, Daniel
Ribeiro, Diogo
Rigobello, Ronaldo
Rizzatti, Eduardo
Rocha, Janaíde Cavalcante
Rocha, Marcelo
Roesler, Jeffery
Rojas, Rosangel
Romanel, Celso
Rossi, Alexandre
Sakata, Rafael Dors
Sanchez, Emil
Sandoval, Gersson Fernando Barreto
Santos, Ana Carolina Parapinski dos
Santos, Daniel
Santos, Sérgio Hampshire C.
Santos, White
Sarker, Prabir K.
Savija, Branko
Schulz, Mauro
Sciarretta, Francesca
Scott, Allan
Seara-Paz, Gumersinda
Setiawan, Andri
Shafigh, Payam
Shi, Jinjie
Shishegaran, Aydin
Silva Filho, José
Silva, Amilton Rodrigues da
Silva, Bruno do Vale
Silva, Fernando Marques da
Silva, José Guilherme da
Silva, Marcelo Araújo da
Silva, Maria Cecília Teixeira da
Silva, Renata Gomes Lanna da
Silva, Valdir
Silva, Wellington Andrade da
Silvestro, Laura
Simonetti, Camila
Siqueira, Gustavo
Snoeck, Didier
Soto, Orieta
Sousa, Adla
Stucchi, Fernando Rebouças
Tamayo, Jorge
Tarabia, Ahmed
Tavares, Maria Elizabeth
Tayeh, Bassam
Thamboo, Julian Ajith
Toralles, Berenice
Trautwein, Leandro
Trindade, Ana Carolina Constância
Tutikian, Bernardo
Valença, Jonatas
Veríssimo, Gustavo
Vianna, Sávio S. V.
Vieira, Geilma
Vieira, Manuel
Wahrhaftig, Alexandre de Macêdo
Wally, Gustavo
Wang, Wen-Wei
Wang, Xiao-Yong
Welter, Nathanaell Vinícius de Camargos
Wong, Patrick
Xie, Tianyu (Anson)
Yang, Shangtong
Yassin, Ahmed
Yu, Runqing



ORIGINAL ARTICLE

Partially grouted concrete masonry shear walls subject to in-plane shear load: a critical review

Paredes de alvenaria de concreto parcialmente grauteadas submetidas a cargas de cisalhamento no plano: uma revisão crítica

Jianyixian Zhu^a

Nigel Shrive^a

^aUniversity of Calgary, Department of Civil Engineering, Calgary, Alberta, Canada

Received 25 November 2022

Accepted 07 February 2023

Abstract: Although structures have been built from masonry for many years, little is still known about the behaviour of a wall subject to in-plane shear. This is particularly true of partially grouted concrete masonry. The factors that are known to affect the strength of this type of masonry are discussed with the varying results and interpretations highlighted. There is consensus that increasing axial stress increases the shear strength and reduces the ductility of the masonry. However, whether reinforcement (both horizontal and vertical) contributes to strength remains an issue of debate, as is the effect of aspect ratio. Most codes and standards do not differentiate fully grouted from partially grouted masonry, often over predicting the shear strength of the latter. Wall versus panel failure is not considered. Much work needs to be done to improve our understanding of this material subject to in-plane shear.

Keywords: concrete masonry, partially grouted, in-plane shear, strength, failure mode.

Resumo: Embora as estruturas sejam construídas em alvenaria há muitos anos, pouco ainda se sabe sobre o comportamento de uma parede sujeita a cisalhamento no plano. Isto é particularmente verdadeiro para alvenaria de concreto parcialmente grauteado. Os fatores que sabidamente afetam a resistência deste tipo de alvenaria são discutidos destacando as variações de resultados e interpretações. É consenso que o aumento da tensão axial aumenta a resistência ao cisalhamento e reduz a ductilidade da alvenaria. No entanto, se a armação (horizontal e vertical) contribui para a resistência permanece uma questão de debate, assim como o efeito da relação de aspecto. A maioria dos códigos e normas não diferencia alvenaria totalmente grauteada de alvenaria parcialmente grauteada, muitas vezes superestimando a resistência ao cisalhamento desta última. A ruptura de parede versus painel não é considerada. Muito trabalho precisa ser feito para melhorar a compreensão deste material sujeito a cisalhamento no plano.

Palavras-chave: alvenaria de concreto, parcialmente rebocada, cisalhamento no plano, resistência, modo de falha.

How to cite: J. Zhu and N. Shrive, "Partially grouted concrete masonry shear walls subject to in-plane shear load: a critical review," *Rev. IBRACON Estrut. Mater.*, vol. 16, no. 3, e16301, 2023, <https://doi.org/10.1590/S1983-41952023000300001>

1 INTRODUCTION

Although masonry has been used for centuries, the structural behaviour of masonry is still not understood thoroughly by researchers and engineers. Within a building, shear walls are structural components that resist in-plane lateral load. Concrete masonry shear walls can be categorized according to different grouting and reinforcement conditions: unreinforced masonry (URM), partially grouted masonry (PGM), and fully grouted masonry (FGM). PGM shear walls are the focus of this review, including the modes of failure, parameters that can impact the masonry shear capacity, and

Corresponding author: Jianyixian Zhu. E-mail: jianyixian.zhu@ucalgary.ca

Financial support: This research project is funded by Natural Sciences and Engineering Research Council (NSERC) of Canada. The first author is granted a two-year scholarship by Canadian Standard Association (CSA) and another two-year scholarship by Alberta Student Aid.

Conflict of interest: Nothing to declare.

Data Availability: the authors are willing to share the reference papers upon request.



This is an Open Access article distributed under the terms of the Creative Commons Attribution License, which permits unrestricted use, distribution, and reproduction in any medium, provided the original work is properly cited.

equations for estimating that shear capacity. In addition, brief discussions on the scaling effect and ductility of masonry are provided.

2 MODES OF FAILURE

There are three commonly recognized independent failure modes for masonry shear walls, namely sliding failure, diagonal shear failure, and flexural / rocking failure [1], as in Figure 1. These failure modes can happen independently or in combinations of any of the two modes, or even all three modes together [2]. The transition points from one failure mode to another are not yet understood, but some parameters have been found to influence the transition or combination of failure modes, such as reinforcement, axial load, and wall aspect ratio [3], [4], [5], [6].

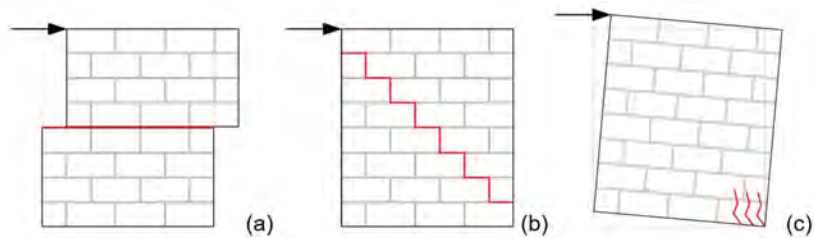


Figure 1. Modes of failure: (a) sliding; (b) diagonal shear; (c) flexural / rocking.

Sliding failure normally occurs along horizontal bed joints, and thus the part of wall above the horizontal crack slides relative to the part below [1]. Gao and Zhai [7] reported that the compressive strength of the mortar and the applied axial load could impact the shear strength of sliding failure, and that the higher these two components were, the higher the shear strength, which could be higher than the strength of the wall in the diagonal failure mode. Diagonal shear failure refers to the step-like cracking pattern that runs diagonally across a wall, with the cracking typically in the head and bed mortar joints but sometimes through the masonry units [1]. Voon and Ingham [3] observed that diagonal cracking started with tension splitting cracks in the compression strut in the wall, so major cracks would develop along the diagonal. The flexural / rocking failure mode is characterized by crushing of the toe and lifting of the heel of the shear wall [1], and this mode can also be accompanied by yielding of steel reinforcement in the wall. Therefore, the flexural failure mode has higher deformation capacity, and can be considered as more ductile than when a wall fails in the diagonal shear mode [4].

When there is an outer frame or confinement, such as reinforced concrete confinement or grouted cores and bond beams, the wall could be seen as a larger wall system consisting of multiple panels in the wall frame [8]. In realistic engineering designs, there could be multiple bays and stories of walls in a structure. Such a shear wall can fail in either wall action, in which the cracks propagate through panel to panel continuously, or in panel action, where the cracks only exist in individual panels separately, as in Figure 2.

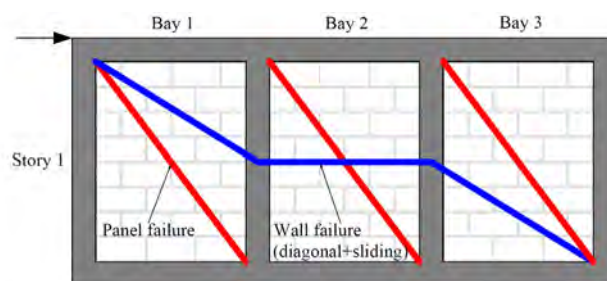


Figure 2. Panel failure and wall failure.

A unique failure mode was reported by Gao and Zhai [7]. They subjected a 2000 x 1300 x 240 mm brick wall with two reinforced bond beams to cyclic loading and observed failure in the lowest panel only, which had very low panel aspect ratio. A combined sliding and diagonal shear failure was observed in their experiment, as in Figure 3. Their other wall specimens failed at the bond beam and panel interfaces or had more vertically angled cracks from the upper panel to the lower panel.

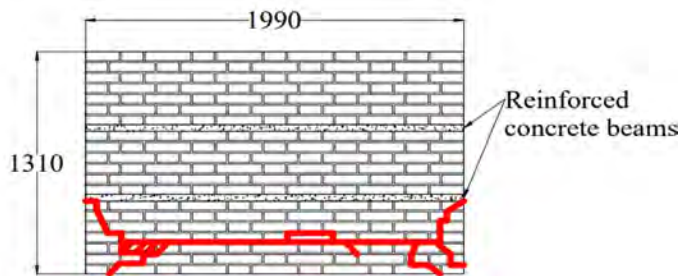


Figure 3. Failure of plain wall with reinforced concrete beams [7].

3 PARAMETERS THAT INFLUENCE SHEAR STRENGTH OF MASONRY WALLS

There are many parameters that have been observed to influence the shear strength of masonry walls. These parameters can be grouped into two categories: material variables such as grouting, mortar, reinforcement; and structural variables such as aspect ratio, axial load, detailing [5], [9], [10], [11]. The variability in masonry causes difficulty in determining whether there is a correlation between the parameter and shear strength or whether the apparent effect was just a random coincidence. In addition, many of the early studies did not have enough experimental group repetitions to validate conclusions statistically, and/or variables were not isolated – for example, changing the horizontal and vertical reinforcement ratios simultaneously, or changing one of these and not accounting for the additional grout so one doesn't know if it was the additional grout that made the difference or the additional steel. The lack of rigour in many studies thus means that the prediction of masonry shear wall performance often has many limitations.

Much of the prediction of masonry shear wall behaviour started from masonry beams [12], which were assumed to have some similarities with reinforced concrete beams. Some early studies had the shear load applied vertically on beams, and walls were thought of as beams rotated through 90 degrees, so the shear load was equivalently applied horizontally. If masonry were homogeneous and isotropic, this assumption might be correct, if shear walls were deep beams. However, masonry is heterogeneous and anisotropic, so the analogy of simply rotating from a beam to a wall may not be accurate.

3.1 Mortar Joints

Mortar plays a critical role in masonry as it binds units together. Mortar normally consists of cement, lime, sand, and water, so different proportions of each component create mortar pastes with different properties which in turn influence the performance of masonry. For example, the more coarse the sand, the higher the compressive strength and tensile bond strength [13]. Curing mortar by covering the masonry with sheets could increase its strength, but this is not very applicable in actual construction.

Whether or not the mortar joints contribute to the ultimate shear strength of masonry, either for small specimen tests or grouted walls, remains controversial. Some researchers found that there was no correlation between the compressive strength of the mortar and the shear strength of the masonry [6], [14], [15], while others found that while higher mortar strength increased the masonry shear strength, the increase was not very significant [7], [16], [17].

3.2 Grouting

Grouting is used in conjunction with reinforcement to connect the reinforcement to the masonry. The impacts of the two materials on shear capacity was not examined separately in some cases, so the researcher might change the reinforcement ratio whilst also changing the grouted area [3]. The strength of the grout, size of aggregate and area of grouting can affect grout performance. Numerical modelling shows the spacing of vertical and horizontal grout has a non-linear relationship with the shear capacity of a wall [18]. As for the net area of PGM, the TMS 402/602-22 standard [19] specifies that the web of a concrete masonry unit and the void space between two units should be accounted for [10]. However, there is not always grout on the web, so a slightly larger net area could result in a lower shear stress.

Since grout strength can be lower, equal to, or higher than the masonry unit strength, results from each case can be quite different. If the grout strength is higher than the strength of the masonry unit, the resulting compressive strength of the grouted masonry can be much higher than that of the ungrouted masonry [20]. If the grout strength is lower or equal to the unit strength, the maximum shear load of PGM can be higher than the maximum load for the equivalent URM, but the shear stress is lower [3], [21], [22]. Cracks normally start where the effective width is reduced, such as in the ungrouted cores or in the mortar joints between the ungrouted and grouted cores.

3.3 Masonry Compressive Strength

Research on concrete beams showed the ultimate shear strength of a reinforced concrete beam is positively related to the square root of the compressive strength of the concrete [23]. The same was deemed to apply to masonry. Drysdale et al. [14] were one of the earliest to normalize the shear strength of brick masonry by its compressive strength. A non-linear increasing trend between the compressive strength and shear strength of masonry was observed by Mastumura [24], [25], and a linear trend was developed between the square root of compressive strength and shear strength by Janaraj and Dhanasekar [8]. Others found that the increasing trend has certain limits: for example, shear load capacity increased by 15% with a 40% increase in compressive strength of PGM walls (from 14.75 MPa), but a further increase in the masonry compressive strength did not affect the load capacity [11].

3.4 Reinforcement

Horizontal and/or vertical steel reinforcement is often used in masonry shear walls to increase their ductility. It is still controversial as to whether these reinforcements contribute to the shear strength of a masonry wall. Some researchers claim that the reinforcement did not yield [25] or did not contribute to wall stiffness until cracking [6], while others reported that the reinforcement yielded before cracking [4]. One of the common findings from the literature is that researchers tended only to compare walls with various type of vertical reinforcement embedded in grout, or horizontal reinforcement together with vertical reinforcement, but neglected to compare their results to walls with grout only or without any reinforcement. Therefore, the impact of each component was unclear, i.e., the variables were not controlled effectively. Discussion is included separately for horizontal and vertical reinforcement in the following sections.

3.4.1 Horizontal reinforcement

Horizontal reinforcement could be in various forms. Continuous steel bars can be placed in the masonry courses with grout to form a bond beam, and the ends of the horizontal steel could be bent to 90-degree or 180-degree hooks. Joint reinforcement, another type of horizontal reinforcement, is normally thinner ladder steel or straight bars placed in the mortar or on top of the mortar between courses. Joint reinforcement can be mounted easily and has better performance in crack control, ductility, and energy dissipation than continuous steel bars [26], [27], [28]. Oan [9] tested 66 squat walls with repetitive specimens in each group. Statistical analysis of the results showed that changing the type of horizontal reinforcement did not have significant impact on shear strength or energy dissipation.

The ratio of horizontal reinforcement to the area is one of the key factors examined. Some studies showed that increasing the reinforcement ratio could increase the ultimate shear capacity [3], [24], [25], [29], while others claimed that there was a threshold for the impact [20]. Researchers mostly examined the performance of horizontal reinforcement on squat or square walls, seldom considering the effect on walls with aspect ratio greater than 1. On the other hand, several researchers have reported that horizontal reinforcement can only be activated after cracking, and thus such reinforcement improved the post cracking performance and ductility of walls, which could cause change from the brittle failure mode to a more ductile failure [4], [5], [6], [16], [20], [30], [31]. It is only the steel in the middle third or so of a square wall that can contribute to ductility as it is only that steel which will have sufficient embedment in the wall to develop tension: bars at the top and bottom of the wall where the cracking is towards the corner will have insufficient development length on the short side of the masonry post-cracking. A statistical analysis showed that neither strength nor area of horizontal reinforcement had impact on masonry shear wall capacity [17]. Some researchers claimed that masonry and horizontal reinforcement had a changing proportion and rate of contribution at different phases in the load-displacement relationship [2], [32]: cracking could decrease the capacity of masonry to carry load, so tension could build up in the steel. The concept of energy dissipation, which is the area under load-displacement curve during cyclic-loading, was used to compare the effect of different levels of horizontal reinforcement: changing the reinforcement ratio did not have significant impact on energy dissipation in shear walls [30].

Since reinforcement can be of different sizes, for the same reinforcement ratio, the choice can be a few bars of large diameter or more bars with smaller diameter. The latter was found to result in smoother strength degradation and thinner but a larger number of cracks than the former [3], [31]. The distribution or spacing of horizontal reinforcement was also an important factor. As the grouted bond beams with horizontal reinforcement could be considered to separate the wall into multiple panels, the angle of a diagonal crack varies with the spacing [22].

3.4.2 Vertical reinforcement

The impact of using vertical reinforcement on the shear strength of a masonry wall is also controversial. Early studies showed that increasing the ratio of vertical reinforcement could increase the ultimate shear capacity [6], [33], [34], but some

researchers did not differentiate the effects of the additional grout vis-a-vis the reinforcement. Others therefore claimed that there was no correlation between vertical reinforcement and the shear strength of masonry walls [2], [5]. Oan and Shrive [5] also explained that the material and structural contribution of reinforcement should be examined separately. When the vertical reinforcement was embedded into the foundation of wall, dowel action would occur during a sliding or diagonal failure, so the steel would bend near the base. Some studies reported that, similar to horizontal reinforcement, vertical reinforcement was also only activated after cracking, and therefore, the ductility of the wall increased [5], [34], [35]. The use of vertical reinforcement could also shift the failure mode from wall failure to panel failure, as the grout and vertical reinforcement could be considered as a frame to the panels [20].

Changing the horizontal spacing of vertical reinforcement did not have a significant effect on the peak load or initial stiffness [20], [35], [34]. A smaller spacing could result in a larger number of narrower cracks [20], [26]. Widely spaced reinforced masonry shear walls are defined differently for various standards. For example, the Canadian standard allows up to 2.4 m spacing [36] and the American standard up to 2.44 m spacing [19], whereas the Australian code specifies that “wide” spacing should be within the range of 0.8 m to 2.4 m [37]. Current standards used literature sources primarily of FGM to determine the masonry shear strength, and the equations were simply factored to obtain an estimation for PGM, but the shear strength and distribution of FGM and PGM was different [10]. Therefore, those clauses should be updated.

3.5 Axial stress

It is commonly reported and agreed that increasing the level of applied axial stress in a masonry shear wall increases its ultimate shear strength, aggregate interlocking forces or friction force, and delays crack initiation [3], [5], [6], [9], [38]. A linear relationship, or the Mohr-Coulomb criterion, was observed by many researchers until a certain limit [4], [6], [7], [9], [14], [24], [25], [39], [40], and then the rate of increase changed or the relationship became more curved [14]. Numerical modelling can present the distribution of stress over the wall, and it was found that increasing the axial load changed the principal stresses of the diagonal compression strut, in which the principal compressive stress increased and principal tensile stress decreased [41], [42]. Increasing the axial stress can also result in changing the failure mode from a more ductile failure to a more brittle failure [3], [5], [6], [33], [34], and cause a smoother degradation in stiffness. With low axial load and high shear load, sliding was the dominant mode of failure; whereas high axial load and low shear load on the other hand could create more vertically angled diagonal cracks [9], [15]. For those specimens with intermediate compressive and shear stress, a mix of the two failure modes occurred. When a wall was reinforced with some vertical steel bars, low or zero axial load could result in partial pull-out of vertical reinforcement, so the tensile straining and strain hardening of steel was lowered, and the contribution of the vertical reinforcement to the ultimate shear capacity was also lowered [6].

3.6 Aspect Ratio

The aspect ratio of a wall is the ratio between the wall height and length and was generally found to correlate negatively with the shear strength of masonry walls [3], [7], [8], [24], [25], [40], [42]. The well-understood range of aspect ratio is from 0.5 to 2.0: shear walls with higher aspect ratios have not been studied thoroughly. Matsumura [24], [25] reported a decreasing hyperbolic relationship, while Hamedzadeh [40] concluded a logarithmic equation of shear stress normalized with the compressive strength of masonry represented the effect more accurately. Schultz et al. [30] were the only exception, finding a positive relationship between aspect ratio and nominal shear stress. They tested 6 fixed brick walls under cyclic loading, with aspect ratios of 0.5, 0.7, and 1.0 with the walls having the same height but changing length. A significant increase in shear strength was found when increasing the aspect ratio from 0.5 to 0.7, but no change was found from 0.7 to 1.0. However, they used the same size and number of vertical reinforcing bars in the outermost cells of the walls, so it was unclear that the impact on peak shear load was caused by the aspect ratio or the different ratios and moments of resistance of the vertical reinforcement.

Increasing the aspect ratio creates a larger moment arm for the horizontal load at the top of a wall and thus a larger moment reaction at the bottom of the wall. Increasing the aspect ratio also causes a narrower compression strut at more a vertically oriented slope [41], [42], [43]. Pan [42] modelled the effect of a circular void lying in the compression strut of a shear wall numerically and explained that the wall could experience higher surface stress, so a crack would be very likely to be initiated at the high tensile stress zone at the void.

The aspect ratios of the wall and the panels within it can be examined separately if there are multiple bays and stories [8]. Hamedzadeh [40] examined the performance of half-scale concrete block walls with various aspect ratios. The walls had vertical reinforcement welded to the foundation to create multiple panels. He reported that with high

axial load on square and squat walls, major diagonal cracks occurred across the middle vertical reinforcement. If there were three panels, the first and second panels (closest to the point of application of the lateral shear load (top left in Figure 4) tended to fail together while the third panel cracked individually.

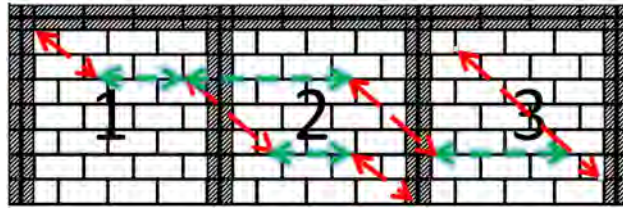


Figure 4. Cracking pattern of multi-panel walls [40].

3.7 Shear Span Ratio

Shear span ratio is a concept that was imported from reinforced concrete beams and applied to masonry beams, and eventually to masonry shear walls. In the beam context, the shear span ratio refers to the ratio of the shear span to the effective depth, shown as a/d [12], as in Figure 5a. In the wall context the concept was rotated 90 degrees from the beam, so the ratio becomes the ratio of the vertical height from the base to the inflection point of the wall to the length of the wall in the shear direction [10]. In some standards, the ratio is often represented as M/Vd , which is the external moment versus shear load times the effective depth, as in Figure 5b. Dillon and Fonseca [10] claimed that this ratio varied with the boundary conditions of tested specimens and that some researchers had mistakenly used the incorrect ratio. However, using the external loads estimated for design to predict strength appears to violate the fundamental concepts of limit states design [44]. Many researchers have tried to prove that there is a relationship between shear span ratio and masonry shear strength. For example, Okamoto et al. [4] reported that increasing shear span ratio could decrease the maximum shear stress but increase the ultimate drift angle of the masonry wall.

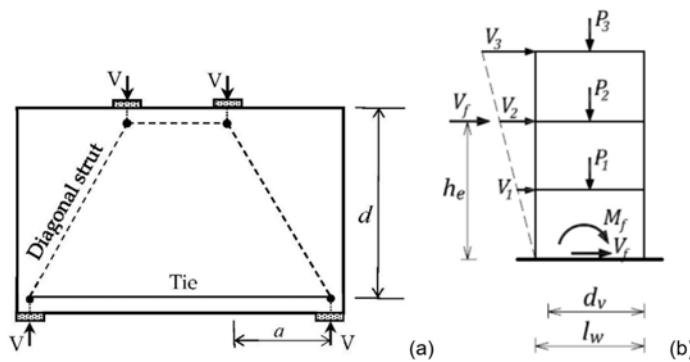


Figure 5. Shear span to depth ratio of: (a) a beam [45]; (b) a wall [46].

3.8 Loading Pattern

Commonly used loading patterns include monotonic, cyclic, and seismic loading [32], as in Figure 6. Monotonic loading is simply a constant rate of increasing load until the specimen fails. Cyclic loading refers to repeated loading at different (typically increasing) amplitudes. Seismic loading is the simulation of past or synthetic seismic activity and could be considered as a type of cyclic loading. The loading pattern and rate will have some influence on the shear capacity, ductility, and strength degradation of a masonry wall [6], [10], [32]. Walls subjected to monotonic loading could have a higher peak shear load than those subjected to cyclic load, since the latter could experience closing and opening of cracks, and the strength of the wall can drop quite significantly after the first loading cycle [10], [33]. Different types of cyclic loading did not result in significant differences in peak load or energy absorption. Therefore, using values obtained from experimental tests should be factored down based on their loading type in the equations for prediction.

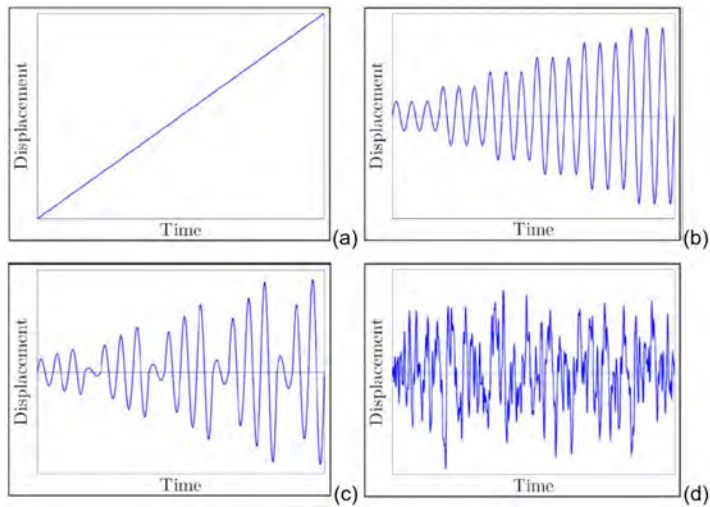


Figure 6. Loading patterns: (a) monotonic; (b) amplified cyclic; (c) sequential-phase cyclic; (d) simulated seismic [10].

Most of the existing studies used one or two actuators on the top of the wall to apply axial load and one actuator on one side of the wall for lateral shear load. Application of a point or distributed load can also create different cracking patterns in the wall [40]. As shown in Figure 7, applying a distributed load can cause the major crack to appear along the diagonal of the shear wall with some minor parallel cracks, but applying a concentrated load can shift the major crack down a couple of courses and cause a slight increase in peak shear load. However, numerical models of the different load applications did not present a distinct change in the compression strut, but the area of extreme compression was slightly wider for those subjected to distributed load [42].

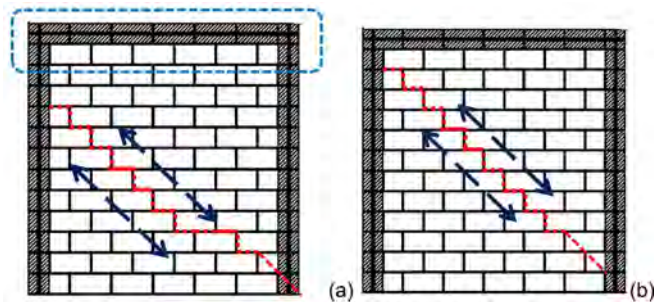


Figure 7. Cracking pattern of (a) concentrated load and (b) distributed load [40].

3.9 Openings

Perforated walls, or walls with window or door openings, have gained more and more attention from researchers [47]. Several studies have considered the effect of the size and location of openings on the behaviour of a shear wall. The presence of an opening can lower the peak load and increase wall deflection [18], [39], [48], [49], [50]. Increasing the size of the opening did not have significant impact on peak load, but could increase the height of the piers, which impacts the wall stiffness and cracking pattern [11], [18], [48], [49], [50], [51]. Increasing the number of stories can also limit the effect caused by openings [18]. Other parameters such as axial load and horizontal reinforcement below the opening can not only increase shear strength, but also alter the cracking pattern of perforated walls [39], [47], [48].

3.10 Confinement

Confined masonry refers to masonry walls with both an infill panel and an outer “frame”, such as grouted outermost cores or a reinforced concrete frame. The former is more convenient and economical to construct but the latter had better performance [52]. The confinement can maintain the integrity of a masonry wall, and thus increase the shear capacity, ductility, and energy dissipation [7], [28], [50]. The level of influence of confinement on the peak shear

capacity is still controversial, with some researchers reporting that confinement can only contribute after cracking. Thus, this would not have a significant impact in terms of shear strength if net area is taken into consideration [52]. The stiffness ratio between the confinement and the infill panel could alter the failure mode of the wall. For example, similar moduli of elasticity of the frame and infill or high cohesion between them can result in wall action and higher mechanical interlocking forces: in contrast, with frames much stiffer than the panels, panel action or local failure could be observed [31], [34], [42], [53], [54].

4 SCALING

Laboratory experiments are often constrained by space, budget, and testing equipment. Therefore, many researchers have explored the possibility to scale down the size of the specimens tested. For instance, 1/2 scale specimens have been used commonly, and sometimes 1/3, 1/4, or 1/6 scale specimens have been considered. The scaling effect of the material properties is of importance as masonry is an anisotropic and heterogenous material. Researchers have found that with similar density, a similar percentage of the cross-section being solid, and similar absorption rate of the bricks and blocks, reducing the size and volume could result in equal or higher compressive strength of the masonry unit and prism [55], [56], [57], [58], [59]. Some explained that smaller sizes of the masonry units could have a lower possibility and distribution of flaws during the manufacturing processes, and smaller-scale prisms had thinner mortar joints. Other properties such as tensile strength, shear strength and initial stiffness were not different based on size effect. However, one major concern was that the experiments have normally been done with only one type of masonry unit, mortar, or grouting, so the effect of different masonry combinations should be examined. Another issue raised was to relate the properties of prisms to those of walls of various sizes. Changing the overall geometry of the wall or adding vertical constraints to the top of the wall could change the peak shear capacity or stiffness [58], [60]. Reports in the literature generally conclude that using reduced size masonry was mostly in agreement with full scale masonry but results should be given careful consideration.

5 DUCTILITY

The ductility of a masonry wall does not have a strict definition, but ductility is normally used to describe the deformation of wall at different loading stages. Tomažević and Žarnić [16] extracted a bi-linear load-displacement relationship from the backbone curves using the theorem of energy conservation, and this relationship has been used in many studies and standards. The commonly used ductility index is the ratio of ultimate displacement to the effective yielding displacement [61], but the definition for the displacements is varied. For example, the effective yielding displacement has been defined as 40% of the displacement at peak load [62], or the displacement at the intercept of the initial stiffness line with a horizontal line through the peak load [61]. The ultimate displacement could be taken as the displacement of the wall corresponding to the load dropping to 80% of the peak load [61], or 67% [27] or 75% [30]. Except for the bi-linear models, the tri-linear approach is also considered by some researchers [34], which accounts for yielding, peak, and post-peak performance, as shown in Figure 8. These methods are all idealized load-displacement responses of masonry shear walls, so researchers could choose the approach that best represents their experimental results for further analysis or numerical modelling.

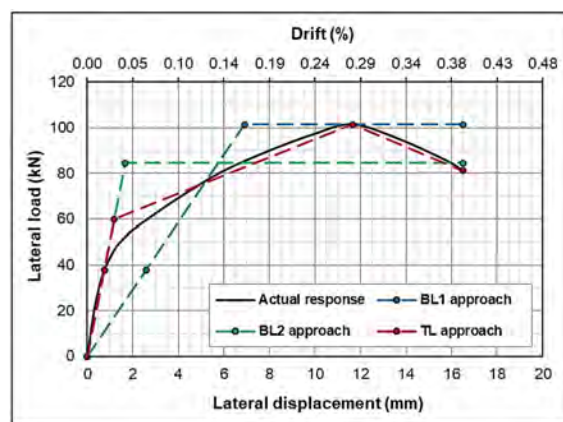


Figure 8. Bi-linear and tri-linear methods [34].

6 STANDARDS AND CODES OF PRACTICE

The estimation of in-plane shear capacity of masonry walls varies for different countries or regions. In this section, some published standards are included and compared with each other.

6.1 Canadian CSA S304-14

The Canadian Standard CSA S304-14 [36] defines the in-plane shear capacity separately for diagonal shear, as Equation 2, and sliding shear failure, as Equation 3. For the diagonal shear equation, three components are considered: masonry shear strength, axial load, and the contribution from the reinforcement. In addition, the term γ_g is a factor to account for the grouting condition. The shear span term was included to determine the shear strength of the masonry, as Equation 1, but including factored loads in the resistance side of a limit state is contradictory to the principle of ultimate limit states design [44]. Many researchers who have examined their own experimental results and other results reported in the literature found that the value predicted by the standard had large variation [8], [9], [18], [40], [43], [63], and that the factor 0.25 for applied axial load could be unconservative at very high or very low axial loads [8]. Some researchers have argued that the standard was developed from FGM, so cannot predict the capacity of PGM accurately, especially with all the different possibilities for PGM (grout and bar spacing, panel failure, etc.) [10], [18].

$$v_m = 0.16 \left(2 - \frac{M_f}{V_f d_v} \right) \sqrt{f'_m} \text{ and } 0.25 < \frac{M_f}{V_f d_v} < 1 \quad (1)$$

$$V_r = \phi_m (v_m b_w d_v + 0.25 P_d) \gamma_g + \left(0.60 \phi_s A_v f_y \frac{d_v}{s} \right) \leq 0.4 \phi_m \sqrt{f'_m} b_w d_w \gamma_g \quad (2)$$

$$V_r = \phi_m \mu C \quad (3)$$

6.2 American TMS 402/602-22

There are similar components in the American TMS 402/602-22 [19] as in the Canadian standard, but there is only one equation for all failure modes, as Equation 4. Although in TMS 402/602-22 there is no stand-alone clause for masonry shear strength, a similar shear span term is included in the shear capacity equation. This standard is developed from the MSJC standards [64], for which the only difference is that the coefficient for masonry contribution changed from 0.083 to 0.042. Studies have found that the MSJC clause significantly overestimates the contribution of horizontal reinforcement and the nominal shear load, especially for PGM and walls with openings [8], [18], [20], [43], [63].

$$F_v = \left\{ 0.042 \left[\left(4.0 - 1.75 \left(\frac{M}{V d_v} \right) \sqrt{f'_m} \right) \right] + 0.25 \frac{P}{A_n} + 0.5 \left(\frac{A_v F_s d_v}{A_n v s} \right) \right\} \gamma_g \quad (4)$$

6.3 Australian AS 3700:2018

Unlike the American and Canadian standards, the Australian standard AS 3700:2018 [37] has separate clauses for plain and reinforced walls. For unreinforced shear walls, Equation 5 includes the shear bond strength and friction strength of the masonry. The shear strength of unreinforced masonry is defined as a factor times the tensile bond strength of the masonry, which are both associated with cohesion: the correlation was verified and considered generally conservative [65]. The default value 0.2 MPa for tensile bond strength could overestimate some masonry combinations. For reinforced masonry, walls with aspect ratios above and below 2.3 are defined differently, and the terms include masonry shear strength and vertical reinforcement, see Equation 6. The clauses were reported to overestimate PGM or multi-panel wall strength significantly [8], [43].

$$V_d \leq V_o + V_l = \phi f'_{ms} A_d + k_v f_d A_d \quad (5)$$

$$V_d \leq \phi (f_{vr} A_d + 0.8 f_{sy} A_s) \text{ for } H/L \leq 2.3 \quad (6)$$

6.4 Brazilian ABNT NBR 16868-1

In the equation to determine shear wall capacity in the Brazilian standard [66], contributions from the masonry and the horizontal reinforcement are included, as in Equation 7.

$$V_{design} \leq V_a + V_s = f_{vd}bd + 0.75f_{yd}bd \frac{A_{sw}}{s} \quad (7)$$

The design shear strength, f_{vd} , should be half of f_{vk} , which for unreinforced masonry includes axial load. For reinforced masonry f_{vk} includes the reinforcement ratio.

- $f_{vk} = 0.10 + 0.5\sigma \leq 1.0$, for mortar strength from 1.5 to 3.4 MPa
- $f_{vk} = 0.15 + 0.5\sigma \leq 1.4$, for mortar strength from 3.5 to 7.0 MPa
- $f_{vk} = 0.35 + 0.5\sigma \leq 1.7$, for mortar strength above 7.0 MPa
- $f_{vk} = 0.35 + 17.5\rho \leq 0.7$

6.5 Chinese GB50003-2011

The Chinese standard GB5003-2011 [67] not only specifies equations for unreinforced and reinforced walls, as Equation 8, but also uses two equations for reinforced shear walls subjected to eccentric compression or tension, Equations 9 and 10, respectively. For the unreinforced walls, terms for the masonry contribution and the applied axial load are included. For reinforced walls, the masonry contribution, the axial load, and the horizontal reinforcement are considered. There are different ways to determine the masonry shear strength in the Chinese standard. For unreinforced masonry, values can be found in a table according to the masonry type and mortar grade. For reinforced masonry with concrete units, values depend on the masonry compressive strength.

$$V \leq (f_v + \alpha\mu\sigma_0)A \quad (8)$$

$$V \leq \frac{1}{\lambda-0.5} \left(0.6f_{vg}bh_0 + 0.12N \frac{A_w}{A} \right) + 0.9f_{yh} \frac{A_{sh}}{s} h_0 \quad (9)$$

$$V \leq \frac{1}{\lambda-0.5} \left(0.6f_{vg}bh_0 - 0.22N \frac{A_w}{A} \right) + 0.9f_{yh} \frac{A_{sh}}{s} h_0 \quad (10)$$

6.6 European Eurocode 2005

The Eurocode [68] also uses different equations for the shear strength of unreinforced and reinforced masonry walls, Equations 11 and 12, respectively. For the unreinforced masonry, the shear capacity of a masonry wall is deemed solely dependent on the masonry contribution, while for the reinforced masonry, the capacity includes contributions from both the masonry and the horizontal reinforcement, and a factor is applied to account for different grouting conditions. The masonry shear strength can be either determined from sample testing, such as the triplet test [69], or using the Mohr-Coulomb criterion with the initial shear strength to determine the characteristic strength. The Eurocode is quite conservative, with an experimental to predicted shear capacity ratio of 2.62 and a 56% COV, but the code can also overestimate some walls in some circumstances [9].

$$V_{Rd} = f_{vd}t l_c \quad (11)$$

$$V_{Rd1} + V_{Rd2} = f_{vd}t l + 0.9A_{sw}f_{yd} \quad (12)$$

7 SHEAR MODELS

As there have been many studies of masonry shear wall capacity completed since the 1970s. Researchers have developed various equations to estimate the in-plane shear capacity of masonry walls with different conditions. Some of the models are included in this section. Some more recently proposed models have not yet been studied by other researchers, so the accuracy and precision of these latter models could be questionable.

7.1 Matsumura (1987, 1988)

Matsumura [24], [25] tested 60 reinforced concrete masonry walls and 30 brick walls and concluded with the following Equation 13 for ultimate shear capacity, including terms for the masonry contribution, aspect ratio, horizontal reinforcement, and axial load. Factors also include the grouting condition and vertical reinforcement. Matsumura was one of the earliest to include the square root of the masonry compressive strength and the horizontal reinforcement in the prediction, and thus influenced many later standards and other models. The ratio of predicted value to experimental value showed both overestimation and underestimation with different grouting conditions, and the horizontal reinforcement term could greatly impact the accuracy [2], [18], [40], [63].

$$V_u = \left(K_u K_p \left(\frac{0.76}{h/d+0.7} + 0.012 \right) \sqrt{f'_m} + 0.18 \gamma \delta \sqrt{\rho_h \sigma_{hy} f'_m + 0.2 \sigma_o} \right) t j \cdot 10^3 \quad (13)$$

7.2 Shing et al. (1990)

Shing et al. [6] tested 22 reinforced masonry walls under both monotonic and cyclic loading and proposed Equation 14 to estimate shear capacity in imperial units. There are terms representing contributions from the masonry, vertical reinforcement, horizontal reinforcement and axial load, as well as the square root of the masonry compressive strength. However, Shing et al. [6] did not test replicate walls, and the accuracy of prediction was of great concern [40], [63].

$$V_n = [0.0018(\rho_v f_y + \sigma_c) + 2] A \sqrt{f'_m} + \left(\frac{l-2d'}{s} - 1 \right) A_h f_y \quad (14)$$

7.3 Anderson and Priestley (1992)

Anderson and Priestley [2] summarized the results of the testing of 69 walls from three sources. All the walls had aspect ratio greater or equal to one, while some had fixed-fixed boundary conditions and others were cantilever wall type tests. The Anderson and Priestly equation (Equation 15) again included terms of the masonry contribution, axial load, and horizontal reinforcement. It was reported that this equation significantly overestimates the capacity of PGM walls [63].

$$V_u = 0.24 \sqrt{f'_m} w t + 0.25 P + 0.50 A_h f_{yh} \frac{d}{s} \quad (15)$$

7.4 Voon and Ingham (2007)

Voon and Ingham [70] summarized their experimental results from 10 cantilever walls [3] and the same literature resources as Anderson and Priestley [2]. They suggested Equation 16 which includes terms for the masonry contribution, axial load, and horizontal reinforcement. Similar factors as the CSA [36] and TMS [19] standards to account for the shear span ratio were included as $C_b = 0.083[4 - 1.75(M/VL)]$. In addition, there were also factors of vertical reinforcement and ductility included in the equation, in which $C_a = 0.022 \rho_v f_{yv}$ and the ductility factor, k , decreased with increasing ductility, as in Figure 9a. Other than the previously mentioned issues of various boundary conditions from the literature, the determination of angle α in the equation was primarily from experimental results for reinforced concrete columns [71], which have much higher aspect ratios than regular masonry shear walls. The definition also varied with single or double curvature, which might be confusing in some cases, as in Figure 9b.

$$V_n = 0.8k(C_a + C_b)A_n \sqrt{f'_m} + 0.9N^* \tan \alpha + A_h f_{yh} \frac{D_{eff}}{s_h} \leq 0.33A_n \sqrt{f'_m} \quad (16)$$

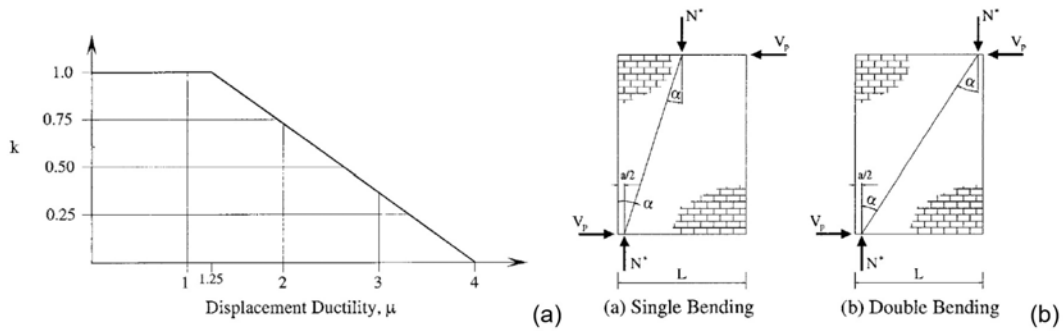


Figure 9. (a) Relationship between ductility and reduction factor; (b) Contribution of axial load to masonry shear strength [70].

7.5 Oan and Shrive (2014)

Oan and Shrive [72] tested 66 masonry walls and used the results of 130 walls from various literature sources to propose a revision to the CSA S304-14 [36] equation for masonry shear capacity. They stated that their proposed equation showed relatively good accuracy and precision to their experimental and the literature results [18]. Their equation including terms accounting for masonry strength, axial load, and vertical reinforcement, as Equation 17. However, they did not change the definition for masonry shear strength, and it was still dependent on masonry compressive strength and the shear span ratio.

$$V_r = \phi_m(v_m d_v b_w \gamma_g) + 0.27P + \phi_s(0.05 A_{sv} f_{yv}) \tag{17}$$

7.6 Dillon and Fonseca (2015)

Dillon and Fonseca [10] completed a meta-analysis of 340 walls from 47 research projects from 1968 to 2010 and concluded that the MSJC equation had acceptable accuracy for FGM but overestimated PGM. The walls tested in the different sources were also subject to various boundary conditions, aspect ratio, axial load, etc. However, the weighting assigned to each study was still based on the terms included in the equation, with the inclusion of some being controversial. Dillon and Fonseca [10] further examined the grouting factor for PGM and confirmed that the current adjustment factor of 0.75 was acceptable, but that a factor of 0.73 would be better [73]. They also confirmed that the strengths of FGM and PGM had different statistical distributions, so it might not be accurate simply to apply a single factor to account for the wall capacity.

7.7 Janaraj and Dhanasekar (2016)

One major difference in the Janaraj and Dhanasekar [8] equation and others was that they ignored the contribution of steel reinforcement and introduced separate terms for panel aspect ratio and wall confinement, as Equation 18. The number of bays was included as n , and number of stories was included as m . The confinement efficiency η was dependent on panel aspect ratio and the type of material in the masonry wall. They used their experimental results of confined masonry walls and literature values from various sources.

$$V_n = [0.17(2 - 0.9\lambda_p)\sqrt{f'_m} A_n + 0.25P] \times (0.9)^{m-1} \times \eta \tag{18}$$

7.8 Bolhassani et al. (2016)

Bolhassani et al. [63] proposed a shear capacity equation for PGM with or without a frame, as Equation 19. They used their experimental results and some existing studies. They claimed that this equation predicted the shear capacity more accurately if the spacing of the reinforcement was larger than 1.2 m.

$$V_n = (n - 1) \left[w t_{eff} \sqrt{f'_m} \cos \theta + \mu P_{infill} + \frac{4M_p}{h} \right] \tag{19}$$

7.9 Izquierdo et al. (2021)

Izquierdo et al. [17] randomly selected 25% of 292 PGM walls from 27 existing studies as their dataset. They used stepwise regression and examined several equations to predict masonry shear capacity from the statistical analysis. Some of their equations showed that the compressive strength of the mortar had a positive impact on masonry shear capacity, but they omitted those equations because they claimed that it was “unconventional”. Izquierdo et al. [17] confirmed that neither the strength nor the area of horizontal reinforcement contributed to the shear strength of a wall. Out of several equations, they selected Equation 20 as their optimal model, which includes wall length, the compressive strength of the grouted masonry, the area and spacing of vertical reinforcement, and the axial load.

$$V_n = 0.0538L + 4.83f'_{mg} + 0.067A_{vf} - 0.0553s_{v,ave} + 0.245P \quad (20)$$

7.10 Medeiros et al. (2022)

Medeiros et al. [18] summarized their numerical modelling results of multi-panel walls with openings and experimental results from various sources and proposed Equation 21, which includes terms of masonry contribution with grouting factors, axial load, and horizontal and vertical reinforcements. For the dataset they utilized, their equation gave the best predictive results, being slightly more consistent than the equations of Oan and Shrive [72], Dillon and Fonseca [10], and Izquierdo et al. [17].

$$V_n = k_{gv}k_{gh}\beta A_{eh}\sqrt{f'_m} + 0.4P_d \tan \theta + 0.02A_v f_{yv}\sqrt{f'_m} + 0.02\rho_h A_{ev} f_{yv}\sqrt{f'_m} \quad (21)$$

8 METHOD OF TESTING

Experimental testing and numerical modeling are both commonly used methods found in existing studies of masonry shear walls. These approaches have both advantages and disadvantages. Testing a wall is normally used to determine the performance, ultimate load and displacement, but construction and handling is very time and budget consuming. Small specimens can be used to reflect some properties, but the properties measured might not represent the actual ones of the wall (because of different boundary conditions, material proportions, construction etc.). On the other hand, numerical modeling can be applied to assess various aspects, but without the input of actual experimental results, the output may not be trustworthy. In this section, some testing methods are discussed.

8.1 Tests for Shear Strength

The triplet test is widely used in Europe to determine the shear strength of masonry [69]. As in Figure 10a, the assembly of a triplet specimen is relatively easy as only three masonry units are required. By supporting the outer units and loading only the middle unit, the mortar joints can experience close to a pure shear load. It is also possible to apply pre-compression to the specimen. The results of many studies involving clay brick specimens generally demonstrate that precompression and shear strength followed a linear Mohr-coulomb relationship [14], [33], [74], [75], [76], [77], but only a few studies have been performed on concrete block specimens (hollow, partially and fully grouted) [78], [79].

The diagonal tension test, as defined by ASTM C1006 [80], is another test to determine the diagonal shear strength of masonry. The specimen is a square wall with dimensions of 1.2 m x 1.2 m: steel loading shoes are placed at each end of the diagonal compression strut, as in Figure 10b and displaced towards each other. The stress distribution induced by the test is different from a typical shear wall in practice, because the specimens can only fail in the diagonal failure mode and suffer from compressive stress concentration around the loading shoes [44], [52], [56], [81], [82]. Moreover, the diagonal tension test is similar to the Brazilian splitting tensile strength test for determining tensile strength of rock samples [83], so the results from this diagonal test may need adjustment before being used as the shear strength of a masonry wall.

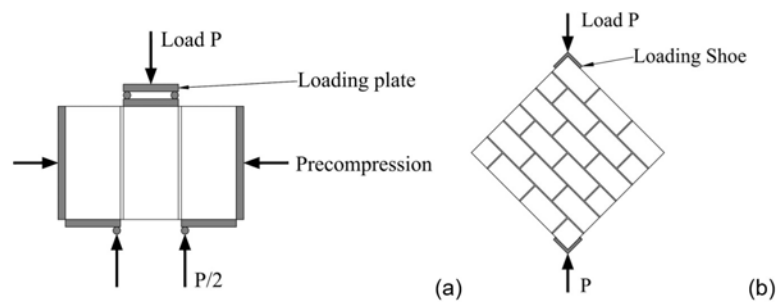


Figure 10. (a) Triplet test; (b) diagonal tension test.

8.2 Numerical Modelling

Numerical modelling is an important and powerful tool to assess structural performance, as it can save time and budget compared to experimental testing. There are three common methods of modelling for masonry structures, namely macro-modelling, simplified micro-modelling, and detailed micro-modelling [40], [41], [42], [84]. Macro-modelling refers to using homogenous material properties and element mesh for the structure, while micro-modelling includes the different properties for each masonry component, i.e., separate sets of properties and elements for unit, mortar, grout, steel, and their interfaces. Simplified micro-modelling treats the mortar and mortar-unit interface as discontinuous elements with units as continuous elements - detailed micro-modelling has only the interface properties as discontinuous elements. There are pros and cons for each method, so researchers should consider which would be more suitable for their project. For example, micro-modelling is helpful to examine local failure of a structure, but macro-modelling could be more applicable for the holistic view of a complex structure. To simulate crack propagation, researchers often use either the discrete or the smeared crack approach [11], [18], [34], [85]. The discrete crack approach allows crack or joint opening from using interface elements, whereas the smeared crack approach displays damaged areas with the distortion or deformation of continuum elements [85]. Researchers should also carefully study mesh sensitivity to make sure that the output is stable and reliable.

9 CONCLUSIONS

Partially grouted masonry (PGM) walls have gained more and more interest worldwide. In this review, parameters influencing the shear strength and capacity of PGM walls that were examined by many researchers were discussed. A few of them have a commonly agreed impact on the strength and stiffness of PGM walls, such as axial load, aspect ratio and loading pattern, but the effects of many parameters remain controversial, such as grouting, reinforcement, and confinement. Standards in different regions have different clauses to estimate the peak shear capacity, and many researchers summarized their findings into their equations. This all shows that a commonly acceptable understanding of the shear behaviour of masonry is deficient. A lot more needs to be learned about the fundamentals of this subject. In terms of experimental testing, reduced sized units are often used due to many constraints, and results are mostly in agreement with full-scale units. A ductility index is a good measurement for the wall performance after peak load. However, the question remains as to how to predict masonry shear strength accurately and precisely, and to convert strength into the masonry contribution component of the shear capacity estimation of PGM. The controversy of the impact of different parameters should be resolved, or at least updated, in the estimation. Furthermore, the transition point of different failure modes or equations to estimate the peak shear load for different failure types should be identified.

ACKNOWLEDGEMENTS

The authors would like to acknowledge the support from the Natural Sciences and Engineering Research Council (NSERC) of Canada and the University of Calgary. The Canadian Standards Association (CSA) and Alberta Student Aid are also appreciated for their scholarships to the first author.

REFERENCES

- [1] N. Shrive, M. Dhanasekar, M. Masia, and A. Page, "The response of concrete masonry with widely-spaced reinforcement to in-plane shear: state-of-the-art and research needs," *Int. J. Mason. Res. Innov.*, vol. 3, no. 4, pp. 369–381, Oct. 2018.

- [2] D. Anderson and M. Priestley, "In plane strength of masonry walls," in *6th Can. Mason. Symp.*, Saskatoon, Canada, Jun. 1992, pp. 223–234.
- [3] K. Voon and J. Ingham, "Experimental in-plane shear strength investigation of reinforced concrete masonry walls," *J. Struct. Eng.*, vol. 132, pp. 400–408, Mar. 2006.
- [4] S. Okamoto, Y. Yamazaki, T. Kaminosono, M. Teshigawara, and H. H. Iraishi, "Seismic capacity of reinforced masonry walls and beams," in *18th Joint Meeting U.S.-Jpn Cooperat. Progr. Natur. Resour. Panel Wind Seismic Effec.*, Washington D.C., United States, 1987, pp. 307–319.
- [5] A. Oan and N. Shrive, "Shear of concrete masonry walls," in *11th Can. Mason. Symp.*, Toronto, Canada, 2009, pp. 1–10.
- [6] P. B. Shing, M. Schuller, and V. S. Hoskere, "In-plane resistance of reinforced masonry shear walls," *ASCE J. Structural Eng.*, vol. 116, no. 3, pp. 619–640, Mar. 1990.
- [7] B. Gao and H. Zhai, "The seismic resistance behaviour of partially reinforced brick walls," in *9th Int. Brick Block Mason. Conf.*, Berlin, Germany, 1991, pp. 481–489.
- [8] T. Janaraj and M. Dhanasekar, "Design expressions for the in-plane shear capacity of confined masonry shear walls containing squat panels," *J. Structural Eng.*, vol. 142, no. 2, p. 04015127, Feb. 2016.
- [9] A. F. Oan, "*Diagonal Shear of Partially Grouted Concrete Masonry Panels*," Calgary, Canada: University of Calgary, 2013.
- [10] P. B. Dillon and F. S. Fonseca, "Nominal shear strength of partially grouted masonry walls," *Mason. Soc. J.*, vol. 33, no. 1, pp. 71–92, Dec. 2015.
- [11] K. Medeiros, K. Chavez, F. Fonseca, G. Parsekian, and N. Shrive, "Parametric study of multi-story, perforated, partially grouted masonry walls subjected to in-plane cyclic actions," *Can. J. Civ. Eng.*, vol. 48, no. 8, pp. 1046–1055, Aug. 2020.
- [12] G. Suter and A. Hendry, "Shear strength of reinforced brickwork masonry," *Struct. Eng.*, vol. 53, no. 6, pp., Jun. 1975.
- [13] C. Anderson and L. Held, "The effect of sand grading on mortar properties and tensile bond strength of brickwork specimens," in *8th Int. Load Bearing Brickwork Symp.*, London, United Kingdom, 1986, pp. 1–6.
- [14] R. Drysdale, R. Vanderkeyl, and A. Hamid, "Shear strength of brick masonry joints," in *5th Int. Brick Mason. Conf.*, Washington D.C., United States, 1979, pp. 106–113.
- [15] A. Hamid and R. Drysdale, "Behaviour of brick masonry under combined shear and compression loading," in *2nd Can. Mason. Symp.*, Ottawa, Canada, 1980, pp. 51–64.
- [16] M. Tomažević and R. Žarnić, "The effect of horizontal reinforcement on the strength and ductility of masonry walls at shear failure," in *7th Int. Brick Block Mason. Conf.*, Melbourne, Australia, 1985, pp. 1291–1302.
- [17] K. Izquierdo, C. Cruz-Noguez, and M. Arash, "Stepwise regressions for predicting the in-plane shear strength of partially grouted masonry walls," in *14th Can. Mason. Symp.*, Montreal, Canada, 2021, pp. 1–12.
- [18] K. A. Medeiros, G. A. Parsekian, N. G. Shrive, and F. S. Fonseca, "Shear load capacity prediction of unperforated and perforated partially grouted masonry walls," *Eng. Struct.*, vol. 256, p. 113927, Apr. 2022.
- [19] The Masonry Society, *Building Code Requirements and Specification for Masonry Structures, TMS 402/602-22*, 2022.
- [20] S. M. Nolph and M. A. ElGawady, "Static cyclic response of partially grouted masonry shear walls," *J. Struct. Eng.*, vol. 138, no. 7, pp. 864–879, Jul. 2012.
- [21] A. Oan and N. Shrive, "Effect of construction method on shear resistance of concrete masonry walls," in *15th Int. Brick Block Mason. Conf.*, Florianópolis, Brazil, 2012, pp. 1–9.
- [22] A. Oan and N. Shrive, "Experimental study on the effect of horizontal reinforcement on the shear strength of concrete masonry walls," *Int. J. Civ. Struct. Eng. Res.*, vol. 6, no. 2, pp. 15–21, Aug. 2018.
- [23] A. Placas, "*Shear Failure of Reinforced Concrete Beams*," London, United Kingdom: Imperial College of Science and Technology, 1969.
- [24] A. Matsumura, "Shear strength of reinforced hollow unit masonry walls – differences between partially grouted walls and fully grouted walls," in *4th North Amer. Mason. Conf.*, Los Angeles, United States, 1987, pp. 50–1–50–16.
- [25] A. Matsumura, "Shear strength of reinforced masonry walls," in *9th World Conf. Earthq. Eng.*, Tokyo, Japan, 1988, pp. 121–126.
- [26] G. Baenziger and M. Porter, "Joint reinforcement for masonry shear walls," in *11th North Amer. Mason. Conf.*, Minneapolis, United States, 2011.
- [27] G. Baenziger and M. Porter, "Joint reinforcement as primary shear reinforcement for concrete masonry shear walls," *Mason. Soc. J.*, vol. 36, no. 1, pp. 49–64, Dec. 2018.
- [28] J. P. Gouveia and P. B. Lourenço, "Masonry shear walls subjected to cyclic loading: influence of confinement and horizontal reinforcement," in *10th North Amer. Mason. Conf.*, St. Louis, United States, 2007, pp. 838–848.
- [29] A. Schultz and R. Hutchinson, "*Seismic Behavior of Partially-Grouted Masonry Shear Walls, Phase 2: Effectiveness of Bed-Joint Reinforcement, Report No. NIST GCR 01-808*," Gaithersburg, United States: National Institute of Standards and Technology, 2001.
- [30] A. Schultz, R. Hutchinson, and G. Cheok, "Seismic performance of masonry walls with bed joint reinforcement," in *Structural Engineers World Congr.*, San Francisco, United States, 1998, p. T119-4.
- [31] M. Bolhassani, A. Hamid, and F. Moon, "Enhancement of lateral in-plane capacity of partially grouted concrete masonry shear walls," *Eng. Struct.*, vol. 108, pp. 59–76, Feb. 2016.

- [32] M. Tomažević, M. Lutman, and L. Petković, “Seismic behavior of masonry walls: experimental simulation,” *J. Struct. Eng.*, vol. 122, no. 9, pp. 1040–1047, Sep. 1996.
- [33] R. Meli, “Behaviour of masonry walls under lateral loads,” in *5th World Conf. Earthq. Eng.*, Rome, Italy, 1973, pp. 853–862.
- [34] K. A. Medeiros, R. A. Palhares, G. A. Parsekian, N. G. Shrive, and F. S. Fonseca, “In-plane behavior and seismic performance of differently detailed, multi-story, perforated, partially grouted masonry walls,” *Eng. Struct.*, vol. 271, p. 114941, Nov. 2016.
- [35] Y. Zhuge and J. Mills, “On behaviour of partially reinforced masonry under simulated earthquake load,” in *12th Int. Brick Block Mason. Conf.*, Madrid, Spain, 1992, pp. 1985–1992.
- [36] Canadian Standards Association, *Design of Masonry Structures, CSA S304-14*, 2015.
- [37] Australian Standard, *Masonry Structures, AS 3700:2018*, 2018.
- [38] A. Oan and N. Shrive, “Effect of steel reinforcement on shear strength of concrete masonry walls,” in *8th Int. Mason. Conf.*, Dresden, Germany, 2010, pp. 1–10.
- [39] A. Hendry and B. Sinha, “*Shear Tests on Full-Scale Single-Storey Brickwork Structures Subjected to Precompression*,” Stoke-on-Trent, United Kingdom: The British Ceramic Research Association, 1971.
- [40] A. Hamedzadeh, “*On the Shear Strength of Partially Grouted Concrete Masonry*,” Calgary, Canada: University of Calgary, 2013.
- [41] H. Pan, A. Isfeld, and N. Shrive, “Modelling of shear tests with different boundary conditions,” in *13th Can. Mason. Symp.*, Halifax, Canada, 2017, pp. 1–11.
- [42] H. Pan, “*Modelling In-plane Shear in Partially Reinforced Concrete Masonry*,” Calgary, Canada: University of Calgary, 2018.
- [43] R. Hassanli, M. ElGawady, and J. Mills, “An evaluation of design code expressions for estimating in-plane shear strength of partially grouted masonry walls,” *Aust. J. Struct. Eng.*, vol. 15, no. 3, pp. 299–320, Nov. 2014.
- [44] J. Zhu, J. Shrestha, G. Iskander, and N. G. Shrive, “Towards determining the in-plane shear strength of masonry,” in *14th Can. Mason. Symp.*, Montreal, Quebec, 2021.
- [45] M. R. Kaloop et al., “Shear strength estimation of reinforced concrete deep beams using a novel hybrid metaheuristic optimized SVR models,” *Sustainability*, vol. 14, no. 9, p. 5238, Mar. 2022.
- [46] S. Brzev and D. Anderson, “Seismic design of masonry walls to CSA S304-14,” in *Seismic Design Guide for Masonry Buildings*. Waterdown, Canada: Canadian Concrete Masonry Producers Association, 2018, pp. 2-2-2-104.
- [47] C. Allen, M. Masia, A. Page, M. Griffith, H. Derakhshan, and N. Mojsilovic, “Experimental testing of unreinforced masonry walls with openings subject to cyclic in-plane shear,” in *16th Int. Brick Block Mason. Conf.*, Padova, Italy, 2016, pp. 1–8.
- [48] K. Voon and J. Ingham, “Experimental in-plane strength investigation of reinforced concrete masonry walls with openings,” *J. Struct. Eng.*, vol. 134, no. 5, pp. 758–768, May. 2008.
- [49] S. Calderón, C. Sandoval, and O. Arnau, “Shear response of partially-grouted reinforced masonry walls with a central opening: testing and detailed micro-modelling,” *Mater. Des.*, vol. 118, pp. 122–137, Mar. 2017.
- [50] F. Yáñez, M. Astroza, A. Holmberg, and O. Ogaz, “Behavior of confined masonry shear walls with large openings,” in *13th World Conf. Earthq. Eng.*, Vancouver, Canada, 2004, p. 3438.
- [51] E. Ortega-G, J. Jiménez-Pacheco, J. Quinde, and H. García, “Macroelement model for nonlinear static pushover analysis of confined,” in *Brick and Block Masonry - from Historical to Sustainable Masonry*, J. Kubica, A. Kwiecień, and Ł. Bednarz, Eds., London, United Kingdom: CRC Press, 2020, pp. 924–932.
- [52] T. Janaraj and M. Dhanasekar, “Effectiveness of two forms of grouted reinforced confinement methods to hollow concrete masonry panels,” *J. Mater. Civil Eng.*, vol. 27, no. 12, p. 04015038, Dec. 2015.
- [53] H. Pan, A. Isfeld, and N. Shrive, “The failure of partially grouted masonry walls subject to in-plane shear is affected by the stiffness of the grouted “frame,”” in *13th North Amer. Mason. Conf.*, Salt Lake City, United States, 2019.
- [54] S. H. Basha and H. B. Kaushik, “Investigation on improving the shear behavior of columns in masonry infilled RC frames under lateral loads,” *Bull. Earthq. Eng.*, vol. 17, no. 7, pp. 3995–4026, Apr. 2019.
- [55] L. Long, A. A. Hamid, and R. G. Drysdale, “Small-scale modelling of concrete masonry using half-scale units: a preliminary study,” in *10th Can. Mason. Symp.*, Banff, Canada, 2005, pp. 1–10.
- [56] V. Singhal and D. C. Rai, “Suitability of half-scale burnt clay bricks for shake table tests on masonry walls,” *J. Mater. Civ. Eng.*, vol. 26, no. 4, pp. 644–657, Apr. 2014.
- [57] N. Sathiparan, W. Anjalee, and K. Kandage, “The scale effect on small-scale modelling of cement block masonry,” *Mater. Struct.*, vol. 49, pp. 2935–2946, Aug. 2016.
- [58] C. Knox, D. Dizhur, and J. Ingham, “Experimental study on scale effects in clay brick masonry prisms and wall panels investigating compression and shear related properties,” *Constr. Build. Mater.*, vol. 163, pp. 706–713, Feb. 2018.
- [59] S. M. Moayedian and M. Hejazi, “Stress-strain relationships for scaled gypsum mortar and cement mortar brick masonry,” *J. Build. Eng.*, vol. 33, pp. 101861, Jan. 2021.

- [60] P. Lourenço, "Simulations of size effect in masonry structures," in *Int. Assoc. Fracture Mechanics for Concrete and Concrete Struct.*, Gifu, Japan, 1998, pp. 2001–2010.
- [61] Applied Technology Council, *Quantification of Building Seismic Performance Factors*, FEMA P695, 2009.
- [62] American Society of Civil Engineers, *Minimum Design Loads for Buildings and Other Structures*, 2010.
- [63] M. Bolhassani, A. Hamid, C. Johnson, and F. Moon, "Shear strength expression for partially grouted masonry walls," *Eng. Struct.*, vol. 127, pp. 475–494, Nov. 2016.
- [64] Masonry Standards Joint Committee, *Building Code Requirements and Specification for Masonry Structures (TMS 402-13/ACI 530-13/ASCE 5-13)*, 2013.
- [65] M. Masia, G. Simundic, and A. Page, "Assessment of the AS3700 relationship between shear bond strength and flexural tensile bond strength in unreinforced masonry," in *15th Int. Brick Block Mason. Conf.*, Florianópolis, Brazil, 2012, pp. 1–10.
- [66] Associação Brasileira de Normas Técnicas, *Alvenaria Estrutural – Parte 1: Projeto*, NBR 16868-1, 2020.
- [67] Ministry of Housing and Urban-Rural Development of the People's Republic of China, *Code for Design of Masonry Structures (GB50003-2011)*, 2011.
- [68] European Committee for Standardization, *Eurocode 6 - Design of Masonry Structures (EN 1996-1-1: 2005)*, 2005.
- [69] European Committee for Standardization, *Methods of Test for Masonry - Part 3: Determination of Initial Shear Strength, EN 1052-3:2002*, 2002.
- [70] K. Voon and J. Ingham, "Design expression for the in-plane shear strength of reinforced concrete masonry," *J. Struct. Eng.*, vol. 133, no. 5, pp. 706–713, May. 2007.
- [71] M. Priestley, R. Verma, and X. Yan, "Seismic shear strength of reinforced concrete columns," *J. Struct. Eng.*, vol. 120, no. 8, pp. 2310–2329, Aug. 1994.
- [72] A. F. Oan and N. G. Shrive, "A simple design model for the diagonal shear of partially grouted concrete masonry panels," in *9th Int. Mason. Conf.*, Guimarães, Portugal, 2014, pp. 1–11.
- [73] P. Dillon and F. Fonseca, "Resistance analysis of partially grouted shear walls," in *12th North Amer. Mason. Conf.*, Denver, United States, 2015.
- [74] L. K. Nuss, J. Noland, and J. Chinn, "The parameters influencing shear strength between clay masonry units and mortar," in *North Amer. Mason. Conf.*, Boulder, United States, 1978, pp. 13-1–13-27.
- [75] S. Barattucci et al., "Shear response and failure mode of masonry triplets subjected to monotonic and cyclic loading," in *Brick and Block Masonry - from Historical to Sustainable Masonry*, J. Kubica, A. Kwiecień, and Ł. Bednarz, Eds., London, United Kingdom: CRC Press, 2020, pp. 813–818.
- [76] M. Ramesh, C. Briceno, M. Azenha, and P. Lourenço, "Impact of type of mortar on shear bond strength of brick masonry," in *Brick and Block Masonry - from Historical to Sustainable Masonry*, J. Kubica, A. Kwiecień, and Ł. Bednarz, Eds., London, United Kingdom: CRC Press, 2020, pp. 591–595.
- [77] P. J. B. B. Lourenço, J. Barros, and J. Oliveira, "Shear testing of stack bonded masonry," *Constr. Build. Mater.*, vol. 18, pp. 125–132, Mar. 2004.
- [78] A. A. Hamid, R. G. Drysdale, and A. C. Heidebrecht, "Effect of grouting on the strength characteristics of concrete block masonry," in *North Amer. Mason. Conf.*, Boulder, United States, 1978, pp. 591–595.
- [79] X. Yang, H. Wu, J. Zhang, and H. Wang, "Shear behavior of hollow concrete block masonry with precast concrete anti-shear blocks," *Adv. Mater. Sci. Eng.*, vol. 2019, p. 9657617, Apr. 2019.
- [80] American Society for Testing and Materials, *Standard Test Method for Splitting Tensile Strength of Masonry Units, ASTM C1006/C1006M-20a*, 2020.
- [81] A. Incerti, A. R. Tilocca, F. Ferretti, and C. Mazzotti, "Influence of masonry texture on the shear strength of FRCM strengthened masonry panels," in *11th Int. Conf. Structural Anal. Historical Constructions*, Cusco, Peru, 2018, pp. 1623–1631.
- [82] M. Nollet, L. Guizani, A. E. Ezz, J. Touraille, E. Boldireff, and P. Moretti, "Experimental evaluation of the mechanical parameters for seismic assessment of traditional brick and stone masonry buildings in eastern Canada," in *CSCE Annu. Conf.*, Montreal, Canada, 2019, pp. GEN170-1–GEN170-10.
- [83] M. N. AlWad, "Modification of the Brazilian indirect tensile strength formula for better estimation of the tensile strength of rocks and rock-like geomaterials," *J. King Saud Univ.-Eng. Sci.*, vol. 34, no. 2, pp. 147–154, Feb. 2022.
- [84] P. J. B. B. Lourenço, "Computational Strategies for Masonry Structures," Porto, Portugal: Universidade do Porto, 1996.
- [85] L. Bejarano-Urrego, E. Verstrynge, G. Giardina, and K. Van Balen, "Crack growth in masonry: numerical analysis and sensitivity study for discrete and smeared crack modelling," *Eng. Struct.*, vol. 165, pp. 471–485, Jun. 2018.

Author contributions: JZ: conceptualization, writing; NS: conceptualization, writing, supervision.

Editors: Leandro Trautwein, Mauro Real, Mario Pimentel.



REVIEW PAPER

Shear and punching shear according to the Critical Shear Crack Theory: background, recent developments and integration in codes

Corte e punçamento de elementos de betão armado de acordo com a Teoria da Fissura de Corte Crítica: enquadramento histórico, desenvolvimentos recentes e integração em normas

Aurelio Muttoni^a João Tiago Simões^a ^aEcole Polytechnique Fédérale de Lausanne, Lausanne, Switzerland

Received 24 February 2023

Accepted 24 March 2023

Abstract: The Critical Shear Crack Theory (CSCT) has been developed since 1985 to assess the shear resistance of members without shear reinforcement and the punching shear resistance of reinforced concrete slabs in a rational manner. The main idea of the CSCT is that the shear resistance is governed by the development of a critical shear crack, its geometry and its kinematics. Recent shear tests with detailed measurements have confirmed that the shear force can be carried through the critical shear crack by a combination of aggregate interlocking, residual tensile strength of concrete, dowel action of the longitudinal reinforcement, inclination of the compression zone and activation of the shear reinforcement crossed by the critical shear crack if present. On the basis of advanced constitutive laws, all these contributions can be calculated as a function of the crack geometry and its kinematic. Simplifications of the resulting general formulations have been implemented in several standards including the *fib* Model Code 2010 and, in its recent closed-form format, in the second generation of the European Standard for Concrete Structures. The generality of the models allows accounting for several materials and cases, as for instance the presence of axial forces, fiber reinforced concrete, non-metallic reinforcements and designing strengthening using several techniques. This document presents the historical framework of the development of the theory, followed by a short presentation of its most up-to-date refined models. The derivation of closed-form solutions based on the CSCT and how it leads to expressions in a format similar to the current European Standard for Concrete Structures is also discussed. Eventually, for the case of punching, some recent developments are shown in what refers to the capability of the refined mechanical model to capture the relationship between the acting punching load, the rotation and the shear deformation during loading and at failure.

Keywords: shear, punching shear, mechanical model, codes, levels-of-approximation.

Resumo: A Teoria da Fissura de Corte Crítica (CSCT, referindo-se à sua definição Critical Shear Crack Theory na Língua Inglesa) tem sido desenvolvida desde 1985 para avaliar a resistência ao corte de elementos de betão armado sem armadura de esforço transversal assim como a resistência ao punçamento de lajes e fundações de betão armado. A principal ideia desta teoria é a de que a resistência é condicionada pelo desenvolvimento de uma fissura de corte crítica, nomeadamente pela sua geometria e cinemática. Ensaios experimentais realizados recentemente demonstram que o esforço transversal pode ser transmitido através da fissura de corte crítica devido à soma de várias contribuições, nomeadamente: engrenamento dos agregados, resistência à tração residual do betão, efeito de ferrolho das armaduras longitudinais, contribuição da zona comprimida e activação da armadura de esforço transversal atravessada pela fissura crítica (nos casos em que esta exista). Todas estas contribuições podem ser devidamente quantificadas em função da geometria e cinemática da fissura de corte crítica, usando para o efeito relações constitutivas adequadas. Versões simplificadas das formulações mais refinadas e gerais dos modelos mecânicos da CSCT foram introduzidas em diversos documentos normativos, tais como o Código Modelo 2010 da *fib* ou, mais recentemente, a segunda geração da Norma Europeia para Estruturas de Betão Armado. A generalidade dos modelos da teoria permite utilizá-los para outros casos particulares, tais como seja a presença de esforço normal, o caso de elementos de betão com fibras, armaduras não metálicas ou o dimensionamento de soluções de reforço estrutural. Este documento apresenta um enquadramento histórico do desenvolvimento da teoria, seguido de uma apresentação muito sucinta dos seus modelos refinados mais atuais.

Corresponding author: Aurelio Muttoni. E-mail: aurelio.muttoni@epfl.ch

Financial support: None.

Conflict of interest: Nothing to declare.

Data Availability: data-sharing is not applicable to this article as no new data were created or analyzed in this study.



This is an Open Access article distributed under the terms of the Creative Commons Attribution License, which permits unrestricted use, distribution, and reproduction in any medium, provided the original work is properly cited.

É ainda discutida a derivação de expressões de forma fechada baseada na CSCT, o que conduz a expressões com um formato idêntico às que constam no atual Eurocódigo 2. Finalmente, para o caso de punçoamento, alguns dos desenvolvimentos mais recentes da teoria são apresentados, nomeadamente no que se refere à capacidade do modelo refinado de relacionar a carga, a rotação e a deformação por corte, não somente na rotura mas também durante o carregamento.

Palavras-chave: corte, punçoamento, modelo mecânico, normas, níveis de aproximação.

How to cite: A. Muttoni and J. T. Simões, “Shear and punching shear according to the Critical Shear Crack Theory: background, recent developments and integration in codes,” *Rev. IBRACON Estrut. Mater.*, vol. 16, no. 3, e16302, 2023, <https://doi.org/10.1590/S1983-41952023000300002>

1 INTRODUCTION

The need for a safe and sound design against brittle failures is a well-established design principle to ensure robust structures. Shear or punching shear are among the most known sources of brittle failures in reinforced concrete structures. In concrete slabs, a major difference between shear and punching is the principal shear force direction with respect to the support [1]. In “one-way shear” (as for instance in the slab supported on two walls with a distributed load as shown in Figure 1b), the shear principal directions are parallel between them and normally perpendicular to the linear supports. In punching shear, or “two-way shear”, the shear principal directions predominantly converge to the support (or propagate from a concentrated load) in a radial manner (see red shear trajectories in Figure 1a). The shear resistance can be the governing design criterion in linear members with shear reinforcement or in planar members without shear reinforcement where linear supports are provided, such as slabs with significant distributed loads (Figure 1b), slabs with discontinuities, shells, retaining walls or slabs with concentrated loads in the vicinity of linear supports (Figure 1c). Punching shear is the common governing design criterion in flat slabs near to columns, wall ends and wall corners, or when concentrated loads are applied to planar members, such as slabs, shells and column bases.

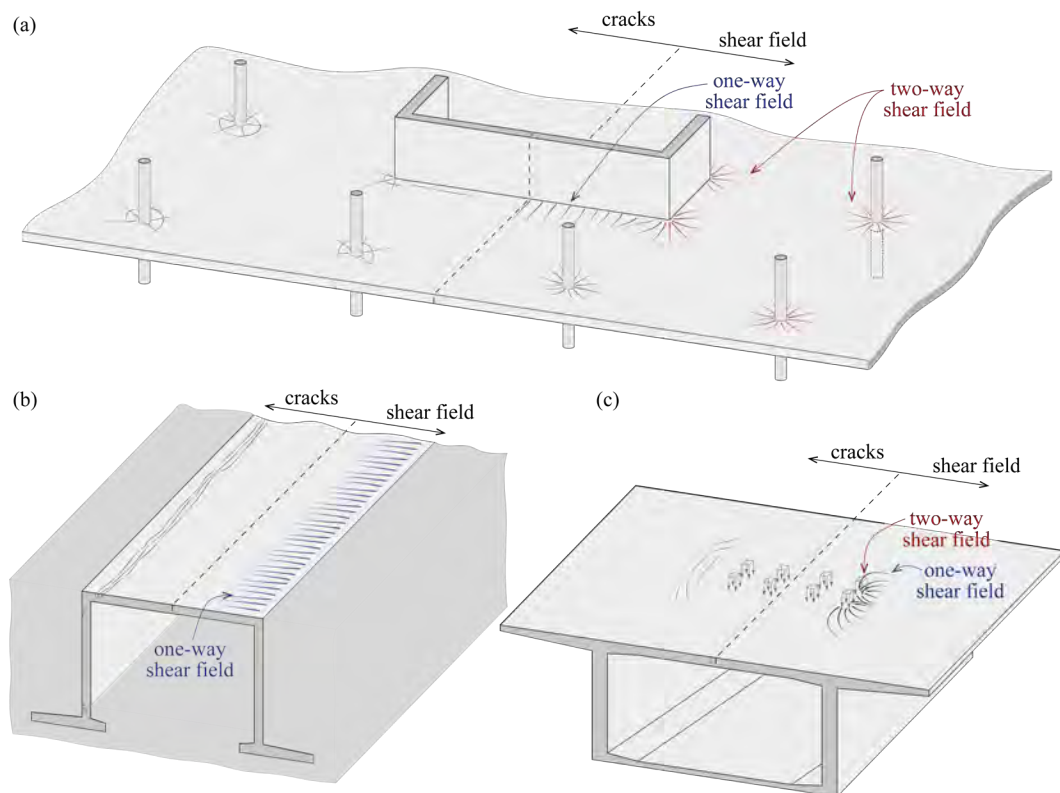


Figure 1. Examples of structural reinforced concrete members where shear or punching shear can be the governing design criterion.

Whitin the group of reinforced concrete members potentially failing in shear, a difference has to be made between members with shear reinforcement (such as beams, columns or transition walls) and members without shear reinforcement (typically slabs, shells and retaining walls). In the former case, if more than minimum shear

reinforcement is provided, the shear failure will occur by yielding of the shear reinforcement or/and crushing of concrete carrying the inclined compression field, thus being associated with a given deformation capacity (distributed cracking, see for instance [2]). On the contrary, shear failures in members without shear reinforcement take place by strain localization along a critical shear crack associated with a very limited deformation capacity [1], [3]. This fundamental difference has led to the development of different design methods for each one of the cases.

For members with shear reinforcement, two different models have been proposed and implemented in standards: (1) the so called “variable truss angle model” based on [2], [4] (implemented for instance in the European Standard for Structural Concrete 5,6); which is in fact a compression field model where the concrete tensile strength is neglected) and (2) the approaches where the compression field contribution is combined with the contributions which can be observed in members without shear reinforcement [5] (implemented for instance in North American Standards [6]).

For members without shear reinforcement, the behavior and the failure mechanism are complex so that the design has been historically based on methods with a strong empirical basis (see for instance [7], [8] for shear in one-way members and [9]–[12] for punching shear). Mechanical considerations and mechanical models have also been proposed in the last century (see for instance [3], [13]–[19] for shear in one-way members and [20]–[23] for punching shear). Some of them were strain-based [3], [18], [20], [22], allowing to explicitly calculate the shear resistance on the basis of the deformations in the localization zone. Nevertheless, until 1993 [24], the size effect was considered in standards only on an empirical basis and mechanically based strain-based models have been implemented for the first time in a standard only in 2003 [25].

It was in this context that the Critical Shear Crack Theory (CSCT) has been proposed some decades ago to account for strain and size effect in a rational manner and allowing to implement for the first time these effects in standards [24], [25]. Since then, the theory has evolved, being nowadays well consolidated for both research and design purposes.

This keynote article presents an overview of the CSCT, starting with the background including an historical overview followed by the recent developments. It discusses not only the advances on the level of the theoretical model (with the development of refined mechanical formulations), but also its implementation in codes of practice.

2 HISTORICAL BACKGROUNDS OF THE CRITICAL SHEAR CRACK THEORY

2.1 Main ideas

The CSCT has been developed since 1985 to assess the shear resistance of members without shear reinforcement and the punching shear resistance of reinforced concrete slabs in a rational manner. The research started with a design proposal for punching [26] and an experimental work on concrete beams without shear reinforcement which has shown that the shear resistance is typically governed by the development of a Critical Shear Crack (CSC) and its kinematics [27], [28]. The CSCs typically develop starting from the tensile zone as flexural cracks, slightly inclined in presence of a shear force. For low load levels, the crack opens mainly in mode I (Figure 2) due to the elongation of the flexural reinforcement. For higher load levels, the crack becomes flatter, the center of rotation follows the tip of the crack so that the crack opens in combined mode I-II with an increasing sliding component (Figure 2).

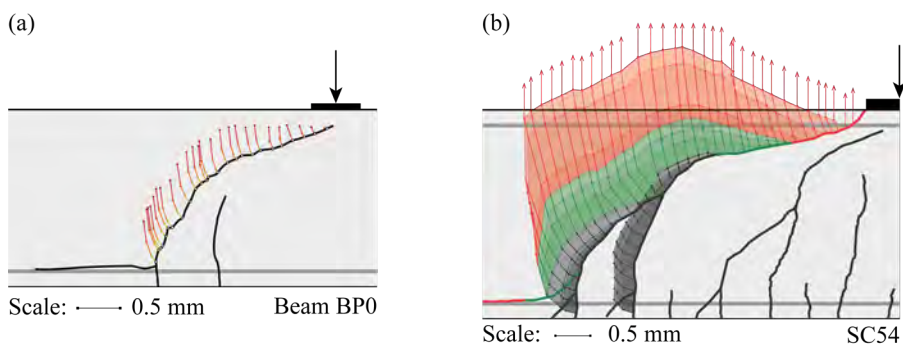


Figure 2. Research on the development of the critical shear crack and associated kinematics: (a) original measurements [27], [28] and (b) recent measurements with refined techniques [29].

The original cardboard model shown in Figures 3a has been prepared at the beginnings of the CSCT to explain the failure process in an intuitive manner: the shear resistance is reached when the opening of the CSC due to bending (Figure 3a1) reduces the capacity to carry shear stresses through the crack by aggregate interlocking. The CSC can thus

almost freely develop in the compression zone (only the activation of the dowel action in the flexural reinforcement and the residual tensile strength in the sub-horizontal branch of the CSC oppose to its development) leading finally to the shear failure (Figure 3a2).

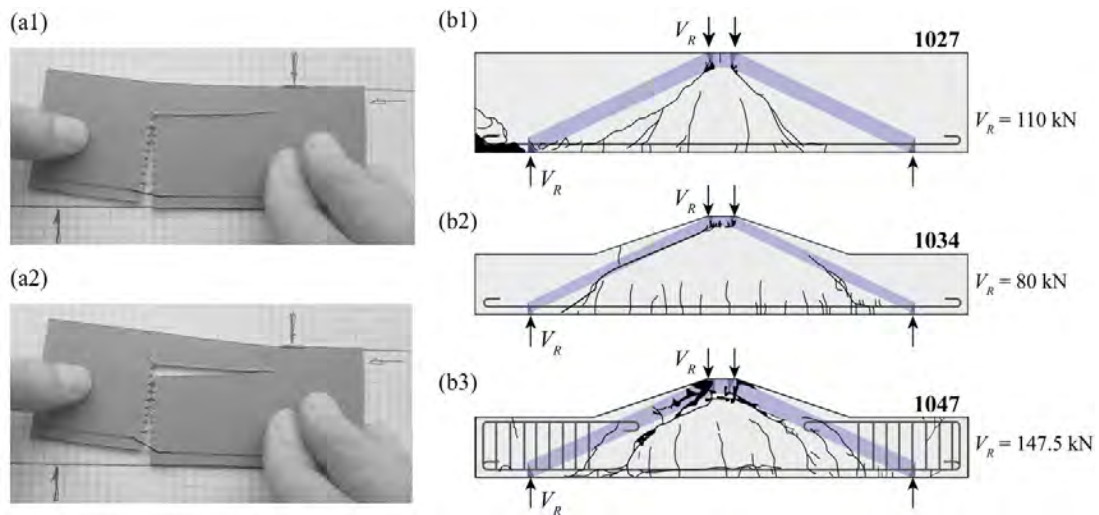


Figure 3. First conceptual ideas and experimental evidence grounding the CSC for shear in beams and slabs without shear reinforcement: (a) original cardboard model from 1985 with (a1) flexural crack in Mode I and (a2) flexural crack in combined mode I-II; (b) figure from reference [28] presenting the experimental results by Mörsch [30], whose interpretation supports the idea that the location and shape of the CSC influences the failure load (theoretical direct struts carrying shear shown in blue).

In addition, a systematic interpretation of test results described in the literature has also shown that the location of the CSC with respect to loads and supports can have a significant influence on the shear resistance. This is mainly due to the fact that if the CSC is not located in a region where a direct strut can develop between load and support, a significant shear force can be carried without activating the aggregate interlocking across the CSC. This is shown for instance in Figure 3b from [28]: in the case of Figure 3b1, the crack developed without interaction with the theoretical direct strut due to poor bond conditions (plain bars were used) and the beam failed eventually due to insufficient anchorage at the support; in the tapered beam of Figure 3b2, the CSC developed in a unfavorable manner reducing significantly the capacity of the direct strut, leading to a strength reduction of 27% compared to previous case; on the contrary, in a very similar beam shown in Figure 3b3, the top reinforcement of the beam ends was sufficiently long to reach the theoretical strut, thus controlling the opening of the CSC, and eventually allowing for an increased shear resistance (134%). This matter of fact explains the significant influence of the load location with respect to the support (loads applied at a distance $< 3d$ from the support) on the shear resistance [13], [14], [28], [31]–[33] and the scatter of the experimental results which can be observed in members without shear reinforcement (as a small deviation of the shape and position of the CSC can have a significant influence on the shear resistance).

2.2 Development of the mechanical model for punching shear and applications

The considerations presented above have been implemented in a mechanical model to calculate the punching shear resistance of slabs without shear reinforcement with the initial aim of quantifying the size effect in a rationally sound manner for the revision of the Swiss Code for concrete structures SIA 162 of 1993 [24]. The main ideas at that time were (see reference [32]):

- The opening in Mode I of the CSC which develops near to the column with an inclination of about 45° is proportional to the product $\psi \cdot d$, where d is the effective depth of the slab and ψ is the slab rotation outside the slab-column connection (see blue arrows in Figure 4a);
- The rotation ψ can be calculated as a function of the acting load (and thus of the shear force) assuming an elastic-plastic flexural behavior of the slab as proposed by Kinnunen and Nylander [20];

- The shear stresses which are activated in the CSC due to crack sliding (combined Mode I-II) can be estimated for the adopted kinematics with the model by Walraven [35]. Their integration provides the shear resistance which is a function of the crack opening (Mode I, and therefore of the product $\psi \cdot d$) leading to the so-called failure criterion.

The failure criterion has been calibrated on the basis of the experimental results available in the literature at that time (Figure 4b) allowing to calculate the punching shear resistance in a reliable manner on the basis of the main parameters. Figure 4c, presented in reference [32] in 1991, depicts for instance the normalized punching shear resistance as a function of the effective depth, showing clearly the size effect which depends also on the flexural reinforcement ratio (with higher detrimental size effects for slabs with higher flexural reinforcement ratios and brittle behavior). With this mechanical model, it was possible to design also tailored solutions as for instance the punching shear resistance in presence of steel shear heads where the contribution of the embedded steel structure and its influence on the deformation could be considered in a rational manner [36].

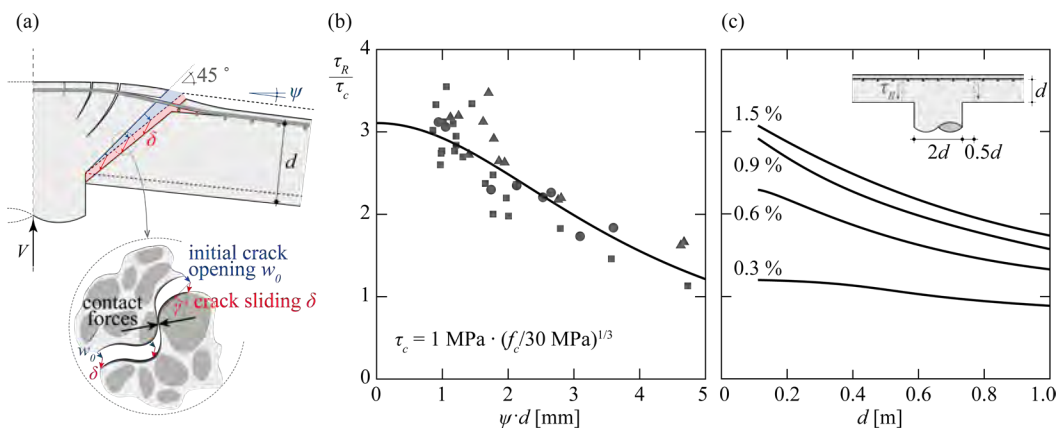


Figure 4. CSCT for punching shear between 1985 to 1991, with: (a) assumptions on the shape and kinematics of the CSC to calculate the interlocking stresses between crack lips (opening in Mode I due to flexure shown in blue, combined Mode I-II due to shear shown in red); (b) adoption of an analytical failure criterion calibrated on the basis of experimental results; (c) calculated normalized punching resistance with the proposed model for different flexural reinforcement ratios as a function of the effective depth (figures (a) adapted from [34], (b) and (c) adapted from [32]).

Since 2000, the principles of the CSCT for punching shear have been improved and applied to several situations and cases:

- Improvement of the load-rotation relationship accounting for tension stiffening and for the uncracked zones; improvement of the failure criterion accounting for the aggregate size in a physical sound manner [37]–[39];
- Experimental validation for different slabs thicknesses, columns sizes and flexural reinforcements ratios [40]–[43];
- Punching of slabs with shear reinforcement [44]–[49];
- Extension of the CSCT to steel fiber reinforced concrete [50];
- Investigation of retrofitting methods with post-installed shear reinforcement [51], [52], using externally bonded fiber reinforced polymers [53] or other techniques [54];
- Investigation of edge and corner connections, internal slab-column connections with non-symmetric reinforcement or rectangular columns [55]–[57];
- Experimental validation for different aggregate sizes, improvement of the analytical definition of the failure criterion, investigation of the effect of significant axial forces in the columns in case of multi-story buildings [58], [59];
- Experimental and theoretical investigation of post-tensioned slabs and slabs with axial forces [60]–[62];
- Internal slab-column connections with unbalanced moments, deformation capacity of flat slabs with imposed horizontal displacements, monotonic and cyclic loading [63]–[66];
- General considerations on the size effect [67];
- Experimental and theoretical investigation of foundation rafts and column bases [68]–[70];
- Experimental and theoretical investigation of the residual load-carrying capacity after punching and on the efficiency of integrity reinforcement to prevent progressive collapse [71];
- Investigation of the influence of compressive membrane actions in flat slabs and redistribution between hogging and sagging moments in continuous slabs [72], [73];

- Verification of actual slabs combining the failure criterion of the CSCT with the rotation calculated on the basis of NLFEA [74]–[81];
- Punching of slabs in case of impact loading [82], [83];
- Detailed measurements to better assess the failure process [84];
- Improvement of the mechanical model to better account for the actual failure mechanism [70], [85], see also subsection 3.2.2 below;
- Development of closed-form solutions to be implemented in standards following current Eurocode 2 format [86]–[88], see also subsection 3.2.3 below;
- Investigation of internal slab-column connections with openings [89];
- Investigation of the serviceability limit state of flat slabs on the basis of the CSCT [90];
- Investigation of the influence of corroded reinforcement on the punching shear resistance and deformation capacity of flat slabs [91];
- Investigation of lightweight aggregate concrete flat slabs with ultra-high fiber reinforced concrete in the compression zone [92].

2.3 Development of the mechanical model for shear in one-way members and applications

With respect to the shear resistance of one-way members without shear reinforcement, the opening of the CSC can be assumed to be proportional to the product of the longitudinal strain and the effective depth (further details will be given in subsection 3.1 below). Since the reinforcement is usually in the elastic range, the governing longitudinal strain can be easily calculated with a sectional analysis. The mechanical model has been presented in 2003 [37], [93] (see [33] for an English translation) and implemented in the Swiss code for concrete structures SIA 262:2003 [25]. Also in this case, based on a failure criterion calibrated on experimental results (Figure 5a), it was possible to calculate the shear resistance on the basis of the main geometrical and mechanical parameters. Figure 5b shows for instance the size effect on the shear resistance. It is interesting to note that, since the normalized shear resistance becomes smaller for deeper members, also the longitudinal reinforced required for bending becomes smaller. This means that for a member designed both for shear and bending, the combined size and strain effect (descending failure criterion in Figure 5a) leads to a more pronounced reduction of the shear resistance for deeper members (see the steeper curve in Figure 5b, see also [94] for further details).

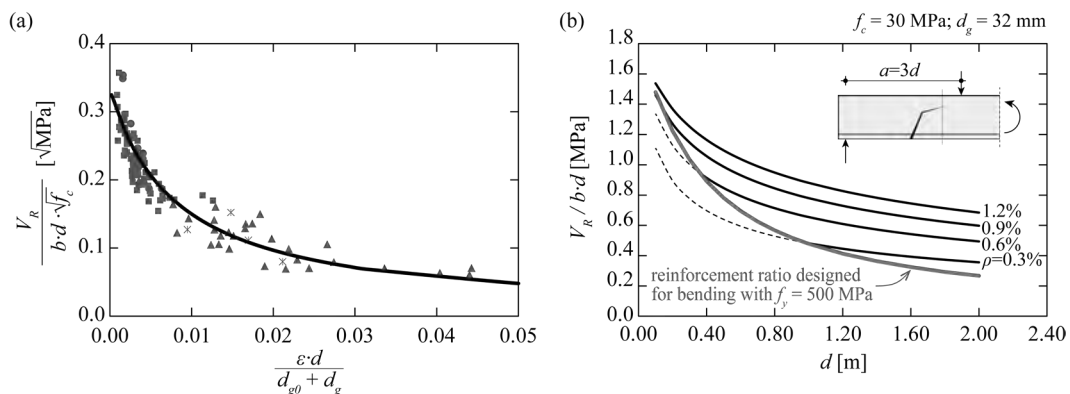


Figure 5. Critical shear crack theory for shear in one-way members between 2000 to 2003, with: (a) adoption of an analytical failure criterion calibrated on the basis of experimental results (adapted from [37], [93]); (b) calculated shear resistance varying the value of the effective depth (according to [37], [93]).

It is also interesting to mention that already in its original form [33], [37], [93], the CSCT allowed to account for the presence of an axial force (which has a direct influence on the reference longitudinal strain, see also subsection 3.1.3 below), lightweight aggregate concrete (reduced aggregate interlocking) and a non-metallic reinforcement (increased longitudinal strain due to the lower elastic modulus, and therefore reduced shear resistance).

Since 2003, the principles CSCT for shear in one-way members without shear reinforcement has been improved and applied to different situations and cases:

- Reduction of the shear resistance in case of yielding of longitudinal reinforcement and calculation of rotation capacity as a function of the shear force in members without shear reinforcement [95], [96];
- Shear force distribution in slabs with concentrated loads near linear supports [97]–[99];
- Detailed analysis of shear-transfer actions in RC members based on measured cracking pattern and failure kinematics [29], [100]–[105];
- Theoretical considerations on the shear transfer actions and implications to size effects [67], [94], [102], [106];
- Influence of distributed loads [102], [103], [107], [108];
- Shear resistance of T-beams [109], tapered [107] and curved members [110];
- Detailed quantification of the shear transfer actions and improvement of the mechanical model [102], [103], [108], see also subsections 3.1.1 and 3.1.2 below;
- Development of closed-form solutions to be implemented in standards [102], [105], [106], see also subsection 3.1.3 below;
- Influence of fatigue loading on shear failures of reinforced concrete members without shear reinforcement [111], [112];
- Development of the model for fiber reinforced concrete and low amounts of shear reinforcement [103];
- Characterization of shear deformations and implications for the shear force redistribution in slabs [113].

Most of the above-mentioned references resulted directly or indirectly from researches performed at École Polytechnique Fédérale de Lausanne, Switzerland, but a large number of other works performed by different research groups have also contributed to further validate and extend the theory (some references are already presented above, without the ambition to be exhaustive).

2.4 Implementation of the CSCT in Standards

The CSCT and its ideas have been implemented in following standards:

- Swiss code for concrete structures SIA 162:1989 [114]: punching provisions including minimum flexural resistances required to limit the rotation [26];
- CEB-FIP MC1990 [115]: implementation of the minimum flexural resistances from [26] in the punching shear provisions;
- Swiss code for concrete structures SIA 162, revision 1993 [24]: implementation of the size effect according to the CSCT [32];
- Swiss code for concrete structures SIA 262:2003 [25]: full implementation of the CSCT for shear in slabs without shear reinforcement [33], [37], [93], and for punching shear [37], [39];
- *fib* Model Code 2010 [116]: implementation of the CSCT in the punching shear provisions [117] and new provision to avoid progressive collapse of flat slabs [71];
- draft for the second generation of Eurocode 2 FprEN 1992-1-1:2023 [118]:
 - closed-form expression of the CSCT for shear in one-way slabs without shear reinforcement based on the development presented in [102], [105], [106] (further details are presented in section 3.1.3 below);
 - closed-form expression of the CSCT for punching without and with shear reinforcement based on the development presented in [34], [86], [87], [88] with further improvements according to [49] (further details are presented in section 3.2.4 below);
 - strain-based approach adapted from [33], [37], [93] for a detailed assessment of the shear resistance of existing slabs (Annex for existing structures);
 - strain-based approach adapted from [37], [39], [117] for a detailed assessment of the punching shear resistance of existing slabs (Annex for existing structures);
 - provisions adapted from [71] to avoid progressive collapse of flat slab.

3 RECENT DEVELOPMENTS OF THE CRITICAL SHEAR CRACK THEORY

3.1 Shear in beams and slabs without shear reinforcement

3.1.1 Recent experimental evidence

The generalization of the use of Digital Image Correlation (DIC) to follow in detail the behavior of reinforced concrete members is allowing steps forward in the understanding of complex phenomena (e.g. [29], [119]). With respect to the shear response of beams and slabs without shear reinforcement, a number of relevant experimental evidence has been presented in recent years (see references [29], [101]–[103], [106] for further details):

- The DIC allows identifying and tracking quasi-continuously the development of the CSC, see Figure 6a. By dividing the actual CSC into a finite number of segments with its measured geometry and kinematics (Figure 6b), the relative contribution of the different shear-transfer actions can be calculated with advanced constitutive laws (Figure 6c). Such procedure applied to different load levels, different specimens with varying boundary and loading conditions, as well as geometrical and mechanical properties, allowed concluding that the sum of all shear-transfer actions contributing to carry shear across the critical section corresponds fairly well with the experimentally acting shear load (during loading and at failure), see Figure 6d for an example. If such a procedure was already possible with conventional techniques [100], DIC allows to conduct the measurement just before and after reaching the maximum load.
- The relative contribution of each shear-transfer action depends on the location and shape of the CSC. When the tip of the CSC is close to the load introduction, the contribution of the compression chord is higher than in the cases where the tip of the CSC is far from the load. In this latter case, shear is mainly carried by aggregate interlocking, residual tensile strength and dowel action.
- DIC also allows to investigate in a systematic manner the geometry of the CSC. As identified long ago by various researchers [18], the CSC for shear in beams and slabs without shear reinforcement can be simplified by a bi-linear shape with a steeper branch on the tension side and a flatter one close to the compression side.
- With respect to the kinematics of the CSC, the crack opening along the height of the CSC shows a linear profile if the crack opening of different secondary flexural crack (associated with bond) is summed in a tributary length. More details can be found in reference [102] which presents a summarized overview on recent findings [29], [101], [103], [106].

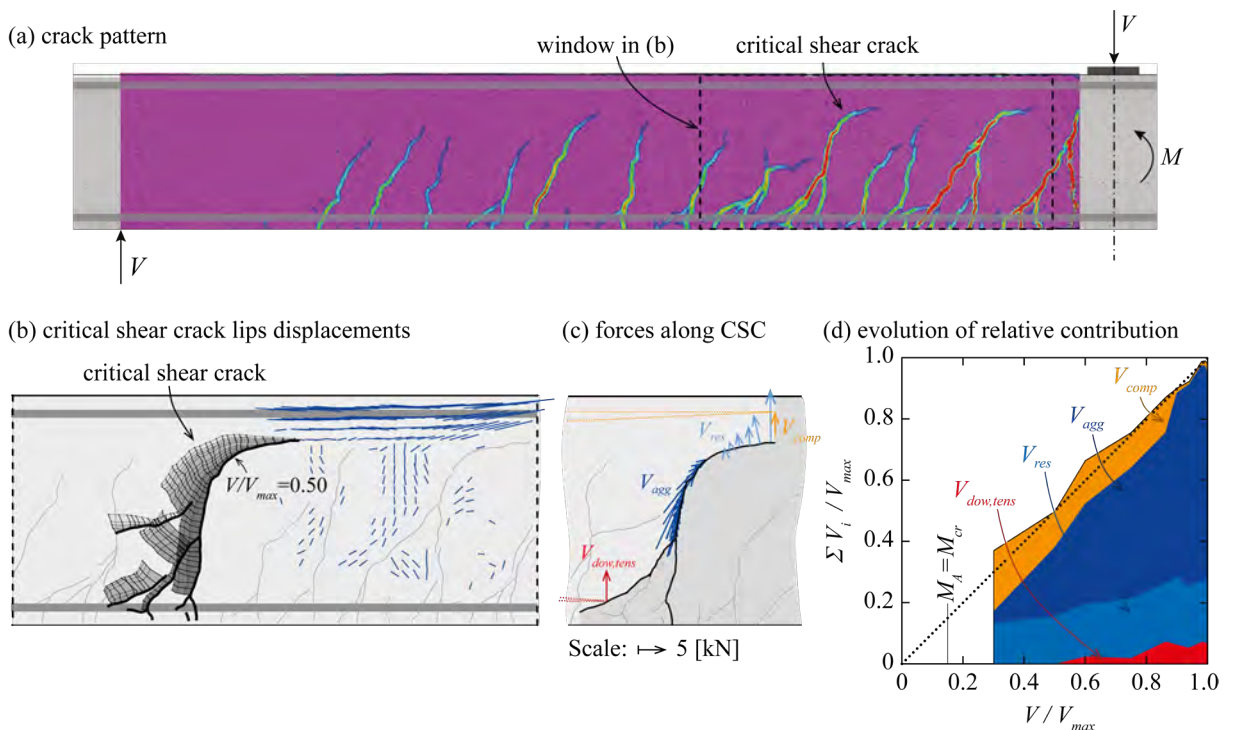


Figure 6. Application of DIC to investigate the cracking development and associated kinematics in specimen SC70 by Cavagnis et al. [101]: (a) crack pattern at V_{max} ; (b) measured crack lips displacements and compressive strains in the shear critical region at V_{max} ; (c) acting forces in the critical shear crack at V_{max} ; (d) evolution of relative contribution of each shear-transfer action during loading. Figure adapted from [102].

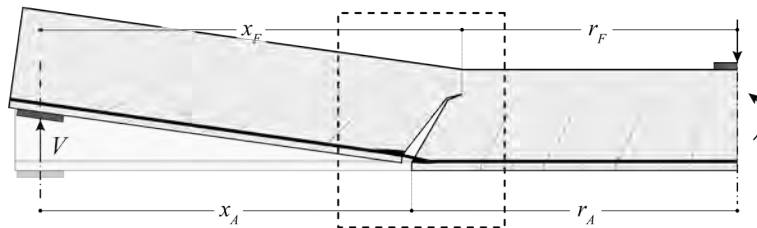
3.1.2 Refined formulation of the mechanical model

Based on the principles of the CSCT (development of flexural shear cracks reducing the shear-carrying capacity), with an assumed bi-linear shape of the CSC (as already considered by [18], see Figure 7a-7b), the crack kinematics can be derived assuming the rotation between rigid bodies (Figure 7c-7e). Using advanced constitutive laws as described

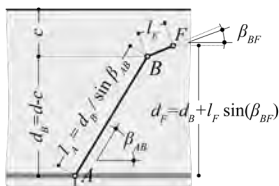
by Cavagnis et al. [102], [108], all different shear transfer actions shown in Figure 7f can be calculated: aggregate interlocking V_{agg} , residual tensile strength after cracking V_{tens} , dowel action of the longitudinal reinforcement V_{dow} and shear carried by the compression zone V_{com} . The sum of all these contributions provides the failure criterion (Figure 7g) and the shear resistance for a given cross-section can be calculated intersecting the load-deformation relationship from equilibrium and stress-strain relationship of the longitudinal reinforcement.

The shear resistance of the member can be calculated for the different sections along the length of the beam (corresponding to different load-strain relationships and shapes of the CSC), eventually allowing to search for the section that yields the minimum resistance (governing section, see Figure 7h).

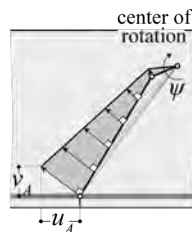
(a) Overview



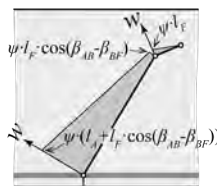
(b) CSC geometry



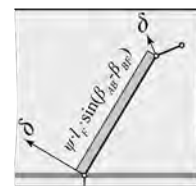
(c) CSC kinematics



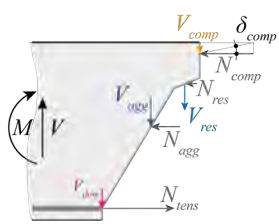
(d) crack opening



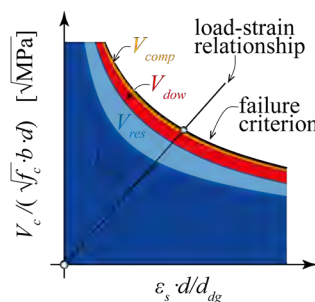
(e) crack sliding



(f) equilibrium



(g) failure load for given section



(h) determination of governing section

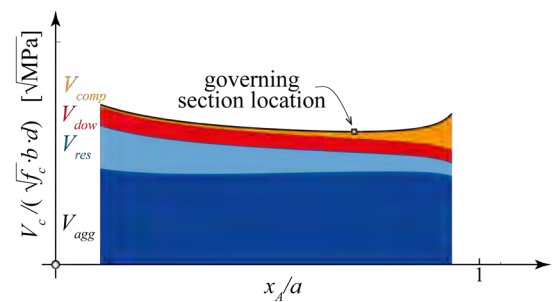


Figure 7. Mechanical model based on the development of a critical shear crack according to [102], [108].
Figure adapted from [102].

3.1.3 Closed-form expressions and Integration to codes of practice

The refinement of the mechanical model by Cavagnis et al. [102], [108] presented above can be used to establish a generalized failure criterion which describes the normalized shear resistance as a function of the normalized crack width. The latter is represented by the ratio $\epsilon_s d / d_{dg}$ (see Figure 7g), where ϵ_s is the strain of the tensile flexural reinforcement and d_{dg} is the reference value of the crack roughness $d_{dg} = 16 \text{ mm} + d_g \leq 40 \text{ mm}$, with d_g being the maximum aggregate size (to be reduced for high strength concretes [120]; value of d_{dg} with upper limit in accordance with [121]). Eventually, as a simplification for practical purposes (see Figure 8 and reference [102] for validation through a systematic parametric study), the analytical failure criterion (V_c) of Equation 1 can be assumed:

$$V_c = 0.015 \cdot k_c \cdot k_\beta \cdot \left(\frac{d_{dg}}{\varepsilon_s \cdot d}\right)^{\frac{1}{2}} \cdot \sqrt{f_c} \cdot b \cdot d \tag{1}$$

where f_c refers to the cylinder compressive concrete strength; b and d to the width and effective depth; k_c and k_β account respectively for the location and shape of the CSC (see reference [102] for details).

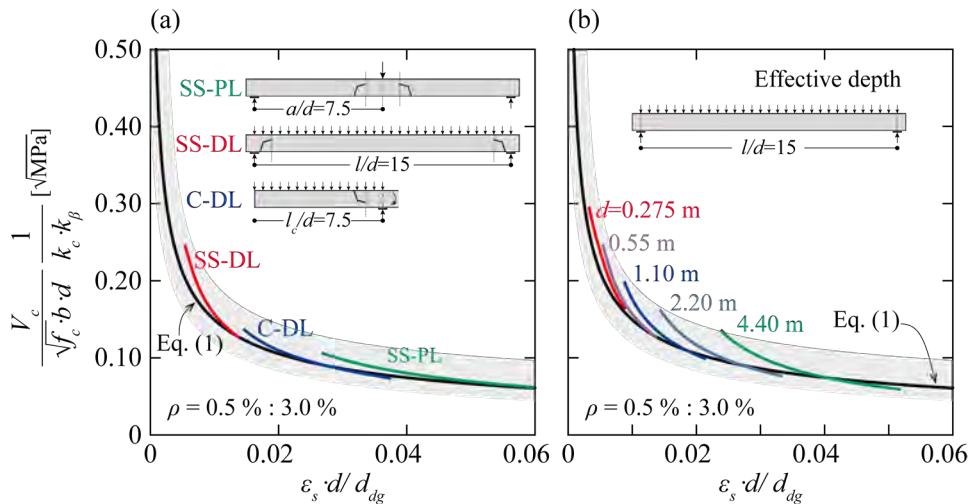


Figure 8. Failure criterion calculated with the refined formulation of the mechanical model of the CSCT obtained varying (a) ρ or (b) d and comparison with the analytical power-law failure criterion (values when not varied: $d=0.55$ m; $f_c=40$ MPa; $d_g=16$ mm). Figure adapted from [102].

Considering that the longitudinal reinforcement remains elastic, the load-deformation relationship can be easily derived from a sectional analysis with the bending moment $V_E \cdot a_{cs}$:

$$\varepsilon_s = \frac{V_E \cdot a_{cs}}{z \cdot \rho \cdot b \cdot d \cdot E_s} \tag{2}$$

where V_E is the acting shear load; a_{cs} is the moment-to-shear ratio at the control section; z is the lever arm; E_s is the modulus of elasticity and ρ is the flexural reinforcement ratio. A closed-form equation can then be obtained for the shear resistance as follows (considering $V_E=V_c=V_R$) [102]:

$$\frac{V_R}{b \cdot d} = 0.75 \cdot (k_c \cdot k_\beta)^{2/3} \cdot \left(100 \cdot \rho \cdot f_c \frac{d_{dg}}{a_{cs}}\right)^{\frac{1}{3}} \tag{3}$$

Equation 3 can be further simplified to (considering a constant value for k_c and a value for k_β as a function of a_{cs} , whose values depend on the adopted control section) [102]:

$$\frac{V_R}{b \cdot d} = 0.75 \cdot \left(100 \cdot \rho \cdot f_c \frac{d_{dg}}{\sqrt{a_{cs}}}\right)^{\frac{1}{3}} \tag{4}$$

This expression is similar to the one in current Eurocode 2 – Concrete Structures [122] (which has completely empirical origin [8]), but accounts for the strain and size effect in a rational manner. In addition, it also acknowledges the influence of the type of concrete (by means of parameter d_{dg}) and the moment-to-shear ratio a_{cs} on the shear resistance of members without shear reinforcement. As discussed above (see also references [102] and [123]), Equation 4 has been integrated in section 8 (Ultimate Limit States) of the second generation of Eurocode 2 – Concrete Structures [118], while the original format of the CSCT (intersection of load-deformation relationship and failure criterion [33], which is more general) has been integrated in Annex I dedicated to a more refined assessment of existing structures.

Since Equation 4 was analytically derived from a mechanical model, the required adaptations to deal with other effects can be easily derived on a rational manner. This is for instance the case of axial or prestressing forces, whose effects can be dealt with in a suitably and straight forward manner in the frame of the CSCT by considering them in the evaluation of the strain in the reinforcement as suggested in reference [105]. Equation 2 can thus be adapted to calculate the reinforcement strain accounting for the presence of axial or prestressing forces. For example, in the case of a centered axial force, Equation 2 becomes (see Figure 9a; see also [105], [123]):

$$\epsilon_s = \frac{v \cdot a' + N \cdot \left(z - \left(\frac{d-h}{2}\right)\right)}{z \cdot \rho \cdot b \cdot d \cdot E_s} = \frac{v}{z \cdot \rho \cdot b \cdot d \cdot E_s} \cdot \left(a' + \frac{N}{V} \cdot \left(z - d + \frac{h}{2}\right)\right) \approx \frac{v}{z \cdot \rho \cdot b \cdot d \cdot E_s} \cdot \underbrace{\left(a' + \frac{N}{V} \cdot \frac{d}{3}\right)}_{a_{cs}} \quad (5)$$

An effective shear span a_{cs} considering the effect of a centered axial force which can be used directly in Equation 4 can thus be established from an analytical (Equation 5) and a graphical manner (Figure 9) (approach valid for both compression and tension axial forces). As shown in Figure 9b, an effective shear span can also be calculated for the cases of prestressing. This approach shows that a case with an external compressive axial force acting on the compression side (Figure 9c) would not lead to an increase of the shear resistance, contradicting the provisions of current standards.

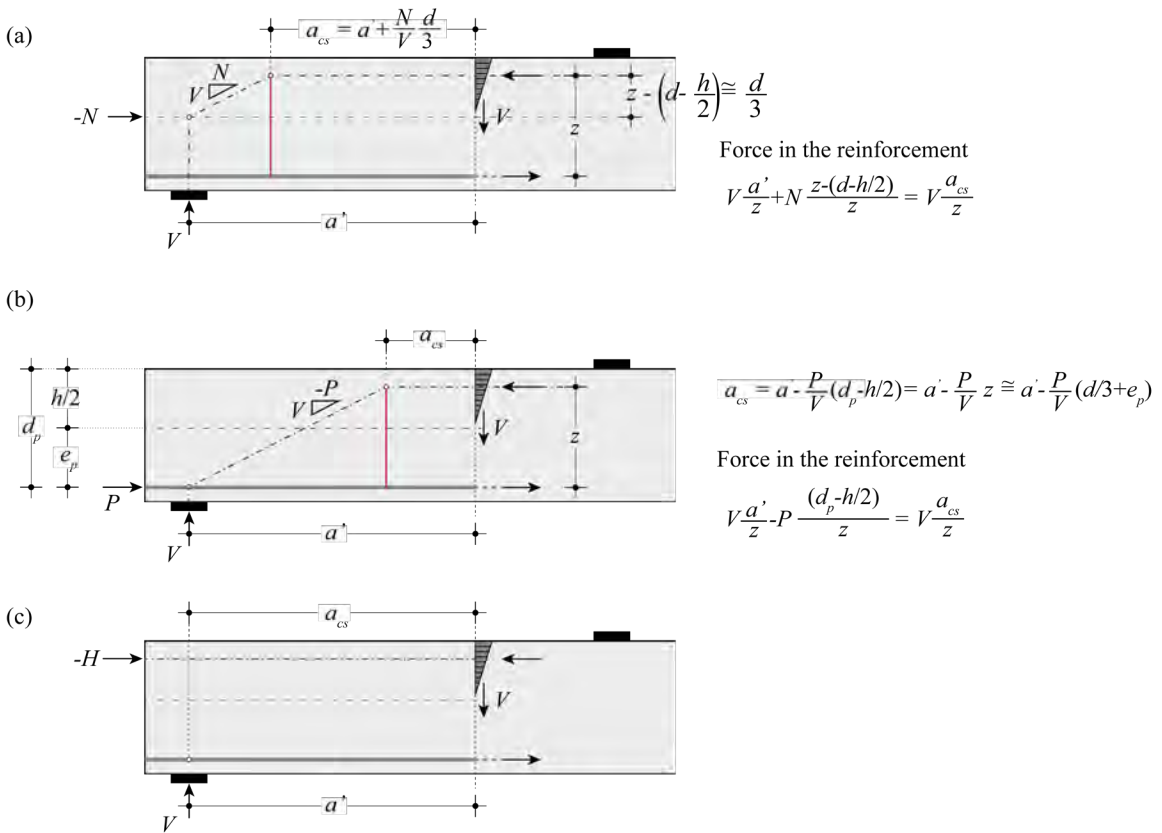


Figure 9. Considering the effects of (a) centered axial forces, (b) prestressing forces and (c) eccentric normal forces on the calculation of the effective shear span. Figure adapted from [105].

3.2 Punching shear

3.2.1 Recent experimental evidence and associated challenges

Beyond the differences between one-way shear and punching shear from a theoretical point of view, there is also an important difference from an experimental point of view. The behavior of one-way slabs without shear reinforcement is typically investigated experimentally on beams with a rectangular cross section with a limited width [99]. This allows tracking and observing the development of cracking over the depth of the members during

loading in an almost instantaneous manner (e.g. [29], [119]). In punching shear tests, with the available measuring techniques today available, it is only possible to follow the development of cracking and strains in bottom and top surfaces and attempts to follow the development of crack inside the slabs in a detailed manner are at the beginning [84]. This lack of insight information makes it difficult to fully validate some of the assumptions of a mechanical model for punching. An additional level of uncertainty with respect to shear results therefore in the interpretation of the phenomena governing the failures. Notwithstanding, a number of interesting experimental evidence are reported in literature, allowing to ground the most relevant hypotheses of a mechanical model. For that purpose, some analogies with the experimental evidence resulting from the shear tests can also be used. This is what has been done by Simões et al. [85], who combined experimental observations with the main principles of the CSCT to develop a more refined mechanical model.

3.2.2 Refined formulation of the mechanical model for punching

As previously discussed, the CSCT for punching considers that the propagation of an inclined tangential flexural crack towards the compression zone governs the capacity to transfer shear forces from the slab to the column [32], [37], [39]. The location, shape and kinematics of this crack are therefore instrumental to calculate the punching shear resistance and the associated deformation capacity [85].

Simões et al. [85] presented a refinement of the mechanical model consisting of an advanced formulation to calculate the failure criterion. Such model is grounded on experimental evidence and theoretical considerations.

The CSC is an inclined surface presenting two regions with distinct behaviors [34] (see Figure 10a): a localized cracking on the tension side and a smeared cracking on the compression side. On the localized cracking region, a crack is formed, and the transmission of forces occurs by aggregate interlocking [35], [58], [108] and residual tensile strength [124]. On the smeared cracking region, a shear band behavior is adopted (inspired on the work by Jensen [125], but adopting a strain-stress relationship for concrete [59] accounting for strain softening [3] and biaxial compression [126]), consisting on the consideration of a distributed cracking (eventually with coalescence at failure) over a given width (corresponding to the width of the band). The location of the CSC at the level of the flexural reinforcement (see the parameter r_0 in Figure 10a-10b) is governed by the formation of the outermost tangential flexural cracks. Its kinematics is composed by the vector sum of a flexural (in blue in Figure 10c) and a shear deformation (in red in Figure 10c), as originally idealized in references [28], [32], considered in [58], [60] and supported from an experimental point-of-view by the work of Clément [60]). On the basis of the calculated displacements between the two crack lips, the shear-transfer forces developing along the CSC can be evaluated based on advanced constitutive laws (see Simões et al. [85] for their description). For a given rotation and the corresponding shear deformation at maximum load, the punching resistance is obtained by summing the contributions of the different shear-transfer actions (Figure 10d). References [85], [86] can be consulted for further details.

The results of the refinement of the mechanical model of the CSCT [85] show a decreasing punching resistance with increasing rotation in accordance with previous failure criteria [32], [37], [39], which is explained by the reduction of the different shear-transfer contributions. Larger rotations mean wider cracks which [85]: (1) reduce the aggregate interlocking stresses in the localizing cracking region; (2) reduce the strength in the smeared cracking region and (3) are normally associated with yielding of radial flexural reinforcement, reducing or even disabling the contribution of dowel-action.

The calculations [70], [85] which reproduce the behavior of tests on slab and footing specimens (databases from [34]) are plotted in Figure 11a in terms of normalized punching shear resistance as a function of a normalized rotation and in Figure 11b in terms of crack opening (at a height $d/2$ from the intrados) as a function of the normalized rotation. Figure 11a shows that: (1) the calculated values fall within a band which can be approximated by a single analytical function (the hyperbolic failure criterion of reference [39] represents a good approximation of such function) [85]; (2) while the simulation of slab specimens are distributed along a wide range of normalized rotations, the results for isolated footings show that these members fail for limited values of the normalized rotation; (3) even if the calculation for the isolated footings are within the ones observed for slender slabs, it seems possible to observe a trend of a more pronounced decrease of the punching resistance with the increase of the normalized rotation for isolated footings than for slender slabs (this could be justified by the rather small values of the column size-to-effective depth ratio occurring in footings, see also Figure 12a for parametric study on the influence of the column size). Figure 11b shows that: (1) a linear correlation between the crack opening and the multiplication of the rotation by the effective depth $w_T \propto \psi \cdot d$ as originally idealized in references [32], [37], [39] to determine the bending related crack opening is a fair approximation of the calculated behavior for medium to large flexural deformations; (2) for limited flexural deformations (low rotations), the shear deformation becomes the governing contribution to the crack opening; (3) the isolated footings are mainly in this regime; (4) these results are in-line with the adoption of power-law failure

criterion [34], [87] with an upper limit corresponding to the maximum achievable punching shear resistance (again, associated to a failure mechanism rather governed by the shear deformations [34]).

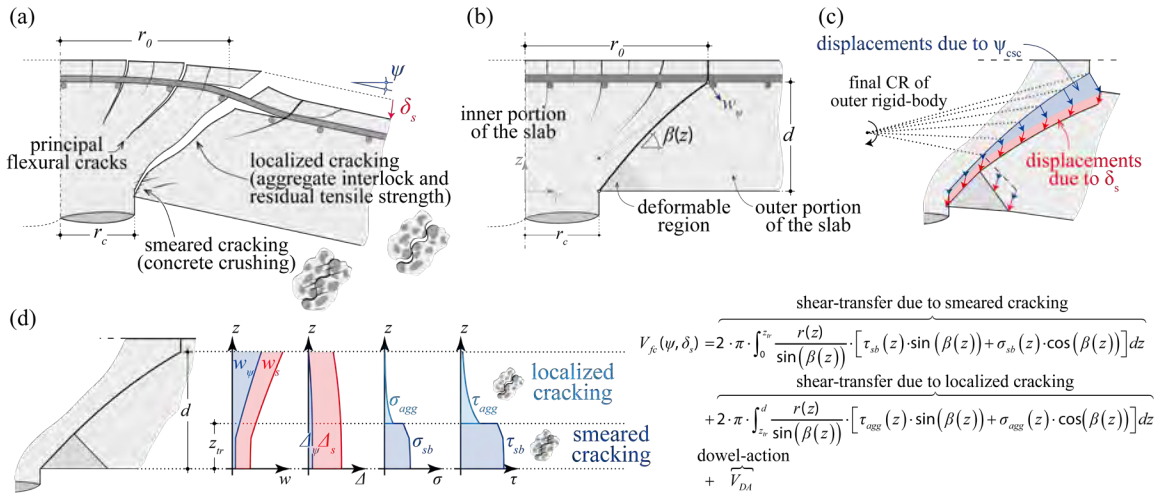


Figure 10. Mechanical model of Simões et al. [85]: (a) main assumptions; (b) different regions of the slab; (c) kinematics; (d) geometry, displacements normal and parallel to the CSC, normal and shear stresses and integration of stresses along the CSC. Figure adapted from [85], [86].

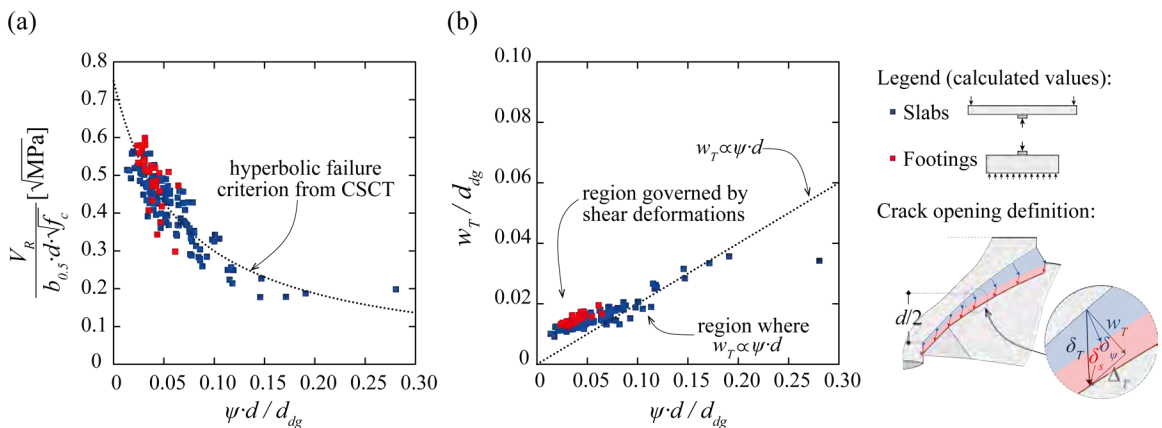


Figure 11. Results of the refined mechanical model of the CSCT for punching [85]: (a) normalized punching resistance calculated for selected tests (databases from [34]) as a function of the calculated normalized rotation; (b) calculated normalized crack opening at $d/2$ from the soffit of the slab as a function of the normalized rotation. Figure adapted from Simões et al. [85].

Another possible interesting application of the CSCT is the calculation of the shear deformation not only at failure, but also during loading. Such a deformation is for instance interesting to investigate (1) the activation of the shear reinforcement, and (2) the redistributions of the shear forces due to nonlinear shear deformation around non-axis-symmetric supports like edge and corner columns or columns with unbalanced moments.

According to the refined mechanical model presented by Simões et al. [85], the shear deformation associated to a given punching load can be calculated with the following iterative procedure: (1) assume a rotation ψ ; (2) calculate the associated acting load based on the load-rotation relationship; (3) assume an initial shear deformation and increase it incrementally until the calculated shear force which can be activated across the CSC corresponds to the load of step (2). The results of such approach are for instance presented in Figure 13 for two slab specimens tested by Einpaul et al. [42] and Einpaul [127]: for the sake of comparison, the calculated vertical displacement at the root of the column (associated to the shear deformation) is compared against the maximum measured deviation from a conical shape deformation of the slab. The calculated and measured values are in excellent agreement, indicating that the refined mechanical model is not only capable of predicting the shear deformation at failure, but can also estimate the shear and flexural deformations for lower load levels. A parametric study relating the rotation-shear deformation-punching load during loading up to failure is shown in Figure 14.

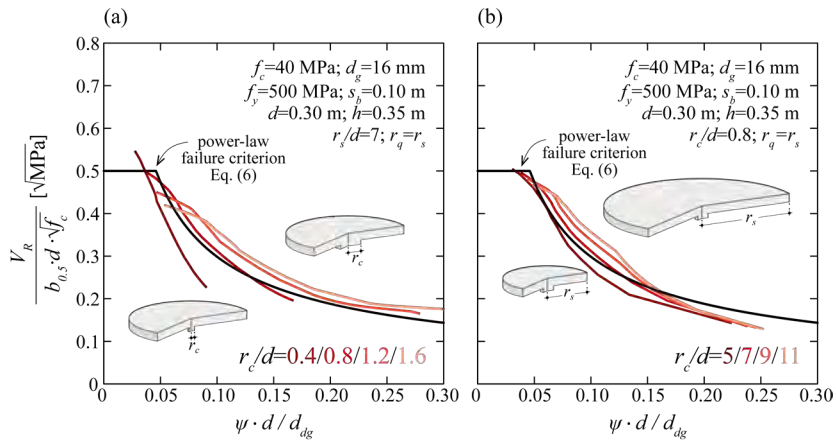


Figure 12. Normalized punching resistance as a function of the normalized rotation calculated with the refined mechanical model [85] and comparison with simplified power-law failure criterion [34], [104] for different: (a) column size-to-effective depth ratios; (b) slenderness-to-effective depth ratios. Figure adapted from [86].

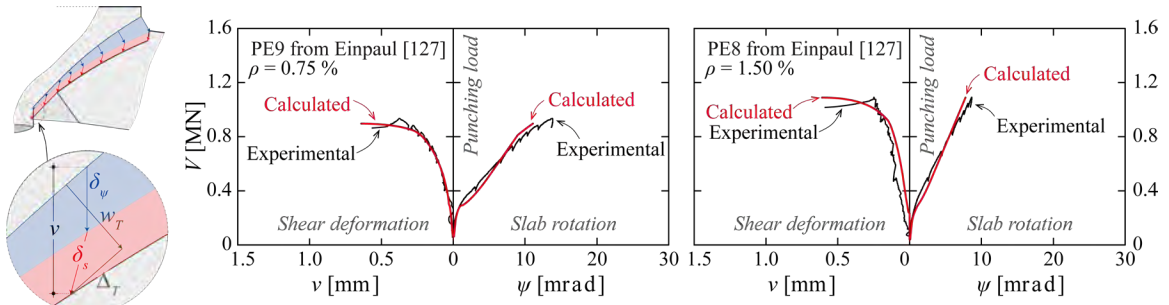


Figure 13. Comparison of the results of the refined mechanical model of the CSCT for punching [85] against experimental results (from [127]) in terms of shear and flexural deformations.

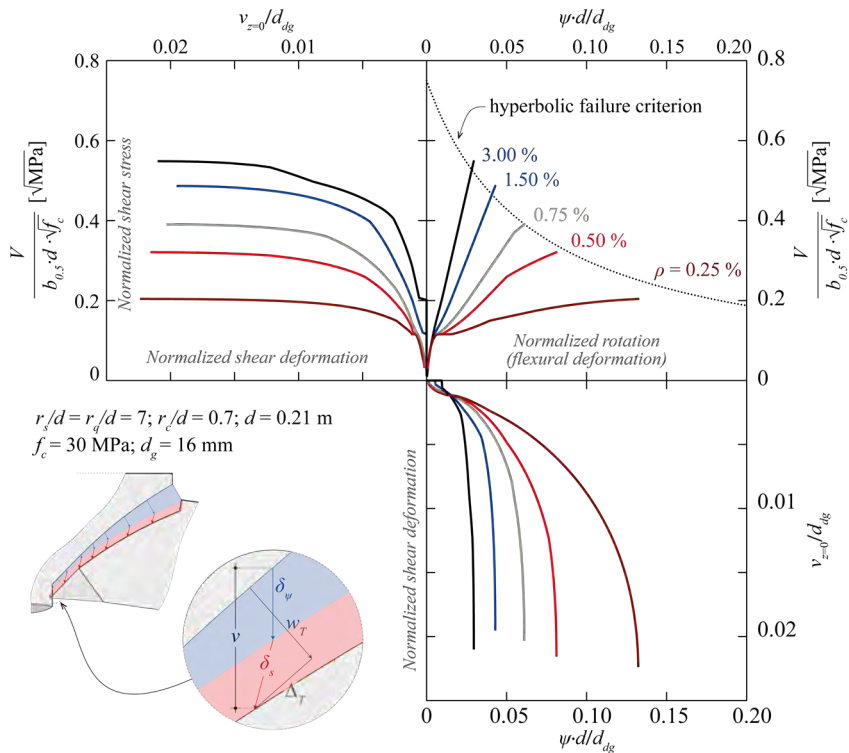


Figure 14. Results of the refined mechanical model of the CSCT for punching [85]: relationship between load, rotation and shear deformation during loading and at failure.

3.2.3 Closed-form expressions and integration to codes of practice

As discussed in Section 2, the strain-based version of the CSCT for punching shear has been integrated in codes of practice since 2003 (Swiss Code SIA 262:2003 [25], see [37], [39], [93]. From a practical point of view, the application of this theory to punching shear design or assessment has been normally performed calculating the resistance associated with the rotation calculated based on the applied design load (considering the appropriate partial safety factor and characteristics values). This methodology is simple to use for the design of new structures, as it consists on a simple comparison of a design resistance to a design load. An iterative procedure is nevertheless required to calculate the load where the design resistance equals the design load, thus corresponding to the punching resistance.

In the scope of the review of the design expressions for the punching shear provisions in the new generation of the Eurocode for reinforced concrete structures [118], one of the objectives was to improve the ease-of-use. Considering that Eurocode 2 provides in its current version an expression for the calculation of the punching resistance that, although empirical (based on Zsutty's work for shear [8]), is closed-form and relatively easy to use, a reformulation of the CSCT expressions has been seen as suitable. It thus resulted in the need to develop analytical closed-form expression for the punching shear design in the framework of the CSCT. As the hyperbolic failure criterion does not allow for the analytical derivation of such expressions, it was necessary to approximate it with a function that could allow it. A power-law failure criterion was considered to be a justified choice as follows [34], [104]:

$$\frac{V_{R,c}}{b_{0.5} \cdot d_v \cdot \sqrt{f_c}} = 0.55 \cdot \left(\frac{d_{dg}}{25 \cdot \psi \cdot d} \right)^{\frac{2}{3}} \leq k_F \tag{6}$$

where d_v is the shear-resisting effective depth, $b_{0.5}$ is the length of the control perimeter at a distance $0.5d_v$ for the column face (see subsection 3.2.5 below) and k_F is the upper limit of the failure criterion (maximum achievable punching shear resistance for small rotations; a value between 0.45 and 0.65 can be considered [34]) being associated to a failure mostly governed by shear deformations (refer to Figure 11b; see [34] for further discussion on this topic). Figure 12 shows a comparison between a parametric study performed with the refined mechanical model of the CSCT [85] and the power-law failure criterion of Equation 6. These results, as others previously presented [34], [85], [86], show that the consideration of an analytical power-law failure criterion is a reasonable compromise between the results of the refined mechanical model and the simplicity required for the derivation of a closed-form solution for the punching resistance of reinforced concrete members to be implemented in a standard.

The load-rotation relationship according to [39], [117] was already a power-law and has been slightly adapted with respect to the influence of a_p to better approximate the results of the refined mechanical model:

$$\psi = k_m \frac{8 \cdot a_{pd} \cdot f_y}{d \cdot E_s} \left(\frac{V}{V_{flex}} \right)^{3/2} \tag{7}$$

where $a_{pd} = \sqrt{a_p \cdot \frac{d}{8}}$, where a_p refers to the distance between the center of the support area and the point of contraflexure.

Based on Equations 6-7, simple expressions for punching shear design can be analytically derived (as already shown in references [34], [87], [88], [128]). For the sake of simplicity, the derivation will be quickly revisited below considering the case of interior columns, without unbalanced moment and without any column penetration ($d_v=d$ considered in the following, i.e. an equal flexural and shear-resisting effective depth).

Introducing Equation 7 into the failure criterion of Equation 6 and solving for $V=V_{R,c}$, the punching shear resistance can be calculated in a closed-form format as follows [87]:

$$V_{R,c} = \sqrt{V_{flex} \cdot 0.55 \cdot b_{0.5} \cdot d \cdot \sqrt{f_c}} \cdot \left(\frac{d_{dg}}{25 \cdot k_m \cdot 8 \cdot a_{pd}} \cdot \frac{E_s}{f_y} \right)^{\frac{1}{3}} \leq k_F \cdot b_{0.5} \cdot d \cdot \sqrt{f_c} \tag{8}$$

Equation 8 allows calculating the punching resistance without any iteration as a function of the different parameters which can be calculated on a mechanical basis (concrete type, reinforcement properties, column size, slab flexural resistance of the slab and slab slenderness). Equation 8 can further be simplified obtaining a direct function of only geometrical and mechanical parameters. For that purpose, it can be assumed that $V_{flex}=a \cdot m_R$, $m_R \approx 0.75 d^2 (\rho f_y)^{0.9} f_c^{0.1}$ [34], [87], $E_s=200\,000$ MPa (applicable only for steel reinforcement), $k_F=0.5$ and $k_m=1.2$ thus eventually yielding the following expression (simplifying exponents with minor influences, refer to [34] for further details on these simplifications):

$$\frac{V_{R,c}}{b_{0.5} \cdot d} = 0.60 \cdot k_{pb} \cdot \left(100 \rho \cdot f_c \cdot \frac{d_{dg}}{a_{pd}} \right)^{1/3} \leq k_F \cdot \sqrt{f_c} \tag{9}$$

where the parameter $k_{pb} = \sqrt{\frac{8}{(1.2)^2} \cdot a \cdot \frac{d}{b_{0.5}}}$ (for the adopted assumptions, i.e. case without any concentration of shear forces along the control perimeter and $d_v=d$). Equation 9 presents a similar format as in current Eurocode 2 [118], but differs by: (a) considering a control perimeter located closer to the supporting area (see discussion in section 3.2.5 for further details); (b) considering the concrete type (by means of the factor d_{dg}); (c) including strain and size effects [67] by means of the factor $(d_{dg}/a_{pd})^{1/3}$.

In addition to the punching shear resistance, the rotation at failure (ψ_{Rc} as represented in Figure 15a) can also be calculated in a closed-form format by introducing Equation 8 into Equation 7 as follows:

$$\psi_{R,c} = \left(\frac{0.55 \cdot b_{0.5} \cdot d \cdot \sqrt{f_c}}{V_{flex}} \right)^{\frac{3}{4}} \left(\frac{k_m \cdot 8}{25} \cdot \frac{a_{pd} f_y d_{dg}}{d E_s d} \right)^{\frac{1}{2}} \leq k_m \frac{8 \cdot a_{pd} f_y}{d E_s} \left(\frac{k_F \cdot b_{0.5} \cdot d \cdot \sqrt{f_c}}{V_{flex}} \right)^{\frac{3}{2}} \tag{10}$$

Equation 10 can be further simplified following the same considerations adopted to simplify Equation 8 to Equation 9 (considering steel reinforcement, rounding exponents and canceling parameter with minor influence), eventually yielding:

$$\psi_{R,c} = C_1 \left(\frac{a_p}{d} \right)^{1/4} (f_c)^{1/3} \left(\frac{1}{\rho} \right)^{2/3} \left(\frac{1}{k_{pb}} \right)^{3/2} \left(\frac{d_{dg}}{d} \right)^{1/2} \leq C_2 \frac{a_{pd}}{d} f_c^{3/5} \frac{1}{k_{pb}^3} \left(\frac{1}{\rho} \right)^{4/3} \tag{11}$$

where C_1 and C_2 are constants cumulating the multiplication of other constants or parameters with minor impact (parameter with exponents smaller than 0.35 are canceled). It is important to note that the left and right sides of the inequalities (Equations 10-11) refer respectively to the situation where the load-rotation relationship intersects the failure criterion in the power-law descending branch and the upper limit of the failure criterion (plateau).

For members with shear reinforcement, failure can occur by (1) crushing of the inclined concrete struts (maximum punching resistance); (2) within the shear-reinforcement zone; and (3) outside the shear-reinforced zone [44]. Other failure modes are also possible if current widely accepted detailing rules related to anchorage and spacing of the shear reinforcement are not respected. Within the framework of the CSCT, the punching resistance related to crushing of the concrete struts is normally determined by multiplying the failure criterion by an enhancement factor which depends on the type and detailing rules of the shear reinforcement [44], [49]. The punching resistance outside the shear-reinforced zone is calculated considering the corresponding control section and a reduced effective depth (function of the type of shear reinforcement) [44].

The derivation of closed-form expressions for the cases of failures due to crushing of concrete struts or outside the shear-reinforced region can be performed in a similar manner as shown above for the case of members without shear reinforcement (see [128] for further details). For failures within the shear reinforced region, the calculation of the punching resistance can be simplified as described in the following. According to reference [44], and as introduced in *fib* Model Code 2010 [116], the punching resistance in this case ($V_{R,cs}$) can be calculated considering the sum of the concrete and shear reinforcement contributions as follows (again, for an axisymmetric case, i.e. without concentration of shear forces along the control perimeter) [44]:

$$V_{R,cs} = V_{R,c,E} + V_{R,s,E} \geq A_{sw} \cdot f_{yw} \tag{12}$$

where $V_{R,c,E}$ and $V_{R,s,E}$ refer respectively to the concrete and shear reinforcement contributions at failure, which are a function of the state of deformations (described by the slab rotation ψ_E associated to the acting punching load V_E).

A relationship between the rotation ψ_E associated to the acting punching load V_E and the rotation at failure of the slab without shear reinforcement (associated to the punching resistance $V_{R,c}$) can be established based on the load-rotation relationship of Equation 7 as follows:

$$\frac{\psi_E}{\psi_{R,c}} = \left(\frac{V_E}{V_{R,c}} \right)^{3/2} \tag{13}$$

The concrete contribution associated to the slab rotation ψ_E can be obtained in a simplified manner using the relationship of Equation 13 together with the failure criterion of Equation 6 as (neglecting in addition the upper-limit of the failure criterion):

$$V_{R,c,E} = V_{R,c} \left(\frac{\psi_{R,c}}{\psi_E} \right)^{\frac{2}{3}} = V_{R,c} \cdot \frac{V_{R,c}}{V_E} = V_{R,c} \cdot \eta_c \tag{14}$$

where $\eta_c = V_{R,c}/V_E \leq 1$ is the analytically derived reduction factor that accounts for the decrease of the concrete contribution with the increased acting shear force allowed by the use of shear reinforcement.

With respect to the shear reinforcement contribution, it can be calculated (again, for an axisymmetric case, i.e. without concentration of shear forces along the control perimeter) multiplying the stress in the shear reinforcement (σ_{sw})

by the total area of shear reinforcement that can be activated (ΣA_{sw} ; located between $0.35d$ and d from the column face according to [116]):

$$V_{R,s} = \Sigma A_{sw} \cdot \sigma_{sw} \tag{15}$$

The activable stress in the shear reinforcement in Equation 15 can be estimated based on the following expression (see [44] for further details on its derivation; second term of the left side of the inequality referring to the increase in the shear reinforcement stress due to bond; see Figure 15b for graphical representation):

$$\sigma_{sw} = \frac{E_{sw}}{6} \cdot \psi + \tau_b \cdot \frac{d}{\phi_w} \leq f_{yw} \tag{16}$$

where E_{sw} is the modulus of elasticity, τ_b is the average bond stress and ϕ_w is the diameter of the shear reinforcement bars. It should be noted that Equation 16 was derived in 2009 [44] neglecting the contribution of shear deformations to the crack opening (see line in Figure 11b), and thus to the shear reinforcement activation. This Equation provides nevertheless reasonable results when compared to the experimental tests.

Considering the relationship of Equation 13 and that $\eta_c = V_{R,c}/V_E$, the rotation ψ_E associated to the acting shear force can be written as a function of the rotation at failure of a member without shear reinforcement and the acting shear force as:

$$\psi_E = \psi_{R,c} \left(\frac{1}{\eta_c} \right)^{3/2} \tag{17}$$

The shear reinforcement stress at failure can be calculated introducing ψ_E according to Equation 17 in Equation 16:

$$\sigma_{sw} = \frac{E_{sw}}{6} \psi_{R,c} \left(\frac{1}{\eta_c} \right)^{3/2} + \tau_b \cdot \frac{d}{\phi_w} \leq f_{yw} \tag{18}$$

Equation 18 can eventually be simplified (to be a direct function of geometrical and mechanical parameters) introducing $\psi_{R,c}$ according to Equation 11 (considering in addition that the intersection with the power-law function is governing, i.e., the rotation is given by the left side of the inequality) as:

$$\sigma_{sw} = \frac{E_{sw}}{6} C_1 \left(\frac{a_p}{d} \right)^{1/4} (f_c)^{1/3} \left(\frac{1}{\rho} \right)^{2/3} \left(\frac{1}{k_{pb} \cdot \eta_c} \right)^{3/2} \left(\frac{d_{dg}}{d} \right)^{1/2} + \tau_b \cdot \frac{d}{\phi_w} \leq f_{yw} \tag{19}$$

From a practical point-of-view, the parameters (a_p/d) and f_c with the least influence on the shear reinforcement stress can be cancelled considering realistic, yet unfavorable values. The influence of the flexural reinforcement ratio can also be cancelled based on the assumption that a rather large value of this parameter is normally used in the case of members with shear reinforcement (to avoid the flexural resistance to be the governing criterion). With such reasonings, Equation 19 can eventually be simplified as follows for slabs with steel shear reinforcement (constant value of E_{sw}):

$$\sigma_{sw} = C_3 \left(\frac{1}{k_{pb} \cdot \eta_c} \right)^{3/2} \left(\frac{d_{dg}}{d} \right)^{1/2} + \tau_b \cdot \frac{d}{\phi_w} \leq f_{yw} \tag{20}$$

where C_3 is a constant absorbing the multiplication of other constant value as well as the constants resulting from the cancelling of the previously mentioned parameters.

Using Equations 14 and 20, Equation 12 can be rewritten in a simpler format as:

$$V_{R,cs} = \eta_c \cdot V_{R,c} + \eta_s \cdot \rho_{sw} \cdot b_{0.5} \cdot d \cdot f_{yw} \geq \rho_{sw} \cdot b_{0.5} \cdot d \cdot f_{yw} \tag{21}$$

where η_s is a factor accounting (1) for the activation of the shear reinforcement and (2) for the fact that a total area of shear reinforcement (ΣA_{sw}) smaller than $\rho_{sw} \cdot b_{0.5} \cdot d$ based on the principle of *fib* Model Code 2010 (where the only the units of shear reinforcement between $0.35d$ and d from the face of the supporting area can be activated; this consideration is slightly relaxed for the lower limit of Equation 21 [128]). This factor is calculated according to Equation 22:

$$\eta_s = \frac{\sigma_{sw}}{f_{yw}} \cdot \frac{\Sigma A_{sw}}{\rho_{sw} \cdot b_{0.5} \cdot d} \leq \frac{\Sigma A_{sw}}{\rho_{sw} \cdot b_{0.5} \cdot d} \tag{22}$$

which yields an equation of the following type:

$$\eta_s = \frac{C_3}{C_4 \cdot C_6} \frac{\Sigma A_{sw}}{\rho_{sw} \cdot b_{0.5} \cdot d} \left(\frac{1}{k_{pb} \cdot \eta_c} \right)^{3/2} \left(\frac{d_{dg}}{d} \right)^{1/2} + \frac{\tau_b}{C_5 \cdot C_6} \frac{\Sigma A_{sw}}{\rho_{sw} \cdot b_{0.5} \cdot d} \cdot \frac{d}{\phi_w} \leq \frac{\Sigma A_{sw}}{\rho_{sw} \cdot b_{0.5} \cdot d} \tag{23}$$

where the values of C_4 to C_6 can be assumed to be constant without a significant loss of generality.

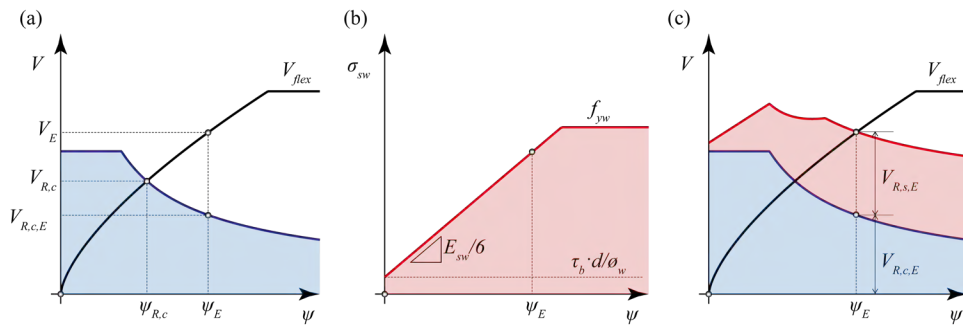


Figure 15. Graphical representation of the analytical derivation of simplified punching shear design formulae for FprEN 1992-1-1:2023 [118] based on the CSCT: (a) closed-form for members without shear reinforcement; (b) activation of shear reinforcement; (c) members with shear reinforcement.

Equations 9 and 21 (together with Equations 14 and 23), formulated in an appropriate safety format [129], are the basis for the punching shear design of the next generation of the European Standards for Concrete Structures [118]. They are derived from the mechanical model, which allows to understand the limitations that result from the process of simplification to enhance their easiness of use. Figure 16 presents for instance the principles of the application of these equations to different control sections, having as objective to reduce the required area of shear reinforcement in the outer perimeters.

The derivation of design expressions from advanced physically sound models ensures also the possibility to have simple design expressions which are consistent with higher Levels-of-Approximation [130]. This is for instance the case of Annex I of FprEN 1992-1-1:2023 [118], dedicated to a refined assessment of critical existing structures, where the application of the original rotation-based formulation of the CSCT for punching (identical to the one included in the *fib* Model Code 2010 [116]) is allowed.

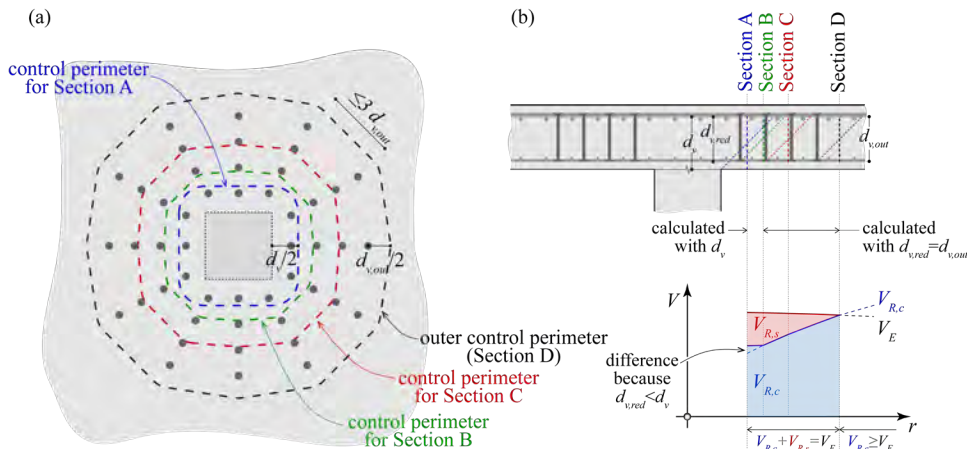


Figure 16. Investigation of the required amount of shear reinforcement by varying the location of the control section as allowed in FprEN 1992-1-1:2023 [118].

3.2.4 Considerations on the control perimeter and the actual level of the support area

Different control perimeters to verify a flat slab for punching have been adopted in standards (see Figure 17a):

- located at a distance $d/2$ from the support area as adopted by several standards (see for instance the ACI 318 [131] and the CEB-FIP Model Code 1978 [132]);
- located at a larger distance from the support area ($2d$ according to CEB-FIP Model Code 1990 [115] and EN 1992-1-1:2004 [122]).

The choice of a larger distance ($2d$) was intended to allow for an assessment of the resistance independently from the column size, but presents several drawbacks (does not represent the reality; is valid only for flat slabs without shear reinforcement and requires to be adapted for slabs with shear reinforcement and for foundations; leads to unsafe predictions for small columns requiring an additional verification nearer to the column) [128].

For the CSCT, since it is a mechanical model, the distance $d/2$, which reproduces more accurately the actual failure mechanism, has been adopted. A theoretical investigation has shown that this choice provides reasonable results for all

combinations of column sizes, slab depths and soil reactions in case of foundations. Since for larger columns, the length of the control perimeter increases, also the total punching shear resistance increases. This has as consequence an increase of the flexural deformation ψ at failure, and thus, a decrease of the punching shear stress resistance (decreasing slope of the failure criteria, see Figures 11a and 12). This effect is explicitly accounted for in the rotation-based approach of the CSCT (and in the *fib* Model Code 2010 [116], since the rotation ψ at failure is explicitly considered), whereas in the analytical derivation of the closed-form approach implemented in the second generation of Eurocode 2 FprEN 1992-1-1:2023 [118], the same effect is accounted for with the coefficient k_{pb} in Equation 9. Interestingly, the choice of a control perimeter located at $2d$ from the column face according to EN 1992-1-1:2004 [122] provides similar results as shown in Figure 17b for circular columns. The same effect is accounted for also in ACI 318 [131], where for large columns, a strength reduction is considered based on empirical observations [133].

For large square and rectangular columns, an additional detrimental effect needs to be considered. In these cases, the slab tends to lean on the column corners and even to lift from the intermediate parts [57]. Due to the brittleness of the failure mode, only a limited redistribution of the internal forces can take place and punching can occur before significant slab shear forces can be activated at the intermediate parts. For these reasons, the length of straight segment of the control perimeter according to *fib* Model Code 2010 [116] and FprEN 1992-1-1:2023 [118] is limited to $3d$ ($1.5d$ at both sides of the corners, see Figure 18a). This reduction of the length of the control perimeter (see Figure 17d) has a consequence on the punching shear resistance (see Figure 17c), although the effect is mitigated by the nonlinearity of the relationship between length of the control perimeter and punching shear resistance (see for instance coefficient k_{pb} in Equation 9).

The phenomenon of the shear force concentrations can be observed also at wall corners and wall ends. In these cases, the punching shear verification should be conducted for the force carried by the end and corner zones with the related control perimeters (Figure 18b-18c).

In some cases, the construction joint between column and slab is higher than the slab intrados (Figure 18d). Since the casted faces of the columns are usually too smooth to carry shear stresses between the column and the slab, it is reasonable to assume that the shear force in the slab must be transferred to the column at the level of the construction joint. For this reason, the punching shear verification should be conducted on the basis of the shear carrying effective depth d_v defined in Figure 18d instead of d [118], [25], [116].

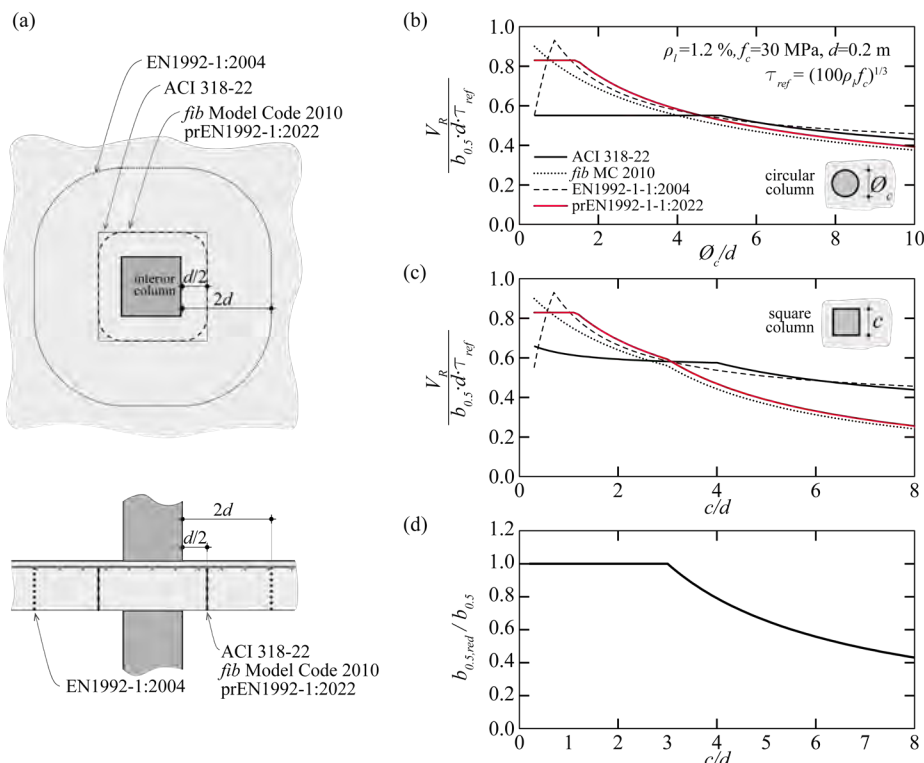


Figure 17. Considerations on the control perimeter: (a) location according to different codes of practice [122], [118], [116], [131]; influence of the column size-to-effective depth ratio on the punching resistance for (b) round and (c) square columns (accounting for stresses concentrations); (d) reduction of control perimeter in square stiff support areas due to stresses concentrations considered in [116] and [118].

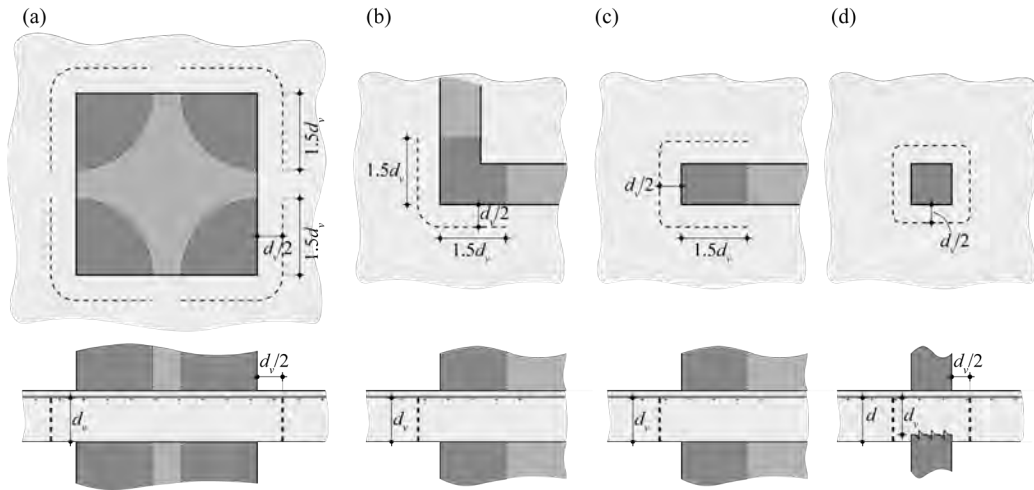


Figure 18. Definition of control perimeter according to [118]: (a) large stiff square support area; (b) corner of wall; (c) wall end; (d) interior column with column penetration.

3.2.5 Models with different levels of refinement and Levels of Approximation Approach

As shown along this document, different levels of refinement can be used in the framework of the CSCT. These different approaches are schematically presented in Figure 19, together with the indication of the cases for which the use of each of them is more interesting (see also [86] for a wider discussion on this topic).

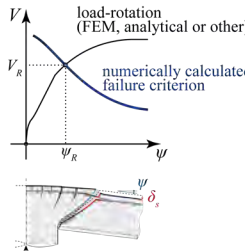
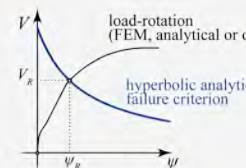
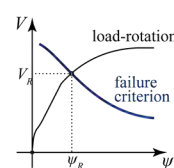
RANGE OF APPLICABILITY	Research		Design
	Assesment of existing structures		
LOAD-ROTATION RELATIONSHIP	FEM, analytical, or other	FEM, analytical, or other	Simplified parabola
FAILURE CRITERION	Integration of stresses along CSC $V_R = \int \sigma \cos(\beta) + \tau \sin(\beta) dA$	Analytical hyperbolic failure criterion	Simplified power-law
METHODOLOGY	Calculation by intersection of the load-rotation relationship and the failure criterion	Calculation by intersection of the load-rotation relationship and the failure criterion	Closed-form expressions
GENERAL COMMENTS	 <p>Refined formulation supporting the need for adaptations on the analytical failure criterion or on the simplified formulations</p>	 <p>Largely validated and extended to other cases</p>	 <p>Closed-form analytically derived solutions</p>
REFERENCES	Guidotti [58] Clément [60] Simões et al. [85]	Muttoni [37] Muttoni [39]	Muttoni et al. [34, 86, 87]

Figure 19. Overview of the framework of the mechanical model of the CSCT for punching.

4 CONCLUSIONS

This document presents a general overview of the Critical Shear Crack Theory for shear in one-way slabs without shear reinforcement and punching of slabs without and with shear reinforcement:

- The first ideas of this theory date back to 1985. Since then, the theory has strongly evolved, notably in the last 20 years. A large number of researchers from a wide range of countries from all over the world have participated in its development and validation and different research groups worldwide are using it for research purposes and to develop practical applications.
- The theory is nowadays well-established and offers the theoretical grounds for the Swiss Code for Concrete Structures since 2003, *fib* Model Code 2010 and the second generation the European standard for Concrete Structures.
- Since it is a mechanical model, it is possible to integrate it in codes via an approach based on the Levels-of-Approximation. It thus allows using closed-form expressions for simple cases, while remaining in a consistent framework which allows applying more advanced approaches for the assessment of critical existing structures and to design strengthening solutions.
- The work performed in the last years allowed the development of refined formulations for both shear and punching which can be continuously improved to incorporate new experimental evidence, new materials and new developments of construction techniques. The analytical expressions can also be easily adapted to cover new practical cases.

ACKNOWLEDGEMENTS

The first author would like to acknowledge the contributions of all the researchers who have collaborated with him in the last two decades in enhancing the Critical Shear Crack Theory.

REFERENCES

- [1] A. Muttoni and M. Fernández Ruiz “Shear in slabs and beams: should they be treated in the same way?” in *fib Bulletin No. 57 – Shear and Punching Shear in RC and FRP Elements*, F. Minelli, G. Plizzari, V. Sigrüst, and S. Foster, Eds., Lausanne, Switzerland: FIB, 2010, pp. 105–128.
- [2] B. Thürlimann, “Plastic analysis of reinforced concrete beams,” in *IABSE Colloq.: Plasticity Reinf. Concr.*, Copenhagen, Denmark, 1979, pp. 71–90.
- [3] F. J. Vecchio and M. P. Collins, “The Modified Compression-Field Theory for reinforced concrete elements subjected to shear,” *ACI J. Proc.*, vol. 83, no. 2, pp. 219–231, 1986.
- [4] J. F. Jensen, M. P. Nielsen, M. W. Bræstrup, and F. Bach, *Some Plastic Solutions Concerning the Load-Carrying Capacity of Reinforced Concrete: Report No. R-101*. Copenhagen, Denmark: Tech. Univ. Denmark/Struct. Res. Lab., 1978 [in Danish].
- [5] E. V. Bentz, F. J. Vecchio, and M. P. Collins, “Simplified modified compression field theory for calculating shear strength of reinforced concrete elements,” *ACI Struct. J.*, vol. 103, no. 4, pp. 614–624, Jul./Aug. 2006.
- [6] American Association of State Highway and Transportation Officials, *Bridge Design Specifications*, 9th ed. Washington, D.C., USA: AASHTO, 2020.
- [7] K. G. Moody and I. M. Viest, “Shear strength of reinforced concrete beams – part 4 – analytical studies,” *ACI J. Proc.*, vol. 51, no. 3, pp. 697–730, 1955.
- [8] C. T. Zsutty, “Beam shear strength prediction by analysis of existing data,” *ACI J. Proc.*, vol. 65, no. 11, pp. 943–951, 1968.
- [9] E. Hognestad, “Shearing strength of reinforced concrete column footings,” *ACI J. Proc.*, vol. 25, no. 3, pp. 189–208, 1953.
- [10] R. C. Elstner and E. Hognestad, “Shearing strength of reinforced concrete slabs,” *ACI Mater. J.*, vol. 53, no. 2, pp. 29–58, 1956.
- [11] C. S. Whitney, “Ultimate shear strength of reinforced concrete flat slabs, footings, beams, and frame members without shear reinforcement,” *ACI J. Proc.*, vol. 54, no. 10, pp. 265–298, 1957.
- [12] J. Moe, *Shearing Strength of Reinforced Concrete Slabs and Footings under Concentrated Loads*. Skokie, IL, USA: Portland Cement Assoc., Res. Develop. Lab., 1961.
- [13] G. N. J. Kani, “The riddle of shear failure and its solution,” *ACI J. Proc.*, vol. 61, no. 4, pp. 441–468, 1964.
- [14] R. C. Fenwick and T. Paulay, “Mechanisms of shear resistance of concrete beams,” *J. Struct. Div.*, vol. 94, no. 10, pp. 2325–2350, 1968.
- [15] H. P. J. Taylor, *Investigation of the Forces Carried Across Cracks in Reinforced Concrete Beams in Shear by Interlock of Aggregate: Technical Report N. 42*. London, UK: Cement Concr. Assoc., 1970.
- [16] M. P. Nielsen, M. W. Braestrup, and F. Bach, “Rational analysis of shear in reinforced concrete beams,” in *IABSE Proc.*, 1978, pp. 15–78.
- [17] Y. D. Hamadi and P. E. Regan, “Behaviour in shear of beams with flexural cracks,” *Mag. Concr. Res.*, vol. 32, no. 111, pp. 67–78, 1980.

- [18] K.-H. Reineck, "Ultimate shear force of structural concrete members without transverse reinforcement derived from a mechanical model," *ACI Struct. J.*, vol. 88, no. 5, pp. 592–602, 1991.
- [19] F. J. Vecchio, "Disturbed stress field model for reinforced concrete: formulation," *J. Struct. Eng.*, vol. 126, no. 9, pp. 1070–1077, Sep. 2000.
- [20] S. Kinnunen and H. Nylander, *Punching of Concrete Slabs Without Shear Reinforcement* (Transactions of the Royal Institute of Technology 158). Stockholm, Sweden: Elan. Boktry. Aktiebol., 1960.
- [21] M. W. Braestrup, M. P. Nielsen, B. C. Jensen, and F. Bach, *Axisymmetric Punching of Plain and Reinforced Concrete: Report No. 75*. Copenhagen, Denmark: Tech. Univ. Denmark, 1976.
- [22] M. Hallgren "Punching shear capacity of reinforced high strength concrete slabs," Doctoral dissertation, Royal Inst. Technol., Stockholm, Sweden, 1996.
- [23] D. Z. Yankelevsky and O. Leibowitz, "Punching shear in concrete slabs," *Int. J. Mech. Sci.*, vol. 41, pp. 1–15, 1999.
- [24] Swiss Society of Engineers and Architects, *Code 162 for Concrete Structures*, 1993.
- [25] Swiss Society of Engineers and Architects, *Code 262 for Concrete Structures*, 2003.
- [26] A. Muttoni, *Punching Shear – Draft Code Proposal, SIA 162, Working Group 5*. Zürich, Switzerland: Swiss Soc. Eng. Archit., 1985.
- [27] A. Muttoni and B. Thürlimann, *Shear Tests on Beams and Slabs Without Shear Reinforcement*. Zürich, Switzerland: Inst. Baustatik Konstr., 1986.
- [28] A. Muttoni, "The applicability of the theory of plasticity in the design of reinforced concrete," Doctoral dissertation, ETHZ: Zürich, Switzerland, 1990 [in German].
- [29] F. Cavagnis, M. Fernández Ruiz, and A. Muttoni, "Shear failures in reinforced concrete members without transverse reinforcement: an analysis of the critical shear crack development on the basis of test results," *Eng. Struct.*, vol. 103, pp. 157–173, 2015.
- [30] E. Mörsch, *The Reinforced Concrete Construction, Ist Theory and Ist Application*, 6th ed., Vol. 1.2. Stuttgart: Konrad Wittwer Ed., 1929 [in German].
- [31] F. Leonhardt and R. Walther, *Shear Tests on Beams With and Without Shear Reinforcement, No. 151*. Berlin, Germany: Deut. Ausschuss Stahlbeton, 1962 [in German].
- [32] A. Muttoni and J. Schwartz, "Behaviour of beams and punching in slabs without shear reinforcement," in *62 IABSE Colloq.*, Stuttgart, Germany, 1991, pp. 703–708.
- [33] A. Muttoni and M. Fernández Ruiz, "Shear strength of members without transverse reinforcement as function of critical shear crack width," *ACI Struct. J.*, vol. 105, no. 2, pp. 163–172, 2008.
- [34] A. Muttoni, M. Fernández Ruiz, and J. T. Simões, "The theoretical principles of the critical shear crack theory for punching shear failures and derivation of consistent closed-form design expressions," *Struct. Concr.*, vol. 19, pp. 174–190, 2018, <http://dx.doi.org/10.1002/suco.201700088>.
- [35] J. C. Walraven, "Fundamental analysis of aggregate interlock," *J. Struct. Eng.*, vol. 107, no. 11, pp. 2245–2270, 1981.
- [36] T. Frangi, D. Tonis, and A. Muttoni, "On the dimensioning of steel shear head: new finding," *Swiss Eng. Architects*, vol. 115, pp. 227–230, 1997 [in German].
- [37] A. Muttoni, "Shear and punching strength of slabs without shear reinforcement," *Bet. Stahlbetonbau*, vol. 98, pp. 74–84, 2003 [in German].
- [38] A. Muttoni, "Introduction to the Swiss Code SIA 262", in *Punching Shear*. Zürich, Switzerland: Swiss Eng. Archit. Document., 2003, pp. 57–66. [in French and German] [D0182].
- [39] A. Muttoni, "Punching shear strength of reinforced concrete slabs without transverse reinforcement," *ACI Struct. J.*, vol. 105, no. 4, pp. 440–450, 2008.
- [40] S. Guandalini, "Poinçonnement symétrique des dalles en béton armé," Ph.D. dissertation, EPFL, Lausanne, Switzerland, 2005.
- [41] S. Guandalini, O. Burdet, and A. Muttoni, "Punching tests of slabs with low reinforcement ratios," *ACI Struct. J.*, vol. 106, no. 1, pp. 87–95, 2009.
- [42] J. Einpaul, J. Bujnak, M. Fernández Ruiz, and A. Muttoni, "Study on influence of column size and slab slenderness on punching strength," *ACI Struct. J.*, vol. 113, no. 1, pp. 135–145, 2016.
- [43] A. Torabiana, B. Isufi, D. Mostofinejada, and A. Pinho Ramos, "Behavior of thin lightly reinforced flat slabs under concentric loading," *Eng. Struct.*, vol. 196, pp. 109327, 2019, <http://dx.doi.org/10.1016/j.engstruct.2019.109327>.
- [44] M. Fernández Ruiz and A. Muttoni, "Applications of the critical shear crack theory to punching of R/C slabs with transverse reinforcement," *ACI Struct. J.*, vol. 106, no. 4, pp. 485–494, 2009.
- [45] S. Lips, "Punching of flat slabs with large amounts of shear reinforcement," Ph.D. dissertation, EPFL, Lausanne, Switzerland, 2012.
- [46] S. Lips, M. Fernández Ruiz, and A. Muttoni, "Experimental investigation on punching strength and deformation capacity of shear-reinforced slabs," *ACI Struct. J.*, vol. 109, no. 6, pp. 889–900, 2012.

- [47] J. Einpaul, F. Brantschen, M. Fernández Ruiz, and A. Muttoni, "Performance of punching shear reinforcement under gravity loading: influence of type and detailing," *ACI Struct. J.*, vol. 113, no. 4, pp. 827–838, 2016.
- [48] R. Cantone, M. Fernández Ruiz, J. Bujnak, and A. Muttoni, "Enhancing punching strength and deformation capacity of flat slabs," *ACI Struct. J.*, vol. 116, no. 5, pp. 261–276, 2019.
- [49] D. Hernández Fraile, J. T. Simões, A. Muttoni, and M. Fernández Ruiz, "A mechanical approach for the maximum punching resistance of shear-reinforced slab-column connections," in *2021 Fib Symp.*, Lisbon, Portugal, Jun. 2021, pp. 1628–1639.
- [50] L. F. Maya, M. Fernández Ruiz, A. Muttoni, and S. J. Foster, "Punching shear strength of steel fibre reinforced concrete slabs," *Eng. Struct.*, vol. 40, no. 3, pp. 83–94, 2012.
- [51] A. Muttoni, M. Fernández Ruiz, and J. Kunz, "Nachträgliche durchstanzbewehrung zur verstärkung von stahlbetonflachdecken," *Bauingenieur*, vol. 83, pp. 503–511. [in German].
- [52] M. Fernández Ruiz, A. Muttoni, and J. Kunz, "Strengthening of flat slabs against punching shear using post-installed shear reinforcement," *ACI Struct. J.*, vol. 107, no. 4, pp. 434–442, 2010.
- [53] D. M. V. Faria, J. Einpaul, A. M. P. Ramos, M. Fernández Ruiz, and A. Muttoni, "On the efficiency of flat slabs strengthening against punching using externally bonded fibre reinforced polymers," *Constr. Build. Mater.*, vol. 73, pp. 366–377, 2014.
- [54] M. Lapi, A. P. Ramos, and M. Orlando, "Flat slab strengthening techniques against punching-shear," *Eng. Struct.*, vol. 180, pp. 160–180, 2019, <http://dx.doi.org/10.1016/j.engstruct.2018.11.033>.
- [55] L. Tassinari, "Non-axisymmetric punching of flat slabs," Ph.D. dissertation, EPFL, Lausanne, Switzerland, 2011 [in French].
- [56] J. Sagaseta, A. Muttoni, M. Fernández Ruiz, and L. Tassinari, "Non-axis-symmetrical punching shear around internal columns of RC slabs without transverse reinforcement," *Mag. Concr. Res.*, vol. 63, no. 6, pp. 441–457, 2011.
- [57] J. Sagaseta, L. Tassinari, M. Fernández Ruiz, and A. Muttoni, "Punching of flat slabs supported on rectangular columns," *Eng. Struct.*, vol. 77, pp. 17–33, 2014.
- [58] R. Guidotti, "Poinçonnement des planchers-dalles avec colonnes superposées fortement sollicitées," Ph.D. dissertation, EPFL, Lausanne, Switzerland, 2010.
- [59] R. Guidotti, M. Fernández Ruiz, and A. Muttoni, "Crushing and flexural strength of slab-column joints," *Eng. Struct.*, vol. 33, no. 3, pp. 855–867, 2011.
- [60] T. Clément, "Influence de la précontrainte sur la résistance au poinçonnement de dalles en béton armé," Ph.D. dissertation, EPFL, Lausanne, Switzerland, 2012.
- [61] T. Clément, A. P. Ramos, M. Fernández Ruiz, and A. Muttoni, "Design for punching of prestressed concrete slabs," *Struct. Concr.*, vol. 14, pp. 157–167, 2013.
- [62] T. Clément, A. P. Ramos, M. Fernández Ruiz, and A. Muttoni, "Influence of prestressing on the punching strength of post-tensioned slabs," *Eng. Struct.*, vol. 72, pp. 59–69, 2014.
- [63] I.-S. Drakatos, A. Muttoni, and K. Beyer, "Internal slab-column connections under monotonic and cyclic imposed rotations," *Eng. Struct.*, vol. 123, pp. 501–516, 2016.
- [64] I.-S. Drakatos, "Seismic behavior of slab-column connections without transverse reinforcement," Ph.D. dissertation, EPFL, Lausanne, Switzerland, 2016.
- [65] I.-S. Drakatos, A. Muttoni, and K. Beyer, "Mechanical model for drift-induced punching of slab-column connections without transverse reinforcement," *ACI Struct. J.*, vol. 115, no. 2, pp. 463–474, 2018.
- [66] A. Muttoni et al., "Deformation capacity evaluation for flat slab seismic design," *Bull. Earthq. Eng.*, vol. 20, pp. 1619–1654, 2022.
- [67] M. Fernández Ruiz and A. Muttoni, "Size effect in shear and punching shear failures of concrete members without transverse reinforcement: differences between statically determinate members and redundant structures," *Struct. Concr.*, vol. 19, no. 1, pp. 65–75, 2018, <http://dx.doi.org/10.1002/suco.201700059>.
- [68] J. T. Simões, D. M. V. Faria, M. Fernández Ruiz, and A. Muttoni, "Strength of reinforced concrete footings without transverse reinforcement according to limit analysis," *Eng. Struct.*, vol. 112, pp. 146–161, 2016.
- [69] J. T. Simões, J. Bujnak, M. Fernández Ruiz, and A. Muttoni, "Punching shear tests on compact footings with uniform soil pressure," *Struct. Concr.*, vol. 17, no. 4, pp. 603–617, 2016.
- [70] J. T. Simões, "The mechanics of punching in reinforced concrete slabs and footings without shear reinforcement," Ph.D. dissertation, EPFL, Lausanne, Switzerland, 2018.
- [71] M. Fernández Ruiz, Y. Mirzaei, and A. Muttoni, "Post-punching behavior of flat slabs," *ACI Struct. J.*, vol. 110, pp. 801–812, 2013.
- [72] J. Einpaul, M. Fernández Ruiz, and A. Muttoni, "Influence of moment redistribution and compressive membrane action on punching strength of flat slabs," *Eng. Struct.*, vol. 86, pp. 43–57, 2015.
- [73] J. Einpaul, C. E. Ospina, M. Fernández Ruiz, and A. Muttoni, "Punching shear capacity of continuous slabs," *ACI Struct. J.*, vol. 113, no. 4, pp. 861–872, 2016.

- [74] B. Belletti, M. Pimentel, M. Scolari, and J. C. Walraven, "Safety assessment of punching shear failure according to the level of approximation approach," *Struct. Concr.*, vol. 46, pp. 366–380, 2015.
- [75] J. Shu, B. Belletti, A. Muttoni, M. Scolari, and M. Plos, "Internal force distribution in RC slabs subjected to punching shear," *Eng. Struct.*, vol. 153, pp. 766–781, 2017.
- [76] B. Belletti, A. Muttoni, S. Ravasini, and F. Vecchi, "Parametric analysis on punching shear resistance of reinforced-concrete continuous slabs," *Mag. Concr. Res.*, vol. 71, no. 20, pp. 1083–1096, 2019.
- [77] B. Belletti, J. C. Walraven, and F. Trapani, "Evaluation of compressive membrane action effects on punching shear resistance of reinforced concrete slabs," *Eng. Struct.*, vol. 95, pp. 25–39, 2015.
- [78] D. Abu-Salma, R. L. Vollum, and L. Macorini, "Design of biaxially loaded external slab column connections," *Eng. Struct.*, vol. 249, pp. 113326, 2021, <http://dx.doi.org/10.1016/j.engstruct.2021.113326>.
- [79] D. Abu-Salma, R. L. Vollum, and L. Macorini, "Modelling punching shear failure at edge slab-column connections by means of nonlinear joint elements," *Structures*, vol. 34, pp. 630–652, 2021.
- [80] A. Setiawan, R. L. Vollum, L. Macorini, and B. A. Izzuddin, "Efficient 3D modelling of punching shear failure at slab-column connections by means of nonlinear joint elements," *Eng. Struct.*, vol. 197, pp. 109372, 2019, <http://dx.doi.org/10.1016/j.engstruct.2019.109372>.
- [81] A. Setiawan, R. L. Vollum, L. Macorini, and B. A. Izzuddin, "Numerical modelling of punching shear failure of reinforced concrete flat slabs with shear reinforcement," *Mag. Concr. Res.*, vol. 73, no. 23, pp. 1205–1224, 2021.
- [82] K. Micallef, J. Sagaseta, M. Fernández Ruiz, and A. Muttoni, "Assessing punching shear failure in reinforced concrete flat slabs subjected to localised impact loading," *Int. J. Impact Eng.*, vol. 71, pp. 17–33, 2014.
- [83] J. Sagaseta, P. Oلماتi, K. Micallef, and D. Cormie, "Punching shear failure in blast-loaded RC slabs and panels," *Eng. Struct.*, vol. 147, pp. 177–194, 2017.
- [84] J. Einpaul, M. Fernández Ruiz, and A. Muttoni, "Measurements of internal cracking in punching test slabs without shear reinforcement," *Mag. Concr. Res.*, vol. 70, no. 15, pp. 798–810, 2018.
- [85] J. T. Simões, M. Fernández Ruiz, and A. Muttoni, "Validation of the Critical Shear Crack Theory for punching of slabs without transverse reinforcement by means of a refined mechanical model," *Struct. Concr.*, vol. 19, pp. 191–216, 2018, <http://dx.doi.org/10.1002/suco.201700280>.
- [86] A. Muttoni, M. Fernández Ruiz, and J. T. Simões, "Recent improvements of the critical shear crack theory for punching shear design and its simplification for code provisions," in *Proc. 2018 Fib Congr.: Better, Smarter, Stronger*, 2019, pp. 116–129.
- [87] A. Muttoni and M. Fernández Ruiz, "The Critical Shear Crack Theory for punching design: from a Mechanical Model to Closed-Form Design Expressions," in *ACI-Fib Int. Symp.: Punching Shear Test Of Structural Concrete Slabs: Honoring Neil M. Hawkins*, 2017, pp. 237–252.
- [88] A. Muttoni, J. T. Simões, D. M. V. Faria, and M. Fernández Ruiz, "A mechanical approach for the punching shear provisions in the second generation of Eurocode 2," *Hormig. Acero.*, 2023, In press, <http://dx.doi.org/10.33586/hya.2022.3091>.
- [89] J. B. Santos, A. Muttoni, and G. S. Melo, "Enhancement of the punching shear verification of slabs with openings," *Struct. Concr.*, pp. 1–18, 2022, In press, <http://dx.doi.org/10.1002/suco.202200714>.
- [90] S. Ravasini, F. Vecchi, B. Belletti, and A. Muttoni, "Verification of deflections and cracking of RC flat slabs with numerical and analytical approaches," *Eng. Struct.*, 2023, In press.
- [91] K. Qian, J.-S. Li, T. Huang, Y.-H. Weng, and X.-F. Deng, "Punching shear strength of corroded reinforced concrete slab-column connections," *J. Build. Eng.*, vol. 45, pp. 103489, 2022.
- [92] M. Góldyn and T. Urban, "UHPFRC hidden capitals as an alternative method for increasing punching of LWAC flat slabs," *Eng. Struct.*, vol. 271, pp. 114906, 2022, <http://dx.doi.org/10.1016/j.engstruct.2022.114906>.
- [93] A. Muttoni, "Shear in Members Without Shear Reinforcement", in *Introduction to the Swiss Code SIA 262*, Zürich, Switzerland: Swiss Eng. Archit. Document., 2003, pp. 47-55.[in French and German] [D0182].
- [94] M. Fernández Ruiz, A. Muttoni, and J. Sagaseta, "Shear strength of concrete members without transverse reinforcement: a mechanical approach to consistently account for size and strain effects," *Eng. Struct.*, vol. 99, pp. 360–372, 2015.
- [95] R. Vaz Rodrigues, "Shear strength of reinforced concrete bridge deck slabs," Ph.D. dissertation, EPFL, Lausanne, Switzerland, 2007.
- [96] R. Vaz Rodrigues, A. Muttoni, and M. Fernández Ruiz, "Influence of shear on rotation capacity of reinforced concrete members without shear reinforcement," *ACI Struct. J.*, vol. 107, no. 5, pp. 516–525, 2010.
- [97] R. Vaz Rodrigues, M. Fernández Ruiz, and A. Muttoni, "Shear strength of R/C bridge cantilever slabs," *Eng. Struct.*, vol. 30, pp. 3024–3033, 2008.
- [98] F. Natário, M. Fernández Ruiz, and A. Muttoni, "Shear strength of RC slabs under concentrated loads near clamped linear supports," *Eng. Struct.*, vol. 76, pp. 10–23, 2014.
- [99] R. Cantone, M. Fernández Ruiz, and A. Muttoni, "Shear force redistributions and resistance of slabs and wide beams," *Struct. Concr.*, vol. 22, no. 4, pp. 2443–2465, 2021.

- [100] S. Campana, M. Fernández Ruiz, A. Anastasi, and A. Muttoni, “Analysis of shear-transfer actions on one-way RC members based on measured cracking pattern and failure kinematics,” *Mag. Concr. Res.*, vol. 65, no. 6, pp. 386–404, 2013.
- [101] F. Cavagnis, M. Fernández Ruiz, and A. Muttoni, “An analysis of the shear transfer actions in reinforced concrete members without transverse reinforcement based on refined experimental measurements,” *Struct. Concr.*, vol. 19, pp. 49–64, 2018.
- [102] F. Cavagnis, J. T. Simões, M. Fernández Ruiz, and A. Muttoni, “Shear strength of members without transverse reinforcement based on development of critical shear crack,” *ACI Struct. J.*, vol. 117, no. 1, pp. 103–118, 2020.
- [103] F. Cavagnis, “Shear in reinforced concrete without transverse reinforcement: from refined experimental measurements to mechanical models,” Doctoral dissertation, EPFL, Lausanne, Switzerland, 2017.
- [104] A. Muttoni, M. Fernández Ruiz, and F. Cavagnis, “Shear in members without transverse reinforcement: from detailed test observations to a mechanical model and simple expressions for codes of practice,” in *fib Bulletin No. 85: Towards a Rational Understanding of Shear in Beams and Slabs*, International Federation for Structural Concrete, Ed., Lausanne, Switzerland: FIB, 2018, pp. 7–23.
- [105] A. Muttoni, M. Fernández Ruiz, and F. Cavagnis, “Shear in members without transverse reinforcement: from detailed test observations to a mechanical model and simple expressions for codes of practice,” in *Fib Int. Workshop on Beam Shear*, Zurich, Switzerland, Sep. 5-6 2016.
- [106] A. Muttoni and M. Fernández Ruiz, “From experimental evidence to mechanical modeling and design expressions: The Critical Shear Crack Theory for shear design,” *Struct. Concr.*, vol. 20, no. 4, pp. 1464–1480, 2019, <http://dx.doi.org/10.1002/suco.201900193>.
- [107] A. Pérez Caldentey, P. Padilla, A. Muttoni, and M. Fernández Ruiz, “Effect of load distribution and variable depth on shear resistance of slender beams without stirrups,” *ACI Struct. J.*, vol. 109, no. 5, pp. 595–603, 2012.
- [108] F. Cavagnis, M. Fernández Ruiz, and A. Muttoni, “A mechanical model for failures in shear of members without transverse reinforcement based on development of a critical shear crack,” *Eng. Struct.*, vol. 157, pp. 300–315, 2018.
- [109] C. R. Ribas González and M. Fernández Ruiz, “Influence of flanges on the shear-carrying capacity of reinforced concrete beams without web reinforcement,” *Struct. Concr.*, vol. 18, no. 5, pp. 720–732, 2017.
- [110] S. Campana, M. Fernández Ruiz, and A. Muttoni, “Shear strength of arch-shaped members without transverse reinforcement,” *ACI Struct. J.*, vol. 111, no. 3, pp. 573–582, 2014.
- [111] F. Natário, M. Fernández Ruiz, and A. Muttoni, “Experimental investigation on fatigue of concrete cantilever bridge deck slabs subjected to concentrated loads,” *Eng. Struct.*, vol. 89, pp. 191–203, 2015.
- [112] M. Fernández Ruiz, C. Zanuy, F. Natário, J.-M. Gallego, and A. Muttoni, “Influence of fatigue loading in shear failures of reinforced concrete members without transverse reinforcement,” *J. Adv. Concr. Technol.*, vol. 13, pp. 263–274, 2015.
- [113] R. Cantone, A. Setiawan, M. Fernández Ruiz, and A. Muttoni, “Characterization of shear deformations in reinforced concrete members without shear reinforcement,” *Eng. Struct.*, vol. 257, pp. 113910, 2022.
- [114] Swiss Society of Engineers and Architects, *Code 162 for Concrete Structures*, 1989.
- [115] Comité Euro-International du Béton, *CEB-FIP Model Code 1990*, 1993.
- [116] International Federation for Structural Concrete, *fib Model Code for Concrete Structures 2010*. Berlin, Germany: Ernst & Sohn, 2013.
- [117] A. Muttoni, M. Fernández Ruiz, E. Bentz, S. J. Foster, and V. Sigrist, “Background to the Model Code 2010 Shear Provisions - Part II Punching Shear,” *Struct. Concr.*, vol. 14, no. 3, pp. 195–203, 2013.
- [118] European Committee for Standardization, *Eurocode 2 - Design of Concrete Structures - Part 1-1: General Rules - Rules for Buildings, Bridges and Civil Engineering Structures*, Final Draft FprEN 1992-1-1:2023, 2023.
- [119] P. Huber, T. Huber, and J. Kollegger, “Investigation of the shear behavior of RC beams on the basis of measured crack kinematics,” *Eng. Struct.*, vol. 113, pp. 41–58, 2016.
- [120] M. P. Collins and D. Kuchma, “How safe are our large, lightly reinforced concrete beams, slabs, and footings,” *ACI Struct. J.*, vol. 96, pp. 482–490, 1999.
- [121] E. G. Sherwood, E. C. Bentz, and M. P. Collins, “Effect of aggregate size on beam-shear strength of thick slabs,” *ACI Struct. J.*, vol. 104, pp. 180–190, 2007.
- [122] European Committee for Standardization, *Eurocode 2. Design of Concrete Structures - Part 1-1: General Rules and Rules for Buildings*, EN 1992-1-1:2004, 2004.
- [123] A. Muttoni, M. Fernández Ruiz, F. Cavagnis, and J. T. Simões, “Shear in members without shear reinforcement,” in *Background Document To FprEN 1992-1-1:2023-04 (Formal-Vote-Draft)*, CEN/TC 250/SC 2: Eurocode 2: Design of Concrete Structures, Ed., Italy, Eurocode, 2021, pp. 1–17.
- [124] D. A. Hordijk, “Tensile and tensile fatigue behaviour of concrete, experiments, modelling and analyses,” *Heron*, vol. 37, no. 1, pp. 3–79, 1992.
- [125] B. C. Jensen, “Lines of discontinuity for displacements in the theory of plasticity of plain and reinforced concrete,” *Mag. Concr. Res.*, vol. 2, no. 2, pp. 143–150, 1975.
- [126] H. Kupfer, K. H. Hubert, and H. Rusch, “Behavior of concrete under biaxial stresses,” *ACI J. Proc.*, vol. 66, no. 52, pp. 656–666, 1969.

- [127] J. Einpaul, "Punching strength of continuous flat slabs," Ph.D. dissertation, EPFL, Lausanne, Switzerland, 2016.
- [128] A. Muttoni et al., "Punching," in *Background document to FprEN 1992-1-1:2023-04 (Formal-Vote-Draft)*, CEN/TC 250/SC 2: Eurocode 2: Design of Concrete Structures, Ed., Italy, Eurocode, 2023, pp. 338–357.
- [129] A. Muttoni and Q. Yu, "Partial safety factor for strain-based formulae," in *Fib TG3.1*, Oslo, Norway, Jun. 2022, pp. 1–12.
- [130] A. Muttoni and M. Fernández Ruiz, "Levels-of-approximation approach in codes of practice," *Struct. Eng. Int.*, vol. 22, no. 2, pp. 190–194, 2012.
- [131] American Concrete Institute Committee, *Building Code Requirements for Structural Concrete and Commentary*, ACI Code 318-19 (22) (Reapproved 2022), 2022.
- [132] Comité Euro-International du Béton, *CEB-FIP Model Code for Concrete Structures*, 1978.
- [133] M. Vanderbilt, "Shear strength of continuous plates," *J. Struct. Div.*, vol. 8, no. 5, pp. 961–973, 1972.

Author contributions: AM: conceptualization, writing; JTS: conceptualization, writing.

Editors: Leandro Trautwein, Mauro Real, Mario Pimentel.



ORIGINAL ARTICLE

Investigation of aggregate interlock contribution to shear strength of reinforced concrete and steel fiber reinforced concrete beams

Investigação da contribuição do engrenamento dos agregados em vigas de concreto armado e concreto reforçado com fibras de aço

Leticia Col Debella^a Luis Alberto Montoya-Coronado^b Thomás Lima de Resende^c Ricardo Pieralisi^d ^aUniversidade Federal do Paraná – UFPR, Programa de Pós-graduação em Engenharia Civil – PPGEC, Curitiba, PR, Brasil^bUniversidad de las Islas Baleares – UIB, Departamento de Ingeniería Industrial y de Construcción, Palma, España^cUniversidade Federal dos Vales do Jequitinhonha e Mucuri – UFVJM, Instituto de Ciência, Engenharia e Tecnologia, Teófilo Otoni, MG, Brasil^dUniversidade Federal do Paraná – UFPR, Centro de Estudos em Engenharia Civil – CESEC, Programa de Pós-graduação em Engenharia Civil (PPGEC), Curitiba, PR, Brasil

Received 20 September 2022

Accepted 31 March 2023

Abstract: Shear strength in reinforced concrete (RC) beams, especially in steel fiber reinforced concrete (SFRC) beams is a subject of great interest in structural engineering. In the case of beams without transverse reinforcement, the failure is explained based on a predefined crack pattern and kinematics, and the transfer of shear force accomplished through different mechanisms. Among these mechanisms, the aggregate interlock is present in most of the existing shear strength mechanical models in the literature, with divergences regarding its performance and preponderance. Thus, this paper focuses on evaluating the contribution of aggregate interlock throughout the critical crack formation process up to the ultimate load by performing bending tests on small-scale rectangular RC and SFRC beams without considering the effect of transverse reinforcement. The Digital Image Correlation (DIC) technique is used to track the patterns of shear cracks and their associated kinematics by measuring the relative displacements of opening (w) and sliding (δ). A detailed description of the shear behavior of these beams is provided by quantifying the aggregate interlock using the simplified Walraven model. The results help to understand the level of contribution of the aggregate interlock, and the main differences between structural elements of concrete with and without steel fibers in the scope of the shear strength.

Keywords: steel fiber reinforced concrete, aggregate interlock, shear.

Resumo: A resistência à força cortante em vigas de concreto armado (CA), especialmente em vigas de concreto reforçado com fibras de aço (CRFA), é um assunto de grande interesse na engenharia estrutural. No caso de vigas sem armadura transversal, a falha é explicada com base em um padrão de fissura pré-definido e sua cinemática, e a transferência da força cortante é feita por diferentes mecanismos. Dentre esses mecanismos, o engrenamento dos agregados está presente na maioria dos modelos existentes na literatura, havendo divergências quanto ao seu desempenho e preponderância. Assim, este trabalho se concentra em avaliar a contribuição do engrenamento dos agregados ao longo do processo de formação das fissuras críticas até a carga última, realizando ensaios de flexão em vigas retangulares de CA e CRFA de pequena escala sem levar em consideração o efeito da armadura transversal. A técnica de Correlação de Imagem Digital (CID) é usada para rastrear os padrões de fissuras de cisalhamento e suas cinemáticas associadas, medindo os deslocamentos relativos de abertura (w) e deslizamento (δ). Uma descrição detalhada do comportamento à força cortante dessas vigas é fornecida pela quantificação do engrenamento dos agregados, usando o modelo simplificado

Corresponding author: Leticia Col Debella. E-mail: leticiacoldebella@hotmail.com

Financial support: This study was financed in part by the Coordenação de Aperfeiçoamento de Pessoal de Nível Superior – Brasil (CAPES) – Finance Code 001, CNPq/MCTI/FNDCT Nº 18/2021 422189/2021-9; RTI2018-099091-B-C22 by 2 MCIN/AEI/10.13039/501100011033 and by “ERDF A way of making Europe”; and BIA2015-3 64672-C4-3-R (AEI – FEDER, UE).

Conflict of interest: Nothing to declare.

Data Availability: The data that support the findings of this study are available from the corresponding author, L. C. Debella, upon reasonable request.



This is an Open Access article distributed under the terms of the Creative Commons Attribution License, which permits unrestricted use, distribution, and reproduction in any medium, provided the original work is properly cited.

de Walraven. Os resultados ajudam a entender o nível de contribuição do engrenamento dos agregados e as principais diferenças entre elementos estruturais de concreto com e sem fibras de aço no âmbito da força cortante

Palavras-chave: concreto reforçado com fibras de aço, engrenamento dos agregados, cisalhamento.

How to cite: L. C. Debella, L. A. Montoya-Coronado, T. L. Resende, and R. Peralisi, "Investigation of aggregate interlock contribution to shear strength of reinforced concrete and steel fiber reinforced concrete beams" *Rev. IBRACON Estrut. Mater.*, vol. 16, no. 3, e16303, 2023, <https://doi.org/10.1590/S1983-41952023000300003>

1 INTRODUCTION

The shear strength of reinforced concrete (RC) elements without transverse reinforcement may be resisted by different shear transfer actions that depend directly on the cracking pattern and its kinematics at the failure load [1]. During the shear failure process in beams without major arching effects, the shear transfer mechanisms that act are the residual stress; the dowel action; the height of the compressed zone; and the aggregate interlock [2].

Studies conducted by [3] and [4] have shown that the direct shear transfer capacity of cracked concrete in steel fiber reinforced concrete (SFRC) beams is significant with the use of fibers. However, there is currently no consensus among researchers regarding the development of critical cracks and activation of failure mechanisms during the process of crack formation leading up to the failure load for both traditional RC and SFRC [4], [5].

The aggregate interlock is one of the most controversial and debated shear transfer actions. Yang et al. [6] proposed a model where the aggregate interlock is the primary shear failure mechanism in conventional RC beams without transverse reinforcement. Other authors [7]–[11] have also suggested that the aggregate interlock plays a significant role in shear transfer. These authors have demonstrated that the mechanism represents a high percentage of shear in the failure process of RC elements, although its contribution may be variable.

In recent years, there have been differences among authors regarding the influence of aggregate interlock on the shear strength of SFRC. For example, in [4] and [12], the authors consider that aggregate interlock has an insignificant contribution to the shear strength. However, in [13] and [14] the authors state that the aggregate interlock is one of the most preponderant mechanisms in the failure of SFRC elements. The authors of [15] and [16] proposed a model that combines the aggregate interlock and pullout equations of steel fibers, claiming that it represents SFRC elements mechanically. Additionally, [17] demonstrates the influence of adding steel fibers to some aggregate interlock models.

This paper aims to evaluate the contribution of aggregate interlock in the process of critical crack formation up to failure load in both traditional RC and RC-SFRC beams. Flexural tests were conducted on small-scale rectangular beams without stirrups. Digital Image Correlation (DIC) technique was used to track critical shear cracking patterns and their associated kinematics throughout the experiment. Geometric characteristics, such as the shape and origin of the cracks, were identified [8]. The simplified Walraven's model [18] was employed to describe the behavior of aggregate interlock during the experimental test. The study provides a detailed understanding of the contribution of steel fibers in the behavior and mechanisms of shear transfer in SFRC structural elements.

2 SHEAR TRANSFER ACTIONS ON CONCRETE ELEMENTS

ACI-ASCE Committee 426 [19] identifies several mechanisms that may transmit internal forces between cracked sections in RC structures subjected to shear stresses. Figure 1 illustrates the main shear transfer actions: the vertical components of the residual stress (V_R); the uncracked compression zone (V_C); the aggregate interlock (V_{agg}); the dowel action (V_D); and, in the case of SFRC, the contribution of the steel fibers (V_F). Additionally, Figure 1 shows the arch action (V_{ARC}), which is related to the theoretical strut of the beam [20].

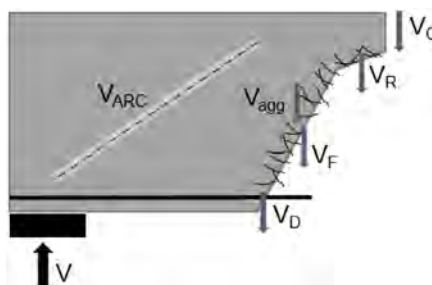


Figure 1. Shear transfer mechanisms in an SFRC beam

In SFRC beams, fibers provide additional tensile capacity along the crack [4], [13], [16]. In the compression zone of the cross-section, uncracked concrete provides shear strength. The residual stress capability comes from the aggregates, which allow the stress to be carried across the crack when the crack width opening (w) is small and there is no sliding (δ). The dowel action is the result of the interaction between the longitudinal rebars and the concrete that surrounds them, generating a sliding displacement (δ) in the fractured plane of the concrete [17]. The arch action of the theoretical strut assumes that no load is transferred through the cracks, and an inclined tension tie balances that shear forces. When the tensile strength of the concrete is reached in the tie, the bending crack propagates and the contribution of the strut is reduced [8], [9].

The aggregate interlock is a result of the contact forces between the aggregates that cross the critical shear crack, allowing the development of shear stresses due to the roughness of the cracked concrete [21]. In the case of the addition of steel fibers, the stress transfer bridge they provide may result in higher values of crack opening (w) and sliding (δ) compared to conventional concrete. This fact may lead to the overestimation of the level of contribution of aggregate interlock [15]–[17].

Walraven [18] proposed a theoretical model for the aggregate interlock shear transfer mechanism. The author approached the physical context of the aggregate interlock, which allowed for the relationship between the opening (w) and sliding (δ) between the cracked surfaces to the normal (σ) and tangential (τ) stresses transferred along critical cracks. The two-phase model (TPM) is mathematically complex, and its formulation makes it difficult to solve without numerical procedures. Therefore, Reinhardt and Walraven [22] proposed a simplified solution with linear equations as follows:

$$\sigma = -\frac{f_{cu}}{20} + [1.35w^{-0.63} + (0.19w^{-0.552} - 0.15)f_{cu}]\delta \tag{1}$$

$$\tau = -\frac{f_{cu}}{30} + [1.8w^{-0.8} + (0.234w^{-0.707} - 0.12)f_{cu}]\delta \tag{2}$$

where f_{cu} is the average compressive strength of cubic specimens (MPa), w is the crack width (mm) and δ is the crack sliding (mm).

The linear model equations were obtained by adapting the original model. This simplified model is limited by a maximum aggregate diameter (D_{max}) less than 32 mm and a compressive strength (f_{cu}) less than or equal to 59 MPa, both of which are met in the present study. In general, the original TPM model produces more stable results [15]–[17], [22] compared to the linear model, although the values are similar. Figure 2 shows the comparison between the two models, reiterating that, despite being more stable, the original TPM provides values close to the linear TPM. It should be noted that the work of Montoya-Coronado et al. [23] demonstrates that for low longitudinal reinforcement ratios (less than $\rho = 0.92$), the Walraven model overestimate the contribution of V_{agg} . This aspect was considered in this experimental campaign to ensure the accuracy of the results.

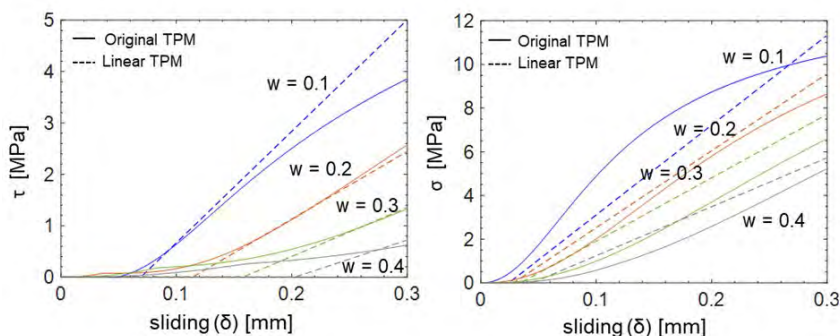


Figure 2. Sliding and opening obtained with the linear simplify TPM and the original TPM

3 CRITICAL SHEAR CRACKS KINEMATICS

Cavagnis et al. [8] employed Digital Image Correlation (DIC) to evaluate the shear transfer mechanisms in traditional RC beams without transverse reinforcement. The authors observed that the failure of the structural

components is closely related to kinematics of cracks, such as the appearance and propagation of critical cracks. Furthermore, Cavagnis et al. [8] noted that critical shear failure may be governed by different mechanisms for beams with similar characteristics, such as concrete dosage and beam geometry. These observations confirmed the conflicting ideas about the existing shear models, particularly the influence of the aggregate interlock contribution on shear strength. This mechanism is more affected by cracks kinematics than any other material characteristic or specificity [8].

Figure 3 illustrates the types of cracks that may appear during shear failure in RC beams under flexure test conditions [8], which can be categorized as follows:

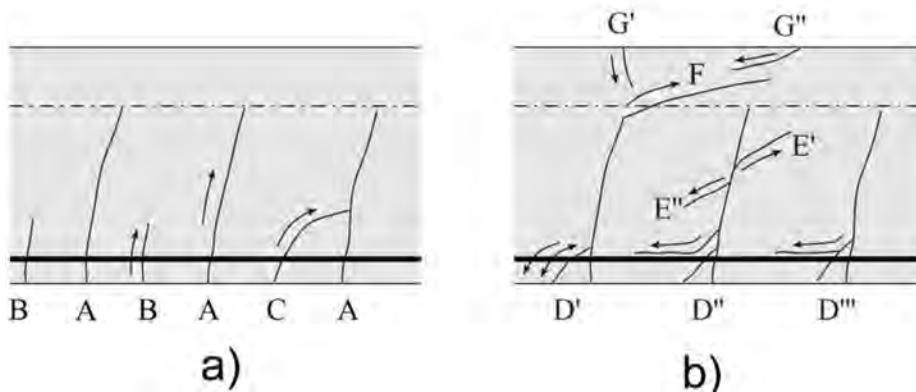


Figure 3. Types of cracks: (a) primary and secondary bending cracks; and (b) cracks caused by shear transfer actions. Source: Cavagnis et al. [8]

- Type A (Figure 2a): primary flexural cracks. These cracks arise from bending moments and typically one of them becomes the critical crack as the load increases.
- Type B (Figure 2a): secondary flexural cracks. These cracks occur between two primary flexural cracks or near the beam supports.
- Type C (Figure 2a): secondary or primary flexural cracks that merge with another primary flexural crack.
- Type D (Figure 2b): dowel cracks that develop at the same level of the flexural reinforcement. They typically join an inclined crack from the surface of the specimen to a primary flexural crack (type A) and often originate at low load levels.
- Type E (2-b): aggregate interlock induced cracks. These cracks form on either side of an existing crack and usually stem from primary or secondary bending cracks that transfer shear by aggregate interlock.
- Type F (Figure 2b): Propagation of a primary flexural crack within the compression zone. This occurs with a flat crack originating from a primary flexural crack, and usually happens at load levels near to failure.
- Type G (Figure 2b): Development of a crack within the compression zone not originating from a primary flexural crack. These cracks develop perpendicularly to the beam edge (G') due to the local bending of the compression chord, or at plane angles near to the load introduction region (G'') due to the large shear forces in the compression zone and /or crushing of the compression chord.

4 EXPERIMENTAL PROGRAM

4.1 Specimens

Nine rectangular (10 x 20 cm) beams were produced, each with a length of 100 cm, resulting in an effective span of 90 cm. The beams were reinforced with rebars and steel fibers, except for three control beams that were only reinforced with rebars. The conventional reinforcement consisted of 2 bars with a diameter of 12.5 mm at the bottom ($\rho = 1.25\%$) and 2 bars with a diameter of 8.0 mm at the top ($\rho = 0.5\%$) of the section, all 4 arranged longitudinally. Additionally, 5.0 mm diameter stirrups were used every 60 mm in the transversal direction in the unmonitored half of the beam to ensure shear failure at other side of the beam (see Figure 4). The nominal concrete cover for the longitudinal and transversal reinforcement was 15 mm.

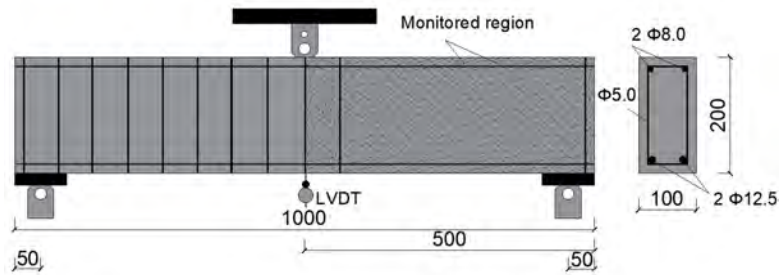


Figure 4. Conventional reinforcement of the beams (units in mm).

4.2 Materials and concrete compositions

A conventional concrete composition (C0) was prepared as a control for the RC beams, along with two SFRC compositions that varied in fiber content. Slightly adjustments were made to the proportion of material and super-plasticizer content to maintain consistency (slump of 100 ± 10) in the fresh state mixes. The experimental program employed Cement type CII F, natural sand, and basaltic coarse aggregate, with maximum diameter (D_{max}) of 12.7mm. The water-to-cement (w/c) was kept constant to ensure similar compressive strength. Hooked-end steel fiber contents of 0.5% (C0.5) and 1.0% (C1.0) in volume (40 kg/m³ and 80 kg/m³, respectively) were tested, and the primary fiber characteristics are shown in Table 1. In addition, super-plasticizer of type Muraplast FK 25 from MC-Bauchemie was used to reduce variations in the fresh-state properties of the concrete during the casting process. Table 2 summarizes the compositions used, along with the reference name assigned to each mix.

Table 1. Steel fiber characteristics

Dramix ® 3D 45/30 BL	
Length l_f (mm)	30
Diameter d_f (mm)	0.62
Aspect ratio (l_f/d_f)	45
Tensile strength f_y (MPa)	1100
Nominal Young's modulus (GPa)	210
Nominal unit weight (g/cm ³)	7.85

Table 2. Characteristics of the concrete

Material	C0	C0.5	C1.0
Cement (kg/m ³)	468	468	468
Sand (kg/m ³)	684.9	684.9	684.9
Coarse aggregate (kg/m ³)	1013.9	1007.3	1000.6
w/c	0.45	0.45	0.45
Superplasticizer (kg/m ³)	0	1.04	1.08
Fiber volume (%)	0	0.5	1

The beams were cast by pouring concrete in accordance with EN 14651 [24], with the central increment being twice the lateral increments. Additionally, also following EN 14651 [24], the molds were filled up to 90% of the volume, and the remaining 10% were filled during vibration. The molds, filled with concrete, were vibrated externally to ensure uniform distribution. The beams were removed from the molds within 24 hours of casting, cured under a plastic sheet for 28 days, and then kept under laboratory conditions until the testing date. Prior to conducting the tests, the side face of the beam dimensioned to fail by shear was painted with a set of randomly spaced points (speckles) with adequate contrast to the surface. This painting is necessary to monitor the occurrence and propagation of cracks using the Digital Image Correlation (DIC) technique (for further details, refer to Section 4.3).

Moreover, for each composition, 8 cylindric samples ($\Phi 100 \times 200$ mm) and 5 prismatic samples (150 x 150 x 550 mm) were cast to characterize the compressive (f_{cm}) (in accordance with NBR 5739: 2018 [25]) and flexural tensile strength ($f_{t,fl}$) (in accordance with NBR 16940:2021 [26]), respectively. The results of this characterization are presented in Table 3, with

the coefficient of variation of the tests in parentheses. Also in Table 3, $f_{R1}, f_{R2}, f_{R3}, f_{R4}$ are the residual flexural strength referring to the crack openings of 0.5 mm, 1.5 mm, 2.5 mm, and 3.5 mm, respectively.

Table 3. Results of the characterization of concrete

		C0	C0.5	C1.0
Flexural Strength	f_{fl} (MPa)	3.39 (10.7%)	4.02 (7.9%)	4.87 (12.5%)
	f_{R1} (MPa)	1.19 (22.3%)	3.29 (16.0%)	4.82 (13.1%)
	f_{R2} (MPa)	[-]	3.11 (17.8%)	4.25 (12.7%)
	f_{R3} (MPa)	[-]	2.72 (20.2%)	3.68 (10.3%)
	f_{R4} (MPa)	[-]	2.27 (18.2%)	3.03 (7.9%)
Compressive Strength	f_{cm} (MPa)	31.14 (4.3%)	35.56 (1.4%)	39.75 (4.3%)

4.3 Test setup

Flexural tests were conducted using an EMIC 23-300 Universal Testing System (from INSTRON®), which has a maximum capacity of 300 kN. The beams were simply supported by two steel roller supports, resulting in a theoretical shear span of 450 mm and the shear span to depth (a/d) of 2.58. During the loading procedure, deflection at the center of the span was measured using a displacement transducer. The test was performed with displacement control at a rate of 0.02 mm/min, enabling a clear observation of crack development and propagation.

In addition, a Canon DSLR EOS Rebel SL3 camera equipped with an EF-S 40mm lens was used to record the test. The camera was placed perpendicular to the surface of the beam. The video was captured at 4 frames per second for each specimen, and a white light reflector was used during image capture to prevent shadows (see Figure 5). Boulekbache et al. [27] provide detailed information on the specimen preparation and DIC measurement technique for the test. The deformation and displacement fields were obtained using GOM Correlate software [28].

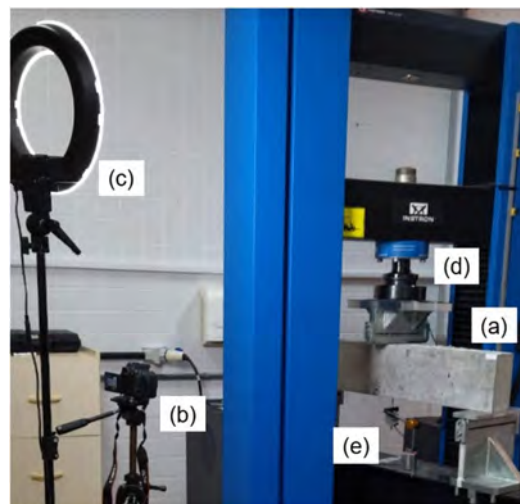


Figure 5. DIC test procedure. a) simply supported beam tested, b) Canon camera, c) light reflector, d) INSTRON press, e) LVDT

Figure 6 illustrates the crack discretization process used for measuring relative displacements (opening w and sliding δ) along the cracks (Figure 6a). Initially, each crack was divided into approximately 8 straight lines (Figure 6b). Each straight line was further subdivided into a set of segments with a length limited to the maximum diameter of the aggregate, as suggested by Cavagnis [9] (Figure 6c). The appropriate trigonometric manipulations of the horizontal and vertical measurements between the control points obtained throughout the experimental test were used to determine the relative displacements of crack opening (w) and sliding (δ). Figure 6 illustrates the crack discretization and the control points on both sides of the opening. Recently, Koščák et al. [29] and Assis et al. [30] presented a similar methodology and concluded that it was effective in measuring relative displacements.

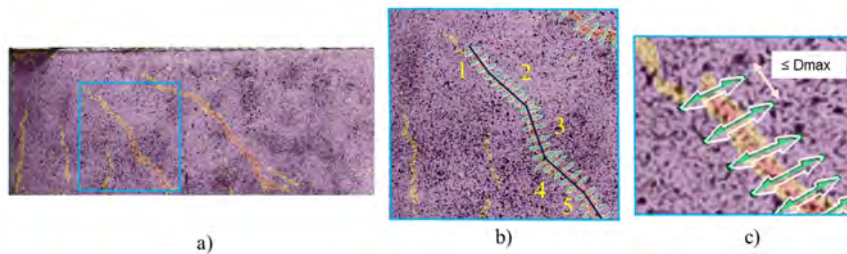


Figure 6. a) shear crack shown as major deformation in DIC, b) crack discretization and c) distance between segments limited by D_{max}

The values of w and δ were used in the Walraven aggregate interlock simplify model (Equation 1 and 2), and transformed into shear force (V_{agg}), as follows:

$$V_{agg} = b_w \left[\int_0^{lcr} \tau \sin(\alpha) dl - \int_0^{lcr} \sigma \cos(\alpha) dl \right] \tag{3}$$

where b_w is the width of the beam, lcr is the total length of the analyzed critical crack, dl is the length for each segment, τ and σ are the tangential and normal stresses, respectively, from the Walraven equation (Equation 1 and 2), and α is the angle between the segment and the horizontal axis.

5 RESULTS AND DISCUSSIONS

The analysis of the results is organized in four subsections. The first three subsections describe the particularities observed during the initiation and propagation of cracks in individual tests carried out on RC beams without fiber reinforcement (C0), with a volume of 0.5% of fibers (C0.5) and with a volume of 1.0% of fibers (C1.0), respectively. The final subsection presents a comparison between all the results obtained.

5.1 Conventional concrete (C0)

Figure 7 shows the shear forces versus mid-span deflection curve with the identification of the moments where cracks arose and the maximum load. The cracks are presented based on the description provided in section 3, with the flexural cracks indicated by the abbreviation FC.

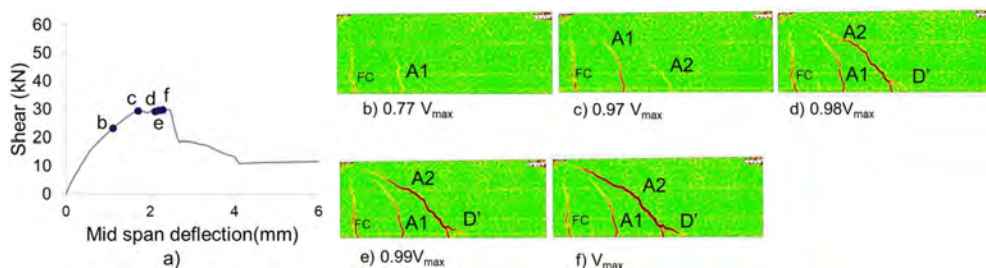


Figure 7. a) Shear force vs displacement curve, and cracking development of C0 in b) $0.77V_{max}$, c) $0.97V_{max}$, d) $0.98V_{max}$, e) $0.99V_{max}$, and f) V_{max}

During the experimental test, at 77% of the maximum shear (Figure 7b), the first shear crack A1 appeared. From that moment on, the relative displacements of opening (w) and sliding (δ) were measured at A1. Later, at another point in time (Figure 7c), another inclined crack (A2) appeared at the longitudinal reinforcement height, and the relative displacements of opening (w) and sliding (δ) for the A2 crack were subsequently measured.

To understand the influence of the aggregate interlock on the cracking process, Figure 8 shows the development of this mechanism throughout the experimental test, measured for the two main critical shear cracks (A1 and A2). It is

important to note that the coordinate axis in Figure 8 represents the amount of the aggregate interlock expressed in terms of shear force for each instant of time in the experimental test. The abscissa axis represents the rate between the shear force at a given point and its maximum value, from beginning of the test to the failure load. The solid grey line represents the experimental shear force applied to the simply supported beams, presented as the applied force (V) divided by the maximum force resisted by the beam (V_{max}). In Figure 8, V represents the punctual shear, V_{agg} represents the shear force attributed to the aggregate interlock, and V_{crit} represents the shear force at which crack opening occurs.

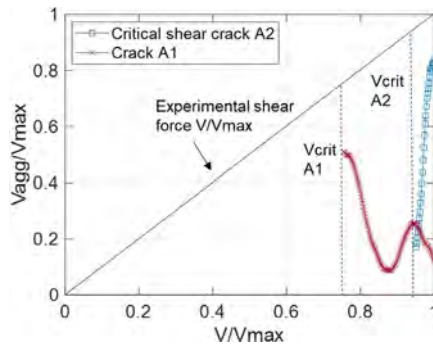


Figure 8. Aggregate interlock through the experimental test for cracks A1 and A2

In Figure 8, the blue curve represents the quantification of aggregate interlock on the critical crack (A2) throughout the experimental test. The A2 curve shows a significant increase in the contribution of aggregate interlock soon after its appearance, already at 97% of the maximum load V_{max} . The connection of a crack type D' with the critical crack triggers a larger opening w in this region, but there is no loss of the aggregate interlock mechanism due to the concomitant development of the crack towards the top of the beam, where the sliding (δ) continues to develop and transfer the aggregate interlock. Figure 9a shows the opening w , and Figure 9b shows the sliding (δ) at different times as a percentage of the maximum load V_{max} . An increase in sliding (δ) was observed in the steepest parts of the A2 crack, as mentioned, keeping the aggregate interlock contribution high. For a better understanding of the aggregate interlock curves, Figure 9 shows the opening and sliding of the two cracks (A1 and A2) throughout the evolution of the applied shear force, until the rupture in V_{max} .

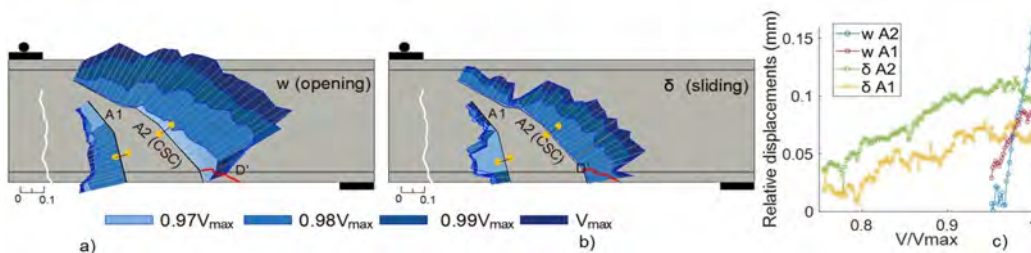


Figure 9. a) opening (w), b) sliding (δ) and c) relative displacements as a function of load variation for beam C0

Concerning the first crack A1, the contribution of aggregate interlock showed a constant decline shortly after its appearance. Figure 9 depicts that the crack widened significantly more than the sliding throughout all the experimental test while the load increased up to failure. The primary reason for this is that the crack A1 remained nearly vertical.

It is important to note that opening (w) and sliding (δ) do not exhibit a fully ascending curve of values (Figure 9c). As cracks propagate, certain sections of these cracks may increase, decrease, or stabilize relative displacements. Depending on the current opening (w) and sliding (δ) combination, the aggregate interlock equation may transmit this phenomenon, oscillating between increasing and decreasing sections of the mechanism. Additionally, cracks initiate at one point and propagate towards the top surface of the beam. Thus, as the load progress, the crack propagates further, and more opening (w) and sliding (δ) measurements are taken. The variations in the aggregate interlock curves are a result of this variation since one section of the crack may have increasing opening development while another section

is still in its initial stages. The contribution of the aggregate interlock near the tensile reinforcement differs from that of the crack tip. Also, this variation may be due to redistribution and activation of other shear force transfer mechanisms.

The moment when the opening (w) of the critical crack A2 at 97% of the maximum load (Figure 7c) and the negligible contribution of the aggregate interlock of the crack A1 at practically the same instant indicate that another shear mechanism is responsible for transmitting the shear force on the beam. The works of Cavagnis et al. [8], and [30] suggest that, in shear failure, the load is initially resisted by mechanisms other than aggregate interlock. When the load application region is near the support, a secondary physical phenomenon, known as the arching action, can contribute to the direct transmission of loads to the support. For small values of a/d , cracks do not propagate through the inclined strut, and other shear modes such as shear-compression failure and arch action are observed. For larger values of a/d , flexure-shear cracks develop through the inclined struts, and a diagonal tension failure is observed. The shear span to depth ratio (a/d) influences the failure mode, as known from Kani's valley [32] and [33]. According to Kani [32], the limiting relationship can be $a/d = 2.5$. However, the author emphasizes that the a/d limit is not entirely decisive, and the mechanical behavior depends on other factors, such as the longitudinal reinforcement ratio.

When the theoretical compressed strut may develop undisturbed by the presence of a shear crack, the plastic shear strength solution may be applied. In such case, direct transmission occurs between the point of application and the support of the specimen. Figure 10 illustrates this phenomenon, where all the shear cracks emerge and propagate below a straight line connecting the load application point and the support, indicating that the theoretical strut has not been disturbed.

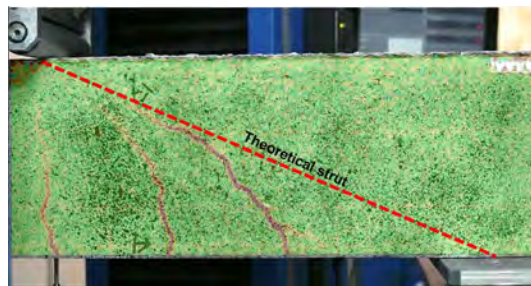


Figure 10. Theoretical strut developed without crack disturbances

Failure occurs when the critical crack crosses the theoretical strut (Figure 6e). In other words, the failure did not occur due to the loss of aggregate interlock linked to a larger crack opening, but rather due to the interruption of transmission by the compressed strut.

5.2 Concrete with 0.5% of steel fiber (C0.5)

Figure 11 illustrates the shear force versus mid-span deflection curve and the development of the cracking process for the beam made of concrete with a steel fiber content of 0.5% in volume (C0.5). Additionally, the flexural cracks that emerged in the middle of the beam span are identified as FC.

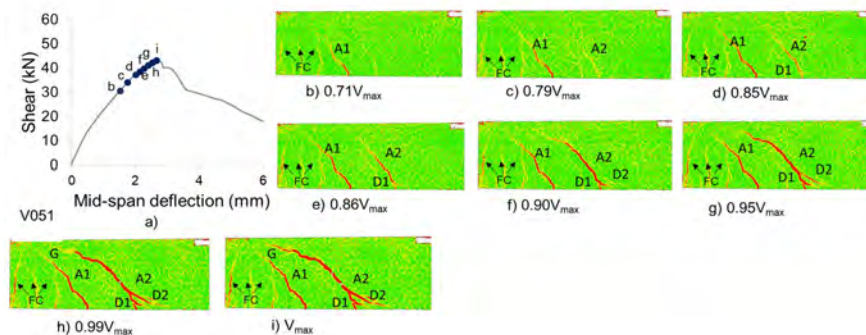


Figure 11. a) Shear force vs mid-span deflection curve, and cracking development of C0.5 in b) $0.71V_{max}$, c) $0.79V_{max}$, d) $0.85V_{max}$, e) $0.86V_{max}$, f) $0.9V_{max}$, g) $0.95V_{max}$, h) $0.99V_{max}$, i) V_{max}

Figure 11 illustrates the relative displacements measured for crack A1 from 71% of the maximum load V_{max} and for crack A2 from 79% of V_{max} , while Figure 12 shows the contribution of the aggregate interlock throughout the experimental test for both critical shear cracks.

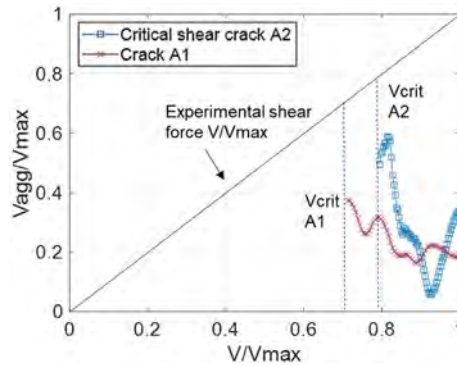


Figure 12. Aggregate interlock throughout the experimental test for the cracks A1 and A2

A D-type crack starts in the vicinity of A2 at 85% de V_{max} (Figure 11d), and soon after, at 86% de V_{max} (Figure 11e), joins A2. This union between D1 and A2 causes an increase in crack opening (w), resulting in a small drop in the contribution of the aggregate interlock, as shown in Figure 13b. This decrease in the contribution of the aggregate interlock due to the union between a type A and a type D crack was also observed in [8] and [31]. The phenomenon is repeated with the union of a new crack, D2, which joins A2 at 95% of V_{max} , again causing a sharp increase in opening (w) and consequently, loss of aggregate interlock. This drop can also be observed in Figure 13b, where the moment before and after the union of cracks A2 and D2 is detailed.

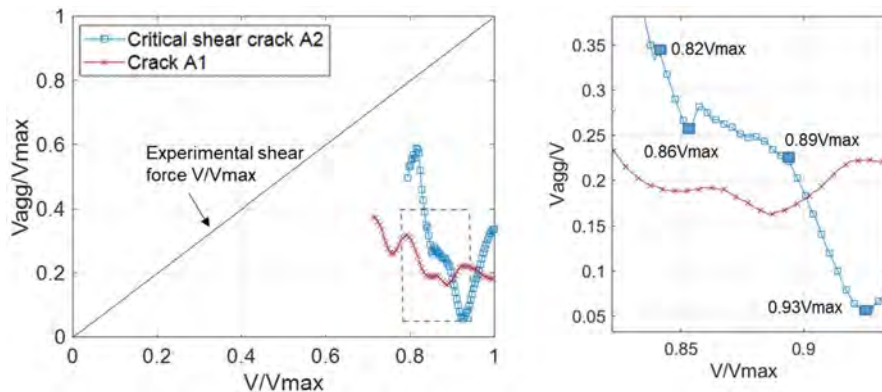


Figure 13. Decrease in the contribution of aggregate interlock due to the union of the crack D1 (0.82 and 0.86 of V_{max}) and D2 (0.89 and 0.93 of V_{max}) with A2

In Figure 11f, the almost horizontal portion develops in the A2 crack develops into a critical crack. The almost horizontal portion activates the residual stress mechanism of the concrete, which is characterized by pure tension without sliding (mode I), according to Yang et al. [6]. Figure 14b confirms that the sliding in the almost horizontal region of the A2 crack is very low, which is consistent with the literature. At this point, the residual stress becomes the main mechanism responsible for the transfer of shear force, with aggregate interlock present only in the steepest part of the crack where there is more sliding, as shown in Figure 14. These observations are consistent with those reported by Cavagnis et al. [8].

The variation of the aggregate interlock between higher and lower values, as shown in the Figure 12, follows the same reasoning presented for concrete C0. In other words, there is variation in both specific opening (w) and sliding (δ) measurements along the crack, where, as the load increases, more parts of the crack are activated.

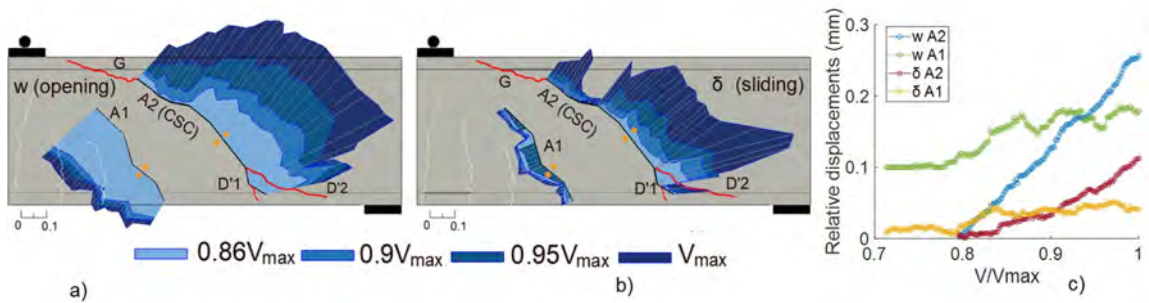


Figure 14. a) opening (w) b) sliding (δ) and c) relative displacements as a function of load variation for beam C0.5

The propagation of critical cracks is accompanied by the action of steel fibers, which act as a transfer bridge and regulate the crack opening, preventing brittle failure. This can be justified by observing the failure mechanism in the beams without fibers (C0) in the present work. With the predominant arching action, the shear cracks did not affect the compressed strut. Failure of the beams without fibers occurred when the compressed zone was crossed by the propagation of one of the main critical cracks, preventing the development of other shear transfer mechanisms due to the absence of large slidings (δ) and openings (w) associated with crack propagation.

After the union of crack D2 to A2, the aggregate interlock increases again from the steepest parts of the crack up to 0.99 of V_{max} . In fact, Figure 14 shows that even in the failure, there were significant values of crack opening (w), but there was also sliding (δ).

At 99% of failure (Figure 12h), a type G crack begins to propagate along the theoretical compressed strut due to the large shear forces in the compressed zone. At 99.9% of V_{max} , crack G merges with the critical crack leading to collapse. Figure 15 illustrates in detail the development of this crack G and its union with the critical crack.

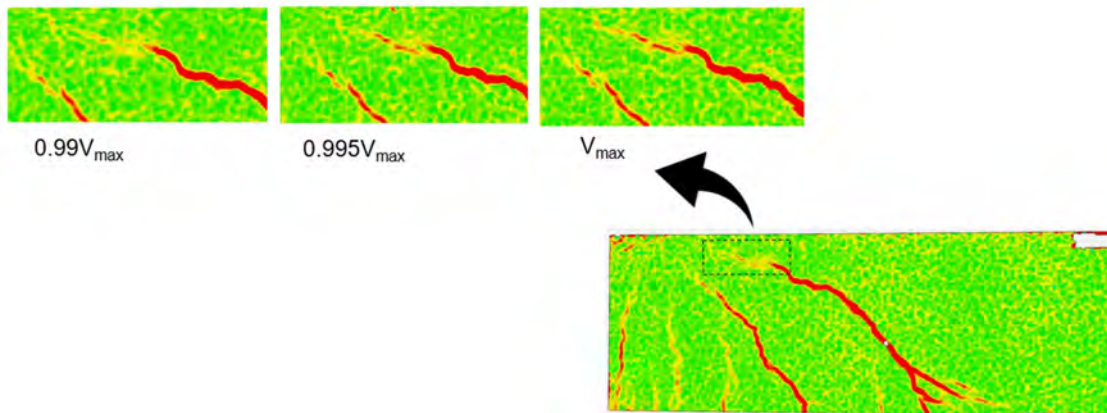


Figure 15. Type G crack developing in the compressed zone

At the tip of the critical crack between the initiation of the type G crack and the failure moment, the crack opening suddenly increased by approximately 30%, leading to a loss of the ability to transfer shear force through aggregate interlock. The specimen reached its maximum capacity when the aggregate interlock decreases due to the union of the critical crack A2 with the crack G of the compressed zone.

5.3 Concrete with 1.0% of steel fiber (C1.0)

For the beam with concrete containing 1.0% steel fibers (C1.0), the evolution of the cracking process, as well as its relationship with the shear force versus mid-span deflection curve, can be observed in Figure 16.

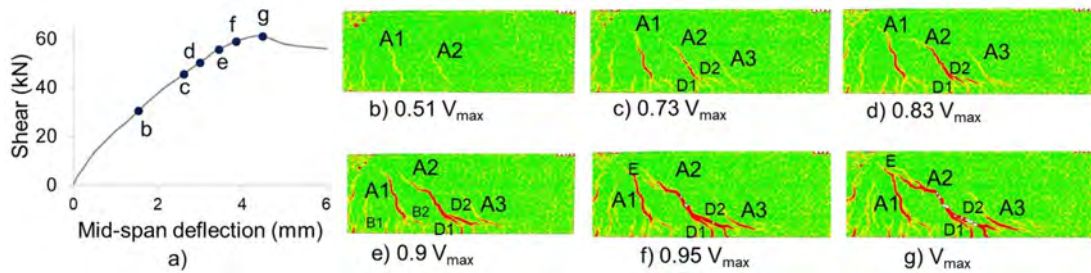


Figure 16. a) Shear force versus mid-span deflection, and cracking development of C1.0 in b) $0.51V_{max}$, c) $0.73V_{max}$, d) $0.83V_{max}$, e) $0.9V_{max}$, f) $0.95V_{max}$, and g) V_{max}

The first two shear cracks (A1 and A2) appear at 51% of the maximum load. At 73% of V_{max} (Figure 16c), two doweling cracks (D1 and D2) appear and quickly join A2, causing a sharp increase in opening (w). A third flexural shear crack, A3, also appears. At 83% of V_{max} (Figure 16d), it can be observed that the A2 crack has developed to the point of being the critical shear crack, with its propagation going towards the upper surface of the beam. At 90% of the total loading (Figure 16e), in addition to the 3 shear cracks (A1, A2 and A3), type B secondary flexural cracks are also observed. In general, at this loading stage, a significant number of secondary bending cracks such as type B and C [8] can be seen appearing in the lower region of the beam, as shown in Figure 17. This fact is justified by the higher dosage of steel fibers in the composition, causing a constant redistribution of stresses in the specimen.

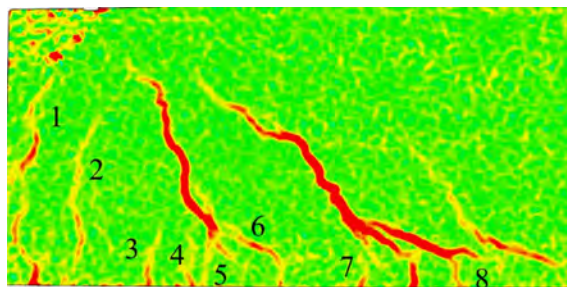


Figure 17. Secondary cracks in the C1.0 beam

At 95% of the maximum load (Figure 16f), a type E crack appears as a branch of the critical crack A2. This type of crack originates from the aggregate interlock, as presented in section 3. To understand the development of aggregate interlock in this beam, Figure 18 shows the simplified Walraven’s model equation applied to the three cracks (A1, A2 and A3) during the experimental test.

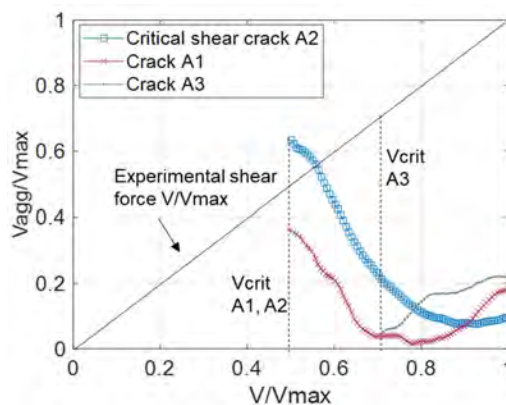


Figure 18. Aggregate interlock throughout the experimental test for cracks A1, A2 and A3

In Figure 18, it can be noted that the main crack (A2) shows a decreasing contribution from its appearance. The small contribution of the aggregate interlock in the main critical shear crack is mainly due to the predominance of the action of steel fibers. According to [15] and [16], the opening (w) in beams with fibers is usually larger than in conventional concrete, which reduces the friction within the crack, and consequently, the performance of the aggregate interlock.

In addition, the contribution of the aggregate interlock on shear strength could be overestimated when there is a no brittle failure as it is shown in Figure 18. This phenomenon can be explained due to high slippage to maintain equilibrium while cracks are forming. Furthermore, the steel fibers, which in this example have the highest dosage in the present experimental campaign, help to reduce the opening of cracks compared to the C0 reference beam. Thus, this issue is related to the sensitivity of the minimum crack opening accounted for in aggregate blocking contribution shear models at the beginning of the critical crack [23].

Figure 19 shows the opening w (Figure 19a) and sliding δ (Figure 19b) at the main test instants. The relative displacements of cracks A1 and A2 are also presented as a function of the load evolution (Figure 19c). It is clear that the opening (w) is greater than the sliding, supporting the hypothesis of little action of the aggregate interlock.

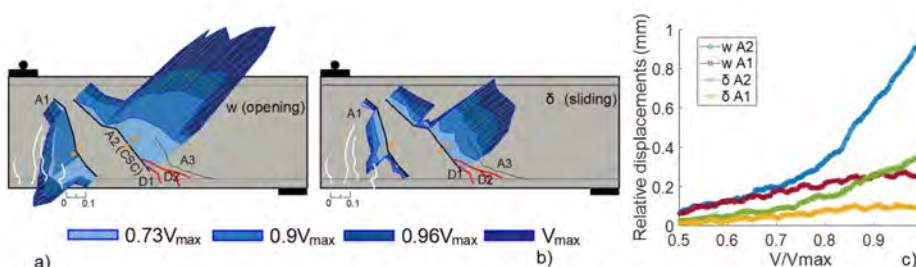


Figure 19. a) opening (w) b) sliding (δ) and c) relative displacements as a function of load variation for beam C1.0

Despite the larger opening in the critical crack, a type E crack emerged, theoretically designated to be the result of the action of the aggregate interlock [8]. In this case, the region where the crack emerged had a high sliding value δ , surpassing the opening w . The steeper and lower part of the crack had lost its contribution from the aggregate interlock due to the larger opening (w), but the crack tip region had more friction between the walls due to the high sliding (δ). Figure 20b shows a detailed view of the crack tip region at 95% of V_{max} (Figure 16f), where it can be observed in Figure 20a that the sliding δ was actually greater than the opening w . Failure occurred when the critical crack A2 gave rise to the crack E, which eventually merged with the crack A1. (Figure 16g).

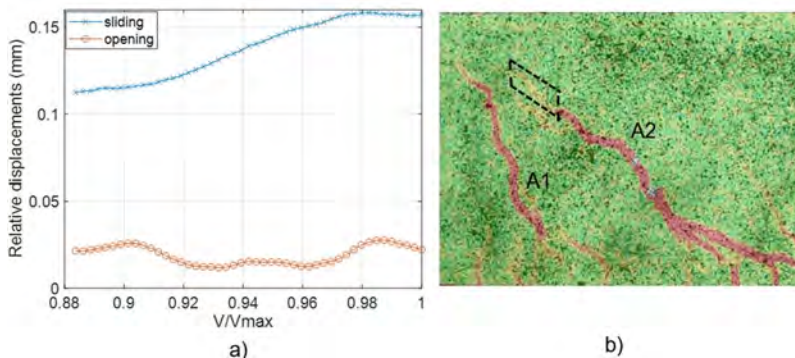


Figure 20. a) Opening (w) and sliding (δ) for the 88% to 95% of V_{max} , from the b) crack tip region

5.4 Comparison between the cases evaluated

To draw a comparison between the 3 evaluated beams, Figure 21 shows the measurement of a control point at of failure. The point was allocated to the steepest portion of each main crack (A2) and the measured opening is referred to as w_{max} , and the sliding as δ_{max} , as shown in Table 4.

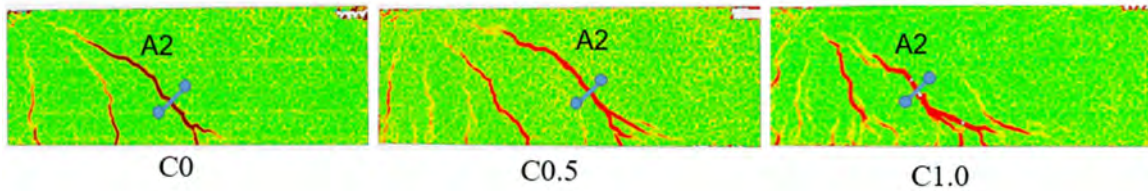


Figure 21. Control points measured at the failure

Table 4. Comparison between the beams.

	V_{max} (kN)	V_{crit} / V_{max}	w_{max} (mm)	δ_{max} (mm)	V_{agg_u} / V_{max}
C0	29.9	0.97	0.152	0.09	0.78
C0.5	43.3	0.79	0.249	0.11	0.34
C1.0	61.3	0.51	0.967	0.346	0.124

Table 4 provides a comparison of the shear forces resulting from the aggregate interlock at the failure (V_{agg_u}), as well as the maximum opening (w_{max}) and sliding (δ_{max}) for each of the three evaluated beams. As more fibers were incorporated into the concrete, the final opening w_{max} was observed to increase, consistent with findings from previous studies [4], [33] and [34]. In fact, the contribution of aggregate interlock was so low for concrete C1.0 that it was essentially negligible at just 12.4% of V_{max} . Conversely, for beam C0.5, aggregate interlock represented 34% of V_{max} .

Table 4 also displays the maximum crack opening for C1.0 concrete. Although this concrete type also experienced an increase in sliding, the considerably larger opening reduces the contribution of aggregate interlock.

Table 4 presents the critical shear value (V_{crit}) corresponding to the onset of the critical crack. By comparing the V_{crit}/V_{max} ratios, it is observed that the higher the fibers content in the concrete, the lower the V_{max} percentage at which the critical crack appears. This early initiation of the critical crack suggests that the FRC is better equipped to redistribute stresses in these elements. Conversely, in the case of C0 concrete without fibers, the critical crack emerged at 97% of the maximum load (V_{max}), propagating rapidly and leading to failure shortly after.

Finally, it is worth noting that the strength of the beams increased with the addition of steel fibers. According to the findings in [35], the proportion and characteristics of the steel fibers can influence the dosage required to effectively control cracking, increase the mechanical strength, and improve the ductility of the element. Specifically, volume contents ranging from 0.5% to 1.0% were found to be effective. In addition, [36] reported that the increase in shear capacity due to an increase in fiber volume depends on the a/d ratio. Specifically, the authors notated that for $a/d = 1$, the shear strength increased by 96.6% when the fiber content was increased from 0% to 1.5%, while for $a/d = 6$, the shear strength increased by 32.2%. The authors also concluded that the fiber volume is a key variable affecting the shear strength of the elements. Nevertheless, there is no known proportional relationship since other factors, such as the a/d ratio, reinforcement ratio, and f_{cm} , can also influence the results.

5 CONCLUSIONS

The present study has evaluated the role of aggregate interlock in shear transfer in RC and SFRC beams using the simplified Walraven’s model. DIC technique was employed to measure relative displacements at the cracks opening (w) and sliding (δ). Based on the analysis of the experimental data, the following conclusions can be drawn:

- The simplified Walraven’s equation was used to calculate the values of w and δ during the experimental test, up to failure. The results demonstrate that this equation accurately captures the phenomenon of aggregate interlock, although some overestimation of the calculated values was observed. Overall, the model provides a reliable representation of the mechanism under study.
- The influence of steel fibers on the mechanical behavior of the concrete was found to increase with the dosage used. In addition to enhancing the strength of the material, steel fibers caused a shift in the cracking pattern, due to their ability to redistribute stresses and alter the mechanisms of fracture in comparison to conventional concrete. As the volume of fibers in the mixture increases, the critical crack opening (w) also increases, leading to decrease in the contribution of aggregate interlock.
- The aggregate interlock plays a fundamental role in the failure process on SFRC beams. Observing the aggregate interlock during experimental tests helps to understand the activation of other shear resisting mechanisms. This fact

justifies exposing data throughout the beam failure process, rather than solely reading at the maximum load strength or the moment of failure.

- The evaluation of V_{crit} in the specimens indicated that the incorporation of more fibers into the concrete resulted in a lower relationship between V_{crit} and V_{max} . This observation supports the idea that fibers enable continuous stress redistribution, thereby promoting the development of the cracking process and activating more stress transfer mechanisms. In the case of C0 concrete, the critical crack occurred at a value very close to V_{max} . Although the aggregate interlock mechanism was not well developed, it proved to be the predominant mechanism in the failure process due to the limited crack opening.
- The C0 beams exhibited direct shear transmission to the support, which was primarily caused by the compressed strut related to Kani's valley phenomenon. Beams with fibers demonstrated a higher incidence of crack formation, resulting in a greater level of aggregate interlock.

Overall, the methodology presented herein provided to be effective in achieving its intended objectives. The test failure facilitated the assessment of aggregate interlock activation and development. Expanding the methodology to include other shear transfer mechanisms appears to be a rational approach for evaluating the individual contributions of each mechanism, particularly those of steel fibers.

ACKNOWLEDGEMENTS

The first author thanks CAPES and CNPQ for their financial support. All authors thank the PPGEC (Postgraduate Program in Civil Engineering) and CESEC (Centre for Civil Engineering Studies) at UFPR for their institutional support.

6 REFERENCES

- [1] M. Tirassa, M. Fernández Ruiz, and A. Muttoni, "Influence of cracking and rough surface properties on the transfer of forces in cracked concrete," *Eng. Struct.*, vol. 225, pp. 111138, 2020.
- [2] M. Fernández Ruiz, A. Muttoni, and J. Sagaseta, "Shear strength of concrete members without transverse reinforcement: a mechanical approach to consistently account for size and strain effects," *Eng. Struct.*, vol. 99, pp. 360–372, 2015.
- [3] M. G. Cardoso, R. M. Lameiras, and V. M. S. Capuzzo, "Influence of concrete strength, fiber content, and aspect ratio in the residual flexural strength of steel fiber reinforced self-compacting concrete," *Rev. IBRACON Estrut. Mater.*, vol. 14, no. 5, e14503, 2021.
- [4] M. R. Zarrinpour and S. H. Chao, "Shear strength enhancement mechanisms of steel fiber-reinforced concrete slender beams," *ACI Struct. J.*, vol. 114, no. 3, pp. 729–742, 2017.
- [5] M. F. Ruiz and A. Muttoni, "Shear strength of members without transverse reinforcement as function of critical shear crack width," *ACI Struct. J.*, vol. 117, no. 1, pp. 103–118, 2020.
- [6] Y. Yang, J. den Uijl, and J. Walraven, "Critical shear displacement theory: on the way to extending the scope of shear design and assessment for members without shear reinforcement," *Struct. Concr.*, vol. 17, no. 5, pp. 790–798, 2016.
- [7] M. Classen, "Shear Crack Propagation Theory (SCPT): the mechanical solution to the riddle of shear in RC members without shear reinforcement," *Eng. Struct.*, vol. 210, pp. 110207, 2020.
- [8] F. Cavagnis, M. Fernández Ruiz, and A. Muttoni, "Shear failures in reinforced concrete members without transverse reinforcement: An analysis of the critical shear crack development based on test results," *Eng. Struct.*, vol. 103, pp. 157–173, 2015.
- [9] F. Cavagnis, "Shear in reinforced concrete without transverse reinforcement: from refined experimental measurements to mechanical models," Ph.D. dissertation, Ec. Polytech. Fed. Lausanne, Lausanne, 2017.
- [10] M. Tirassa, M. Fernández Ruiz, and A. Muttoni, "Influence of cracking and rough surface properties on the transfer of forces in cracked concrete," *Eng. Struct.*, vol. 225, pp. 111138, 2020.
- [11] M. Schmidt, P. Schmidt, S. Wanka, and M. Classen, "Shear response of members without shear reinforcement- experiments and analysis using shear crack propagation theory (SCPT)," *Appl. Sci. (Basel)*, vol. 11, no. 7, pp. 3078, 2021.
- [12] A. Mari Bernat, N. Spinella, A. Recupero, and A. Cladera, "Mechanical model for the shear strength of steel fiber reinforced concrete (SFRC) beams without stirrups," *Mater. Struct.*, vol. 53, no. 2, pp. 28, 2020.
- [13] S. Gali and K. V. L. Subramaniam, "Influence of cohesive stresses on shear capacity of reinforced SFRC beams without stirrups: A discrete crack approach," *Eng. Fract. Mech.*, vol. 206, pp. 218–232, 2019.
- [14] T. Soetens and S. Matthys, "Shear-stress transfer across a crack in steel fibre-reinforced concrete," *Cement Concr. Compos.*, vol. 82, no. May, pp. 1–13, 2017.
- [15] W. Kaufmann, A. Amin, A. Beck, and M. Lee, "Shear transfer across cracks in steel fibre reinforced concrete," *Eng. Struct.*, vol. 186, pp. 508–524, 2019.

- [16] L. M. P. Matos, J. A. O. Barros, A. Ventura-Gouveia, and R. A. B. Calçada, "Constitutive model for fibre reinforced concrete by coupling the fibre and aggregate interlock resisting mechanisms," *Cement Concr. Compos.*, vol. 111, pp. 103618, 2020.
- [17] T. L. Resende, D. C. Taissum Cardoso, and L. C. D. Shehata, "Experimental and theoretical investigation on the stress transfer across cracks due to combined action of steel fibers and aggregate interlock," *Cement Concr. Compos.*, vol. 124, pp. 104239, 2021.
- [18] J. C. Walraven, "Fundamental analysis of aggregate interlock," *J. Struct. Div.*, vol. 107, no. 11, pp. 2245–2270, 1981, <http://dx.doi.org/10.1061/JSDEAG.0005820>.
- [19] ACI-ASCE Committee 426, "The shear strength of reinforced concrete members," *J. Struct. Div.*, vol. 99, no. ST6, pp. 1091–1187, Jun 1973.
- [20] A. Nouri et al., "Quantification of shear strength in reinforced concrete beams using digital image correlation: Experimental and analytical study," *Adv. Struct. Eng.*, vol. 24, no. 1, pp. 147–164, 2021.
- [21] T. Huber, P. Huber, and J. Kollegger, "Influence of aggregate interlock on the shear resistance of reinforced concrete beams without stirrups," *Eng. Struct.*, vol. 186, pp. 26–42, 2019.
- [22] H. W. Reinhardt and J. C. Walraven, "Cracks in concrete subject to shear," *J. Struct. Div.*, vol. 108, pp. 207–224, 1982.
- [23] L. A. Montoya-Coronado, C. Ribas, J. G. Ruiz-Pinilla, and A. Cladera, "Time-history analysis of aggregate interlock in reinforced concrete beams without stirrups," *Eng. Struct.*, vol. 283, pp. 115912, 2023.
- [24] International Union of Laboratories and Experts in Construction Materials, Systems and Structures, "Recommendations of RILEM TC 162-TDF: Test and design methods for steel fibre reinforced concrete Design of steel fibre reinforced concrete using the sigma-epsilon method: principles and applications," *Mater. Struct.*, vol. 35, no. 249, pp. 262–278, 2002.
- [25] Associação Brasileira de Normas Técnicas, *Concreto – Ensaio de Compressão de Corpos de Prova Cilíndricos*, ABNT NBR 5739, 2018.
- [26] Associação Brasileira de Normas Técnicas, *Concreto Reforçado com Fibras — Determinação das Resistências à Tração na Flexão (Limite de Proporcionalidade e Resistências Residuais) — Método de Ensaio*, ABNT NBR 16940, 2021.
- [27] B. Boulekbache, M. Hamrat, M. Chemrouk, and S. Amziane, "Failure mechanism of fibre reinforced concrete under splitting test using digital image correlation," *Mater. Struct.*, vol. 48, no. 8, pp. 2713–2726, 2015.
- [28] G. O. M. Aramis, *User Manual v6*. Braunschweig: GOM mbH, 2007.
- [29] J. Koščak, D. Damjanović, M. Bartolac, and I. Duvnjak, "Shear behavior of RC beams without transverse reinforcement: An analysis of crack kinematics and transfer mechanisms based on stereophotogrammetric measurements," *Eng. Struct.*, vol. 255, pp. 2021, 2022.
- [30] L. S. Assis, J. T. Assis, J. R. C. Pessoa, and A. D. Tavares Jr., "Elaboration of fracture prediction map using 2D digital image correlation - 2D CID," *Rev. IBRACON Estrut. Mater.*, vol. 15, no. 4, e15403, 2022.
- [31] F. Cavagnis, M. Fernández Ruiz, and A. Muttoni, "A mechanical model for failures in shear of members without transverse reinforcement based on development of a critical shear crack," *Eng. Struct.*, vol. 157, pp. 300–315, 2018, <http://dx.doi.org/10.1016/j.engstruct.2017.12.004>.
- [32] G. N. J. Kani, "Basic facts concerning shear failure," *ACI J. Proc.*, vol. 63, pp. 675–692, 1966.
- [33] E. O. L. Lantsoght, "How do steel fibers improve the shear capacity of reinforced concrete beams without stirrups," *Compos., Part B Eng.*, vol. 175, pp. 107079, 2019.
- [34] T. D. Dang, D. T. Tran, L. Nguyen-Minh, and A. Y. Nassif, "Shear resistant capacity of steel fibres reinforced concrete deep beams: An experimental investigation and a new prediction model," *Structures*, vol. 33, pp. 2284–2300, 2021.
- [35] D. Carnovale and F. J. Vecchio, "Effect of fiber material and loading history on shear behavior of fiber-reinforced concrete," *ACI Struct. J.*, vol. 111, no. 5, pp. 1235–1244, 2014.
- [36] S. A. Ashour, G. S. Hasanain, and F. F. Wafa, "Shear behavior of high-strength fiber reinforced concrete beams," *ACI Struct. J.*, vol. 89, no. 2, pp. 176–184, 1992.

Author contributions: LCD: writing, conceptualization, methodology, experimental program data curation, formal analysis, and paper review. LAMC: methodology, formal analysis, and paper review. TLR: methodology and formal analysis. RP: methodology, conceptualization, supervision, formal analysis, and paper review.

Editors: Leandro Trautwein, Mauro Real, Mario Pimentel.



ORIGINAL ARTICLE

Identification of the failure modes of CFRP shear-strengthened reinforced concrete beams by the finite element method

Identificação dos modos de ruptura de vigas de concreto armado reforçadas ao cisalhamento com PRFC pelo método dos elementos finitos

Palloma Borges Soares^a

Paula Manica Lazzari^a

Américo Campos Filho^a

Bruna Manica Lazzari^b

Alexandre Rodrigues Pacheco^a

^aUniversidade Federal do Rio Grande do Sul, Programa de Pós-Graduação em Engenharia Civil, Porto Alegre, RS, Brasil

^bPontifícia Universidade Católica do Rio Grande do Sul, Escola Politécnica, Porto Alegre, RS, Brasil

Received 15 September 2022

Accepted 4 March 2023

Abstract: The rehabilitation and strengthening of concrete structures using carbon fiber reinforced polymers (CFRP) has become an interesting alternative for a series of important aspects. This material has a low specific weight, high tensile strength, corrosion and fatigue resistance, a high modulus of elasticity, and is a versatile material, with ease and speed in its application. Nevertheless, its consideration and design tend to require more sophisticated analyses to evaluate and predict the behavior of the strengthened structural element. For this reason, numerical methods, such as the Finite Element Method (FEM), can be used in such complex analyses to simulate to a high degree the actual performance of the structure. Thus, this work presents computer simulations of reinforced concrete beams shear strengthened with CFRP through the Finite Element Method in a customized ANSYS model. Special attention is given to the bond behavior between the CFRP sheets and the concrete surface of the beams through contact elements and bilinear cohesive zone models, which allowed for the identification of the debonding failure modes. Twenty-one reinforced concrete beams reported in the literature were simulated: twelve simply supported and nine continuous, with and without CFRP shear strengthening. The beams showed failure modes in shear, bending, concrete splitting, and debonding of the strengthening CFRP sheets. The numerical model developed predicted with good accuracy the beams' behavior in terms of load vs. displacement, load vs. strain, as well as their ultimate loads and failure modes.

Keywords: strengthened reinforced concrete beams, carbon fiber reinforced polymers, finite element method, ANSYS, failures modes.

Resumo: A crescente necessidade de reabilitar e reforçar estruturas de concreto armado, assim como os problemas apresentados por técnicas de reforço tradicionais, tornou a utilização de polímeros reforçados com fibras de carbono (PRFC) uma alternativa interessante, uma vez que este material apresenta propriedades como baixo peso específico, elevada resistência à tração, à corrosão e à fadiga, alto módulo de elasticidade, assim como versatilidade, facilidade e rapidez de execução. A fim de avaliar e prever o comportamento do PRFC, é necessário realizar uma análise mais aprofundada dos elementos estruturais reforçados com esse material. Para isso, utilizam-se métodos numéricos, como é o caso do método de elementos finitos (MEF), que permite analisar estruturas complexas, bem como realizar análises não lineares de estruturas de concreto armado. Diante disso, o objetivo deste trabalho é apresentar uma modelagem computacional de vigas de concreto armado, reforçadas ao cisalhamento com PRFC, através do método dos elementos finitos com o emprego do software ANSYS customizado. Especial atenção foi dada ao comportamento da aderência entre o reforço e a viga de concreto, através da utilização de elementos de contato e de modelos de zona coesiva bilineares, possibilitando identificar, durante as simulações computacionais, falhas por perda de aderência do sistema de reforço.

Corresponding author: Palloma Borges Soares. E-mail: pallomaborges24@gmail.com

Financial support: This study was fully financed by the Civil Engineering Graduate Program (PPGEC) of the Federal University of Rio Grande do Sul (UFRGS) and by the Brazilian governmental research institutions CAPES and CNPQ.

Conflict of interest: Nothing to declare.

Data Availability: the data that support the findings of this study are available from the corresponding author, [P. B. Soares].



This is an Open Access article distributed under the terms of the Creative Commons Attribution License, which permits unrestricted use, distribution, and reproduction in any medium, provided the original work is properly cited.

Neste estudo foram testadas vinte e uma vigas de concreto armado reportadas na literatura, doze biapoiadas e nove contínuas, com e sem reforço ao esforço cortante com PRFC. Estas vigas apresentaram modos de ruptura por cisalhamento, por flexão, por fendilhamento do concreto, assim como pelo descolamento da camada de reforço. Constatou-se que os modelos numéricos desenvolvidos foram capazes de prever com boa precisão o comportamento das vigas simuladas, tanto em termos de carga-deslocamento e carga-deformação, como a carga e o modo de ruptura.

Palavras-chave: reforço estrutural de vigas de concreto armado, polímeros reforçados com fibras de carbono, método dos elementos finitos, ANSYS, modos de ruptura.

How to cite: P. B. Soares, P. M. Lazzari, A. Campos Filho, B. M. Lazzari, and A. R. Pacheco, "Identification of the failure modes of CFRP shear-strengthened reinforced concrete beams by the finite element method," *Rev. IBRACON Estrut. Mater.*, vol. 16, no. 3, e16304, 2023, <https://doi.org/10.1590/S1983-41952023000300004>

1 INTRODUCTION

A reduction in the performance of concrete structures tends to occur along their lifespan because of many factors and, eventually, they may present deficient strength to resist their design forces. Several strengthening methods can be applied to structural elements, such as externally bonded steel plates or fiber-based composite materials. The latter consists of the application of composite materials known as Fiber Reinforced Polymer (FRP), which present properties of low density, high tensile strength, corrosion resistance, high fatigue resistance, and high-impact resistance. Among the types of composite materials, carbon fiber reinforced polymers (CFRP) are the most used for structural strengthening since carbon fibers offer the best mechanical properties. Therefore, according to Dias [1] and Mhanna et al. [2], significant increases in the load capacity of structural elements are obtained through a small amount of strengthening.

The finite element method (FEM) can evaluate the actual behavior of structural elements strengthened with CFRP. Using FEM, it is possible to simulate various geometric arrangements, boundary and loading conditions, and analyze the bond between concrete and the strengthening system.

This work aims to demonstrate the viability of computational simulations of the behavior of reinforced concrete beams shear-strengthened with CFRP via the Finite Element Method through the software ANSYS, version 19.2. As recommended by Soares [3], special attention is given to the identification of the different failure modes of the simulated beams.

2 MATERIAL CONSTITUTIVE MODELS

Concrete constitutive models implemented by Lazzari et al. [4], Lazzari et al. [5], and Hoffman et al. [6], were adopted in the ANSYS UPF (User Programmable Features) customization tool. An elastoplastic model with hardening represented the concrete behavior under compression, while a linear elastic model up to crack formation described the concrete behavior under tension, with a smeared crack model considered afterward.

The concrete under compression model comprises a failure criterion, a plastification criterion, and a hardening rule. The failure surface of Ottosen [7] was adopted for the failure criterion, as recommended by the *fib* Model Code 2010 [8]. Additionally, the concrete under compression was considered to present an isotropic hardening, and the plastification surface had the same shape as the rupture surface.

The movement of the plastification surfaces (loading surfaces) during the plastic deformation was given by the hardening rule. This rule was determined by the relation between the effective stress and the effective plastic strain, allowing extrapolations of simple uniaxial tests to multiaxial situations. The curve corresponding to the stress vs. strain diagram for the concrete under uniaxial compression proposed by the *fib* Model Code 2010 [8] was adopted as a hardening rule for those extrapolations.

The model suggested by Hinton [9] was used to represent the behavior of the concrete under tension, with the concrete modeled as an elastic material with softening, i.e., behaving elastically until rupture, when a smeared cracking model with tension stiffening takes place. The smeared cracking model was specified by a cracking criterion, a rule for the concrete contribution between cracks, and a model for transferring shear stresses.

Each local direction's stiffness was considered independently when a determined integration point cracked. Therefore, stress vs. strain diagrams corresponding to uniaxial internal forces were used for each of the two principal directions in the crack plane. The stress vs. strain diagram for concrete under compression was adopted when a shortening occurred in one of those directions, and the diagram for concrete under tension when an elongation was detected.

Titello [10] introduced a new criterion to the cracked concrete model where the consideration of the tension stiffening would depend on the reinforcement orientation. This would provide a better result when analyzing beams without shear reinforcement, which happens in some cases studied herein. Thus, when no stirrups were used, the effect was considered only for the vertical cracks, i.e., the ones with an inclination up to 15° with the vertical direction.

Typically, steel rebars are considered to resist only axial forces in reinforced concrete structures. Therefore, a uniaxial model was adopted to describe the behavior of the steel reinforcements. According to Lazzari et al. [11], and Machado et al. [12], rebar products differ due to their fabrication process: there are laminated products with well-defined yielding plateaus, which are modeled with a perfect elastoplastic model; and cold-formed steel products, which are modeled with an elastoplastic model with linear hardening up from 0.85 of its yielding stress.

Several approaches can be considered to numerically model interfaces, with the Cohesive Zone Model (CZM) as the typical choice when the thickness of the bonding region is negligible. This model is commonly used in analyses of problems that involve composite materials since it avoids singularities and can be easily implemented numerically in Finite Element formulations. Additionally, CZM uses relative stress-slip relation for interface analyses [13], [14].

Medeiros [15] mentions that most numerical simulations consider that the interface between concrete and CFRP is dominated by tangential slips, i.e., Mode II of separation [16]. Therefore, a Mode II behavior is considered in this work, with bilinear tangential stress vs. slip relation, as illustrated in Figure 1.

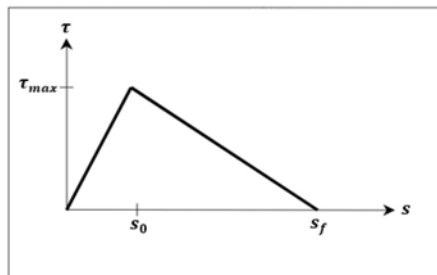


Figure 1. Bilinear relation between bonding stress and slip [17].

The bilinear model by Lu et al. [18] was considered to evaluate the parameters of the formulation implemented in ANSYS. This model can be considered to represent the concrete-strengthening interface behavior. To accomplish that, the curve that governs the behavior is determined as a function of the bond stress and its corresponding slip. Therefore, the Equations 1-10 mathematically describe the bilinear model considered in this work:

$$\tau = \tau_{max} \frac{s}{s_0}, s \leq s_0 \tag{1}$$

$$\tau = \tau_{max} \frac{s_f - s}{s_f - s_0}, s_0 < s \leq s_f \tag{2}$$

$$\tau = 0, s > s_f \tag{3}$$

$$s_f = \frac{2G_f}{\tau_{max}} \tag{4}$$

$$\tau_{max} = 1,5\beta_w f_t \tag{5}$$

$$\beta_w = \sqrt{\frac{2,25 - b_f/b_c}{1,25 + b_f/b_c}} \tag{6}$$

$$f_t = 0,395 f_{cu}^{0,55} \tag{7}$$

$$f_{cu} = \frac{f_c}{0,76} \tag{8}$$

$$s_0 = 0,0195\beta_w f_t \quad (9)$$

$$G_f = 0,308\beta_w^2 \sqrt{f_t} \quad (10)$$

The coefficient β_w is the factor that correlates the CFRP strengthening width (b_f) and the concrete beam width (b_c); f_t is the concrete tensile strength related to the concrete cube compressive strength (f_{cu}). Equation 8 correlates strength f_{cu} with the mean compressive strength (f_c). The measured slip when the bonding stress is at a maximum (s_0) is defined in Equation 9. Lastly, the measured slip when displacement occurs (s_f) is calculated from the fracture energy in the interface (G_f) and from the maximum bonding stress (τ_{max}), as shown in Equation 4.

3 COMPUTATIONAL MODEL

The Finite Element Method was used to carry out the numerical simulation since it is one of the most efficient ways to analyze the non-linear behavior of concrete and steel materials. The method also considers failures due to bonding loss of strengthening systems by introducing particular finite elements in the interface regions. ANSYS version 19.2 was used to carry out these finite element analyses. It presents a library with many finite elements that can be chosen according to the type of problem to be analyzed.

The 3D quadratic finite element SOLID186 was considered to represent the concrete. This element has 20 nodes with three degrees of freedom each, corresponding to the translations in the X, Y, and Z axes. This finite element was chosen because of its good answer under coarser meshes, which considerably reduces the processing time during structural analyses. Additionally, the element presents compatibility with the finite element REINF264, which is needed to represent reinforced concrete with its discretized rebars. REINF264 is a reinforcing finite element that can be used together with beam elements, shells, and even solid elements. This element is adequate for simulations of reinforcing fibers randomly oriented, with every fiber modeled individually and presenting only axial stiffness. The nodal coordinates, degrees of freedom, and connectivities of element REINF264 are identical to those of the base finite element. In this work, the element REINF264 is used to discretize the steel rebars embedded in concrete in a perfectly bonded incorporated approach.

The finite element SHELL281 was used to model the strengthening CFRP sheets. This finite element presents 8 nodes with 6 degrees of freedom each, considering membrane and bending stiffnesses. However, only the membrane stiffnesses were defined for the element since the CFRP sheets would develop mainly tension forces, resulting in only three degrees of freedom per node (translations in the X, Y, and Z axes).

An association of a contact element and a target element was adopted to model the interface between concrete and the strengthening system. Thus, the finite elements CONTA174 and TARGE170 were used to represent the slip that may occur in the interface between the solid and the shell elements.

Regarding the constitutive models, an elastoplastic model with cracking was implemented for the concrete in the USERMAT3D subroutine, which is available for customization purposes in the software through FORTRAN commands. This subroutine is compatible with the 3D element used to represent the concrete, i.e., SOLID186. The constitutive model BISO (*Bilinear Isotropic Hardening*), was used to represent the reinforcing bars and was already available in the ANSYS library.

4 STRUCTURAL CHARACTERISTICS

Khalifa [19] tested twenty-one full-scale reinforced concrete beams with a rectangular section and designed to collapse under shear. The beams were grouped into two main series called A and B. Series A comprised twelve beams simply supported, and series B by nine continuous beams. The A-series beams were subdivided into two main groups (A-SW and A-SO) depending on the existence or not of stirrups in the right half of the beam. The A-SW group consisted of four beams, which had steel stirrups along the entire length of the beam, and the dimensions and details of this group are shown in Figure 2a. The A-SO group was composed of eight beams, which did not have stirrups in the right half of the beam, as shown in Figure 2b. As shown in Figure 2c, all beams had the same cross-section of 150 x 305 mm, and upper, and bottom reinforcement was composed of two 32mm in diameter rebars. The shear reinforcement was formed of 10mm in diameter stirrups spaced by 80mm and 125mm, as shown in Figure 2a-2b.

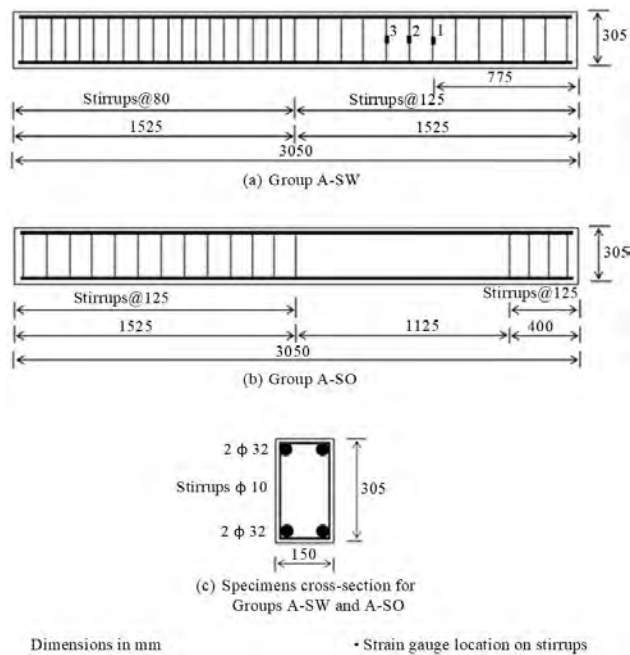


Figure 2. Configuration and reinforcement details for Series A beams [20].

Series B was divided into three groups: B-CW, B-CO, and B-CF. Each group had different rates for flexural and shear reinforcement. The B-CW group is composed of two beams with stirrups along the entire length of the beam. Part of the right span had less shear reinforcement to force shear failure in this position. The dimensions and details of this group are shown in Figure 3a. The B-CO group consists of three beams with longitudinal reinforcement equal to group B-CW. These beams had no stirrups in the shear span tested, as shown in Figure 3b. The four beams of the B-CF group had no shear reinforcement, as can be seen in Figure 3c. Table 1 presents the properties of the materials of the beams in series A and B.

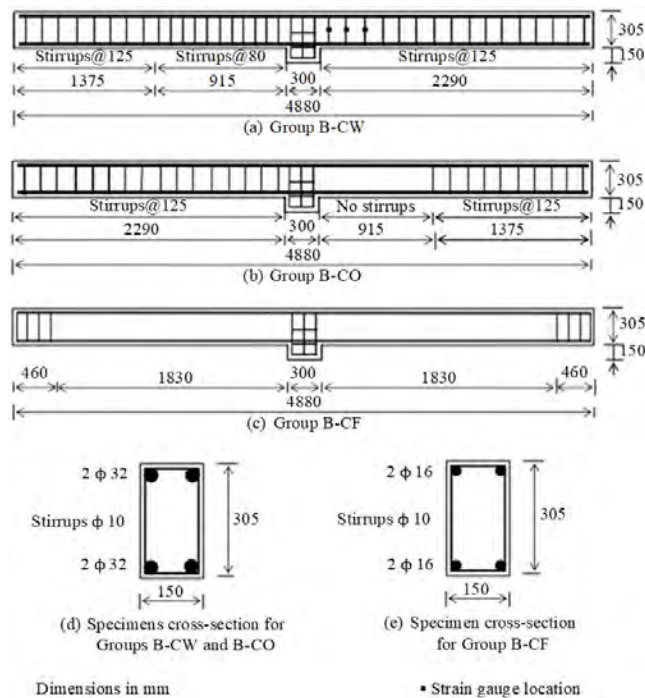


Figure 3. Configuration and reinforcement details for Series B beams [21].

Table 1. Material properties [21].

Material	Specification	Compressive strength (MPa)	Yielding stress (MPa)	Ultimate tensile strength (MPa)	Modulus of elasticity (GPa)
Concrete	Group A-SW	19.3	-	2.2	20
	Group A-SO	27.5	-	2.7	25
	Group B-CW	27.5	-	2.7	25
	Group B-CO	20.5	-	2.2	22
	Group B-CF	50.0	-	4.1	33
Steel	$\phi = 32$ mm	-	460	730	200
	$\phi = 16$ mm	-	430	700	200
	$\phi = 10$ mm	-	350	530	200
CFRP	$t_{fa} = 0.165$ mm	-	-	3790	228
	$t_{fb} = 0.165$ mm	-	-	3500	228

Both series SW and SO were subdivided according to their shear span to effective depth ratio (a/d), and since a/d ratios of 3 and 4 were considered, four subgroups were then obtained: SW3, SW4, SO3, and SO4. Four of the twelve tested beams were not strengthened with CFRP sheets, i.e., one in each of the subgroups, denominated SW3-1, SW4-1, SO3-1, and SO4-1. The eight beams that were strengthened with externally bonded CFRP laminates in three different configurations (see Figure 4) were denominated SW3-2, SW4-2, SO3-2, SO3-3, SO3-4, SO3-5, SO4-2, and SO4-3.

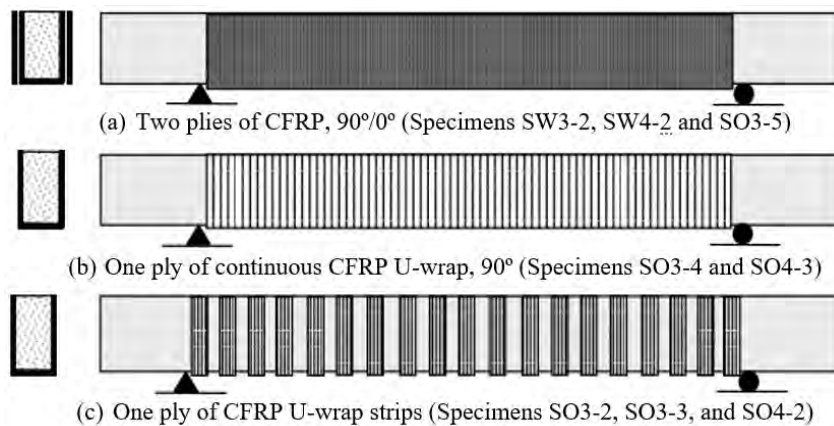


Figure 4. Schematic representation of CFRP strengthening schemes for beam specimens of Series A [20].

All Series A beams were four-point bending tested by applying a load to a steel load-distribution element to produce two concentrated loads at certain positions. These positions are represented in Figure 5a for the beams with an a/d ratio equal to 3 and, in Figure 5b, for the beams with an a/d ratio equal to 4. Four LVDTs (*linear variable differential transformers*) were used to measure the vertical displacements at specific points of the beams, as shown in Figure 5. Two of them were positioned at midspan on each side of the beams, while the other two were positioned at the supports.

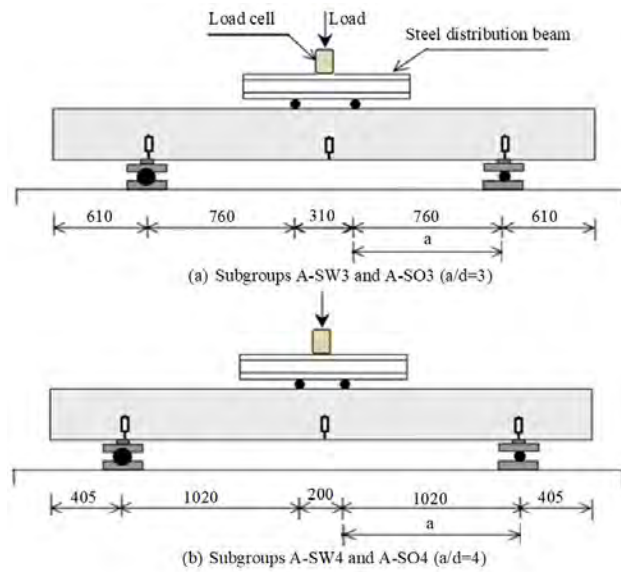


Figure 5. Schematic representation of test set-up for Series A [20].

For group B, one beam from each subgroup was not strengthened with CFRP. These beams were called B-CW1, B-CO1, and B-CF1, as shown in Figure 6a. The other six beams were strengthened with CFRP, following four different configurations, as shown in Figure 6, and were called B-CW2, B-CO2, B-CO3, B-CF2, B-CF3, and B-CF4. All beams in Series B were tested as continuous and subjected to concentrated loads in the center of each span, as can be seen in Figure 6. Five LVDTs were used in each beam: two fixed at midspan and the other three at the supports.

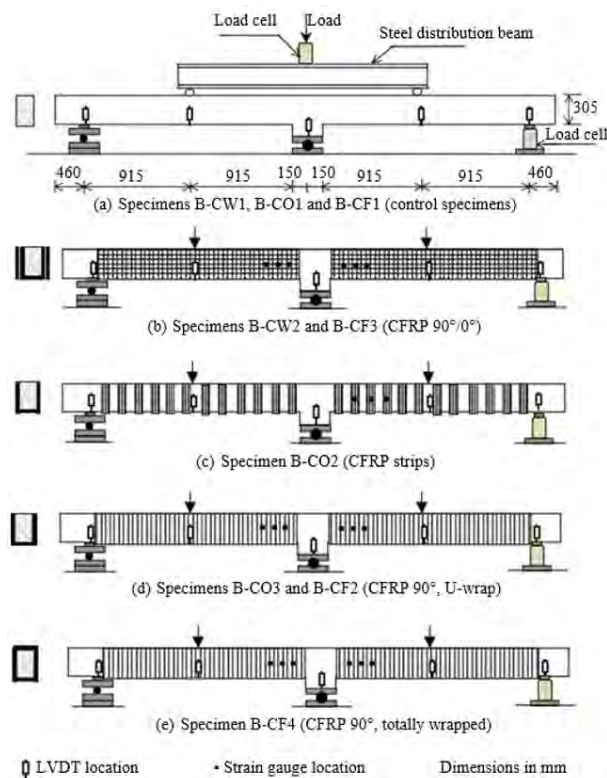
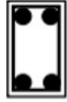


Figure 6. Strengthening schemes and test set-up for Series B beams [21].

Table 2 summarizes the characteristics of the beams in Series A and B, such as dimensions and details of the cross-sections, shear span and effective depth ratio (a/d), concrete compressive strength, shear reinforcement, and CFRP strengthening configurations.

Table 2. Summary of beam characteristics [21].

N ^o	Specimen designation	Structural system and cross-section details	a/d ratio	Concrete strength (MPa)	Shear reinforcement	
					Steel stirrups in the test region	CFRP
1	A-SW3-1		3	19.3	φ 10@125mm	-
2	A-SW3-2		3	19.3	φ 10@125mm	Two plies (90°/0°)
3	A-SW4-1		4	19.3	φ 10@125mm	-
4	A-SW4-2		4	19.3	φ 10@125mm	Two plies (90°/0°)
5	A-SO3-1	Simply supported beams	3	27.5	-	-
6	A-SO3-2	2 φ 32 	3	27.5	-	U-wrap strips, 50 @ 125mm
7	A-SO3-3		3	27.5	-	U-wrap strips, 75 @ 125mm
8	A-SO3-4	2 φ 32 	3	27.5	-	One-ply continuous U-wrap
9	A-SO3-5		3	27.5	-	Two plies (90°/0°)
10	A-SO4-1		4	27.5	-	-
11	A-SO4-2		4	27.5	-	U-wrap strips, 50 @ 125mm
12	A-SO4-3		4	27.5	-	One-ply continuous U-wrap
13	B-CW1		3.6	27.5	φ 10@125mm	-
14	B-CW2	Continuous beams	3.6	27.5	φ 10@125mm	Two plies (90°/0°)
15	B-CO1	2 φ 32 	3.6	20.5	-	-
16	B-CO2	2 φ 32 	3.6	20.5	-	U-wrap strips, 50 @ 125mm
17	B-CO3		3.6	20.5	-	One-ply continuous U-wrap
18	B-CF1	Continuous beams	3.6	50	-	-
19	B-CF2	2 φ 16 	3.6	50	-	One-ply continuous U-wrap
20	B-CF3		3.6	50	-	Two plies (90°/0°)
21	B-CF4	2 φ 16 	3.6	50	-	One-ply totally wrapped

5 NUMERICAL MODEL

In the computational analysis of the beams tested by Khalifa [19], only half of the width of the beams was modeled since they present symmetry of geometry and load along the cross-section. Hexahedral 20-node quadratic finite elements (SOLID186) were used to represent concrete. REINF264 elements discretized inside the solid elements represented the embedded reinforcement in the beams. Furthermore, at the loading points and supports, plates of SOLID186 elements, with dimensions of 10 x 2 x 7.5 cm, were included to avoid the concentration of stresses at those locations.

Figure 7 presents the mesh discretization for simply supported beams. Figure 7a shows the beam without CFRP strengthening and with an a/d ratio equal to 4 (A-SO4-1), and Figure 7b shows the A-SW3-2 beam, which is strengthened with continuous CFRP and had an a/d ratio equal to 3. Figure 8 illustrates the characteristics of continuous beams with strengthening in bands and with total involvement. Figure 8a corresponds to the model of the B-CO2 beam, and Figure 8b shows the B-CF4 beam. Figure 9a-9b present the cross-sections of the beams without strengthening. Figure 9c-9d show the cross-sections of the beams strengthened in a U-shape and with total wrapping, respectively.

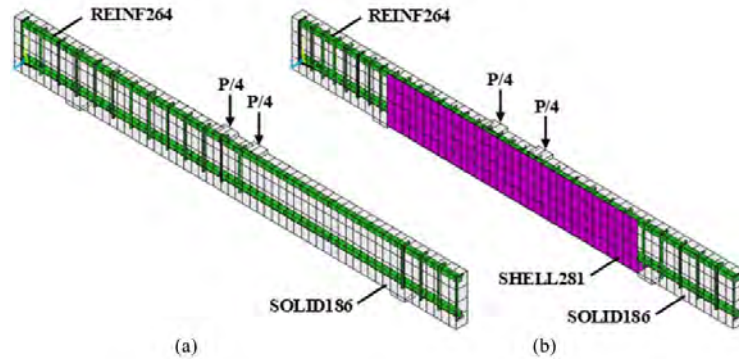


Figure 7. Finite element discretization of the beams: (a) A-SO4-1, and (b) A-SW3-1.

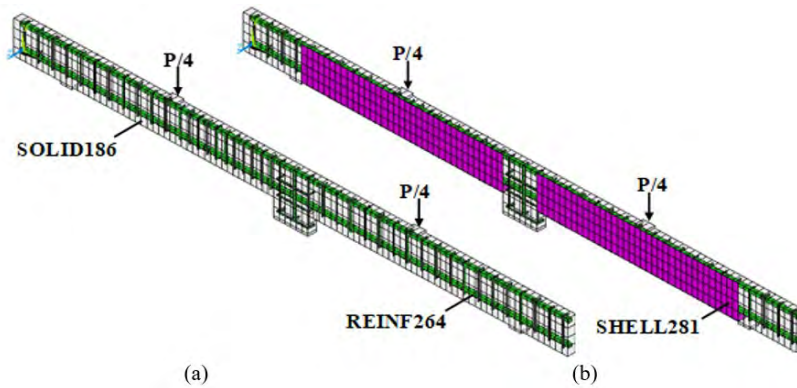


Figure 8. Finite element discretization of the beams: (a) B-CO2, and (b) B-CF4.

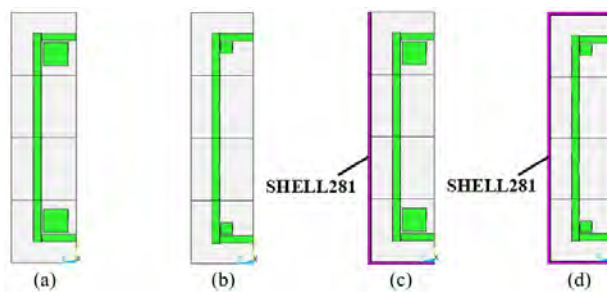


Figure 9. Cross-sections of the beams: (a) A-SW, A-SO, B-CW, and B-CO without CFRP; (b) B-CF without CFRP; (c) CFRP U-wrap; and (d) CFRP, totally wrapped.

The adhesive, used to bond the CFRP composite to the concrete surface, was modeled in two layers of 20-node quadratic hexahedral finite elements (SOLID186). One layer was modeled on the surface of the SOLID186 elements (concrete) and the other on the surface of the SHELL281 elements (CFRP composite), enabling the positioning of CONTA174 and TARGE170 elements in these adhesive layers, as can be seen in Figure 10.

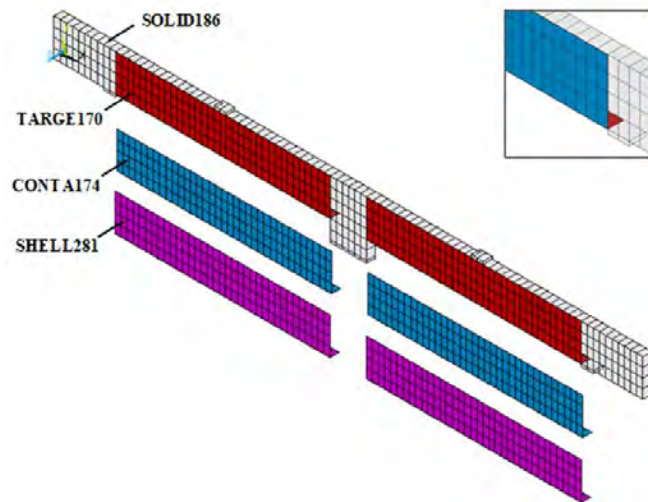


Figure 10. CONTA174 and TARGE170 elements for modeling beam B-CW2.

The interface properties were determined from the model and formulation proposed by Lu et al. [18]. Substituting the parameters of the beams tested by Khalifa [19] in the formulation presented in item 2, it was possible to determine the values of maximum bond stress, tangential interface stiffness, and maximum slip for each group of beams, as shown in Table 3.

Table 3. Interface model parameters.

Group	Maximum bonding stress τ_{t1} (kN/cm ²)	Tangential stiffness K_t (kN/cm ³)	Maximum slip s_0 (cm)
A-SW	0.317	77	0.0182
A-SO	0.366	77	0.0169
B-CW	0.366	77	0.0169
B-CO	0.324	77	0.0180
B-CF	0.479	77	0.0148

6 RESULT ANALYSIS

This item presents a comparative analysis between the numerical and the experimental results of Khalifa [19], Khalifa and Nanni [20], Khalifa et al. [21], and Khalifa et al. [22] for beams in Series A and B. Load vs. displacement diagrams in the central section of each beam are presented, as well as stresses and strains in concrete, reinforcement, and CFRP strengthening. In addition, the behavior of the interface is analyzed through the results of bond stresses and slips obtained from the contact elements.

The short-term behavior for all simulated beams was determined. It is essential to point out that the values presented in this item are net values, i.e., the values corresponding to self-weight have been discounted. Next, the results of only some beams analyzed according to the type of failure observed are presented. Complete results can be found in Soares [3].

6.1 Shear failure

Figure 11 presents the load vs. displacement diagram for the experimental tests and the numerical analyses of the simply supported beams A-SW3-1, A-SO4-1, and the continuous beam B-CF1.

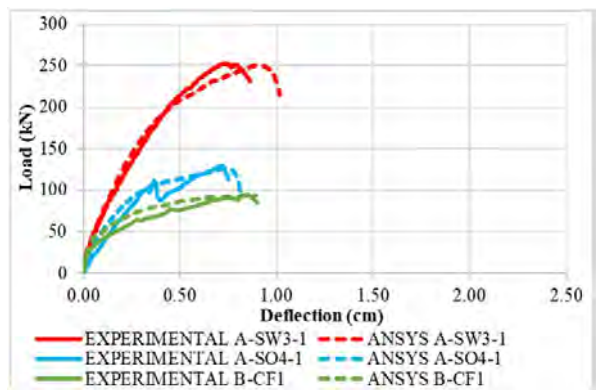


Figure 11. Load vs. displacement diagram of beams with shear failure.

Regarding the failure mode, it was found, through the simulations, that these beams had a shear failure. It was observed through the stress distribution in the reinforcements, Figure 12-12b (stirrups of the shear span of interest) for beam A-SW3-1, that the stirrups reached the yield stress (35 kN/cm²) before yielding in the longitudinal reinforcement (46 kN/cm²), indicating shear failure. As for beam A-SO4-1, it was possible to observe that the concrete reached a high principal tensile deformation at the web, Figure 13, which indicated shear failure due to the formation of a diagonal crack. This failure was predictable since the analyzed beam did not have shear reinforcement in the shear span. Similar behavior was observed in the failure of beam B-CF1, with high elongations in its web, Figure 14, indicating failure by shear. These results followed what was observed in the experimental tests carried out by Khalifa [19]. Figure 15 illustrates the failure of beams A-SW3-1 and B-CF1.

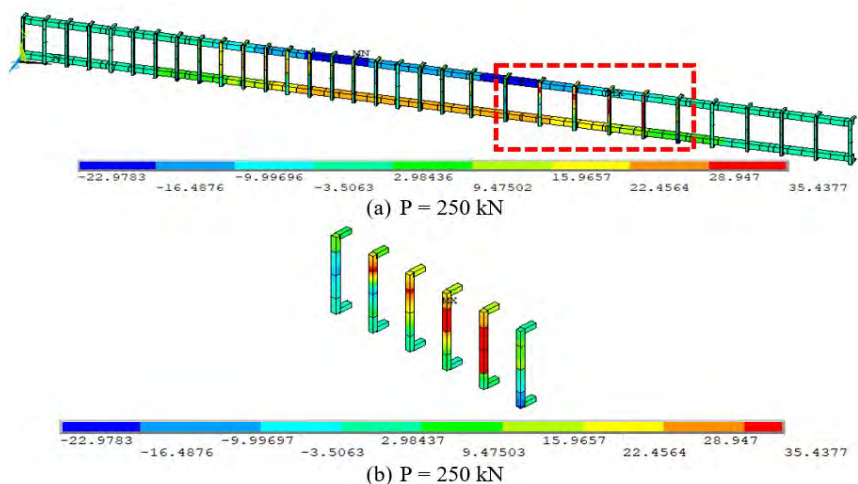


Figure 12. Stress σ_x in the reinforcement of beam A-SW3-1 (kN/cm²).

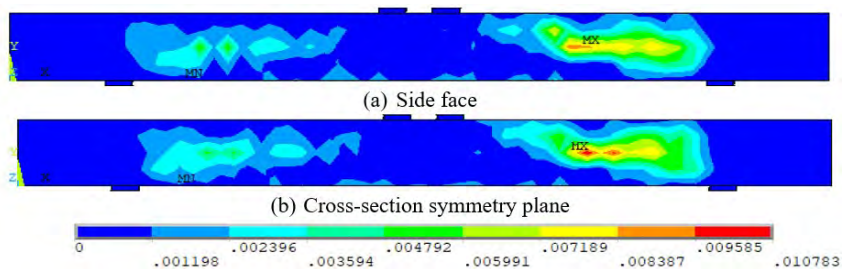


Figure 13. Principal strain ϵ_1 in the concrete of beam A-SO4-1 (cm/cm).

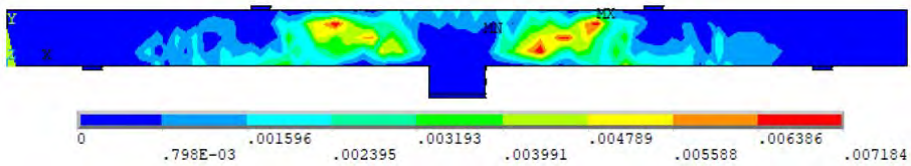


Figure 14. Principal strain ϵ_1 in the concrete of beam B-CF1 (cm/cm).



Figure 15. Failure modes observed in the beam tests [19].

6.2 Failure by splitting

Figure 16 presents the load vs. midspan deflection diagram, for the experimental tests and the numerical analyses, of beams A-SW3-2, A-SW4-2, and B-CW2.

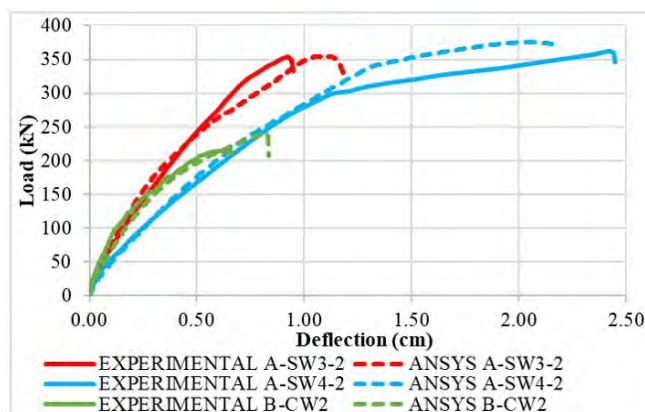


Figure 16. Load vs. midspan deflection diagram for the beams with splitting failure.

Results from the computational analysis, Figure 17, show that the stress in the concrete in the Z-direction (beam width) for beam A-SW3-2 reaches very high values at failure, characterizing failure by concrete splitting. A similar situation occurred for beams A-SW4-2 and B-CW2, where it was verified that the concrete presented, in the plane of symmetry, principal tensile strains with very high values, as shown in Figure 18 and Figure 19, respectively. This corroborates with what was determined in the experimental tests, where the failure occurred due to concrete splitting, as seen in Figure 20a for beam A-SW3-2 and Figure 20b for beam B-CW2.

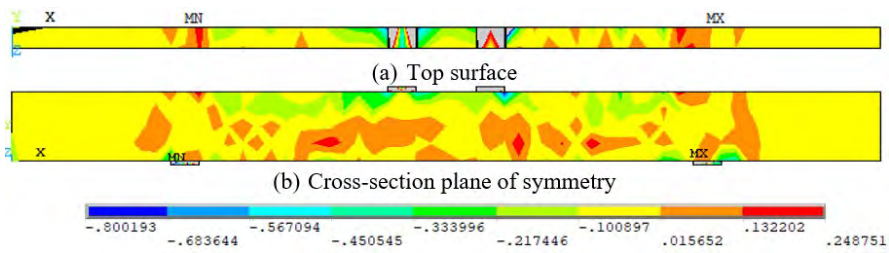


Figure 17. Stress σ_z in concrete for beam A-SW3-2 (kN/cm²).

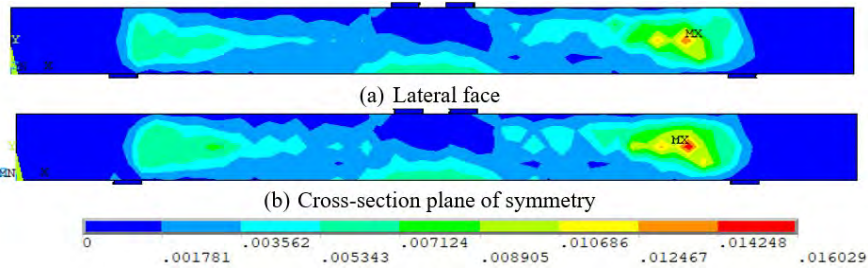


Figure 18. Principal strain ϵ_1 in concrete for beam A-SW4-2 (cm/cm).

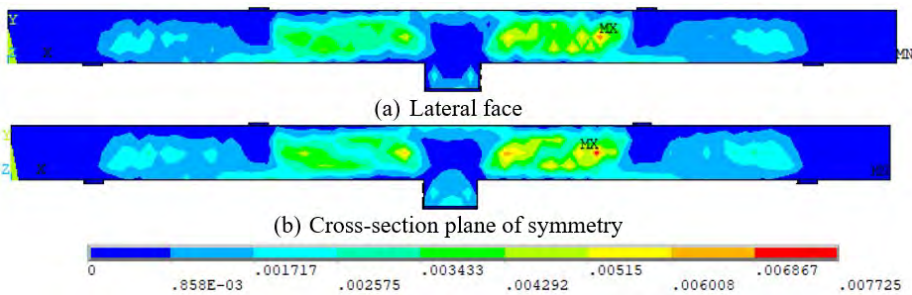
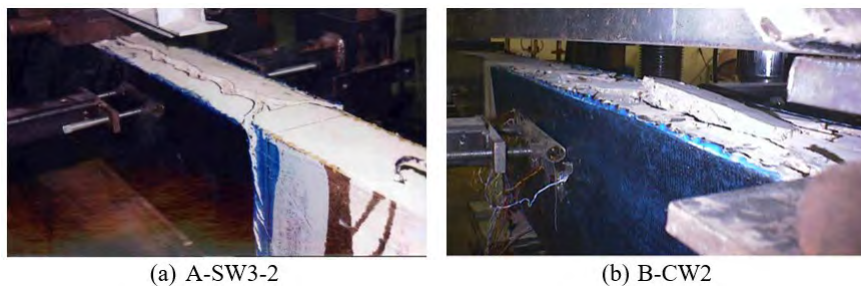


Figure 19. Principal strain ϵ_1 in concrete for beam B-CW2 (cm/cm).



(a) A-SW3-2 (b) B-CW2

Figure 20. Failure modes observed in the experiments [19].

6.3 Failure by CFRP debonding

The diagram load vs. midspan deflection in Figure 21 compares numerical and experimental results for beams A-SO3-3, ASO4-2, and B-CO2. Figure 22 shows the stress distribution in the lateral strengthening of beam A-SO3-3, where it is possible to observe that the highest stress value in the shear span occurs for a load of 188 kN, Figure 22a. As the load increases, this tensile stress decreases, indicating failure in the connection between the strengthening and the beam surface. At this time, a reduction in the stiffness of the load-displacement curve is observed. Then, an increase in stresses in the strengthening on the opposite side of the beam occurs when the ultimate load is reached, Figure 22b.

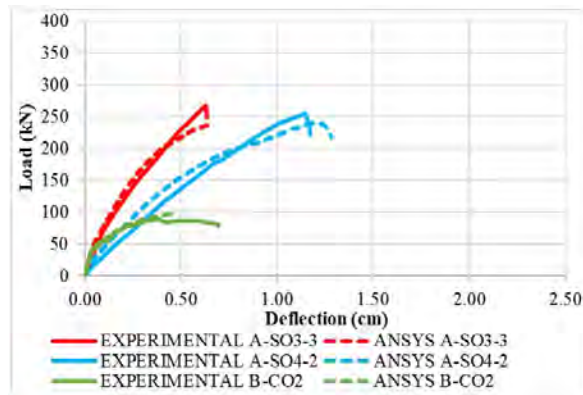


Figure 21. Load vs. midspan deflection diagram for beams with debonding failure.

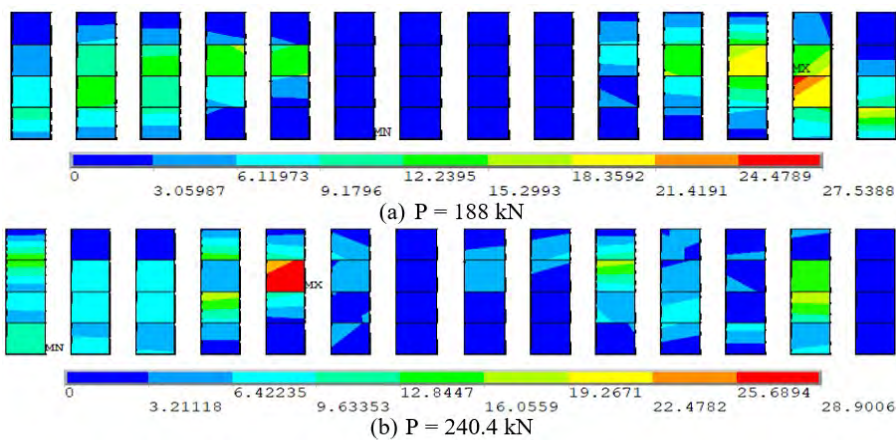


Figure 22. Evolution of the principal stress σ_1 in the CFRP strengthening for beam A-SO3-3 (kN/cm²).

Figures 23-24 show that the concrete-strengthening interface reached the maximum bond stress (0.366 kN/cm²) and the maximum slip (0.0169 cm), respectively. This indicates that the debonding of the CFRP strengthening occurred in the shear span, reproducing the behavior observed in the experimental test carried out by Khalifa [19]. Beam A-SO4-2 presented a similar behavior. Figure 25 shows the stress distribution in the reinforcement, and Figures 26-27 show the bond stress and slip at the interface, respectively. It was observed in Figure 28, for beam B-CO2, that the regions of maximum stress are located in the shear span and that this stress value is much lower than the ultimate stress of CFRP (350 kN/cm²). It was also verified, in Figures 29-30, that the beam reached the maximum bond stress (0.324 kN/cm²) for a load of approximately 85 kN and the maximum slip (0.0180 cm) for a load of 96 kN, respectively. This indicates that strengthening debonding occurs in the numerical simulation, as observed in the experimental test. Figure 31 illustrates the failure of beams A-SO3-3 and B-CO2.

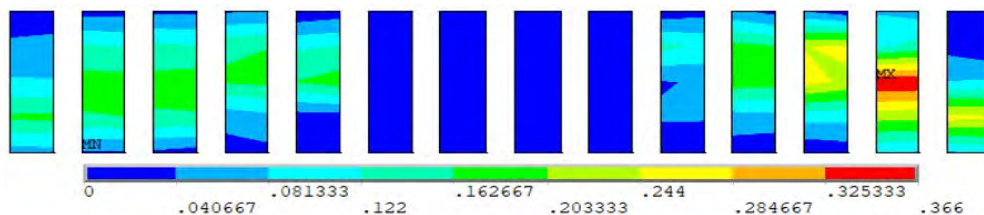


Figure 23. Bond stress in the interface of beam A-SO3-3 (kN/cm²).

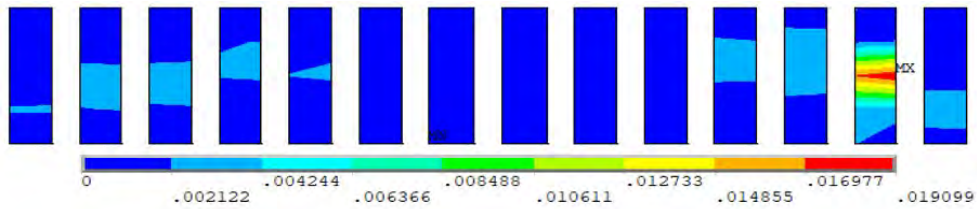
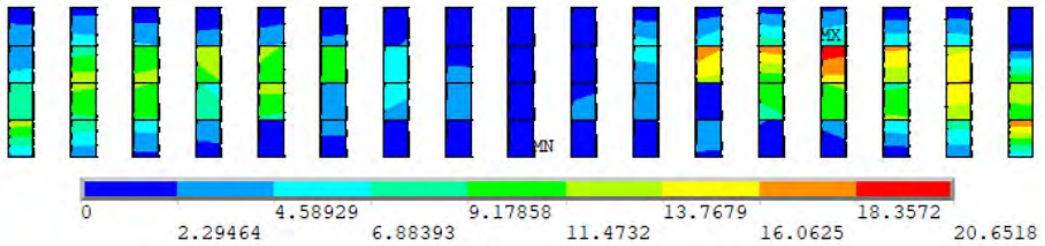
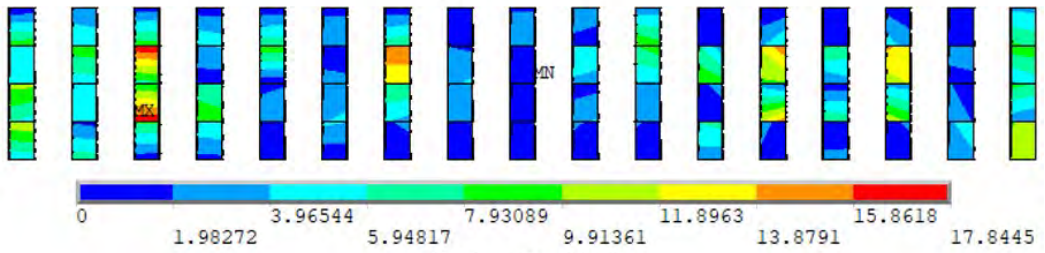


Figure 24. Slip in the interface of beam A-SO3-3 (cm).



(a) P = 150 kN



(b) P = 238.9 kN

Figure 25. Evolution of the principal stress σ_1 in the CFRP strengthening for beam A-SO4-2 (kN/cm²).

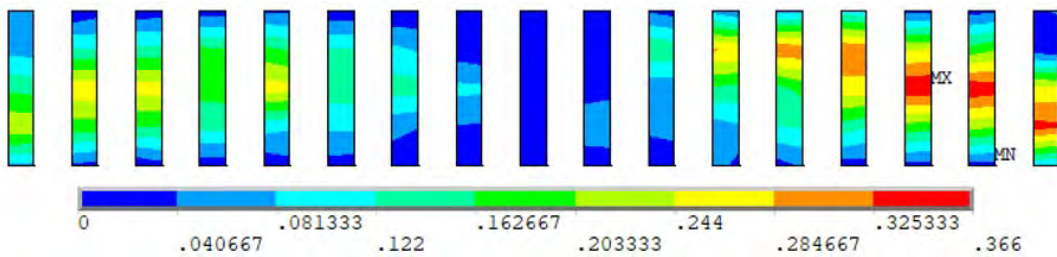


Figure 26. Bond stress in the interface of the beam A-SO4-2 (kN/cm²).

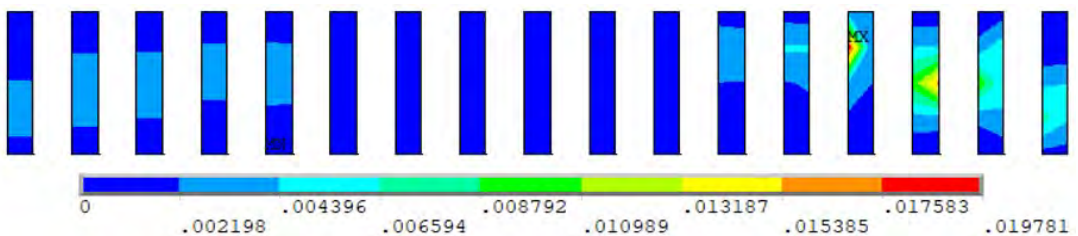


Figure 27. Slip in the interface of beam A-SO4-2 (cm).

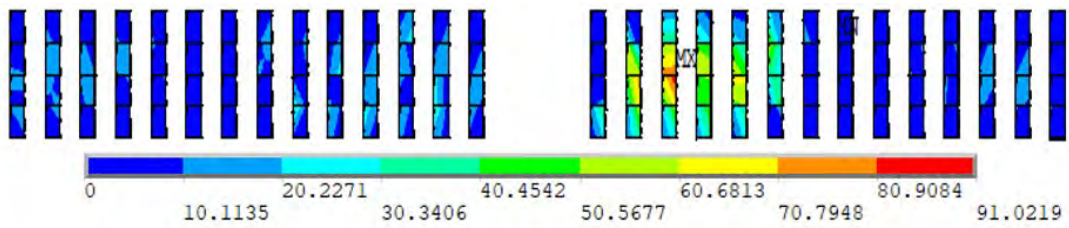


Figure 28. Principal stress σ_1 in the CFRP strengthening of beam B-CO2 (kN/cm²).

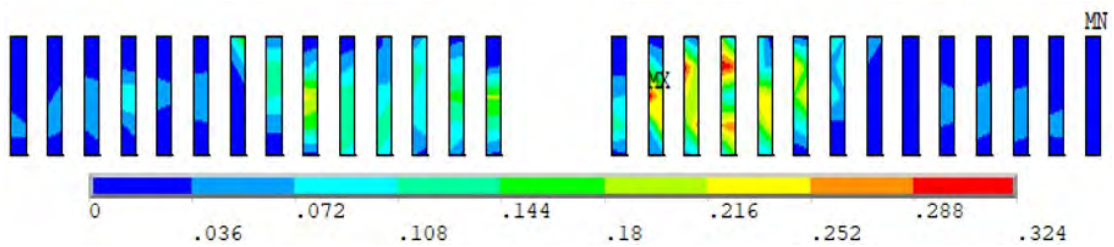


Figure 29. Bond stress in the interface of beam B-CO2 (kN/cm²).

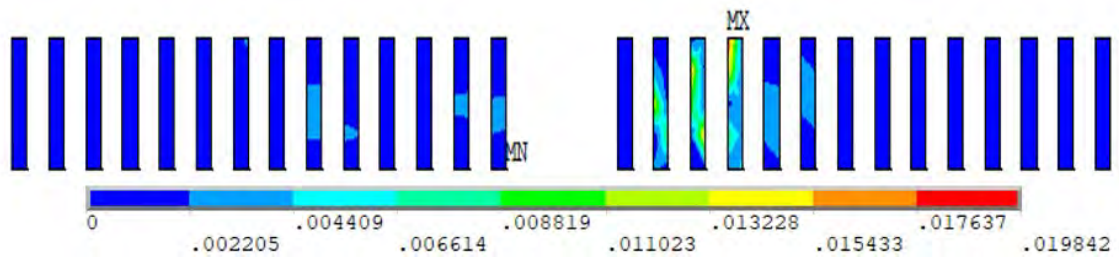


Figure 30. Slip in the interface of beam B-CO2 (cm).



Figure 31. Failure modes observed in the experiments [19].

6.4 Flexural failure

Figure 32 presents the comparison between the experimental and numerical results obtained from the proposed modeling, in terms of load vs. midspan deflection for beams B-CF2 and B-CF4.

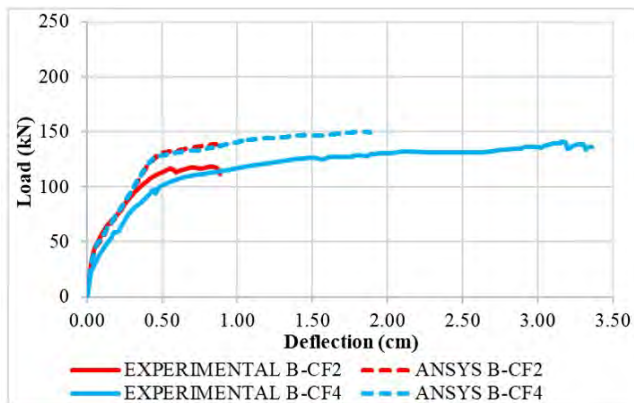


Figure 32. Load vs. midspan deflection diagram for beams with bending failure.

According to the computational model, the longitudinal reinforcement yields at the ultimate condition, as shown in Figures 33-34 for beams B-CF2 and B-CF4, respectively. This indicates that failure occurs due to bending. Figure 35 shows the stress distribution in the CFRP strengthening of beam B-CF2. The bottom strengthening, Figure 35b, presents more significant stresses than those at the lateral strengthening, Figure 35a, due to the bending failure mode of the structural element.

When evaluating the bond stresses and slips at the concrete-strengthening interface, it can be observed that, at the rupture of beam B-CF2, the interface presents the maximum value of bond stress (0.479 kN/cm²), Figure 36, as well as of slip (0.0148 cm), Figure 37, indicating that the strengthening had a debonding failure. The debonding of the strengthening, after the failure of the beam due to bending, was also observed in the experimental test. It was observed for beam B-CF4 that the CFRP strengthening at the bottom face reached its ultimate stress value (350 kN/cm²), Figure 38c, which corroborates that the bending failure caused the strengthening to fail, which is in agreement with what was observed in the experimental test. Figure 39 illustrates the failure of beams B-CF2 and B-CF4.

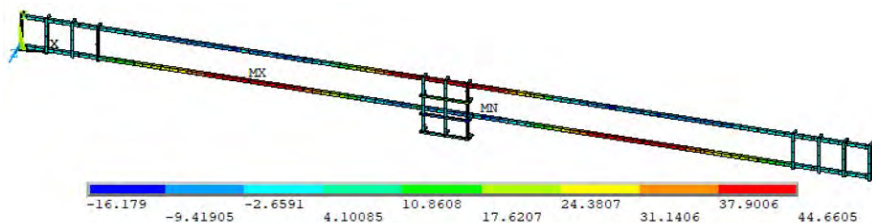


Figure 33. Stress σ_x in the reinforcement of beam B-CF2 (kN/cm²).

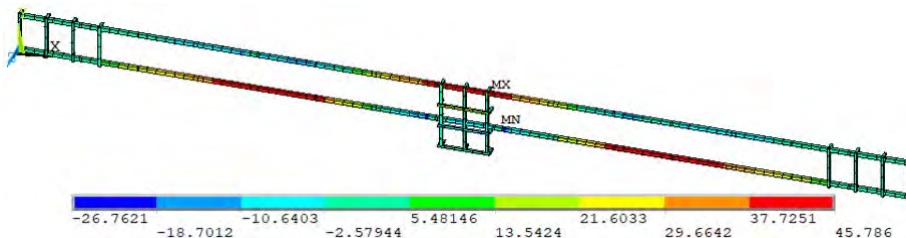


Figure 34. Stress σ_x in the reinforcement of beam B-CF4 (kN/cm²).

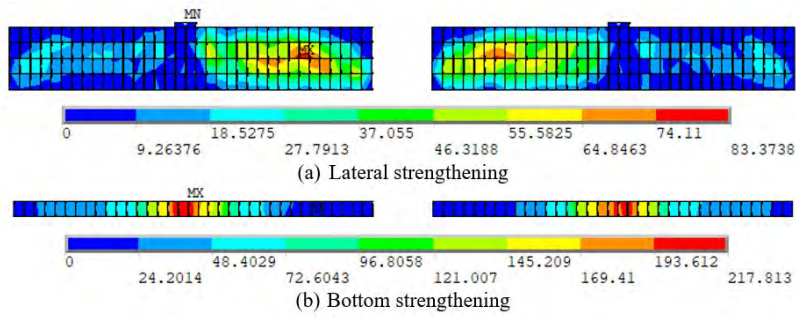


Figure 35. Principal stress σ_1 in the CFRP strengthening of beam B-CF2 (kN/cm²).

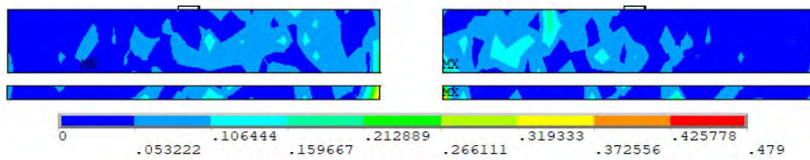


Figure 36. Bond stress in the interface of beam B-CF2 (kN/cm²).

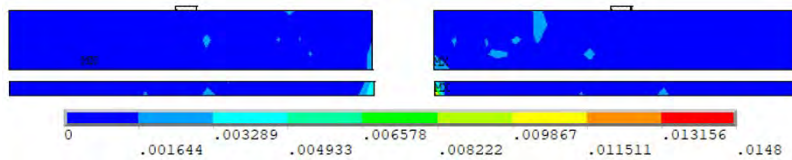


Figure 37. Interface slip of beam B-CF2 (cm).

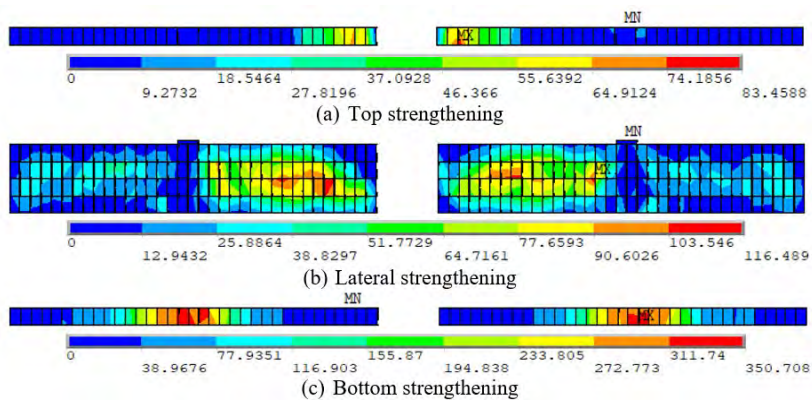


Figure 38. Principal stress σ_1 in the CFRP strengthening of beam B-CF4 (kN/cm²).

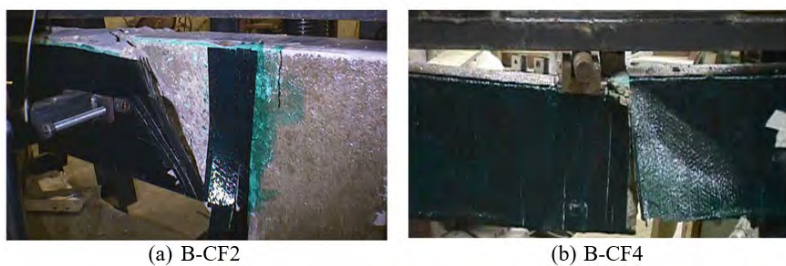


Figure 39. Failure modes observed in the experiments [19].

6.5 Summary of Results

Table 4 presents the type of reinforcement for each beam, the experimental and numerical results of failure mode and ultimate load, and the variation of that load for the twenty-one beams. The numerical simulations identified the same failure mode observed in the experimental tests for all the beams in Series A. In addition, ultimate load values were close to those observed by Khalifa [19]. Nine beams presented a variation in the ultimate load of up to 10%, and three beams had a slightly higher variation, with a maximum value of 16.6%.

For the beams in group B, the numerical simulations identified the same failure mode observed in the experimental tests for eight of the nine beams. The only beam that did not show the same experimental failure mode was beam B-CO3. In this case, it was found that, at the ultimate condition, the maximum bond stress and slip values were lower than the values established for this group of beams, thus indicating that the numerical analysis was interrupted when the concrete failed. Probably the reinforcement debonding observed in the experimental test was a post-rupture effect, which was not identified in the numerical simulation.

Regarding the ultimate load values, two beams had the same ultimate load observed in the experimental tests, five beams had a variation of less than 15%, and two beams had variations greater than 15%. Therefore, it was found that, in general, the proposed model could accurately predict the beams' behavior in terms of failure mode and ultimate load.

Table 4. Summary of test results.

N°	Specimen designation	CFRP shear reinforcement	Experimental		Numerical		Variation (%)
			Failure mode	Load (kN)	Failure mode	Load (kN)	
1	A-SW3-1	-	Shear	252.8	Shear	249.9	-1.1
2	A-SW3-2	Two plies (90°/0°)	Splitting	354.6	Splitting	355.3	0.2
3	A-SW4-1	-	Shear	201.2	Shear	231.6	15.1
4	A-SW4-2	Two plies (90°/0°)	Splitting	361.6	Splitting	372.8	3.1
5	A-SO3-1	-	Shear	151	Shear	151	0
6	A-SO3-2	U-wrap strips, 50 @ 125mm	Debonding	261.9	Debonding	235	-10.3
7	A-SO3-3	U-wrap strips, 75 @ 125mm	Debonding	267.1	Debonding	240.4	-10.0
8	A-SO3-4	One-ply continuous U-wrap	Debonding	289	Debonding	337.1	16.6
9	A-SO3-5	Two plies (90°/0°)	Splitting	339.4	Splitting	321.2	-5.4
10	A-SO4-1	-	Shear	129.4	Shear	126.3	-2.4
11	A-SO4-2	U-wrap strips, 50 @ 125mm	Debonding	254.9	Debonding	240.5	-5.6
12	A-SO4-3	One-ply continuous U-wrap	Splitting	311.1	Splitting	341.5	9.8
13	B-CW1	-	Shear	175	Shear	175	0
14	B-CW2	Two plies (90°/0°)	Splitting	214	Splitting	241	12.6
15	B-CO1	-	Shear	48	Shear	43	-10.4
16	B-CO2	U-wrap strips, 50 @ 125mm	Debonding	88	Debonding	99	12.5
17	B-CO3	One-ply continuous U-wrap	Debonding	113	Splitting	140	23.9
18	B-CF1	-	Shear	93	Shear	93	0
19	B-CF2	One-ply continuous U-wrap	Flexural	119	Flexural	139	16.8
20	B-CF3	Two plies (90°/0°)	Flexural	131	Flexural	150	14.5
21	B-CF4	One-ply; totally wrapped	Flexural	140	Flexural	150	7.1

7 CONCLUSIONS

This work aimed to present a FEM computational program to simulate the behavior of reinforced concrete beams shear-strengthened with CFRP laminates through the customization of the software ANSYS, version 19.2. The results showed that the non-linear models considered could accurately predict the behavior of the tested beams selected from the literature, both in terms of load vs. deflection, as well as when ultimate loads and failure modes were evaluated.

In addition, the ANSYS post-processing visual resources allowed the analysis of stress and strain distributions in the concrete, in the steel rebars and stirrups, and in the CFRP strengthening system considered, as well as facilitating the evaluation of the bond stresses and slips at the concrete-strengthening interface.

It was observed that the simply supported beams A-SW3-1, A-SW4-1, A-SO3-1, and A-SO4-1, and the continuous beams B-CW1, B-CO1, and B-CF1, failed by shear. This confirmed what was already expected in the experiments since they had no strengthening and were indeed designed to fail in shear. Nevertheless, the simply supported beams, A-SW3-2, A-SW4-2, A-SO3-5, and A-SO4-3, and the continuous beam, B-CW2, which were strengthened with CFRP, did not reach the maximum bond stress and slip values at the interface. There was no strengthening debonding, and the concrete failed by reaching stresses and strains above its limits, agreeing again with the experiments, which showed concrete splitting.

Three different behaviors were observed in the numerical simulations for the beams with experimental failure mode due to CFRP debonding. The first one was observed in the simply supported beams strengthened with CFRP strips (A-SO3-2, A-SO3-3, and A-SO4-2), where the interface reached the maximum bond stress followed by a maximum slip in the shear length (between a support and the concentrated load). There was a reduction in the beam stiffness exactly at the CFRP debonding. Then, the stresses decreased toward one end of the beam, reaching the maximum value in the strips located on the opposite end when the ultimate load approached. The second behavior was observed in the simply supported beam with continuous strengthening, A-SO3-4, and in the continuous beam with strip strengthening, B-CO2. The failure of these beams occurred when CFRP debonding took place, with the interfaces reaching the maximum slip value at the ultimate load. The third behavior occurred for the continuous beam with continuous strengthening, B-CO3, wherein the maximum bond stress and slip values were lower than the limiting values that would lead to a collapse. In this case, the numerical analysis was interrupted when the concrete failed. Therefore, the strengthening debonding observed in the experiments was probably a post-rupture effect.

Lastly, one more failure mode observed was due to bending and occurred in the tests of the continuous beams B-CF2, B-CF3, and B-CF4, which had their structural response satisfactorily simulated numerically.

ACKNOWLEDGEMENTS

The authors wish to acknowledge the financial support given by the Civil Engineering Graduate Program (PPGEC) of the Federal University of Rio Grande do Sul (UFRGS) and by the Brazilian governmental research institutions CAPES and CNPQ.

REFERENCES

- [1] S. J. E. Dias, "Investigação experimental e analítica no reforço ao corte de vigas de betão armado com a técnica da inserção de laminados de CFRP," Ph.D. dissertation, Esc. Eng., Univ. Minho, Guimarães, Portugal, 2008.
- [2] H. H. Mhanna, R. A. Hawileh, and J. A. Abdalla, "Shear behavior of RC T-beams externally strengthened with anchored high modulus carbon fiber-reinforced polymer (CFRP) laminates," *Compos. Struct.*, vol. 272, p. 114198, May 2021, <http://dx.doi.org/10.1016/j.compstruct.2021.114198>.
- [3] P. B. Soares, "Simulação através do Método dos Elementos Finitos do reforço ao esforço cortante de vigas de concreto utilizando polímeros reforçados com fibras de carbono," Master thesis, Prog. Pós-Grad. Eng. Civil, Univ. Fed. Rio Grande do Sul, Porto Alegre, Brazil, 2022.
- [4] B. M. Lazzari, A. Campos Fo., P. M. Lazzari, and A. R. Pacheco, "Using element-embedded rebar model in ANSYS for the study of reinforced and prestressed concrete structures," *Comput. Concr.*, vol. 19, pp. 347–356, Apr. 2017, <http://dx.doi.org/10.12989/cac.2017.19.4.347>.
- [5] P. M. Lazzari, A. Campos Fo., B. M. Lazzari, A. R. Pacheco, and R. Gomes, "Numerical simulation of the constructive steps of a cable-stayed bridge using ANSYS," *Struct. Eng. Mech.*, vol. 69, pp. 269–281, Feb. 2019, <http://dx.doi.org/10.12989/sem.2019.69.3.269>.
- [6] I. S. Hoffman, B. M. Lazzari, A. Campos Fo., P. M. Lazzari, and A. R. Pacheco, "Finite element numerical simulation of a cable-stayed bridge construction through the progressive cantilever method," *Struct. Concr.*, vol. 23, pp. 632–651, Feb. 2022, <http://dx.doi.org/10.1002/suco.202100662>.
- [7] N. S. Ottosen, "A failure criterion for concrete," *J. Eng. Mech. Div.*, vol. 103, no. 4, pp. 527–535, 1977.
- [8] Fédération Internationale du Béton, *fib Model Code for Concrete Structures 2010*. Lausanne, Switzerland: FIB, 2013.
- [9] E. Hinton, *Numerical Methods and Software for Dynamic Analysis of Plates and Shells*. Swansea, UK: Pineridge Press Limited, 1988.

- [10] E. P. Titello, "Análise da confiabilidade de vigas em concreto armado reforçado com fibras de aço em relação aos esforços transversais," Master thesis, Prog. Pós-Grad. Eng. Civil, Univ. Fed. Rio Grande do Sul, Porto Alegre, Brazil, 2020.
- [11] P. M. Lazzari, A. Campos Fo., B. M. Lazzari, and A. R. Pacheco, "Structural analysis of a prestressed segmented girder using contact elements in ANSYS," *Comput. Concr.*, vol. 20, pp. 319–327, Sep. 2017, <http://dx.doi.org/10.12989/cac.2017.20.3.319>.
- [12] G. G. Machado, A. Campos Fo., P. M. Lazzari, B. M. Lazzari, and A. R. Pacheco, "Numerical simulation by the finite element method of the constructive steps of a precast prestressed segmental bridge," *Struct. Eng. Mech.*, vol. 85, no. 2, pp. 163–177, Jan. 2023, <http://dx.doi.org/10.12989/sem.2023.85.2.163>.
- [13] F. D. M. Sarturi, "Simulação computacional de estruturas de concreto reforçadas com aço e compósitos de fibra de carbono," Master thesis, Prog. Pós-Grad. Metod. Num. Eng., Univ. Fed. Paraná, Curitiba, Brazil, 2014.
- [14] Z. Ouyang and G. Li, "Cohesive zone model based analytical solutions for adhesively bonded pipe joints under torsional loading," *Int. J. Solids Struct.*, vol. 46, no. 5, pp. 1205–1217, Mar. 2009, <http://dx.doi.org/10.1016/j.ijsolstr.2008.10.021>.
- [15] M. V. Medeiros, "Simulação numérica do comportamento de peças fletidas reforçadas com PRFC," Master thesis, Prog. Pós-Grad. Eng. Civil, Univ. Fed. Rio Grande do Sul, Porto Alegre, Brazil, 2019.
- [16] ANSYS, Inc., *ANSYS Help System Version 19.2*. Canonsburg, PA, USA: ANSYS, Inc., 2021.
- [17] Fédération Internationale du Béton, *Externally Bonded FRP Reinforcement for RC Structures: Bulletin D'information, N. 14*. Lausanne, Switzerland: FIB, 2001.
- [18] X. Z. Lu, J. G. Teng, L. P. Ye, and J. J. Jiang, "Bond-slip models for FRP sheets/plates bonded to concrete," *Eng. Struct.*, vol. 27, no. 6, pp. 920–937, May 2005, <http://dx.doi.org/10.1016/j.engstruct.2005.01.014>.
- [19] A. Khalifa, "Shear performance of reinforced concrete beams strengthened with advanced composites," Ph.D. dissertation, Struct. Eng. Depart., Alexandria Univ., Alexandria, Egypt, 1999.
- [20] A. Khalifa and A. Nanni, "Rehabilitation of rectangular simply supported RC beams with shear deficiencies using CFRP composites," *Constr. Build. Mater.*, vol. 16, no. 3, pp. 135–146, Jan. 2002.
- [21] A. Khalifa, A. Belarbi, and A. Nanni, "Shear performance of RC members strengthened with externally bonded FRP wraps," in *Proc. 12th World Conf. Earthq. Eng.*, New Zealand National Society for Earthquake Engineering, Org. (Auckland, New Zealand), Jan. 2000, pp. 1–8.
- [22] A. Khalifa, G. Tumialan, A. Nanni, and A. Belarbi, "Shear strengthening of continuous RC beams using externally bonded CFRP sheets," in *Proc. 4th Int. Symp. FRP Reinf. Concr. Struct.*, American Concrete Institute, Org. (Baltimore, MD, USA), Nov. 1999, pp. 995–1008.

Author contributions: PBS: conceptualization, writing, data curation, formal analysis, and methodology; PML and ACF: conceptualization, formal analysis, methodology, and supervision; BML: conceptualization and methodology; ARP: conceptualization.

Editors: Leandro Trautwein, Mauro Real, Mario Pimentel.



ORIGINAL ARTICLE

Experimental analysis of concrete flat slabs with internal stud-type shear reinforcement

Análise experimental de lajes lisas de concreto armado com armadura de cisalhamento do tipo stud interno

Diego Borja Ferreira^{a,b} Leandro Mouta Trautwein^a Jeovan Pereira das Virgens^{a,c} Ronaldo Barros Gomes^c Luiz Carlos de Almeida^a ^aUniversidade Estadual de Campinas – UNICAMP, Engenharia Civil, Campinas, SP, Brasil^bInstituto Federal de Educação Ciências e Tecnologia, Engenharia Civil, Cidade de Goiás, GO, Brasil^cUniversidade Federal de Goiás – UFG, Engenharia Civil, Goiânia, GO, Brasil

Received 20 September 2022

Accepted 12 March 2023

Abstract: This study evaluates seven flat slabs made with reinforced concrete. There are three reference slabs, one of them doesn't present any shear reinforcement. Four slabs have a new model of shear reinforcement of stud type, internally anchored to the flexural reinforcements. That reinforcement has an additional element, called on this study by the name: anti-cracking pins. The main objective of the research is to find the ideal spacing between these pins to achieve a failure mode and a failure load similar to the reference slabs that have conventional studs. For that, are evaluated: vertical displacements, rotation, shear reinforcement deformation, load capacity and failure mode. The slabs with the new stud have a load gain of 40% to 106% compared to the slab without studs LRef. The slab L-5-13 presented a load and a failure mode similar to the slab of reference, LRef-AC.

Keywords: flat slab, punching, shear reinforcement.

Resumo: Esse estudo avalia sete lajes lisas de concreto armado. São três lajes de referência, dessas uma não apresenta armadura de cisalhamento, e quatro com uma novo modelo de armadura de cisalhamento do tipo stud, ancorado internamente às armaduras de flexão. Essa armadura possui um elemento adicional, denominado nessa pesquisa de pinos anti-fissuração. O objetivo principal da pesquisa é encontrar o espaçamento ideal entre esses pinos para atingir um modo e carga de ruptura semelhante às lajes de referência com studs convencionais. Para tanto são avaliados deslocamentos verticais, rotação, deformação das armaduras de cisalhamento, capacidade de carga e modo de ruptura. As lajes com o novo stud apresentam ganho de carga de 40% a 106% com relação à laje sem studs LRef. A laje L-5-13 apresentou carga e modo de ruptura similar à sua laje de referência LRef-AC.

Palavras-chave: lajes lisas, punção, armadura de cisalhamento.

How to cite: D. B. Ferreira, L. M. Trautwein, J. P. Virgens, R. B. Gomes, and L. C. Almeida, "Experimental analysis of concrete flat slabs with internal stud-type shear reinforcement," *Rev. IBRACON Estrut. Mater.*, vol. 16, no. 3, e16305, 2023, <https://doi.org/10.1590/S1983-41952023000300005>

1 INTRODUCTION

The use of flat slabs made with reinforced concrete is standing out in civil engineering due to its advantages in the construction process. The absence of beams reduces cuts in the production process of formwork. Therefore, it reduces

Corresponding author: Diego Borja Ferreira. E-mail: diego.ferreira@ifg.edu.br

Financial support: This research was financed in part by the Coordenação de Aperfeiçoamento de Pessoal de Nível Superior-Brasil (CAPES) - Finance Code 001.

Conflict of interest: Nothing to declare.

Data Availability: The data that support the findings of this study are available from the corresponding author, DBF, upon reasonable request.



This is an Open Access article distributed under the terms of the Creative Commons Attribution License, which permits unrestricted use, distribution, and reproduction in any medium, provided the original work is properly cited.

costs and rationalizes construction. The increased flexibility in the conception of projects for building and architectural installations is also a possibility in the use of this slab model.

As any structural system, the use of flat slabs must take into account some unfavorable aspects. The large vertical displacements presented by this structural model points to the use of elements that increase its stiffness [1].

Another preponderant factor in the use of this type of slab concerns to the punching effects in the columns area. The high concentration of shear forces can lead the structural element to collapse. Figure 1 shows the loaded region, it is possible to observe the development of cone-shaped cracking around the columns, the use of mechanisms can minimize these effects.

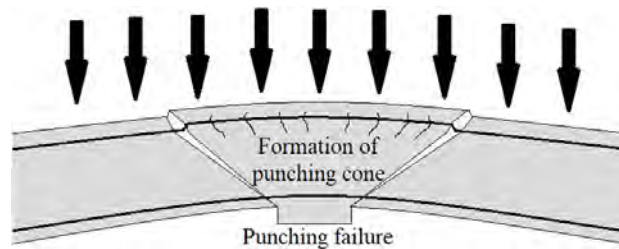


Figure 1: Failure by punching.

One of the possibilities to minimize the punching effects is to increase the concrete cross section in the region of the connection with the columns, but this technique causes problems in the architectural project. Another technique to combat this effect is the use of reinforcement, is the most efficient method to increase the capacity and ductility of flat slabs [2], [3].

The use of shear reinforcement to combat punching effects can lead to three distinct failure modes: failure by crushing of the compression strut near the column face (Figure 2a); failure by yielding of the shear reinforcement in the internal region of the reinforcement (Figure 2b); failure outside the region of the shear reinforcement with characteristics similar to the failure of slabs without shear reinforcement (Figure 2c), [2].

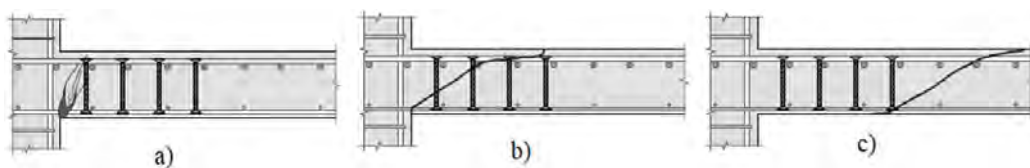


Figure 2: Crack patterns [4]

Several studies [1], [5]–[8], used internal-type shear reinforcement point to a specific type of failure called delamination, in which the failure surface touches the bases of the reinforcement (Figure 3) anticipating collapse.



Figure 3: Crack delamination patterns.

The work in question presents a comparative study of flat slabs investigating the effects of two models of stud-type shear reinforcement, which differ in terms of anchorage in the flexural reinforcement (Figure 4). The structural performance was evaluated by analyzing the strength and stiffness, as well as possible the benefits in the mounting process in the construction environment.

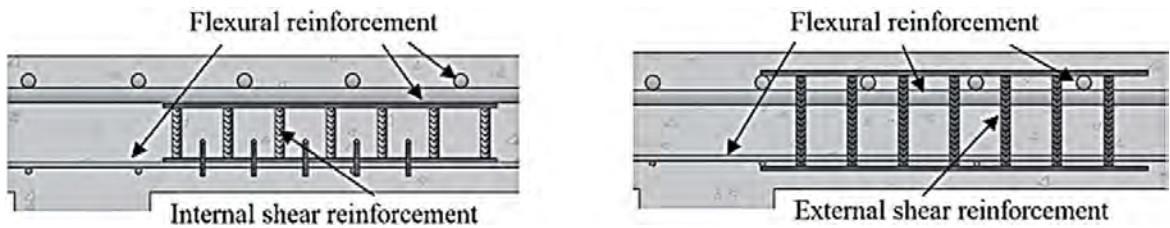


Figure 4: Shear reinforcement with different anchorage types.

2 EXPERIMENTAL PROGRAM

The experimental program reproduced a reinforced concrete panel with a central column with side dimensions 150mm x 150mm, simulating the behavior of punching effects in flat slabs.

The experimental analysis was made through tests until the failure of seven square flat slabs with 2400 mm side and 150 mm thick, with a flexural reinforcement ratio sufficient to prevent failure by this reinforcement. All slabs have the same characteristics varying only the shear reinforcement.

2.1 Characteristics of the slabs

The study is composed by a reference slab that has no shear reinforcement named LRef, two slabs with conventional stud-type shear reinforcement with external anchorage in the flexural reinforcement, named LRef-AC and LRef-AC-I and four other slabs with a new proposal of stud-type shear reinforcement anchored internally in the flexural reinforcement, named L-5-13, L-5-6, L-5-13-I and L-5-6-I. The slabs with studs that are identified with “I” have internal failure prediction for the current standards and the others, external failure prediction.

Figure 5 shows the slab models tested and Figure 6 shows the details of the studs distribution.

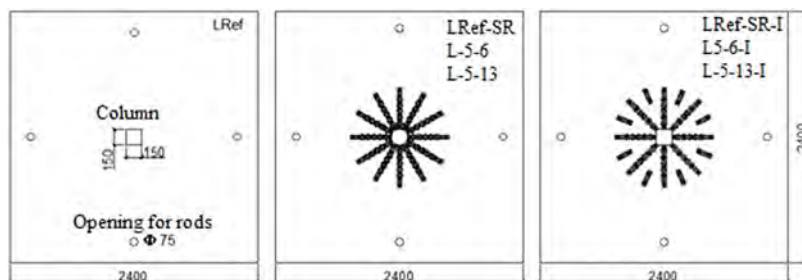


Figure 5: Distribution of studs and reference slab LRef.

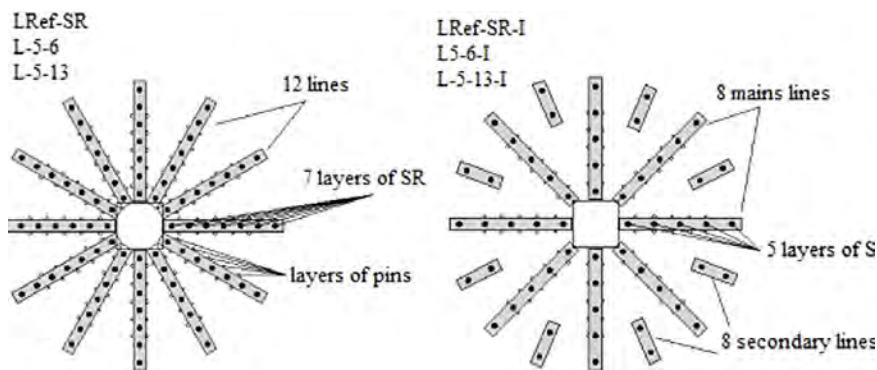


Figure 6: Detail of the stud distribution.

The new stud proposal is based on previous researches [9], [10] that presented excellent results for the use of shear reinforcement anchored internally on the flexural reinforcement. The authors identified some fragility regarding the

development of cracks, noting the appearance of horizontal cracks that tangent the bases of the reinforcement causing a decrease in the ultimate strength.

The slabs L-5-13, L-5-6, L-5-13-I and L-5-6-I use a proposal of internal stud, which have an auxiliary reinforcement in order to minimize the effects of the cracking, this reinforcement has an inverted “U” shape called anti-cracking pin, welded to the bottom plate of the pieces.

In order to neutralize the effects of exudation which can weaken the concrete in the region of the bottom plate, openings of 8 mm in diameter were made – it also contributes to the anchoring of the material. The details of this type of stud can be seen in Figure 7.

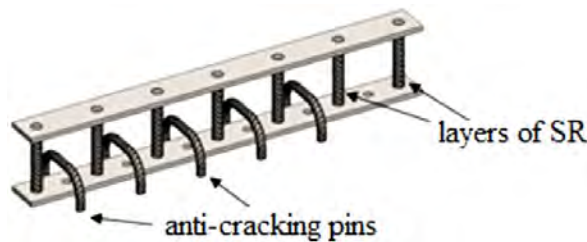


Figure 7: Internal stud model used.

The slabs LRef-AC, L-5-13 and L-5-6 were reinforced due to the prediction of external failure, being composed by 12 lines of studs with 7 layers of shear reinforcement of 10 mm diameter. The slabs LRef-AC-I, L5-13-I and L-5-6-I were reinforced due to the internal failure prediction, consisting in 8 lines of studs with 5 layers of shear reinforcement of 6.3 mm diameter.

The slabs with internal studs have 13 and 6 layers of 5.0 mm anti-cracking pins. The location for using these pins has been defined considering that [1] concluded that the use of pins similar to the one used in this research were efficient in covering the control perimeter region C' defined by NBR 6118 [11] as 2d of the column face. Figure 8 shows the details of the shear reinforcement used in the research.

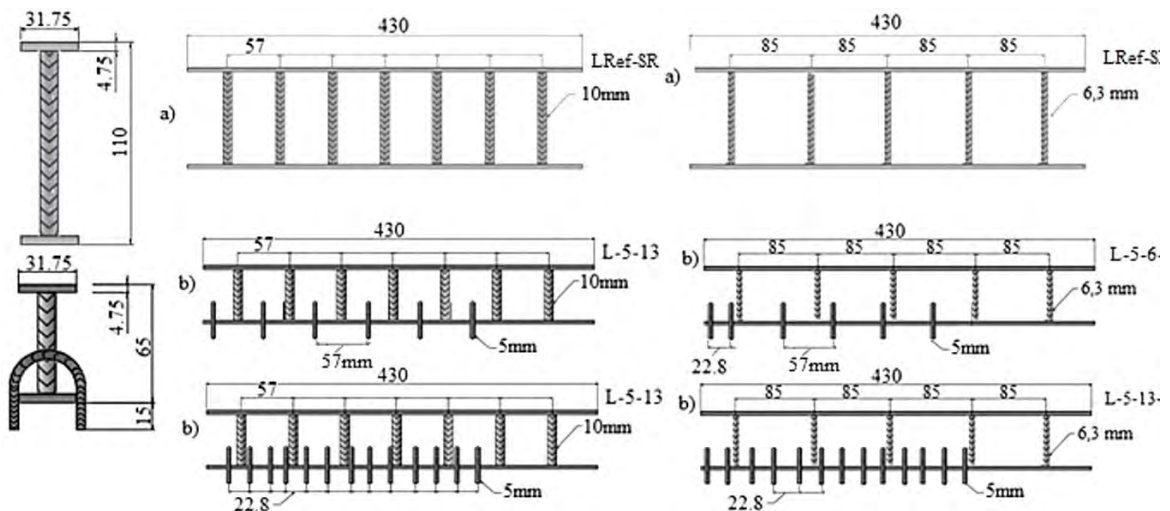


Figure 8: Models of studs.

To combat the effects of flexural forces the slabs were reinforced with 40 straight bars with 16.0 mm diameter of CA-50 steel distributed in cross on the top face and 20 bars with 6.3 mm diameter distributed in cross on the bottom face. In order to increase the anchorage of the bars, 10.0 mm diameter hooks were installed at the slabs ends. The details of the flexural reinforcement are shown in Figure 9.

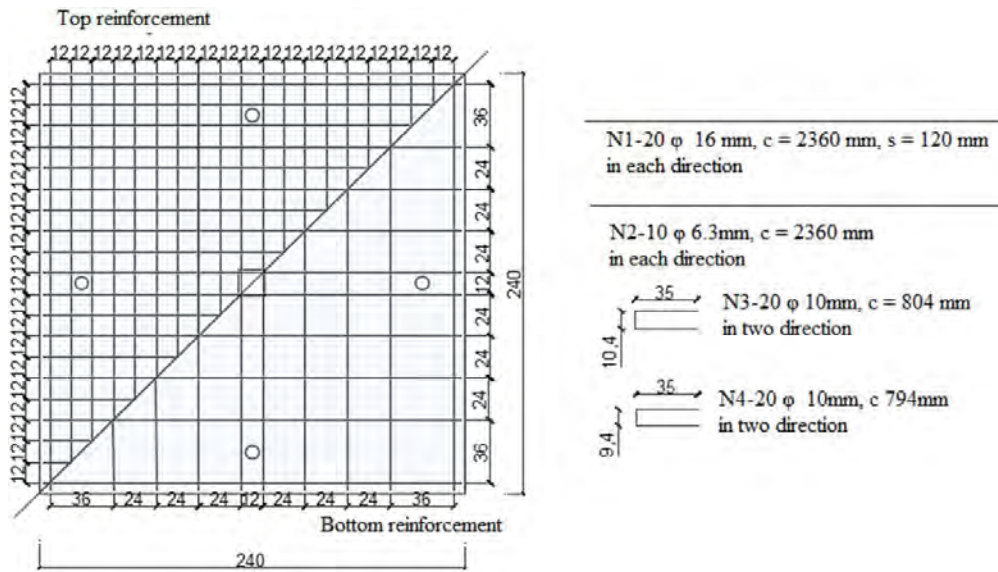


Figure 9: Detailing of the flexural reinforcement.

Conventional studs make it difficult to position bending and shear reinforcement with the ideal spacing foreseen in the design due to the dense amount of reinforcement required in this region, as can be seen in the slabs analyzed by [1], [6], [8] and [12] presented in Figure 10.

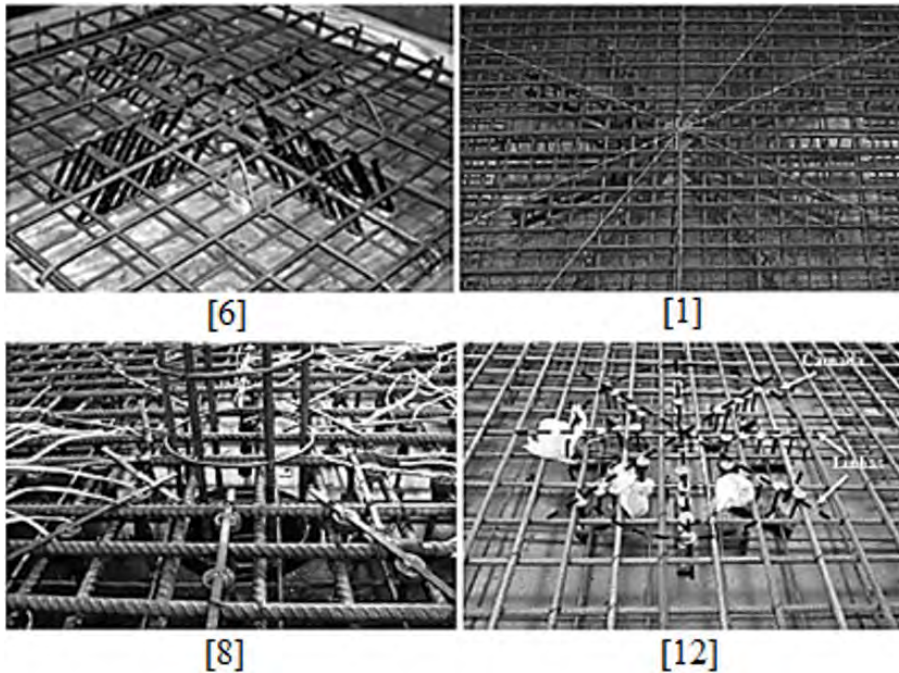


Figure 10: Flexural reinforcements in the region of the slab-column connection.

The use of internal studs presents an advantage in the assembly process, since there is no need to pass the bending bars between the shear reinforcements, which was observed during the assembly of the slabs in this research [1].

The slab reinforcement procedure occurred in the following order: positioning of the bottom bending reinforcement grid (compressed), radial positioning of the studs with the proper angles, positioning of the upper bending reinforcement grid (tensioned), closing with lateral hooks. The reinforcement installing procedure is shown in Figure 11.

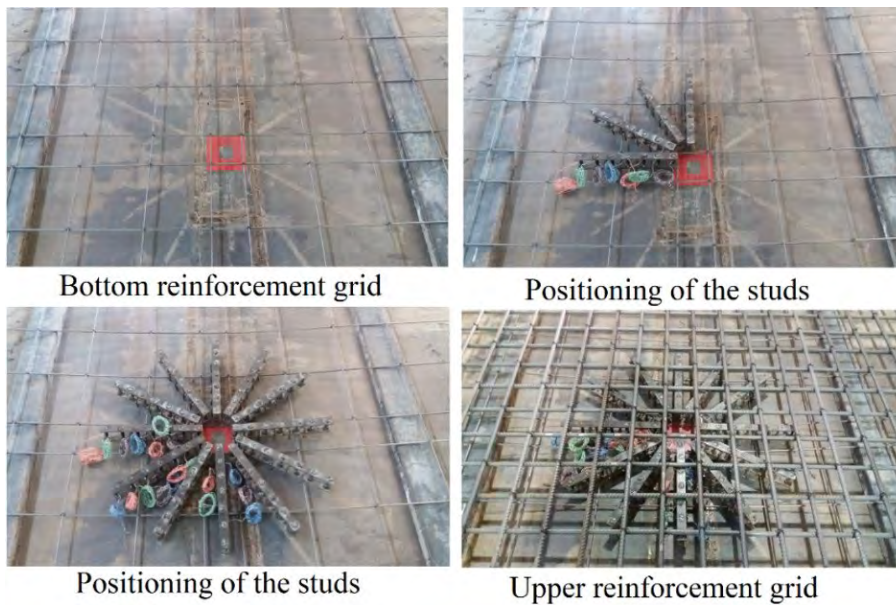


Figure 11: Installing the slab’s reinforcement

2.2 Test system

The loading system was set up simulating an internal column, using a hydraulic actuator with capacity of 1000 kN positioned at the bottom of the slab, applying load on a square metal plate of 150 mm side simulating a column, between the plate and the actuator was positioned a load cell to measure the applied load (Figure 12).

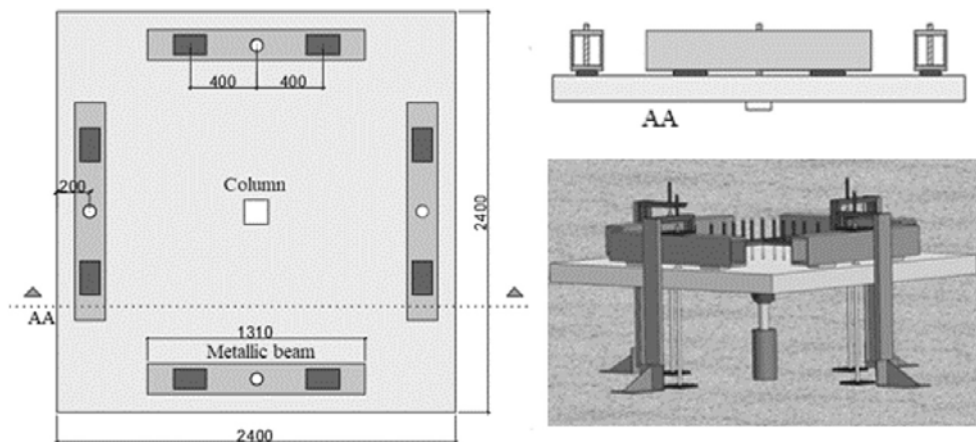


Figure 12: Test system.

3 RESULTS AND DISCUSSIONS

3.1 Load and failure mode

The load obtained by the load cell considers the self-weight of the slabs and metallic beams of the experimental apparatus. The slabs were submitted to loadings at intervals of 50 kN, with constant monitoring of deformations and displacements. As the deformations indicated a possible failure, load intervals were reduced to refine the data obtained, improving the analysis of the structural element behavior.

The failure load calculations and the predicted failure mode were based on NBR 6118 [11] for conventional studs are exposed in Table 1.

Table 1: Characteristics, load and failure mode.

Slabs	d (mm)	h (mm)	ρ (%)	f_c (MPa)	P_u (kN)	P_{calc} (kN)	P_u/P_{calc} (kN)	Failure mode	
								Predicted	Real
LRef-AC	116	155	1.65	47.2	665	632	1.05	EP**	EP**
L-5-6	113	153	1.73	44.3	500	610	0.82	EP**	IP*
L-5-13	115	155	1.67	42.0	660	602	1.10	EP**	EP**
LRef-AC-I	113	154	1.73	46.5	551	478	1.15	IP*	IP*
L-5-6-I	113	154	1.73	46.7	450	479	0.94	IP*	IP*
L-5-13-I	116	157	1.65	46.4	525	485	1.08	IP*	IP*
LRef	116	155	1.65	47.2	320	310	1.03	Punching	Punching

*IP: Internal Punching (in the region of shear reinforcement) according to NBR 6118 [11]. **EP: External Punching (after the region of the shear reinforcement) according to NBR 6118 [11]

All slabs analyzed showed a failure load higher than the design load defined by NBR 6118 [11], except for the slabs that used only 6 layers of anti-cracking pins (L-5-6 and L-5-6-I). Only the slab L-5-6 did not present failure mode with the normative prediction.

Compared to the reference slab LRef the load gain with the use of conventional shear reinforcement was 107% for LRef-AC and 72% for LRef-AC-I. With the use of the proposed reinforcement the gain was 106% for L-5-13 and 64% for L-5-13-I.

When performing the comparison of the reinforcement models with their respective reference slabs, despite not reaching higher loads, the slabs with internal shear reinforcement yielded a capacity very similar to the slabs with external reinforcement. The difference in load was less than 1% between LRef-AC and L-5-13 and 4% between LRef-AC-I and L-5-13-I.

It is possible to identify the interference of the number of layers of anti-cracking pins in the strength and failure mode, in such a way that the slabs with fewer layers have the lowest failure loads of the slabs with shear reinforcement. This behavior is valid both for slabs with external failure prediction, as for slabs with internal failure prediction.

3.2 Vertical displacement

The vertical displacements were monitored by 13 LVDT's in only one quadrant of the slabs in directions perpendicular to each other and centered, as shown in Figure 13. LVDTs were installed in the ties in order to subtract their displacements, obtaining the real displacement of the slabs.

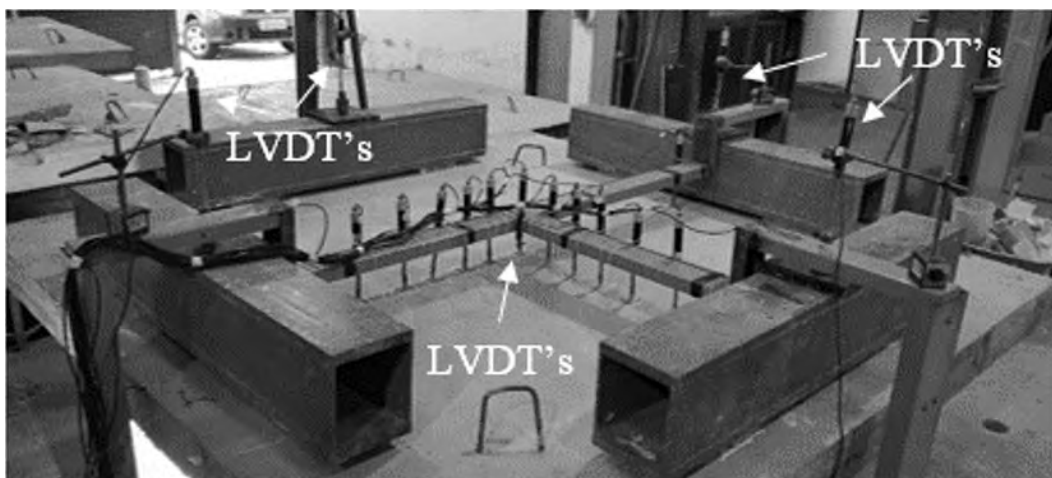


Figure 13: Positioning of the LVDT's.

In all slabs, the maximum displacement was obtained in the central region (LVDT 1) gradually decreasing as approaching the edges, it was possible to observe a certain symmetry in the displacement in the equidistant perpendicular axes. Figures 14 to 17 show the vertical displacement in different loading ranges.

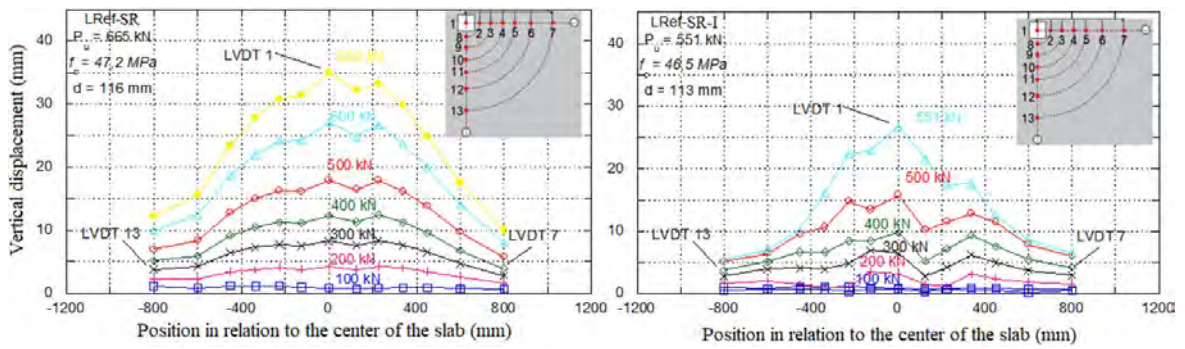


Figure 14: Vertical displacement of slabs LRef-SR and LRef-SR-I.

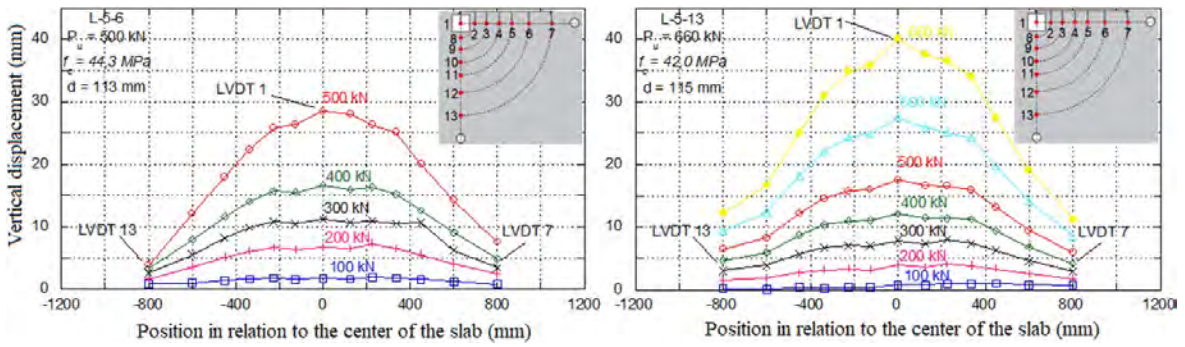


Figure 15: Vertical displacement of slabs L-5-6 and L-5-13.

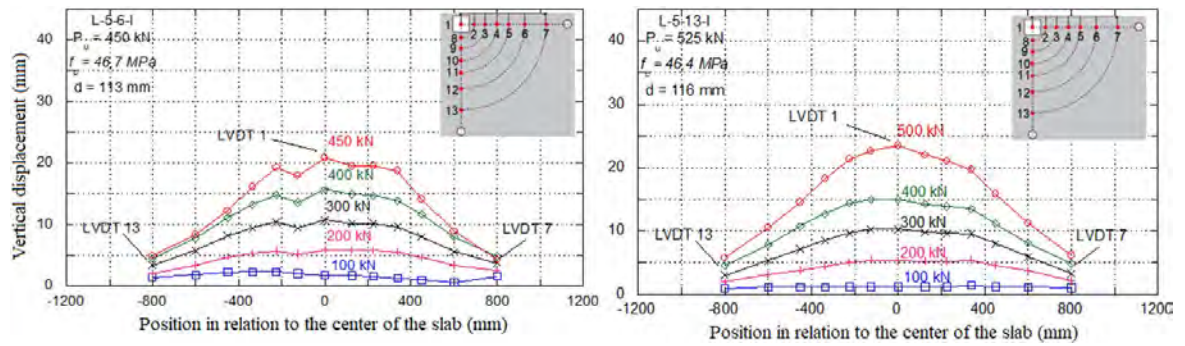


Figure 16: Vertical displacement of slabs L-5-6-I and L-5-13-I.

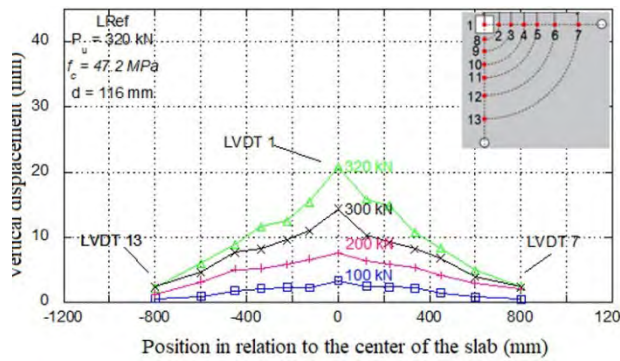


Figure 17: Vertical displacement of slabs LRef.

Analyzing the displacement in the loading range of 300 kN, a load close to the failure of the LRef slab, an increase in the rigidity of the slabs with shear reinforcement is observed. This increase was in the order of 50% (L-5-6-I, L-5-13-I, L-5-6) and 47% (L-5-13, LRef-SR, LRef-SR-I).

Regarding the maximum displacement, the slabs that showed greater ductility with higher displacements were: L-5-13-I with external failure prediction, and LRef-SR-I with internal failure prediction.

3.3 Strain of the flexural reinforcement

Figure 18 shows the mapping of the yield radius of the flexural reinforcement, it used data from strain gauges (SG) installed in the most loaded bars (outermost). The analysis area is divided into 5 bands delimited by the position of the SG's, the radii have the following distances from the center of the column: 6 cm, 25 cm, 37 cm, 49 cm and 85 cm.

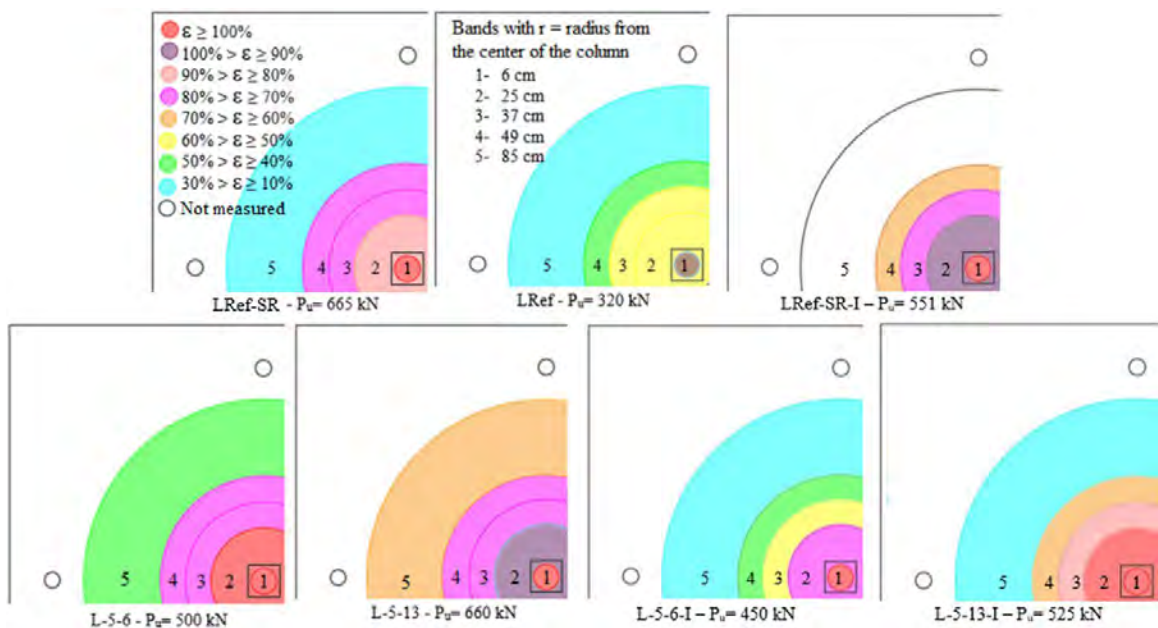


Figure 18: Mapping the yield radius.

In all slabs, it is possible to observe the yield of the reinforcement in the central region (column region, with the exception of the reference slab LRef that showed in this same region strain above 90% of the yield strain).

Analyzing the slabs with internal failure prediction (LRef-SR-I, L-5-6-I and L-5-13-I), it can be seen that there was a greater load distribution in the slab L-5-13-I increasing the yield radius until the second range. Slab L-5-6-I, range 2, showed strain between 80% and 70% while the same range in reference slab LRef-SR-I showed strain between 90% and 100%.

Regarding the slabs of external failure prediction, the slab L-5-13 had greater load distribution, its yield radius was concentrated in the first range, but the fifth and the final range of analysis showed the highest strain among the slabs analyzed with a strain between 60% and 70% of the yield strain characteristic.

This behavior shows the marked ductility of this slab, which was visually verified during the failure of this model.

3.4 Strain of the shear reinforcement

The shear reinforcement strains were measured with electrical resistance strain gauges (SG) in all layers of the same stud line.

Figure 19 shows the shear reinforcement strains of the LRef-SR and LRef-SR-I slab, and indicate higher strains in the layers closest (SG's 1 and 2) to the loaded region (column).

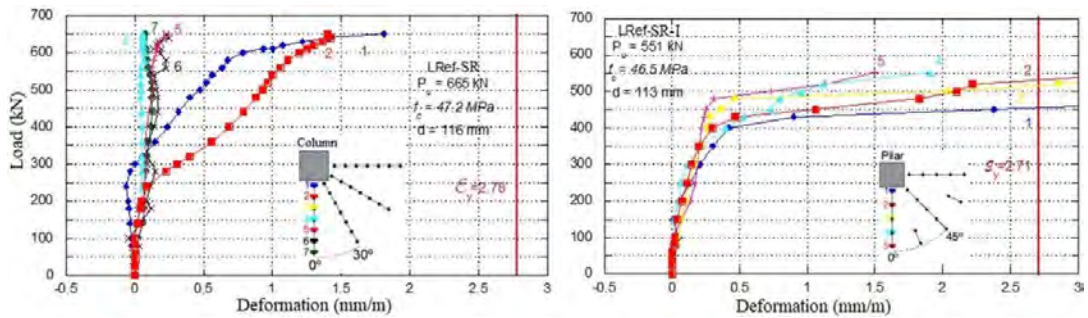


Figure 19: Strain of shear reinforcement, slabs LRef-SR and LRef-SR-I.

The LRef-SR slab showed external failure surface to the region of the shear reinforcement, the late horizontality of the curves demonstrate this behavior, while the LRef-SR-I slab shows horizontality at lower loads and strains that reached the yield strain characteristic of steel. This behavior indicates an internal failure, since the crossing of the failure surface line by a layer of shear reinforcement causes its yielding.

Figure 20 shows the shear strains of the slabs L-5-6 and L-5-13.

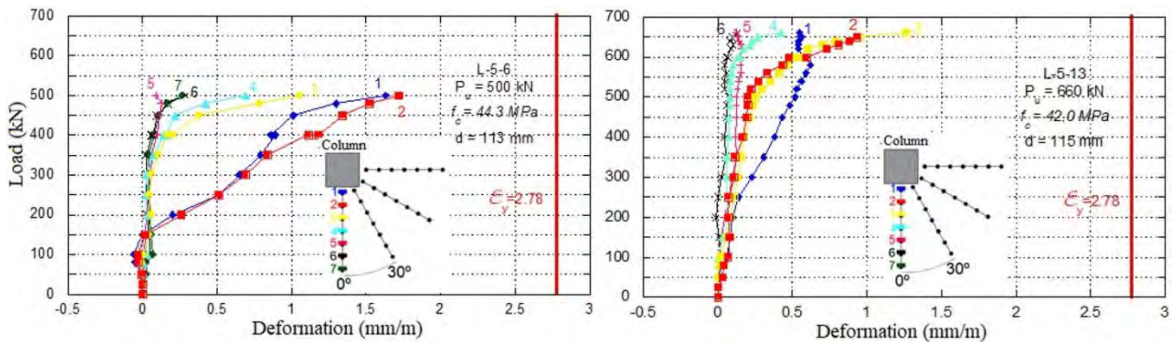


Figure 20: Strain of the shear reinforcement of slab L-5-6 and L-5-13.

The slab L-5-6 presented higher strains in the layers closest to the column region (layers 1 and 2), and no layer reached the characteristic yield strain. The maximum strain recorded reached approximately 62% of the yield strain obtained in the characterization test.

The slab L-5-13 presents lower strains than LRef-AC, and in order of 35% of the yield strain. Layer 1 showed greater strain at initial loads, and at 85% of the final load the curve shows a stress relief, which may have occurred due to the loss of the SG gauging capacity. The horizontality of the curves in the failure loads demonstrate a tendency for the reinforcement to yield.

The shear reinforcement strains of the slabs L5-6-I and L-5-13-I are presented in Figure 21.

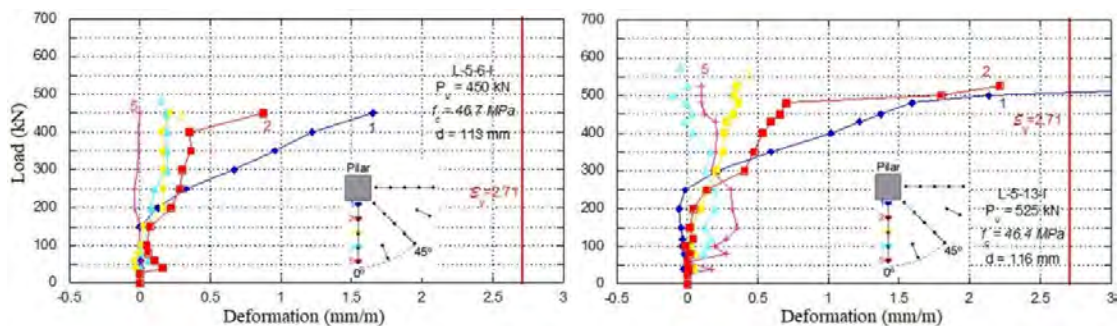


Figure 21: Strain of the shear reinforcement slab L-5-6-I and L-5-13-I.

The slab L-5-6-I has shear reinforcement strains smaller than the characteristic yield strain, layers 1 and 2 had the largest strains, showing the appearance of cracks in this region. Despite not reaching the yield strain, the horizontality of the curves of these layers indicates that the failure surface passed through these layers, which was visually verified in the slab.

The slab L-5-13-I showed strains that reached the yield strain, the most strained layers are the two closest to the column, indicating that the failure surface passed through them, which was also visually observed in the slab.

3.5 Strain on the anti-cracking pins

All the one line anti-cracking pins were instrumented, there was no characteristic yield strain in any case, but as in the shear reinforcement there was a horizontality on the strain curves of the ultimate loads. It is possible to observe that the largest strains occurred in the pins closest to the column region, decreasing linearly as they move away (Figures 22 and 23).

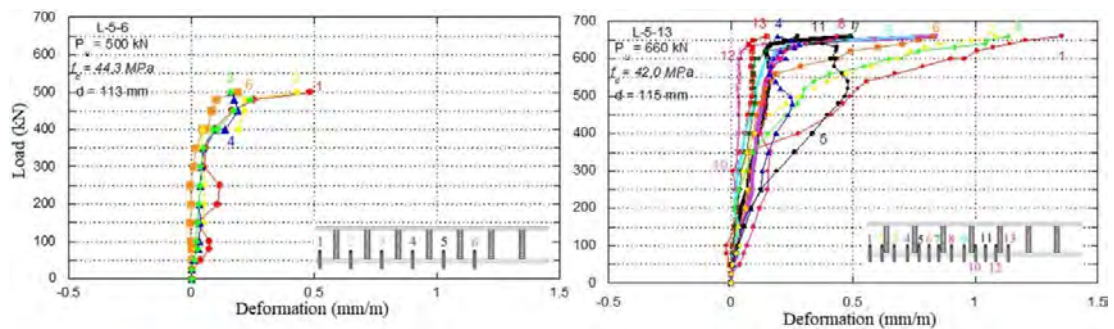


Figure 22: Strain of the anti-cracking pins of slabs L-5-6 and L-5-13.

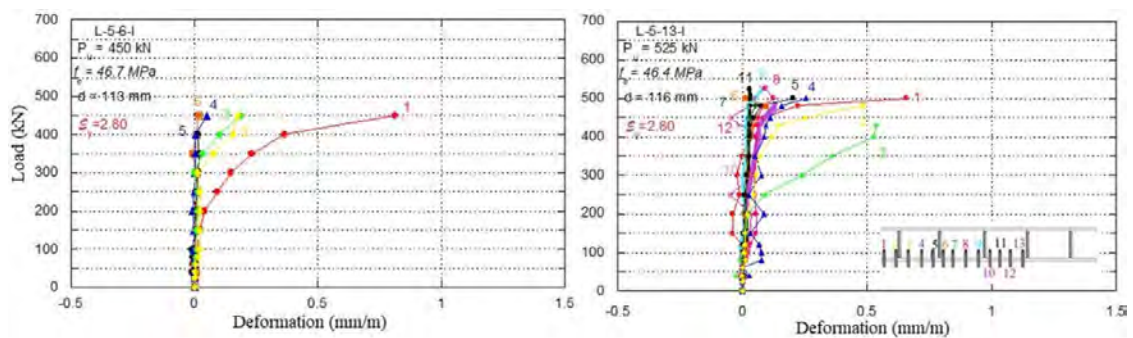


Figure 23: Strain of the anti-cracking pins of slabs L-5-6-I and L-5-13-I.

The maximum strains recorded were at the pin closest to the column with 47% (L-5-13) and 25% (L-5-13-I) of the yield strain. The stresses are more concentrated in the pins as the load increases.

In slab L-5-13-I it can be seen that the most distant pins experience very little strains, which may even reduce the amount of pins in this slab, unlike the slab L-5-13 in which even the most distant pins have larger strains with horizontal behavior in the ultimate loads.

3.6 Comparison of the experimental failure load with loads predicted in analytical models.

For the purpose of comparative analysis between the slabs tested with codes and standards, it was decided to evaluate the failure load with the results theoretically obtained by such normative instructions. Comparative data are shown in Table 2.

One must note that there is no normative forecast for the internal stud-type shear reinforcement model proposed in this study. The following codes were used for this analysis: ACI 318 [13], Eurocode 2 [14], NBR 6118 [11].

The ACI 318 [13] code establishes, for the design of slabs subject to punching, the application of Equation 1:

$$V_n = V_c + V_s \tag{1}$$

Where “ V_n ” is the shear strength, constituted by the contribution portion of the concrete (V_c) and the contribution portion of the steel of the shear reinforcement (V_s). For slabs without shear reinforcement, the failure load at the punch of the slab-column connection must be equal to the smallest result obtained with the application of Equations 2 to 4:

$$V_c = 0,33\lambda_s\lambda\sqrt{f'_c} \tag{2}$$

$$V_c = 0,17\left(1 + \frac{2}{\beta}\right)\lambda_s\lambda\sqrt{f'_c} \tag{3}$$

$$V_c = 0,083\left(2 + \frac{\alpha_s d}{b_0}\right)\lambda_s\lambda\sqrt{f'_c} \tag{4}$$

For slabs with shear reinforcement, the calculation of the resistant portion of concrete V_c for slabs with reinforcement, composed of stirrups must be done in the two control perimeters by Equation 5:

$$V_c = 0,17\lambda_s\lambda\sqrt{f'_c} \tag{5}$$

Concerning the slabs with reinforcement composed of studs, the shear force at the first critical perimeter must be equal to the lowest value obtained by Equations 6 to 8:

$$V_c = 0,25\lambda_s\lambda\sqrt{f'_c} \tag{6}$$

$$V_c = \left(0,17 + \frac{0,33}{\beta}\right)\lambda_s\lambda\sqrt{f'_c} \tag{7}$$

$$V_c = \left(0,17 + \frac{0,083\alpha_s d}{b_0}\right)\lambda_s\lambda\sqrt{f'_c} \tag{8}$$

Figure 24 shows the control perimeters established by ACI 318 [13].

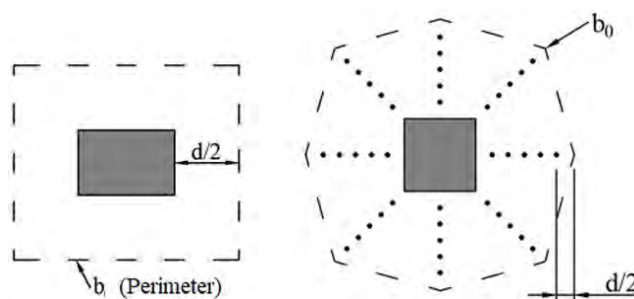


Figure 24: Adapted ACI 318 [13] control perimeter.

Eurocode 2 [4] recommends, establishing for the proper dimensioning of slabs subject to punching, that the maximum shear force must not exceed the maximum shear force capacity according to Equations 9 to 11.

$$V_{Ed} \leq V_{Rd} \tag{9}$$

$$V_{Ed} = \beta \frac{F_{sd}}{u_0 d} \tag{10}$$

$$V_{Rd,max} = 0,4\left(1 - \frac{f_{ck}}{250}\right)f_{cd}u_0d \quad (11)$$

For slabs without shear reinforcement, only the contribution portion of the concrete must be considered in the calculation of the punching ultimate load. Equation 12 calculates the shear force capacity from concrete.

$$V_{Rd,c} = 0,18k(100\rho f_{ck})^{1/3} \geq V_{min} \quad (12)$$

Where: $V_{min} = 0,035k^{2/3}f_{ck}^{1/2}$

Equations 13 and 14 give the calculation of shear strength in the region with shear reinforcement.

$$V_{Ed} \leq V_{Rd,cs} \quad (13)$$

$$V_{Rd,cs} = 0,75V_{R,dc} + 1,5\frac{d}{s_r}A_{sw}f_{ywd,ef}\left(\frac{1}{u_1d}\right)\text{sen}\alpha \quad (14)$$

Equations 15 and 16 are used to calculate shear strength for regions external to the shear reinforcement.

$$v_{Ed} \leq v_{Rdc,ext} \quad (15)$$

$$V_{Rd,cs,ext} = V_{Rd,c}\mu_{out}d \quad (16)$$

Figure 25 details the control perimeter for this analysis.

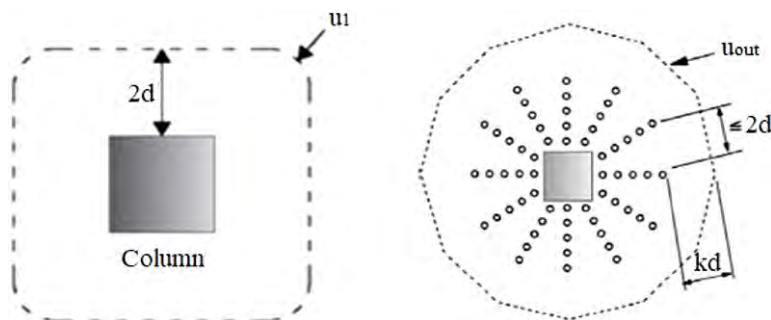


Figure 25: Adapted Eurocode 2 [14] control perimeter.

NBR 6118 [11] establishes that for symmetrical loading in internal columns, the stress on critical surfaces C and C' is calculated by Equation 17:

$$\tau_{sd} = \frac{F_{sd}}{\mu d} \quad (17)$$

To avoid cracking by diagonal compression of the concrete on the critical surface C, the verification in flat slabs with or without shear reinforcement must be solved by Equation 18.

$$\tau_{sd} \leq \tau_{Rd2} = 0,27\alpha_v f_{cd} \quad (18)$$

To verify the shear stress acting on the critical surface C' in flat slabs without shear reinforcement, Equation 19 is used.

$$\tau_{sd} \leq \tau_{Rd1} = 0,13(1 + \sqrt{\frac{20}{d}})(100\rho f_{ck})^{1/3} \tag{19}$$

To verify the shear stress acting on the critical surface C' in flat slabs with shear reinforcement, Equation 20 is used.

$$\tau_{sd} \leq \tau_{Rd1} = 0,13(1 + \sqrt{\frac{20}{d}})(100\rho f_{ck})^{1/3} + 1,5 \frac{d}{s_r} \frac{A_{sw} f_{ywd} \sin \alpha}{\mu d} \tag{20}$$

The control perimeters established by NBR 6118 [11] are shown in Figure 26.

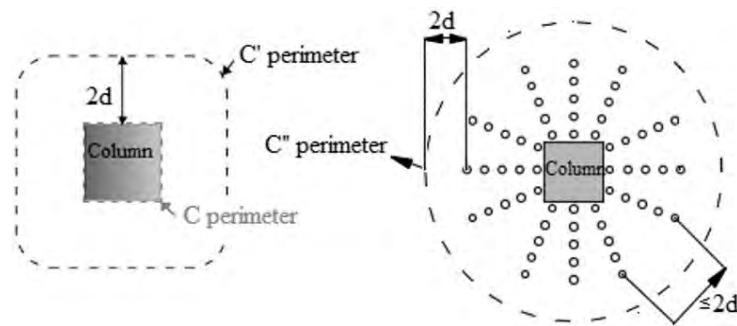


Figure 26: Adapted NBR 6118 [11] control perimeter.

The comparison of the experimental results with that predicted by the calculation according to NBR 6118 [11] is presented in Table 2. Regarding the result (Pu/Pcalc), it is possible to observe that the LRef, LRef-SR, and L5-13 slabs presented a failure load greater than that calculated with this code formulation. The others slabs cracked with a load lower than the predicted, ranging between 8% and 18% lower.

Table 2: Comparison of experimental results with codes specifications.

Slabs	Pu kN	ACI 318 [13]				Eurocode 2 [14]				NBR 6118 [11]			
		Pcalc kN	Pu/Pcalc	b0 mm	b0sr mm	Pcalc kN	Pu/Pcalc	u1 mm	uout mm	Pcalc kN	Pu/Pcalc	C' mm	C'' mm
LRef-SR	665	426	1.56	1064	3144	691	0.96	2080	3874	632	1.05	2080	4244
L-5-6	500	401	1.25	1052	3134	656	0.76	2020	3836	610	0.82	2020	4235
L-5-13	660	398	1.66	1060	3140	655	1.01	2045	3854	602	1.10	2045	4231
LRef-SR-I	551	398	1.39	1052	3134	404	1.36	2020	3836	478	1.15	2020	4235
L-5-6-I	450	397	1.13	1052	3134	405	1.11	2020	3836	479	0.94	2020	4235
L-5-13-I	525	409	1.28	1064	3144	419	1.25	2080	3874	485	1.08	2080	4244
LRef	320	254	1.14	1064	-	371	0.86	2080	-	310	1.03	2080	-

Compared to ACI 318 [13], no slab presented a failure load lower than that predicted by the code; Pu/Pcalc results range from 13% (L-5-6-I) to 66% (L-5-13).

When comparing with Eurocode 2 [14], the L-5-13 and LRef-SR slabs presented a Pu practically equal to Pcalc, while the slabs LRef and L-5-6 presented a Pu lower than Pcalc, varying between 14% and 24% respectively, thus the obtained results (Pu/Pcalc) are against security. All slabs predicted to failure internally reached a failure load greater than the design load. The control perimeter 1.5d away from the last layer of shear reinforcement was adopted.

4 CONCLUSION

The use of internal stud-type shear reinforcement looks promising, since the increase in strength of the slab without shear reinforcement reached the order of 106% in L-5-13 and 64% in L-5-13-I. These same slabs compared to the

models that used standardized studs showed very close failure loads, L-5-13 less than 1% lower than LRef-AC and L-5-13-I 5% lower than LRef-AC-I.

The data points to a direct relationship between the amount of anti-cracking pins and the capacity of the structural element. The smaller the spacing between pins in the 2d control perimeter the greater the capacity and ductility.

The anti-cracking pins in the layers farthest from the column in the slabs with internal failure prediction, presented small strains, indicating that the positioning of the pins in slabs with this failure prediction can be installed covering a smaller region, different from the 2d control perimeter proposed in this study.

The pins fulfilled the function of preventing the development of cracks tangential to the base of the studs as observed in previous research, avoiding the failure designated as delamination.

Regarding normative specifications, further studies are necessary to develop an adequate design model that can describe the behavior of the proposed reinforcement.

About the on-site assembly process, the proposed model shows to be efficient given the ease of assembly of the structural components and the guarantee of the design specifications, such as the spacing between the flexural reinforcement and the perfect radial distribution of the shear reinforcement lines, something that proved to be complicated for slabs with conventional studs.

ACKNOWLEDGEMENTS

The authors thank the Federal University of Goiás - UFG in the person of Professor PhD. Janes for the availability of the Structure Laboratory to carry out the tests of this research. They are also grateful to the Coordination for the Improvement of Higher Education Personnel-Brazil (CAPES) for the partial financial support given to this research.

5 REFERENCES

- [1] L. M. Trautwein, T. N. Bittencourt, R. B. Gomes, and Bella, J.C.D., "Punching strength of flat slabs with unbraced shear reinforcement," *ACI Struct. J.*, vol. 108, pp. 197–205, 2011.
- [2] R. B. Gomes, "Punching resistance of reinforced concrete flat slabs with shear reinforcement," Ph.D. dissertation, Polytech. Cent. London, London, 1991.
- [3] C. E. Broms, "Elimination of flat plate punching failure mode," *ACI Struct. J.*, vol. 97, no. 1, pp. 94–101, Jan-Feb 2000.
- [4] J. Hegger, A. G. Sherif, D. Kueres, and C. Siburg, "Efficiency of various punching shear reinforcement systems for flat slabs," *ACI Struct. J.*, vol. 114, no. 3, pp. 631–642, 2017.
- [5] F. Samadian, "Shear reinforcement against punching in reinforced concrete flat slabs," *Struct. Eng.*, vol. 79, no. 10, pp. 24–31, 2001.
- [6] K. Pilakoutas and X. Li, "Alternative shear reinforcement for reinforced concrete flat slabs," *J. Struct. Eng.*, vol. 129, no. 9, pp. 1164–1172, 2003.
- [7] S. Lips, M. Fernández Ruiz, and A. Muttoni, "Experimental investigation on punching strength and deformation capacity of shear-reinforced slabs," *ACI Struct. J.*, vol. 109, no. 6, pp. 889–900, 2012.
- [8] M. P. Ferreira, R. N. M. Barros, M. J. M. Pereira Filho, L. S. Tapajós, and F. S. Quaresma, "One-way shear resistance of RC members with unconnected stirrups," *Lat. Am. J. Solids Struct.*, vol. 13, no. 15, pp. 2970–2990, 2016.
- [9] M. A. S. Andrade, "Punção em lajes cogumelo – estudo do posicionamento da armadura de cisalhamento em relação à armadura de flexão," M.S. thesis, Esc. Eng. Civ., UFG, Goiânia, 1999.
- [10] L. M. Trautwein, "Punção em lajes cogumelo de concreto armado: análise experimental e numérica," Ph.D. dissertation, Dep. Eng. Estru. Fund., Esc. Politéc., Univ. São Paulo, 2006, 350p.
- [11] Associação Brasileira de Normas Técnicas, *Projeto de Estruturas de Concreto - Procedimento*, ABNT NBR 6118, 2014.
- [12] M. G. Marques, E. A. P. Liberati, R. B. Gomes, and L. M. Trautwein, "Study of failure mode of reinforced concrete flat slabs with openings and studs," *ACI Struct. J.*, vol. 117, no. 4, pp. 39–48, 2020.
- [13] American Concrete Institute, *Building Code Requirements for Structural Concrete and Commentary (ACI 318R-11)*, ACI 318-19, 2019.
- [14] European Committee for Standardization, *Eurocode 2, Design of Concrete Structures – Part 1-1 General Rules and Rules for Buildings*, CEN EN 1992-1-1:2004/prA1:2013, 2014.

Author contributions: Contribution description of each co-author for the study. LMT: conceptualization, funding acquisition, data curation, supervision, writing; JPV: experimental tests, data curation; RBG and LCA: data curation, formal analysis.

Editors: Mauro Real, Mario Pimentel.



ORIGINAL ARTICLE

Analysis of size effect in shear transfer mechanisms and size effect suppression by transversal reinforcement – contributions to NBR 6118

Análise de efeito de escala nos mecanismos complementares de resistência ao cisalhamento e sua supressão por reforço transversal – contribuições para a NBR 6118

Igor José Santos Ribeiro^a José Renato de Castro Pessôa^b Túlio Nogueira Bittencourt^a André Teófilo Beck^c ^aUniversidade de São Paulo – USP, Programa de Pós-graduação em Engenharia Civil, São Paulo, SP, Brasil^bUniversidade Estadual de Santa Cruz – UESC, Programa de Pós-graduação em Ciência, Inovação, e Modelagem de Materiais, Ilhéus, BA, Brasil^cUniversidade de São Paulo – USP, Escola de Engenharia de São Carlos, São Carlos, SP, Brasil

Received 20 September 2022

Accepted 25 March 2023

Abstract: Size effects are known to be relevant in the shear transfer mechanisms of quasi-brittle materials like concrete. Bažant proposed an asymptotic approximation between plasticity theory and Linear Elastic Fracture Mechanics (LEFM), showing a proportionality of concrete nominal resistance with $d^{-1/2}$, where d is beam depth. Recently, the long-standing shear transfer mechanism expressions of ACI 318:2014 have been updated (ACI 318:2019), with introduction of a size effect factor. In Brazil, recent publications identified non-conservative trends in predictions of ABNT NBR 6118:2014 for larger beam depths; yet, the Brazilian code never considered size effects because they are suppressed by transverse reinforcement. Considering this background, in this manuscript we make a comprehensive analysis of NBR 6118:2014 shear strength predictions using as a reference the papers of ACI-ASCE DatStb 445-D database. The results exhibit strong tendencies in the model error regarding longitudinal reinforcement and effective depth for beams without transversal reinforcement. A two-step analysis is made herein to describe model errors: first, a nonlinear regression for longitudinal reinforcement is made; second, a linear regression is made for size effect. The reliability analysis corroborates that model error may be reduced by introducing size effect and longitudinal reinforcement factors. Next, for beams with transversal reinforcement, smoother tendencies regarding beam depth are noted, indicating a size effect suppression for the beams depths available in the database. However, as the analysis shows that the higher beam depths concentrate most of the results with unconservative model errors, further studies are necessary to accurately describe how transversal reinforcement suppress the size effect.

Keywords: fracture mechanics, size effect, shear transfer mechanisms, size effect suppression, model error.

Resumo: A relevância do efeito escala é conhecida nos mecanismos de transferência de cisalhamento em materiais quase-frágeis, como o concreto. Bažant propôs uma abordagem assintótica entre a teoria da plasticidade e a Mecânica da Fratura Elástica Linear, exibindo uma proporcionalidade da resistência nominal do concreto com $d^{-1/2}$, sendo d a altura útil da viga. Recentemente, a expressão do código norte americano ACI 318:2014 para os mecanismos complementares de cisalhamento foi atualizada (ACI 318:2019), com a inserção de um fator de efeito de escala. No Brasil, publicações recentes identificaram tendências não conservadoras nas previsões da NBR 6118:2014 para maiores valores de d ; ainda assim, o código brasileiro nunca considerou efeito escala devido à aparente supressão pelo reforço transversal. Considerando esse cenário, esse artigo faz uma análise abrangente das previsões normativas da NBR 6118:2014 para a resistência ao cisalhamento usando como referência os artigos da base de dados ACI-ASCE DatStb 445-D. Os resultados exibem fortes tendências da variável erro de modelo em relação à taxa de reforço longitudinal e altura útil para as vigas sem reforço transversal. Uma análise em duas etapas é efetuada neste trabalho: primeiro, uma

Corresponding author: Igor José Santos Ribeiro. E-mail: igorjsribeiro@usp.br

Financial support: Fundação de Amparo à Pesquisa do Estado da Bahia (FAPESB), Fundação para o Desenvolvimento Tecnológico da Engenharia (FDTE).

Conflict of interest: Nothing to declare.

Data Availability: the data that support the findings of this study are available from the corresponding author, upon reasonable request.



This is an Open Access article distributed under the terms of the Creative Commons Attribution License, which permits unrestricted use, distribution, and reproduction in any medium, provided the original work is properly cited.

regressão não-linear é realizada, em termos da taxa de reforço longitudinal; na sequência, uma regressão linear é realizada para a altura da viga. A análise de confiabilidade estrutural corrobora os resultados apontando que a incorporação dos fatores para efeito escala e taxa de reforço longitudinal leva à redução do erro de modelo. Para vigas com reforço transversal, são observadas tendências mais sutis de variação do erro de modelo com a altura útil da viga. Contudo, a análise mostra que as maiores alturas de viga ainda concentram a maior parte dos resultados para as quais o modelo é não conservador; logo, mais estudos são necessários para descrever precisamente como o reforço transversal suprime o efeito escala.

Palavras-chave: mecânica da fratura, efeito escala, mecanismos complementares de resistência ao cisalhamento, supressão do efeito escala, erro de modelo.

How to cite: I. J. S. Ribeiro, J. R. C. Pessôa, T. N. Bittencourt, and A. T. Beck, "Analysis of size effect in shear transfer mechanisms and size effect suppression by transversal reinforcement – contributions to NBR 6118," *Rev. IBRACON Estrut. Mater.*, vol. 16, no. 3, e16306, 2023, <https://doi.org/10.1590/S1983-41952023000300006>

1 INTRODUCTION

Use of increasingly larger cross-sections in structural elements, together with catastrophic failures observed in recent years, point to a need to better comprehend size effects in predictions of current design codes. The shear transfer mechanism is one of the crucial design variables which recent studies related to scalability problem, i.e., size effect. Illustrating this, the American Code ACI 318: 2019 [1], included a factor to consider the observed transitional trend between theory of plasticity and Linear Elastic Fracture Mechanics predictions.

For quasi-brittle materials, such as concrete, Bažant and Oh [2] was a pioneer analyzing the effect of increasing the depth dimension on the fracture energy. The author laid the foundations for adjustments, like those made in ACI 318:2019, which included a factor showing a proportionality of concrete nominal resistance with $d^{-1/2}$, where d is beam depth.

Regarding the beams without transverse reinforcement, both code and recent publications show, from the ACI445-D database covering a wide range of depth variation, that more reliable designs may be obtained through Bažant's approach. In addition, it was also found that the slopes of the adjustment curve were correctly predicted according to the type-II size effect law, as well as the divergence from the usual normative values that disregard it [3], [4]. Nevertheless, authors such as Collins et al. [5] state that when a minimum transversal reinforcement is provided, there is no need to consider size effect due to the suppression occurrence.

In Brazil, the shear resistance of complementary mechanism is calculated through expressions that do not consider size effect for reinforced concrete beams, when transversal reinforcement is provided or not. According to results obtained by Kuchma et al. [6] when investigating the previous ACI 318:2014 [7], which has trends like those present in ABNT NBR 6118:2014 [8], ignoring size effects may result in unconservative design for higher beams depths. Therefore, it is important to analyze the Brazilian code to incorporate a size factor as well.

2 FRACTURE MECHANICS AND SIZE EFFECT

2.1 Fracture Mechanics

Fracture mechanics studies the phenomena of crack appearance and propagation in materials, until complete fracture. For this to occur, it is necessary that tensile stresses have sufficient intensity to successively break the bonds between the atoms that make up the crystalline structure, until there is partial or total separation of the material. According to the way this phenomenon occurs, it is possible to divide the materials into three groups: brittle, quasi-brittle and ductile.

Brittle materials undergo a cleavage process, characterized by break of atomic bonds as the crack propagates along specific crystallographic planes, orthogonal to the loading and with little deformation before rupture. In these materials, as soon as the maximum tensile stress (f_t') is reached, continuity is lost. The type of rupture that is linked to quasi-brittle materials, demonstrate the behavior known as strain-softening. This is characterized by the fact that the load gradually decays after f_t' as the deformations increase.

This rupture characterization for the different materials comes from Linear Elastic Fracture Mechanics (LEFM) and Elastic-Plastic Fracture Mechanics (EPFM). While the former describes materials with a small fracture process zone (FPZ), the latter extends to more materials, since it considers plasticity ahead of the crack tip. At the structural level, global aspects, such as carrying capacity or deflections, may be correctly determined only by considering plasticity in the crack propagation until the material complete discontinuity [9].

Observing concrete compressive tests, Hillerborg et al. [10] sought to describe the crack displacement from the analysis of the stress vs deformation curve ($\sigma \times \epsilon$), from a uniaxial concrete stress test. The authors observed that after the peak load the deformations were predominantly located at the tip of the crack, until the body was completely fractured. Considering this curve as a function of crack width, the fracture energy (G_F) was established as equivalent to the area under the curve.

Planas et al. [11] also define fracture energy as the external energy required for the expansion of one unit of cohesive crack area to occur. Following the authors [11], the characteristic length (l_{ch}), result of Irwin’s formulations estimation for the FPZ dimension applied to the cohesive crack, can be expressed by Equation 1:

$$l_{ch} = \left(\frac{K_{IC}}{f'_t}\right)^2 = \frac{E'G_F}{f_t'^2} \tag{1}$$

where K_{IC} is the critical stress intensity factor for mode I, E' is the modulus of elasticity in plane stress. The smaller l_{ch} , the smaller the area of inelastic processes, the more brittle the material will be. Authors such as Hoover et al. [12] attest that l_{ch} , together with G_F , remain necessary to characterize concrete’s post peak curve. Values of l_{ch} for an infinite concrete body, where it would be possible to apply LEFM, usually vary between 0.15 to 0.45m, whereas l_{ch} varies from 0.30 to 2 m for a fully developed FPZ. Thus, it is attested that LEFM is not applicable to concrete in the usual dimensions. This conclusion also points that size effect might occur as the beams increase its dimensions.

2.2 Size Effect Law (SEL)

Two types of size effect are described in the literature, within the energetic approach. Type I, or statistical size effect, is usual for simple concrete structures, is caused by stress redistribution, and occurs as a large crack propagates continuously from a small region containing micro-cracks. The location of this finite region will depend on the material’s random resistance, i.e., this approach is energetic and statistical [13], [14].

Type II, in turn, which is more common for reinforced concrete structures, occurs when the propagation of a crack in the quasi-brittle material is preceded by a redistribution of stresses, which occurs in the FPZ. In these cases, the size effect is deterministic for structures already weakened by a wide crack with stable growth, or non-negligible notch in relation to the cross section and larger than the FPZ [15], [16].

Figure 1 exhibits Bažant and Oh’s [2] observations of nominal shear resistance (v) and the logarithm of the ratio between beam depth (D) and transitional dimension (D_0). The second parameter was defined initially as an empirical adjustment parameter, plotted as a vertical line. On the upper part, the horizontal line (blue) represents the classical formulations predictions, which had no dependence on size. As the beam depth increases, the FPZ decreases and the LEFM may be used to describe the shear resistance. From that, the author proposed and transitional approach between plasticity theory and LEFM, as represented by the dashed purple line with slope of 1/2 in Figure 1. The size effect law is plotted as the continuous green curve, describing how v decreases as the depth increases.

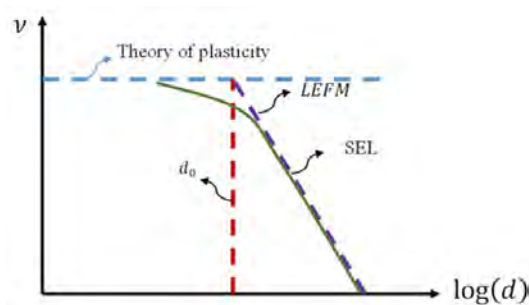


Figure 1 – SEL asymptotic approach: nominal shear strength (v) in terms of cross-session depth d (log scale).

Hence, the size effect law of Type II (SEL-II) was obtained by making an asymptotic correspondence for geometrically similar structures by varying their depth, as expressed in Equation 2:

$$v = \frac{\hat{B} f_t'}{\sqrt{1 + \frac{d}{d_0}}} \quad (2)$$

where d is the effective depth, d_0 is the transitional dimension and \hat{B} is defined in the Equation 3:

$$\hat{B} = E' G_f / c_f g'(\alpha_0) \quad (3)$$

where G_f is the initial fracture energy, c_f is the effective length of fracture zone, $g'(\alpha_0)$ is the energy release rate, as function of α_0 , the initial crack extension normalized by depth. Later, Bažant and Oh [2] stated that the transitional behavior observed in concrete can be related to the size of FPZ which is not negligible with the increase of member dimensions [16].

3 SHEAR TRANSFER MECHANISMS

3.1 Shear resistance of complementary mechanism parameters

Since the first approaches to analyze shear in concrete structures, several updates were made to insert the discovered shear transfer mechanisms that change the initial truss and tie model predictions. The studies revealed differences due to pin effect, interface friction, cantilever effect, concrete residual tensile strength, among others, and these are considered in the shear resistance codes through a parameter named shear resistance of complementary mechanisms (V_c).

In turn, the current Brazilian code defines expressions based on two models: the fixed angle truss and the variable angle truss. The former has a fixed value for any load, given by:

$$V_c = 0.6 f_{ctd} b_w d \quad (4)$$

where f_{ctd} is the design concrete tensile strength that is calculated by Equation 5:

$$f_{ctd} = \frac{f_{ctk,inf}}{\gamma_c} = \frac{0.7 f_{ctm}}{1.4} = 0.5 f_{ctm} \quad (5)$$

where γ_c is the concrete partial safety factor and f_{ctm} is the mean of concrete tensile resistance calculated according to Equation 6 for concrete with compressive strength up to 50 MPa and Equation 7 from 55 to 90 MPa. The ABNT: NBR 8953:2015 [17] also establishes class C100, which is not covered by the ABNT: NBR 6118:2014 in its current version.

$$f_{ctm} = 0.3 (f_{ck})^{\frac{2}{3}} \quad (6)$$

$$f_{ctm} = 2.11 \ln(1 + 0.11 f_{ck}) \quad (7)$$

The second model starts from the consideration of a truss with variable angle and is divided into different expressions that seek to adjust the load distribution of the classic truss, with possible relief in the struts by reducing the vertical component. This leads to a change in the model for calculating the V_c parameter which, in this approach, depends on the load.

3.2 Size Effect in Shear Resistance of concrete beams

One of the factors that contributes to V_c is the size effect. Different approaches have been made, such as the Canadian standard CSA A23 [18], or the methodology incorporated in the ACI 318:2019 [1], the SEL-II. There is still no consensus on how this should be considered, or even if there is an actual need when the minimum transverse reinforcement is provided [5].

By analyzing geometrically similar structures with different heights, Kani [19] observed that the predicted values for the larger beam depths led to results up to 40% smaller than those predicted by the current formulation.

Based on a probabilistic approach but considering beam depths between 10 and 300cm and distributed loads, Iguro et al. [20] stated that a proportionality of the shear resistance to $d^{-1/4}$ may be considered, to obtain more conservative results.

In the Toronto series, Podgorniak-Stanik [21] considered 7 different beam depths, varying the percentage of longitudinal reinforcement ratio, for specified compressive strength of $f_{cr}=37$ MPa, and high strength concrete ($f_{cr} = 99$ MPa), with minimum transverse reinforcement. The author affirmed existence of the size effect, which is more prominent for larger beam depths. Nevertheless, the author [22] also supposed that the stirrups would be sufficient to control cracking. However, according to Bažant et al. [3] it is wrong to infer this from the results. There is a notable reduction for beams reinforced transversally for the considered sizes, although not as significant as for beams without stirrups. The authors also point out that the predictions should be based on the parameter of characteristic compressive strength in the quantile of 9% (f'_c), instead of f_{cr} , and that the curve adjustment should be done at the edge of the dispersion band, instead of in the middle. After comparison with simulations, Bažant et al. [3] concluded that there is a significant reduction due to use of minimal transverse reinforcement, but insufficient for the size effect to become negligible.

Testing beams with effective depths of 300 and 4000 mm, and comparing several proposed predictions, Quach [22] demonstrated that the consideration of the size effect for large sections was necessary for an optimized design. Afterwards, Collins et al. [5], in an article referring to these same specimens, together with the ones from the Toronto series, affirmed an apparent suppression of the size effect based on the more brittle behavior observed. However, this series has maximum value for the beam depth of $d = 1840$ mm, insufficient to conclude about a complete size effect suppression. Furthermore, this beam has an $a/d < 2.4$ where the arc action is still the main shear transfer mechanism.

From the database selected by the ACI 445-D committee, Bažant et al. [3] applied an algorithm to randomly eliminate data at intervals to fix the variance of other parameters than beam depth. As their variance affects the size effect, the influence of beam depth become even more notorious after applying Equation 2 to this transformed database, with nominal shear strength proportional to $d^{-1/2}$.

Later, applying the ACI 318 (2014) formulation to the updated database, Yu et al. [4] observed that for small beam depths, the plastic analysis was satisfactory. They also inferred that consideration of a probabilistic approach of the size effect for concrete was not justifiable, given the usual stress redistribution as well as the cracking pattern of the concrete beams under analysis.

3.3 A note on datasets

Different approaches are possible in constructing datasets and subsets. For instance, to reflect advances in materials technology, which are expected to reduce standard deviation, test data could be split into prior and posterior to 1980, as done in [23], [24], [25]. The coefficient of variation per interval depends both on heterogeneity of data and on the formulations. As model predictions are made to all collected data, it is important to consider what goals the authors had when developing the original studies. Due to data heterogeneity, the COV of a larger dataset tends to be larger than that of a smaller dataset.

4 MATERIALS AND EXPERIMENTAL PROGRAM

4.1 Shear test database

4.1.1 Slender beams without transversal reinforcement

Ribeiro et al. [26] analyzed the trends concerning the main complementary mechanisms to shear transfer in ACI 318:2014, ACI 318:2019, Frosch et al. [27] and ABNT NBR 6118:2014 considering slender beams (where the complementary mechanisms have greater influence) from a dataset encompassing 1356 tests available in the ACI-DafStb, filtered as proposed by Reineck et al. [28] and additionally with a $f_{ck}>20$ MPa to select only concrete with structural propose as defined by ABNT NBR 8953:2015.

The results show the most influents mechanisms to the model error and points towards the possible adjust through minimum square regression concerning longitudinal reinforcement ratio and later a linear regression to beam depth. Therefore, we start from the same database focused solely on propose an adjusted model to reduce the previously observed trends.

4.1.2 Slender beams with transversal reinforcement

Size effect suppression with use of stirrups was pointed out by Collins et al. [5], corroborated by Kuchma et al. [6] and opposed by Yu and Bažant [29]. To verify size effect suppression, the database provided by Reineck et al. [30] was employed herein: 886 beams were selected, of which 556 had $a/d > 2.4$.

After applying the filters recommended by Reineck et al. [30], removing beams that suffered rupture other than by shear, as well as spurious or missing data, a set of 170 beams with no axial forces, was obtained. Also, this database is like the one used by the ACI 445-D committee for adequacy. Similarly, a filter was applied for structural concrete, which removed only 6 beams from the sample set. The data taken from 39 authors is reported in Annex A.

4.2 Calculation of shear resistance of complementary mechanisms (V_c)

4.2.1 Beams without stirrups

From the ABNT: NBR6118:2014, solely the Model I, previously exposed in Section 3.1 and calculated by Equation 4 was used by Ribeiro et al. [26] because of the available data for calculations.

4.2.2 Beams with stirrups

To verify the size effect suppression, the strength of beams with stirrups is calculated. The formulations by Frosch et al. [27], ACI 318: 2014 [7] and ACI 318: 2019 [1] have the same normative prescription for the transversal reinforcement resistance, for beams where reinforcement is greater than the minimum. The Brazilian formulation is like the *fib* Model Code [31].

4.2.2.1 Approach from ACI 318 and Frosch et al. [27]

Based on the fixed-angle truss model with contribution of complementary mechanisms, the standards prescribe that the strength of a beam with transverse reinforcement will be given by Equation 8:

$$V_n = V_s + V_c \quad (8)$$

For ACI 318:2019, the shear strength of the complementary mechanisms follows the expressions of ACI 318:2014 when at least minimum transversal reinforcement is provided. The transversal reinforcement shear strength is calculated by Equation 9:

$$V_s = \frac{A_{sw}}{s_w} f_{yw} d \quad (9)$$

Substituting the respective expressions, the value of the ultimate shear strength of a beam is calculated by Equation 10:

$$V_u = 0.166 \sqrt{f'_c} b_w d + \frac{A_{sw}}{s_w} f_{yw} d \quad (10)$$

For the expression by Frosch et al. [27], Equation 11 must be used:

$$V_u = 0.415 \sqrt{f'_c} b_w c + \frac{A_{sw}}{s_w} f_{yw} d \quad (11)$$

Where c is the depth of the cracked cross-section, calculated by Equation 12:

$$c = kd \quad (12)$$

Where k is a coefficient relating reinforcement and concrete given by Equation 13:

$$k = \sqrt{2\rho_L n + (\rho_L n)^2} - \rho_L n \quad (13)$$

Where ρ_L is the longitudinal reinforcement ratio (%) and n is the ration between reinforcement end elasticity modules.

4.2.2.2 Code NBR 6118 (2014)

Since the Brazilian code also starts from the fixed angle truss model with V_c contribution, Equation 8 will be used. Therefore, for the Brazilian standard, the resistance is calculated by Equation 14:

$$V_u = 0.6f_{ctd}b_w d + \frac{A_{sw}}{s_w} 0.9d f_{yw} \quad (14)$$

4.3 Model error

The model for the beams without stirrups in Equation 4 provides one estimate of shear strength (V_c) for each of the beams of the experimental database. Similarly, for beams with stirrups the model in Equations 20-22 provides one estimate of total shear resistance V_u . If V_M is the shear strength predicted by the model (M), and V_E is the shear strength observed in the experiment (E), then observations of a model error variable (ME) can be obtained by Equation 15:

$$ME = \frac{V_E}{V_M} \quad (15)$$

The model error ratio (ME) shows how the predictions are close to the actual tests results. If $ME < 1$, the experimental strength is smaller than the model-predicted strength, potentially leading to an unsafe design. The higher the value of ME , the more conservative is the model prediction. Beck et al. [32] used ME to identify tendencies in circular steel concrete-filled steel columns regarding the slenderness ratio and later applied non-linear regression to describe the relation between parameters.

Based on a statistical analysis of a set of model error observations, statistics like mean (μ_{ME}), standard deviation (σ_{ME}) and coefficient of variation ($\delta_{ME} = \sigma_{ME}/\mu_{ME}$) can be computed. The ideal model should have $\mu_{ME} = 1$ and $\delta_{ME} = 0$, but this is unrealistic due the uncertainties inherent to any model. A good engineering model will have $\mu_{ME} \approx 1$ and δ_{ME} as small as possible. When $\mu_{ME} > 1$ we say that, on average, the model is conservative; but this may not be sufficient if δ_{ME} is large!

In this manuscript, we interpret model error results by reporting the mean (μ_{ME}) and coefficient of variation (δ_{ME}), as well as the percentage of results for which $ME < 1$ (potentially unsafe). Also, we report model error results for two upper fractiles (UF), corresponding to 90 and 95%. These fractiles highlight models that are excessively conservative, when $UF \gg 1$.

5 RESULTS AND DISCUSSIONS

5.1 Application of a size effect factor to ABNT: NBR 6118:2014

There is a strong influence of the size effect, demonstrated with the increase in effective depth. Considering that Barros et al. [33] exhibit trends regarding the minimum longitudinal reinforcement to slabs, Ribeiro et al. [26] to beams, and that this parameter is expected to change with increasing effective depth, a two steps regression is proposed.

First the same dataset in terms of longitudinal reinforcement ratio (ρ_L) is exhibited in Figure 2. For the Brazilian code the model error increases with ρ_L from unconservative design for lightly reinforced beams ($ME < 1$) to excessively conservative design. The tendencies in model error concerning longitudinal reinforcement ratio per range are more detailed in Table 1.

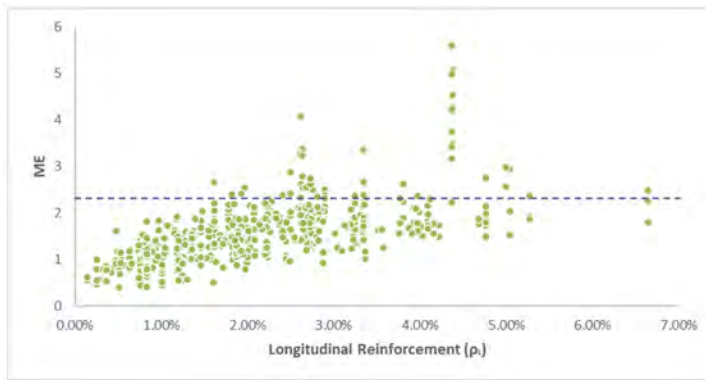


Figure 2 – ME x ρ_L for NBR 6118:2014

Table 1 – ME with respect to longitudinal reinforcement ratio

N	ρ_L (%)	ME <1 (%)	μ_{ME}	δ_{ME}
125	0-1.30	44.0%	1.05	0.32
207	1.30 – 2.60	5.13%	1.54	0.25
149	2.60 – 3.90	0.00%	1.86	0.27
68	3.90 – 6.70	0.00%	2.39	0.42

To correct these tendencies a power function is proposed, similarly to ACI 318:2019, given by Equation 16:

$$V_{c0} = 0.6f_{ctd}b_w(a\rho_L^b) \tag{16}$$

where a and b are parameters of a power function to be determined by regression. By way of minimum squares regression analysis, the following Equation 17 is obtained:

$$V_{c0} = 0.6f_{ctd}b_w(8.6\rho_L^{0.44}) \tag{17}$$

The ACI 318 (2019) uses $\rho_L^{0.33}$, close to the obtained result. Next, the model in Equation 17 is applied to the same database, obtaining new ME results which do not have trends concerning ρ_L as presented in Figure 3. Also, the 90% fractile is $UF = 1.4$ for this correction. After implementing Equation 17, the ME data still exhibits a trend with respect to beam depth, as seen in Figure 4.

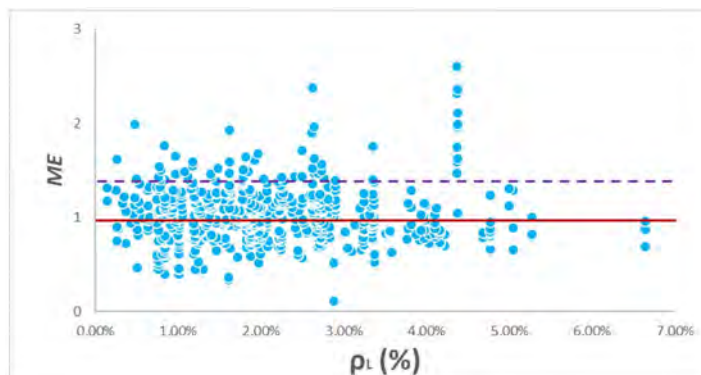


Figure 3 – ME results in terms of ρ_L , after applying ρ factor of Equation 17

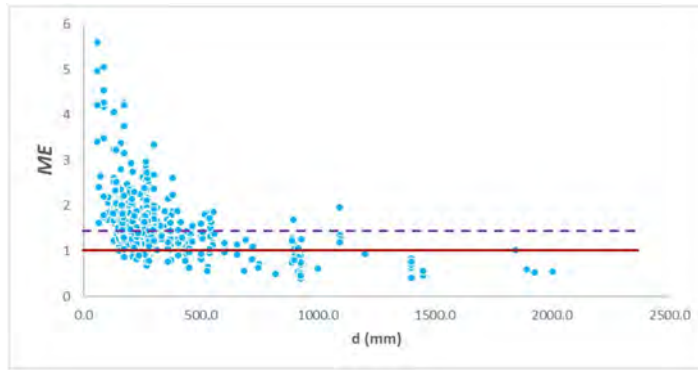


Figure 4 – ME in terms of d after application of ρ_L factor

Therefore, as the size effect law is already defined, a change of variable in d is made to (tentatively) linearize the data in Equation 18:

$$y' = \frac{1}{\sqrt{1+\frac{d}{d_0}}} \tag{18}$$

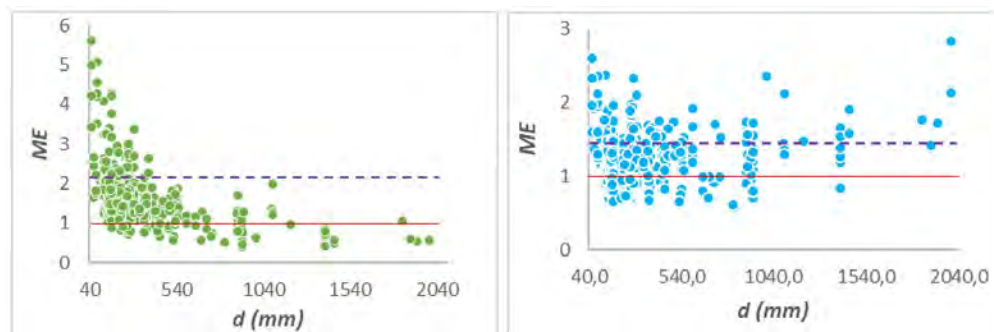
where $d_0 = 254 \text{ mm}$. Once the data is (tentatively) linearized, a linear regression analysis is made on variable y' , to determine the coefficient a , of the Equation 19:

$$y = ay' \tag{19}$$

Once determined, it can be used to correct the model as proposed in the size effect factor defined by Equation 20:

$$\gamma_e = \sqrt{\frac{1,53}{1+d/d_0}} \tag{20}$$

Applying the model error correction of (Equation 20), the distribution of data points in Figure 5 is obtained. On (a) the ME for ABNT NBR6118:2014 and on (b) for the corrected model.



(a)

(b)

Figure 5 – ME results for ABNT NBR 6118:2014 without (a) and with (b) ρ_L and γ_e factors.

Clearly, there are no more tendencies in the new proposed design, exhibiting that the proposed equation correctly describes the functional relation among the parameters. The 90% fractile is $UF = 1.60$, indicating a less conservative approach, since the NBR 6118:2014 had $UF = 2.24$. Since the insertion of the factor ρ_L does not foresee that as the beam height increases the pin effect reduce its role in the shear resistance output, this is the most likely cause of the increasing in ME for higher beam depths. The final proposed expression, to be adjusted accordingly the desirable safety is given in Equation 21:

$$V_c = 5.2\gamma_e f_{cta} b_w d \rho_L^{0.44} \quad (21)$$

This expression may be corrected through a reliability analysis establishing a target reliability index.

5.2 Structural Reliability Analysis

To further evaluate the proposed expression the First Order Reliability Method (FORM) was applied to both the proposed expression (18), and the current code. First, same beam depth intervals used in Ribeiro et al. [26] were used. The mean of ME (μ_{ME}) and the coefficient of variation (δ_{ME}) of each range was used to compute the standard deviation by:

$$\sigma = \delta_{ME} \times \mu_{ME} \quad (22)$$

The beam width was considered a deterministic parameter with $b_w = 200mm$. Since size effect takes place to $d > 254mm$ and varies among the intervals, beams depth of 375, 625, 875, and 1500mm were considered.

Since the most of dataset is comprehended between $20 < f_{ck} < 40 MPa$, compressive strengths of 20, 30 and 40 MPa were used in this analysis as random variables with normal distribution. Finally, to analyze how the longitudinal reinforcement ratio affect the model were used $\rho_{L,min}$, $\rho_{L,m}$ and $\rho_{L,max}$, where $\rho_{L,min}$ correspond to the design code minimum longitudinal reinforcement to the beams in analysis, $\rho_{L,max}$ corresponds to the maximum value observed in dataset and $\rho_{L,m}$ is the median of this parameter. As b_w , d and ρ_L were considered as deterministic variable the resistance in the limit function state depends only on f_c for both the current design code and the proposed.

Regarding the loads, dead load (D) was considered with a normal distribution, live load (L) and wind load (W) as Gumbel Distributions. The load combination was made as the design code NBR 6118:2014 applying the so-called Turkstra combination, considering the maximum of Live Loads (L) for 50 years and the maximum annual wind load (W_1). In turn, for both mean model error of resistance ($E_{M,R}$) and for the loads ($E_{M,S}$), normal distributions were considered. Next, the limit state equations were considered as Equation 23:

$$g(f_c, D, L, W_1, E_{m,r}, E_{m,l}) = E_{M,R} * R(f_c) - E_{M,S} * S(D + L_{50} + W_1) \quad (23)$$

As aforementioned, $E_{M,R}$ was considered for the same beam depth intervals in Table 2. The $E_{M,S}$ was used accordingly JCSS [34] with mean value of 1.00 to shear and $\delta_{E_{M,S}} = 0.10 R(f_c)$ is given by Equations 4 and 21, for the Brazilian code and for the proposal, respectively, resulting in Equations 24 and 25:

$$g_1(R, S) = E_{M,R} * 0.6 * \left(0.21 f_c^{\frac{2}{3}}\right) b_w d - E_{M,S} * (D + L_{50} + W_1) \quad (24)$$

$$g_2(R, S) = E_{M,R} * 5.2 * \left(0.21 f_c^{\frac{2}{3}}\right) b_w d * \rho_L^{0.44} - E_{M,S} * (D + L_{50} + W_1) \quad (25)$$

The function g_1 , is the limit state function when ABNT NBR 6118:2014 is considered and g_2 , when the proposal is used. The Tables 3-4 summarizes the distribution data to resistance and load parameters, respectively, available in Santiago et al. [35] and Costa et al. [36] to live loads.

Table 2- Concrete compressive strength distribution parameters

Random Variable	Compressive Strength Class	Distribution	Mean(μ)	C. O. V. (δ)
f_c	C20	Normal	$1.30f_c$	0.20
	C30	Normal	$1.22f_c$	0.15
	C40	Normal	$1.16f_c$	0.11

Table 3- Loads distribution parameters

Random Variable	Distribution	Mean(μ)	C. O. V. (δ)
D	Normal	$1.06D_n$	0.12
L	Gumbel	$0.92L_n$	0.25
W1	Gumbel	$0.33W_n$	0.47

Where D_n , L_n and W_n refer to nominal values of Dead Load, Live Load and Wind Load, respectively. The Dead Load parameters were taken from Santiago et al. [35]. The Live Load values were taken from Costa et al. [36], who made a comprehensive study of stochastic models for live loads, including comparison to design values of NBR 6120:2019. Finally, the Wind Loads used are based in the results obtained by Beck and Souza [37]. The failure probability may be obtained by:

$$p_f = \int_{g(x) \leq 0} f_x(x) dx \tag{26}$$

Where $g(x) \leq 0$ is the failure probability domain, and $f_x(x)$ is the joint probability distribution function of the random variables in this problem. When FORM is applied, the previous equation, and its limits state function described in Equations 25-26, is mapped into a standard gaussian space, and the design point may be found, representing the point over failure domain closest to the standard space origin. Hence, the reliability index (β) may be determined as, precisely, this distance. By solving this problem using FORM, sensitivity coefficients (α) that are used on interpreting the results by identifying the relative contribution of each random variable.

5.2.1 Structural reliability results

The Figure 6 shows the obtained result to C20. The three longitudinal reinforcement ratio used are represented as $r_1 = \rho_{L,min}$, $r_2 = \rho_{L,m}$ and $r_3 = \rho_{L,max}$.

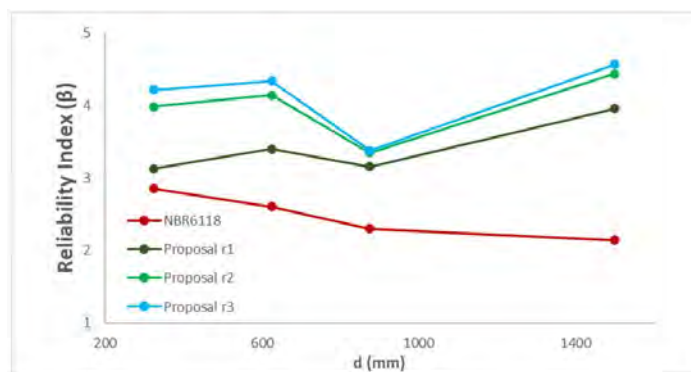


Figure 6 – Reliability indexes (β) in relation to d to NBR6118:2014 and proposal: C20

The Figure exhibit a notorious trend in the NBR 6118:2014 to reduce β as the beam depth increases. On the other hand, the introduction of the correction factors concerning ρ_L and d leads to higher β values to the beams considered. The higher ρ_L is, the higher β becomes. The sensitivity factors to NB 6118 are shown in the Figure 7 and on Figure 8 to Proposal-r1 where the model error changes were higher.

Although there is some other small contribution, the Figure 7 shows that for this analysis the model error of resistance variables is the more influent parameter to resistance.

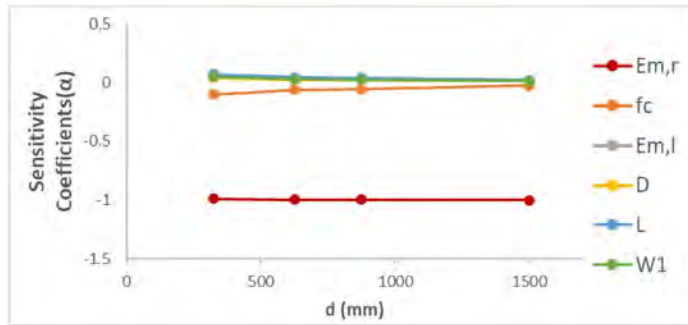


Figure 7 – Sensitivity coefficients to NB6118:2014 to C20

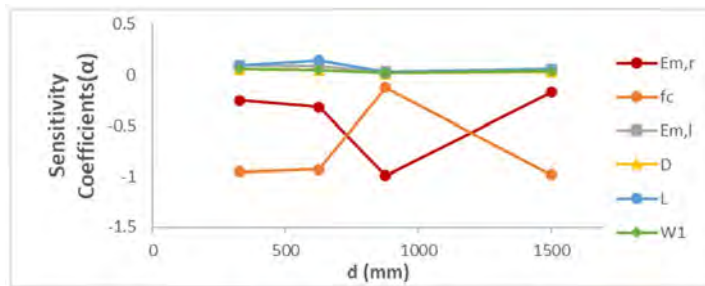


Figure 8 – Sensitivity coefficients to Proposal- r_1 to C20

In turn, the Figure 8 show a significant contribution of this variable in 500-1250mm intervals, indicating the model proposed has a better performance to light reinforced beams. Concerning the loads, the Live Load was the most influent parameter in this analysis until beam depth of 750mm. Considering the Compressive Strength Class C30, the Figure 9 is obtained.

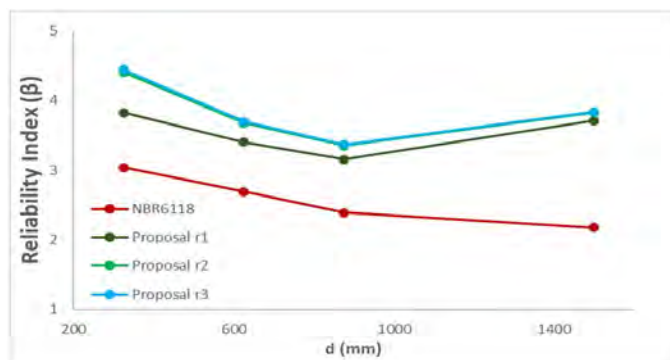


Figure 9 – Reliability indexes (β) in relation to d to NBR6118:2014 and proposal: C30

The reliability index exhibits the same pattern, reducing as the beam depth increases. Similarly, the same trends are obtained to de proposal with slightly higher values for the first considered beam depth.

The sensitivity coefficients from the FORM are show at Figure 10 to NBR 6118:2014 and at Figure 11 to Proposal- r_1 . The tendencies now are similar in Figures 12-13, even though the proposal still holds smaller values to the considered beam depth and higher values to Live loads.

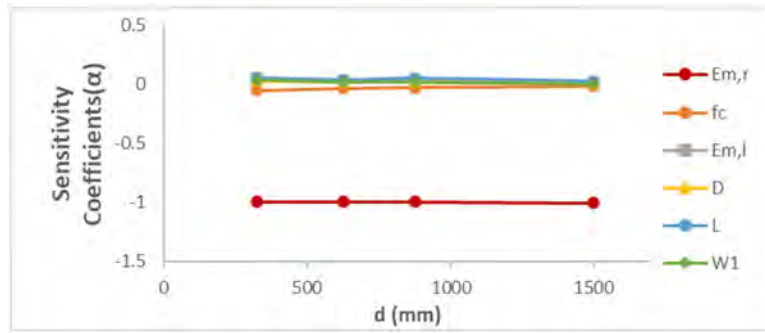


Figure 10 – Sensitivity coefficients to NB6118:2014 to C30

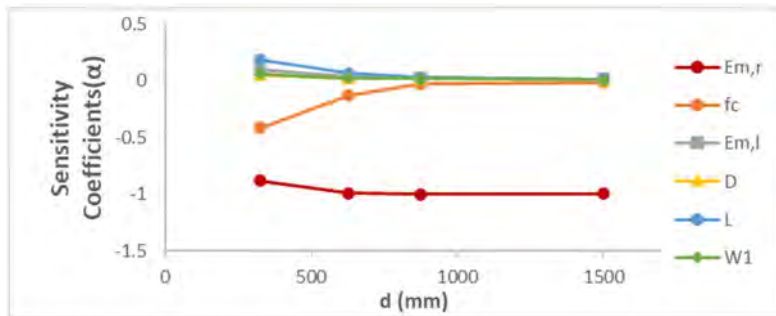


Figure 11 – Sensitivity coefficients to Proposal-r1 to C30

This change with concrete compressive strength may be a consequence of considering only compressive resistance as a random variable. Considering C40, the Figure 14 is obtained.

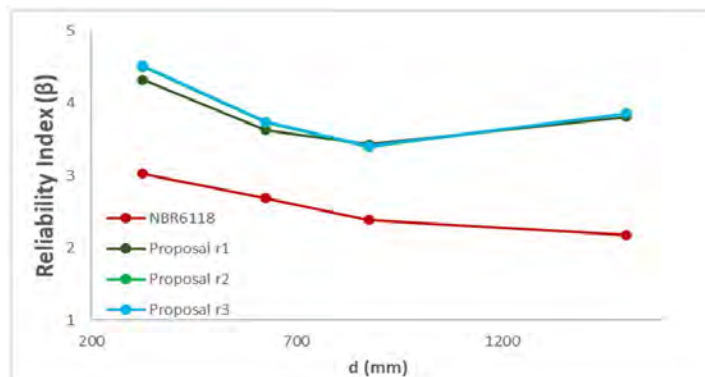


Figure 12 – Reliability indexes (β) in relation to d to NBR6118:2014 and proposal: C40

The NBR 6118:2014 reach lower values to β , but it still holds the same pattern as C20 and C30. Meanwhile the difference between the maximum and the minimum β becomes larger as compressive strength increases.

The sensitivity coefficients to C40 are shown in Figure 13 to NBR 6118 and in Figure 14 to Proposal- r_1 . The pattern remains alike both designs and slightly smaller to NBR 6118 (2014). The live loads had greater influence in the current code than the proposed formulation to this concrete class.

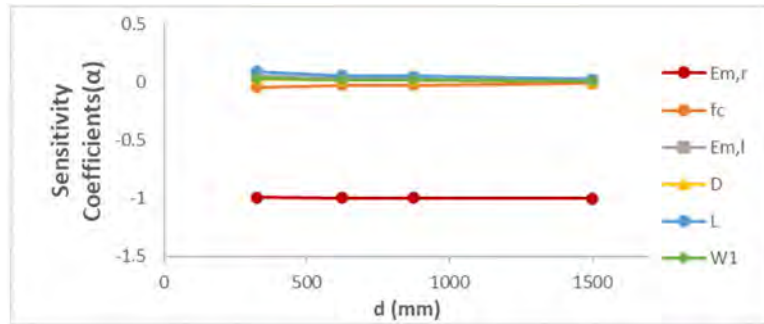


Figure 13 – Sensitivity coefficients to NB6118:2014 to C40

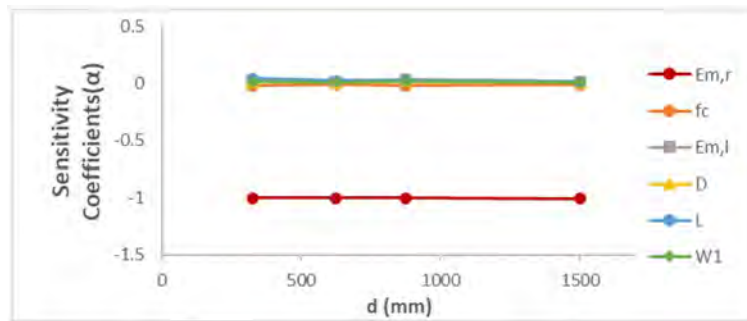


Figure 14 – Sensitivity coefficients to Proposal-r1 to C40

5.3 Size effect analysis in beams with transversal reinforcement

From the database for reinforced concrete beams with stirrups, the parameter d distributions in Figure 15 are obtained. For the effective depth, fewer samples higher than 1000 mm are noted, where the formulations under analysis present most of the values for which $ME < 1$.

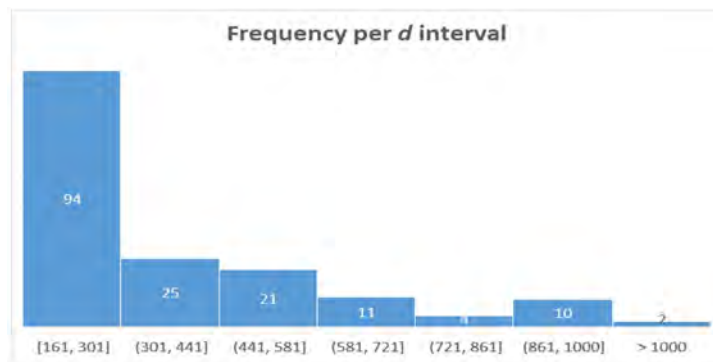


Figure 15 – Effective depth distribution (mm).

Table 4. Model error 90% fractile and percentage of results above fractile, for different beam depths and codes.

	Code	ACI 318 2014	NBR6118 2014	Frosch [27]
	90% ME fractile	1.71	2.10	2.06
N	Beam depth d (mm)	Fraction of results above the 90% fractile		
23	0-250	34.78%	13.04%	13.04%
112	250-500	7.21%	12.61%	13.51%
15	500-750	0.00%	0.00%	0.00%
15	750-1300	0.00%	0.00%	0.00%

As observed in Table 3, most of the results above the upper fractile are in the same range where most of the data is, i.e., between zero and 500 mm.

In this dataset, even though the tendencies are smaller, they are still observable only in effective depth in Figure 16, where (a) is ACI 318 (2019), (b) is the NBR 6118 (2014), and (c) is the Frosch [27]. Whenever transversal reinforcement is provided the ACI 318:2014 remains in the newest code version (ACI 318:2019).

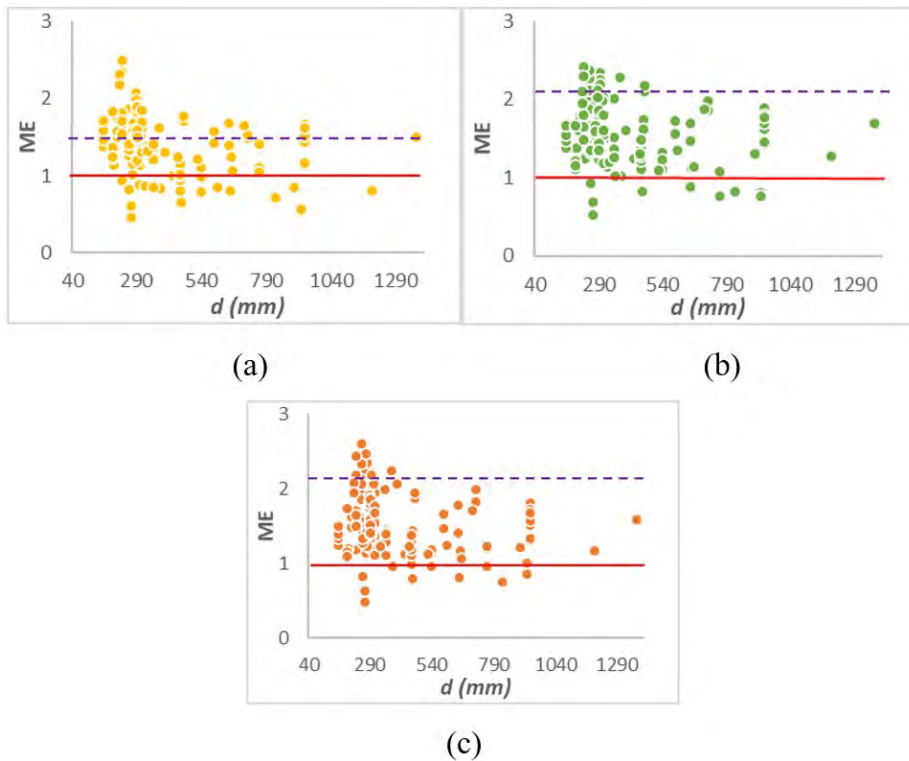


Figure 16 – ME x $d(mm)$ for beams with transversal reinforcement: ACI 318: 2019 (a), NBR 6118-14 (b), and Frosch et al. [27] (c)

As observed by Kuchma et al. [6] for the ACI 318:2014 and by Frosch et al. [27] for the unified approach, whenever a minimum reinforcement is provided, the size effect is suppressed. The same behavior occurs in the NBR 6118:2014. Nevertheless, compared to the beams without transversal reinforcement, the beams depths are limited to 1360 mm. Additionally, more studies are required to better describe how the transversal reinforcement ratio may be related to size effect suppression.

6 CONCLUSIONS

This manuscript addressed size effects in the shear strength of RC beams without transversal reinforcement. It was shown how the introduction of a size-effect factor in the formulation of NBR ABNT NBR 6118:2014 produces shear strength predictions which are more uniform with respect to longitudinal reinforcement ratio and beam depth. A new shear strength design equation was proposed for NBR 6118 that still may be calibrated to exhibit adequate reliability index. The formulation includes a correction term for reinforcement ratio, and another correction term for beam depth. It also provided higher reliability indexes and smaller model error contribution to the failure. This analysis may be improved using more uniform data, or a statistical analysis that considers the heterogeneity of data. The beam depth correction term is based on the transition between plastic and linear elastic behavior, as identified by Bažant. The notorious suppression of size effects by transversal reinforcement was also identified. Further studies are needed aiming to describe how the transversal reinforcement changes transitional dimension and suppresses size effects as effective depth increases.

REFERENCES

- [1] American Concrete Institute, *Building Code Requirements for Structural Concrete*. Farmington Hills, MI, USA: Amer. Concrete Inst., 2019.
- [2] Z. P. Bažant and B. H. Oh, "Crack band theory for fracture of concrete," *Mater. Constr.*, vol. 16, pp. 155–177, 1983.
- [3] Z. P. Bažant, Q. Yu, W. Gerstle, J. Hanson, and J. W. Ju, "Justification of ACI 446 proposal for updating ACI code provisions for shear design of reinforced concrete beams," *ACI Struct. J.*, vol. 105, no. 4, pp. 512–515, 2008.
- [4] Q. Yu, J. L. Le, M. H. Hubler, R. Wendner, and G. Cusati, "P. Bažant, "Comparison of main models for size effect on shear strength of reinforced and prestressed concrete beams," *Struct. Concr.*, vol. 17, no. 5, pp. 778–789, 2016.
- [5] M. P. Collins, P. T. Quach, and E. C. Bentz, "Shear behavior of thick slabs," *ACI Struct. J.*, vol. 117, no. 4, pp. 115–126, 2020.
- [6] D. A. Kuchma, S. Wei, D. H. Sanders, A. Belarbi, and L. C. Novak, "Development of the one-way shear design provisions of ACI 318-19 for reinforced concrete," *ACI Struct. J.*, vol. 116, no. 4, pp. 285–296, 2019.
- [7] American Concrete Institute, *Building Code Requirements for Structural Concrete*. Farmington Hills, MI, USA: Amer. Concrete Inst., 2014.
- [8] Associação Brasileira de Normas Técnicas, *Projeto de Estruturas de Concreto: Procedimentos*, NBR 6118:2014, 2014.
- [9] R. Wendner, A. Strauss, and D. Novák, "The role of fracture mechanics in reliability analyses," in *SP-300: Fracture Mechanics Applications in Concrete*, C. Gaedicke, Ed., Farmington Hills, MI, USA: Amer. Concrete Inst., 2015, pp. 117–142.
- [10] A. M. Hillerborg, P. Modéer, and P. E. Petersson, "Analysis of crack formation and crack growth in concrete by means of fracture mechanics and finite elements," *Cement Concr. Res.*, vol. 6, no. 6, pp. 773–781, 1976.
- [11] J. Planas, B. Sanz, and J. M. Sancho, "Vectorial stress-separation laws for cohesive cracking: in concrete and other quasibrittle materials," *Int. J. Fract.*, vol. 223, no. 1, pp. 77–92, 2020.
- [12] C. G. Hoover and Z. P. Bažant, "J. V., R. Wendner and M. H. Hubler, "Comprehensive concrete fracture tests: description and results," *Eng. Fract. Mech.*, vol. 114, pp. 92–103, Dec 2013.
- [13] Z. P. Bažant, M. Rasoolinejad, A. Dönmez, and W. Luo, "Dependence of fracture size effect and projectile penetration on fiber content of FRC," *IOP Conf. Series Mater. Sci. Eng.*, vol. 596, no. 1, pp. 012001, 2019.
- [14] C. Carloni, G. Cusatis, M. Salviato, J. L. Le, C. G. Hoover, and Z. P. Bažant, "Critical comparison of the boundary effect model with cohesive crack model and size effect law," *Eng. Fract. Mech.*, vol. 215, pp. 193–210, May 2019.
- [15] J. Le, C. G. Hoover, and Z. P. Bažant, "Problems with Hu-Duan boundary effect model and its comparison to size-shape effect law for quasi-brittle fracture," *J. Eng. Mech.*, vol. 136, no. 1, pp. 40–50, Jun 2010.
- [16] C. G. Hoover and Z. P. Bažant, "Cohesive crack, size effect, crack band and work of fracture compared to comprehensive concrete fracture tests," *Int. J. Fract. Mech.*, vol. 187, pp. 133–143, 2014.
- [17] Associação Brasileira de Normas Técnicas, *Concretos para fins estruturais*, NBR 8953:2015, 2015.
- [18] Canadian Standard Association, *Design of Concrete Structures*, CAN3 A23.3-94, 2014.
- [19] G. N. Kani, "The riddle of shear failure and its solution," *ACI J. Proc.*, vol. 61, no. 4, pp. 441–468, 1964.
- [20] M. Iguro, T. Shioya, Y. Nojiri and H. Akiyama, "Experimental studies on shear strength of large reinforced," *Concr. Libr. JSCE*, vol. 1, no. 345, pp. 137–154, 1984.
- [21] B. A. Podgorniak-Stanik, "The influence of concrete strength distribution of longitudinal reinforcement amount," Master thesis, Grad. Dept. Civil Eng., Toronto Univ., Toronto, Canada, 1998.
- [22] P. Quach, "Understanding and safely predicting the shear response of large-scale reinforced concrete structures," Master thesis, Dept. Civil Eng., Toronto Univ., Toronto, Canada, 2016.
- [23] A. Agarwal, S. J. Foster, and M. G. Stewart, "Model error and reliability of reinforced concrete beams in shear designed according to the Modified Compression Field Theory," *Struct. Concr.*, vol. 22, pp. 3711–3726, 2021.
- [24] S. J. Foster et al., "Calibration of Australian Standard AS3600 concrete structures: part I statistical analysis of material properties and model error," *Aust. J. Struct. Eng.*, vol. 17, no. 4, pp. 242–253, 2016.
- [25] S. Foster et al., *A Re-Evaluation of the Safety and Reliability Indices for Reinforced Concrete Structures Designed to AS3600: UNICIV Report R-464*. Sydney, Australia: Univ. New South Wales, 2015.
- [26] I. J. S. Ribeiro, J. R. C. Pessoa, and T. N. Bittencourt, "Analysis of shear strength of complementary mechanisms "trends in reinforced concrete beams," *Rev. IBRACON Estrut. Mater.*, vol. 16, no. 2, pp. e16208, 2023.
- [27] R. J. Frosch, Q. Yu, G. Cusatis, and Z. P. Bažant, "A unified approach to design," *Concr. Int.*, vol. 1, no. 582, pp. 147–158, 2017.
- [28] K. H. Reineck, E. C. Bentz, B. Fitik, D. A. Kuchma, and O. Bayrak, "ACI-DAfStb database of shear tests on slender reinforced concrete beams without stirrups," *ACI Struct. J.*, vol. 110, no. 5, pp. 867–948, 2013.
- [29] Q. Yu and Z. P. Bažant, "Can stirrups suppress size effect on shear strength of RC beams," *J. Struct. Eng.*, vol. 137, no. 5, pp. 607–617, 2011.
- [30] K. H. Reineck, E. C. Bentz, B. Fitik, D. A. Kuchma, and O. Bayrak, "ACI-DAfStb database of shear tests on slender reinforced concrete beams with stirrups," *ACI Struct. J.*, vol. 110, no. 5, pp. 1, 2014.

- [31] Fédération Internationale du Béton, *Fib Model Code for Concrete Structures 2010*. Lausanne, Switzerland: FIB, 2013.
- [32] A. T. Beck, W. L. A. Oliveira, S. Nardim, and A. L. H. C. ElDebs, "Reliability-based evaluation of design code provisions for circular concrete-filled steel columns," *Eng. Struct.*, vol. 31, pp. 2299–2308, 2009.
- [33] V. P. de Barros, A. T. Beck, and T. N. Bittencourt, "Shear failure in reinforced concrete members without transverse reinforcement: analysis of model error of NBR6118:2014," *Rev. IBRACON Estrut. Mater.*, vol. 14, no. 1, pp. e14112, 2021.
- [34] Joint Committee on Structural Safety. "JCSS probabilistic model code – part 2: load models." JCSS-LC.org. <https://www.jcss-lc.org/jcss-probabilistic-model-code/> (accessed Mar. 25, 2022).
- [35] W. C. Santiago and H. Machado, "S. Hampshire S., F. R. Stucchi and A. T. Beck. "Reliability-based calibration of main Brazilian structural design codes," *Lat. Am. J. Solids Struct.*, vol. 17, no. 1, pp. e245, 2020.
- [36] L. G. L. Costa, W. C. Santiago, and A. T. Beck, "Probabilistic models for live loads in buildings: critical review, comparison to Brazilian design standards and calibration of partial safety factors," *Rev. IBRACON Estrut. Mater.*, vol. 16, no. 2, pp. e16204, 2023.
- [37] A. T. Beck and A. C. Souza Jr., "A first attempt toward a reliability-based calibration of Brazilian structural design codes," *J. Braz. Soc. Mech. Sci. Eng.*, vol. 32, pp. 119–127, 2010.

Author contributions: IJSR: conceptualization, data curation, formal analysis, writing, methodology; JRCP: supervision, writing, methodology; TNB: conceptualization, data curation, formal analysis, writing, methodology; ATB: conceptualization, data curation, formal analysis, writing, methodology.

Editors: Leandro Trautwein, Mauro Real, Mario Pimentel.

Annex A. DATA FOR CONCRETE BEAMS WITH STIRRUPS

- Ahmad, S.H.; Park, F.; El-Dash, K. (1995): Web reinforcement effects on shear capacity of reinforced high-strength concrete beams. Magazine of Concrete Research 47 (Sep.1995), No. 172, 227-233
- Ahmad, S.H.; Xie, Y.; Yu, T. (1996): Effectiveness of Shear Reinforcement for Normal and High-Strength Concrete Beams. Structural Engineering Review, V.8 (1996), No.1, 65-78
- Angelakos, D.; Bentz, E.C (2001): Collins, M.P.: Effect of concrete strength and minimum stirrups on shear strength of large members. ACI Structural Journal 98 (2001), Title 98-S28, May-June, 290 - 300
- Aparicio, A.; Calavera, J.; del Pozo, F.J. (1997): Testing strut compression shear failure in beams. Polytechnic University of Madrid, 1997. pp. 55 [see also: Gettu et al (1997); Rozas Hernando et al. (1997)]
- Bernhardt, C.J.; Fynboe, C.C. (1986): High strength concrete beams. Nordic Concrete Research, Norske Betongforening, Oslo 1986
- Bhal, N.S. (1968): Über den Einfluß der Balkenhöhe auf die Schubtragfähigkeit von einfeldrigen Stahlbetonbalken mit und ohne Schubbewehrung. Otto-Graf-Institut, H.35, Stuttgart, 1968
- Bræstrup, M.W.; Nielsen, M.P.; Bach, F.; Jensen, B. Chr. (1976): Shear Tests on Reinforced Concrete T-Beams. Series T. Structural Research Laboratory, Technical University of Denmark, rapport Nr.R 72,1976
- Cladera, A.; Mari, A.R. (2002): Shear Strength of Reinforced High -Strength and Normal -Strength Concrete Beams. A New Smimplified Shear Design Method. Universitat Politècnica de Catalunya, 1-19, 2002
- Cederwall, K.; Hedman, O.; Losberg, A. (1974): Shear strength of partially prestressed beams with pretensioned reinforcement of high grade deformed bars. SP 42 - 9
- Gabriellson, H. (1993): High Performance Concrete Beams Tested in Shear. Comparison between the Traditional Approach and the Modified Compression Field Theory. 169-176 in: Holand, I.; Sellevold, E. (Editors): 'Utilization of High Strength Concrete', 3rd Symp. in Lillehammer, Norway, 20.-23. June 1993, Proc. V.1. Norwegian Concrete Assoc., Oslo 1993. ISBN 82-91341-00-1
- Guido, C. C.; Radogna E. F. (1963): Contributo teorico sperimentale allo studio della precompressione parziale. Giomate del Precompresso. Venezia (Okt. 1963)
- Hamadi, Y.D. (1976): Force transfer across cracks in concrete structures. PhD-thesis, Polytechnic of Central London, 1976
- Hegger, J.; Görtz, S.; Will, N.; Drössler, C.; Tigges, C. (2001): Tragfähigkeit von Bauteilen aus selbstverdichtendem Beton. BuStb 96 (2001), H. 11, 691-697
- Hegger, J.; Görtz, S. (2003): Analyse des Schubrissverhaltens und dessen Auswirkungen auf die Querkrafttragfähigkeit. RWTH Aachen, Institut für Massivbau, Schlussbericht DBV 227, Institutsbericht-Nr. 86/2003, Aachen, September 2003
- Hegger, J.; Görtz, S.; Neuser, J.U. (1999): Hochfester Beton für Spannbetonbalken mit sofortigem Verbund. Schlußbericht (DBVNr.192), Institutsbericht Nr. 55/99, RWTH Aachen, 1999
- Kautsch, R. (2010): Beitrag zur Nachweisführung von Querkraftbewehrten Stahlbeton- und Spannbetonquerschnitten unter kombinierter Biege- und Schubbeanspruchung auf Grundlage der erweiterten technischen Biegelehre. (Analysis of shear reinforced r.c.- and p.c.-crosssections subjected to combined bending and shear on basis of the extended bending theory). Diss. Fachbereich Architektur / Raum- und Umweltplanung / Bauingenieurwesen der TU Kaiserslautern. D 386, Kaiserslautern 2010. pp. 251
- Kong, F.-K.; Robins, P.J.; Cole, D.P. (1970): Web Reinforcement Effects on Deep Beams. ACI-Journ. V.67 (1970), No.12, Dec., 1010-1017
- Leonhardt, F.; Walther, R. (1962b): Versuche an Plattenbalken mit hoher Schubbeanspruchung. DAfStb H.152, Beuth Verlag Berlin, 1962
- Leonhardt, F.; Walther, R. (1962c): Versuche an schlaff bewehrten Rechteck- und Plattenbalken mit Schubbewehrung; 1. Teil; Forschungsreihe über die Tragfähigkeit auf Schub von Stahl- und Spannbetonbalken, FMPA (Otto-Graf-Institut), Stuttgart, März 1962
- Leonhardt, F.; Walther, R. (1962d): Versuche an schlaff bewehrten Rechteckbalken und Platten ohne Schubbewehrung; 2. Teil; Forschungsreihe über die Tragfähigkeit auf Schub von Stahl- und Spannbetonbalken, FMPA (Otto-Graf-Institut), Stuttgart, März 1962
- Leonhardt, F., Walther, R. (1962e): Versuche an schlaff bewehrten Rechteckbalken und Platten ohne Schubbewehrung; Zusammenfassung und vorläufige Schlußfolgerungen; Forschungsreihe über die Tragfähigkeit auf Schub von Stahl- und Spannbetonbalken, FMPA (Otto-Graf-Institut), Stuttgart, April 1962 DAfStb H. 617: Report on ACI-DAfStb Shear Databases 2015 - Part 4.1: Attachment 4.2-1 4 2016
- Leonhardt, F., Walther, R. (1963): Schubversuche an Plattenbalken mit unterschiedlicher Schubbewehrung. DAfStb H.156, Beuth Verlag, Berlin, 1963
- Levi, F.; Marro, P. (1989): Shear Tests up to Failure of Beams made with Normal and High Strength Concrete. p. 11-24 in: CEB-Bulletin No.193 (1989)
- Levi, F.; Marro, P. (1993): Shear Tests on HSC Prestressed Beams - Proposals of new Interpretative Models. High-Strength Concrete (1993), Proceedings V.1, 293-305
- Mariyama, K.; Rizkalla, S.H. (1988): Shear design consideration for pretensioned prestressed beams. ACI-Journ. V.85 (1988), No.5, Sep.-Oct., 492-498
- Moayer, M.; Regan, P.E. (1974): Shear strength of prestressed and reinforced concrete T-beams. 183-214 in: Shear in reinforced concrete. Vol. 1, Publ. SP 42, ACI Detroit. 1974
- Özden, K. (1967): An Experimental Investigation on the Shear Strength of Reinforced Concrete Beams. Structural Research Laboratory (1967), Technical University of Denmark
- Ozcebe, G.; Ersoy, U.; Tankut, T. (1999): Evaluation of minimum shear reinforcement requirements for higher strength concrete. ACI Struct. Journ. V.96 (1999), No. 3, May-June
- Petersson, T. (1972): Shear and Torsion in reinforced concrete beams. National Swedish Building Research, Document D10:1972
- Quast, U. (1999): Einfluß von Langzeitwirkungen auf den Neigungswinkel von Schubrissen. Schlußbericht zum Forschungsvorhaben QU 48/5-1. Arbeitsbereich Massivbau, Technische Universität Hamburg-Harburg (TUHH), 31.03. 1999. pp. 36 + 121 Anlagen DAfStb H. 617: Report on ACI DAfStb Shear Databases 2015 - Part 4.1: Attachment 4.2-1 5, 2016
- Reineck, K.-H.; Wohlfahrt, R.; Hardjasaputra, H. (2001): Verformungsverhalten und Tragfähigkeit dünner Stege von Stahlbeton- und Spannbetonträgern mit hoher Betongüte (Deformations and strength of thin webs of reinforced and prestressed high strength concrete beams). DAfStb-Heft 517, Beuth Verlag, Berlin 2001
- Roller, J.J., Russel, H.G. (1990): Shear Strength of High-Strength Concrete Beams with Web Reinforcement. ACIJourn. V.87, N. 2, (1990), March-April, 191-198
- Rosenbusch, J.; Teutsch, M. (2002): Trial Beams in Shear. Brite/Euram project 97-4163, Final Report Sub task 4.2, Institut für Baustoffe, Massivbau und Brandschutz, TU Braunschweig, January, 2002
- Rosenbusch, J. (2003): Zur Querkrafttragfähigkeit von Balken aus stahlfaserverstärkten Stahlbeton. Diss., Fachbereich Bauingenieurwesen, Technische Universität Carolo-Wilhelmina zu Braunschweig, Juni 2003. pp. 199
- Sarsam, K.F.; Al-Musawi, J.M.S. (1992): Shear Design of High-and Normal Strength Concrete beams with Web Reinforcement. ACI-Journ. V.89 (1992), No.6, Nov.-Dec., 658-664
- Soerensen, H.C. (1974): Shear Test on 12 Reinforced Concrete T-Beams. Structural Research Laboratory (1974), Rapport Nr. R 60, Technical University of Denmark
- Stroband, J. (1997): Shear Capacity of High-Strength Concrete Beams with Shear Reinforcement. Progress in Concrete, V.5 (1997), TU Delft, 87-96 Sunderland, A. (1947): Shear strength of reinforced concrete rectangular and T-beams, Ph. D. Thesis, University of Leeds (1947)
- Tan, K.-H.; Kong, F.-K.; Teng, S.; Weng, L.-W. (1997): Effect of web reinforcement on high-strength concrete deep beams. ACI Structural Journal, V. 94, No. 5, Sep.-Oct. 1997, 572-582
- Tan, K.-H.; Kong, F.-K.; Teng, S.; Guan, L. (1995): High-strength concrete deep beams with effective span and shear span variations. ACI Structural Journal, V. 92, N. 4, July-Aug. 1995, 395-405
- Tan, K.; Teng, S.; Kong, F.-K.; Lu, H. (1997): Main Tension Steel in High Strength Concrete Deep and Short Beams. ACI Structural Journal, November- December 1997, 752- 768
- Yoon, Y.-S.; Cook, W.D.; Mitchell, D. (1996): Minimum Shear Reinforcement in Normal, Medium and HighStrength Concrete Beams. ACI-Journ., V.93 (1996), No.5, Sept.-Oct., 576-584
- Yoshida, Y. (2000): Shear Reinforcement for Large, Lightly Reinforced Concrete Members. Master Thesis, Grad.Dep. of Civil Eng., University of Toronto (2000)



ORIGINAL ARTICLE

Punching shear design with control perimeters subjected to asymmetrical bending

Verificação à punção com perímetros de controle submetidos à flexão assimétrica

Mariana Nunes Souza^a Mayra Soares Pereira Lima Perlingeiro^a Mauro Schulz^a ^aUniversidade Federal Fluminense – UFF, Civil Engineering Department, Niteroi, RJ, Brasil

Received 19 September 2022

Accepted 23 March 2023

Abstract: A numerical procedure is proposed for asymmetrical plastic shear diagrams in punching control perimeters. Asymmetrical diagrams occur for edge and corner columns and for internal columns with biaxial unbalanced moments. The procedure intends to support the use of NBR 6118, which covers asymmetrical shear distributions due to internal moments of edge and corner columns. The study of columns in different positions of the slab proves the robustness and numerical efficiency of the proposal. The practical application of the procedure is tested against Model Code 1990, Eurocode 2, NBR 6118, and with combinations of criteria from these codes. The estimated capacities are compared with experimental data from the literature. Eurocode 2 initially presents better results, but this code does not consider moments with internal eccentricities in edge and corner columns. The Eurocode 2 evaluations are significantly improved by the inclusion of NBR 6118 criteria that partially apply these moments, whose asymmetrical shear diagrams can be determined by the proposed procedure.

Keywords: flat slabs, punching shear, unbalanced moments, plastic analysis.

Resumo: Um procedimento numérico é proposto para diagramas plásticos de cisalhamento assimétricos em perímetros de controle de punção. Diagramas assimétricos ocorrem para pilares de borda e de canto e para pilares internos com momentos desbalanceados biaxiais. O procedimento visa auxiliar a utilização da NBR 6118, que considera as distribuições assimétricas de cisalhamento associadas aos momentos internos de pilares de borda e de canto. O estudo de pilares em diferentes posições da laje comprova a robustez e a eficiência numérica da proposta. A aplicação prática do procedimento é testada com o Model Code 1990, o Eurocode 2, a NBR 6118 e com combinações de critérios desses códigos. As capacidades estimadas são comparadas com dados experimentais da literatura. O Eurocode 2 apresenta inicialmente melhores resultados, mas este código não considera os momentos com excentricidades internas em pilares de borda e de canto. As estimativas do Eurocode 2 são significativamente melhoradas pela inclusão de critérios da NBR 6118 que aplicam parcialmente esses momentos, cujos diagramas de cisalhamento assimétricos podem ser determinados pelo procedimento proposto.

Palavras-chave: lajes lisas, punção, momentos desbalanceados, análise plástica.

How to cite: M. N. Souza, M. S. P. L. Perlingeiro, and M. Schulz, “Punching shear design with control perimeters subjected to asymmetrical bending,” *Rev. IBRACON Estrut. Mater. J.*, vol. 16, no. 3, e16307, 2023, <https://doi.org/10.1590/S1983-41952023000300007>

1 INTRODUCTION

The design of flat slabs is often controlled by the punching shear strength of the slab-column connections. Slab-column connections are usually subjected to unbalanced moments that yield additional shear stresses and reduce the punching shear capacity.

Corresponding author: Mauro Schulz. E-mail: mschulz@id.uff.br

Financial support: None.

Conflict of interest: Nothing to declare.

Data Availability: Data-sharing is not applicable to this article as no new data were created in this study.



This is an Open Access article distributed under the terms of the Creative Commons Attribution License, which permits unrestricted use, distribution, and reproduction in any medium, provided the original work is properly cited.

Eurocode 2 [1] and the Brazilian code NBR 6118 [2] adopt the Model Code 90 [3] punching shear design model with modifications. In this work, these codes are referenced by the abbreviations EC2, NBR6118, and MC90, respectively. The MC90 model compares acting stresses with resisting stresses in control perimeters.

Shear forces due to normal forces are assumed to be uniformly distributed along control perimeters or reduced control perimeters. Shear forces distributed due to unbalanced moments are considered fully plastic in both positive and negative directions. The positive and negative parts of the perimeter may show symmetry, but they are often asymmetrical. Plastic asymmetrical bending diagrams require nonlinear solutions.

This paper proposes a numerical procedure for the determination of asymmetrical plastic shear diagrams in arbitrary control perimeters. The procedure is tested together with the empirical equations set forth in MC90, EC2, and NBR6118. The results are compared with experimental data from the literature.

2 SELECTED RECOMMENDATIONS FROM THE CODES

Research that influenced the design of the MC90 model is discussed by Regan [4] and Regan and Braestrup [5]. The ACI 318-19 [6] and Model Code 2010 [7] recommendations are not discussed here. ACI 318-19 adopts the linear elastic hypothesis proposed by di Stasio and van Buren [8]. Model Code 2010 verifies plastic distributions based on the Critical Shear Crack Theory (Muttoni [9] and Ruiz and Muttoni [10]).

MC90, EC2, and NBR6118 verify the capacity of slabs without transverse reinforcement at Perimeter 1. Perimeter 1 is at distance $2d$ from the column face, where d is the effective depth of the slab. Considering elements without shear reinforcement, the punching strength of slabs at Perimeter 1 corresponds to the shear strengths of the linear members (FIB Bulletin 2 [11]). The three codes present equivalent expressions for design shear stresses τ_{Rd} , whose parameters are determined using the respective partial safety factors for concrete γ_c .

Compressive stresses in concrete struts are verified at Perimeter 0, which is adjacent to the column. Although the τ_{Rd} expressions are similar at Perimeter 0, MC90, EC2, and NBR6118 reduce the diagonal compressive capacity by different factors.

Perimeter n is tested when transverse reinforcement is required. The distance between this perimeter and the outer reinforcement contour is kd . MC90 and NBR6118 use $k = 2$, while EC2 uses $k = 1.5$. The three codes define maximum stresses for transverse reinforcement but use different approaches.

The differences between the codes are more significant in the control perimeters submitted to bending. The plastic diagrams of internal columns subjected to biaxial bending are asymmetrical. This issue is only addressed in EC2, which indicates an empirical solution. MC90 and EC2 ignore moments with internal eccentricity in edge and corner columns. NBR6118 partially includes internal moments of edge and corner columns when their eccentricities are greater than the eccentricities between the columns and the reduced control perimeters.

3 PUNCHING SHEAR DESIGN WITH UNBALANCED MOMENTS

Any evaluation of shear forces along a control perimeter must consider that the bending and torsional moments resist part of the unbalanced moment. The K factor is defined as the fraction of the unbalanced moment that is resisted by shear forces.

The moments transferred to the slab by bending and shear are experimentally investigated by Hanson and Hanson [12] on square columns. The ratios of unbalanced moments resisted by shear are analytically discussed by Mast [13] for internal columns (Figure 1). The corresponding K factor is estimated by the elastic solution of a plate subjected to a concentrated moment. The plate is simply supported in the main direction and is infinite in the other direction (Girkmann [14]). The K factor can be defined as a function of the control perimeter shape in the region close to the column.

Design K values indicated in MC90 are compared with Mast's [13] approximate elastic solution (Figure 1). The analytical values assume that lengths a and b vary between $L/20$ and $L/5$, where L is the span between the columns. Figure 1 also shows the elastic distribution of shear forces along a square perimeter, where $a = b = L/10$.

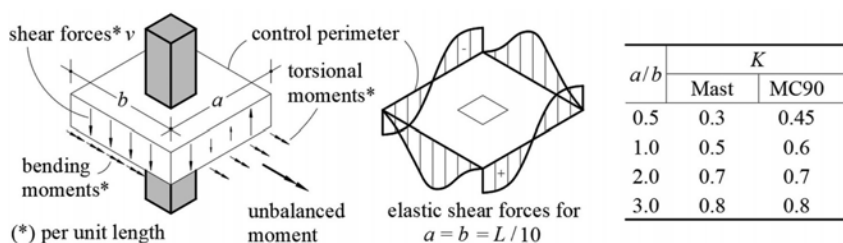


Figure 1. Unbalanced moment transfer in slab-column connections

Shear force distribution in reinforced concrete flat slabs has also been studied by nonlinear finite element analyses. Shu et al. [15] investigate internal columns without unbalanced moments in flat slabs without shear reinforcement. The shear force distributions along the control perimeters are determined by shell and solid nonlinear finite element models. The results show that reinforcement arrangement, cracking and nonlinear material behavior influence the shear force distribution. Laguta [16] uses a concrete damaged plasticity material model to describe the nonlinear behavior of the concrete and present a typical shear stress distribution at a control perimeter under combined vertical load and unbalanced moment.

Normal force and bending moment are considered separately in the MC90 design model and produce distinct plastic shear force diagrams per unit length (Figure 2). The plastic shear forces related to normal force F and bending moment M are respectively denoted by v_F and v_M .

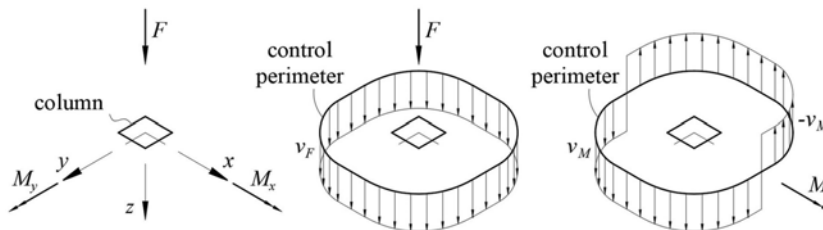


Figure 2. Coordinate system, applied forces and moments, and distributed shear forces

MC90 defines an effective normal force F_{ef} , including the effect of unbalanced moment. The plastic diagrams for normal force F and bending moment M determine the effective force F_{ef} . EC2 uses the same methodology, presented by coefficient β , such that $F_{ef} = \beta F$.

F_{ef}^j is here defined as the effective force that is calculated on Perimeter j . The following expressions apply:

$$v_F^j = \frac{F}{u^j} \quad ; \quad v_F^{*j} = \frac{F}{u^{*j}} \quad ; \quad v_M^j = \frac{M}{W_p^j} \tag{1}$$

where W_p^j is the plastic modulus and u^j is the developed length of Perimeter j . Reduced lengths u^{*j} are defined for edge and corner columns. Reduced lengths u^{*j} correspond to developed lengths u^j in internal columns.

The combined shear force per unit length v_{MF}^j is expressed by

$$v_{MF}^j = v_F^{*j} + v_M^j \tag{2}$$

The effective force F_{ef}^j on Perimeter j is given by

$$F_{ef}^j = \frac{v_{MF}^j}{v_F^j} F \tag{3}$$

4 PLASTIC MODULUS FOR ASYMMETRICAL BENDING

A numerical procedure is used to determine the plastic shear diagram and the plastic flexural modulus of an arbitrary perimeter, which is subjected to a bending moment M about an oblique axis.

M_x and M_y are the vector components of bending moment M about the x – and y – axes, respectively (Figure 3).

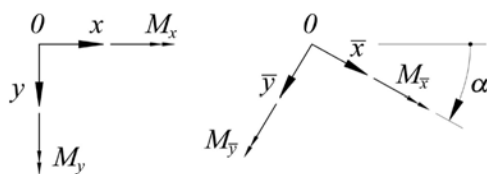


Figure 3. Rotated coordinate system associated with the principal moments

4.1 Moments in the principal coordinate system

Figure 3 presents the principal coordinate system $\bar{x}\bar{y}$. The system is rotated from the xy coordinate system by an angle α , which is defined by

$$\cos \alpha = \frac{M_x}{\sqrt{M_x^2 + M_y^2}} \quad ; \quad \sin \alpha = \frac{M_y}{\sqrt{M_x^2 + M_y^2}} \quad (4)$$

Considering $\bar{x} = x \cos \alpha + y \sin \alpha$ and $\bar{y} = -x \sin \alpha + y \cos \alpha$, the equilibrium conditions of the shear forces per unit length v along the perimeter U yield

$$M_{\bar{x}} = \int_U v \bar{y} ds = \int_U v (-x \sin \alpha + y \cos \alpha) ds = M_x \cos \alpha + M_y \sin \alpha = \sqrt{M_x^2 + M_y^2} \quad (5)$$

$$M_{\bar{y}} = \int_U -v \bar{x} ds = \int_U -v (x \cos \alpha + y \sin \alpha) ds = -M_x \sin \alpha + M_y \cos \alpha = 0 \quad (6)$$

where $M_{\bar{x}}$ and $M_{\bar{y}}$ are the moments about the \bar{x} – and \bar{y} –axes (Figure 3).

4.2 Distribution of shear forces per unit length

Shear forces $v = -v_M$ and $v = +v_M$ (Figure 2) are considered uniformly distributed along perimeter lengths U^- and U^+ , respectively. The equilibrium conditions in the z –direction and about the x – and y –axes lead to the following equations:

$$\int_{U^-} (-v_M) ds + \int_{U^+} (+v_M) ds = 0 \quad (7)$$

$$M_{\bar{x}} = \int_{U^-} (-v_M) \bar{y} ds + \int_{U^+} (+v_M) \bar{y} ds \quad (8)$$

$$M_{\bar{y}} = - \int_{U^-} (-v_M) \bar{x} ds - \int_{U^+} (+v_M) \bar{x} ds \quad (9)$$

Collecting like terms in Equations 7 to 9 yields

$$\int_{U^-} (-1) ds + \int_{U^+} (+1) ds = 0 \quad (10)$$

$$W_{p\bar{x}} = \int_{U^-} (-1) \bar{y} ds + \int_{U^+} (+1) \bar{y} ds \quad (11)$$

$$W_{p\bar{y}} = - \int_{U^-} (-1) \bar{x} ds - \int_{U^+} (+1) \bar{x} ds \quad (12)$$

where the plastic flexural moduli $W_{p\bar{x}}$ and $W_{p\bar{y}}$ are

$$W_{p\bar{x}} = \frac{M_{\bar{x}}}{v_M} \quad ; \quad W_{p\bar{y}} = \frac{M_{\bar{y}}}{v_M} \quad (13)$$

A numerical algorithm establishes perimeter lengths U^- and U^+ .

4.3 Discretization and parametrization of the control perimeter

The perimeter is divided into linear and arc segments for the application of the numerical procedure.

The developed length of the control perimeter is defined as u . The numerical procedure demands that all segments have lengths less than the semi-perimeter $u/2$. This condition is satisfied by the division into segments shown in Figure 4.

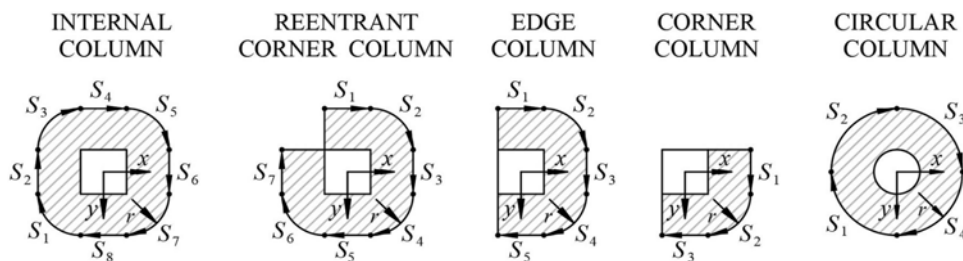


Figure 4. Discretization of control perimeters into segments S_i

The points that divide the segments are numbered from 1 to N . The control perimeter is parameterized according to the developed length s , where $s_1 = 0$ at start point 1 and $s_N = u$ at endpoint N (Figure 5).

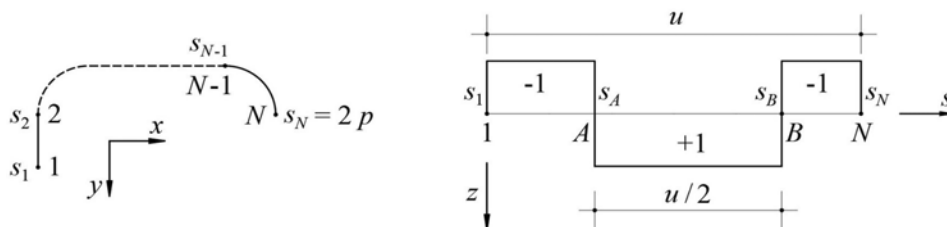


Figure 5. Parameter s and unit shear force distribution along the control perimeter

This parameterization is valid for open and closed perimeters. Points 1 and N are distinct for open perimeters but coincident for closed perimeters.

Figure 5 also presents a flat diagram of unit shear forces per unit length. The longitudinal axis indicates parameter s , which is the developed length from the origin ($s_1 = 0$). The unit shear forces change signs at points A and B . The perimeter length of positive shear forces U^+ is defined between points A and B . The perimeter length of negative shear forces U^- is defined in intervals $1 - A$ and $B - N$.

Equation 10 shows that the developed lengths of the perimeter lengths U^- and U^+ are both equal to the semi-perimeter $u/2$.

4.4 Plastic flexural modulus

The parameters s of points A and B are defined as s_A and s_B , respectively. Equation 10 is automatically respected by adopting the following

$$s_B = s_A + \frac{u}{2} \tag{14}$$

A parameter s_A yields s_B by Equation 14. Perimeter lengths U^- and U^+ are defined in Figure 5. The plastic flexural moduli $W_{p\bar{x}}(s_A)$ and $W_{p\bar{y}}(s_A)$ are determined by Equations 11 and 12, respectively.

The algorithm searches for a parameter s_A^* that yields $W_{p\bar{y}}(s_A^*) \approx 0$. The solution s_A^* yields a unit diagram proportional to the shear force diagram that satisfies Equations 5 and 6.

The plastic flexural modulus W_p and the shear force per unit length v_M are given by

$$W_p = |W_{p\bar{x}}(s_A^*)| \tag{15}$$

$$v_M = \frac{M_{\bar{x}}}{W_p} = \frac{\sqrt{M_{\bar{x}}^2 + M_{\bar{y}}^2}}{W_p} \tag{16}$$

where v_M is always positive.

If \bar{y} coordinates are always negative in U^- and positive in U^+ , or always positive in U^- and negative in U^+ , Equations 11 and 15 yield

$$W_p = \int_U |\bar{y}| ds \tag{17}$$

Equation 17 cannot be used in the general case, but it is valid for symmetrical perimeters about the \bar{x} - axis. It is applicable in specific cases, such as edge columns subjected to moments $M_{\bar{x}} = M_x$ (Figure 4).

4.5 Partial integration of a same-sign length of a segment

Changes in the sign of unit shear forces can occur in linear and arc segments. Equations 11 and 12 yield the plastic flexural moduli $W_{p\bar{x}}$ and $W_{p\bar{y}}$ by integrating lengths with shear forces of the same sign.

A segment's start and end points are defined as I and J , respectively (Figure 6). Points P and Q determine a length with positive shear forces.

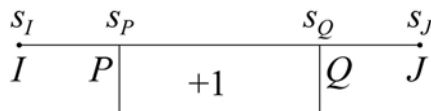


Figure 6. Partial integration between points P and Q

The variables associated with points P , Q , I , and J that are known are the parameters s_I , s_J , s_P , and s_Q and the coordinates \bar{x}_I , \bar{y}_I , \bar{x}_J , and \bar{y}_J . The dimensionless factors ζ_{GI} and ζ_{GJ} of a generic point G on the segment are defined by

$$\zeta_{GI} = \frac{(s_J - s_G)}{(s_J - s_I)} \quad ; \quad \zeta_{GJ} = \frac{(s_G - s_I)}{(s_J - s_I)} \tag{18}$$

In the case of linear segments, H is defined as the barycenter of PQ . The parameter s_H and coordinates \bar{x}_H and \bar{y}_H are equal to

$$s_H = \frac{(s_P + s_Q)}{2} \tag{19}$$

$$\bar{x}_H = \zeta_{HI}\bar{x}_I + \zeta_{HJ}\bar{x}_J \quad ; \quad \bar{y}_H = \zeta_{HI}\bar{y}_I + \zeta_{HJ}\bar{y}_J \tag{20}$$

where $W_{p\bar{x}}^{PQ}$ and $W_{p\bar{y}}^{PQ}$ are the contributions of PQ to the plastic moduli $W_{p\bar{x}}$ and $W_{p\bar{y}}$. In linear segments, they are expressed by

$$W_{p\bar{x}}^{PQ} = \Delta s \bar{y}_H \quad ; \quad W_{p\bar{y}}^{PQ} = -\Delta s \bar{x}_H \tag{21}$$

$$\Delta s = s_Q - s_P \tag{22}$$

where Δs is the length between P and Q .

In arc segments, the following variables are also considered: angles α_I and α_J at points I and J , coordinates x_C and y_C of the center, and radius r . Angles α_P and α_Q are interpolated by

$$\alpha_P = \zeta_{PI}\alpha_I + \zeta_{PJ}\alpha_J \quad ; \quad \alpha_Q = \zeta_{QI}\alpha_I + \zeta_{QJ}\alpha_J \tag{23}$$

The following expressions yield the contributions of PQ to the plastic moduli $W_{p\bar{x}}$ and $W_{p\bar{y}}$ in arc segments:

$$W_{p\bar{x}}^{PQ} = \int_{\alpha_P}^{\alpha_Q} 1 \bar{y} ds = \int_{\alpha_P}^{\alpha_Q} 1 (\bar{y}_C + r \sin \alpha) r d\alpha = \Delta s \bar{y}_C + r^2 (\cos \alpha_Q - \cos \alpha_P)$$

$$W_{p\bar{y}}^{PQ} = - \int_{\alpha_P}^{\alpha_Q} 1 \bar{x} ds = - \int_{\alpha_P}^{\alpha_Q} 1 (\bar{x}_C + r \cos \alpha) r d\alpha = -\Delta s \bar{x}_C - r^2 (\sin \alpha_Q - \sin \alpha_P) \tag{24}$$

The developed length Δs between P and Q is

$$\Delta s = r(\alpha_Q - \alpha_P) \tag{25}$$

4.6 Full segment integration

Unit shear forces on lengths PQ (Figure 6) can be positive or negative. Figure 7 discusses the positive and negative shear forces that should be considered during the complete integration of a segment IJ .

Each segment cannot simultaneously contain points A and B , since all segments have a developed length less than the semi-perimeter $u/2$. The discretization into segments shown in Figure 4 meets this requirement.

Parameters s_A and s_B define segments S_A and S_B , which respectively contain points A and B .

Table 1 defines the coordinates s_P and s_Q of each segment S integration step, according to its location. Equations 21 and 24 are established for a positive unit shear force. The effective signs of unit shear forces will be considered as indicated in the table.

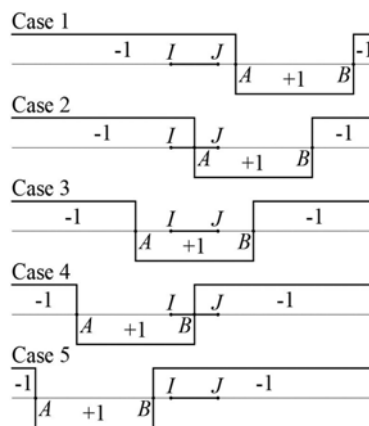


Figure 7. Unit shear force along the control perimeter

Table 1. Integration of segment IJ

Case	Condition	Segment parts	s_P	s_Q	v
1	$S < S_A$	1	s_I	s_J	-1
2	$S = S_A$	2	s_I s_A	s_A s_J	-1 1
3	$S < S_B$	1	s_I	s_J	1
4	$S = S_B$	2	s_I s_B	s_B s_J	1 -1
5	$S > S_B$	1	s_I	s_J	-1

5 IMPLEMENTATION AND EXAMPLES

The previous steps define an iteration that yields the plastic flexural moduli $W_{p\bar{x}}(s_A)$ and $W_{p\bar{y}}(s_A)$ as a parameter function s_A . The parameter s_A^* associated with $W_{p\bar{y}}(s_A^*) \cong 0$ gives the principal plastic modulus $W_p = |W_{p\bar{x}}(s_A^*)|$, which depends on the direction of the applied bending moment M . The solution s_A^* is searched for in the interval $0 \leq s_A < \frac{u}{2}$.

As the computational cost of the procedure is low, the solution can be investigated by sequentially examining many values in the range. This process can be optimized by dividing the original interval into m subintervals. The solution subinterval is identified by the change in the sign of $W_{p\bar{x}}$ at its endpoints, but the endpoints themselves should be previously verified as possible solutions. The solution subinterval is iteratively divided into m subintervals until the required tolerance is reached. This work uses $m = 20$.

Figure 8 shows examples of internal, reentrant corner, edge, and corner columns. All columns are subjected to unbalanced moments about an oblique \bar{x} -axis, which is rotated 60 degrees from the x -axis, in the counterclockwise direction. Perimeter 1 unit shear diagrams are shown.

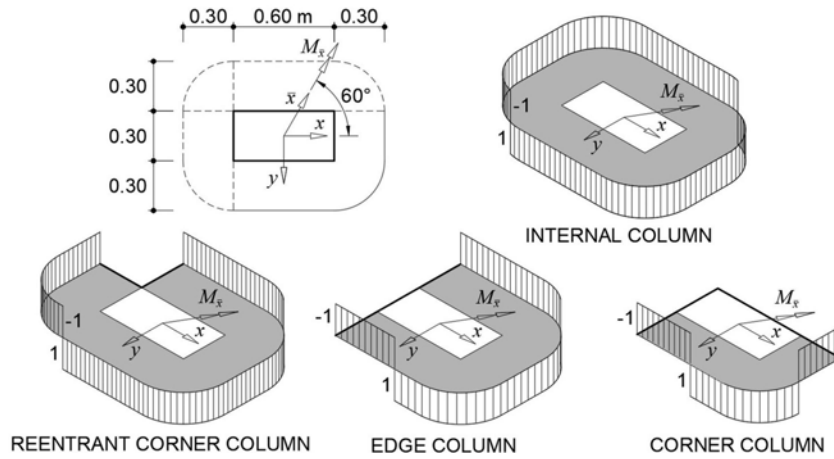


Figure 8. Examples: asymmetrical diagrams of unit shear forces

The sections of all the columns are 0.60 x 0.30 m, and all the slabs have 0.15 m effective depth.

The signs of the shear forces change in the arc and linear segments. The shear force diagrams depend on the direction of the acting bending moment and do not show symmetry.

6 COMPARISON WITH EXPERIMENTS IN THE LITERATURE

Experimental results in the literature are analyzed using MC90, EC2, and NBR6118 together with the proposed procedure.

Asymmetrical bending results can be compared with values usually accepted by these codes as the dataset also includes tests that yield symmetrical diagrams in bending.

The formulas from the codes are used with $\gamma_f = \gamma_c = \gamma_s = 1$, where γ_f is the partial factor for actions. Parameters γ_c and γ_s are the partial factors for concrete and reinforcing steel, respectively.

Shear reinforcement arrangements are always distributed uniformly in the literature tests discussed in this work. Perimeter n may be discontinuous since perimeter lengths with distances greater than d to the nearest transverse reinforcement will not be considered. For uniformly distributed shear reinforcement, the effective shear force $v_{MF,ef}$ is estimated by the following equation:

$$v_{MF,ef} = v_{MF} \frac{s_{avg}}{s_{max}} \geq v_{MF} \tag{26}$$

The combined shear force v_{MF} for continuous perimeters is determined according to each code. The average spacing between transverse bars in the outer reinforcement contour is s_{avg} . The maximum spacing s_{max} is defined as $2d$.

Although the procedures in EC2 and NBR6118 are based on MC90, the differences between them significantly affect the results. The following code criteria are discussed in this work:

a. Size effect (ξ)

In MC90, EC2, and NBR6118, design shear stress τ_{Rd} depends on the size effect parameter $\xi = 1 + \sqrt{\frac{0.2m}{d}}$. EC2 also assumes $\xi \leq 2$.

b. Reinforcement ratio for longitudinal reinforcement (ρ)

Design shear stress τ_{Rd} is also a function of the longitudinal reinforcement ratio $\rho = \sqrt{\rho_x \rho_y}$ in MC90, EC2, and NBR6118. Parameters ρ_x and ρ_y are the ratios in the x - and y -directions, respectively. EC2 also assumes $\rho \leq 0.02$.

c. Effective design yield stress of shear reinforcement ($f_{ywd,ef}$)

All the codes limit the effective design yield stress of shear reinforcement $f_{ywd,ef}$. MC90 adopts $f_{ywd,ef} \leq 300\text{MPa}$. In EC2, the maximum value depends on the effective depth d of the slab. NBR6118 defines different limits for connectors and stirrups depending on total depth h . In this work, the NBR6118 formulation is adapted for effective depth $d = h - 0.03m$.

d. Distance between Perimeter n and the outer transverse reinforcement contour (kd)

MC90 and NBR6118 establish the distance $kd = 2d$ between Perimeter n and the outer transverse reinforcement contour. EC2 assumes $kd = 1.5d$.

e. Edge and corner column moments with internal eccentricity (M^*)

MC90 and EC2 do not consider moments with internal eccentricity in edge and corner columns. NBR6118 partially includes internal moments that are larger than M^* , which are the moments that can be resisted by eccentricities between columns and reduced control perimeters.

f. Perimeter 0 length on edge and corner columns (u^{0*})

In edge and corner column connections, MC90 and EC2 assume a reduced length for Perimeter 0, which is here denoted as u^{0*} . NBR6118 does not assume a reduced length for Perimeter 0.

g. Effective normal force due to unbalanced moments (F_{ef})

F_{ef}^j is defined as the effective normal force that is calculated on a control Perimeter j . MC90 uses F_{ef}^1 and F_{ef}^n on Perimeters 1 and n , respectively, and reuses F_{ef}^1 on Perimeter 0. EC2 only calculates F_{ef}^1 , which is used as the effective normal force on all perimeters. Effective forces are not discussed in NBR6118.

h. Concrete strength reduction factor in diagonal compression (α_θ)

The concrete stress in diagonal compression is limited to $\alpha_\theta \alpha_V f_{cd}$ at Perimeter 0, where f_{cd} is the concrete design strength and $\alpha_V = \left(1 - \frac{f_{ck}}{250\text{MPa}}\right)$. The reduction factor α_θ is given as 0.30, 0.24, and 0.27 in MC90, EC2, and NBR6118, respectively.

Ten combinations (C1 to C10) of eight criteria from the codes are presented in Table 2. Combinations C1 to C3 correspond to MC90, EC2, and NBR6118, respectively. C4 to C10 investigate the response of different criteria a to h in EC2 and NBR6118.

Table 2. Combinations of criteria from Model Code 90, Eurocode 2, and NBR 6118

Combinations of criteria from codes	Criteria from the codes								$\psi \geq 0.95$	ψ_{mean}	ψ_{min}
	a	b	c	d	e	f	g	h			
	ζ	ρ	$f_{ywd,ef}$	kd	M^*	u^{0*}	F_{ef}	α_θ			
C1	MC90	MC90	MC90	MC90	MC90	MC90	MC90	MC90	64%	1.06	0.12
C2	EC2	EC2	EC2	EC2	EC2	EC2	EC2	EC2	94%	1.29	0.18
C3	NBR 6118	NBR 6118	NBR 6118	NBR 6118	NBR 6118	NBR 6118	NBR 6118	NBR 6118	67%	1.14	0.71
C4	EC2	EC2	EC2	EC2	NBR 6118	EC2	EC2	EC2	99%	1.42	0.92
C5	EC2	EC2	NBR 6118	EC2	NBR 6118	EC2	EC2	EC2	99%	1.42	0.92
C6	NBR 6118	NBR 6118	NBR 6118	EC2	NBR 6118	EC2	EC2	EC2	84%	1.20	0.71
C7	EC2	EC2	NBR 6118	NBR 6118	NBR 6118	EC2	EC2	EC2	97%	1.39	0.89
C8	EC2	EC2	NBR 6118	EC2	NBR 6118	NBR 6118	EC2	EC2	99%	1.42	0.92
C9	EC2	EC2	NBR 6118	EC2	NBR 6118	EC2	MC90	EC2	98%	1.40	0.89
C10	EC2	EC2	NBR 6118	EC2	NBR 6118	EC2	EC2	NBR 6118	98%	1.41	0.82
C5 - Asym.	EC2	EC2	NBR 6118	EC2	NBR 6118	EC2	EC2	EC2	100%	1.66	1.06

MC90 = Model Code 90; EC2 = Eurocode 2; NBR = Norma Brasileira (Brazilian Code); ψ = ratio between the experimental and estimated capacities; ψ_{mean} = mean value of ψ ; ψ_{min} = minimum value of ψ

Ninety-four experiments of slab-column connections subjected to punching shear were compiled from the literature and their experimental capacity was compared with the theoretical capacity given by the combinations in Table 2. The dataset contains internal, reentrant corner, edge, and corner columns subjected to normal forces, with and without unbalanced moments. The tests include slabs without shear reinforcement. Transverse reinforcement is provided by shear studs.

Table 3. C5 results for experiments in Stamenkovic [17] and Stamenkovic and Chapman [18].

Exp.	Case	d (mm)	c_x (mm)	c_y (mm)	ρ (%)	f_{ck} (MPa)	F (kN)	M_x (kNm)	M_y (kNm)	F_{ef}^1 (kN)	A_{sw}^ϕ (cm ²)	n_p	n_r	s_0 (mm)	s_r (mm)	f_{yw} (MPa)	$f_{yw,ef}$ (MPa)	s_{avg} (mm)	s_{max} (mm)	Crit. per.	ψ	
V_I_1	INTERNAL	56	127	127	1.17	40.14	119.7	-	-	119.7	-	-	-	-	-	-	-	-	-	-	1	1.36
V_I1_1	INTERNAL	56	127	127	1.17	38.68	104.5	-	-	104.5	-	-	-	-	-	-	-	-	-	-	1	1.20
V_I2_1	INTERNAL	56	127	127	2.34	56.26	129.9	-	-	129.9	-	-	-	-	-	-	-	-	-	-	1	1.10
V_I_2	INTERNAL	56	127	127	1.17	27.54	117.4	-	-	117.4	-	-	-	-	-	-	-	-	-	-	1	1.51
V_Ir_1	INTERNAL	56	152	76	1.17	26.72	108.5	-	-	108.5	-	-	-	-	-	-	-	-	-	-	1	1.48
V_E_1	EDGE	56	127	127	1.17	30.47	74.7	-	-	74.7	-	-	-	-	-	-	-	-	-	-	1	1.86
V_C_1	CORNER	56	127	127	1.17	34.23	27.1	-	-	27.1	-	-	-	-	-	-	-	-	-	-	1	1.30
C_I_1	INTERNAL	56	127	127	1.17	38.27	84.5	-	-7.3	120.6	-	-	-	-	-	-	-	-	-	-	1	1.39
C_I_2	INTERNAL	56	127	127	1.17	31.53	62.3	-	-10.5	114.0	-	-	-	-	-	-	-	-	-	-	1	1.41
C_I_3	INTERNAL	56	127	127	1.17	27.13	33.8	-	-13.6	101.1	-	-	-	-	-	-	-	-	-	-	1	1.31
C_I_4	INTERNAL	56	127	127	1.17	26.67	20.9	-	-16.7	103.1	-	-	-	-	-	-	-	-	-	-	1	1.34
C_Ir_1	INTERNAL	56	152	76	1.17	24.03	85.7	-	-7.3	127.0	-	-	-	-	-	-	-	-	-	-	1	1.79
C_Ir_2	INTERNAL	56	152	76	1.17	31.06	67.3	-	-10.9	128.6	-	-	-	-	-	-	-	-	-	-	1	1.66
C_Ir_3	INTERNAL	56	152	76	1.17	30.36	39.9	-	-15.7	128.6	-	-	-	-	-	-	-	-	-	-	1	1.68
C_Ir_4	INTERNAL	56	152	76	1.17	28.25	21.6	-	-16.8	116.5	-	-	-	-	-	-	-	-	-	-	1	1.56
Ct_E_1	EDGE	56	127	127	1.17	29.60	45.8	4.9	-	59.6	-	-	-	-	-	-	-	-	-	-	1	1.50
Ct_E_2	EDGE	56	127	127	1.17	30.18	34.9	5.7	-	51.1	-	-	-	-	-	-	-	-	-	-	1	1.28
Ct_E_3	EDGE	56	127	127	1.17	29.65	23.5	9.4	-	50.1	-	-	-	-	-	-	-	-	-	-	1	1.26
Ct_E_4	EDGE	56	127	127	1.17	31.06	12.9	10.1	-	41.6	-	-	-	-	-	-	-	-	-	-	1	1.03
Cn_E_1	EDGE	56	127	127	1.17	32.70	73.2	-	-5.6	73.2	-	-	-	-	-	-	-	-	-	-	1	1.78
Cn_E_2	EDGE	56	127	127	1.17	27.54	54.7	-	-9.2	76.4	-	-	-	-	-	-	-	-	-	-	1	1.97
Cn_E_3	EDGE	56	127	127	1.17	28.89	24.9	-	-10.1	85.5	-	-	-	-	-	-	-	-	-	-	1	2.17
Cn_E_4	EDGE	56	127	127	1.17	29.19	10.9	-	-8.8	75.7	-	-	-	-	-	-	-	-	-	-	1	1.91
C_C_1	CORNER	56	127	127	1.17	32.35	24.9	-	-6.2	56.7	-	-	-	-	-	-	-	-	-	-	1	2.78
C_C_2	CORNER	56	127	127	1.17	30.06	15.9	-	-6.4	60.0	-	-	-	-	-	-	-	-	-	-	1	3.01
C_C_3	CORNER	56	127	127	1.17	27.43	8.0	-	-6.2	59.6	-	-	-	-	-	-	-	-	-	-	1	3.08
C_C_4	CORNER	56	127	127	1.17	32.53	3.6	-	-5.6	55.1	-	-	-	-	-	-	-	-	-	-	1	2.69

Table 4. C5 results for experiments in Ferreira [19] and Ferreira et al. [20].

Exp.	Case	d (mm)	c_x (mm)	c_y (mm)	ρ (%)	f_{ck} (MPa)	F (kN)	M_x (kNm)	M_y (kNm)	F_{ef}^1 (kN)	A_{sw}^ϕ (cm ²)	n_p	n_r	s_0 (mm)	s_r (mm)	f_{yw} (MPa)	$f_{yw,ef}$ (MPa)	s_{avg} (mm)	s_{max} (mm)	Crit. per.	ψ
LC01	CIRCULAR	143	270	270	1.5	48.00	858.4	-	-	858.4	0.79	6	10	70	100	573.0	363.0	436	286	n	1.06
LC02	CIRCULAR	140	360	360	1.55	47.00	955.7	-	-	955.7	0.79	6	10	70	100	573.0	360.0	465	280	n	1.25
LC03	CIRCULAR	142	450	450	1.41	49.00	1076.8	-	-	1076.8	0.79	6	10	70	100	573.0	362.0	493	284	n	1.41
LC05	CIRCULAR	140	360	360	2.05	50.00	1117.5	-	-	1117.5	0.79	6	10	70	100	573.0	360.0	465	280	n	1.32
LC06	CIRCULAR	143	360	360	1.45	49.00	1077.9	-	-	1077.9	0.79	6	10	70	100	573.0	363.0	465	286	n	1.36
LC07	CIRCULAR	144	360	360	1.6	49.00	1110.4	-	-	1110.4	0.79	7	10	55	80	573.0	364.0	442	288	n	1.31
LC08	CIRCULAR	144	360	360	1.62	48.00	1058.9	-	-	1058.9	0.79	6	12	70	100	573.0	364.0	387	288	n	1.06

Table 5. C5 results for experiments in Ferreira [19] and Ferreira et al. [21].

Exp.	Case	d (mm)	c_x (mm)	c_y (mm)	ρ (%)	f_{ck} (MPa)	F (kN)	M_x (kNm)	M_y (kNm)	F_{ef}^1 (kN)	A_{sw}^ϕ (cm ²)	n_p	n_r	s_0 (mm)	s_r (mm)	f_{yw} (MPa)	$f_{yw,ef}$ (MPa)	s_{avg} (mm)	s_{max} (mm)	Crit. per.	ψ	
LS01	INTERNAL	145	300	300	1.54	48.00	1021.5	-	-	1021.5	0.79	2	12	70	100	573.0	364.0	177	290	n	1.38	
LS02	INTERNAL	143	300	300	1.46	49.00	1127.5	-	-	1127.5	0.79	4	12	70	100	573.0	363.0	278	286	n	1.14	
LS03	INTERNAL	145	300	300	1.54	50.00	698.5	-	-189.0	1071.5	0.79	2	12	70	100	573.0	364.0	177	290	n	1.43	
LS04	INTERNAL	143	300	300	1.46	49.00	721.7	-	-190.0	1099.9	0.79	4	12	70	100	573.0	363.0	278	286	n	1.12	
LS05	INTERNAL	143	300	300	1.58	50.00	779.0	-	-	779.0	-	-	-	-	-	-	-	-	-	-	1	1.18
LS06	INTERNAL	144	300	300	1.56	50.00	528.3	-	-140.7	807.2	-	-	-	-	-	-	-	-	-	-	1	1.21
LS07	INTERNAL	143	300	300	1.7	49.00	1196.8	-	-	1196.8	1.23	4	12	70	100	530.0	363.0	280	286	n	1.15	
LS08	INTERNAL	144	300	300	1.68	48.00	934.1	-	-190.9	1312.5	1.23	4	12	70	100	530.0	364.0	280	288	n	1.27	

Table 6. C5 results for experiments in Feliciano [22].

Exp.	Case	d (mm)	c_x (mm)	c_y (mm)	ρ (%)	f_{ck} (MPa)	F (kN)	M_x (kNm)	M_y (kNm)	F_{ef}^1 (kN)	A_{sw}^ϕ (cm ²)	n_p	n_r	s_0 (mm)	s_r (mm)	f_{yw} (MPa)	$f_{yw,ef}$ (MPa)	s_{avg} (mm)	s_{max} (mm)	Crit. per.	ψ	
L1	EDGE	152	300	300	0.75	45.10	293.0	-	-87.8	293.0	-	-	-	-	-	-	-	-	-	-	1	1.06
L2	EDGE	152	300	300	0.75	45.10	300.0	-	-	300.0	-	-	-	-	-	-	-	-	-	-	1	1.09
L3	EDGE	152	300	300	0.75	45.10	242.0	-	72.5	493.7	-	-	-	-	-	-	-	-	-	-	1	1.79
L4	EDGE	152	300	300	0.75	45.10	198.0	-	79.0	472.1	-	-	-	-	-	-	-	-	-	-	1	1.72

Table 7. C5 results for experiments in Barbosa [23].

Exp.	Case	<i>d</i>	<i>c_x</i>	<i>c_y</i>	ρ	<i>f_{ck}</i>	<i>F</i>	<i>M_x</i>	<i>M_y</i>	<i>F_{ef}¹</i>	<i>A_{sw}^φ</i>	<i>n_p</i>	<i>n_r</i>	<i>s₀</i>	<i>s_r</i>	<i>f_{ywk}</i>	<i>f_{ywk,ef}</i>	<i>s_{avg}</i>	<i>s_{max}</i>	Crit. per.	ψ	
		(mm)	(mm)	(mm)	(%)	(MPa)	(kN)	(kNm)	(kNm)	(kN)	(cm ²)			(mm)	(mm)	(MPa)	(MPa)	(mm)	(mm)			
L01	REENTRANT	144	300	300	1.4	57.90	300.0	111.4	-111.4	624.7	-	-	-	-	-	-	-	-	-	-	1	1.23
L02	REENTRANT	144	300	300	1.4	57.90	488.0	120.8	-120.8	840.2	0.5	3	10	70	100	587.0	364.0	231	288	<i>n</i>	1.25	
L03	REENTRANT	144	300	300	1.4	57.90	550.0	136.1	-136.1	946.9	0.78	4	10	70	100	562.0	364.0	282	288	<i>n</i>	1.22	
L04	REENTRANT	144	300	300	1.4	57.90	347.0	85.9	-85.9	597.4	-	-	-	-	-	-	-	-	-	-	1	1.18

Table 8. C5 results for experiments in Oliveira [24].

Exp.	Case	<i>d</i>	<i>c_x</i>	<i>c_y</i>	ρ	<i>f_{ck}</i>	<i>F</i>	<i>M_x</i>	<i>M_y</i>	<i>F_{ef}¹</i>	<i>A_{sw}^φ</i>	<i>n_p</i>	<i>n_r</i>	<i>s₀</i>	<i>s_r</i>	<i>f_{ywk}</i>	<i>f_{ywk,ef}</i>	<i>s_{avg}</i>	<i>s_{max}</i>	Crit. per.	ψ	
		(mm)	(mm)	(mm)	(%)	(MPa)	(kN)	(kNm)	(kNm)	(kN)	(cm ²)			(mm)	(mm)	(MPa)	(MPa)	(mm)	(mm)			
LN01	INTERNAL	143	400	200	1.58	55.10	1084.0	-	-	1084.0	0.5	3	14	70	100	573.0	363.0	201	286	<i>n</i>	1.17	
LN02	INTERNAL	143	400	200	1.58	53.80	1144.0	-	-	1144.0	0.5	6	14	70	100	573.0	363.0	334	286	1	1.08	
LN03	INTERNAL	143	400	200	1.58	51.20	786.0	-	-	786.0	-	-	-	-	-	-	-	-	-	-	1	1.18
LN04	INTERNAL	143	400	200	1.58	55.50	966.0	-	-	966.0	0.31	4	14	70	100	651.0	363.0	245	286	1	1.13	
LN05	INTERNAL	142	400	200	1.6	54.80	1143.0	-	-	1143.0	1.23	5	14	70	100	602.0	362.0	290	284	<i>n</i>	0.97	
LS01	INTERNAL	143	400	200	1.58	53.60	425.0	-	-114.0	673.9	-	-	-	-	-	-	-	-	-	-	1	0.99
LS02	INTERNAL	144	400	200	1.56	53.90	763.0	-	-218.0	1237.0	0.5	3	14	70	100	573.0	364.0	201	288	<i>n</i>	1.33	
LS03	INTERNAL	142	400	200	1.6	54.40	775.0	-	-234.0	1287.9	0.5	6	14	70	100	573.0	362.0	334	284	1	1.23	
LS04	INTERNAL	143	400	200	1.58	51.30	712.0	-	-183.0	1111.5	0.31	4	14	70	100	651.0	363.0	245	286	1	1.32	
LS05	INTERNAL	142	400	200	1.6	51.00	926.0	-	-272.0	1522.2	1.23	5	14	70	100	602.0	362.0	290	284	<i>n</i>	1.32	
LS06	INTERNAL	143	400	200	1.58	53.00	904.0	-	-252.0	1454.1	0.79	6	14	70	100	597.0	363.0	334	286	<i>n</i>	1.27	
LW01	INTERNAL	141	200	400	1.62	50.20	446.0	-	-124.0	648.0	-	-	-	-	-	-	-	-	-	-	1	0.99
LW02	INTERNAL	143	200	400	1.58	52.20	711.0	-	-189.0	1016.0	0.5	3	14	70	100	573.0	363.0	201	286	<i>n</i>	1.11	
LW03	INTERNAL	142	200	400	1.6	51.50	733.0	-	-195.0	1049.2	0.5	6	14	70	100	573.0	362.0	319	284	1	1.01	
LW04	INTERNAL	142	200	400	1.6	51.50	617.0	-	-131.0	829.4	0.31	4	14	70	100	651.0	362.0	245	284	1	0.99	
LW05	INTERNAL	142	200	400	1.6	50.60	815.0	-	-241.0	1205.8	1.23	5	14	70	100	602.0	362.0	290	284	<i>n</i>	1.05	

Table 9. C5 results for experiments in Trautwein et al. [25].

Exp.	Case	<i>d</i>	<i>c_x</i>	<i>c_y</i>	ρ	<i>f_{ck}</i>	<i>F</i>	<i>M_x</i>	<i>M_y</i>	<i>F_{ef}¹</i>	<i>A_{sw}^φ</i>	<i>n_p</i>	<i>n_r</i>	<i>s₀</i>	<i>s_r</i>	<i>f_{ywk}</i>	<i>f_{ywk,ef}</i>	<i>s_{avg}</i>	<i>s_{max}</i>	Crit. per.	ψ
		(mm)	(mm)	(mm)	(%)	(MPa)	(kN)	(kNm)	(kNm)	(kN)	(cm ²)			(mm)	(mm)	(MPa)	(MPa)	(mm)	(mm)		
L1	INTERNAL	159	200	200	1.2	36.80	1050.0	-	-	1050.0	1.25	11	16	35	60	500.0	375.0	300	318	0	1.10
L4	INTERNAL	164	200	200	1.2	43.40	1038.0	-	-	1038.0	2	11	16	35	60	500.0	379.0	300	328	0	0.92
L9	INTERNAL	154	200	200	1.3	39.40	933.0	-	-	933.0	0.8	11	16	35	60	500.0	371.0	300	308	0	0.95

Table 10. C5 results for experiments in Albuquerque et al. [26] and Albuquerque [27].

Exp.	Case	<i>d</i>	<i>c_x</i>	<i>c_y</i>	ρ	<i>f_{ck}</i>	<i>F</i>	<i>M_x</i>	<i>M_y</i>	<i>F_{ef}¹</i>	<i>A_{sw}^φ</i>	<i>n_p</i>	<i>n_r</i>	<i>s₀</i>	<i>s_r</i>	<i>f_{ywk}</i>	<i>f_{ywk,ef}</i>	<i>s_{avg}</i>	<i>s_{max}</i>	Crit. per.	ψ	
		(mm)	(mm)	(mm)	(%)	(MPa)	(kN)	(kNm)	(kNm)	(kN)	(cm ²)			(mm)	(mm)	(MPa)	(MPa)	(mm)	(mm)			
L01	REENTRANT	148	300	300	2.07	48.00	325.0	114.9	-114.9	655.5	-	-	-	-	-	-	-	-	-	-	1	1.17
L02	REENTRANT	148	300	300	2.07	48.00	513.0	127.7	-127.7	880.3	0.5	3	10	70	100	587.0	367.0	231	296	<i>n</i>	1.19	
L03	REENTRANT	145	300	300	2.17	48.00	575.0	141.9	-141.9	987.3	0.78	4	10	70	100	560.0	364.0	282	290	<i>n</i>	1.19	
L04	REENTRANT	147	300	300	2.1	48.00	372.0	91.8	-91.8	637.0	-	-	-	-	-	-	-	-	-	-	1	1.15
L05	REENTRANT	143	300	300	0.91	44.00	250.0	89.1	-89.1	510.7	-	-	-	-	-	-	-	-	-	-	1	1.29
L06	REENTRANT	145	300	300	0.88	44.00	282.0	68.4	-68.4	480.8	-	-	-	-	-	-	-	-	-	-	1	1.20
L07	REENTRANT	141	300	300	1.35	44.00	358.0	88.3	-88.3	618.3	-	-	-	-	-	-	-	-	-	-	1	1.40
L08	REENTRANT	146	300	300	1.27	44.00	345.0	84.7	-84.7	590.2	-	-	-	-	-	-	-	-	-	-	1	1.29
L09	REENTRANT	148	300	300	2.08	43.00	550.0	135.7	-135.7	940.4	0.78	5	13	60	90	528.0	367.0	250	296	<i>n</i>	1.07	
L10	REENTRANT	148	300	300	2.08	43.00	500.0	176.1	-176.1	1006.5	0.78	5	10	70	90	528.0	367.0	334	296	<i>n</i>	1.28	
L11	REENTRANT	147	300	300	2.11	43.00	640.0	120.8	-120.8	988.7	0.78	5	10	70	90	528.0	366.0	334	294	<i>n</i>	1.27	
L12	REENTRANT	145	300	300	1.28	43.00	345.0	65.4	-65.4	535.0	-	-	-	-	-	-	-	-	-	-	1	1.19

Table 11. C5 results for experiments in Albuquerque [28] and Albuquerque et al. [29].

Exp.	Case	d	c_x	c_y	ρ	f_{ck}	F	M_x	M_y	F_{ef}^1	A_{sw}^ϕ	n_p	n_r	s_0	s_r	f_{ywk}	$f_{ywk,ef}$	s_{avg}	s_{max}	Crit. per.	ψ
		(mm)	(mm)	(mm)	(%)	(MPa)	(kN)	(kNm)	(kNm)	(kN)	(cm ²)			(mm)	(mm)	(MPa)	(MPa)	(mm)	(mm)		
L1	EDGE	147	300	300	1	46.80	308.0	-	-92.0	308.0	-	-	-	-	-	-	-	-	-	1	1.06
L2	EDGE	146	300	300	1.25	44.70	315.0	-	-	315.0	-	-	-	-	-	-	-	-	-	1	1.03
L3	EDGE	146	300	300	1.25	45.10	256.0	-	77.0	527.2	-	-	-	-	-	-	-	-	-	1	1.72
L4	EDGE	146	300	300	1.25	46.00	210.0	-	84.0	505.8	-	-	-	-	-	-	-	-	-	1	1.64
L5	EDGE	146	300	300	1.25	51.40	374.0	-	37.0	504.3	-	-	-	-	-	-	-	-	-	1	1.58
L6	EDGE	146	300	300	1.25	52.10	330.0	-	66.0	562.4	-	-	-	-	-	-	-	-	-	1	1.75
L7	EDGE	146	300	300	1.52	50.00	288.0	-	115.0	693.0	-	-	-	-	-	-	-	-	-	1	2.05
L8	EDGE	146	300	300	1.4	50.50	320.0	-	128.0	770.8	-	-	-	-	-	-	-	-	-	1	2.34
L9	EDGE	146	300	300	1.25	57.60	489.0	-	-	489.0	0.5	4	7	70	100	580.0	365.0	287	292	n	0.96
L10	EDGE	146	300	300	1.52	59.30	445.0	-	89.0	758.4	0.5	4	7	70	100	580.0	365.0	287	292	n	1.39
L11	EDGE	146	300	300	1.52	43.10	304.0	-	110.0	691.4	-	-	-	-	-	-	-	-	-	1	2.15
L12	EDGE	146	300	300	1.52	43.60	347.0	-	55.0	540.7	-	-	-	-	-	-	-	-	-	1	1.68
L13	EDGE	146	300	300	1.52	44.10	357.0	-	125.0	797.2	-	-	-	-	-	-	-	-	-	1	2.46

Tables 3 to 11 present the results of all the experiments retrieved from the literature for the C5 combination. The sides of the columns are c_x and c_y , respectively, in the x – and y –directions. Characteristic strength f_{ck} is substituted in the code equations by the as-tested compressive strength of concrete. Transverse reinforcement is arranged in n_p contours and n_r rails. A_{sw}^ϕ is one bar area. The distance from the first reinforcement contour to the column and the distance between the reinforcement contours are denoted as s_0 and s_r , respectively.

The slab capacity is verified at Perimeters 0, 1, and n . The critical control perimeters are shown in Tables 3 to 11. The prediction ratio ψ is the ratio between the experimental and estimated capacities, considering $\gamma_f = \gamma_c = \gamma_s = 1$.

A brittle failure of a slab-column connection can cause the progressive collapse of the structure. Table 2 shows the percentages of experiments with $\psi \geq 0.95$ in each combination, which indicates the reliability of the combination. Table 2 also presents the mean and the minimum ψ ratios of each combination, which are denoted as ψ_{mean} and ψ_{min} , respectively.

C1, C2, and C3 correspond to MC90, EC2, and NBR6118, respectively. Among them, C2 (EC2) gives the highest number of predictions with $\psi \geq 0.95$ (94%). C2 yields inadequate predictions in some cases. The minimum C2 prediction ratio ($\psi_{min} = 0.18$) is associated with the corner column connection C_C_4 in Stamenkovic and Chapman [18], which is subjected to unbalanced moment. The normal force is relatively small.

Combination C4 corresponds to EC2 with the moment approach proposed by NBR6118 for edge and corner columns (criteria e). Combinations C5 to C10 discuss the effect of replacing other criteria in C4.

Combinations C4, C5, and C8 yield $\psi \geq 0.95$ for 99% of the dataset. The average and minimum prediction ratios are $\psi_{mean} = 1.42$ and $\psi_{min} = 0.92$, respectively. The minimum prediction ratio is associated with the specimen L4 in Trautwein et al. [25], which fails at Perimeter 0 by diagonal compression in concrete. The moment criterion proposed by NBR6118 yields good capacity predictions for edge and corner column connections with internal eccentricities.

Combinations C4 and C5 show that the criteria proposed by NBR6118 and EC2 for effective yield stress $f_{ywd,ef}$ provide similar results.

Combination C8 investigates the criterion f from NBR 6118, by which the effective length of Perimeter 0 is not reduced in edge and corner columns. New studies are needed as the current dataset does not contain failures due to diagonal compressive stresses in edge and corner column connections.

Combinations C6, C7, and C10 show that criteria a (ξ), b (ρ), d (kd), and h (α_θ) from NBR6118 do not contribute to C5 predictions.

Combinations C5 and C9 apply the effective forces F_{ef}^1 and F_{ef}^n at Perimeter n , as recommended by EC2 and MC90, respectively. They both yield similar predictions, but this conclusion is limited to the uniformly distributed reinforcement arrangements of the dataset. Non-uniform reinforcement distributions can change the effective F_{ef}^n forces. Cross arrangements of shear reinforcement demand further investigation.

The dataset contains 16 reentrant corner columns, five corner columns, and 18 edge columns yielding asymmetrical plastic shear diagrams. Row “C5-Asym.” of Table 2 discusses the results of combination C5 for the asymmetrical subset. Relations $\psi_{mean} = 1.66$ and $\psi_{min} = 1.06$ are considered adequate and compatible with the results of the complete set.

7 CONCLUSIONS

A numerical procedure yields plastic diagrams of shear forces in arbitrary control perimeters subjected to asymmetrical bending. Examples of internal, reentrant corner, edge, and corner columns are subjected to unbalanced moments about an axis oblique to the principal axes. The proposed procedure is fast, robust, and accurate.

Experimental results in the literature are compared to the MC90, EC2, and NBR6118 design methods, which are applied together with the proposed procedure.

Although the recommendations in EC2 and NBR6118 are based on MC90, they contain some differences, which are discussed as they significantly affect the results.

EC2 performed better than the other two codes. A similar conclusion is reported by Ferreira et al. [21] when comparing ACI, EC2 and Model Code 2010 [7]. However, some results of EC2 were not considered satisfactory, because this code disregards the moments of corner and edge columns with internal eccentricities.

NBR6118 considers the portions of the unbalanced moments that exceed the moments that can be resisted by the eccentricities between columns and reduced control perimeters of corner and edge columns. The best performance is obtained by combining EC2 with the NBR6118 moment criterion. Ninety-nine percent of the dataset yields prediction to experimental results ratios greater than 0.95. All prediction to experimental rates are greater than 0.92.

The prediction to experimental ratios of cases with symmetrical and asymmetrical plastic diagrams are compatible.

Asymmetrical shear diagrams are found not only in edge and corner column connections but also in internal column connections. The proposed procedure considers the asymmetrical plastic diagrams that usually occur in all column connections due to biaxial bending.

Connections of edge and corner columns, critical at Perimeter 0, and plastic shear diagrams, discontinuous due to cross-arranged reinforcement, are themes for future studies.

REFERENCES

- [1] Comité Européen de Normalisation, *Eurocode 2 - Design of concrete structures – Part 1-1: General rules and rules for Buildings*, Stockholm, Sweden: Comité Européen de Normalisation, 2004.
- [2] Associação Brasileira de Normas Técnicas, *Design of Concrete Structures – Procedures, NBR 6118*, 2014.
- [3] Comité Euro-International du Béton, *Model Code 1990 for structures*. London, England: Comité Euro-International du Béton, 1993.
- [4] P. E. Regan, *Behavior of Reinforced Concrete Flat Slabs. Report 89*. London, England: CIRIA, 1981.
- [5] P. E. Regan and M. W. Braestrup, *Punching Shear in Reinforced Concrete* (Bulletin d'Information, 168). London, England: Comité Euro-International du Béton, Jan., 1985.
- [6] American Concrete Institute, *Building Code Requirements for Structural Concrete and Commentary*, ACI 318R-19, 2019.
- [7] Fédération Internationale du Béton, *fib Model Code for Concrete Structures, Model Code 2010*. Lausanne, Switzerland: Fédération Internationale du Béton, 2012.
- [8] J. di Stasio and M. P. van Buren, "Transfer of bending moment between flat plate floor and column," *ACI J. Proc.*, vol. 57, pp. 299–314, Jan 1960, <http://dx.doi.org/10.14359/8022>.
- [9] A. Muttoni, "Punching shear strength of reinforced concrete slabs without transverse reinforcement," *ACI Struct. J.*, vol. 105, no. 4, pp. 440–450, Jul 2008, <http://dx.doi.org/10.14359/19858>.
- [10] M. F. Ruiz and A. Muttoni, "Applications of critical shear crack theory to punching of reinforced concrete slabs with transverse reinforcement," *ACI Struct. J.*, vol. 106, no. 4, pp. 485–494, Jul. 2009, <http://dx.doi.org/10.14359/56614>.
- [11] Fédération Internationale du Béton, *Textbook on Behaviour, Design and Performance, vol. 2: Basis of Design* (Bulletin d'Information, 2). Lausanne, Switzerland: Fédération Internationale du Béton, 1999.
- [12] N. W. Hanson and J. N. Hanson, "Shear and moment transfer between concrete slabs and columns", *J. of the PCA Rsrch. and Devel. Lab.*, vol. 10, no. 1, pp. 2–16, Jan. 1968.
- [13] P. E. Mast, "Stresses in flat plates near columns," *ACI J. Proc.*, vol. 67, no. 10, pp. 761–768, Oct. 1970, <http://dx.doi.org/10.14359/7306>.
- [14] K. Girkmann, *Flaechentragwerke : Einführung in Die Elastostatik der Scheiben, Platten, Schalen und Falwerke*, 5th ed. Wien, Austria, Springer-Verlag, 1959.
- [15] J. Shu, B. Belletti, A. Muttoni, M. Scolari, and M. Plos, "Internal force distribution in RC slabs subjected to punching shear," *Eng. Struct.*, vol. 153, pp. 766–781, Dec 2017, <http://dx.doi.org/10.1016/j.engstruct.2017.10.005>.
- [16] M. Laguta, "Effect of unbalanced moment on punching shear strength of slab- column joints", M.S. thesis, Civil and Env. Eng., Univ. Waterloo, Ontario, 2020. [Online]. Available: <https://uwspace.uwaterloo.ca/handle/10012/15931?show=full>
- [17] A. Stamenkovic, "Local strength of flat slabs at column heads", Ph.D. thesis, Imperial Coll. of Sci. and Tec., Univ. of London, London, 1969. [Online]. Available: <https://spiral.imperial.ac.uk/bitstream/10044/1/16718/2/Stamenkovic-A-1970-PhD-Thesis.pdf>

- [18] A. Stamenkovic and J. C. Chapman, "Local strength at column heads in flat slabs subjected to a combined vertical and horizontal loading," *Proc. Inst. Civ. Eng.*, vol. 57, pp. 205–232, Jun. 1974, <http://dx.doi.org/10.1680/iicep.1974.4054>.
- [19] M. P. Ferreira, "Punção em lajes lisas de concreto armado com armaduras de cisalhamento e momentos desbalanceados", Ph.D. dissertation, Fac. Tecnol., Univ. Brasília, Brasília, 2010. [Online]. Available: <https://repositorio.unb.br/handle/10482/8965>
- [20] M. P. Ferreira, G. S. S. A. Melo, P. E. Regan, and R. L. Vollum, "Punching of reinforced concrete flat slabs with double-headed shear reinforcement," *ACI Struct. J.*, vol. 111, no. 2, pp. 363–374, Jan. 2014, <http://dx.doi.org/10.14359/51686535>.
- [21] M. P. Ferreira, M. H. Oliveira, and G. S. S. A. Melo, "Tests on the punching resistance of flat slabs with unbalanced moments," *Eng. Struct.*, vol. 196, no. July, 2019, <http://dx.doi.org/10.1016/j.engstruct.2019.109311>.
- [22] F. M. H. Feliciano, "Punção em lajes lisas de concreto armado com pilares de borda e excentricidade externa", M.S. thesis, Fac. Tecnol., Univ. Brasília, Brasília, 2011. [Online]. Available: <https://repositorio.unb.br/handle/10482/9354>
- [23] W. C. S. Barbosa, "Punção em lajes lisas de concreto armado com pilares de canto reentrante", M.S. thesis, Fac. Tecnol., Univ. Brasília, Brasília, 2012. [Online]. Available: <https://repositorio.unb.br/handle/10482/10968>
- [24] M. H. Oliveira, "Punção em lajes lisas com armadura de cisalhamento submetidas a carregamento excêntrico e apoiadas sobre pilares retangulares", Ph.D. dissertation, Fac. Tecnol., Univ. Brasília, Brasília, 2013. [Online]. Available: <https://repositorio.unb.br/handle/10482/13624>.
- [25] L. M. Trautwein, R. B. Gomes and G. S. S. A. Melo, "Puncionamento em lajes planas de concreto armado com armadura de cisalhamento interna", vol. 7, no. 1, pp. 38-49, Nov., 2013, <http://dx.doi.org/10.5216/reec.v7i1.24333>.
- [26] E. J. P. Albuquerque, G. S. S. A. Melo, A. M. P. Ramos and V. J. G. Lúcio, "Estudo teórico-experimental da resistência ao punçoamento de lajes fungiformes de betão armado com pilar de canto reentrante sem armadura de punçoamento", In 5ª JPEE, Lisboa, Portugal, 2014. <http://dx.doi.org/10.13140/2.1.1473.1849>.
- [27] E. J. P. Albuquerque, "Punção em lajes lisas com armadura de cisalhamento e pilar de canto reentrante", Ph.D. dissertation, Fac. Tecnol., Univ. Brasília, Brasília, 2015. [Online]. Available: <https://repositorio.unb.br/handle/10482/18905>
- [28] N. G. B. Albuquerque, "Comportamento das ligações de lajes lisas de concreto armado com pilares de borda sujeitas a excentricidades interna e externas", Ph.D. dissertation, Fac. Tecnol., Univ. Brasília, Brasília, 2014. [Online]. Available: <https://repositorio.unb.br/handle/10482/17442>
- [29] N. G. B. Albuquerque, G. S. S. A. Melo, and R. L. Vollum, "Punching shear strength of flat slab-edge column connections with outward eccentricity of loading," *ACI Struct. J.*, vol. 113, no. 5, pp. 1117–1129, Sep. 2016, <http://dx.doi.org/10.14359/51689156>.

Author contributions: MNS: literature review, numerical tests, validation, writing, proofreading; MSPLP: conceptualization, literature review, methodology, writing, proofreading, supervision; MS: conceptualization, literature review, methodology, formal analysis, computer programming, validation, writing, proofreading, supervision.

Editors: Leandro Trautwein, Mauro Real, Mario Pimentel.



ORIGINAL ARTICLE

Recommendations to assess the shear and punching capacity of one-way slabs under concentrated loads according to the ABNT NBR 6118:2014

Recomendações para avaliação da resistência à força cortante e punção de lajes unidirecionais sob cargas concentradas de acordo com a ABNT NBR 6118:2014

Alex Micael Dantas de Sousa^a

Eva Olivia Leontien Lantsoght^{b,c}

Daniel de Lima Araújo^d

Lisiane Pereira Prado^e

Mounir Khalil El Debs^a

^aUniversidade de São Paulo – USP, Escola de Engenharia de São Carlos – EESC, São Carlos, SP, Brasil

^bUniversidad San Francisco de Quito – UFSQ, Quito, Ecuador

^cDelft University of Technology – TU Delft, Delft, The Netherlands

^dUniversidade Federal de Goiás – UFG, Goiânia, Brasil

^eUniversidade Estadual Paulista “Júlio de Mesquita Filho” – UNESP, Guaratinguetá, Brasil

Received 14 September 2022

Accepted 27 February 2023

Abstract: This study describes a set of recommendations to improve the precision of shear and punching shear capacity predictions for one-way slabs under concentrated loads, regardless of the governing failure mechanism, using the ABNT NBR 6118:2014 code provisions. For this purpose, a database of 143 test results was developed, including one-way slabs with different support conditions and loading layouts and that failed by different shear failure mechanisms: one-way shear, punching shear or a mixed mode. The key parameters influencing the load capacity and failure mechanism of these slabs were considered for the proposed recommendations: load position and slab width. Adjustments to the effective shear width definition and shear resisting control perimeter were described. Arching action for loads close to the support was also considered in both one-way shear and punching shear predictions. Considering the whole database and without separation by the failure mechanism, the ratio between tested and predicted resistances with the one-way shear expressions shows an average value of 1.22 and a coefficient of variation of 18.3%. The respective ratio between tested and predicted resistances with the punching shear expressions reached an average ratio of 1.23 with a coefficient of variation of 21.3%. Therefore, the proposed recommendations allow for reaching enhanced levels of precision in assessing the shear and punching shear capacity of one-way slabs under concentrated loads, regardless of the governing failure mechanism of the slabs.

Keywords: one-way shear, punching shear capacity, one-way slabs, concentrated loads.

Resumo: Este estudo descreve um conjunto de recomendações para melhorar a precisão nas previsões de resistência ao cisalhamento e à punção de lajes unidirecionais sob cargas concentradas, independentemente do mecanismo governante na ruptura, utilizando as disposições da norma ABNT NBR 6118:2014. Para isso, foi organizado um banco de dados com 143 resultados de ensaios, incluindo lajes unidirecionais com diferentes condições de apoio e configurações de carregamento e que apresentaram diferentes mecanismos de ruptura por cisalhamento. Os principais parâmetros que influenciam a capacidade de carga e o mecanismo de ruptura dessas lajes foram considerados nas recomendações propostas. Ajustes para a definição da largura

Corresponding author: Alex Micael Dantas de Sousa. E-mail: alex_dantas@usp.br

Financial support: The authors acknowledge the financial support provided by the São Paulo Research Foundation (FAPESP) (grant number #2018/21573-2, grant number #2019/20092-3 and grant number #2021/13916-0) and by Brazilian National Council for Scientific and Technological Development (CNPq) (grant number #303438/2016-9). This study was also partially financed by the Coordenação de Aperfeiçoamento de Pessoal de Nível Superior – Brasil (CAPES) – Finance Code 001.

Conflict of interest: Nothing to declare.

Data Availability: the main database used in the investigations is available through the open-access repository Zenodo at: <https://zenodo.org/record/5911469> (accessed on 24/11/2022). Other supplementary data that support the findings of this study are available from the corresponding author, [AMDS], upon reasonable request.



This is an Open Access article distributed under the terms of the Creative Commons Attribution License, which permits unrestricted use, distribution, and reproduction in any medium, provided the original work is properly cited.

efetiva de cisalhamento e perímetro de controle resistente ao cisalhamento foram descritos. A ação de arqueamento para cargas próximas ao apoio também foi considerada nas previsões de resistência ao cisalhamento unidirecional e ao puncionamento. Considerando todo o banco de dados, a razão entre as resistências testadas e previstas com as expressões de cisalhamento unidirecional apresenta um valor médio de 1.22 e um coeficiente de variação de 18.3%. A respectiva relação entre as resistências testadas e previstas com as expressões de puncionamento atingiu uma relação média de 1.23 com um coeficiente de variação de 21.3%. Portanto, as recomendações propostas permitem alcançar maiores níveis de precisão na previsão da resistência ao cisalhamento e ao puncionamento de lajes unidirecionais sob cargas concentradas, independentemente do mecanismo de ruptura governante das lajes.

Palavras-chave: cisalhamento unidirecional, resistência à punção, lajes unidirecionais, cargas concentradas.

How to cite: A. M. D. Sousa, E. O. L. Lantsoght, D. L. Araújo, L. P. Prado, and M. K. E. Debs, "Recommendations to assess the shear and punching capacity of one-way slabs under concentrated loads according to the ABNT NBR 6118:2014," *Rev. IBRACON Estrut. Mater.*, vol. 16, no. 3, e16308, 2023, <https://doi.org/10.1590/S1983-41952023000300008>

1 INTRODUCTION

In the last decades, many bridges built between 1960 and 1970 are reaching the end of their designed service life [1]. To extend the service life of these structures, it is necessary to attest that these bridges meet the requirements of the current design codes, considering that sometimes traffic loads and intensities have increased and the resistance models have become more conservative for certain applications. In this context, many bridge deck slabs (Figure 1a – Brazilian design truck) were rated as critical in shear assessments, despite these structures not showing any signs of distress upon inspection. Consequently, it was concluded that some widespread evaluation approaches could be overly conservative, which motivated the testing of one-way reduced-scale slabs under concentrated loads (Figure 1b) in laboratories from several countries, mainly in Europe [2]–[7].

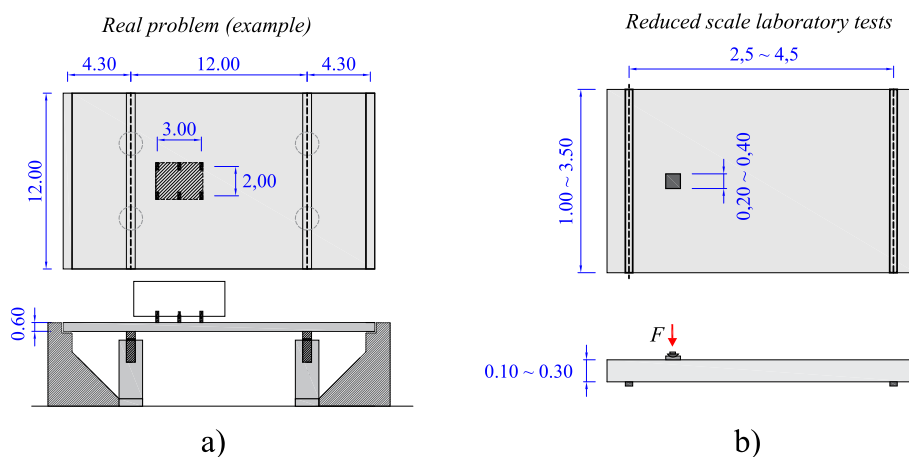


Figure 1 – a) Example of one-way slabs loaded by the design truck prescribed in Brazilian code ABN NBR 7188:2013 [8]; b) example of reduced-scale laboratory test of a one-way slab under a single concentrated load. Dimensions in m.

One-way slabs under concentrated loads may present a more complex failure mechanism compared to beams loaded over the entire width (Figure 2a) or with slab-column connections under concentric loads (Figure 2b). In fact, these members may fail either by one-way shear as wide beams or by punching shear around the load, depending on the load position, slab width b_{slab} , and other parameters. In addition, two-way flexure influences the outcomes. Nevertheless, until now, most publications addressed only how to check the one-way shear capacity of such slabs [4], [6], [7], [9], sometimes neglecting that the evaluated slabs failed by punching. Additionally, most analytical approaches to evaluate the one-way shear capacity or punching capacity of these slabs with design code expressions show a large scatter between tested and predicted resistances [3], [10]. In practice, most available approaches to evaluate the one-way shear capacity of these slabs overestimate the contributing slab strip to the shear capacity (frequently named the effective shear width b_{eff}) when the distance from the load to the support increases [3], [9]. Besides that, no design codes address how the slab width could influence the effective contribution of some sides of the control perimeter to the punching capacity. At this point, the reader shall realize that the free edges decrease the shear flow that goes through the sides of the control perimeter in the transverse direction, depending on the slab width [11] (see Figure 2c).

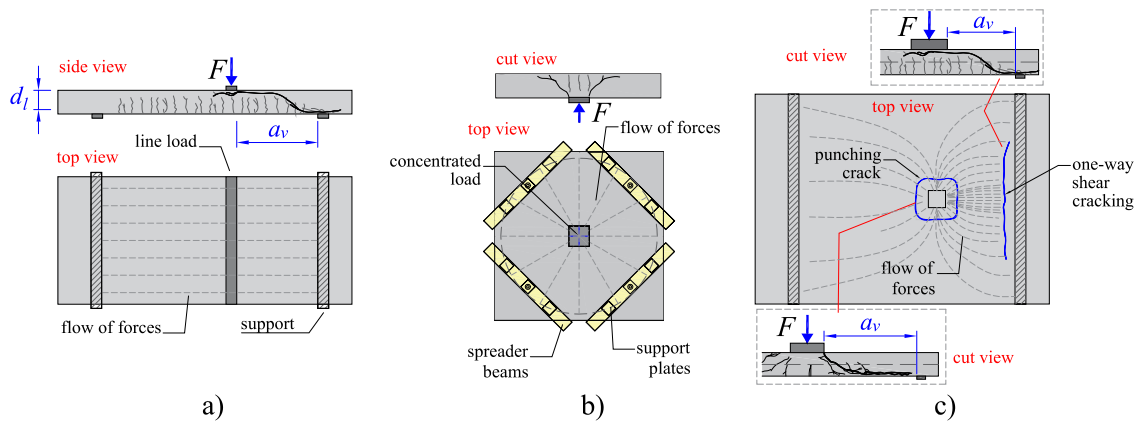


Figure 2 - One-way slabs loaded over the entire width failing in one-way shear; b) slab-column connections failing in punching; and c) one-way slabs under concentrated loads subjected to both one-way shear and punching shear failures (adapted from [12]).
 Note: a_v is the clear distance between the faces of support and load and d_t is effective depth to longitudinal reinforcement.

In 2019, the preliminary investigation of one-way slabs under concentrated loads with the Brazilian code expressions for shear and punching shear was performed using the most traditional rules to define the effective shear width b_{eff} and the shear resisting control perimeter for punching [3]. At that time, some shortcomings were highlighted: (i) it was concluded that the one-way shear predictions tend to become unsafe when the slabs fail by punching, (ii) additionally, the predictions of punching capacity also became unsafe when the tests failed in one-way shear as wide beams. Since the most critical failure mechanism of the slabs is not known in most cases and depends on a large number of parameters, it would be important to assure conservative predictions regardless of the most critical failure mechanism of the slabs being the one-way shear or punching shear. Until now, no specific recommendation has been published addressing this issue regarding the ABNT NBR 6118:2014 code expressions.

In this study, we propose to describe a set of enhanced recommendations to assess the shear and punching capacity of one-way slabs under concentrated loads using the current ABNT NBR 6118:2014 [13] expressions for one-way shear and two-way shear (punching). Since these slabs may fail either by one-way shear or two-way shear, the idea of this work is to improve the level of accuracy of both one-way shear and punching resistance approaches in such a way as to provide the most accurate predictions of failure load, regardless of the most critical failure mechanism.

Section 2 discusses the traditional approaches to define the effective shear width and shear resisting control perimeter for punching capacity evaluations. In Section 3, the one-way shear and punching shear expressions of the ABNT NBR 6118:2014 [13] are presented. At this point, the Section 2 and Section 3 combination represents the approach to be used in the evaluations, which can be compared with the proposed approach. Next, Section 4 brings the recommendations developed to improve the predictions of shear and punching capacity with the Brazilian code expressions, regardless of the governing failure mechanism of the slabs being one-way shear or punching. In Section 5, the database of one-way slabs under concentrated loads used to validate the proposed recommendations is discussed (143 test results). In the end, a comparison between tested and predicted resistances using one-way shear and punching shear expressions is described (Section 6), comparing the predictions with and without the proposed recommendations.

2 BACKGROUND

2.1 One-way shear

The traditional approach to evaluate the one-way shear capacity of one-way slabs under concentrated loads is based on the definition of a slab strip that it is supposed to contribute effectively to the one-way shear capacity, called effective shear width b_{eff} . Theoretically, this effective shear width can be defined based on the distribution of shear demand v_E (shear force per unit length) from linear elastic finite element analyses, for instance (Figure 3a). In this way, the effective shear width would be defined as the length that multiplied by the peak shear demand equals the total shear force V_E . However, analytically, the most traditional approaches to defining the effective shear width are based on the assumption of a horizontal load spreading from the loading plate to the supports under a fixed angle, typically 45 degrees (Figure 3b-3c).

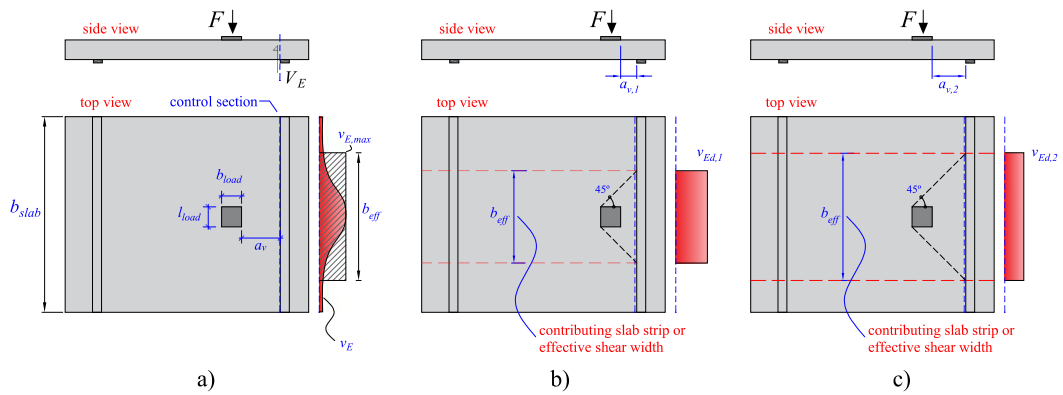


Figure 3 – a) Definition of the effective shear width based on the distribution of the unitary shear demand v_E ; b) and c) effective shear width according to the French guidelines varying the clear shear span a_v .

The effective shear width calculated as in Figure 3b is commonly named the French effective shear width, as it was first identified on the French guidelines of design [14], [15]. This approach has already been demonstrated to provide good predictions of shear capacity, mainly for loads close to the support $a_v < 2d_t$ [2], [3]. However, Figure 3c shows that this approach assumes that the effective shear width increases by increasing the clear shear span a_v (herein, a_v is the clear distance between load and support). Because of this, some studies have already identified that this approach leads to an overestimation of the one-way shear capacity for tests that failed in punching [16].

2.2 Punching shear

In evaluating the punching capacity of one-way slabs under concentrated loads with the Brazilian code expressions, a well-consolidated approach compares different layouts of the control perimeter to define the most critical mechanism (Figure 4). The shear resisting control perimeter (blue lines) is considered at the distance of $2d_{avg}$ of the loaded area ($k = 2$ in Figure 4).

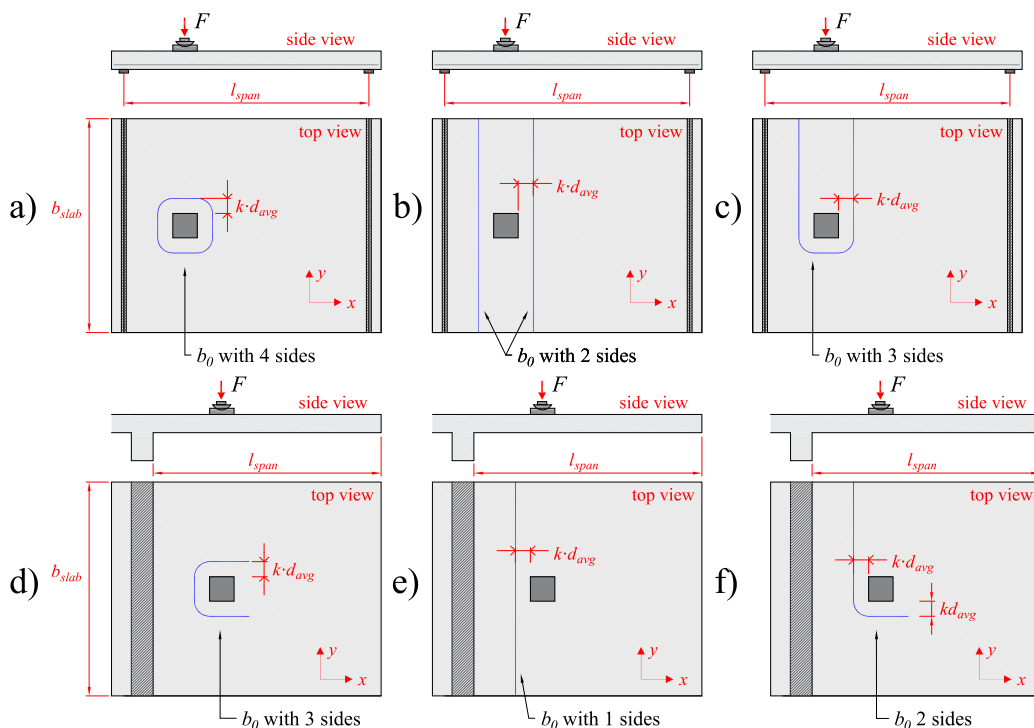


Figure 4 – Possible definition of the shear resisting control perimeter for simply supported (a, b and c) and cantilever slabs (d, e and f) (adapted from [12]). Note: in the Brazilian code [13], $k = 2$; d_{avg} is the average effective depth of the tensiled reinforcement; b_{slab} is the slab width.

In practice, the reader may realize that the most critical shear resisting control perimeter will be a function of parameters such as the slab width and load position. For instance, the control perimeter b_0 with two sides tends to govern over the perimeter with four sides for slabs with a reduced slab width (Comparing Figure 4a and Figure 4b). In the same way, the control perimeter with three sides governs when the concentrated loads are placed close to the free edges of simply supported slabs (layout of Figure 4c).

In the Brazilian code ABNT NBR 6118:2014 [13], the shear stress concentration in the case of loads close to the free edge of simply supported slabs (Figure 5a-5b) and cantilever slabs (Figure 5c-5d) is considered through the definition of a reduced control perimeter (dashed red lines) that is a function of the slab effective depth d_{avg} and size of the concentrated load). In Figure 5b-5d, note that the lengths b_{load} and l_{load} refer to the size of the concentrated loads in the spanning and transverse directions, respectively. B_1 and B_2 refer to the size of the control perimeter considered in the transverse and spanning directions (x and y) to consider the shear stress concentration at the load corners depending on the loaded area geometry.

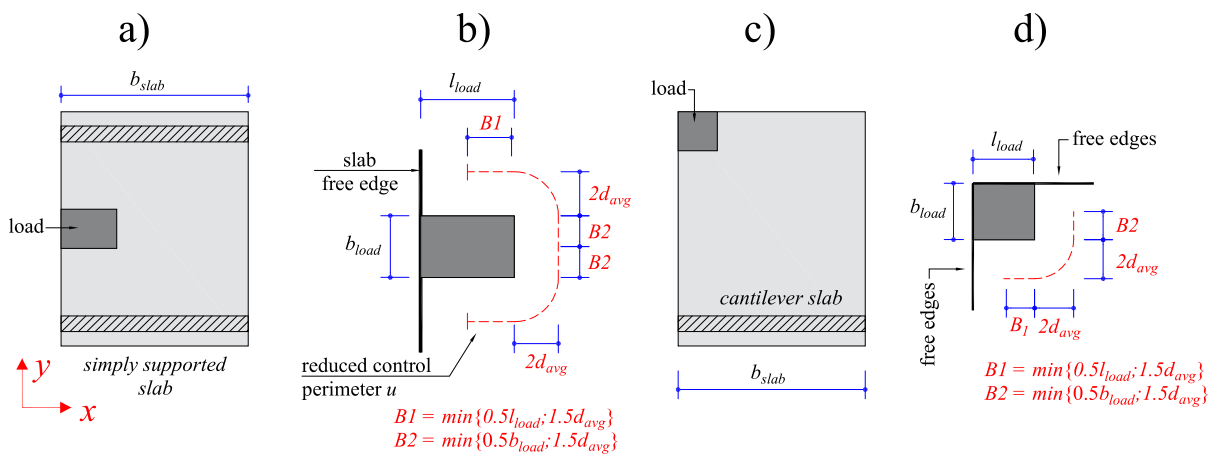


Figure 5 - Definition of the reduced control perimeter for a) and b) concentrated loads close to free edges of simply supported slabs; and for c) and d) corner of cantilever slabs according to the ABNT NBR 6118:2014. Note: l_{load} and b_{load} refer to the size of the concentrated loads; B_1 and B_2 refer to the lengths of the control perimeter.

No clear mention about the influence of the rectangular index of the load α in the definition of the control perimeter is provided in the current Brazilian code, with α given by Equation 1:

$$\alpha = \max\{l_{load}; b_{load}\} / \min\{l_{load}; b_{load}\} \tag{1}$$

In practice, when the rectangular index α increases and the load becomes more elongated in the span direction, the shear stresses concentrate in the corners (Figure 6a.1). However, when the elongated side is running parallel to the line support (Figure 6a.2), the shear flows in the elongated side is predominant, and hence, a lower reduction in the resisting control perimeter occurs [17]. Since the effect of the rectangular index is similar to that of edge and corner columns [17] for flat slabs, it is assumed that the sketch of Figure 6 should be used in the case of rectangular loads evaluated in this study. In the same context, cantilever slabs under concentrated loads should be evaluated as slab-edge column connections in the definition of the reduced control perimeter (Figure 6b).

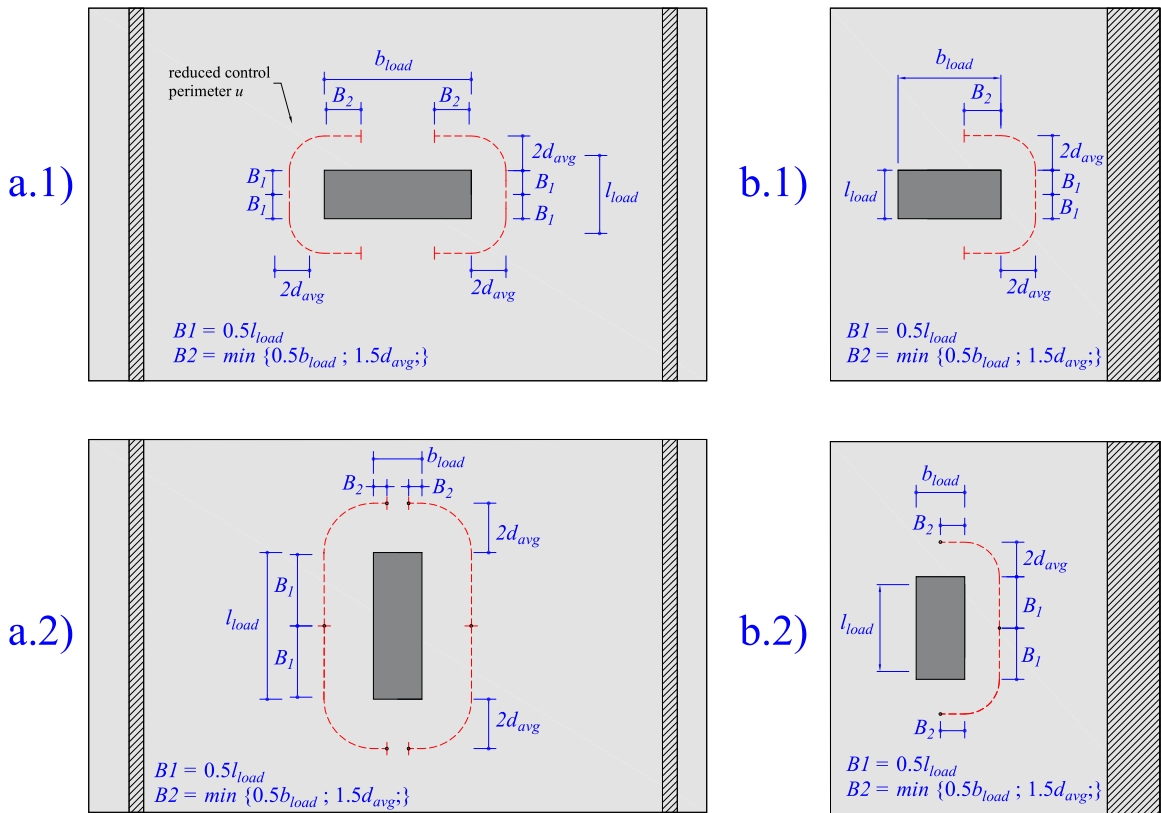


Figure 6 - Definition of the reduced control perimeter for simply supported and cantilever slabs under concentrated loads according to the Brazilian code ABNT NBR 6118:2014 [13].

3 EXPRESSIONS TO EVALUATE THE ONE-WAY SHEAR AND PUNCHING CAPACITY ACCORDING TO THE ABNT NBR 6118:2014

The one-way shear capacity V_R of slabs is predicted by multiplying the nominal shear capacity (shear force per unit length $v_{R,shear}$) of these slabs by an effective shear width b_{eff} (Equation 2):

$$V_R = v_{R,shear} \cdot b_{eff} \quad (2)$$

The punching capacity P_R , in the same way, is calculated by multiplying the nominal punching capacity (shear capacity per unit length $v_{R,punch}$) by the shear resisting control perimeter b_0 (Equation 3):

$$P_R = v_{R,punch} \cdot b_0 \quad (3)$$

3.1 One-way shear capacity according to the ABNT NBR 6118:2014

According to the ABNT NBR 6118:2014 [13], the nominal one-way shear capacity of reinforced concrete members without stirrups is calculated as follows (Section 19.4, SI units, Equation 4):

$$v_{R,shear} = \left[\tau_{Rd} \cdot k_{shear} \cdot (1.2 + 40 \cdot \rho_1) + 0.15 \cdot \sigma_{cp} \right] \cdot d_l \quad (4)$$

with τ_{Rd} and σ_{cp} in [MPa]

$$\tau_{Rd} = 0.25 \cdot f_{ctd} \tag{5}$$

$$f_{ctd} = f_{ctk,inf} / \gamma_c \tag{6}$$

$$f_{ctk,inf} = 0.7 f_{ctm} \tag{7}$$

$$f_{ctm} = \begin{cases} 0.3 f_{ck}^{2/3} & \text{for } f_{ck} \leq 50 \text{ MPa} \\ 2.12 \ln(1 + 0.11 f_{ck}) & \text{for } 50 \text{ MPa} < f_{ck} \leq 90 \text{ MPa} \end{cases} \tag{8}$$

$$\rho_l = \frac{A_s}{b_w \cdot d_l} \leq 0.02 \tag{9}$$

$$k_{shear} = \begin{cases} 1, & \text{if at least } 0.50A_s \text{ does not reach the support} \\ |1.6 - d_l|, & \text{with } d_l \text{ in [m], for the other cases} \end{cases} \tag{10}$$

τ_{Rd} is the design shear capacity of the concrete (in MPa, Equation 5); k_{shear} is the size effect factor for one-way shear in the Brazilian code (see Equation 10); ρ_l is the reinforcement ratio in the longitudinal direction (Equation 9); σ_{cp} is the external axial stress in the section (tensile stress are considered with a negative signal); d_l is the effective depth towards the longitudinal reinforcement; f_{ctd} is the design value of the tensile strength of concrete (Equation 6); $f_{ctk,inf}$ is the lower bound value of the characteristic tensile strength of concrete (Equation 7); γ_c is the concrete safety factor (assumed equal to 1 in the comparisons between tested and predicted resistances from this paper and 1.4 in design calculations from professional practice); f_{ctm} is the mean value of tensile strength of concrete (Equation 8); f_{ck} is the characteristic value of compressive strength of concrete (in the comparisons between tested and predicted resistances, f_{ck} was replaced by f_{cm}); b_w is the considered length in the evaluation of A_s and; A_s is the are of longitudinal reinforcement distributed along b_w .

The ABNT NBR 6118:2014, as well as most design codes, does not guide how to define the effective shear width of slabs under concentrated loads. In the ABNT NBR 6118:1980 [18] (replaced version), the following expression was provided (Equations 11 and 12):

$$b_{NBR} = l_{load} + h_{slab} \tag{11}$$

$$\text{if } b_{NBR} > l_{span} : b_{eff,NBR} = b_{NBR}$$

$$\text{if } b_{NBR} \leq l_{span}, b_{eff,NBR} = \begin{cases} b_{NBR} + 0.5 \cdot a \cdot \left(1 - \frac{b_{NBR}}{l_{span}}\right), & \text{if cantilever slab} \\ b_{NBR} + a \cdot \left(1 - \frac{b_{NBR}}{l_{span}}\right), & \text{for simply sup. and continuous slabs} \end{cases} \tag{12}$$

Herein, h_{slab} is the slab thickness; l_{load} is the side of the load in the width direction of one-way slabs; b_{load} is the side of the load in the spanning direction of one-way slabs; l_{span} is the span length, a is the shear span between axes of support and load; and a_v is the clear distance between the support and the load.

In most publications [3], [10], however, the commonly named French effective shear width model is employed (Equation 13, see Figure 3b-3c):

$$b_{eff, french} = l_{load} + 2 \cdot (a_v + b_{load}) \leq b_{slab} \tag{13}$$

This occurs since it leads to reasonable levels of accuracy for the tests that fail as wide beams in one-way (WB) shear [16] or for loads close to the support [2] compared to other approaches. Figure 7 compares the effective shear widths $b_{eff,NBR}$ and $b_{eff,french}$ for a simply supported slab ($b_{load} = l_{load} = 0.40$ m; $b_{slab} = 3.0$ m and $h_{slab} = 0.30$ m). As can be seen, the predicted effective shear width with the replaced Brazilian code is significantly lower than that predicted with the French effective shear width.

In this study, it was verified that the predictions with the French effective shear width model would provide the best results between the two approaches, mainly for the tests with $a_v/d_l \leq 2$. Based on that, the one-way shear capacity with the reference approach was assumed as Equation 14:

$$V_{R,reference} = v_{R,shear} \cdot b_{eff, french} \tag{14}$$

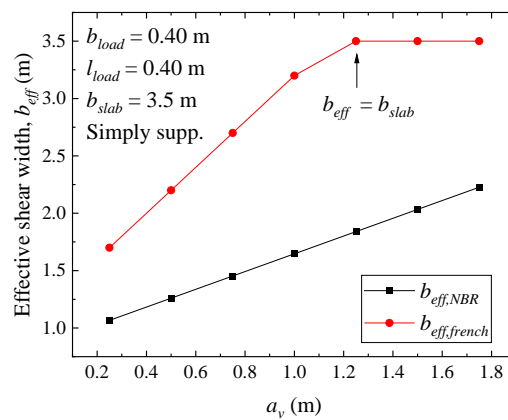


Figure 7 - Comparison between the predicted effective shear with according to the replaced Brazilian code $b_{eff,NBR}$ (ABNT NBR 6118:1980) and the French effective shear width model $b_{eff,french}$.

3.2 Nominal punching capacity according to the ABNT NBR 6118:2014

According to ABNT NBR 6118:2014, Section 19.5.3.2, the nominal punching capacity $v_{R,punch}$ (shear force per unit length), can be calculated as in Equation 15:

$$v_{R,punch} = \frac{0.18}{\gamma_c} k_{punch} (100 \rho_{avg} f_{ck})^{1/3} \cdot d_{avg} \tag{15}$$

$$\rho_{avg} = (\rho_l \cdot \rho_t)^{1/2} \tag{16}$$

$$d_{avg} = (d_l + d_t) / 2 \tag{17}$$

$$k_{punch} = 1 + \sqrt{\frac{200}{d_{avg}}} \leq 2, \text{ with } d_{avg} \text{ in [mm] and } f_{ck} \text{ in [MPa]} \tag{18}$$

k_{punch} is the size effect factor for punching (Equation 18). In the current code [13], k_{punch} is not explicitly limited to 2. In practice, this recommendation appears only in the book of recommendations and examples of the code application [19], which was followed in the study; ρ_{avg} is the average reinforcement ratio considered for punching (Equation 16); ρ_l and ρ_t are the reinforcement ratios in the longitudinal and transverse directions, respectively, d_{avg} is the average effective depth of the reinforcement for punching (Equation 17).

In the case of slabs with large thicknesses, the self-weight may significantly increase the shear demand around the control perimeter (Figure 8). In this case, it shall be noted that the control perimeter shall resist the stresses caused by the concentrated load and the those caused by the self-weight. In the literature, it is usually considered that the self-weight acts only in the longitudinal direction of one-way slabs (based on the shear flow considering only the self-weight) [20]. Using this assumption, a net shear resistance can be calculated on the sides of the control perimeter influenced by the self-weight $v_{R,net}$. In this way, the shear demand caused by the self-weight (v_{sw}) shall be subtracted from the unitary shear resistance calculated by the code expression $v_{R,punch}$ (see Equation 19):

$$v_{R,net} = v_{R,punch} - v_{sw} \tag{19}$$

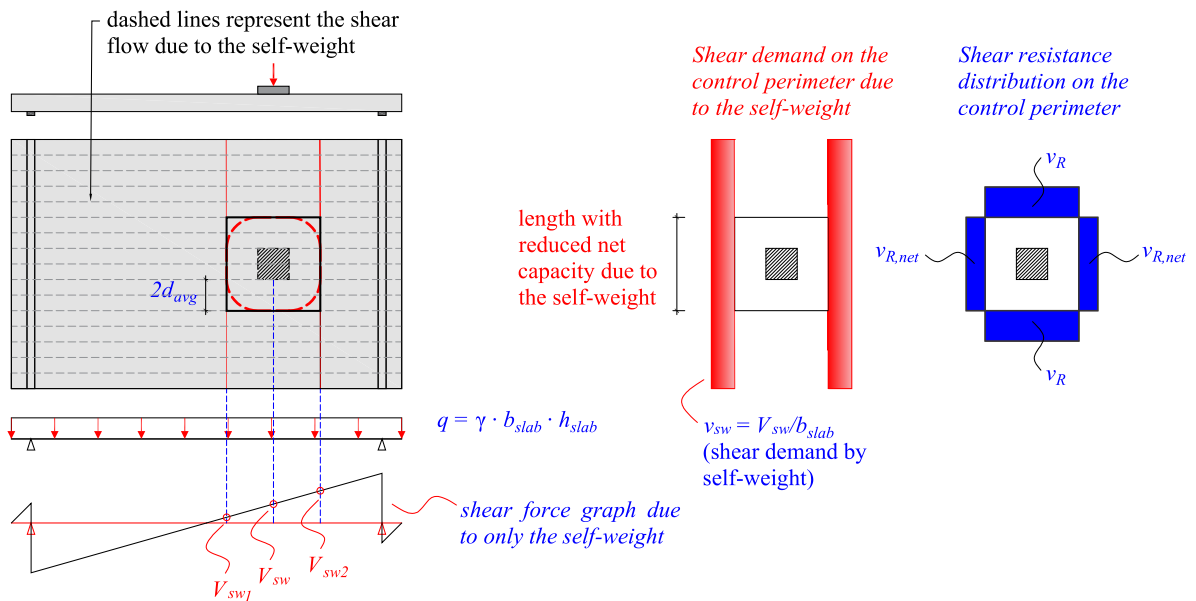


Figure 8 - Effect of the self-weight on the shear demand around the control perimeter and definition of the net shear resistance (the control perimeter was represented with a square shape for simplicity).

In this study, the reference punching capacity (without taking into account the arching action and other parameters influencing the problem) can be expressed as in Equation 20:

$$P_{R,reference} = v_{R,net} \cdot (b_{0,x1} + b_{0,x2}) + v_{R,punch} \cdot (b_{0,y1} + b_{0,y2}), \text{ for SS and CS slabs} \tag{20}$$

$$P_{R,reference} = v_{R,net} \cdot b_{0,x1} + v_{R,punch} \cdot (b_{0,y1} + b_{0,y2}), \text{ for CT slabs}$$

4 PROPOSED APPROACHES

4.1 Proposed approach for the one-way shear predictions

Loads close to the support ($a_v/d_l \leq 2$) benefit from arching action to transmit the load to the supports [21]. In the current Brazilian code [13], this effect is mentioned only for beams. To avoid overly conservative predictions of the shear capacity for loads close to the support, the arching action is considered for slabs in the proposed approach through a factor β , as suggested in the *fib* Model Code 2010 [22] and current European codes [23] (Equation 21):

$$\beta = \frac{a_v}{2d_l}, \text{ with } 0.25 \leq \beta \leq 1 \quad (21)$$

Along the effective shear width, it is assumed that the unitary shear capacity can be enhanced using the following expressions (Equation 22):

$$V_{R,proposed} = (v_{R,shear} \cdot \mu_{shear,1}) \cdot b_{eff,proposed} \quad (22)$$

$$\mu_{shear,1} = 1 / \beta$$

Another key aspect of the predictions of one-way shear capacity is the definition of the effective shear width [2], [3]. Some publications identified that the French effective shear width tends to overestimate the contributing slabs strip for one-way shear predictions when the loads are placed far away from the support ($a_v/d_l > 2$, for instance) or when the slabs are critical in punching instead of one-way shear [3], [16]. Consequently, the predicted one-way shear capacity commonly exceeds the tested one-way shear resistance V_{test} (sectional shear reached in the test). Since for the design or assessment of existing structures, we do not know a priori which is the most critical failure mechanism, conservative predictions for shear and punching capacities should be obtained.

Since the French effective shear width model $b_{eff,french}$ provides good levels of predictions combined with the ABNT code expressions for loads close to the support ($a_v/d_l < 2$) [2], [3], [16], this approach is used as a starting point. Based on regression analyses of $V_{test}/V_{R,predicted}$ using $\mu_{shear,1}$ and $b_{eff,french}$, a factor $\mu_{shear,2}$ was derived to correct the predicted effective shear width according to the shear slenderness a_v/d_l (Equation 24). In this way, the predicted effective shear width $b_{eff,proposed}$ (Equation 23), decreases as the load distance from the support increases. Consequently, the predictions of the one-way shear capacity improve for the tests that present a local failure close to the load by asymmetrical punching:

$$b_{eff,proposed} = b_{eff,french} \cdot \mu_{shear,2} \begin{cases} \leq b_{slab} \\ \geq l_{load} + 4d_l \end{cases} \quad (23)$$

$$\mu_{shear,2} = -0.184 \cdot a_v / d_l + 1.376, \text{ for CT} \quad (24)$$

$$\mu_{shear,2} = -0.128 \cdot a_v / d_l + 1.280, \text{ for CS and SS}$$

On which CT = load applied on cantilever slab, CS = loads close to continuous support and SS = load close to simple support (hinged support).

4.2 Proposed approach for the punching shear predictions

Inspired by the work from Regan [24], this paper suggests considering the enhanced shear capacity for the side of the control perimeter facing to the support when the load is placed at distances $a_v \leq 2d_l$. This is accomplished by multiplying the unitary shear capacity $v_{R,net}$ in $b_{0,xl}$ by the factor μ_{punch1} (see Figure 9), which has the same expressions as $\mu_{shear,1}$. In this way, the arching action for loads close to the support is considered only for the relevant part of the control perimeter.

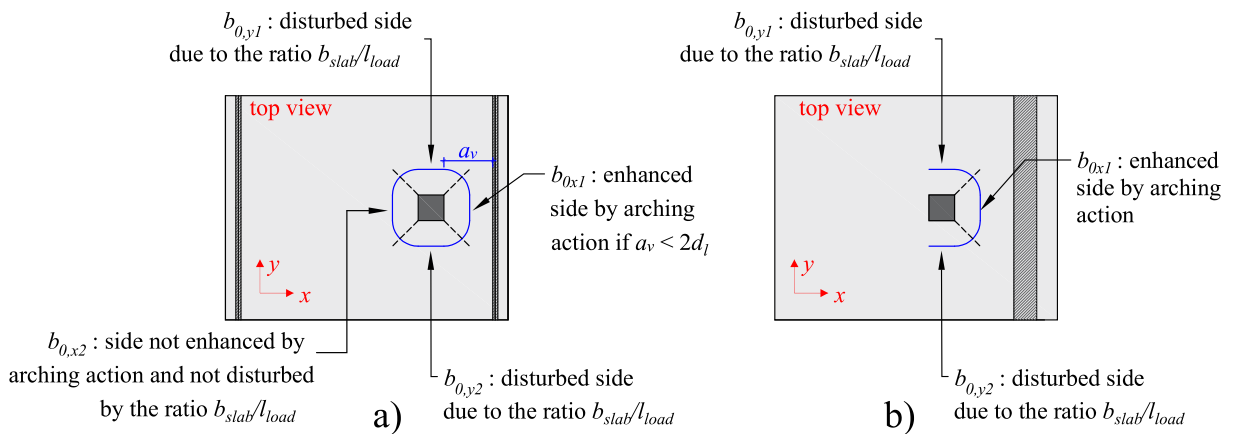


Figure 9 - Sketch of the assumed control perimeter sides enhanced by arching action according to the ratio a_v/d_l , and disturbed according to the ratio b_{slab}/l_{load} (adapted from [12]).

When the loads are placed close to the support, the intersection of the control perimeter with the support should be considered in the definition of the sides of the control perimeter (Figure 10a). In practice, different assumptions could be used to define the length $b_{0,x1}$, $b_{0,x2}$, $b_{0,y1}$ and $b_{0,y2}$. For instance, someone could consider $b_{0,x1}$ as only the straight length that touches the support between the dashed blue lines (Figure 10c). However, this tends to underestimate the length $b_{0,x1}$ when the control perimeter when the load is placed too close of the support ($a_v \approx 0$). Another definition can be based on the variable angle of the reference dashed lines (blue lines in Figure 10). For instance, Figure 10d assumes that the reference line touches the intersection of the support with the control perimeter, which also underestimates the length of the side $b_{0,x1}$ when the load is place at $a_v = 2d_{avg}$. In this study, it is assumed that the reference dashed line always touches the middle of the rounded side to define the length $b_{0,x1}$ (Figure 10e). In summary, we start calculating the point on which the control perimeter intercepts the support and, after, we calculate the length of the rounded corner. In the end, we add the straight length with half of the rounded corners to define $b_{0,x1}$.

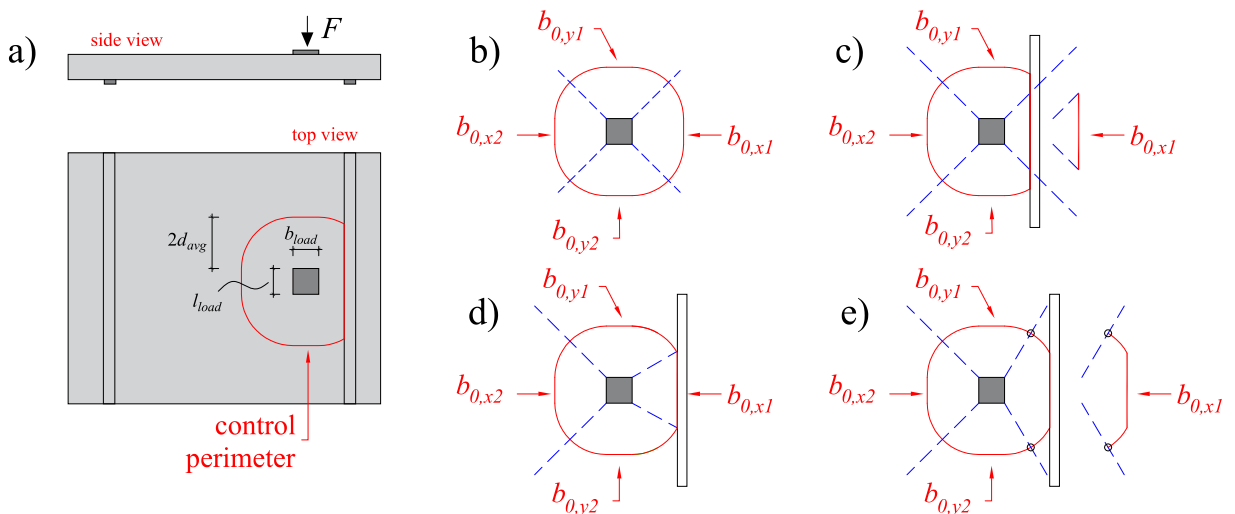


Figure 10 - Definition of the lengths $b_{0,x1}$, $b_{0,x2}$, $b_{0,y1}$ and $b_{0,y2}$ when the control perimeter intercepts the support: a) sketch of the control perimeter when the load is placed at $a_v < 2d_{avg}$; b) original control perimeter without intersection with the support; c) approach 1 with a fixed angle of the reference dashed line; d) approach 2 with a variable angle of the reference dashed line and e) approach 3 with a variable angle of the reference dashed line (used in this study).

Additionally, the second aspect to be considered in the punching capacity predictions is the effect of the slab width-to-load size (b_{slab}/l_{load}) in the effective contribution of the lateral sides of the control perimeter ($b_{0,y1}$ and $b_{0,y2}$). In

practice, by decreasing the slab width and fixing other parameters, a lower shear flow is transferred by the lateral sides of the control perimeter ($b_{0,y1}$ and $b_{0,y2}$) [12]. Therefore, these sides provide a lower contribution to the punching capacity compared to the sides $b_{0,x1}$ and $b_{0,x2}$.

In this study, it is proposed to multiply the unitary shear resistance of the sides $b_{0,y1}$ and $b_{0,y2}$ by the factors $\mu_{punch,2}$ (Equation 25):

$$\mu_{punch,2} = \begin{cases} 0.14 \cdot \lambda - 0.14, & \text{if } \lambda \leq 8 \\ 1, & \text{for } \lambda > 8 \end{cases} \quad (25)$$

$$\lambda = (b_{slab} - l_{load}) / (2 \cdot d_{avg})$$

The effect of the non-proportional shear demand between the frontal and back sides of the load also influences the ultimate capacity of the slabs. In practice, this can be explained by the asymmetrical punching failure around the load for such slabs when the loads are placed closer to the support [6]. Since one side of the control perimeter is more heavily loaded than the other, the less demanded side contributes less to the punching capacity. Comparisons between tested and predicted resistances in this study, however, indicate that this effect would have a considerable influence only for cantilever slabs, which behave as edge columns. However, for concentrated loads close to the free edge of simply supported or continuous slabs, a similar effect can be expected (in this study, we evaluated only slabs under concentrated loads placed at mid-width). Therefore, a third factor that considers the non-proportional shear demand in the shear span direction is employed only for cantilever slabs (Equation 26):

$$\mu_{punch,3} = \begin{cases} 1, & \text{for simply supported and continuous slabs} \\ 0.728 \cdot (a / l_{span})^{0.71}, & \text{for cantilever slabs } (a / l_{span} \geq 0.20) \end{cases} \quad (26)$$

Therefore, the total punching capacity can be calculated for simply supported and continuous slabs as in Equation 27:

$$P_{R,proposed} = (v_{R,net} \cdot \mu_{punch,1}) \cdot b_{0,x1} + v_{R,net} \cdot b_{0,x2} + v_{R,punch} \cdot (b_{0,y1} + b_{0,y2}) \cdot \mu_{punch,2} \quad (27)$$

and can be calculated for cantilever slabs as in Equation 28:

$$P_{R,proposed} = \left[(v_{R,net} \cdot \mu_{punch,1}) \cdot b_{0,x1} + v_{R,punch} \cdot (b_{0,y1} + b_{0,y2}) \cdot \mu_{punch,2} \right] \cdot \mu_{punch,3} \quad (28)$$

Since the effect of the self-weight in the shear demand calculated at the control perimeter sides v_{sw} was limited when compared to $v_{R,punch}$ in the database, (due to the large reinforcement ratios and thickness employed in most tests), one can replace the term $v_{R,net}$ by $v_{R,punch}$ for simplicity. However, such simplifications shall be avoided in the evaluation of bridge decks slabs, on which the self-weight is considerably larger than for laboratory tests [20], [25].

5 DATABASE OF TEST RESULTS

A database of test results was organized for the evaluation of the proposed approach and it was published in the public domain [26]. This dataset contains 143 test results of slabs under concentrated loads failing by shear as wide beams (WB: 91 tests), punching (P: 40 tests) or a mixed mode between shear and punching (WB+P: 12 tests).

The dataset includes tests from the following references: Bui et al. [5], Carvalho [27], Coin and Thonier [14], Damasceno [28], Ferreira [29], Lantsoght [30], Natário et al. [7], [31], Reiffen [32], Regan [24], Regan and Rezai-Jarobi [33], Rombach and Latte [34], [35], Rombach and Henze [36], Vaz Rodrigues [37] and Vida and Halvonik [38].

Table 1 - Ranges of parameters in the database.

Parameter	min	max
h [m]	0.10	0.30
b_{slab} [m]	0.60	4.50
l_{span} [m]	0.90	4.00
b_{slab}/l_{load} [-]	1.67	23.08
b_{slab}/d_l [-]	5.66	29.41
a_v/d_l [-]	0.24	7.66
f_c [MPa]	19.20	77.74
ρ_l [%]	0.602	2.150
ρ_t [%]	0.132	1.526

Table 1 shows the ranges of parameters in the database. The reinforcement ratio of the slabs ρ_l and ρ_t reported in the database and used in the calculations was recalculated based on the spacing of the flexural rebars. The value of the compressive strength measured on cube specimens was corrected by a factor of 0.82 to estimate the compressive strength on cylinder specimens [2]. Only tests with a ratio $b_{slab}/d_l \geq 5$ were included in the dataset to fit the requirement of the ABNT NBR 6118:2014 regarding the definition of the slab members. Besides, only tests with $(b_{slab}-l_{load}) > 4d_l$ were evaluated in this dataset to increase the proportion of tests that could be critical to both shear and punching failures. At this point, the reader shall realize that including members almost loaded over the entire width $(b_{slab}-l_{load})/2d_l \leq 4$ would significantly increase the proportion of tests failing as wide beams over the tests that failed by punching.

6 RESULTS AND DISCUSSIONS

6.1 Comparison between tests and studied methods

Figure 11 compares the ratio between tested and predicted resistances for one-way shear and punching shear analyses. In the comparisons between tested and predicted resistances, partial safety factors were assumed equal to 1 and measured material properties were used instead of characteristic values. The results "No μ s" are the ones following the traditional approaches of evaluation according to the Brazilian code (Section 2 and 3 of this paper) and do not include the proposed factors μ for shear and punching capacity predictions. In this way, $V_{R,predicted}$ and $P_{R,predicted}$ are equal, respectively, to $V_{R,reference}$ and $P_{R,reference}$ for "No μ s". The results "with μ s" are the ones following the recommendations of Section 4 of this paper. In this way, $V_{R,predicted}$ and $P_{R,predicted}$ are equal to $V_{R,proposed}$ and $P_{R,proposed}$, respectively. In Figure 9, the following notations are applied: WB: test failed as a wide beam in one-way shear; P: test failed by punching; and WB+P: the test failed by a mixed mode between one-way shear and punching.

Figure 11a shows two main aspects of the results without the proposed recommendations (No μ s): (i) neglecting the arching action for slabs under concentrated loads close to the support can significantly underestimate the ultimate capacity of the slabs in one-way shear (see Detail 1 in Figure 11a); and (ii) the predictions of one-way shear capacity become critically unsafe for large shear slenderness, for instance, when $a_v/d_l > 4$. In the last case, this occurs because the French effective shear width increases by increasing the shear slenderness a_v/d_l and the ultimate load that causes the failure (P_{test}) does not increase by increasing a_v/d_l [6]. In fact, most tests with $a_v/d_l > 4$ failed by punching or a mixed mode between one-way shear and punching (see Detail 2 in Figure 11a). For such tests, increasing the ratio a_v/d_l increases the slab rotations around the load and, consequently, the crack opening for the same load level, which results in lower punching capacities according to the Critical Shear Crack Theory [39]. Consequently, the predicted one-way shear capacity increased excessively by increasing the shear slenderness.

Using the proposed recommendations through the factors $\mu_{shear,1}$ and $\mu_{shear,2}$ (Section 4), the average ratio $V_{test}/V_{R,predicted}$ changes from 1.37 to 1.22 and the coefficient of variation decreases from 63.7% to 18.3% (see Figure 11c). Therefore, using the proposed recommendations allows for reaching enhanced predictions of shear capacity, even when the tests failed by punching for large values of a_v/d_l .

Figure 11b shows that without the proposed recommendations for punching (No μ s), the predictions of punching capacity can be critically unsafe for the slabs that failed as wide beams in one-way shear (WB) due to the small ratio b_{slab}/l_{load} (see Detail 1 in Figure 11b). Besides, the predictions of punching capacity can, in the same way, be overly conservative if arching action is not considered in the calculations (tests of Detail 2 in Figure 11b), regardless if the test failed as a wide beam or by punching. Using the proposed recommendations for punching capacity predictions (Figure 11d), the average ratio $P_{test}/P_{R,predicted}$ changes from 1.44 to 1.23, and the coefficient of variation decreases from 40.1% to 21.3%.

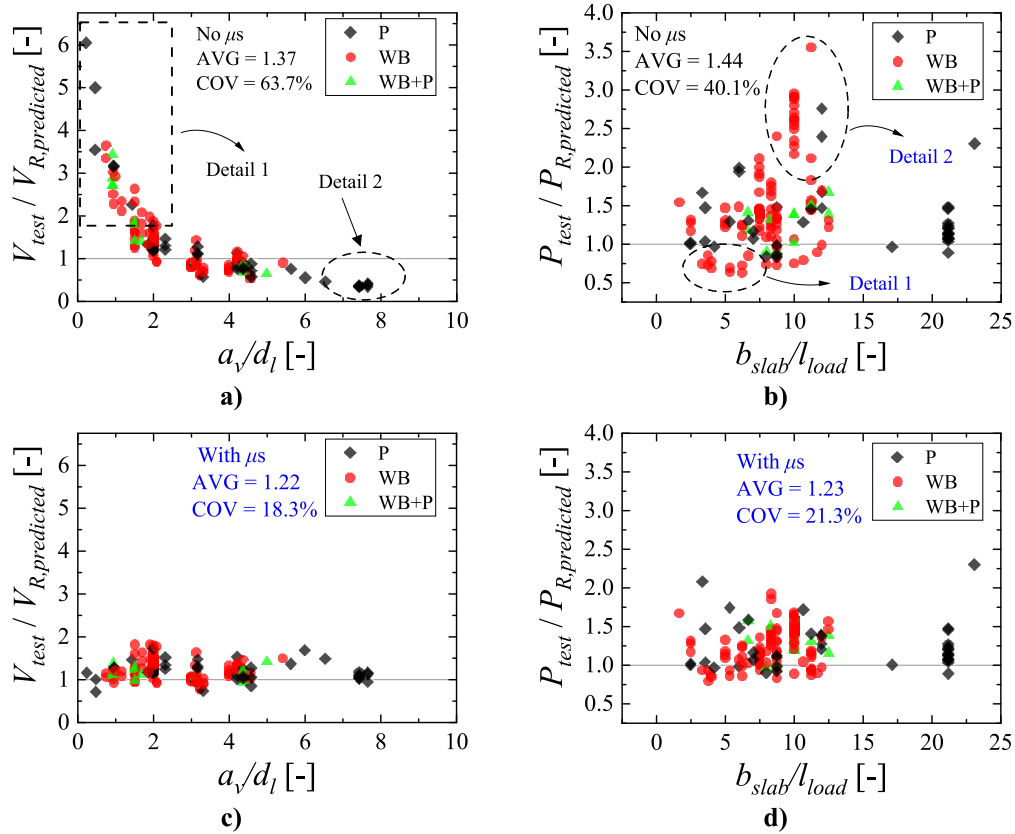


Figure 11 - Comparison between tested and predicted resistances with the reference and proposed approaches for: a) and c) one-way shear; and b) and d) punching shear expressions. The results “No μ_s ” are the ones following the reference approach (Section 3) and the results “With μ_s ” are reached with the proposed recommendations (Section 4). Note: P = punching failure; WB = wide beam shear failure in one-way shear; WB+P = mixed mode between one-way shear and punching.

Comparing the predictions of shear and punching capacity using the proposed recommendations, it can be observed that the predictions are quite similar. The average ratio between tested and predicted resistances (1.22 and 1.23) differs by less than 1%, and the coefficients of variation (18.3% and 21.3%) differ by less than 15%.

In this study, however, it can be observed that the predictions of one-way shear capacity performed better than those for punching (with a lower coefficient of variation) and used a fewer number of correction factors (2 for shear and 3 for punching). In practice, this occurs because of the more significant number of tests that failed as wide beams in the database but also because the one-way shear failure mode seems to represent better the local failure between the load and the support. In this study, it is assumed that the one-way shear approach represents the problem closely because it directly considers the more significant influence of the resistance and shear demand on the front side of the load close to the support. In this context, it is important to note that in the punching capacity predictions, a uniform shear resistance and shear demand around the load is assumed with the Brazilian code expressions. Consequently, it would be necessary to consider the different contributions of each side of the control perimeter (unbalanced shear resistance and unbalanced shear demand) around the load to reach better predictions with the punching expressions.

6.2 Resistance model uncertainty

The analysis of the resistance model’s uncertainty partial safety factor (γ_{Rd}) concerning the shear and punching capacity using the proposed recommendations is carried out. When considering structural reliability, model uncertainties can be related to models for action effects and for resistance models, which are based on simplified relationships or complex numerical models. Therefore, the model uncertainty can be defined as a basic variable related to the accuracy of the physical model. It is commonplace to consider model uncertainty as a random variable.

In this paper, the principles presented in the *fib* Model Code 2010 [22] and other references are used [40]–[44] to estimate the resistance model uncertainty. For this analysis, the model error (ME) is defined as in Equation 29:

$$ME = \frac{\text{Experimental Capacity}}{\text{Capacity calculated from proposed model}} \tag{29}$$

Goodness of fit tests provide a statistical tool for selecting an appropriate type of probability distribution. A normal distribution is usually used to represent the lower tail of model uncertainty for resistance functions. However, the normality test, using the Shapiro-Wilk test at the 0.05 significance level, concluded that data for both analyses were not significantly drawn from a normality distributed population. Figure 12 presents the frequency histogram of shear and punching capacity using the proposed recommendations. Both the Chi-square and the Kolmogorov-Smirnov tests have confirmed at the 0.05 significance level the possibility to adopt log-normal probabilistic distributions for both analyses.

Figure 12 also presents the sample versus theoretical probability plot for the natural logarithm of ME. The horizontal axis (x) represents the expected value of the standard normal distribution, and the vertical axis (y) denotes the natural logarithm of ME. The good linear fit confirms that the log-normal probabilistic distribution is suitable for the model error. The mean and standard deviation of the model error can be obtained using the fit linear on log-normal probability paper and are presented in Table 2.

Equation 29 also includes the variability of the test procedures and the specimen geometry, so it represents more than just the accuracy of the model. The variability of the model error COV_{ME} can be estimated as in Equation 30 [45]:

$$COV_{ME} = \sqrt{COV_m^2 - COV_{test}^2 - COV_{spec}^2} \tag{30}$$

Where COV_m is the coefficient of variation of the measured and predicted strengths by the proposed recommendations obtained from statistical analysis of Figure 12, COV_{test} is the coefficient of variation of the measured test loads, and COV_{spec} is the uncertainty of specimen dimensions in the tests. The values of $COV_{test} = 0.02$ and $COV_{spec} = 0.04$, as proposed in reference [45], are used herein. The resulting model statistical parameters are presented in Table 2.

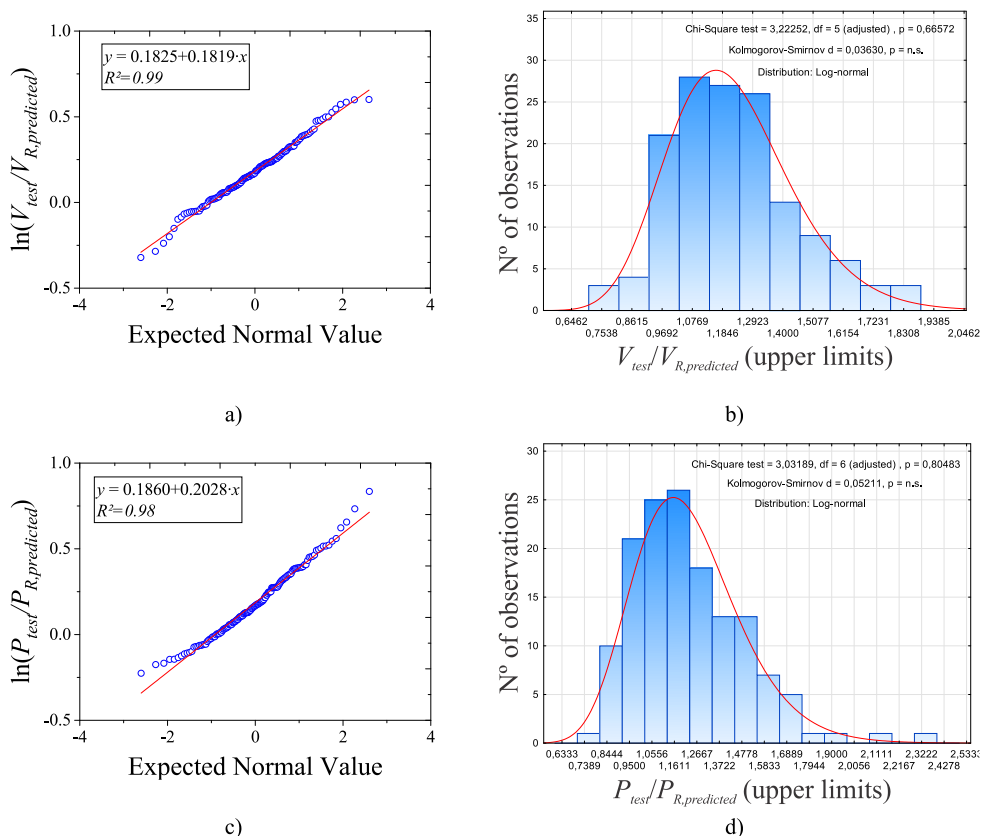


Figure 12 - Normal probability plot and frequency histogram for model error (ME).

Table 2 - Statistical parameters for model error and model uncertainty factors.

Proposed approach	Full data set		Statistical parameters				γ_{Rd}	
	Mean	COV	μ_R	σ_R	COV _m	COV _{ME}	$\alpha_R = 0.32$	$\alpha_R = 0.8$
One-way shear resistance	1.220	0.183	1.220	0.224	0.183	0.178	1.02	1.41
Punching shear resistance	1.230	0.213	1.229	0.252	0.205	0.200	1.04	1.49

Finally, under the lognormal distribution hypothesis, the resistance model uncertainties γ_{Rd} can be determined, according to references [22], [43], as follows (Equation 31):

$$\gamma_{Rd} = \frac{1}{\mu_R} \exp(\alpha_R \beta \text{COV}_{ME}) \tag{31}$$

where μ_R is the mean value of the ratio between the resistance obtained through the tests and the resistance achieved through the proposed recommendations and COV_{ME} is the coefficient of variation of the resistance model uncertainties. The first-order-reliability method (FORM) sensitivity factor for the variables (α_R) can be assumed to be 0.32 or 0.8 [41], [43], accounting for the hypothesis of non-dominant and dominant variables, respectively, and the term β denotes the reliability index. For new structural systems with moderate consequences due to a structural failure and a 50-year lifetime, *fib* Model Code 2010 [22] recommends $\beta = 3.8$ (i.e., a failure probability of 7×10^{-5}).

The value of the model uncertainty factor γ_{Rd} is dependent on the quality of the resistance model formulation. *Fib* Model Code 2010 [22] has recommended values of 1.06 for models with low uncertainties and 1.1 for models with high uncertainties. Table 2 shows the values of γ_{Rd} for the proposed recommendations, with resistance uncertainty as a non-dominant and dominant variable. The values for the non-dominant hypotheses are below the values recommended by the *fib* Model Code 2010 [22]. However, the non-dominant hypothesis of the model uncertainty factor γ_{Rd} can be adopted if the coefficient of variation (COV_{ME}) reported in Table 2 is less than 0.15, which is the coefficient of variation associated with the compressive strength of concrete according to references [22], [43]. Therefore, the dominant hypothesis should be adopted for the shear and punching recommendations proposed herein. Consequently, and as a simplification, it would be recommended to use a $\gamma_{Rd} = 1.5$ for both one-way shear and punching shear resistance predictions with the proposed approaches.

7 CONCLUSIONS

In this study, the expressions and most traditional approaches to predict the shear and punching capacity of one-way slabs under concentrated loads are evaluated, with emphasis to the ABNT NBR 6118:2014 code provisions. Based on the described analyses and proposed recommendations, the following conclusions can be drawn:

- The one-way shear and punching shear capacity enhance significantly for loads close to the support, here assumed at distances $a_v \leq 2d_l$. Using the factors $\mu_{shear,1}$ and $\mu_{punching,1}$ to consider the enhanced unitary shear and punching capacity of the slabs allows for improving the predictions of ultimate capacity when the load is placed relatively close to the support.
- For loads far away from the support, typically when $a_v/d_l > 4$, the predictions of one-way shear capacity with the Brazilian code combined with the French effective shear width model can be critically unsafe. This occurs because the French effective shear width model overestimates the contributing slabs strip to the one-way shear capacity. Using the factor $\mu_{shear,2}$ allows correcting the predicted effective shear width in a simple and effective way. Besides, this approach improves considerably the relation between tested and predicted resistances using the expressions of one-way shear resistance, even when the tests fail by punching.
- The predicted punching capacity with the Brazilian code expressions can be critically unsafe if the influence of the slab width is not considered for tests that are critical in one-way shear. This occurs because by decreasing the slab width, the shear flow concentrates on the sides of the control perimeter in the spanning direction and the sides parallel to the free edges present a smaller contribution to the punching capacity. In this study, it is proposed to apply a factor $\mu_{punching,2}$ as a function of the slab width on the sides of the control perimeter parallel to the free edges. Using this factor, the predicted punching capacity for tests critical in one-way shear are enhanced significantly (see Figure 11b-11d).
- One-way shear and punching capacity expressions can provide similar and enhanced predictions for one-way slabs under concentrated loads if parameters that influence the transition from shear to punching failure mechanisms (and vice-versa) are considered. In this study, the average ratio between tested and predicted resistances $V_{test}/V_{R,predicted}$

was 1.22 with a coefficient of variation of 18.3% using the proposed recommendations. The respective average ratio $P_{test}/P_{R,predicted}$ was 1.23 with a coefficient of variation of 21.3%.

- The uncertainty of the resistance model for shear and punching capacity were calculated using the recommended approaches. The coefficients of variation of the model error were greater than 0.15, so that the dominant hypothesis was adopted. Therefore, the resistance model uncertainties γ_{Rd} for the one-way shear and punching capacities were 1.41 and 1.49, respectively. As a general recommendation, the value of $\gamma_{Rd} = 1.5$ could be adopted for both one-way shear and punching shear.

ACKNOWLEDGEMENTS

The authors acknowledge the financial support provided by the São Paulo Research Foundation (FAPESP) (grant number #2018/21573-2, grant number #2019/20092-3 and grant number #2021/13916-0) and by Brazilian National Council for Scientific and Technological Development (CNPq) (grant number #303438/2016-9). This study was also partially financed by the Coordenação de Aperfeiçoamento de Pessoal de Nível Superior – Brasil (CAPES) – Finance Code 001.

REFERENCES

- [1] E. O. L. Lantsoght, A. Boer, and C. van der Veen, “Levels of approximation for the shear assessment of reinforced concrete slab bridges,” *Struct. Concr.*, vol. 18, no. 1, pp. 143–152, 2017.
- [2] E. O. L. Lantsoght, C. van der Veen, and J. C. Walraven, “Shear in one-way slabs under concentrated load close to support,” *ACI Struct. J.*, vol. 110, no. 2, pp. 275–284, 2013.
- [3] A. M. D. Sousa and M. K. el Debs, “Shear strength analysis of slabs without transverse reinforcement under concentrated loads according to ABNT NBR 6118:2014,” *Rev. IBRACON Estrut. Mater.*, vol. 12, no. 3, pp. 658–693, 2019.
- [4] L. Henze, G. A. Rombach, and M. Harter, “New approach for shear design of reinforced concrete slabs under concentrated loads based on tests and statistical analysis,” *Eng. Struct.*, vol. 219, pp. 110795, 2020.
- [5] T. T. Bui, A. Limam, W. S. A. Nana, E. Ferrier, M. Bost, and Q.-B. Bui, “Evaluation of one-way shear behaviour of reinforced concrete slabs: experimental and numerical analysis,” *Eur. J. Environ. Civ. Eng.*, vol. 24, no. 2, pp. 190–216, 2017.
- [6] K. Reißer, M. Classen, and J. Hegger, “Shear in reinforced concrete slabs-Experimental investigations in the effective shear width of one-way slabs under concentrated loads and with different degrees of rotational restraint,” *Struct. Concr.*, vol. 19, no. 1, pp. 36–48, Feb. 2018.
- [7] F. Natário, M. Fernández Ruiz, and A. Muttoni, “Shear strength of RC slabs under concentrated loads near clamped linear supports,” *Eng. Struct.*, vol. 76, pp. 10–23, 2014.
- [8] Associação Brasileira de Normas Técnicas, *Carga Móvel Rodoviária e de Pedestres em Pontes, Viadutos, Passarelas e Outras Estruturas*, ABNT NBR 7188:2013, 2013.
- [9] J. Halvonik, A. Vidaković, and R. Vida, “Shear capacity of clamped deck slabs subjected to a concentrated load,” *J. Bridge Eng.*, vol. 25, no. 7, pp. 04020037, Jul. 2020.
- [10] E. O. L. Lantsoght, C. van der Veen, J. C. Walraven, and A. de Boer, “Database of wide concrete members failing in shear,” *Mag. Concr. Res.*, vol. 67, no. 1, pp. 33–52, Jan. 2015.
- [11] A. M. D. Sousa, E. O. L. Lantsoght, A. Setiawan, and M. K. El Debs, “Transition from one-way to two-way shear by coupling LEFEA and the CSCT models,” in *Proc. fib Symp. 2021. Concr. Struct. New Trends Eco-Effic. Perform.*, 2021, pp. 1710–1719.
- [12] A. M. D. Sousa, E. O. L. Lantsoght, and M. K. El Debs, “Transition between shear and punching in RC slabs: review and predictions with ACI code expressions,” *ACI Struct. J.*, vol. 120, no. 2, pp. 115–128, Nov. 2023.
- [13] Associação Brasileira de Normas Técnicas, *Design of Concrete Structures — Procedure*, ABNT NBR 6118:2014, 2014. In Portuguese.
- [14] A. Coin and H. Thonier, “Essais sur le cisaillement des dalles en béton arme,” in *Annal. Batim. Trav. Publics*, 2007, pp. 7–16.
- [15] D. Chauvel, H. Thonier, A. Coin, and N. Ile, *Shear Resistance of Slabs not Provided With Shear Reinforcement*, CEN/TC 250/SC 02 N 726, 2007.
- [16] A. M. D. Sousa, E. O. L. Lantsoght, Y. Yang, and M. K. El Debs, “Extended CSCT model for shear capacity assessments of bridge deck slabs,” *Eng. Struct.*, vol. 234, p. 111897, May 2021.
- [17] J. Sagaseta, L. Tassinari, M. Fernández Ruiz, and A. Muttoni, “Punching of flat slabs supported on rectangular columns,” *Eng. Struct.*, vol. 77, pp. 17–33, 2014.
- [18] Associação Brasileira de Normas Técnicas, *Design and Execution of Reinforced Concrete Buildings*, ABNT NBR 6118:1980, 1980. In Portuguese.
- [19] Comitê Técnico Conjunto ABECE/IBRACON - CT 301 Projeto de Estruturas de Concreto. *ABNT NBR 6118:2014 - Comentários e Exemplos de Aplicação*. São Paulo: IBRACON, 2015.
- [20] E. O. L. Lantsoght, C. van der Veen, and A. de Boer, “Extended strip model for slabs subjected to load combinations,” *Eng. Struct.*, vol. 145, pp. 60–69, 2017.

- [21] A. M. D. Sousa, E. O. L. Lantsoght, and M. K. El Debs, "One-way shear strength of wide reinforced concrete members without stirrups," *Struct. Concr.*, vol. 22, no. 2, pp. 968–992, 2020.
- [22] Fédération Internationale du Béton, *Fib Model Code for Concrete Structures 2010, Vol. 1–2*. Lausanne, Switzerland: Ernst & Sohn, 2012.
- [23] Comité Européen de Normalisation, *EN 1992-1-1: Eurocode 2: Design of Concrete Structures -Part 1-1: General Rules and Rules for Buildings*, EN 1992-1-1:2005, 2005.
- [24] P. E. Regan, *Shear Resistance of Concrete Slabs at Concentrated Loads Close to Supports*. London, United Kingdom: Polytechnic of Central London, 1982.
- [25] E. O. L. Lantsoght, C. van der Veen, A. Boer, and S. D. B. Alexander, "Bridging the gap between one-way and two-way shear in slabs," in *ACI-Fib Int. Symp. Punching Shear Struct. Concr. Slabs*, Apr. 2017, pp. 187–214.
- [26] A. M. D. Sousa, E. O. L. Lantsoght, and M. K. eL Debs, "Databases of one-way slabs under concentrated loads: parameter analyses and validation of the proposed approach." *Zenodo.*, 2022. Accessed: Feb. 27, 2023. [Online]. Available: <https://zenodo.org/record/5911469>
- [27] A. S. Carvalho, "Análise experimental de lajes lisas de concreto armado de alta resistência com metacaulim apoiadas em pilares retangulares e armadas à punção," Master thesis, Depart. Eng. Civil, Univ. Fed. Pará, Belém, Brazil, 2006.
- [28] L. S. R. Damasceno, "Análise experimental de lajes lisas unidirecionais de concreto armado com pilares retangulares ao puncionamento," Master thesis, Depart. Eng. Civil, Univ. Fed. Pará, Belém, Brazil, 2007.
- [29] M. P. Ferreira, "Análise experimental de lajes lisas unidirecionais de concreto armado ao puncionamento simétrico ou assimétrico," Master thesis, Univ. Fed. Pará, Belém, Brazil, 2006.
- [30] E. O. L. Lantsoght, "Shear in reinforced concrete slabs under concentrated loads close to supports," Ph.D. dissertation, Fac. Civil Eng. Geosci., Delft Univ. Technol., Delft, The Netherlands, 2013.
- [31] F. Natário, M. Fernández Ruiz, and A. Muttoni, "Experimental investigation on fatigue of concrete cantilever bridge deck slabs subjected to concentrated loads," *Eng. Struct.*, vol. 89, pp. 191–203, Apr. 2015.
- [32] K. Reißer, "Zum querkrafttragverhalten von einachsigen gespannten stahlbetonplatten ohne querkraftbewehrung unter einzellasten," Doctoral dissertation, Fac. Civil Eng., RWTH Aachen Univ., Aachen, Germany, 2016.
- [33] P. E. Regan and H. Rezaei-Jorabi, "Shear resistance of one-way slabs under concentrated loads," *ACI Struct. J.*, vol. 85, no. 2, pp. 150–157, 1988.
- [34] G. A. Rombach and S. Latte, "Shear resistance of bridge decks without shear reinforcement," in *Proc. Int. fib Symp.*, 2008, pp. 519–525.
- [35] G. Rombach and S. Latte, "Querkrafttragfähigkeit von fahrbahnplatten ohne querkraftbewehrung," *Beton Stahlbet.*, vol. 104, no. 10, pp. 642–656, 2009.
- [36] G. Rombach and L. Henze, "Querkrafttragfähigkeit von stahlbetonplatten ohne querkraftbewehrung unter konzentrierten einzellasten," *Beton Stahlbet.*, vol. 112, no. 9, pp. 568–578, Sep. 2017.
- [37] R. Vaz Rodrigues, *Essai d'un Porte-À-Faux de Pont Sous Charge Concentrée*. Lausanne, Switzerland: EPFL, 2002.
- [38] R. Vida and J. Halvonik, "Experimentálné overovanie šmykovej odolnosti mostovkových dosiek," *Inžin. Stav.*, vol. 4, pp. 2–6, 2018.
- [39] A. Muttoni, "Punching shear strength of reinforced concrete slabs without transverse reinforcement," *ACI Struct. J.*, vol. 105, no. 4, pp. 440–450, Jul. 2008.
- [40] D. L. Araújo, S. A. Coelho, S. R. M. Almeida, and M. K. El Debs, "Computational modelling and analytical model for two-step corbel for precast concrete system," *Eng. Struct.*, vol. 244, p. 112699, Oct. 2021.
- [41] P. Castaldo, D. Gino, G. Bertagnoli, and G. Mancini, "Resistance model uncertainty in non-linear finite element analyses of cyclically loaded reinforced concrete systems," *Eng. Struct.*, vol. 211, p. 110496, May 2020.
- [42] D. L. Araújo, M. W. R. Sales, R. P. M. Silva, C. F. M. Antunes, and M. A. Ferreira, "Shear strength of prestressed 160 mm deep hollow core slabs," *Eng. Struct.*, vol. 218, p. 110723, Sep. 2020.
- [43] P. Castaldo, D. Gino, G. Bertagnoli, and G. Mancini, "Partial safety factor for resistance model uncertainties in 2D non-linear finite element analysis of reinforced concrete structures," *Eng. Struct.*, vol. 176, pp. 746–762, Dec. 2018.
- [44] M. Holický, J. V. Retief, and M. Sýkora, "Assessment of model uncertainties for structural resistance," *Probab. Eng. Mech.*, vol. 45, pp. 188–197, Jul. 2016.
- [45] S. J. Foster and A. Parvez, "Assessment of model error for reinforced concrete beams with steel fibers in bending," *Struct. Concr.*, vol. 20, no. 3, pp. 1010–1021, Jun. 2019.

Author contributions: AMDS: conceptualization, methodology, resources, data curation, writing - original draft, writing - review & editing; EOLL: conceptualization, supervision, writing - review & editing; DLA: methodology, writing - review & editing; LPP: writing - review & editing; MKED: supervision, project administration, funding acquisition.

Editors: Leandro Trautwein, Mauro Real, Mario Pimentel.



ORIGINAL ARTICLE

Evaluation of shear design criteria of beams according to NBR6118 applying the modified compression field theory

Avaliação dos critérios de verificação a cisalhamento segundo a NBR6118 aplicando a teoria do campo de compressão modificada

Marcelo Araújo de Sá^a Sergio Hampshire de Carvalho Santos^b Julio Jeronimo Holtz Silva Filho^b ^aConsórcio Brucke – Arte Pontes, Niterói, RJ, Brasil^bUniversidade Federal do Rio de Janeiro – UFRJ, Escola Politécnica, Departamento de Estruturas, Rio de Janeiro, RJ, Brasil

Received 12 December 2022

Accepted 10 March 2023

Abstract: It is known that design deficiencies in shear design are more dangerous than bending, as shear failures can occur in a fragile way and without possibility of redistributing internal forces. Unlike bending design, designing for shear loads by different standards can generate significantly different results for the same element, as long as design models have been under discussion for many years. This paper analyses the evaluation of the behavior of the combined bending and shear loads in reinforced concrete beams for different pairs of these forces. For this purpose, the verification presented in ABNT NBR 6118 was used and compared to a more improved theory currently used, the Modified Compression Field Theory - MCFT. This theory is able to predict the relationships of specific loads and strains, as well as the shear strength of sections with great precision, being parameterized by several tested elements. As the use of this theory is not practical for manual calculations, the Response-2000 software, developed at the University of Toronto by Evan C. Bentz, was used. The program allows the analysis of beams and columns subject to moments, shear forces and axial loads, for any type of geometry, material properties and reinforcement arrangement, resulting in accurate responses of the behavior of the sections using MCFT as a basis.

Keywords: reinforced concrete, shear, modified compression field theory, Response 2000.

Resumo: Sabe-se que deficiências de projeto no dimensionamento à força cortante são mais perigosas que as de flexão, pois rupturas por cisalhamento podem ocorrer de forma frágil e sem possibilidade de redistribuição dos esforços internos. Diferentemente do dimensionamento à flexão, o dimensionamento a solicitações cisalhantes por diferentes normas, podem gerar resultados significativamente distintos para um mesmo elemento, visto que os modelos de dimensionamento seguem em discussão por muitos anos. Este trabalho considera a avaliação do comportamento da ação das solicitações combinadas de flexão e força cortante em vigas de concreto armado para diferentes pares de momentos fletores e forças cortantes. Para tanto foi utilizada a verificação definida na ABNT NBR 6118, comparada a uma teoria mais aprimorada utilizada atualmente, a Teoria do Campo de Compressão Modificada (*Modified Compression Field Theory - MCFT*). Essa teoria é capaz de prever as relações entre carregamentos e deformações específicas, bem como a resistência à força cortante de seções com grande precisão, sendo parametrizada por diversos elementos ensaiados. Como a utilização dessa teoria não é prática para os cálculos manuais, foi utilizado o *software* Response-2000, desenvolvido na Universidade de Toronto por Evan C. Bentz. O programa permite a análise de vigas e pilares sujeitos a momentos, forças cortantes e cargas axiais, para qualquer tipo de geometria, propriedades de materiais e arranjo de armaduras, resultando em respostas precisas do comportamento das seções utilizando como base a *MCFT*.

Palavras-chave: concreto armado, força cortante, teoria do campo de compressão modificada, Response-2000.

How to cite: M. A. de Sá, S. H. C. Santos, and J. J. H. Silva Filho, "Evaluation of shear design criteria of beams according to NBR6118 applying the modified compression field theory," *Rev. IBRACON Estrut. Mater.*, vol. 16, no.3, e16309, 2023, <https://doi.org/10.1590/S1983-41952023000300009>

Corresponding author: Sergio Hampshire de Carvalho Santos. E-mail: sergiohampshire@gmail.com

Financial support: None.

Conflict of interest: Nothing to declare.

Data Availability: The data that support the findings of this study are openly available in <http://www.repositorio.poli.ufrj.br/dissertacoes/dissertpoli10034745.pdf>



This is an Open Access article distributed under the terms of the Creative Commons Attribution License, which permits unrestricted use, distribution, and reproduction in any medium, provided the original work is properly cited.

1 INTRODUCTION

Although the subject of shear resistance of reinforced concrete beams is studied throughout the several last decades, this problem of the determination of the shear resistance determination is nowadays still in discussion. The different design standards still present very different recommendations for the shear design.

For the flexural design, the Navier-Bernoulli hypothesis of plane sections is universally accepted for the design of slender elements, and consequently the forecast of flexural resistance is very similar in the different standards. Differently, for the shear design, the part of the resistance due to the concrete resistance is based on empirical equations, and there is not a consensus on a universally theoretical basis for these equations (Bentz et al. [1]).

Usually, the shear resistance equations are based on the truss model developed by Ritter [2] and Mörsch [3] approximately a century ago. This model does not correspond to the sophistication of the numerical procedures developed internationally throughout the last decades, also considering the computational capacity available nowadays for the structural engineering.

Recent research on the shear resistance of structural concrete is much concentrated nowadays in the study of the rupture mechanisms. This research led to the development of the Compression Field Theory (CFT) and later to the Modified Compression Field Theory (MCFT), as described by Bentz et al. [1]. These theories have been developed from the analysis of a great number of tests in reinforced concrete elements subjected to pure bending and shear combined with axial forces.

The analysis of the of several conducted tests have shown great agreement with the theories, for a great diversity of structural members, such as beams subjected to bending, shear, torsion, deep beams, shear walls, columns, plates, and shells (Vecchio [4]).

The tests shown also that the shear rupture of concrete members presents a different behavior compared with the flexural rupture, are relatively fragile and without the possibility of redistribution of internal forces (Collins et al., [5]). In this way, the understanding of the mechanisms of shear behavior is of the utmost importance.

Another point analyzed herein is that the theories are supported mostly in experiments performed in simply supported beams of small dimensions, very different from the beams of actual structures. Actual continuous beams present points of inversion of the sign of the bending moment, i.e., points of null moment. In these points, shear forces can be high as is in the beam supports, but without the favorable effect of the high vertical compressive forces present in the supports (Kotsovou [6]).

This paper intends to evaluate the criteria for shear design defined in Brazilian Standard ABNT NBR 6118 [7] applying the MCFT for the several scenarios of combined action of shear forces and bending moments in a reinforced concrete section, using the software Response-2000 [8]. This software, developed in the University of Toronto by Evan C. Bentz, uses the MCFT for the analysis of beams and columns subjected to bending moments, shear forces and axial forces, leading to precise results.

The paper summarizes the results obtained in the M.Sc. Thesis of Sá [9].

2 METHODOLOGY

Regarding a better understanding of the behavior of beams near the rupture, when subjected to simultaneous action of bending moments and shear forces, as well as to analyze the safety of the criteria defined in the ABNT NBR 6118 [7], a standardized rection of a reinforced concrete beam has been analyzed, for different pairs of forces and different values of flexural reinforcement ratio. The design according ABNT NBR 6118 [7] is based on the generalized truss shown in Figure 1.

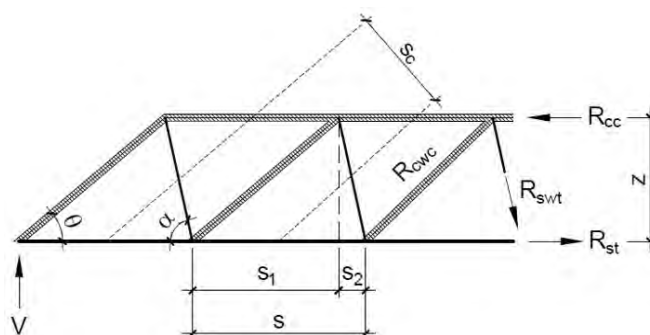


Figure 1. Generalized concrete strut

In this concrete truss, the considered variables are:

- R_{swt} : resulting forces in the inclined tensioned ties (stirrups);
- R_{cwc} : resulting forces in the compressed diagonal strut;
- R_{cc} : resulting force in the horizontal compressed strut;
- R_{st} : resulting force in the horizontal tensioned tie (main flexural reinforcement);
- V : acting shear force;
- z : level arm between the horizontal main struts and ties;
- s : spacing between inclined tensioned ties;
- s_c : width of the compressed diagonal struts;
- α : angle of the inclined tensioned ties;
- θ : angle of the compressed diagonal struts.

For defining the different values of flexural reinforcement, nine values of the non-dimensional depth of the neutral axis/effective beam height ($k_x = x/d$) were considered, varying from 0.05 to 0.45, that is the limiting value defined in Brazilian Standard for usual concrete ($f_{ck} \leq 50$ MPa).

From each defined parameter k_x , the corresponding value of maximum resistant bending moment (M_d) can be evaluated. From the obtained values of these maximum bending moments, different pairs of moments and shear forces are evaluated, i.e., for obtaining the maximum resistant value of the shear force corresponding to a certain value of fraction of the maximum resistant bending moment.

Ten values of fraction of the maximum moment are analyzed, varying between 0.1 M_d to 1.0 M_d . For each value of moment fraction, the maximum simultaneous allowed shear force is evaluated, following the criteria of ABNT NBR 6118 [7], considering also its limits for verification of maximum compressive stresses in the inclined struts.

Concerning the inclination of the concrete struts (θ), three different values were investigated:

- a) $\theta_1 = 45^\circ$, according to Model I of resistance of ABNT NBR 6118 [7];
- b) $\theta_2 = 30^\circ$, minimum value according to Model II of ABNT NBR 6118 [7];
- c) θ_3 - angle evaluated in each case according *fib* Model Code 2010 [10].

For evaluating the eventual contribution of secondary reinforcement in flexural resistance, present in all actual structures, three different situations of actual reinforcement were considered (see Figure 2):

- a) only basic flexural and shear reinforcement (Model A);
- b) Model A reinforcement plus top horizontal reinforcement (Model B);
- c) Model B reinforcement plus skin reinforcement.

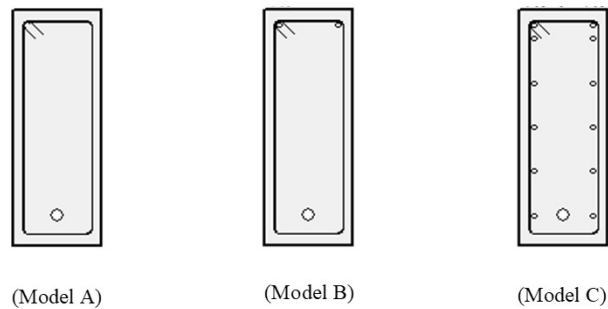


Figure 2. Transversal sections of the models for analysis

It is important to note that the flexural reinforcement of model A correspond to the conventional design defined in ABNT NBR 6118 [7]. In order to evaluate the influence of the secondary superior reinforcement (Model B) and this secondary reinforcement plus the skin reinforcement (Model C), these reinforcements were added to the flexural reinforcement according to the recommendations of this Standard.

3 PROPERTIES OF THE ANALYZED BEAM

For the several analyses, a rectangular beam has been considered, of 30 cm width and 80 cm height. Considered concrete cover is 3 cm. Concerning the materials, concrete class C25 ($f_{ck} = 25$ MPa), steel reinforcement CA 50 ($f_{yk} = 500$ MPa, $f_{yd} = 435$ MPa) and nominal coarse aggregate diameter 10 mm are considered.

The stress-strain relationship for the concrete, in its parabolic branch, as defined in ABNT NBR 6118 [7], is reproduced in Equation 1, in which, for concrete with $f_{ck} \leq 50$ MPa, the considered values are $n = 2$, $\epsilon_{c2} = 2.0$ mm/m and $\epsilon_{cu} = 3.5$ mm/m (in rupture).

$$\sigma_c = 0.85 f_{cd} \left[1 - \left(1 - \frac{\epsilon_c}{\epsilon_{c2}} \right)^n \right] \quad (1)$$

The value for maximum tension of concrete is, according to ABNT NBR 6118 [7], $f_{ctd,inf}$, as defined in Equation 2, being:

$$f_{ctd,inf} = \frac{f_{ctk,inf}}{1.4} \quad (2)$$

and:

$$f_{ctk,inf} = 0.7 f_{ct,m} \quad (3)$$

where:

$$f_{ct,m} = 0.3 f_{ck}^{2/3} \quad (4)$$

Considering $f_{ck} = 25$ MPa, for input in the software, the tension concrete resistance is $f_{ctd,inf} = 1.28$ MPa. The inferior value of the concrete tension resistance was adopted to be consistent with the ABNT NBR 6118 [7] criterion for the shear concrete resistance, that considers this value.

4 LOAD CASES TO BE ANALYZED

As previously stated, nine cases are analyzed, for different values of parameter k_x varying between 0.05 to 0.45, and for each of these values, maximum bending moments resisted by the section are evaluated, considering:

$$k_z = 1 - 0.4 k_x \quad (5)$$

$$k_{md} = 0.68 k_x k_z \quad (6)$$

Where k_z is the non-dimensional value of level arm/effective beam height (z/d) and k_{md} is a non-dimensional bending moment, as defined in Equation 7.

$$M_d = k_{md} b_w d^2 f_{cd} \quad (7)$$

Equations 5 to 7 allows for the evaluation of the maximum bending moments M_d as a function of k_x . From the values of M_d , the corresponding values of the flexural reinforcement A_s are evaluated, with Equation 8:

$$A_s = \frac{M_d}{k_z d f_{yd}} \quad (8)$$

Table 1 presents the numerical values associated with each analyzed case.

Table 1. Summary of numerical values of each case

Case	k_x	k_z	k_{md}	M_{sd} (kNm)	A_s (cm ²)
1	0.050	0.980	0.033	87.47	2.93
2	0.100	0.960	0.065	171.36	5.87
3	0.150	0.940	0.096	251.69	8.80
4	0.200	0.920	0.125	328.44	11.73
5	0.250	0.900	0.153	401.63	14.66
6	0.300	0.880	0.180	471.24	17.60
7	0.350	0.860	0.205	537.29	20.53
8	0.400	0.840	0.228	599.76	23.46
9	0.450	0.820	0.251	658.67	26.39

For each of the nine cases presented next, ten different pairs of maximum bending moments x shear forces were evaluated, each of them associated with a different fraction of the maximum moment M_d . These fractions correspond to values between $0.1 M_d$ to $1.0 M_d$.

The maximum shear forces corresponding to each value of fraction of the maximum moment M_d are evaluated considering Equation 9 from ABNT NBR 6118 [7], which defines the forces $F_{sd,cor}$ in the flexural reinforcement, for the simultaneous action of bending moments and shear forces.

$$F_{sd,cor} = \left[\frac{M_{sd}}{z} + |V_{sd}|(\cot \theta - \cot \alpha) \frac{1}{2} \right] \leq \frac{M_{sd,max}}{z} \tag{9}$$

With:

$$F_{sd,cor} = f_{yd} A_s \tag{10}$$

$$z = k_z d \tag{11}$$

Therefore, the maximum allowed shear force is as defined in Equation 12.

$$V_{sd} = \left(F_{sd,cor} - \frac{M_{sd}}{z} \right) \frac{2}{(\cot \theta - \cot \alpha)} \tag{12}$$

For the angle α , the value 90° is taken (vertical stirrups). For the angle θ , three possibilities are analyzed, $\theta_1=45^\circ$, $\theta_2=30^\circ$ e θ_3 evaluated according to *fib* Model Code 2010 [10]. The *fib* expression for the minimum value of θ is reproduced in Equation 13.

$$\theta_{min} = 20^\circ + 10000 \varepsilon_x \tag{13}$$

Where:

$$\varepsilon_x = \frac{M_{Ed} + V_{Ed} + 0.5 N_{Ed}}{2 E_s A_s} \leq 0.003 \tag{14}$$

and:

ε_x : specific stress at the center of the effective height

M_{Ed} : acting bending moment

N_{Ed} : acting axial force

E_s : steel Young modulus

If the value of ϵ_x results in negative values, it should be taken as zero.

Since for the evaluation of the shear force as defined in Equation 12 is necessary to know the value of θ , and for the evaluation of θ_{min} , as defined in Equation 13 in necessary to know the value of the shear force, a interactive process is necessary until the values of the two angles be coincident.

Then, it is possible to proceed with the evaluation of the shear reinforcement, according to Equation 15.

$$V_{sd} \leq V_{Rd3} = V_c + V_{sw} \tag{15}$$

In order to fix one of the variables of the design, the stirrup spacing is defined as 20 cm, and for defining the necessary shear reinforcement per meter, (A_{sw}/s), a fictitious stirrup ‘‘leg’’ area A_θ is defined as:

$$A_\theta = s_{adot} A_{sw}/s \frac{1}{n} \tag{16}$$

Where:

s_{adot} : adopted stirrup spacing;

A_{sw}/s : necessary shear reinforcement per meter;

n : number of stirrup ‘‘legs’’, fixed in this study as two;

A_θ : area of one stirrup ‘‘leg’’.

For the evaluation of the eventual contribution of the superior secondary reinforcement in the flexural resistance, two bars of 8 mm diameter were considered in the analyses.

Besides this secondary reinforcement, the eventual contribution of the skin reinforcement is also considered. According to ABNT NBR 6118 [7], skin reinforcement is necessary on beams with height superior to 60 cm, with area per meter equal to 0.10% of the concrete section in each vertical face, not superior to 5 cm²/m per face and with spacing not superior to 20 cm.

The defined data can be then introduced in the software Response-2000 [8]. The main screen of the software is shown in Figure 3.

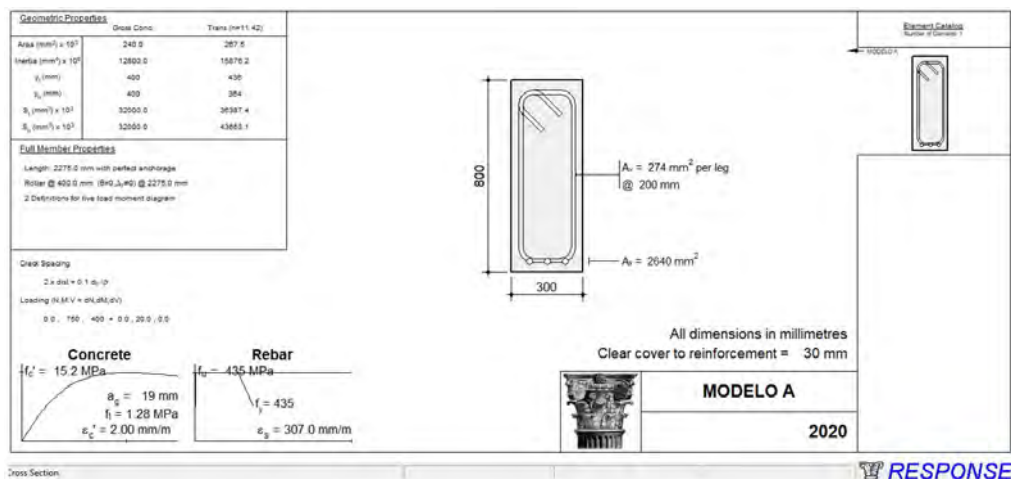


Figure 3. Main screen of Response-2000

For the Response-2000 [8] runs it is necessary to point out that the concrete resistance f_c' considered in the program, correspond to the maximum concrete stress $0.85 f_{cd}$ defined in the Brazilian Standard.

5 RESULTS

Complete results of the performed analysis can be found in Sá [9]. For the sake of concision, results presented herein are only for the value $k_x=0.45$ which correspond to the maximum flexural reinforcement without compression reinforcement.

The presented results correspond to the three considered angles of the diagonal compression struts. For each of them, results corresponding to three reinforcement models are presented: flexural and shear reinforcement (Model A); Model A plus top secondary reinforcement (Model B); Model B plus skin reinforcement (Model C).

Each set of results, initially are presented tables in which: “Case” refers to a fraction, between 1.0 and 0.1 of the maximum moment $M_{sd,max}$ resisted with the reinforcement evaluated with $V_{sd} = 0$ in Equation 9; “ M_{sd} ” correspond to $M_{sd,max}$ times the fraction corresponding to the analyzed case; “ V_{sd} ” is the shear force evaluated according to Equation 12; “ V_{sd}^{final} ” is “ V_{sd} ” limited to V_{rd2} which is the maximum shear force defined in ABNT NBR 6118 [7] corresponding to the maximum compression stress in the diagonal strut (in the analyzed case $V_{rd2} = 911.25 \text{ kN}$); “ V_c ” is the part of the shear force resisted by the complimentary mechanisms in concrete according to ABNT NBR 6118 [7]; “ V_{sw} ” is the part of the shear force resisted by the shear reinforcement. This is the shear reinforcement that will be considered in Response-2000 [8] runs, also considering the minimum shear reinforcement of $3.08 \text{ cm}^2/\text{m}$.

Then, Tables 2 to 5 and Figures 4 and 5 are presented with the relationships between bending moments and allowable shear forces, obtained with the equations of ABNT NBR 6118 [7] and with Response-2000 [8] for reinforcement Models A, B and C.

- Results for $\theta_l = 45^\circ$ (according to Model I of resistance of ABNT NBR 6118 [7])

Table 2. Shear design for θ_l .

Case	M_{sd} (kNm)	V_{sd} (kN)	V_{sd}^{final} (kN)	V_c (kN)	V_{sw} (kN)
1	658.67	0.00	0.00	161.59	0.00
2	592.80	229.50	229.50	161.59	67.91
3	526.93	459.00	459.00	161.59	297.41
4	461.07	688.50	688.50	161.59	526.91
5	395.20	918.00	911.25	161.59	749.66
6	329.33	1147.50	911.25	161.59	749.66
7	263.47	1377.00	911.25	161.59	749.66
8	197.60	1606.50	911.25	161.59	749.66
9	131.73	1836.00	911.25	161.59	749.66
10	65.87	2065.50	911.25	161.59	749.66

Table 3. Shear forces obtained with θ_l .

Case	NBR 6118		Model A		Model B		Model C	
	M_{sd} (kNm)	V_{sd}^{final} (kN)	V_{Rd} (kN)	V_{Rd}/V_{sd}	V_{Rd} (kN)	V_{Rd}/V_{sd}	V_{Rd} (kN)	V_{Rd}/V_{sd}
1	658.67	0.00	0.00	-	0.00	-	0.00	-
2	592.80	229.50	131.05	0.57	142.18	0.62	173.06	0.75
3	526.93	459.00	374.62	0.82	392.18	0.85	444.02	0.97
4	461.07	688.50	640.57	0.93	653.22	0.95	696.78	1.01
5	395.20	911.25	838.44	0.92	845.87	0.93	840.64	0.92
6	329.33	911.25	817.53	0.90	813.25	0.89	850.21	0.93
7	263.47	911.25	704.44	0.77	757.79	0.83	798.83	0.88
8	197.60	911.25	581.64	0.64	713.25	0.78	735.30	0.81
9	131.73	911.25	433.88	0.48	588.94	0.65	698.29	0.77
10	65.87	911.25	306.19	0.34	381.61	0.42	591.55	0.65

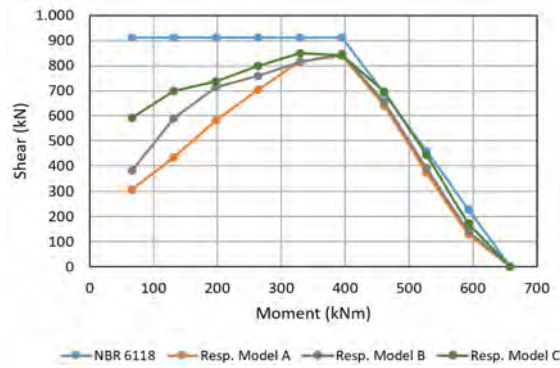


Figure 4. Shear forces obtained with θ_1 .

- Results for $\theta_2 = 30^\circ$ (according to Model II of resistance of ABNT NBR 6118 [7])

Table 4. Shear design for θ_2 .

Case	M_{sd} (kNm)	V_{sd} (kN)	V_{sd}^{final} (kN)	V_{ct} (kN)	V_{sw} (kN)
1	658.67	0.00	0.00	161.59	0.00
2	592.80	132.50	132.50	161.59	0.00
3	526.93	265.00	265.00	134.97	130.04
4	461.07	397.51	397.51	100.85	296.66
5	395.20	530.01	530.01	66.73	463.28
6	329.33	662.51	662.51	32.61	629.90
7	263.47	789.17	789.17	0.00	789.17
8	197.60	789.17	789.17	0.00	789.17
9	131.73	789.17	789.17	0.00	789.17
10	65.87	789.17	789.17	0.00	789.17

Table 5. Shear forces obtained with θ_2 .

Case	NBR 6118		Model A		Model B		Model C	
	M_{sd} (kNm)	V_{sd}^{final} (kN)	V_{Rd} (kN)	V_{Rd}/V_{sd}	V_{Rd} (kN)	V_{Rd}/V_{sd}	V_{Rd} (kN)	V_{Rd}/V_{sd}
1	658.67	0.00	0.00	-	0.00	-	0.00	-
2	592.80	132.50	131.05	0.99	142.18	1.07	173.06	1.31
3	526.93	265.00	170.74	0.64	176.86	0.67	186.88	0.71
4	461.07	397.51	314.43	0.79	317.08	0.80	329.62	0.83
5	395.20	530.01	464.19	0.88	466.90	0.88	471.03	0.89
6	329.33	662.51	603.87	0.91	603.09	0.91	602.99	0.91
7	263.47	789.17	628.72	0.80	624.69	0.79	664.25	0.84
8	197.60	789.17	520.28	0.66	563.75	0.71	597.17	0.76
9	131.73	789.17	388.99	0.49	509.99	0.65	557.52	0.71
10	65.87	789.17	277.25	0.35	342.70	0.43	496.57	0.63

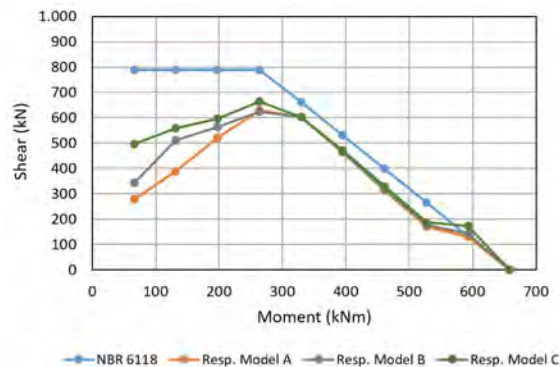


Figure 5. Shear forces obtained with θ_2 .

- Results for θ_3 (according to *fib* Model Code 2010 [10])

For obtaining the maximum allowable shear force, it is necessary firstly to define the strut angle θ . For determining θ_{min} is necessary to know the maximum shear force. Therefore, an interactive process is necessary for equaling the two angles. Tables 6 to 8 present the determination of the angles θ for each considered case.

Table 6. Values of inclination angles θ according to *fib* Model Code 2010 [10]

Case	c	M _{sd} (kNm)	Θ (°)	V _{sd} (kN)	ε _x	θ _{min} (°)
1	1.0	658.67	30.35	0.00	0.00104	30.35
2	0.9	592.80	30.54	135.39	0.00105	30.54
3	0.8	526.93	30.74	273.02	0.00107	30.74
4	0.7	461.07	30.97	413.28	0.00110	30.97
5	0.6	395.20	31.23	556.69	0.00112	31.23
6	0.5	329.33	31.53	703.91	0.00115	31.53
7	0.4	263.47	31.86	855.83	0.00119	31.86
8	0.3	197.60	32.25	1013.63	0.00122	32.25
9	0.2	131.73	32.71	1179.02	0.00127	32.71
10	0.1	65.87	33.26	1354.47	0.00133	33.25

Table 7. Shear design for θ_3 .

Case	M _{sd} (kNm)	V _{sd} (kN)	Θ (°)	V _{rd2} (kN)	V _{sd} ^{final} (kN)	V _{cl} (kN)	V _{sw} (kN)
1	658.67	0.00	30.35	794.70	0.00	161.59	0.00
2	592.80	135.39	30.54	797.59	135.39	161.59	0.00
3	526.93	273.02	30.74	800.74	273.02	133.42	139.60
4	461.07	413.28	30.97	804.21	413.28	98.30	314.98
5	395.20	556.69	31.23	808.04	556.69	62.83	493.86
6	329.33	703.91	31.53	812.31	703.91	26.92	676.99
7	263.47	855.83	31.86	817.09	817.09	0.00	817.09
8	197.60	1013.63	32.25	822.48	822.48	0.00	822.48
9	131.73	1179.02	32.71	828.64	828.64	0.00	828.64
10	65.87	1354.47	33.26	835.74	835.74	0.00	835.74

Table 8. Shear forces obtained with θ_3 .

Case	NBR 6118		Model A		Model B		Model C	
	M _{sd} (kNm)	V _{sd} ^{final} (kN)	V _{Rd} (kN)	V _{Rd} /V _{sd}	V _{Rd} (kN)	V _{Rd} /V _{sd}	V _{Rd} (kN)	V _{Rd} /V _{sd}
1	658.67	0.00	0.00	-	0.00	-	0.00	-
2	592.80	135.39	131.05	0.97	142.18	1.05	173.06	1.28
3	526.93	273.02	170.74	0.63	176.86	0.65	186.88	0.68
4	461.07	413.28	336.91	0.82	337.12	0.82	352.40	0.85
5	395.20	556.69	501.69	0.90	504.68	0.91	509.20	0.91
6	329.33	703.91	653.14	0.93	651.32	0.93	651.91	0.93
7	263.47	817.09	654.76	0.80	653.61	0.80	699.52	0.86
8	197.60	822.48	534.64	0.65	605.11	0.74	638.77	0.78
9	131.73	828.64	398.11	0.48	549.75	0.66	604.55	0.73
10	65.87	835.74	295.46	0.35	356.29	0.43	538.47	0.64

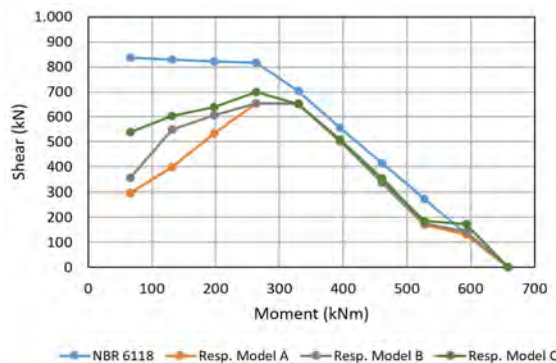


Figure 6. Shear forces obtained with θ_3

6 DISCUSSION OF RESULTS

Observing the results illustrated in Figures 4 to 6, it can be observed that shear design criteria defined in ABNT NBR 6118 [7] are in good agreement with results obtained with the Response-2000 [8] analyses.

However, for low values of bending moments, the allowable shear forces predicted by ABNT NBR 6118 [7] are not attained in the Response-2000 [8] runs. This is because for low values of bending moments, shear forces cause tension forces in the superior part of the beams, where there is not enough flexural reinforcement.

This can occur, as already pointed out by Kotsovou [6], in continuous beams, in spans where there is a change of sign of the bending moments, particularly in points where the bending moments are equal to zero and an important value of shear force is present.

Clearly, the safety in this point can only be achieved with the consideration of an adequate compression reinforcement. For showing this, another situation is analyzed, considering a compression reinforcement equal to the main flexural reinforcement. This is done for the already defined Model A. The analyzed section is presented in Figure 7.

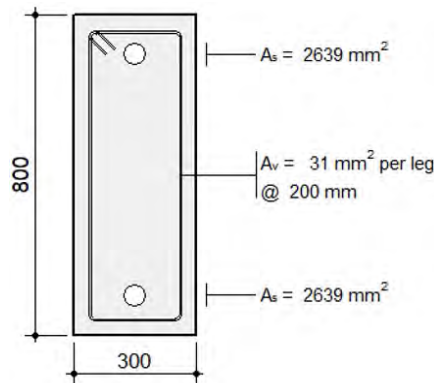


Figure 7. Transversal section with symmetrical reinforcement

The section is processed again, considering the compression reinforcement, being the results presented in Tables 9 to 11 and in Figures 8 to 10. The tables also present the relationship between allowable shear forces obtained with Response-2000 [8] and the ones predicted by ABNT NBR 6118 [7].

Considering the scope of this study, values of this relationship smaller than 1.00 would indicate the cases in which that ABNT NBR 6118 [7] is not safe enough. These can be considered as the final results of the study.

Table 9. Relationship between allowable shears, NBR6118/Response-2000, angle θ_l

Case	NBR 6118		Model A	
	M_{sd} (kNm)	V_{sd}^{final} (kN)	V_{Rd} (kN)	V_{Rd}/V_{sd}
1	658.67	0.00	0.00	-
2	592.80	229.50	180.24	0.79
3	526.93	459.00	411.22	0.90
4	461.07	688.50	656.28	0.95
5	395.20	911.25	840.72	0.92
6	329.33	911.25	851.88	0.93
7	263.47	911.25	853.98	0.94
8	197.60	911.25	820.61	0.90
9	131.73	911.25	817.65	0.90
10	65.87	911.25	818.31	0.90

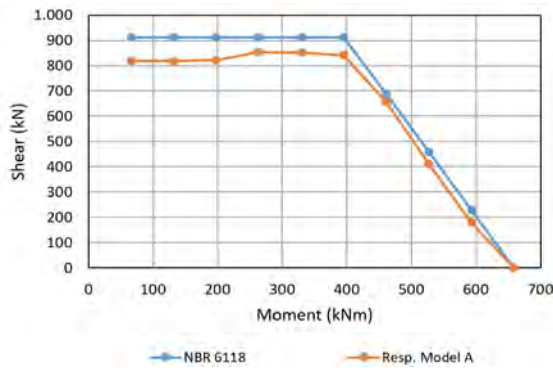


Figure 8. Shear forces obtained with θ_1 . symmetrical reinforcement

Table 10. Relationship between allowable shear, NBR6118/Response-2000, angle θ_2 .

Case	NBR 6118		Model A	
	M_{sd} (kNm)	V_{sd}^{final} (kN)	V_{Rd} (kN)	V_{Rd}/V_{sd}
1	658.67	0.00	0.00	-
2	592.80	132.50	180.24	1.36
3	526.93	265.00	191.63	0.72
4	461.07	397.51	337.01	0.85
5	395.20	530.01	480.50	0.91
6	329.33	662.51	597.44	0.90
7	263.47	789.17	687.46	0.87
8	197.60	789.17	676.36	0.86
9	131.73	789.17	653.55	0.83
10	65.87	789.17	653.82	0.83

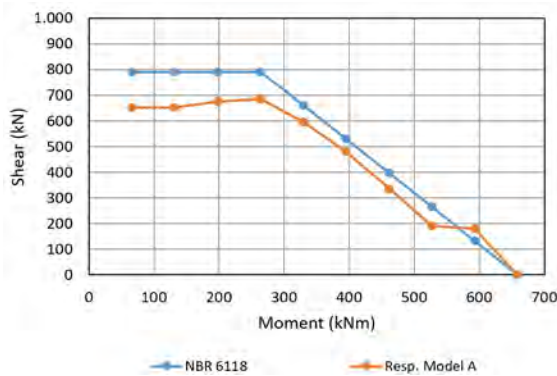


Figure 9. Shear forces obtained with θ_2 . symmetrical reinforcement

Table 11. Relationship between allowable shear, NBR6118/Response-2000, angle θ_3 .

Case	NBR 6118		Model A	
	M_{sd} (kNm)	V_{sd}^{final} (kN)	V_{Rd} (kN)	V_{Rd}/V_{sd}
1	658.67	0.00	0.00	-
2	592.80	135.39	180.24	1.33
3	526.93	273.02	191.63	0.70
4	461.07	413.28	358.75	0.87
5	395.20	556.69	515.81	0.93
6	329.33	703.91	646.83	0.92
7	263.47	817.09	722.71	0.88
8	197.60	822.48	721.19	0.88
9	131.73	828.64	709.27	0.86
10	65.87	835.74	720.36	0.86

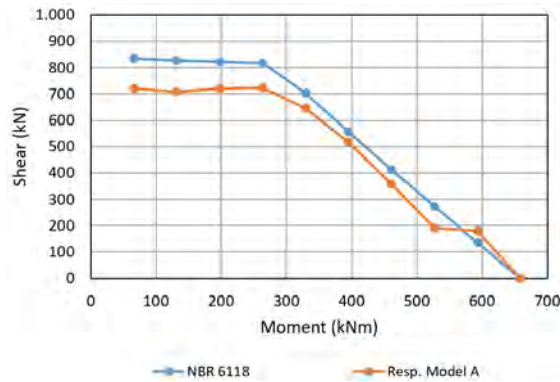


Figure 10. Shear forces obtained with θ_3 . symmetrical reinforcement

Another important issue is the value of V_c , part of the shear force resisted by the complimentary mechanisms of concrete, to be considered in the design. Some standards, such as Eurocode 2 even neglect this contribution. Only for angle θ_2 , a comparison is made, as shown in Figures 11 and 12, with/ without V_c , in which is clear that, without the consideration of V_c , better results are achieved.

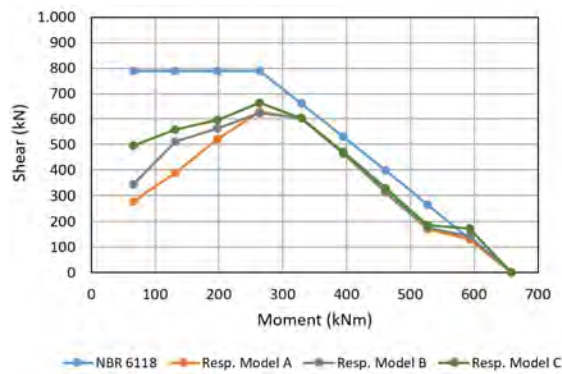


Figure 11. Comparison of results for θ_2 – With V_c

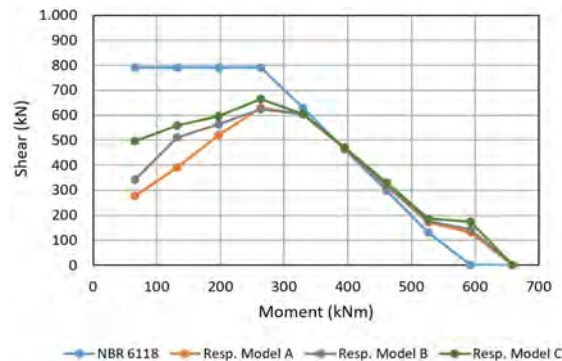


Figure 12. Comparison of results for θ_2 – Without V_c

7 PRACTICAL EXAMPLE

To evaluate the eventual consequence in the current design of beams of the presented results, an example is presented, taken from an actual project.

For the analysis and design of the beam, the system TQS [11] has been used. This system of complete analysis and design of building structures is presently one of the most used in Brazil.

Figures 13 and 14 show, respectively, formwork and perspective drawings of the analyzed beam.

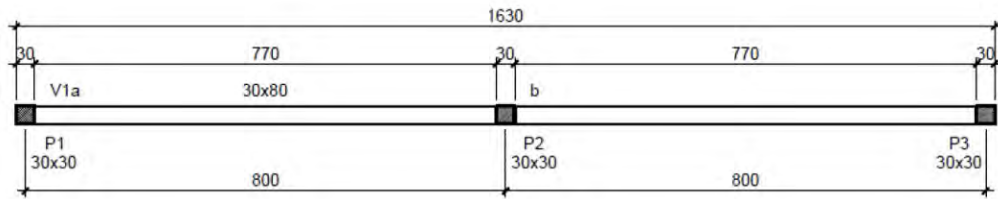


Figure 13. Formwork drawing of the analyzed beam

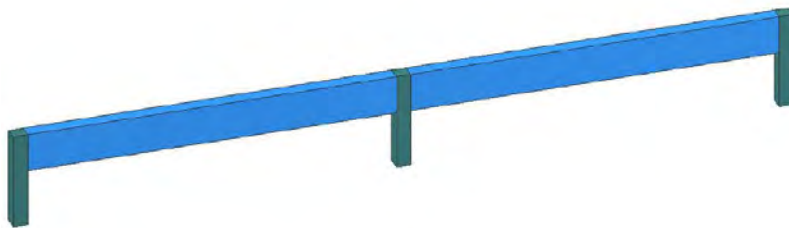


Figure 14. Perspective of the model.

Applied distributed loads in the beam are of 50 kN/m, besides the self-weight, automatically determined by the software. This loading has been adequately chosen in order that the limit of $k_x = 0.45$ be attained. The beams are considered as simply supported in the extreme supports.

Figure 15 shows the bending forces and shear forces diagrams, as well as the selected sections in which the analyses are made: Sections S1 and S4 are a distance d of the supports, Section S2 is in the point of maximum positive bending moment and Section S3 is in the point of zero moment.

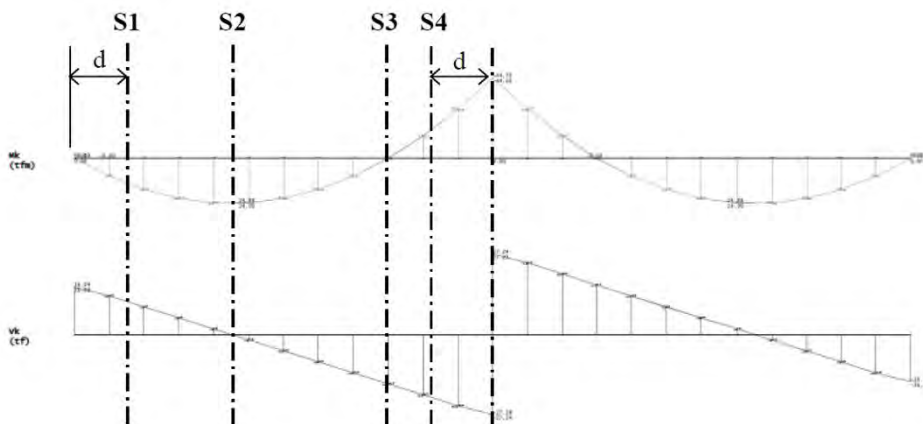


Figure 15. Diagrams of bending moments and shear forces and selected sections.

The shear design is done according to Model I of ABNT NBR 6118 [7]. Table 12 present bending moments and shear forces in the selected sections, with their characteristic and design values, considering $\gamma_f = 1.4$.

Table 12. Characteristic and design forces

Section	TQS Characteristic		TQS Design	
	M_k (kNm)	V_k (kN)	M_d (kNm)	V_d (kN)
S1	108.44	126.23	151.82	176.72
S2	249.00	0.00	348.60	0.00
S3	0.00	-167.90	0.00	-235.06
S4	-254.74	-237.84	-356.64	-332.98

Figure 16 presents the complete reinforcement detailing, automatically performed by the software TQS [11].

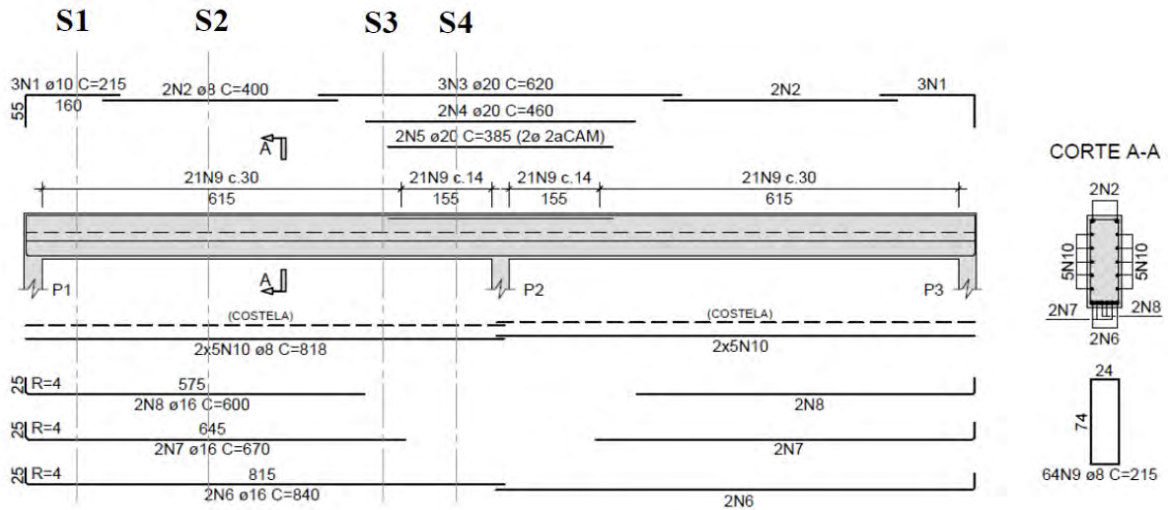


Figure 16. Reinforcement detailing

Tables 13 and 14 show the manual shear design of the selected sections, in order to check the design done by TQS [11].

Table 13. Shear design. Forces.

Section	$ V_d $ (kN)	b_w (m)	d (m)	V_{Rd2} (kN)	V_c (kN)	V_{sw} (kN)
S1	176.72	0.30	0.75	976.34	173.14	3.58
S2	0.00	0.30	0.75	976.34	173.14	0.00
S3	235.06	0.30	0.75	976.34	173.14	61.92
S4	332.98	0.30	0.75	976.34	173.14	159.84

Table 14. Shear design. Reinforcement.

Section	A_{sw}/s^{calc} (cm ² /m)	A_{sw}/s^{min} (cm ² /m)	A_{sw}/s (cm ² /m)	N_{pernas}	ϕ (mm)	s (cm)
S1	0.12	3.08	3.08	2	8.0	32.66
S2	0.00	3.08	3.08	2	8.0	32.66
S3	2.11	3.08	3.08	2	8.0	32.66
S4	5.45	3.08	5.45	2	8.0	18.46

The shear design of the central section is presented in Tables 15 and 16. It can be observed that the shear reinforcement designed by TQS [11] is correct.

Table 15. Shear design. Central support. Forces.

$ V_{d,máx} $ (kN)	b_w (m)	d (m)	V_{Rd2} (kN)	V_c (kN)	V_{sw} (kN)
381.36	0.30	0.75	976.34	173.14	208.22

Table 16. Shear design. Central support. Reinforcement.

A_{sw}/s^{calc} (cm ² /m)	A_{sw}/s^{min} (cm ² /m)	A_{sw}/s (cm ² /m)	N_{pernas}	ϕ (mm)	s (cm)
7.10	3.08	7.10	2	8.0	14.17

The obtained reinforcement is input for analyses with the software Response-2000 [8].

Table 17 shows a comparison between maximum shear forces obtained with TQS [11] and the ones obtained with Response-2000 [8].

Table 17. Comparison between maximum allowable shear forces.

Section	Response-2000		TQS	V_{Rd}/V_{sd}
	$M_{S,d}$ (kNm)	$V_{R,d}$ (kN)	$V_{S,d}$ (kN)	
S1	151.82	253.05	176.72	1.43
S2	348.60	191.14	0.00	-
S3	0.00	-236.18	-235.06	1.00
S4	-356.64	-421.49	-332.98	1.27

In all the analyzed sections, the effective resistant shear forces are equal or superior to the acting shear force, showing the safety of the criteria of ABNT NBR 6118 [7].

Special attention is given to the point of zero moment. For a better understanding of the behavior in S3, some results obtained with Response-2000 [8] are presented in Figures 17 to 19.

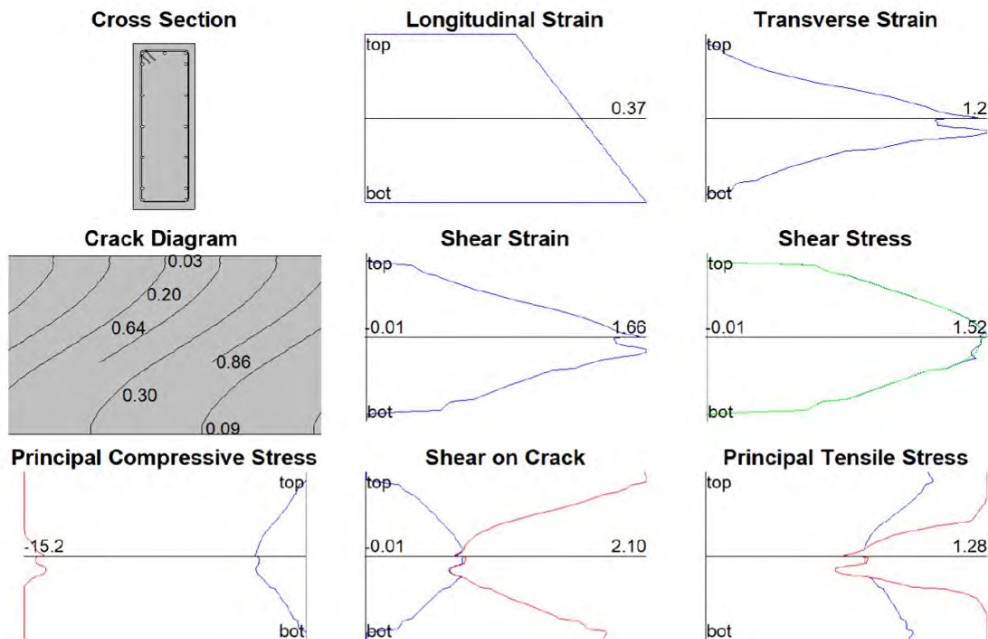


Figure 17. General results of the section – Response-2000

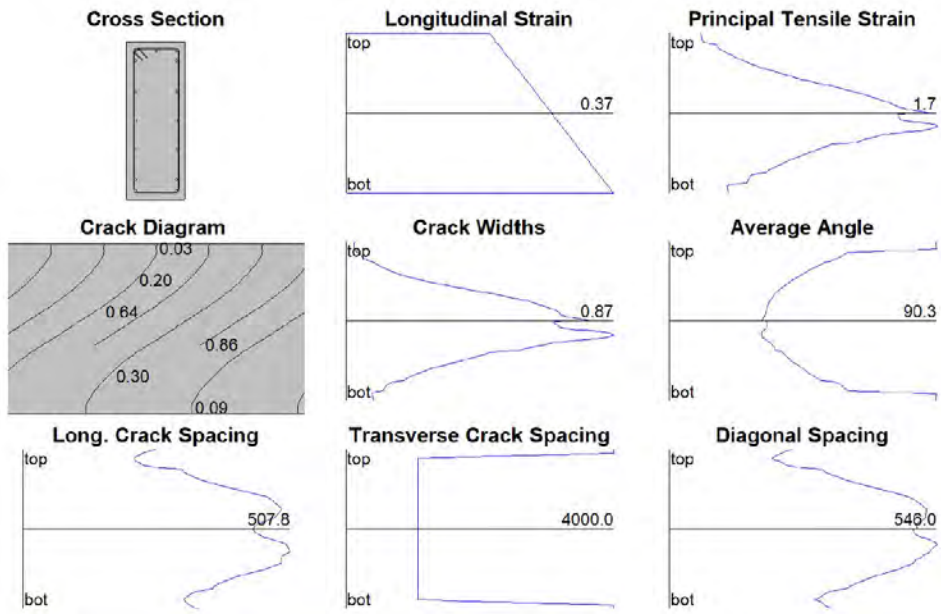


Figure 18. Results related to the cracks – Response-2000

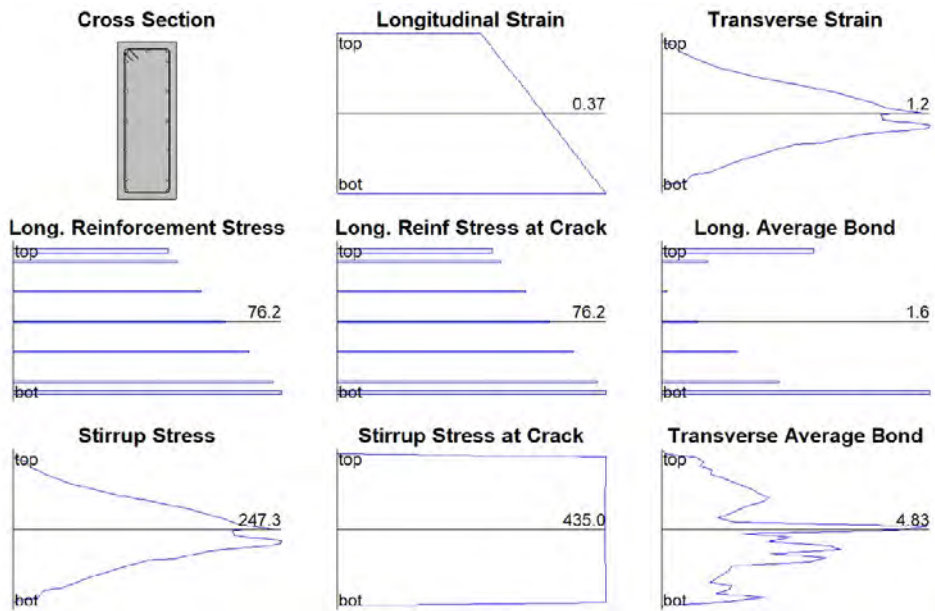


Figure 19. Results related to the reinforcement – Response-2000

It can be observed that the section is fully cracked throughout its height. This is due to the fact that, since the moment is null, the compression due to the flexural binary does not exist, being then the beam totally tensioned by the force due to the compressed diagonal, making all the section more fragile.

Evaluating the results related to the reinforcement, the rupture of the section is due to the yielding of the transversal reinforcement in the cracks, which is a verification made in the MCFT, not done in the usual shear design.

Another observation is that the MCFT considers the presence of all the reinforcement present in the section, including the skin reinforcement, not considered in the usual design. For evaluate the importance of this detail, the beam is verified also without the skin reinforcement. Results are presented in Table 18.

Table 18. Comparison between maximum allowable shear forces. No skin reinforcement.

Section	Response-2000		TQS	V_{Rd}/V_{sd}
	$M_{S,d}$ (kNm)	$V_{R,d}$ (kN)	$V_{S,d}$ (kN)	
S1	151.82	264.79	176.72	1.50
S2	348.60	80.51	0.00	-
S3	0.00	-218.04	-235.06	0.93
S4	-356.64	-415.95	-332.98	1.25

As seen in Table 18, without the skin reinforcement, the relationship resisting/ acting shear force is now 0.93, i.e. the beam is not able to resist to the acting shear force according to the MCFT.

Another analysis is done, considering skin reinforcement, but not respecting the minimum reinforcement of ABNT NBR 6118 [7]. The shear design is shown in Table 19.

Table 19. Shear design. No minimum reinforcement.

Section	A_{sw}/s^{calc} (cm^2/m)	N_{pernas}	ϕ (mm)	s (cm)
S1	0.12	2	5.0	321.48
S2	0.00	2	5.0	-
S3	2.11	2	6.3	29.55
S4	5.45	2	8.0	18.46

Since the design of section S1 led to a great reinforcement spacing a value of 30 cm is adopted for the Response-2000 [8] runs. For section S2 the same spacing is considered.

Comparison between allowable shear forces is presented in Table 20.

Table 20 Comparison between maximum allowable shear forces. No minimum shear reinforcement

Section	Response-2000		TQS	V_{Rd}/V_{sd}
	$M_{S,d}$ (kNm)	$V_{R,d}$ (kN)	$V_{S,d}$ (kN)	
S1	151.82	191.29	176.72	1.08
S2	348.60	100.33	0.00	-
S3	0.00	-224.68	-235.06	0.96
S4	-356.64	-347.03	-332.98	1.04

In this case, the results of the previous analytical results are confirmed, and a safety relationship is usually slightly superior to 1.00.

However, in section S3, although not being the one of maximum shear force, present insufficient safety. The TQS design, strictly in accordance with ABNT NBR 6118 [7], presents a resisting shear force of 235.06kN. The shear force evaluated with Response-2000 [8] is 224.68kN, showing that the section of null moment could be the critical one in a continuous beam, for the design following the criteria of ABNT NBR 6118 [7].

8 CONCLUSIONS

From the extensive studies summarized herein, some conclusions can be drawn.

Considering the sophisticated design criteria of MCFT, the state-of-the-art criteria for the combined bending moments-shear forces design according to the *fib* Model Code 2000 [10], the results obtained applying the criteria of ABNT NBR 6118 [7] led to a safe and economical design.

Nevertheless, in situations of small bending moments and high shear forces, such as points of zero moments in continuous beams, the actual criteria can lead to results against safety. As shown in the text, in these regions the situation of the concrete section presents great fragility, being tensioned throughout its high. Critical design situations can be presented in these regions, not considered in the usual design.

Another point that deserves future attention is that better results are obtained with the shear forces being totally resisted by the shear reinforcement ($V_c = 0$), indicating that perhaps the value of V_c could be overestimated by ABNT NBR 6118 [7].

Regarding the secondary reinforcement, it has been shown that the superior horizontal reinforcement can be considered in the usual evaluation of the resistance, but its contribution is small. Inversely, skin reinforcement is not usually considered in the evaluation of the resistance, but its contribution can be relatively important.

As pointed out by Schulz [12] shear rupture mechanisms in reinforced concrete sections are very complex, of fragile character and without possibility of redistribution of forces. This opens a vast field of research in this subject.

REFERENCES

- [1] E. C. Bentz, F. J. Vecchio, and M. P. Collins, "Simplified Oents," *ACI Struct. J.*, vol. 103, no. 4, pp. 614–624, Jul-Aug 2006.
- [2] W. Ritter, *Die Bauweise Hennebique (Construction Techniques of Hennebique)*. Zürich: Schweizerische Bauzeitung, 1899.
- [3] E. Mörsch, *Concrete Steel Construction*. New York: McGraw-Hill, 1909.
- [4] F. J. Vecchio, "Analysis of shear-critical reinforced concrete beams", *ACI Struct. J.*, vol. 97, no. 1, pp. 102-110, Jan-Feb, 2000.
- [5] M. P. Collins, E. C. Bentz, P. T. Quach, and G. T. Proestos, "Predicting the shear strength of thick slabs," in *Towards a Rational Understanding of Shear in Beams and Slabs*, Switzerland, FIB International, 2018, fib. Bulletin, ch. 3, vol. 85, no. 3, <https://dx.doi.org/10.35789/fib.BULL.0085.Ch03>.
- [6] G. Kotsovou, "Assessment of reinforced concrete shear design methods and proposed improvements," *ACI Struct. J.*, vol. 116, no. 2, pp. 41–52, Mar 2019.
- [7] Associação Brasileira de Normas Técnicas, *Projeto de Estruturas de Concreto – Procedimento*, ABNT NBR 6118, 2014.
- [8] E. C. Bentz, M. P. Collins, *User Manual – Membrane-2000, Response-2000, Triax-2000, Shell-2000. Version 1.1*, Toronto, University of Toronto, Sept. 2001.
- [9] M. A. de Sá "Avaliação dos critérios de verificação a cisalhamento segundo a NBR 6118 aplicando a teoria do campo de compressão modificada", M.Sc. Thesis, Dept. Estrut., Esc. Politécnica, Univ. Fed. Rio de Janeiro, Rio de Janeiro, RJ, 2021.
- [10] International Federation for Structural Concrete, *fib Model Code for Concrete Structures 2010*, Hoboken: Wiley, 2013.
- [11] TQS Informática. "V21", TQS. <https://www.tqs.com.br/v21/#/> (accessed Dec. 12, 2022).
- [12] M. Schulz, "Análise de Peças Lineares de Concreto Armado Baseada na Mecânica das Estruturas", M.Sc. Thesis, Inst. Alberto Luiz Coimbra de Pós-grad. Pesq. Eng., Univ. Fed. Rio de Janeiro, Rio de Janeiro, RJ, 1981.

Author contributions: SHCS conceptualization, supervision, writing; MAS: data processing, writing; JJHSF: revision.

Editors: Leandro Trautwein, Mauro Real, Mario Pimentel.



ORIGINAL ARTICLE

Numerical simulation of punching shear failure in recycled aggregate concrete slabs with steel fiber reinforcement

Simulação numérica de ruptura por punção em lajes de concreto com agregado reciclado com reforço de fibra de aço

Alana Helena Cara Siqueira^a Marcela Gimenes^a Osvaldo Luís Manzoli^a Eduardo Alexandre Rodrigues^a

^aUniversidade Estadual Paulista, Departamento de Engenharia Civil e Ambiental, Bauru, SP, Brasil

Received 02 December 2022

Accepted 04 April 2023

Abstract: The use of construction waste as aggregate in the production of concrete is becoming a more frequent alternative due to the advantages associated with the sustainability aspect. Results obtained in experimental tests with recycled aggregate concrete suggest that mechanical properties such as elastic modulus, compressive, tensile and flexural strength tend to reduce with partial or total replacement of natural aggregate by recycled one. On the other hand, the use of steel fiber reinforcement can minimize the reduction of these properties, since the fibers tend to improve the material strength and ductility. This work proposes a numerical approach, seeking to better predict and understand the structural mechanical behaviors and failure patterns of reinforced recycled aggregate concrete slabs with and without steel fiber. Based on the finite element method, an appropriated constitutive damage model is employed to represent the nonlinear behavior of the conventional/recycled concrete, while an elastic-perfectly plastic model is used to describe the mechanical behavior of the reinforcements. To couple the independent FE meshes and incorporate the mutual interaction between the different components, rigid and non-rigid coupling technique is used to represent the perfect adherence or the bond-slip behavior. Seven concrete slabs were numerically analyzed either with different percentages of recycled aggregate replacement (0, 50 and 100%) or steel fibers content (0.0, 0.5 and 1.0%) and the results were compared with the experimental ones. The results showed that the applied methodology is capable of simulating with good accuracy the punching shear failure mechanism of the slabs. It was observed that the punching ultimate load decreased with increase of recycled aggregate content, as well as that the steel fiber addition can minimize the negative effects of recycled aggregate employment.

Keywords: recycled aggregate, steel fiber, punching failure, finite element, constitutive models.

Resumo: A utilização de resíduos da construção civil como agregado na produção de concreto vem se tomando uma alternativa cada vez mais frequente devido às vantagens associadas ao aspecto da sustentabilidade. Resultados obtidos em ensaios experimentais com concreto de agregado reciclado sugerem que propriedades mecânicas como módulo de elasticidade, resistência à compressão, tração e flexão tendem a diminuir com a substituição parcial ou total do agregado natural pelo reciclado. Por outro lado, a utilização de reforço de fibras de aço pode minimizar a redução dessas propriedades, uma vez que as fibras tendem a melhorar a resistência e a ductilidade do material. Este trabalho propõe uma abordagem numérica, buscando melhor prever e entender os comportamentos mecânicos estruturais e os modos de falha de lajes de concreto com agregado reciclado armado com e sem fibra de aço. Com base no método dos elementos finitos, um modelo constitutivo de dano apropriado é empregado para representar o comportamento não linear do concreto convencional/reciclado, enquanto que um modelo elástico-perfeitamente plástico é usado para descrever o comportamento mecânico das armaduras. Para acoplar as malhas de EF independentes e incorporar a interação mútua entre os diferentes componentes, a técnica de acoplamento rígido e não rígido é usada para representar a aderência perfeita ou o comportamento de perda de aderência (*bond-slip*). Sete lajes de concreto foram analisadas numericamente com diferentes porcentagens de substituição de agregado reciclado (0, 50 e 100%) ou teores de fibras de aço (0,0; 0,5 e 1,0%) e os resultados foram comparados com os experimentais. Os resultados mostraram que a metodologia aplicada é capaz de simular com boa precisão o mecanismo de ruptura por punção das lajes. Observou-se que a capacidade de carga à

Corresponding author: Alana Helena Cara Siqueira. E-mail: alana.hc.siqueira@unesp.br

Financial support: CAPES (Finance Code 001), CNPq (Proc.: 423379/2016-0 and 310401/2019-4) and FAPESP (Process: 2020/16789-6).

Conflict of interest: Nothing to declare.

Data Availability: The data that support the findings of this study are available from the corresponding author, AHCS, upon reasonable request.



This is an Open Access article distributed under the terms of the Creative Commons Attribution License, which permits unrestricted use, distribution, and reproduction in any medium, provided the original work is properly cited.

punção diminuiu com o aumento do teor de agregado reciclado, assim como que a adição de fibra de aço pode minimizar os efeitos negativos do emprego de agregado reciclado.

Palavras-chave: agregado reciclado, fibras de aço, falha por punção, elementos finitos, modelos constitutivos.

How to cite: A. H. C. Siqueira, M. Gimenes, O. L. Manzoli, and E. A. Rodrigues, "Numerical simulation of punching shear failure in recycled aggregate concrete slabs with steel fiber reinforcement" *Rev. IBRACON Estrut. Mater.*, vol. 16, no. 3, e16310, 2023, <https://doi.org/10.1590/S1983-41952023000300010>

1 INTRODUCTION

Flat reinforced concrete slabs can suffer punching shear failure under the action of concentrated load, in general, at the column location. Some conditions which influence punching behavior are slab area, position of force application, concrete compressive strength, span length, slab thickness, flexural reinforcement and supporting conditions. Due to its brittle and sudden failure mechanism, combined with environmental actions that seek to partially or totally replace the natural coarse aggregates by recycled aggregate, the punching shear failure in recycled aggregate concrete (RAC) slabs has been a topic of great interest for the scientific community, since the use of recycled aggregates can significantly reduce the mechanical properties of the concrete, contributing negatively to this failure mode [1]–[3].

Driven by some of its advantages, such as its easy molding and both relatively high compressive strength and low cost, concrete is one of the most widely used building materials, requiring a large availability of natural aggregates, around 60%–75% of the total concrete volume, whose production contributes significantly to carbon emission [4]. Another result of concrete large-scale use for decades is the large amount of waste produced by construction activities or demolitions, whose disposal also negatively contributes to the environment [5]. Thus, the use of recycled concrete aggregates (RCA), which are obtained by crushing concrete waste, brings great economic and environmental advantages, being an alternative to natural aggregates [4], [5]. However, its effects on the mechanical properties of the new recycled aggregate concrete need to be better understood. Due to its high degree of heterogeneity, recycled concrete may have lower mechanical properties than conventional concrete, such as, for example, lower compressive and tensile strengths, as well as significant reductions in the modulus of elasticity and fracture energy [6]–[9].

Seeking to overcome these disadvantages, recent studies have investigated the benefits arising from the inclusion of steel fibers in their composition, which could improve the mechanical properties of the recycled aggregate concrete [10]–[12]. As demonstrated in the studies carried out by these authors, the appropriate addition of steel fiber volumetric ratios can mitigate the disadvantages provided by the replacement percentages of recycled aggregates, such as compressive, tensile and bending strengths, providing beneficial effects on the fracture propagation process in recycled concrete. Experimental results performed by Xie et al. [13] also indicate a significant increase in flexural and tensile strength, highlighting the bridging effect provided by the fibers, which works to contain fracture initiation and propagation. Previous experiments carried out by Carneiro et al. [14] also showed similar results, as the addition of fibers resulted in the increase of all mechanical properties and better controlled the fracture propagation process in recycled concrete. The experimental studies provided by Xiao et al. [1] also show that steel fibers can improve the punching shear and energy dissipation capacities, as well as the ductility and deformations, even for the slabs with a total replacement of natural aggregate by recycled one.

Efforts have been made to develop numerical models to simulate and better understand the effects arising from both the natural aggregate and the partial or total replacement of natural aggregate by recycled aggregate, on the mechanical properties of conventional and fiber-reinforced recycled concrete [15]–[20]. In these models, more realistic geometric representations of the recycled concrete constituents can be adopted, making it possible to explicitly consider some of its heterogeneity, normally observed in the micro and mesoscopic scales, to the numerical analyses. Although this explicit representation can bring more accurate answers, the analyzes can become extremely computationally expensive, making it impossible to carry out 3D problems or perform a large number of simulations, considering varied conditions, for example, different replacement percentages of recycled aggregates. On the other hand, macroscopic models can be used, considering recycled concrete as a homogeneous material, using homogenized elastic and fracture properties (average properties), making it possible to carry out three-dimensional analyzes with much less computational time, and still bring valuable answers about the mechanical behavior of this material.

Therefore, this work proposes a numerical approach to predict and better understand the punching failure behavior of reinforced recycled aggregate concrete slabs either with different replacement percentages of recycled concrete or steel fiber volumetric ratios, which were experimentally performed by Xiao et al. [1], comparing both the experimental found in the literature [1] and numerical responses obtained. The numerical model is based on the Finite Element Method, in which regular tetrahedral finite elements are used to discretize the recycled concrete domain on the

macroscopic scale, while unidimensional finite elements are used to discretize the steel bars and fibers reinforcements. Based on the Continuum Damage Mechanics Theory (CDMT), the constitutive damage model proposed by Cervera et al. [21] is used to represent the nonlinear behavior of the recycled concrete, while an elastic-perfectly plastic model described in Simo and Hughes [22] is employed to simulate the yielding process of steel bars and fibers. To couple these independent FE meshes, the rigid and non-rigid coupling scheme proposed by Bitencourt et al. [23], [24] is properly used to respectively represent the perfect bond or the complex bond-slip phenomenon between the recycled concrete and the steel bars and fibers reinforcements. Seeking to improve the computational stability and robustness of the solution involving cracks propagation in the RAC, mechanical behavior of steel bars and fiber-RAC bond-slip relation, for all the constitutive models adopted the implicit-explicit integration scheme proposed by Oliver et al. [25] and efficiently applied for elastoplasticity problems by Prazeres et al. [26] is employed.

2 METHODOLOGY

The proposed 3D numerical model to simulate reinforced recycled aggregate concrete slabs with different contents of recycle aggregates and steel fibers is based on the Finite Element Method, assuming a macroscopic scale approach, in which the concrete is treated as a homogeneous material, employing homogenized material properties. The main ingredients of the numerical modeling process, formulated and implemented an *in-house* FE computer program in MATLAB®, can be divided into two parts: the FE modeling strategy, in which the tasks still in the pre-processing stage are performed; the constitutive models applied to simulate the individual mechanical behavior of the different components of the slabs (i.e. recycled concrete, steel bars and fibers and even the mutual interaction between them) that working together are able to represent the complex punching failure phenomenon of RAC slabs.

2.1 FE Modeling strategy

The first modeling step is to geometrically design the slab components and apply the boundary conditions (essential and natural), as illustrated in Figure 1, where due to the symmetry of problem, only a quarter of slab is numerically modeled, in which the normal displacements on the two symmetry-planes are restricted. Then, the independent FE meshes of the recycled concrete, steel bars and fibers reinforcements are generated, as illustrated in Figure 2, using the pre and post processing program GiD®, developed by CMNE (“International Center for Numerical Methods in Engineering”) of the Polytechnic University of Catalonia. The concrete domain is discretized by conventional tetrahedral finite elements and both the steel bars and fibers by one-dimensional truss elements. The support that allows upward vertical displacement is also modeled by one-dimensional bar elements.

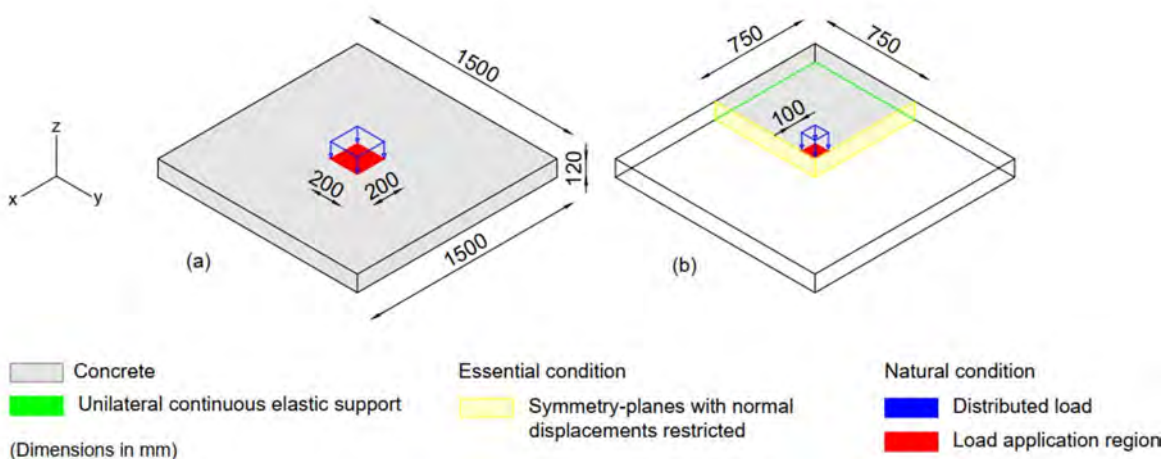


Figure 1. Dimensions of experimental (a) and numerically modeled slab, with its boundary conditions (b).

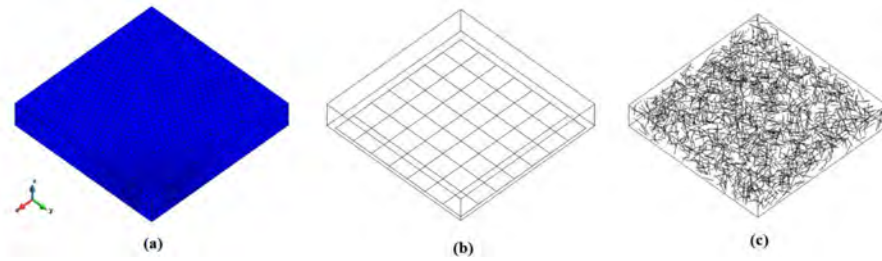


Figure 2. Independent meshes of concrete (a), steel bars (b) and fibers (c).

To couple these independent meshes, the coupling finite elements (CFEs) proposed by Bitencourt et al. [21] are used, as illustrated in Figure 3. These coupling elements are defined from the conventional four-noded tetrahedral elements with an additional node that corresponds to the node of the bars or fibers, called as loose node by the authors [21], located in the domain of the corresponding tetrahedron (Figure 4). As demonstrated by the authors, the CFEs technique do not increase the number of degrees of freedom of the system and both rigid and non-rigid coupling scheme can be assumed [23], [24].

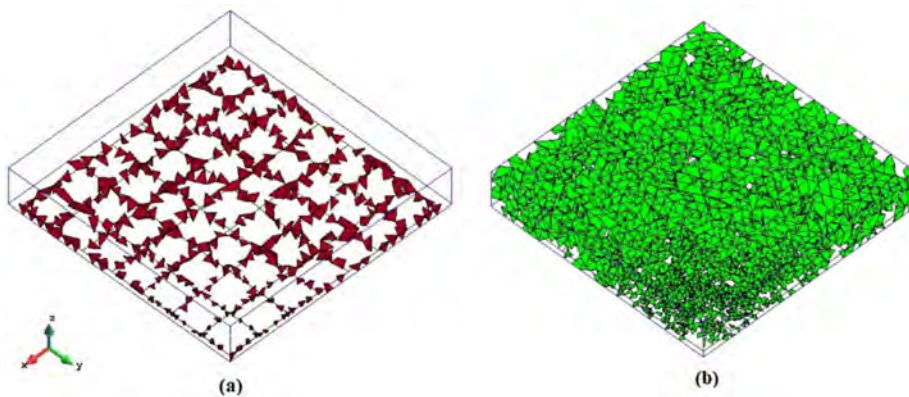


Figure 3. Details about the CFEs meshes used to couple the steel bars (a) and fibers (b) in the RAC mesh.

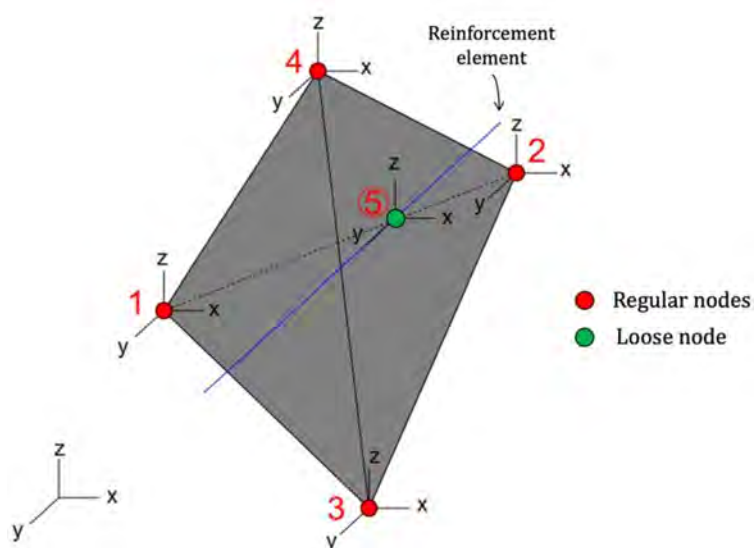


Figure 4. CFE defined from four-noded tetrahedral element with the additional coupling node.

2.2 Constitutive models

2.2.1 Continuum damage model for RAC

To represent the nonlinear behavior of the RAC, the damage model proposed by Cervera et al. [21] is used, in which for the sake of simplicity the compressive behavior is assumed to be linear elastic. Thus, the effective stress tensor ($\bar{\sigma}$) is split in tensile ($\bar{\sigma}^+$) and compressive ($\bar{\sigma}^-$) components, and only the tensile damage variable (d^+) is defined and applied to reduce the effective tensile stress ($\bar{\sigma}^+$), as described by Equation 1.

$$\sigma = (1 - d^+) \bar{\sigma}^+ + \bar{\sigma}^- \quad (1)$$

where $0 \leq d^+ \leq 1$ and σ is the current stress tensor.

The equivalent effective tensile norm $\bar{\tau}^+$ is defined according to Equation 2, as:

$$\bar{\tau}^+ = \sqrt{\bar{\sigma}^+ : \mathbf{D}_0^{-1} : \bar{\sigma}^+} \quad (2)$$

where \mathbf{D}_0^{-1} is the inverse fourth-order linear-elastic constitutive tensor.

To determine the elastic domain and the beginning of degradation growth, the damage criteria g^+ (tension) is introduced by Equation 3:

$$g^+(\bar{\tau}^+, r^+) = \bar{\tau}^+ - r^+ \leq 0 \quad (3)$$

The variable r^+ is the current damage thresholds and its evolution can be obtained by assuming the highest value reached by $\bar{\tau}^+$, as described by Equation 4.

$$r^+ = \max(r_0^+, \max(\bar{\tau}^+)) \quad (4)$$

The initial value of the initial damage thresholds r_0^+ is the tensile strength of the material (f_t).

Finally, the damage evolution rule for tension is given by Equation 5:

$$d^+ = 1 - \frac{r_0^+}{r^+} e^{A^+ (1 - \frac{r^+}{r_0^+})} \quad (5)$$

where A^+ is the softening parameter derived from the fracture energy and the characteristic length.

More details about this model can be found Cervera et al. [21].

2.2.2 Elastoplastic model for steel bars and fibers reinforcements

To represent the mechanical behavior of the steel bars and fibers a perfect elastoplastic model is used. As illustrated in Figure 5, the stress-strain constitutive relation is based on the Young's modulus E_s and the yield stress f_y properties of the material. Details about this model can be found in Simo and Hughes [22].

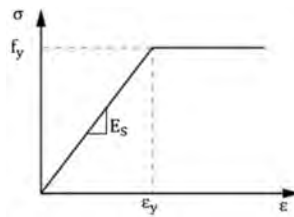


Figure 5. Perfect elastoplastic model assumed for the bars and fibers.

2.2.3 CFE model for bars and fibers reinforcements-RAC interactions

To represent the mutual interaction between the reinforcements (steel bars and fibers) and the RAC, the rigid and non-rigid coupling technique proposed by Bitencourt et al. [23], [24] is used, which has also recently been used to couple non-conforming meshes in multiscale concrete approaches [27]–[29].

According to this technique, in which independent FE meshes can be assumed, the reinforcement contribution is added according to the global internal force vector (\mathbf{F}^{int}) and stiffness matrix (\mathbf{K}) presented in Equations 6 and 7.

$$\mathbf{F}^{int} = \underbrace{\mathbf{A}_{e=1}^{nel\Omega^C} \mathbf{F}_{e,\Omega^C}^{int}}_{\text{concrete elements}} + \underbrace{\mathbf{A}_{e=1}^{nel\Omega^B} \mathbf{F}_{e,\Omega^B}^{int}}_{\text{bars}} + \underbrace{\mathbf{A}_{e=1}^{nel\Omega^F} \mathbf{F}_{e,\Omega^F}^{int}}_{\text{fibers}} + \underbrace{\mathbf{A}_{e=1}^{nel\Omega^{CFE}} \mathbf{F}_{e,\Omega^{CFE}}^{int}}_{\text{coupling elements}} \quad (6)$$

$$\mathbf{K} = \underbrace{\mathbf{A}_{e=1}^{nel\Omega^C} \mathbf{K}_{e,\Omega^C}}_{\text{concrete elements}} + \underbrace{\mathbf{A}_{e=1}^{nel\Omega^B} \mathbf{K}_{e,\Omega^B}}_{\text{bars}} + \underbrace{\mathbf{A}_{e=1}^{nel\Omega^F} \mathbf{K}_{e,\Omega^F}}_{\text{fibers}} + \underbrace{\mathbf{A}_{e=1}^{nel\Omega^{CFE}} \mathbf{K}_{e,\Omega^{CFE}}}_{\text{coupling elements}} \quad (7)$$

In these equations \mathbf{A} is the conventional FE assembly operator. The first, second and third terms are related to the respective independent FE meshes of the RAC, steel bars and fibers. The fourth term is associated with the CFE scheme.

As demonstrated by the authors [23], [24] this technique can be used to represent rigid coupling (perfect bond) between the reinforcements and the RAC. In this case, it is sufficient to assume a linear relationship between reaction force, \mathbf{F} , and relative displacement, $[\mathbf{U}]$, described in Equation 8, and assume high values for the penalty parameters \tilde{C} presented in Equation 9.

$$\mathbf{F} = \mathbf{C}[\mathbf{U}] \quad (8)$$

$$\mathbf{C} = \begin{bmatrix} \tilde{C} & 0 & 0 \\ 0 & \tilde{C} & 0 \\ 0 & 0 & \tilde{C} \end{bmatrix} \quad (9)$$

On the other hand, a non-rigid coupling can be considered, in which the complex bond-slip phenomenon between reinforcements and RAC is explicitly simulated. Thus, the relationship described in Equation 8 is now governed by an appropriate constitutive damage model with a hardening/softening law formulated to properly describe the bond-slip curve proposed by CEB *Fib* Model Code [30] (See Figure 6), in which the shear stress (τ) as a function of the relative displacement (s) for monotonic pullout test is given by Equation 10.

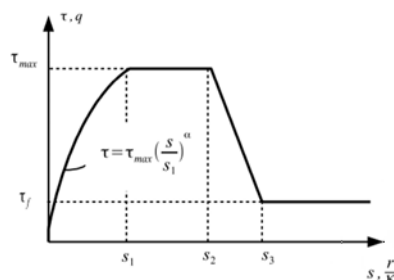


Figure 6. Interface stress bond-slip relationship (monotonic loading) proposed by CEB *Fib* Model Code [30].

$$\tau(s) = \begin{cases} \tau_{max} \left(\frac{s}{s_1}\right)^\alpha & \text{if } s \leq s_1 \\ \tau_{max} & \text{if } s_1 \leq s \leq s_2 \\ \tau_{max} - \frac{(\tau_{max}-\tau_f)(s-s_2)}{(s_3-s_2)} & \text{if } s_2 \leq s \leq s_3 \\ \tau_f & \text{if } s > s_3 \end{cases} \quad (10)$$

It is important to note that α , maximum shear stress τ_{max} , residual shear stress τ_f and the relative displacements s_i ($i = 1, 2, 3$) are parameters associated with concrete strength (f_{ck}), bar geometry, confining situation and bond condition [30]. More details description of this model can be found in Bitencourt et al. [23], [24].

For the sake of simplicity, in the proposed approach a rigid coupling (perfect-bond) between the steel bars and RAC is assumed, while the described non-rigid coupling is used to represent the bond-slip behavior between the steel fibers and the RAC.

3 NUMERICAL SIMULATIONS

The numerical modeling performed in this study was based on the experimental tests proposed by Xiao et al. [1], in which a series of reinforced concrete slabs with different contents of recycled coarse aggregate and steel fibers were tested in laboratory, in order to investigate the complex punching shear behavior. The natural coarse aggregates were gravel stones, and the recycled coarse aggregates used came from the demolition of concrete with average compressive strength of 30 MPa, with diameter size dimensions varying from 5 to 15 mm and from 15 to 25 mm. The steel fibers were wire-type shaped with angles on both ends, average length of 50 mm, diameter of 0.9 mm, with volumetric ratios of 0.5% (39.3 kg/m³) and 1.0% (78.5 kg/m³) being used. The reinforcements were hot-rolled ribbed bars, with 12 mm diameter, 100 mm apart with reinforcement ratio of 1.142%. The slabs were positioned in a reinforced concrete frame with an angle steel frame in four simply-supported edges boundary conditions, applying concentrated load with constant speeds, until the complete failure of the slabs.

In this paper, the slabs numerically simulated are: 0% (RAC0), 50% (RAC50-0%) and 100% (RAC100-0%) of recycled aggregate replacement with bars and without fibers; 50% of recycled aggregate with bars and varying the amount of fibers in 0.5% and 1% (SFRAC50-0.5% and SFRAC50-1%, respectively) and 100% of recycled aggregate, with bars varying the fiber content in 0.5% and 1%. (SFRAC100-0.5% and SFRAC100-1%, respectively).

The numerical parameters used are presented in Table 1. The Young's modulus was provided by the experimental results [1] and the Poisson's ratio, as its value was not informed in the experiment, the typical value of 0.2 was adopted. The average tensile strength ($f_{ct,m}$) was obtained by Equation 11 (NBR 6118 [31]), for concrete classes up to C50:

$$f_{ct,m} = 0,3 f_{ck}^{\frac{2}{3}} \quad (11)$$

where f_{ck} is the characteristic compressive strength of concrete.

The value of fracture energy (G_F) was given by Equation 12, according to CEB *Fib* Model Code [30].

$$G_F = G_{F0} \left(\frac{f_{cm}}{10}\right)^{0,7} \quad (12)$$

where f_{cm} is the average compressive strength and G_{F0} is constant, determined by the maximum diameter of the coarse aggregates (CEB *Fib* Model Code [30]). The aggregates in the experiment had a maximum diameter of 25 mm. Thus, the value $G_{F0} = 0.04575 \text{ Nmm/mm}^2$ is used.

Table 1. Parameters assumed for the RAC.

Specimen	Modulus of elasticity (MPa) (x 10 ⁴)	Tensile strength (MPa)	Fracture energy (N/mm)	Poisson Ratio
RAC0	3.73	3.50	0.1205	0.2
RAC50-0%	2.96	3.10	0.1061	0.2
SFRAC50-0,5%	2.96	3.10	0.1061	0.2
SFRAC50-1%	2.96	3.10	0.1061	0.2
RAC100-0%	2.74	2.80	0.0952	0.2
SFRAC100-0,5%	2.74	2.80	0.0952	0.2
SFRAC100-1%	2.74	2.80	0.0952	0.2

For the steel bars and fibers the perfect elastoplastic model described in subsection (2.2.2) is used, assuming the same Young’s modulus of $E_s = 200 \text{ GPa}$ and yield strength of $f_y = 390 \text{ MPa}$ for both. According to the models presented in subsection (2.2.3), a perfect bond between the steel bars and RAC is considered by using the penalty parameter value of $\tilde{C} = 10^7 \text{ N/mm}$, while a bond-slip between the steel fibers and RAC is modeled by assuming $\tau_{max} = 8.50 \text{ MPa}$, $\tau_f = 4.50 \text{ MPa}$, $S_1 = 0.01 \text{ mm}$, $S_2 = 0.01 \text{ mm}$, $S_3 = 6.50 \text{ mm}$ and $\alpha = 0.4$.

One-dimensional finite elements (truss elements) with linear elastic model only in compression were used to model the interaction between the slabs and the unilateral continuous elastic support, in which the loss of contact between them can occur freely.

The stiffness was obtained by multiplying the influence area by the support reaction modulus of 0.4 MPa/mm , that showed to be an adequate value to represent the reinforced concrete frame with an angle steel frame and also the initial stiffness of the numerical curves.

In all analyzes performed the load was incrementally applied in 1500 steps, controlling the vertical displacement in 0.04 mm per step.

3.1 Concrete with 0%, 50% and 100% of recycled aggregates without fibers

Herein the numerical responses written in terms of the Force vs. displacements curves are compared against the experimental developed by Xiao et al. [1] for the reinforced concrete slabs with 0% (reference concrete), 50% and 100% of recycled aggregates with conventional steel bars and without fibers, as well as the failure pattern, are presented.

Figure 7 illustrates both the numerical and experimental curves obtained for the reference concrete (RAC0). In general, the numerical responses reproduced well some notable experimental results aspects, especially the ultimate load and the typical punching failure pattern (punching cone formation) shown in Figures 8 and 9. In Figure 8 the displacement field in the vertical direction (z-direction) is showed, while in Figure 9a-e the tensile damage distribution is presented, in which the mentioned punching failure propagation process can be observed for different loading steps. In the initial stage of loading no crack occurs. With increasing load, it is possible to notice that cracks propagate radial to the slab from the applied load location to the edge (Figure 9a-c). At more advanced levels of loading, it is possible to observe the formation of curved cracks around the loading area (Figure 9d and 9e), which agrees with the experimental results reported by Xiao et al. [1].

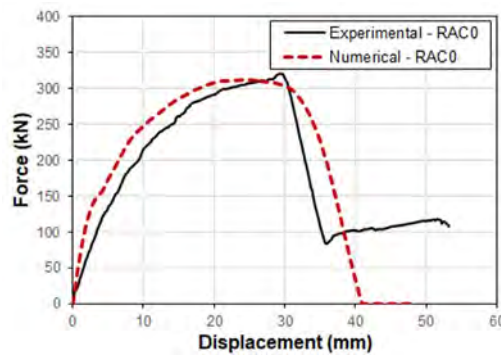


Figure 7. Force x displacement curves of RAC0 slabs.

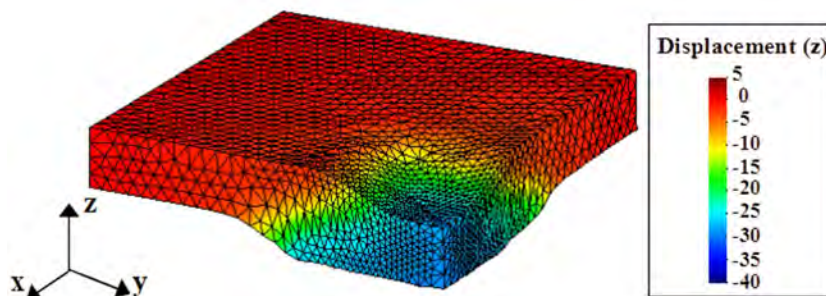


Figure 8. Deformed configuration (scaling factor of 2 times) with the displacement field (in mm) of RAC0 slab, at the end of loading.

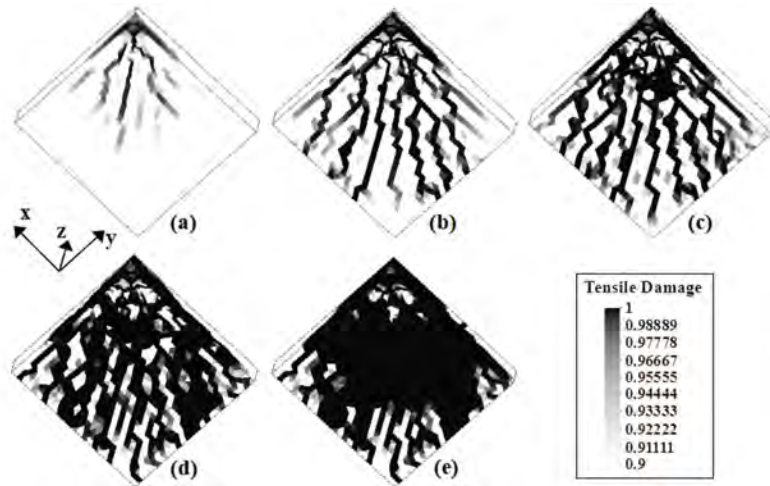


Figure 9. Tensile damage distribution obtained for different loading steps: (a) 100, (b) 300, (c) 500, (d) 1000 and (e) 1500.

The numerical force-displacements curves for the recycled concrete with 50% and 100% of recycled aggregates are plotted with the experimental curves in Figure 10a and 10b. It is possible to note that the responses obtained with the proposed methodology are in good agreement with the results found in the literature [1]. The deformed configurations (scaling factor of 2 times the original one) with the displacement fields in the z-directions of these slabs are illustrated in Figure 11, in which the punching failure patterns with an oblique cone formation can also be observed.

The numerical curves obtained for the three replacement percentages of recycled aggregates are presented in Figure 12. It is worth noting how the peak-load (punching ultimate load) and the energy dissipation are reduced as the percentage of recycled aggregates is increased, showing that the applied methodology can reproduce well the recycled aggregate effect by reducing the homogenized fracture properties as the recycled aggregate content is increased.

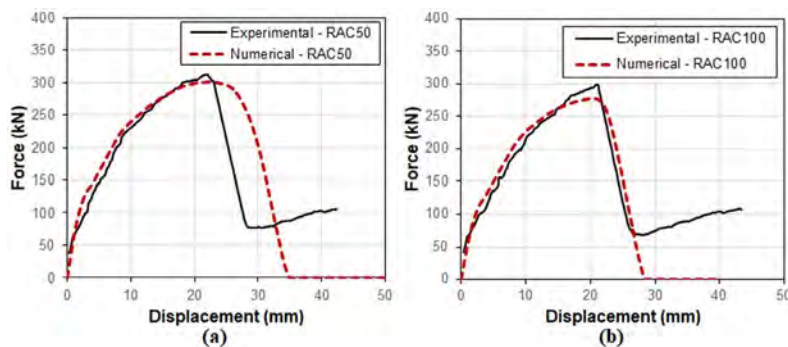


Figure 10. Force x displacement curves of (a) RAC50 and (b) RAC100 slabs.

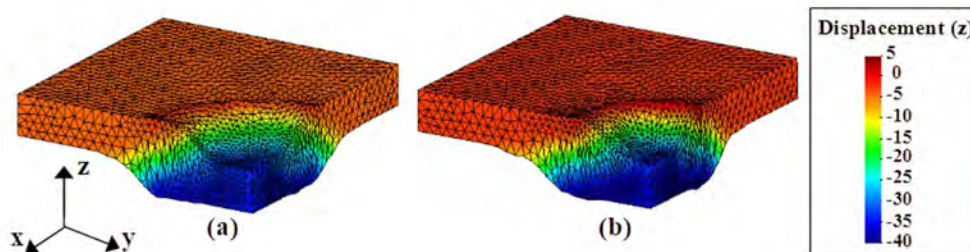


Figure 11. Deformed shapes (scaling factor of 2 times) with the displacement fields (in mm) of the (a) RAC50 and (b) RAC100 slabs, at the end of loading.

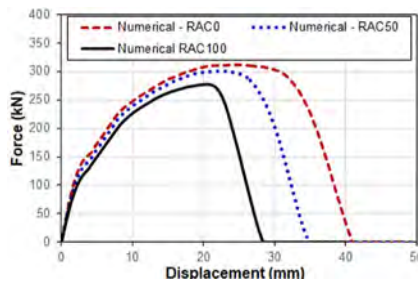


Figure 12. Numerical force x displacement curves of RAC0, RAC50 and RAC100 slabs.

3.2 Concrete with 50% of recycled aggregates and 0.5% and 1.0% of fibers

This section presents the numerical results obtained for the recycled concrete with 50% of replacement of recycled coarse aggregates, assuming 0.5% and 1.0% of steel fibers. Figure 13a and 13b illustrates the numerical force-displacement curves obtained compared with the experimental responses provided by Xiao et al. [1]. Comparing the plotted results it is worthy to note how the proposed approach can reproduce the experimental results, as well as how the addition of fibers is able to mitigate the disadvantages provided by the replacement of natural by recycled aggregates, as it can be proven in Figure 14, in which both numerical curves showed in this section are compared against the experimental one obtained for the reference concrete (RAC0) showed in section 3.1. The mentioned advantages may be related to the bridging effect provided by the fibers, which works to contain fracture initiation and propagation, as described by Xie et al. [13]. It is important to point out that these same beneficial effects on the mechanical properties of the RAC produced by the addition of fiber were observed in experimental studies obtained by other authors [10] [11] [12]. In Figure 15a-c it is possible to observe the tensile stress field of the fibers for different loading steps, which work to prevent crack propagation in the RAC and, consequently, contributing to the reduction of the drawbacks of replacement of the natural aggregates by the recycled aggregates.

Figure 16a-d shows the distribution of the tensile damage variable at step 1000 in two different views for the slabs with 0.5% (Figure 16a and 16c) and 1.0% (Figure 16b and 16d) of steel fibers. It is important to note that in both analyzes the oblique cone formation is observed. However, with the increasing of steel fibers volumetric ratio the cut cone integrity is improved, as illustrated in Figure 16c and 16d, in which the initial transition process of the punching failure pattern to bending-punching failure pattern is observed, in agreement with the experimental results.

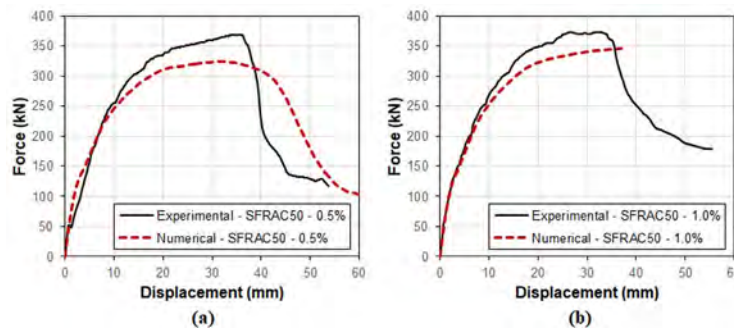


Figure 13. Force x displacement curves of (a) SFRAC50-0.5% and (b) SFRAC50-1.0% slabs.

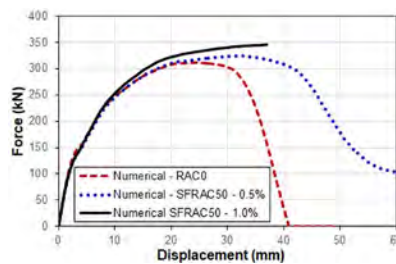


Figure 14. Numerical force x displacement curves obtained for slabs with RAC0, SFRAC50-0.5% and SFRAC50-1.0%.

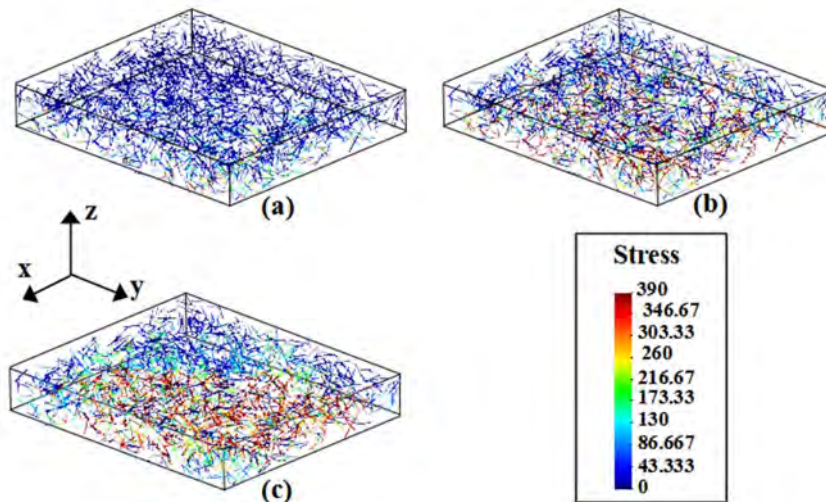


Figure 15. Tensile stress field obtained for the fibers for different loading steps: (a) 100, (b) 500 and (c) 1500.

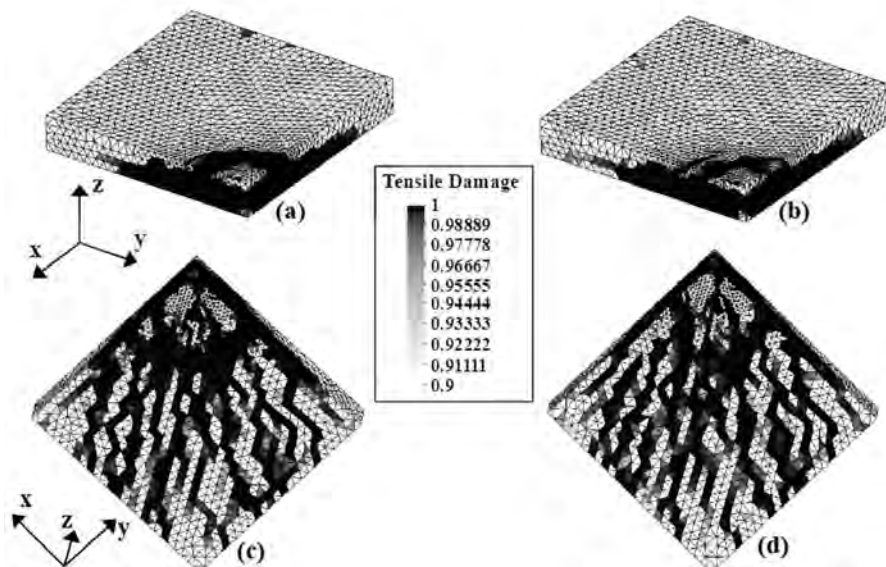


Figure 16. Tensile damage distribution in two different views at step 1000 for slabs with 50% of recycled aggregates and steel fiber volumetric ratios of 0.5% (a and c) and 1.0% (b and d).

3.3 Concrete with 100% of recycled aggregates and 0.5% and 1.0% of fibers

Figure 17a and 17b illustrates the numerical force-displacement curves obtained compared against the experimental responses provided by Xiao et al. [1]. Again, the numerical responses were able to represent well the experimental responses, as well as the beneficial effects produced by the addition of steel fibers, that is, reducing the drawbacks caused by the complete replacement of the natural aggregates by the recycled aggregates, as it can also be seen in both numerical curves obtained in this section, plotted with the curve obtained for the reference concrete in section 3.1, illustrated in Figure 18. Note that, with the increasing of steel fibers volumetric ratio, the punching ultimate load is improved. Also note that even for the total replacement of the natural aggregate, the numerical responses with the addition of fibers show better results than that obtained for the reference concrete, such as the ultimate load, ductility, and energy consumption. However, the punching failure patterns with the cut oblique cone formations are still observed by the distribution of the tensile damage variable illustrated in Figure 19a-d. However, for the steel fiber volumetric ratio of 1.0%, again the transition process of the punching failure pattern to bending-punching failure pattern is noted.

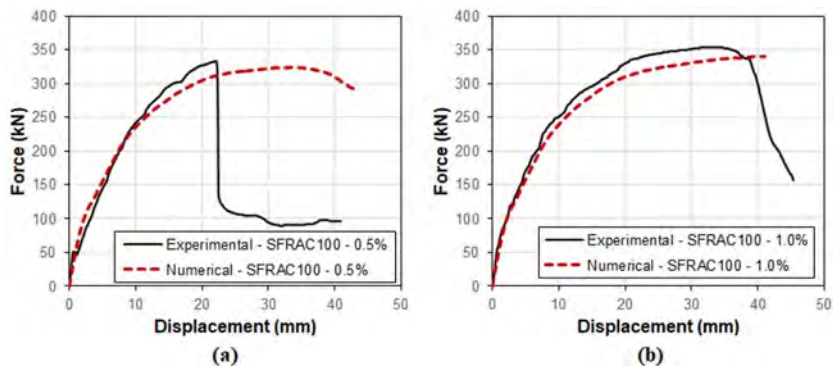


Figure 17. Force x displacement curves of (a) SFRAC100-0.5% and (b) SFRAC100-1.0% slabs.

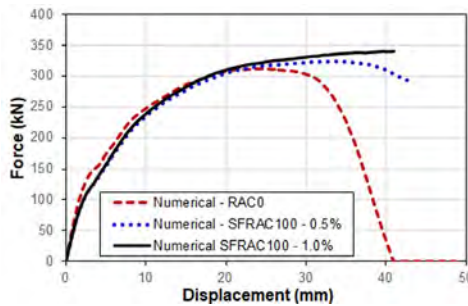


Figure 18. Numerical force x displacement curves obtained for slabs with RAC0, SFRAC100-0.5% and SFRAC100-1.0%.

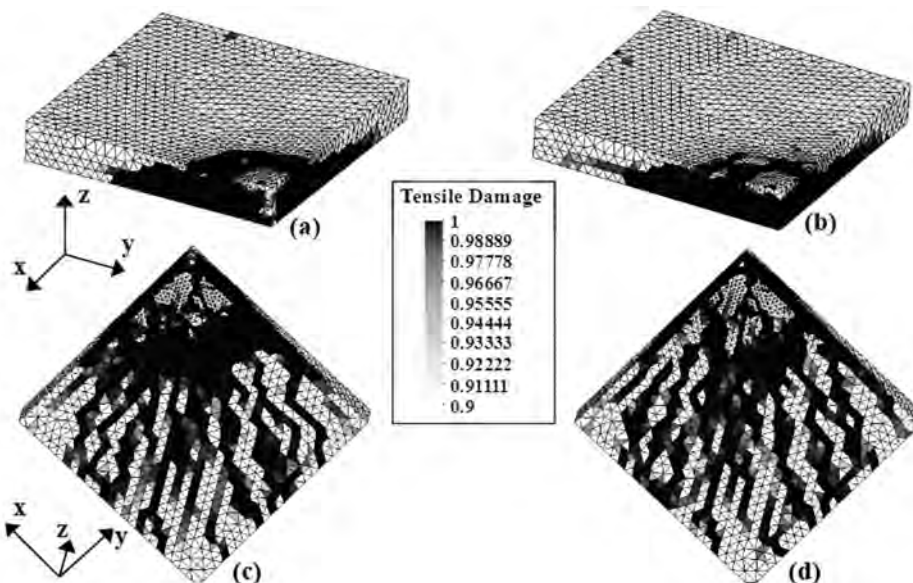


Figure 19. Tensile damage distribution in two different views at step 1000 for slabs with 100% of recycled aggregates and steel fiber volumetric ratios of 0.5% (a and c) and 1.0% (b and d).

4 CONCLUSIONS

In the present paper a numerical approach implemented into an *in-house* finite element code has been proposed to simulate and to better understanding the punching failure behavior of reinforced concrete slabs (i) without fibers with only natural coarse aggregates (natural/reference concrete) and with recycled aggregate replacement percentages of 50% and 100%, and (ii) also using different steel fibers volumetric ratios of 0.5% and 1.0% for slabs with recycled aggregates. To simulate the nonlinear

behavior of the natural and recycled concrete the constitutive damage model proposed by Cervera et al. [21] was used, while an elastic-perfectly plastic model found in Simo and Hughes [22] was used to represent the mechanical behavior of the reinforcing steel bars and fibers. The coupling scheme proposed by Bitencourt et al. [23], [24], either to simulate the perfect-bond (rigid coupling) between the steel bars and recycled concrete or to model the complex bond-slip phenomenon (non-rigid coupling) defined by the CEB *Fib* Model Code [30] between the steel fiber and recycled concrete, was also properly implemented. To improve the stability and robustness of the solution involving cracks propagation in the RAC, mechanical behavior of steel bars and the fiber-RAC bond-slip relation, the implicit-explicit integration scheme (Impl-Ex) proposed by Oliver et al. [25] was employed for all these constitutive models adopted.

In this context, the slabs described above were simulated, in which the qualitative and quantitative numerical results obtained presented good agreement with the experimental responses provided by Xiao et al. [1]. For the slabs without fibers, with the increase of the recycled aggregate replacement percentages, the punching ultimate load is reduced, as well as the ductility and the energy consumption. The punching failure pattern was observed, with both integrity reduced and formation of a more pronounced oblique cone, as the percentage of recycled aggregate is increased. On the other hand, with the addition and increase of steel fiber volumetric ratio, the punching ultimate load, the ductility and energy consumption were improved, mitigating the disadvantages provided by the replacement of natural aggregate by recycled one, and even showing better results than that obtained for the reference concrete, proving to be in full agreement with the experimental results found in the literature [1] and [10]–[12].

Therefore, based on the good numerical results obtained, it can be highlighted that the proposed approach to simulate the punching failure behavior of reinforced concrete slabs is very efficient, and can provide valuable answers about this failure mechanism, mainly in the presence of alternative materials such as recycled aggregate and fibers. It is also important to highlight that the different materials can be discretized in a completely independent way. Furthermore, the constitutive models used are relatively simple and easy to be implemented in conventional FE programs, which used together are able to efficiently represent the complex punching failure phenomenon.

ACKNOWLEDGEMENTS

The authors wish to acknowledge the financial support of the National Council for Scientific and Technological Development – CNPq (Proc.: 423379/2016-0 and 310401/2019-4), Coordination for the Improvement of Higher Education Personnel – CAPES (Finance Code 001) and São Paulo Research Foundation (FAPESP) (Process: 2020/16789-6).

REFERENCES

- [1] J. Xiao, W. Wang, Z. Zhou, and M. M. Tawana, "Punching shear behavior of recycled aggregate concrete slabs with and without steel fibres," *Front. Struct. Civ. Eng.*, vol. 13, no. 3, pp. 725–740, Jun 2019, <http://dx.doi.org/10.1007/s11709-018-0510-6>.
- [2] H. Marzouk and A. Hussein, "Experimental investigation on the behavior of high-strength concrete slabs," *ACI Mater. J.*, vol. 88, no. 6, pp. 701–713, 1991.
- [3] S. Guandalini, O. L. Burdet, and A. Muttoni, "Punching tests of slabs with low reinforcement ratios," *ACI Mater. J.*, vol. 106, no. 1, pp. 87–95, 2009.
- [4] T. R. Sonawane and S. S. Pimplikar, "Use of recycled aggregate in concrete," *Int. J. Eng. Res. Technol.*, vol. 2, no. 1, pp. 1–9, 2013.
- [5] M. Malešev, V. Radonjanin, and S. Marinković, "Recycled concrete as aggregate for structural concrete production," *Sustainability*, vol. 2, no. 5, pp. 1204–1225, 2010, <http://dx.doi.org/10.3390/su2051204>.
- [6] M. Casuccio, M. Torrijos, G. Giaccio, and R. Zerbino, "Failure mechanism of recycled aggregate concrete," *Constr. Build. Mater.*, vol. 22, no. 7, pp. 1500–1506, 2008, <http://dx.doi.org/10.1016/j.conbuildmat.2007.03.032>.
- [7] A. E. B. Cabral, V. Schalch, D. C. C. Dal Molin, and J. L. D. Ribeiro, "Mechanical properties modeling of recycled aggregate concrete," *Constr. Build. Mater.*, vol. 24, no. 4, pp. 421–430, Apr 2010, <http://dx.doi.org/10.1016/j.conbuildmat.2009.10.011>.
- [8] J. Brito and N. Saikia, *Recycled Aggregate in Concrete: Use of Industrial, Construction and Demolition Waste*. New York: Springer, 2013.
- [9] B. S. Hamad and A. H. Dawi, "Sustainable normal and high strength recycled aggregate concretes using crushed tested cylinders as coarse aggregates," *Case Stud. Constr. Mater.*, vol. 7, pp. 228–239, Dec 2017, <http://dx.doi.org/10.1016/j.cscm.2017.08.006>.
- [10] N. V. Ramana, "Performance of crimped steel fibre reinforced recycle aggregate concrete," *Int. J. Adv. Technol. Eng. Sci.*, vol. 4, no. 1, pp. 152–159, 2016.
- [11] Y. Paluri, S. Mogili, H. Mudavath, and V. Noolu, "Effect of fibres on the strength and toughness characteristics of recycled aggregate concrete," *Mater. Today Proc.*, vol. 38, pp. 2537–2540, 2021, <http://dx.doi.org/10.1016/j.matpr.2020.07.555>.

- [12] S. Jahandari et al., "Mechanical properties of recycled aggregate concretes containing silica fume and steel fibres," *Materials*, vol. 14, no. 22, pp. 7065, Nov 2021, <http://dx.doi.org/10.3390/ma14227065>.
- [13] J. Xie, S. Kou, H. Ma, W.-J. Long, Y. Wang, and T.-H. Ye, "Advances on properties of fiber reinforced recycled aggregate concrete: Experiments and models," *Constr. Build. Mater.*, vol. 277, pp. 122345, Mar 2021, <http://dx.doi.org/10.1016/j.conbuildmat.2021.122345>.
- [14] J. A. Carneiro, P. R. L. Lima, M. B. Leite, and R. D. Toledo Filho, "Compressive stress-strain behavior of steel fiber reinforced-recycled aggregate concrete," *Cement Concr. Compos.*, vol. 46, pp. 65–72, Feb 2014, <http://dx.doi.org/10.1016/j.cemconcomp.2013.11.006>.
- [15] Y. Peng, H. Chu, and J. Pu, "Numerical simulation of recycled concrete using convex aggregate model and base force element method," *Adv. Mater. Sci. Eng.*, vol. 2016, pp. 1–10, 2016., <http://dx.doi.org/10.1155/2016/5075109>.
- [16] E. A. Rodrigues, O. L. Manzoli, L. A. Bitencourt Jr., and T. N. Bittencourt, "2D mesoscale model for concrete based on the use of interface element with a high aspect ratio," *Int. J. Solids Struct.*, vol. 94-95, pp. 112–124, 2016, <http://dx.doi.org/10.1016/j.ijsolstr.2016.05.004>.
- [17] M. Guo, F. Grondin, and A. Loukili, "Numerical analysis of the failure of recycled aggregate concrete by considering the random composition of old attached mortar," *J. Build. Eng.*, vol. 28, pp. 101040, Mar 2020, <http://dx.doi.org/10.1016/j.jobbe.2019.101040>.
- [18] N. Kachouh, T. El-Maaddawy, and H. El-Hassan, "Numerical modelling of steel fiber recycled aggregate concrete deep beams," in *Proc. 5th World Congr. Civil Struct. Environ. Eng. (CSEE'20)*, Avestia, 2020. (Virtual Conference).
- [19] E. A. Rodrigues, M. Gimenes, L. A. Bitencourt Jr, and O. L. Manzoli, "A concurrent multiscale approach for modeling recycled aggregate concrete," *Constr. Build. Mater.*, vol. 267, pp. 121040, Jan 2021, <http://dx.doi.org/10.1016/j.conbuildmat.2020.121040>.
- [20] M. Gimenes, E. A. Rodrigues, L. A. Bitencourt Jr, and O. L. Manzoli, "2D mesoscale modeling of compressive fracture in concrete using a mesh fragmentation technique," *Int. J. Solids Struct.*, vol. 260-261, pp. 112031, 2023, <http://dx.doi.org/10.1016/j.ijsolstr.2022.112031>
- [21] M. Cervera, J. Oliver, and O. Manzoli, "A rate-dependent isotropic damage model for the seismic analysis of concrete dams," *Earthquake Eng. Struct. Dynam.*, vol. 25, no. 9, pp. 987–1010, Sep 1996, [http://dx.doi.org/10.1002/\(SICI\)1096-9845\(199609\)25:9<987::AID-EQE599>3.0.CO;2-X](http://dx.doi.org/10.1002/(SICI)1096-9845(199609)25:9<987::AID-EQE599>3.0.CO;2-X).
- [22] J. C. Simo and T. J. R. Hughes, *Computational Inelasticity*. New York: Springer-Verlag, 1998.
- [23] L. A. G. Bitencourt Jr., O. L. Manzoli, P. G. C. Prazeres, E. A. Rodrigues, and T. N. Bittencourt, "A coupling technique for non-matching finite element meshes," *Comput. Methods Appl. Mech. Eng.*, vol. 290, pp. 19–44, Jun 2015, <http://dx.doi.org/10.1016/j.cma.2015.02.025>.
- [24] L. A. G. Bitencourt Jr., O. L. Manzoli, Y. T. Trindade, E. A. Rodrigues, and D. Dias-da-Costa, "Modeling reinforced concrete structures using coupling finite elements for discrete representation of reinforcements," *Finite Elem. Anal. Des.*, vol. 149, pp. 32–44, Sep 2018, <http://dx.doi.org/10.1016/j.finel.2018.06.004>.
- [25] J. Oliver, A. Huespe, and J. Cante, "An implicit/explicit integration scheme to increase computability of non-linear material and contact/friction problems," *Comput. Methods Appl. Mech. Eng.*, vol. 197, no. 21-24, pp. 1865–1889, 2008, <http://dx.doi.org/10.1016/j.cma.2007.11.027>.
- [26] P. G. Prazeres, L. A. Bitencourt Jr., T. N. Bittencourt, and O. L. Manzoli, "A modified implicit–explicit integration scheme: an application to elastoplasticity problems," *J. Braz. Soc. Mech. Sci. Eng.*, vol. 38, no. 1, pp. 151–161, 2016, <http://dx.doi.org/10.1007/s40430-015-0343-3>.
- [27] E. A. Rodrigues, O. L. Manzoli, L. A. Bitencourt Jr., T. N. Bittencourt, and M. Sánchez, "An adaptive concurrent multiscale model for concrete based on coupling finite elements," *Comput. Methods Appl. Mech. Eng.*, vol. 328, pp. 26–46, 2018, <http://dx.doi.org/10.1016/j.cma.2017.08.048>.
- [28] E. A. Rodrigues, O. L. Manzoli, and L. A. Bitencourt Jr., "3D concurrent multiscale model for crack propagation in concrete," *Comput. Methods Appl. Mech. Eng.*, vol. 361, pp. 112813, 2020, <http://dx.doi.org/10.1016/j.cma.2019.112813>.
- [29] M. Gimenes, E. A. Rodrigues, M. A. Maedo, L. A. Bitencourt Jr., and O. L. Manzoli, "2D crack propagation in high-strength concrete using multiscale modeling," *Multiscale Sci. Eng.*, vol. 2, no. 2-3, pp. 169–188, 2020, <http://dx.doi.org/10.1007/s42493-020-00049-y>.
- [30] International Federation for Structural Concrete, *fib Model Code for Concrete Structures 2010*. Lausanne: Ernst & Sohn, 2013.
- [31] Associação Brasileira de Normas Técnicas. *Design of Concrete Structures – Procedure*, ABNT NBR 6118, 2014 (in Portuguese).

Author contributions: AHCS and MG: formal analysis, methodology, validation, visualization, writing-original draft; OLM and EAR: conceptualization, supervision, writing-review, editing & data curation.

Editors: Leandro Trautwein, Mauro Real, Mario Pimentel.



ORIGINAL ARTICLE

Computational modeling of plain and steel fiber-reinforced concrete beams without transverse reinforcement

Modelagem computacional de vigas de concreto simples e reforçadas com fibras de aço sem armadura transversal

Daniel de Lima Araújo^a Cleiton Rodrigues Siqueira Filho^a Fausto Arantes Lobo^a ^aUniversidade Federal de Goiás – UFG, Escola de Engenharia Civil e Ambiental, Goiânia, GO, Brasil

Received 18 September 2022

Accepted 23 March 2023

Abstract: Finite element analysis with nonlinear material behavior modeling can be used to design concrete structures. This study aimed to develop a computational model to represent the shear behavior of concrete beams without transverse reinforcement described in the literature, with or without steel fibers. Two different approaches of finite element analysis were investigated, namely smeared and discrete crack models. The results of the smeared crack model were compared with the results of double-notched push-through tests, and an empirical equation for the shear retention factor of plain concrete was suggested. The computational model using a discrete crack approach with representation of the aggregate interlocking mechanism was compared with the results of push-of test, and an accurate correlation was observed up to the maximum shear stress. It was concluded that the discrete crack approach provided the most accurate representation of the shear behavior of a non-reinforced beam with a shear span-to-depth ratio of 2.17. However, for a non-reinforced beam with a shear span-to-depth ratio of 2.66, the smeared crack approach accurately represents the shear strength and stiffness of the beam. The shear retention factor had little influence on the overall behavior of a steel fiber-reinforced concrete beam. Finally, it was concluded that a variable shear retention factor should be used in the smeared crack approach with fixed crack, as a constant shear retention factor tends to overestimate the shear strength of beams.

Keywords: nonlinear finite element analysis, shear, steel fiber-reinforced concrete, shear retention.

Resumo: O Método dos elementos finitos considerando o comportamento não-linear do material pode ser usado no projeto de estruturas de concreto. Este trabalho teve como objetivo desenvolver um modelo computacional para representar o comportamento ao cisalhamento de vigas de concreto sem armadura transversal descritas na literatura, com ou sem a incorporação de fibras de aço. Duas abordagens diferentes pelo método dos elementos finitos foram investigadas, a saber, modelos com fissuração discreta ou distribuída. Os resultados da modelagem com fissuração distribuída foram comparados com os resultados de ensaios de cisalhamento direto em corpos de prova com duplo entalhe, sendo proposta uma equação empírica para o fator de retenção ao cisalhamento do concreto simples. O modelo computacional usando uma abordagem de fissuração discreta com representação do mecanismo de intertravamento do agregado foi comparado com os resultados de ensaios de cisalhamento direto, tendo sido observada uma boa correlação até a tensão de cisalhamento máxima. Concluiu-se que a melhor representação do comportamento de uma viga de concreto armado sem estribos e com uma relação entre vão cisalhamento e altura de 2,17 foi obtida com a abordagem de fissuração discreta. No entanto, para uma viga sem estribos e com uma relação entre vão de cisalhamento e altura de 2,66, a abordagem de fissuração distribuída representou com precisão a resistência ao cisalhamento e a rigidez da viga. O valor escolhido para o fator de retenção ao cisalhamento teve pouca influência no comportamento de uma viga de concreto reforçado com fibras de aço. Por fim, concluiu-se que na abordagem com fissuração distribuída e fissura fixa deve-se utilizar um fator de retenção ao cisalhamento variável, pois o fator de retenção ao cisalhamento constante tende a superestimar a resistência à força cortante das vigas.

Palavras-chave: análise não linear pelo método dos elementos finitos, cisalhamento, concreto reforçado com fibras de aço, fator de retenção ao cisalhamento.

Corresponding author: Daniel de Lima Araújo. E-mail: dlaraujo@ufg.br

Financial support: This study was financed in part by the Brazilian Federal Agency for Support and Evaluation of Graduate Education (CAPES, Finance Code 001). The authors would also like to thank the Goiás State Research Foundation (FAPEG, grant no. 2017.10.267000.513) and the Brazilian National Council for Scientific and Technological Development (CNPq, grant no. 552118/2011-7) for financing this research.

Conflict of interest: Nothing to declare.

Data Availability: The data that support the findings of this study are available from the corresponding author, D.L. Araújo, upon reasonable request.



This is an Open Access article distributed under the terms of the Creative Commons Attribution License, which permits unrestricted use, distribution, and reproduction in any medium, provided the original work is properly cited.

How to cite: D. L. Araújo, C. R. Siqueira Filho, and F. A. Lobo, "Computational modeling of plain and steel fiber-reinforced concrete beams without transverse reinforcement," *Rev. IBRACON Estrut. Mater.*, vol. 16, no. 3, e16311, 2023, <https://doi.org/10.1590/S1983-41952023000300011>

1 INTRODUCTION

Several parameters have a significant influence on the shear resistance of concrete. In normal-strength concrete, cracking commonly occurs throughout the matrix and in the interface zone between the matrix and coarse aggregate because of the high strength of the latter. High-strength concrete has a different mode of fracture in that cracks develop through coarse aggregate, creating a smoother crack surface. This mechanism is known as aggregate interlock.

Shear transfer along a rough crack depends on aggregate size, crack width, and concrete compressive strength. Aggregate interlock experiments show that the resistance on the crack surface depends not only on tangential crack displacements but also on normal crack displacements and their interaction. This phenomenon is denoted as crack dilatancy.

Deng et al. [1] demonstrated that coarse aggregate size does not directly influence the cracking load of a beam without transverse reinforcement tested in shear. However, the ultimate load of the beam was found to increase with increasing aggregate size, indicating that aggregate size directly influences shear capacity. Sells et al. [2] showed that coarse aggregate size had little impact on shear resistance, but the effect of aggregate type appeared to be highly significant. Compared to limestone aggregate, a material with a weak nature, river gravel improved the shear resistance of reinforced concrete beams.

It is recognized that the use of steel fibers in concrete promotes greater tensile strength, creating a bridging effect on cracks. As a result, aggregate interlock linked to coarse aggregates can be optimized, given that fibers reduce crack width, thereby increasing interlocking between coarse aggregates on the fracture surface [3], [4].

There are several methods for modeling cracking in nonlinear finite element analyses of reinforced concrete, with smeared and discrete approaches being the most common. Araújo et al. [5] suggested that the discrete crack model is preferable for structures with few cracks. The discrete crack approach considers a crack to be a geometric discontinuity in the finite element mesh; therefore, it is necessary to define the direction and position of cracks before proceeding with the analysis. This approach can be used to solve problems involving push-off tests and pre-cracked structures, among others. In this approach, the aggregate interlock phenomenon can be implemented in interface elements by using empirical and analytical formulas that simulate the transfer of shear stresses through cracked concrete planes. Examples of empirical and analytical formulations for aggregate interlock can be found in previous studies [6]–[9].

In the smeared model, a crack is not represented by a single crack but rather by a cracked element area. The finite element mesh does not need to be redefined during the analysis, unlike in the discrete crack approach. The smeared crack concept is suitable for analyses of adequately reinforced structures where cracks are distributed. When the maximum principal stress exceeds the ultimate strength of the material, cracks will appear in the direction perpendicular to the direction of the maximum principal stress at Gauss points of finite elements. Smeared crack models commonly use a total strain-based approach, typically assuming a rotating or fixed crack direction.

As cracks appear in concrete and crack width increases, the ability of the crack surface to transmit shear stresses decreases. In smeared crack models, such a loss is accounted for by a shear retention factor ($0 \leq \beta \leq 1$), which reduces the elastic shear modulus upon cracking of concrete. Slobbe et al. [10] explain that the shear retention factor can be interpreted as a means of modeling aggregate interlock. The relationship between the shear retention factor and the crack shear modulus – a mode II fracture parameter of concrete – can be explained by noting that the reduced shear stiffness is associated with the total strain, while the crack shear modulus is associated with the crack strain.

The assumption of a linear relationship between shear stresses and strains after cracking creates multiple problems. Smeared crack models are extremely sensitive to the shear retention factor, which is either taken as a constant or as a function of current crack normal strain [11]. This is particularly relevant because the β value is often chosen rather arbitrarily. Large values for the β factor can result in stress locking, whereas small values may lead to convergence problems.

Several authors have proposed different values for the shear retention factor. For example, Araújo et al. [5] used a constant β value of 0.01 when modeling the results of direct shear and bending tests of reinforced concrete beams. The same authors used β values of up to 0.5 for steel fiber-reinforced concrete beams. Sagaseta [12] reported that a constant β value of 0.1 or 0.2 is commonly used but noted, however, that, according to experimental evidence, this factor is not constant and decreases as crack width increases. Scotta et al. [13] showed that the adoption of constant β values greater than 0.2 overestimates the strength of concrete beams without stirrups. Furthermore, the authors did not observe any variation in beam resistance with β values above 0.2. Because of this, they recommended that a variable value should

be used for the shear retention factor, with a linear decay rate ranging from 1 to 0. This conclusion agrees with the observations of Hendriks et al. [14], who strongly recommended the adoption of a variable shear retention factor in fixed crack models. Models with constant shear retention are not recommended, because they tend to overestimate the stiffness of beams and slabs. Moreover, for beams and slabs without transverse reinforcement, the adequacy of a variable shear retention factor should be explicitly verified. Alternatively, for beams, shear stiffness could be gradually reduced to zero when the crack width is half the average aggregate size.

Several studies in the literature have proposed expressions for the reduced shear modulus of cracked concrete. These expressions are dependent on the crack normal strain (ε_{nn}) and the stress-free crack normal strain ($\varepsilon_{nn,ult}$). In these studies, the shear retention factor decreases as the crack normal strength increases, which is attributed to the reduction in interlock of aggregate particles as the crack opening increases. When the shear retention factor tends to zero, it indicates that the shear stiffness from aggregate interlock across macro-cracks is being disregarded. This has no significant consequences if the crack normal stress is tensile instead of compressive.

Al-Mahaidi [15] proposed a variable β value that depends on tensile strength (f_t), modulus of elasticity (E), and crack normal total strain (ε_{nn}), according to Equation 1.

$$\beta = 0.4 \frac{f_t}{E \varepsilon_{nn}} \quad (1)$$

Figueiras [16] proposed a linear decay model for the shear retention factor that starts at 0.25 and depends on the crack normal total strain and ultimate normal strain of the element ($\varepsilon_{nn,ult} = 0.0045$). Equation 2 expresses this relationship.

$$\beta = 0.25 \left(1 - \frac{\varepsilon_{nn}}{\varepsilon_{nn,ult}} \right) \quad (2)$$

Rots and Blaauwendraad [17] proposed a similar decay model that depends on the crack normal strain of the element and factor k , which is generally equal to 1, as given by Equation 3.

$$\beta = \left(1 - \frac{\varepsilon_{nn}}{\varepsilon_{nn,ult}} \right)^k \quad (3)$$

Červenka et al. [18] proposed a logarithmic decay model as a function of the crack normal strain and the geometric rate of reinforcement (ρ) that crosses the section, expressed by Equation 4.

$$\beta = \frac{-1}{10-167(\rho-0.005)} \ln \left(\frac{1000\varepsilon_{nn}}{7+333(\rho-0.005)} \right) \quad (4)$$

In the previous equations, the stress-free crack normal strain ($\varepsilon_{nn,ult}$) is not considered a separate material in tension. Instead, it is a result of the crack bandwidth and the properties of the concrete in tension, such as tensile strength, fracture energy, and the chosen softening diagram for concrete.

Although a variable shear retention factor is more adequate to describe shear transfer in fixed cracked models than a constant shear retention factor [17], it has certain limitations in representing shear transfer through a macro-cracked plane. Therefore, studies investigating the most appropriate value for the shear retention factor in finite element modeling of concrete structures are still needed.

2 EXPERIMENTAL PROCEDURES

Tests were carried out to obtain in advance the parameters for the computational modeling of concrete beams without transverse reinforcement subjected to shear failure. Two types of direct shear tests were performed: a double-notched push-through test and a push-off test on a specimen with a pre-cracked shear plane. Details of test procedures are described elsewhere [3].

2.1 Double-notched push-through tests

These tests were conducted on a plain concrete mixture comprising a coarse aggregate with a maximum dimension of 9.5 mm (F-00-1) and 12.5 mm (F-00-2). The mechanical properties of the concrete used in these tests are shown in Table 1. At least three 150 × 150 × 500 mm prismatic specimens were used for each mixture. Prior to the test, 35 mm deep, 5 mm wide notches were cut along the perimeter of the transversal section of the specimens, in the middle third of the span. Therefore, each specimen had two shear crack planes 163 mm from the end, with approximate dimensions of 80 × 80 mm. After the test, the effective dimension of the shear plane was evaluated.

Table 1. Mechanical properties of concrete.

Mixture	v_f (%)	f_{cm} (MPa)		f_{ctm} (MPa)		E_{cm} (GPa)		G_f^I (N/mm)	
		Mean	SD	Mean	SD	Mean	SD	Mean	SD
F-15-2	1.50	68.74	8.57	3.93	1.02	40.39	1.84	5.96	0.97
F-00-2	0.00	65.08	4.73	4.13	0.90	39.04	0.74	0.16	0.01
F-00-1	0.00	66.29	6.54	5.18	-	37.96	1.67	-	-

v_f : volume of steel fibers; f_{cm} : mean value of compressive strength of concrete; f_{ctm} : mean value of axial tensile strength of concrete; E_{cm} : mean value of modulus of elasticity of concrete; G_f^I : fracture energy of concrete.

The specimen was supported by two edges 163 mm apart. Thus, a narrow region of the specimen between the loading and support edges was directly subjected to shear stress. One end was supported by a bearing surface, which provided both horizontal and vertical restraining forces. At the other end, a roller support produced only a vertical restraining force. Additional roller supports were used on the upper face of the specimen where force was applied by the machine. In the original test setup, the shear plane is always accompanied by a normal stress due to loads and reactions acting centrally on the loading plates. Consequently, the shear plane is subject to global bending and arch effect, which compress the upper face of the shear plane and tended to overestimate its shear capacity [3], [19], [20]. However, the test setup used in this study was modified and does not introduce a normal stress on the shear planes due to the roller supports used on the specimen supports and the machine's load cell. Furthermore, specimens were instrumented to measure shear slip and crack dilatancy on both shear planes. The test apparatus is shown in Figure 1.

Displacement was applied to the middle part of the specimen between two shear planes using a non-closed loop machine. The velocity of displacement was set at 0.02 mm/min throughout the test.

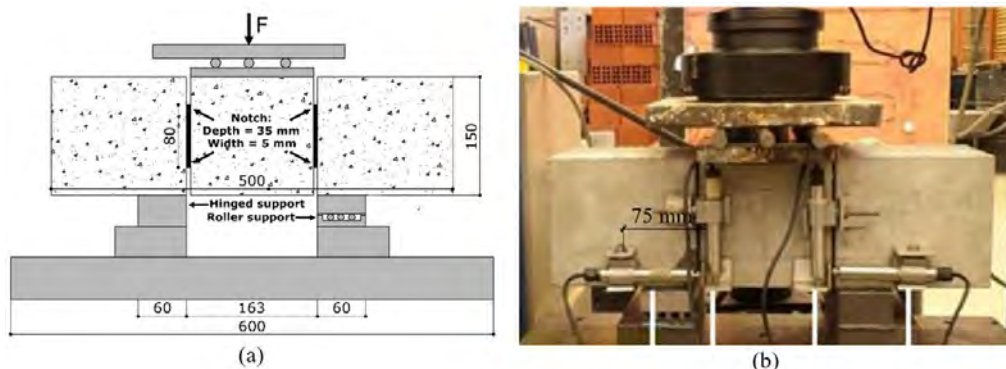


Figure 1. (a) Double-notched push-through test setup (dimensions in mm) and (b) instrumentation.

2.2 Push-off tests

Six Z-type push-off specimens with dimensions of 160 × 250 × 612 mm were cast. Three specimens were prepared using a plain concrete (F-00-2) and another three using a concrete mixture with 1.5% steel fibers (F-15-2). Coarse aggregate with a maximum dimension of 12.5 mm was used. Steel fibers with a hooked end and a circular cross-section were used. According to the manufacturer, the fiber length is 35 mm, the diameter is 0.55, and the aspect ratio is 64. The minimum tensile strength of fibers was 1150 MPa. The mechanical properties of the concrete used in these tests are also shown in Table 1. In these specimens, the shear plane measured 120 × 120 mm.

Specimens were reinforced with a pair of 6.3 mm diameter stirrups (connectors) oriented normal to the shear plane. These stirrups were used to provide normal stress to the shear plane during the test. Adhesion between stirrups and concrete was eliminated near the shear plane in order to reduce its influence on crack dilatancy and shear strength resulting from the dowel action of the bar. This was achieved by wrapping the bar with scotch tape and grease at a distance of 120 mm from the shear plane. A previous study [7] suggested that this procedure is adequate to eliminate the dowel action of the reinforcement, which would only contribute to the normal compression of the shear plane. Strain gages were placed on the stirrups, near the shear plane, to measure the strain of bars during the test.

Push-off tests were conducted in two steps. In the first step, the shear plane of specimens was pre-cracked by applying a splitting load. On both sides of the specimens, there was a 20 mm deep notch where two knives were positioned to induce the pre-cracking of the shear plane. This procedure is similar to one previously described [21]. Loading was applied by displacement control at a rate of 0.010 mm/min until an average crack width of 0.10 mm was produced in the shear plane. Then, the rate was decreased to 0.005 mm/min and kept constant until the average crack width reached about 0.30 mm. Shear crack width was measured using three linear transducers and a clip gage, as shown in Figure 2. Measurements were taken in loading and unloading stages. The strain in stirrups was also measured during this step. It was verified that the stirrup stress did not reach the yield strength of steel on any of the specimens; i.e., all stirrups remained within the linear elastic regime in this first step of the test.

In the second step, the specimen was placed under an electromechanical machine. Load was applied to the top side of the specimen. A roller bearing was attached between plates positioned on the lower side of the specimen to avoid any external horizontal restraint of crack dilatancy during the test. Loading was applied by displacement control at the following rates: 0.004 mm/min for 3 min, 0.02 mm/min until the maximum load was achieved, and 0.05 mm/min until the end of the test.

Four horizontal and two vertical linear transducers were used to measure crack width (w) and the average slip of the shear plane. All instrumentation had an accuracy of 0.01 mm. The instrumentation layout is shown in Figure 3.

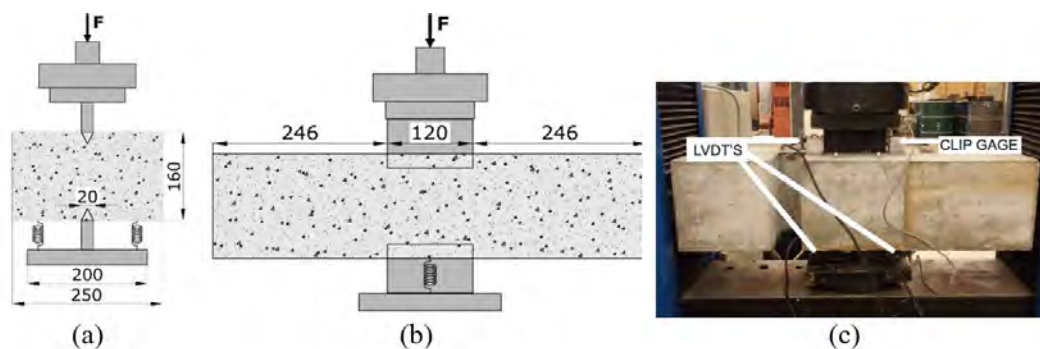


Figure 2. Test setup in the pre-cracking stage: (a) frontal view of specimen (dimensions in mm), (b) lateral view of specimen (dimensions in mm), and (c) splitting test.

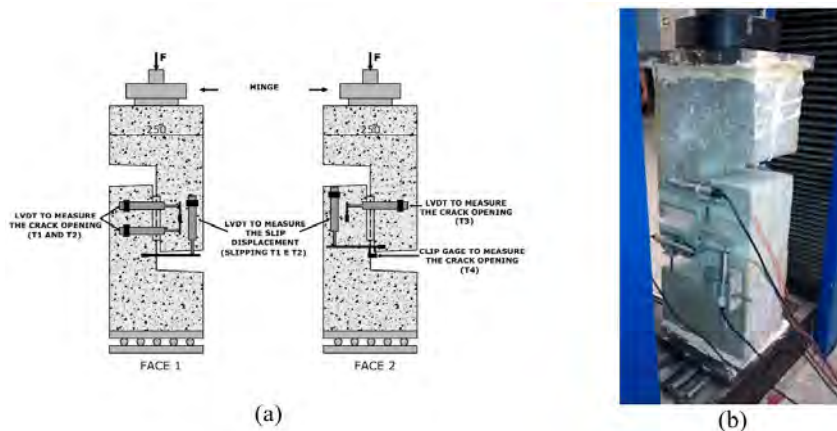


Figure 3. Push-off test instrumentation: (a) front and opposite faces and (b) test setup in the push-off stage.

3 FINITE ELEMENT ANALYSIS OF DIRECT SHEAR TEST RESULTS

In this study, finite element analysis was performed using the commercial software DIANA FEA 10.1 [22], which includes several constitutive models for concrete and masonry.

3.1 Double-notched push-through specimen

A 3D finite element model with a smeared crack approach was used to model specimen with F-00-2 mixture, as shown in Table 1. The objective of this analysis was to determine values for the shear retention factor (β) of concrete without steel fibers.

3.1.1 Mesh, material properties, and loading

The geometry and constraints of the finite element model match those of test supports, as shown in Figure 4. The geometry in black represents specimen supports and the load plate (upper side) on which displacement was imposed. The geometry in red illustrates the notch region. Points a and b , in green, were used to determine the relative slip of the shear plane.

Because of finite element size limitations imposed by the notch width, which limits the finite element size to 5 mm in the notch region, a regular mesh with 5 mm elements was used. The isoparametric elements with linear interpolation (HX24L element type) were used to model concrete and steel plates, resulting in a total of 98,130 elements in the computational model.

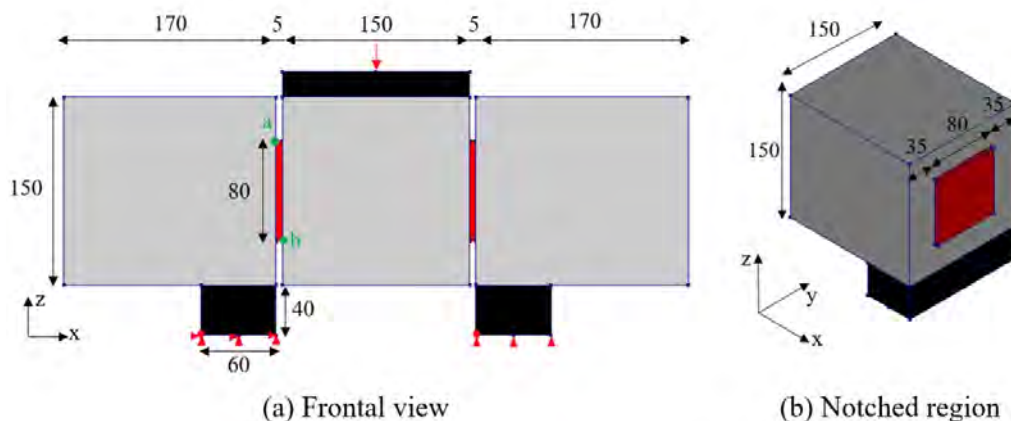


Figure 4. Geometry of the double-notched push-through specimen with uncracked planes (dimensions in mm).

Concrete was described by a total strain model with fixed crack. The equation proposed in Section 5.1.8.1 of Model Code 2010 [23] was used to define the uniaxial compressive behavior of concrete. The uniaxial tensile behavior of concrete without steel fiber was modeled as a linear softening model based on mode I fracture energy. Table 1 shows the values of compression strength, uniaxial tensile strength, modulus of elasticity, and mode I fracture energy determined experimentally. The steel plates used as supports and for applying loads were modeled assuming a linear elastic behavior with a modulus of elasticity of 210 GPa and a Poisson's ratio of 0.3.

Analyses were run in displacement control mode to obtain a post-peak response. Displacement was imposed in 33 steps of 0.03 mm in the z -direction, resulting in a total displacement of 0.99 mm on the upper face of the specimen. The maximum slip values observed in the tests were much lower than this value. The quasi-Newton iteration method, based on the Broyden-Fletcher-Goldfarb-Shanno (BFGS) algorithm, was used to reduce processing time, with a maximum of 40 iterations per load step. A convergence criterion based on an energy criterion with a tolerance of 0.1% was used as it is often easier to satisfy than the force criterion.

3.1.2 Result analysis

A parametric study was conducted for different values of the β factor, which was considered constant. Figure 5a shows the relationship between shear stress and shear slip measured using the finite element model. As expected, this

figure indicates an increase in shear resistance as the β values increase. Figure 5b presents the outcomes obtained using the variable shear retention factor suggested by Al Mahaidi [15], Figueiras [16], Rots and Blaauwendraad [17], and Červenka *et al.* [18]. It was noted that different equations for the β factor may influence shear behavior, including the maximum shear stress of the shear plane.

Because of the roller support used in the test, there was no impediment to crack dilatancy in the shear plane after matrix cracking. Therefore, the reduction in the shear stiffness of the shear plane was estimated by measuring the crack width in the shear plane adjacent to the roller support of the specimen with mixture F-00-1, as shown in Figure 6. Table 2 and Figure 7a present a proposed trilinear model for the β factor. Before concrete cracking, full shear retention should be employed ($\beta = 1$). After concrete cracking, the β factor was adjusted according to the decrease in the slope of the relationship between shear stress and crack width observed in the test data (Figure 6). A minimum β factor of 0.01 was set, and an ultimate normal strain of 0.0045 was admitted, in accordance with values used by several authors, such as Figueiras [16] and Rots and Blaauwendraad [17].

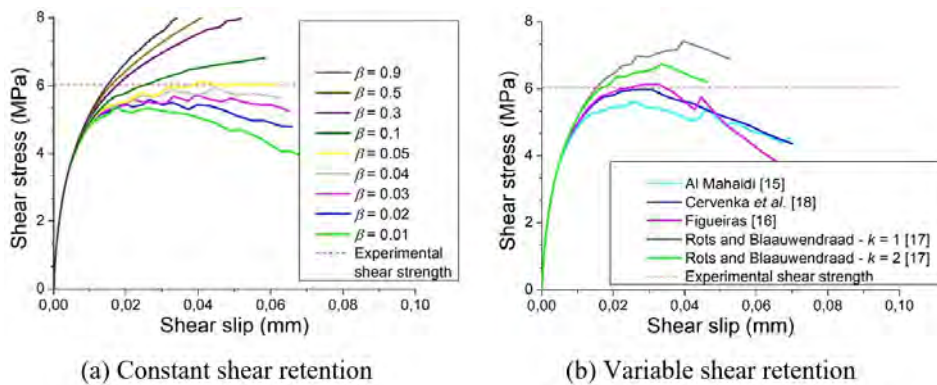


Figure 5. Influence of (a) constant shear retention factor and (b) variable shear retention factor on double-notched push-through test results (F-00-2).

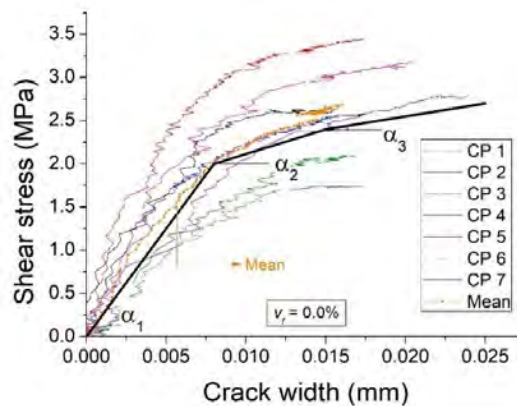


Figure 6. Relationship of shear stress and crack width in double-notched push-through tests (F-00-1).

Table 2. Empirical values of variable shear retention factor (β) estimated from double-notched push-through test results (F-00-1).

Stage	Shear stress (τ) (MPa)	Crack width (w) (mm)	α (MPa/mm)	β	Normal strain (ϵ_{nn}) $\times 10^{-3}$
1	2.0	0.008	250	1	0.107
2	2.4	0.015	57	0.228	0.200
3	-	-	-	0.01	4.500

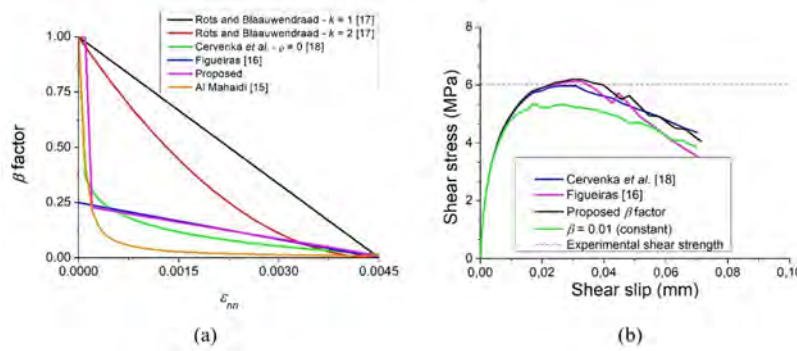


Figure 7. (a) Proposed equations for the variable shear retention factor (β) and (b) shear stress–slip curves obtained using the finite element model and several variable shear retention equations.

Despite the roller support not applying normal stress on the shear plane, the acting and reaction forces were not aligned, resulting in bending in the shear plane. Consequently, the crack width measured on the bottom face of the specimen was divided by the distance between the neutral axis and the position of the horizontal linear variable displacement transducer (LVDT) during the elastic phase to obtain the strain. In the test setup, this distance is approximately half the height of the specimen, or 75 mm. Table 2 shows the normal strain and corresponding β factor, which were determined based on the reduction of stiffness (α) in the relationship between shear stress and crack width (or normal strain) presented in Figure 6. In the first stage, β factor was assumed to be 1 because the value of the normal strain at the end of this stage ($\tau = 2$ MPa) is close to the theoretical elastic distortion strain for concrete, i.e., $\gamma = \tau / G = 0.126 \times 10^{-3}$. For this analysis, G was adopted as $E / [2(1 + \nu)] = 15817$ MPa, where the coefficient of Poisson of concrete (ν) was assumed to be 0.2. Therefore, in the first stage, the slope would be close to the elastic shear modulus of the concrete used in the tests.

Figure 7a shows the final proposed curve for the β factor. In the figure, the curve is compared with other shear retention curves available in the literature. The empirical β factor determined experimentally exhibits similar behavior to the equations suggested by Figueiras [16] and Červenka et al. [18], which demonstrate the effectiveness of the test setup used in this analysis for estimate the values of the β factor. This was possible because, without normal stress confining the shear plane and assuming a plane strain state, the maximum shear strain can be assumed to be approximately equal to the maximum normal strain measured by the LVDT. Figure 7b shows the relationship between shear stress and shear slip estimated by the finite element model using several variable shear retention equations, including the β factor suggested in this study. The use of the empirical β factor and the other two equations for variable shear retention factor results in no significant difference in the curves.

Table 3 presents the maximum resistance load of specimens obtained from both the tests and finite element analysis. With the use of the empirical β factor suggested in this study, as well as the equations proposed by Figueiras [16] and Červenka et al. [18], a difference of less than 5% was observed in the maximum load between the finite element analysis and test results, indicating the similarity between these three proposed formulations for variable β factor. It is noteworthy that the difference of less than 5% with constant shear retention was also obtained with a β factor of approximately 0.05.

Table 3. Maximum resistance load of the double-notched push-through specimen.

Shear retention factor	Maximum load (kN)	Difference from test result
Experimental result (F-00-2)	79.62 ± 3.2	-
$\beta = 0.01$ (constant)	68.71	-13.70%
$\beta = 0.02$ (constant)	71.15	-10.64%
$\beta = 0.03$ (constant)	73.28	-7.96%
$\beta = 0.04$ (constant)	76.41	-4.03%
$\beta = 0.05$ (constant)	78.62	-1.25%
Al Mahaidi [15] (variable)	70.51	-11.44%
Červenka et al. [18] (variable)	76.79	-3.55%
Rots and Blaauwendraad, $k = 1$ [17] (variable)	95.04	19.37%
Rots and Blaauwendraad, $k = 2$ [17] (variable)	86.17	8.23%
Figueiras [16] (variable)	78.41	-1.52%
Proposed β factor (variable)	79.43	0.24%

3.2 Push-off specimens

In this phase of the study, aggregate interlock resistance was modeled using the discrete crack approach with the interface elements available in DIANA FEA 10.1 software. The same method was used by Blomfors et al. [24] to simulate beams without stirrups and with pre-existing cracks. However, the authors used a three-dimensional model and did not explicitly consider aggregate interlock resistance. In this study, two-dimensional plane stress was used because of the limitation of the software version, which only contained analytical equations for crack dilatancy in two-dimensional interface elements.

3.2.1 Mesh, material properties, and loading

The geometry of the push-off specimen is shown in Figure 8, with translational constraints in the x -direction on the right face of the specimen and in the y -direction at the base. In this configuration, the left L-shaped block is free to move along the x -direction, as it was during the test.

Stirrups are represented by L2TRU truss elements inserted across the shear plane. In the shear plane, given the elimination of adhesion, truss elements had no connection with concrete elements of the mesh. The physical thickness of the specimen is 160 mm; however, the finite element model is only 120 mm thick, which is the thickness of the shear plane.

The mesh of concrete and steel plates is composed of plane stress elements with quadratic interpolation (CQ16M type). The finite element size was set at 25 mm (Figure 8). The constructive reinforcement of the model was represented by embedded reinforcement. Within the shear plane, interface elements that incorporate some analytical equations of aggregate interlock were used (CL12I type).

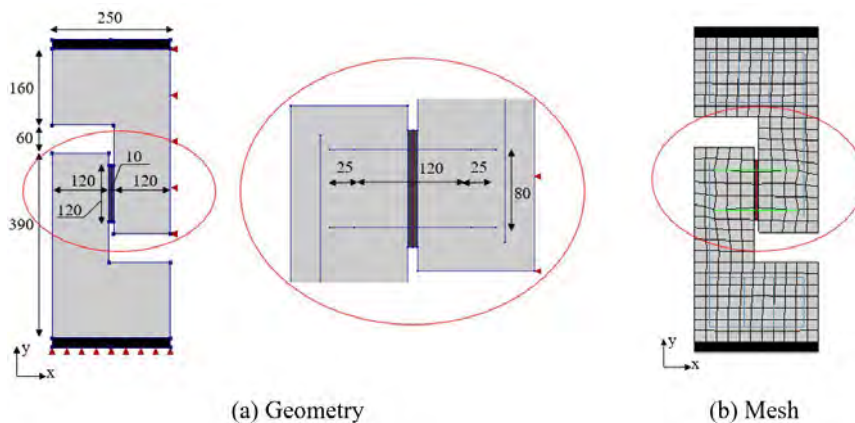


Figure 8. Push-off specimen with pre-cracked shear plane (dimensions in mm).

The mechanical properties of plain (F-00-2 mixture) and fiber-reinforced concrete (F-15-2 mixture) are presented in Table 1. The constitutive law used to model the push-off plain concrete specimen is the same as that described by the finite element model of the double-notched push-through specimen with the variable shear retention factor proposed in this study.

Embedded reinforcements were assumed to have linear elastic behavior, with a modulus of elasticity of 210 GPa, representing the steel used as constructive reinforcement. The truss elements that cross the shear plane were assumed to have non-linear behavior, which was determined from a characterization test of the steel. The modulus of elasticity of the reinforcement was set at 202 GPa, also obtained from the steel characterization test.

Normal and tangent stiffnesses of interface elements were defined by inverse analysis: the values for the finite element model that best matched the initial stiffness were selected. Normal stiffness was found to be 1×10^8 N/mm; and tangential stiffness, 1×10^6 N/mm.

Aggregate interlock was considered in the interface element of the finite element model. Thus, crack dilatancy, which is more advanced than standard discrete cracking for sliding along rough macro-cracks, was used in interface elements. The parameters of the crack dilatancy model were maximum aggregate size (12.5 mm), compressive strength, and mode I fracture energy (values shown in Table 1). Given that the shear plane was pre-cracked before the direct shear test, the tensile strength of the interface was assumed to be zero. The software contains various models for aggregate interlock in two-dimensional interface elements. Variation of the crack dilatancy model did not influence the

results of computational modeling; therefore, the two-phase model proposed by Walraven and Reinhardt [7] was applied to the current finite element model.

A bilinear tension softening diagram was constructed for finite element modeling of the push-off specimen with steel fiber-reinforced concrete. The stress–strain diagram of steel fiber-reinforced concrete was obtained through inverse analysis of toughness test results of F-15-2 mixture, which was performed according to ASTM C1609 [25]. In the referred test, an unnotched prismatic specimen ($150 \times 150 \times 500 \text{ mm}^3$) is bent by four-point loading. Inverse analysis consists in generating a stress–strain diagram via computational modeling of toughness test data, providing a load–displacement curve similar to the curve obtained from the test.

It is worth noting that the smeared crack approach assumes that the deformations of a single crack can be distributed over a characteristic length (l_c). In the case of plain reinforced concrete modeling, this characteristic length is approximately equal to the size of one finite element. For steel fiber-reinforced concrete, the same assumption can be made, but some considerations may be required when modeling a combination of fiber-reinforced concrete and conventional reinforcement. When cracks are distributed throughout the structure, rather than localized to a specific crack, the characteristic length may need to be adjusted. If the crack pattern is unrealistic and too many elements are cracked, the ductility and load resistance can be overestimated if the characteristic length is assumed to be the size of one finite element. In this scenario, the characteristic length should be selected as the size of multiple elements, but not exceeding the average expected crack spacing [26]. For this reason, the mesh size used in the inverse analysis of the prismatic specimen was chosen to be the same as that used in the finite element modeling of the push-off specimen, which was 25 mm. Therefore, the characteristic length was not determined in this analysis and the stress-strain diagram obtained is specific to this mesh size. It should be adjusted using an appropriate characteristic length for other mesh sizes.

Figure 9a and Table 4 show the bilinear tension softening diagram of steel fiber-reinforced concrete obtained by inverse analysis. Figure 9b compares the load–displacement curve obtained from the ASTM C1609 test [25] to that of the finite element model. The area under the curve of the inverse analysis differed in less than 5% from the area under the curve of the test.

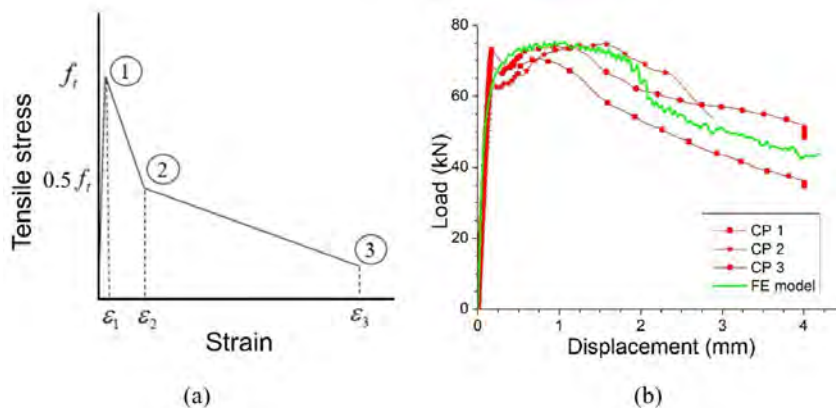


Figure 9. (a) Bilinear tension softening diagram for steel fiber-reinforced concrete and (b) load–displacement curve obtained according to ASTM C1609 for F-15-2 mixture.

Table 4. Points of the bilinear tension softening diagram for steel fiber-reinforced (F-15-2 mixture).

Point	Tensile stress (MPa)	Total strain ($\times 10^{-3}$)
1	3.93	0.09
2	1.80	50
3	0.7	1000

Analyses were also run under displacement control to obtain the post-peak response. Displacement was imposed with 400 steps of 0.005 mm in the y-direction, resulting in a total displacement of 2 mm on the upper face of the push-off specimen. The maximum slip values observed in the tests were close to this value. The quasi-Newton iteration method based on the BFGS algorithm was also used, but the maximum iterations per load step were increased to 1000 due to the difficulty in satisfying the convergence criterion with the interface elements. In this analysis, a convergence criterion based on an energy criterion with a tolerance of 0.1% was also used.

3.2.2 Result analysis

Figure 10 shows the relationships between shear stress, normal stress, crack width, and shear plane slip for the push-off specimen without steel fibers (F-00-2 mixture). For a crack width of zero, the stiffness predicted by the finite element model was equal to experimental values. For increasing crack widths, the model curve ranged within the limits of test curves. The maximum shear stress predicted by the finite element model (6.89 MPa) showed reasonable agreement with the average stress obtained from the test (6.99 MPa), differing by only 1.4%.

The finite element model had a similar behavior to the experimental specimen. It is noted that, in the initial stage, normal stress was low and there was no crack width on the shear plane. Then, the normal stress across the crack increased with crack width and shear slip at the interface. Normal reinforcement did not yield when the maximum shear stress was reached, different from the observed in the test specimen. Nevertheless, the finite element model successfully simulated the relationship between experimental shear stress and normal stress up to the maximum shear stress.

As observed in the test, steel fibers increased shear strength according to the finite element model (Figure 11). The maximum shear stress estimated by the finite element model was 9.46 MPa, being 8.5% lower than the average value obtained in the test (10.34 MPa). The finite element model adequately predicted crack width evolution up to the maximum shear stress but differed from experimental specimens in the post-peak stage, given that the DIANA FEA analysis does not consider steel fibers in aggregate interlock models. As explained by Araújo et al. [3], steel fibers crossing the shear plane begin to contribute to shear strength only after the maximum aggregate interlock capacity is reached, and their contribution depends on maximum aggregate size.

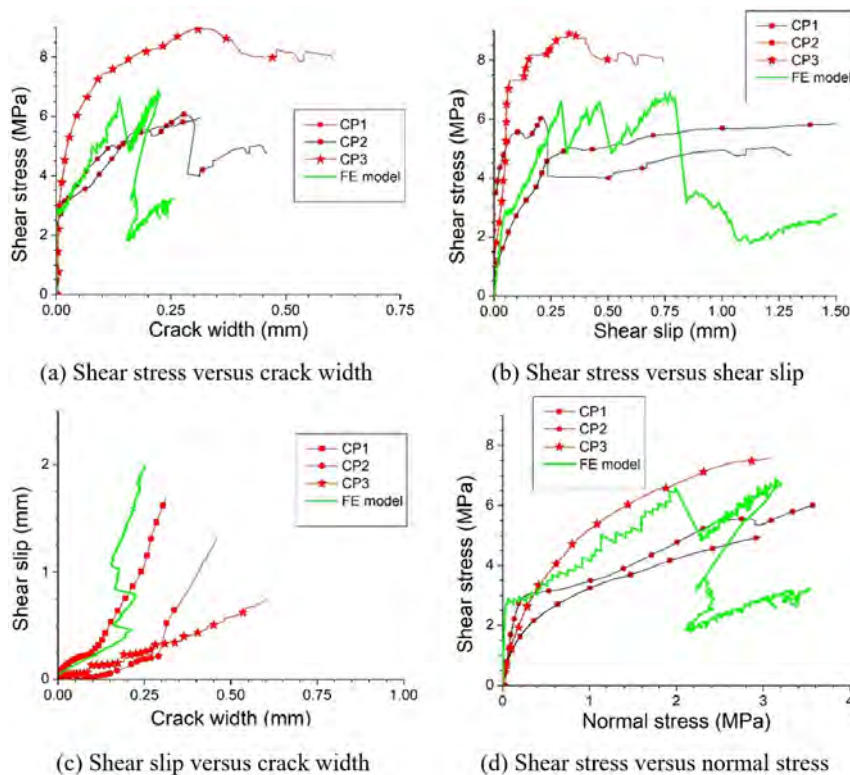


Figure 10. Relationship curves for the push-off specimen without steel fibers (F-00-2).

A good correlation between experimental and model results for the normal stress versus shear stress curve was observed up to maximum shear stress, even though the finite element model showed a smaller crack width in the shear plane. After this, the finite element model showed a decrease in shear stress, which was not observed in the test specimen because of the normal reinforcement. It is concluded that the finite element model was able to accurately represent the push-off specimen with steel fiber-reinforced concrete only up to the maximum shear stress because the finite element model did not consider the presence of steel fibers crossing the cracked plane. Previous studies explicitly

simulated steel fibers in the cracked plane in mode I fracture but did not consider the interaction between fibers and aggregate interlock in the cracked plane [27]. Other studies have analyzed the interaction between steel fibers and aggregate interlock and proposed analytical solutions, but did not present computational modeling [28], [29]. Some other studies have proposed constitutive models for fiber-reinforced concrete by coupling the fiber and the aggregate interlock, but they have not correlated their results with the shear retention factor [30], [31].

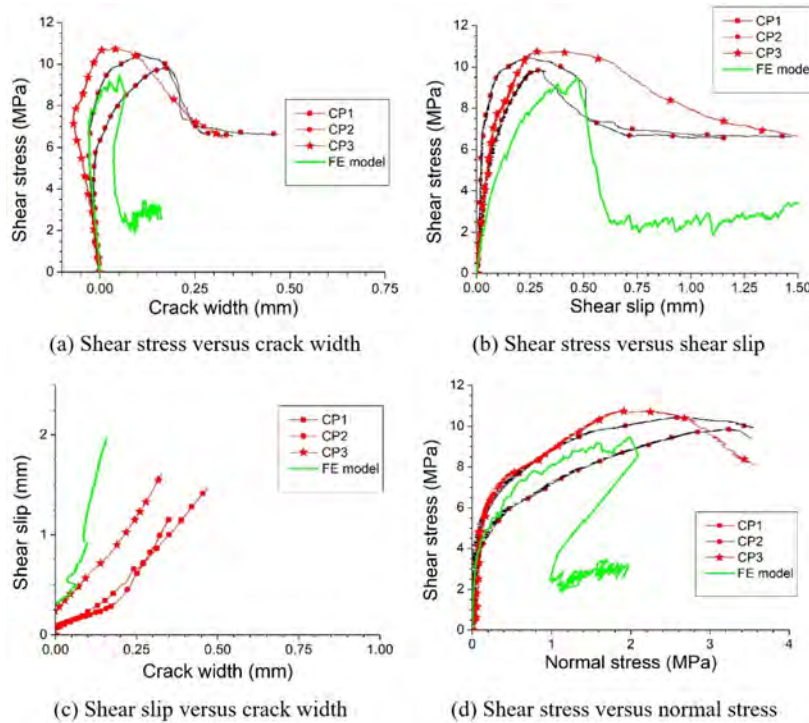


Figure 11. Relationship curves for the push-off specimen with steel fibers (F-15-2).

Despite the limitations of the finite element model in simulating aggregate interlock with steel fibers, it was able to predict the influence of steel fibers on the shear strength (Figure 12). Therefore, an interface element with crack dilatancy models associated with the tensile behavior of steel fiber-reinforced concrete can be used to simulate a push-off specimen of fibrous concrete with a pre-cracked shear plane only up to the maximum shear stress. More studies should be conducted on the representation of the crack shear modulus of steel fiber-reinforced concrete through a shear retention factor, primarily to characterize the mode II fracture parameter of the steel fiber-reinforced concrete.

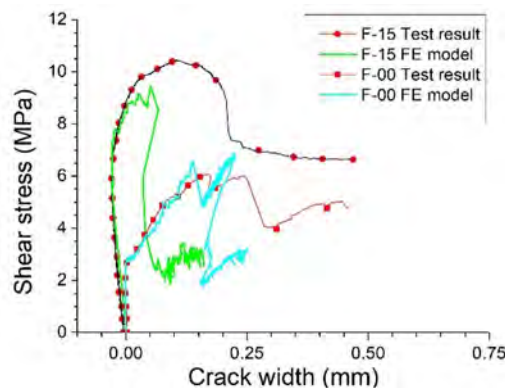


Figure 12. Shear stress versus crack width for push-off specimens with and without steel fibers.

4 FINITE ELEMENT MODEL OF REINFORCED CONCRETE BEAMS WITHOUT STIRRUPS

In the current study, two approaches were used to model the shear strength of reinforced concrete beams with a shear span-to-depth ratio (a/d) less than 3 and no transverse reinforcement, under plane stress. Two beams tested by Araújo et al. [32] and one beam tested by Garcia [33] were used. Of the beams tested by Araújo et al. [32], the V-0-0 and V-1-0 beams were selected, which had a shear span-to-depth ratio (a/d) of 2.17. The first beam was composed of plain concrete, and the second beam contained 1% steel fibers, similar to the fibers used in the experimental procedure presented in item 2. Both beams had a maximum aggregate size of 12.5 mm (Figure 13a). Of the beams tested by Garcia [33], the beam 1R was selected, which had a shear span-to-depth ratio (a/d) of 2.66, no steel fibers, and maximum aggregate size of 19 mm (Figure 13b).

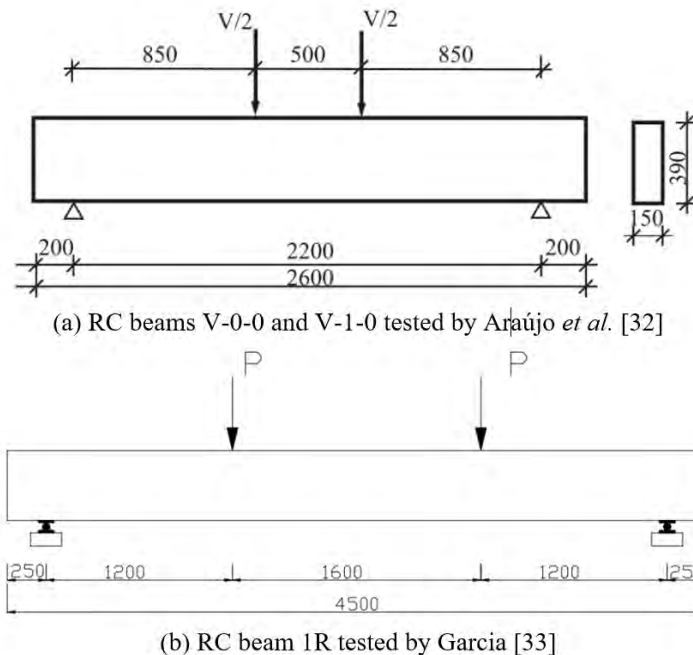


Figure 13. Geometry of reinforced concrete (RC) beams used for modeling (dimensions in mm).

These beams cover two types of potential shear failure. Beams with shear span that are short, with an aspect ratio (a/d) ranging from 1 to 2.5, develop inclined cracks near the supports and can support loads through arch action. The ultimate failure of these beams occurs due to a splitting failure or crushing of the compression zone over the top of the crack, which is referred to as shear compression-failure. In shear spans that are slender, with an aspect ratio ranging from about 2.5 to about 6, the beam fails with inclined cracks due to the combined effect of shear force and bending moment. This failure type mobilizes several mechanisms in the reinforced concrete beam, such as cantilever action, residual tensile strength action, dowel action, and aggregate interlock [34, 35].

4.1 Finite element mesh

In the finite element model with a discrete crack approach, the shear crack in reinforced concrete beams was described by interface elements, and aggregate interlock was represented by the crack dilatancy model. This modeling approach was used only for beams with plain concrete, as finite element modeling results of the push-off specimen demonstrated that aggregate interlock models did not accurately represent the post-peak behavior of specimens with steel fiber-reinforced concrete. For all reinforced concrete beams, only the mid-span was modeled, given the symmetry of the beam and the applied loading.

A shear crack with an angle of 42° was observed in V-0-0 beam, which started from the point of applied load up to the longitudinal reinforcement on the lower face of the beam. The finite element mesh shown in Figure 14a was generated, where red lines represent the interface elements used to simulate the shear crack of the beam. In the smeared crack approach, the beam had the same finite element mesh as in the discrete crack approach but without interface elements to simulate the shear crack (see Figure 14b). The size of finite elements was 10 mm in both approaches for the V-0-0 beam. The mesh for the V-1-0 beam was identical, with the exception that only the smeared crack approach was used to model this beam.

During testing of beam 1R, a shear crack with an angle of 45° was observed, and a finite element mesh (shown in Figure 15a) was developed. Interface elements were also used to model the shear crack. Figure 15b shows the mesh used in the smeared crack approach. Each finite element mesh had a dimension of 10 mm. All beams were modelled using a finite element with quadratic interpolation. Beam reinforcements were represented by embedded reinforcement elements.

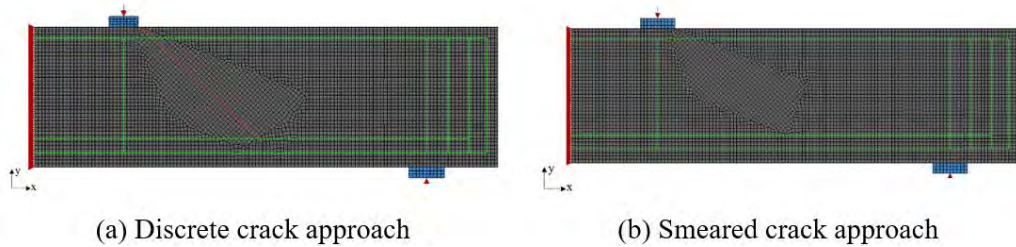


Figure 14. Finite element mesh of reinforced concrete beam V-0-0.

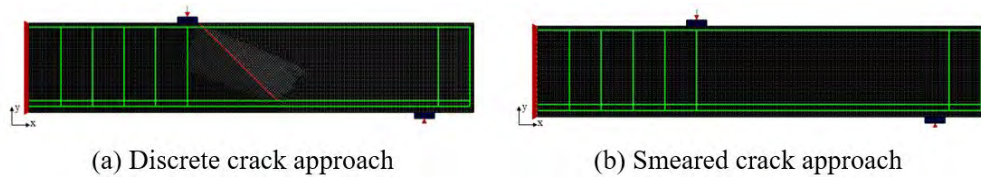


Figure 15. Finite element mesh of reinforced concrete beam 1R.

4.2 Material properties and constitutive laws

The mechanical properties of plain concrete and steel fiber-reinforced concrete beams are described in Table 5, and the mechanical properties of beam reinforcements are given in Table 6.

The compressive behavior of concrete was modeled using a parabolic curve based on fracture energy, and the tensile behavior of plain concrete was modeled using a linear softening diagram based on mode I fracture energy. For plain concrete, the crack bandwidth was automatically calculated as the square root of the finite element area, according to the method proposed by Rots [36]. The compressive fracture energy was defined as 100 times the mode I fracture energy.

Table 5. Mechanical properties of concrete.

Beam	Fiber content (%)	Coarse aggregate (mm)	f_c (MPa)	f_{ct} (MPa)	E_c (GPa)	G_f^I (N/mm)	G_c (N/mm)	ν
V-0-0	0.00	12.50	46.30	3.70	27.73	0.146	14.6	0.3
V-1-0	1.00	12.50	56.87	3.28	31.78	Table 6	341.1	0.3
1R	0.00	19.00	70.20	3.24	28.82	0.156	15.59	0.3

f_c : compressive strength of concrete; f_{ct} : axial tensile strength of concrete; E_c : modulus of elasticity of concrete; G_f^I : fracture energy of concrete; G_c : compressive fracture energy of concrete; ν : Poisson’s ratio of concrete.

Table 6. Mechanical properties of beam reinforcements.

Beam	1R	V-0-0 and V-1-0
Bar diameter (mm)	6.3	20.0
Modulus of elasticity (GPa)	173.33	210.00
Yield strength (MPa)	390	500

The tensile behavior of the steel fiber-reinforced concrete in the V-1-0 beam was represented by a bilinear tension softening diagram, as shown in Figure 9a. The stress and strain values for this diagram were obtained by Araújo et al. [5] using an inverse analysis on prismatic specimens under four-point loading, as presented in Table 7. The compressive fracture energy was defined as 100 times the area under the tensile stress-strain curve multiplied by the crack bandwidth, which was adopted as the size of the finite element (10 mm).

Table 7. Bilinear tension softening of the steel fiber-reinforced concrete of beam V-1-0.

Point	Tensile stress (MPa)	Strain (%)
1	3.28	0.103
2	1.64	12.00
3	0.00	50.00

The same stiffnesses that were determined by finite element analysis of the push-off test were applied for the discrete crack approach using interface elements. However, for beams, the tensile strength of the interface element was assumed to be equal to the tensile strength of concrete, given that the shear plane of beams was not previously cracked. Different crack dilatancy models in interface elements were used for computational modeling of beams.

4.3 Result analysis

Table 8 shows the maximum load of beams obtained using the smeared crack approach and different values for the shear retention factor (β). The use of the empirical β factor proposed in this study (Table 2) allowed good representation of the maximum load of the two test beams without fibers. The equation proposed by Al Mahaidi [15] has a similar variation of the empirical β factor and also displays good precision in evaluating the maximum load of beams without fibers. The equations proposed by Figueiras [16] and Červenka et al. [18] allowed good representation of the maximum load of the beams V-0-0 and 1R, respectively. For V-1-0 beam with steel fiber-reinforced concrete, the equations proposed by Červenka et al. [18] and Figueiras [16] and the empirical β factor proposed in this study (Table 2) predicted the maximum load of steel fiber-reinforced concrete beams with an error of less than 10%.

Table 8. Maximum load of beams estimated by the finite element model using the smeared crack approach.

Shear retention factor	V-0-0		V-1-0		1R	
	Maximum load (kN)	Difference from test	Maximum load (kN)	Difference from test	Maximum load (kN)	Difference from test
Experimental result	172.50	-	260.00	-	133.00	-
$\beta = 0.01$	145.66	-15.56%	276.77	6.45%	153.67	15.54%
$\beta = 0.05$	153.95	-10.75%	263.97	1.53%	128.75	-3.20%
$\beta = 0.10$	153.77	-10.86%	248.54	-4.41%	127.46	-4.17%
$\beta = 0.30$	184.76	7.11%	287.71	10.66%	132.88	-0.09%
Al Mahaidi [15]	169.05	-2.00%	170.10	-34.58%	135.62	1.97%
Červenka et al. [18]	198.95	15.33%	279.78	7.61%	128.07	-3.71%
Rots and Blaauwendraad, $k = 1$ [17]	204.11	18.32%	231.34	11.02%	128.56	-3.34%
Figueiras [16]	177.13	2.68%	248.54	-4.41%	105.10	-20.98%
Proposed β factor	174.47	1.14%	282.44	8.63%	138.74	4.32%

When a constant β factor is used, the resistance of the finite element model usually increases with increasing β . However, there is no unique value that can be used to accurately estimate the strength of the three beams, and the best prediction for each beam was obtained with different β values.

Table 9 describes the results obtained using the discrete crack approach, represented by interface elements, for beams without steel fiber-reinforced concrete. The models for crack dilatancy proposed by Walraven and Reinhardt [7] and Li et al. [9] were the ones that best predicted the maximum load for V-0-0 beam. For beam 1R, all models predicted the maximum load of the beam with an error of less than 10%.

Figure 16 compares the load–displacement curves of the V-0-0 beam obtained from the experimental test and the finite element model using the two approaches. For low constant β factor values, the stiffness of the cracked beam estimated by the finite element model was found to be similar to the initial experimental stiffness, but the maximum load of the beam was lower. By contrast, the finite element model with the variable β factor estimated the maximum load of the beam with more precision. However, it also exhibited less displacement than was observed during the test after the formation of the flexural cracks. On the other hand, the finite element model with a discrete crack approach accurately represented the cracking shear load of the beam. i.e., 96.2 kN in the model compared to 87.5 kN in the test. Furthermore, beam stiffness was accurately represented after formation of the shear crack. It is important to note that

vertical beam displacement was not measured up to the maximum load; thus, the analysis refers to the loading where the vertical displacement was measured in the test.

Table 9. Maximum load of beams estimated by the finite element model using the discrete crack approach.

Crack dilatancy model	V-0-0		1R	
	Maximum load (kN)	Difference from test	Maximum load (kN)	Difference from test
Experimental result	172.50	-	133.00	-
Li et al. [9]	164.05	-4.89%	141.73	6.62%
Walraven and Reinhardt [7]	172.09	-0.24%	140.73	5.71%
Walraven [6]	134.18	-22.21%	137.35	3.27%
Gambarova and Karakoç [8]	155.21	-10.03%	143.62	7.98%

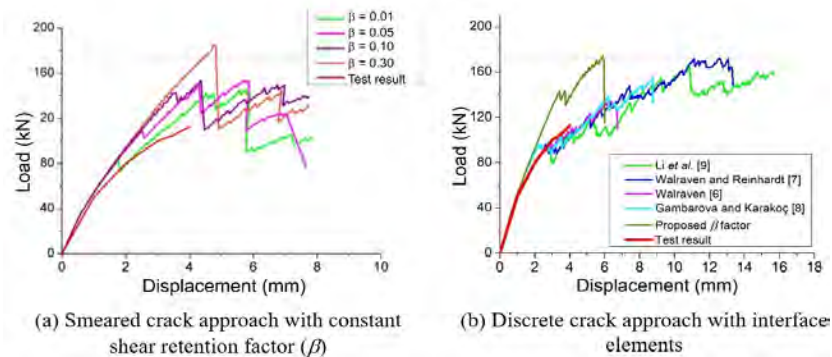


Figure 16. Load–displacement curve of the mid-span of the reinforced concrete beam V-0-0 ($a/d = 2.17$).

The good results of the discrete crack approach with interface elements for representation of the shear crack of the V-0-0 beam can be explained by the crack pattern. Both modeling approaches had a crack pattern similar to that observed at the end of the test (Figure 17); however, the finite element model with the discrete crack approach showed a wider crack width and more sliding along the crack, as simulated by interface elements, than the smeared crack approach. A secondary shear crack was observed, with branches near the point of load application. Hence, the discrete crack approach was capable of providing a more precise estimation of the stiffness of short shear-span beams when failure occurred due to shear-compression with a single shear crack and a low quantity of flexural cracks.

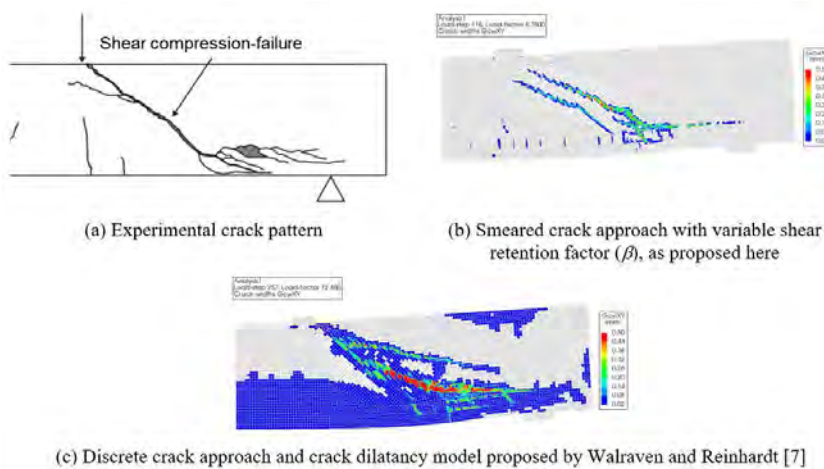


Figure 17. Crack pattern of the reinforced concrete beam V-0-0 ($a/d = 2.17$).

Figure 18 shows the load–displacement curves of beam 1R, which were estimated from the experimental test and the finite element model using two modeling approaches. Overall, minimal variations in maximum load were observed when the smeared crack approach was utilized, regardless of whether a constant β factor ($0.05 < \beta < 0.3$) or a variable β factor. Also, the use of the discrete crack approach with interface elements provided similar maximum load values, regardless of the crack dilatancy model used.

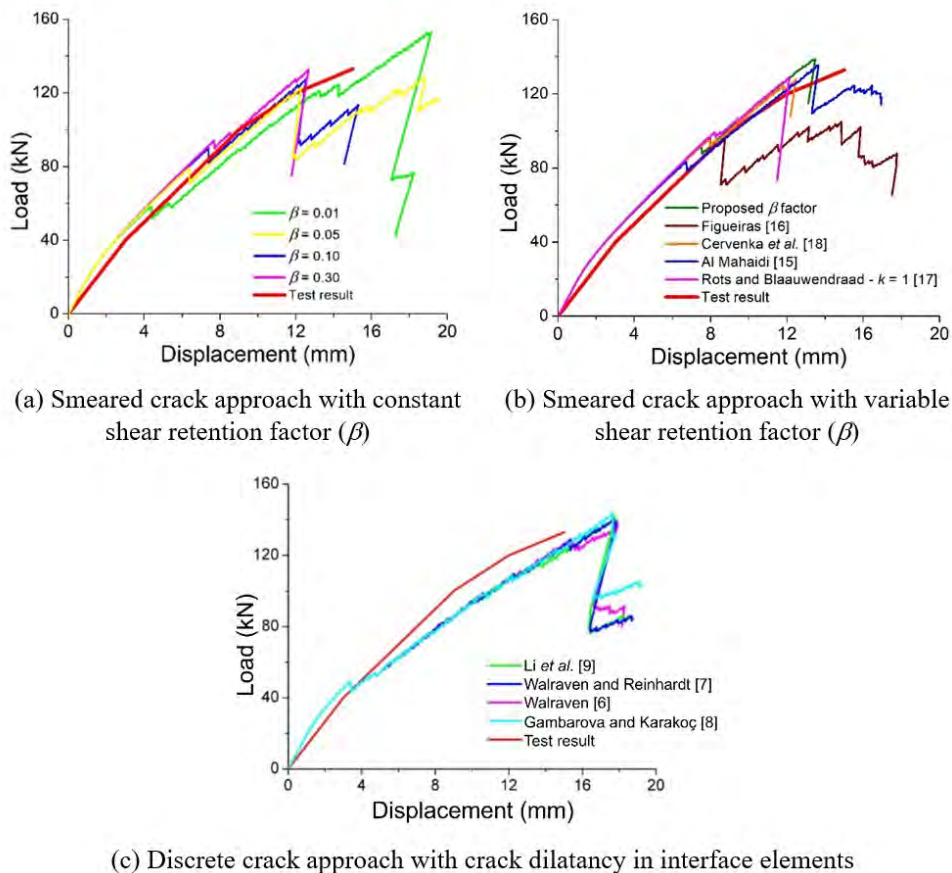


Figure 18. Load–displacement curves of the mid-span of the reinforced concrete beam 1R ($a/d = 2.66$).

The cracking behavior of beam 1R was well represented by both smeared and discrete crack approaches. Such a finding is due to the failure mode of the beam, which has a shear span-to-depth ratio (a/d) of 2.66. Because the concentrated load was further from the support, the beam developed several flexural cracks before the appearance of the main shear crack, which defined the maximum load of the beam (Figure 19). This ensured that beam displacement was not predominantly influenced by sliding along the main shear crack, having a greater contribution from flexural cracks. Thus, the discrete crack approach simulated a main shear crack with the same pattern as that predicted by the smeared crack approach. In this beam, with slender shear-span, the smeared crack approach was sufficient to represent the stiffness of the beam after concrete cracking.

Figure 20 compares the experimental and predicted load–displacement curves of the fibrous concrete beam V-1-0. The smeared crack approach revealed a small influence of the shear retention factor on the response of the beam. The different β factor values afforded similar maximum loads. This finding demonstrates that the tensile behavior of fibrous concrete is more important than the shear retention factor of steel fiber-reinforced concrete beams, even in the case of shear failure.

The crack pattern of beam V-1-0 is depicted in Figure 21. Given that steel fibers provide greater resistance to flexural cracking, there is greater flexural cracking during the test. Thus, although the beam had a shear span-to-depth ratio (a/d) of 2.17, unlike reinforced concrete beam V-0-0 without fibers, the smeared crack approach adequately represented beam stiffness after concrete cracking.

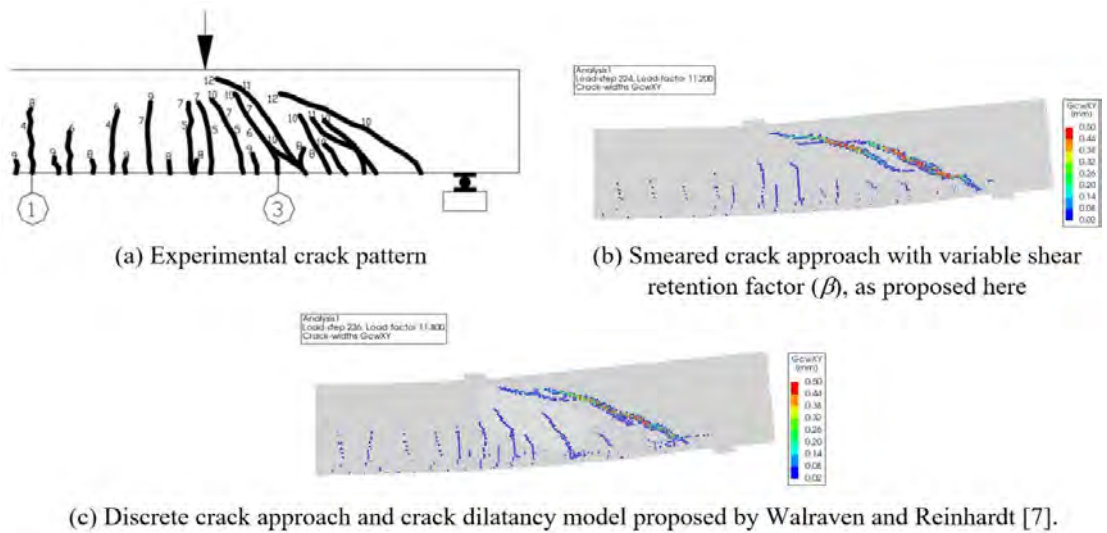


Figure 19. Crack pattern of the reinforced concrete beam 1R ($a/d = 2.66$).

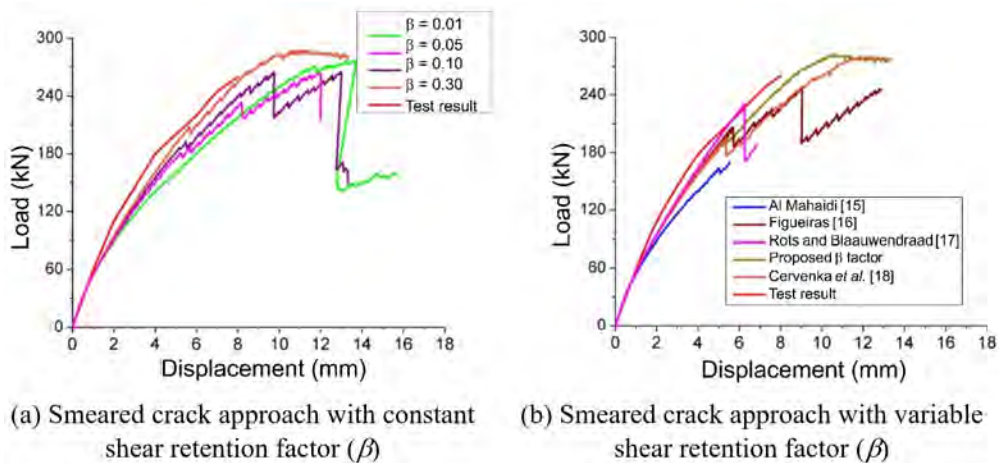


Figure 20. Load–displacement curves of the mid-span of the fibrous concrete beam V-1-0 ($a/d = 2.17$).

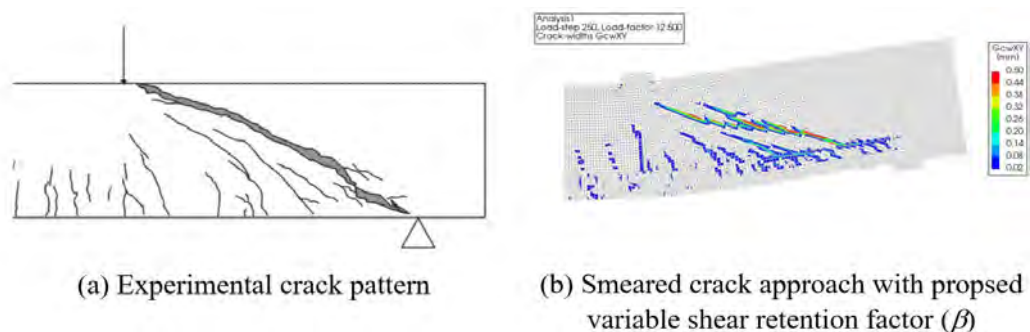


Figure 21. Crack pattern of the fibrous concrete beam V-1-0 ($a/d = 2.17$).

5 CONCLUSIONS

In this study, finite element models were developed to simulate direct shear tests and reinforced concrete beams without transverse reinforcement and with span-to-depth ratios of 2.17 and 2.66. Several shear retention factors (β)

factor) were used to determine their effectiveness. The empirical β factor was deduced from double-notched push-through tests, which predicted well the shear strength of reinforced concrete beams without steel fibers. The behavior of the proposed β factor was similar to the equations proposed by Figueiras [16] and Červenka *et al.* [18], which confirms the effectiveness of the test setup adopted in this study. Furthermore, the variable β factor suggested by Al Mahaidi [15] was also accurate to predict the shear strength of reinforced concrete beams without steel fibers.

On the other hand, when a constant β factor is used, the shear strength of finite element models usually increases as β factor increases. However, there is no unique value that can precisely estimate the shear strength of reinforced concrete beams. This conclusion is consistent with the observations of Hendriks *et al.* [14], who strongly recommended utilizing a variable shear retention factor in fixed crack models. Constant β factor models are not advisable since they tend to overestimate the stiffness of beams and slabs.

A finite element model was developed to simulate push-off specimens with a pre-cracked shear plane using crack dilatancy models implemented in interface elements. Different models for aggregate interlock did not provide significant differences, suggesting that they are equivalent for simulating push-off specimens. Finite element models predicted greater shear slip and lower crack width than that observed in the test, indicating the need for further analysis of the interaction between aggregate interlock, steel fiber, and dowel rebar.

Finite element modeling using the smeared crack approach for beams without transverse reinforcement is a viable alternative for cases where the shear crack fracture is unknown. In this case, the smeared crack approach was precise enough to estimate the resistance, stiffness, and crack pattern of beams without transverse reinforcement and a shear span-to-depth ratio of 2.66. This was due to the densely distributed flexural and shear cracks that governed the overall behavior of the beam.

For beams without transverse reinforcement and with a shear span-to-depth ratio of 2.17, the stiffness of the cracked beam was better represented by the discrete crack approach. These beams exhibited only a few flexural cracks before the appearance of the critical shear crack, indicating that the smeared crack approach is not suitable for accurately representing the overall behavior of these beams. An appropriate solution for beam with shear compression-failure is to use the smeared crack approach as a qualitative predictor of crack localization, followed by a more precise analysis using the predefined crack, which can be represented by the discrete crack approach with interface elements.

For beams with steel fiber-reinforced concrete, the shear retention factor had a slight influence on beam behavior due to the greater ductility in tension of the fibrous concrete. Additionally, different values of the β factor in finite element analysis with the smeared crack approach had little impact on the stiffness and shear strength of the beam. If a constant β factor is used in modeling, a value less than 0.1 is recommended.

It is important to note that these conclusions were obtained from modeling only three beams, and thus, further research should be conducted to confirm these results for beams with different concrete strength and geometry. Nevertheless, these results are a significant contribution to guiding designers in finite element modeling of beams and slabs without transverse reinforcement.

ACKNOWLEDGEMENTS

This study was financed in part by the Brazilian Federal Agency for Support and Evaluation of Graduate Education (CAPES, Finance Code 001). The authors would also like to thank the Goiás State Research Foundation (FAPEG, grant no. 2017.10.267000.513) and the Brazilian National Council for Scientific and Technological Development (CNPq, grant no. 552118/2011-7) for financing this research.

REFERENCES

- [1] Q. Deng, W.-J. Yi, and F.-J. Tang, "Effect of coarse aggregate size on shear behavior of beams without shear reinforcement," *ACI Struct. J.*, vol. 114, no. 5, pp. 1131–1142, 2017, <http://dx.doi.org/10.14359/51689720>.
- [2] E. Sells, J. J. Myers, and J. S. Volz, "Aggregate interlock push-off test results of Self-Consolidating Concrete (SCC) for use in infrastructure element," in *Proc. ISEC 2013 - 7th Int. Struct. Eng. Constr. Conf. New Dev. Struct. Eng. Constr.*, 2013, pp. 917–922, <http://dx.doi.org/10.3850/978-981-07-5354-2-St-194-552>.
- [3] D. L. Araújo, F. A. Lobo, and B. G. Martins, "A shear stress-slip relationship in steel fibre-reinforced concrete obtained from push-off testing," *Constr. Build. Mater.*, vol. 293, pp. 123435, 2021, <http://dx.doi.org/10.1016/j.conbuildmat.2021.123435>.
- [4] S. Lee, J.-Y. Cho, and F. J. Vecchio, "Analysis of steel fiber-reinforced concrete elements subjected to shear," *ACI Struct. J.*, vol. 113, no. 2, pp. 275–285, 2016., <http://dx.doi.org/10.14359/51688474>.

- [5] D. L. Araújo, L. C. Carmo, F. G. T. Nunes, and R. D. Toledo Filho, "Modelagem computacional de vigas de concreto armado reforçado com fibras de aço submetidas a cisalhamento," *Rev. IBRACON Estrut. Mater.*, vol. 3, no. 1, pp. 68–94, 2010., <http://dx.doi.org/10.1590/S1983-41952010000100005>.
- [6] J. C. Walraven, *Aggregate Interlock: a Theoretical and Experimental Analysis*. Delft Univ. Technol., 1980. Accessed: Sep. 18, 2022. [Online]. Available: <https://repository.tudelft.nl/islandora/object/uuid:c33a2890-f9c1-4176-929e-6988f0f23640/datastream/OBJ/download>
- [7] J. C. Walraven and H. W. Reinhardt, "Theory and experiments on the mechanical behaviour of cracks in plain and reinforced concrete subjected to shear loading," *Heron*, vol. 26, no. 1A, pp. 1–68, 1981.
- [8] P. G. Gambarova and C. Karakoc, "A new approach to the analysis of the confinement role in regularly cracked concrete elements," in *H - Struct. Eng. Prestressed Reac. Pressure Vessels Other Struct. H5 - Failure, Fracture Propag. Ductility SMIRT 7*, 1983, pp. 251–261.
- [9] B. Li, K. Maekawa, and H. Okamura, "Contact density model for stress transfer across cracks in concrete," *J. Fac. Eng. Univ. Tokyo*, vol. XL, no. 1, pp. 9–52, 1989.
- [10] A. T. Slobbe, M. A. N. Hendriks, and J. G. Rots, "Sequentially linear analysis of shear critical reinforced concrete beams without shear reinforcement," *Finite Elem. Anal. Des.*, vol. 50, pp. 108–124, 2012, <http://dx.doi.org/10.1016/j.finel.2011.09.002>.
- [11] J. A. O. Barros, H. Baghi, S. J. E. Dias, and A. Ventura-Gouveia, "A FEM-based model to predict the behaviour of RC beams shear strengthened according to the NSM technique," *Eng. Struct.*, vol. 56, pp. 1192–1206, 2013, <http://dx.doi.org/10.1016/j.engstruct.2013.06.034>.
- [12] J. Sagaseta, *The Influence of Aggregate Fracture on the Shear Strength of Reinforced Concrete Beams*. Imp. Coll. London, 2008. Accessed: Sep. 18, 2022. [Online]. Available: <https://ibeton.epfl.ch/Pubs/2008/Sagaseta08a.pdf>
- [13] R. Scotta, R. Vitaliani, A. Saetta, E. Oñate, and A. Hanganu, "Scalar damage model with a shear retention factor for the analysis of reinforced concrete structures: theory and validation," *Comput. Struct.*, vol. 79, no. 7, pp. 737–755, 2001, [http://dx.doi.org/10.1016/S0045-7949\(00\)00178-4](http://dx.doi.org/10.1016/S0045-7949(00)00178-4).
- [14] M. A. N. Hendriks, A. de Boer, and B. Belletti, *Guidelines for Nonlinear Finite Element Analysis of Concrete Structures*. Rijkswaterstaat Cent. Infrastruct., Report RTD:1016-1:2017, 2017.
- [15] DIANA FEA, *User's Manual - Material Library - DIANA Release 10.0*, 1st ed. Delft: TNO DIANA BV, 2016.
- [16] J. A. Figueiras, *Ultimate Load Analysis of Anisotropic and Reinforced Concrete Plates and Shells*. Univ. Coll. Swansea, 1983. Accessed: Sep. 18, 2022. [Online]. Available: [https://repositorio-aberto.up.pt/bitstream/10216/11772/2/Texto integral.pdf](https://repositorio-aberto.up.pt/bitstream/10216/11772/2/Texto%20integral.pdf)
- [17] J. G. Rots and J. Blaauwendraad, "Crack models for concrete: discrete or smeared? Fixed, multi-directional or rotating," *Heron*, vol. 34, no. 1, pp. 1–59, 1989.
- [18] V. Červenka, L. Jendele, and J. Červenka, *ATENA Program Documentation - Part 1 - Theory*. Prague: Cervenka Consulting Ltd., 2005.
- [19] A. G. Soto and W. Kaufmann, "Effect of test setups on the shear transfer capacity across cracks in FRC," in *Fibre Reinforced Concrete: Improvements and Innovations* (BEFIB 2020. RILEM Bookseries 30), P. Serna, A. Llano-Torre, J. R. Martí-Vargas and J. Navarro-Gregori, Eds., Cham: Springer, 2021, http://dx.doi.org/10.1007/978-3-030-58482-5_15
- [20] W. Kaufmann, A. Amin, A. Beck, and M. Lee, "Shear transfer across cracks in steel fibre reinforced concrete," *Eng. Struct.*, vol. 186, pp. 508–524, 2019, <http://dx.doi.org/10.1016/j.engstruct.2019.02.027>.
- [21] J. Echegaray-Oviedo, J. Navarro-Gregori, E. Cuenca, and P. Serna, "Modified push-off test for analysing the shear behaviour of concrete cracks," *Strain*, vol. 53, no. 6, pp. 1–17, 2017, <http://dx.doi.org/10.1111/str.12239>.
- [22] DIANA FEA, *User's Manual - iDIANA Release 10.0*, 1st ed. Delft: TNO DIANA BV, 2016.
- [23] fib, *fib Model Code for Concrete Structures 2010*. Berlin: Wilhelm Ernst & Sohn, 2013.
- [24] M. Blomfors, C. G. Berrocal, K. Lundgren, and K. Zandi, "Incorporation of pre-existing cracks in finite element analyses of reinforced concrete beams without transverse reinforcement," *Eng. Struct.*, vol. 229, pp. 111601, 2021, <http://dx.doi.org/10.1016/j.engstruct.2020.111601>.
- [25] American Society for Testing Materials, *Standard Test Method for Flexural Performance of Fiber-Reinforced Concrete (Using Beam With Third-Point Loading)*, ASTM C1609, 2019.
- [26] I. Löfgren, "Fibre-reinforced concrete for industrial construction: a fracture mechanics approach to material testing and structural analysis," Ph.D. dissertation, Dept. Civ. Environ. Eng. Struct. Eng., Chalmers Univ. Technol., Göteborg, Sweden, 2005. Accessed: Sep. 18, 2022. [Online]. Available: <https://publications.lib.chalmers.se/records/fulltext/8627/8627.pdf>
- [27] L. A. G. Bitencourt, O. L. Manzoli, T. N. Bittencourt, and F. J. Vecchio, "Numerical modeling of steel fiber reinforced concrete with a discrete and explicit representation of steel fibers," *Int. J. Solids Struct.*, vol. 159, pp. 171–190, 2019, <http://dx.doi.org/10.1016/j.ijsolstr.2018.09.028>.
- [28] T. L. Resende, D. C. T. Cardoso, and L. C. D. Shehata, "Experimental and theoretical investigation on the stress transfer across cracks due to combined action of steel fibers and aggregate interlock," *Cement Concr. Compos.*, vol. 124, pp. 104239, 2021, <http://dx.doi.org/10.1016/j.cemconcomp.2021.104239>.

- [29] T. Soetens and S. Matthys, "Shear-stress transfer across a crack in steel fibre-reinforced concrete," *Cement Concr. Compos.*, vol. 82, pp. 1–13, 2017, <http://dx.doi.org/10.1016/j.cemconcomp.2017.05.010>.
- [30] L. M. P. Mato, J. A. O. Barros, A. Ventura-Gouveia, and R. A. B. Calçada, "Constitutive model for fibre reinforced concrete by coupling the fibre and aggregate interlock resisting mechanisms," *Cement Concr. Compos.*, vol. 111, pp. 103618, 2020, <http://dx.doi.org/10.1016/j.cemconcomp.2020.103618>.
- [31] F. Soltanzadeh, J. A. O. Barros, and R. F. C. Santos, "High performance fiber reinforced concrete for the shear reinforcement: experimental and numerical research," *Constr. Build. Mater.*, vol. 77, pp. 94–109, 2015, <http://dx.doi.org/10.1016/j.conbuildmat.2014.12.003>.
- [32] D. L. Araújo, F. G. T. Nunes, R. D. Toledo Fo., and M. A. S. Andrade, "Shear strength of steel fiber-reinforced concrete beams," *Acta Sci. Technol.*, vol. 36, no. 3, pp. 389–397, 2014., <http://dx.doi.org/10.4025/actascitechnol.v36i3.19005>.
- [33] S. L. G. Garcia, *Taxa de armadura transversal mínima em vigas de concreto armado*. Univ. Fed. Rio de Janeiro, 2002.
- [34] F. Cavagnis, M. F. Ruiz, and A. Muttoni, "Shear failures in reinforced concrete members without transverse reinforcement: An analysis of the critical shear crack development on the basis of test results," *Eng. Struct.*, vol. 103, pp. 157–173, 2015., <http://dx.doi.org/10.1016/j.engstruct.2015.09.015>.
- [35] J. K. Wight and J. G. Macgregor, *Reinforced Concrete: Mechanics and Design*, 6th ed. Prentice Hall, 2011.
- [36] J. G. Rots, *Computational Modeling of Concrete Fracture*. Delft Univ. Technol., 1988. Accessed: Sep. 18, 2022. [Online]. Available: <https://repository.tudelft.nl/islandora/object/uuid%3A06985d0d-1230-4a08-924a-2553a171f08f>

Author contributions: DLA: supervision, project administration, funding acquisition, methodology, formal analysis, writing. CRSF: methodology, formal analysis, investigation. FAL: methodology, investigation.

Editors: Leandro Trautwein, Mauro Real, Mario Pimentel.



ORIGINAL ARTICLE

Post punching shear pattern and progressive collapse of flat slab building

Comportamento pós punção e colapso progressivo em uma estrutura em laje lisa

Bernardo Cruz Pereira Galdino^a Guilherme Sales Melo^a ^aUniversidade de Brasília – UnB, Department of Civil and Environmental Engineering, Brasília, DF, BrasilReceived 23 June 2022
Accepted 23 March 2023

Abstract: The possibility of the occurrence of a second punching shear failure and of a Progressive Collapse after a punching shear failure had occurred in one flat slab column connection is investigated in two building structures, using Eberick and SAP2000 softwares and the Yield Line Method, and codes ACI318:2019, EUROCODE2:2004 and NBR6118:2014. It is shown that slab column connections should be designed and detailed to prevent Progressive Collapse and that Integrity Reinforcement should always be present, and that the remaining capacity of floors after punching failures depends on the *i*) post-punching resistance of the connection being punched; *ii*) post-punching resistance of the neighbors' connections; *iii*) flexural resistance of the slabs, and that the flexural resistance of the slab's floors can be evaluated by the Yield Line Method.

Keywords: progressive collapse, flat slab, punching shear, yield line theory.

Resumo: A possibilidade da ocorrência de uma segunda ruptura por punção e colapso progressivo depois de uma ruptura por punção em uma ligação laje-pilar foi investigado em duas estruturas, usando os softwares Eberick e SAP2000, Método das Linhas de Ruptura e as normas ACI318:2019, EUROCODE2:2004 e NBR6118:2014. Verifica-se que a ligação laje-pilar deve ser projetada para prevenir o colapso progressivo, as armaduras contra o colapso progressivo devem estar sempre presentes, a capacidade remanescente da laje lisa depois de uma ruptura por punção depende da resistência pós punção da ligação punccionada, resistência pós punção das ligações vizinhas sobrecarregadas, resistência de flexão da laje conforme o Método das Linhas de Ruptura.

Palavras-chave: colapso progressivo, laje lisa, punção cisalhante, linhas de ruptura.

How to cite: B. C. P. Galdino and G. S. Melo, "Post punching shear pattern and progressive collapse of flat slab building," *Rev. IBRACON Estrut. Mater.*, vol. 16, no. 3, e16312, 2023, <https://doi.org/10.1590/S1983-41952023000300012>

1 INTRODUCTION

This study aims to verify using a software the post-punching shear behavior of reinforced concrete flat slab structures considering the partial or total failure of the slab-column connection, using SAP 2000 [1] and Eberick 2022 [2] software's.

When a slab-column connection fails, there may be an overload on neighboring supports and new failures may occur in a chain reaction [3]. Thus, the effect known as progressive collapse arises.

The causes of this phenomenon include improper renovation of structure, fire, vehicle collision, substandard material, design and/or execution errors. The accident that occurred with the Liberdade Building, in Rio de Janeiro, highlights the tragic damage caused after the loss of a support [4].

Progressive collapse of a building can be triggered by a punching shear failure even eight months after a slab-column connection punching shear resistance was exceeded by almost four times [5].

Corresponding author: Bernardo Cruz Pereira Galdino. E-mail: eng.bernardogaldino@gmail.com

Financial support: None.

Conflict of interest: Nothing to declare.

Data Availability: The data that support the findings of this study are available from the corresponding author, [B.C.P. Galdino], upon reasonable request.



This is an Open Access article distributed under the terms of the Creative Commons Attribution License, which permits unrestricted use, distribution, and reproduction in any medium, provided the original work is properly cited.

Flat slabs are structural elements that are rested by columns and are very susceptible to progressive collapse, as there is less capacity for redistribution of loads and a brittle failure by punching with few pathology warnings. The advantages of using this structural system are lower ceiling heights, concrete forms simplifications and lower costs during construction.

In order to avoid progressive collapse and improve post-punching shear behavior, well anchored reinforcement can be used at the bottom of slab-column connections and is necessary to create alternative load paths, ductility, and continuity in the structure [6], [7], and this integrity bottom reinforcement is required and adopted in most codes [8]–[10].

The utilization of the Yield Line Theory to evaluate the post punching capacity of a flat floor submitted to a punching shear failure and its relation to the possibility of the occurrence of a progressive collapse has been adopted for some time [6], [11], and this use has been continued [12].

And as progressive collapse is not a well comprehensively explored phenomenon, due to its many implications [13], investigations continue to being done on the subject [14], [15], as post-punching shear behavior is one of the main factors that will interfere on the behavior of the floor slab and on the possibility of a progressive collapse and its possible tragic consequences.

2 METHODOLOGIES

Two flat slab buildings structures are analyzed, first the support reactions are obtained, then one column is removed, simulating a punching shear failure at this connection, and the redistribution of the support reactions at the remaining columns are followed, checking for the possibility of a progressive collapse at all slab columns connections.

After the slab punching shear failure, the loads found were compared with the loads obtained according to the intact structure, thus verifying the increase or decrease of the reactions at the connections.

It was then analyzed if there was a possibility of new failures at the most loaded connections by means of a new verification of the punching shear, considering the acting and the shear strength stresses.

The possibility of punching shear failures was checked using the codes ACI 318 [16], EUROCODE [9] and NBR 6118 [10], according to its requirements regarding critical surfaces, punching shear reinforcement, and checking the possibility of splitting or crushing of the concrete.

According to NBR 6118 [10], with the presence of shear reinforcement at the column region there are three calculated design stresses (τ_{Sd1} , τ_{Sd2} , τ_{Sd3}) determined with Equation 1, where F_{Sd} = reaction at the connection; u = critical perimeter; d = effective height; M_{Sdx} and M_{Sdy} = bending moments; K_1 and K_2 depends on the columns sides ratio; and W_{p1} and W_{p2} = plastic resistant modulus, while the resistant stresses are determined by Equations 2 to 4, where f_{ck} and f_{cd} = respectively the characteristic and design concrete strength; ρ = reinforcement ratio; A_{sw} and s_r = respectively the shear reinforcement area and spacing and f_{ywd} = design yielding limit.

$$\tau_{Sd} = \frac{F_{Sd}}{u \cdot d} + \frac{K_1 \cdot M_{Sdx}}{W_{p1} \cdot d} + \frac{K_2 \cdot M_{Sdy}}{W_{p2} \cdot d} \quad (1)$$

$$\tau_{Rd1} = 0.27 \cdot \left(1 - \frac{f_{ck}}{250}\right) \cdot f_{cd} \quad (2)$$

$$\tau_{Rd2} = 0.10 \cdot \left(1 + \sqrt{\frac{20}{d}}\right) \cdot (100 \cdot \rho \cdot f_{ck})^{\frac{1}{3}} + 1.5 \cdot \frac{d}{s_r} \cdot \frac{A_{sw} \cdot f_{ywd}}{u \cdot d} \quad (3)$$

$$\tau_{Rd3} = 0.13 \cdot \left(1 + \sqrt{\frac{20}{d}}\right) \cdot (100 \cdot \rho \cdot f_{ck})^{1/3} \quad (4)$$

For EUROCODE [9] the three calculated design stresses (σ_{Sd1} , σ_{Sd2} e σ_{Sd3}) are determined by Equation 5, similar to Equation 1, according to Equations 6 to 8, similar to Equations 2 to 4, but with a limit for a size effect on the slab thickness and a higher load factor.

$$\sigma_{Sd} = \frac{F_{Sd}}{u \cdot d} + \frac{K_1 \cdot M_{Sdx}}{W_{p1} \cdot d} + \frac{K_2 \cdot M_{Sdy}}{W_{p2} \cdot d} \quad (5)$$

$$\sigma_{Rd1} = 0.30 \cdot \left(1 - \frac{f_{ck}}{250}\right) \cdot f_{cd} \quad (6)$$

$$\sigma_{Rd2} = 0.09 \cdot \left(1 + \sqrt{\frac{20}{d}}\right) \cdot (100 \cdot \rho \cdot f_{ck})^{\frac{1}{3}} + 1.5 \cdot \frac{d}{s_r} \cdot \frac{A_{sw} \cdot f_{ywd}}{u \cdot d} \quad (7)$$

$$\sigma_{Rd3} = 0.12 \cdot \left(1 + \sqrt{\frac{20}{d}}\right) \cdot (100 \cdot \rho \cdot f_{ck})^{1/3} \quad (8)$$

ACI 318 [16] presents Equations 9 to 13, the first for the determination of the acting and the others for the resistant shear stresses, where V = load transferred by the slab; b_o = critical perimeter; M_{SC} = bending moment at the connection; J_c = geometric property of the section; γ_v = parcel of the moment transferred by shear and C_{AB} = eccentricity of the critical perimeter; β = ratio between the column sides and λ_s = size effect; f'_c = concrete strength; A_v and s = respectively the shear reinforcement area and spacing and f_{yt} = design yielding limit; α_s depends on the column position.

$$V_u = \frac{V}{b_o \cdot d} + \frac{\gamma_v \cdot M_{SC} \cdot C_{AB}}{J_c} \quad (9)$$

$$v_n = 0.75 \cdot 0.17 \cdot \left(1 + \frac{2}{\beta}\right) \cdot \lambda_s \cdot \sqrt{f'_c} + 0.75 \cdot \frac{A_v \cdot f_{yt}}{s \cdot b_o} \quad (10)$$

$$v_n = 0.75 \cdot 0.083 \cdot \left(\frac{\alpha_s \cdot d}{b_o} + 2\right) \cdot \lambda_s \cdot \sqrt{f'_c} + 0.75 \cdot \frac{A_v \cdot f_{yt}}{s \cdot b_o} \quad (11)$$

$$v_n = 0.75 \cdot 0.25 \cdot \lambda_s \cdot \sqrt{f'_c} + 0.75 \cdot \frac{A_v \cdot f_{yt}}{s \cdot b_o} \quad (12)$$

$$v_{cout} = 0.75 \cdot 0.17 \cdot \lambda_s \cdot \sqrt{f'_c} \quad (13)$$

The reinforcement against progressive collapse (integrity reinforcement) were determined according to Equations 14 to 17, according respectively to the NBR 6118:2014 [10], GSA:2013 [17], CEB:2010 [8] e ACI 352:2011 [18], where α_{ult} = angle between the reinforcement and the plan of the slab; and L_1 e L_2 = spans at the two directions.

$$A_s \geq \frac{1.5 \cdot F_{Sd}}{f_{yd}} \quad (14)$$

$$A_s \geq \frac{(0.17 \cdot b \cdot d \cdot f_{cd})}{f_{yd}} \quad (15)$$

$$A_s \geq \frac{F_{Sd}}{f_{yd} \cdot (f_t/f_y)_k \cdot \sin \alpha_{ult}} \quad (16)$$

$$A_s \geq \frac{0.5 \cdot W_u \cdot L_1 \cdot L_2}{f_{yd}} \quad (17)$$

The Yield Line Theory was also used to analyze the possibility of progressive collapse in the structure after the failure of a slab-column connection. The remaining flexural capacity of the slab was verified in the region where a support was removed using the Virtual-Work Method, procedure that has been used before [6], [11], and [12].

3 RESULTS AND DISCUSSIONS

3.1 First example

The analysis of the structure was carried out according to a structural design available in two lecture notes used in the UFMG (Federal University of Minas Gerais) course, authored by Chaves [19], and Silva [20].

The post-punching shear behavior was analyzed using the computer program SAP2000 [1] using the Finite Element Method. A comparison of the Integrity Reinforcement according to NBR 6118:2014 [10], GSA:2013 [17], CEB:2010 [8] and ACI 352:2011 [18] was also presented.

As shown in Figure 1, there is an advance of the slab at the edges (overhang) to increase the stiffness of the connection and there is no presence of beams or openings at the floor for the passage of electrical or hidro-sanitary pipes.

The reinforced concrete building has three floors, a ceiling height of 289 cm and twelve columns. The slabs were designed with a thickness of 16 cm, and with columns with a square cross section of 30 cm x 30 cm.

The concrete strength is 30 MPa and the reinforcement steel grade of 500 MPa. The Elasticity Modulus of the concrete was taken as 26072 MPa. The reinforcement adopted at the analysis was the same used at the lecture notes of UFMG [19] and [20], designed by the Equivalent Frame Method. In general bars with eight millimeters of diameter each 15 or 20 centimeters were used at the two directions, and for the connections close to the corners ten millimeters bars each 10 centimeters were used at the two directions. For the internal connections 12.5 mm bars each 12 centimeter was used at the two directions. Besides this, all connections presented punching shear reinforcement.

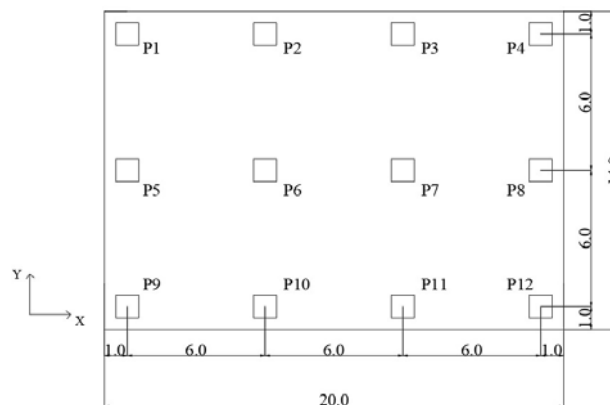


Figure 1. Floor plan of the structure – Dimensions in m.

According to the structural design in the lecture notes and NRB 6120 [21], a live load of 1.50 kN/m² and a total dead load of 8.08 kN/m², considering also distributed on the floor a wall located in the middle of the slab and a wall located at the periphery of the floor slab were used in the structural analysis, as shown in Table 1.

Table 1. Load used.

Overview	Amount
Dead load (distributed):	Load (kN/m ²)
Self-weight of slab (h = 16.0 cm)	25.0 · 0.16 = 4.00
Cladding	0.80
Wall (middle of the slab)	1.00
Wall (periphery of the slab)	2.28
Live load:	Load (kN/m ²)
Load in residential building	1.50

The slab was modeled with a “Four nodes Thin-Shell element type”, considering at the analysis only the translation normal to the slab plane. In the discretization of the slab, rectangular elements measuring 20 cm x 20 cm were used and the columns were modeled in the structural frame as frame-type connected in an element node.

Only a linear elastic structural analysis of the structure was performed, therefore, the reinforcement at columns was not determined and second-order effects were not considered.

3.1.1 Punching shear assessment

According to the results obtained by the codes NBR 6118:2014 [10], EUROCODE 2:2004 [9] and ACI 318:2019 [16], it was found that the slab-column connections presented a satisfactory strength to punching shear in order to withstand the loads that act on the intact structure. According to Table 2, the reactions and bending moments of the supports of the undamaged structure were obtained from the software SAP2000 [1].

Table 2. Reactions and the moments of the support in the structure without damage.

Column	N_k (kN)	M_x (kNm)	M_y (kNm)	Column	N_k (kN)	M_x (kNm)	M_y (kNm)
P1	177.10	21.80	23.00	P7	290.50	0.00	4.20
P2	228.60	4.50	18.10	P8	239.30	20.50	0.00
P3	228.60	4.50	18.10	P9	177.10	21.80	23.00
P4	177.10	21.80	23.00	P10	228.60	4.50	18.10
P5	239.30	20.50	0.00	P11	228.60	4.50	18.10
P6	290.50	0.00	4.20	P12	177.10	21.80	23.00

The effective depth (13 cm) and reinforcement ratio were determined according to the structural design presented at the reference. All connections presented studs type shear reinforcement, with four layers 6.23 cm² each at columns P1, P4, P9 and P12, and five layers 6.23cm² each for the other columns, spacing between studs equal to 10 cm and 6 cm from the first layer to the column face. Table 3 shows the shear stresses in the slab-column connections analyzed.

Table 3. Shear stresses at the critical section.

Codes	Stress (MPa)	P1	P2	P6
NBR 6118	τ_{rd3}	0.70	0.74	0.78
	τ_{sd3}	0.48	0.48	0.57
	τ_{rd2}	1.53	1.56	1.60
	τ_{sd2}	1.03	1.06	1.17
	τ_{rd1}	5.09	5.09	5.09
	τ_{sd1}	3.73	3.15	2.86
	σ_{rd3}	0.58	0.61	0.64
EUROCODE	σ_{sd3}	0.52	0.51	0.61
	σ_{rd2}	1.42	1.45	1.48
	σ_{sd2}	1.03	1.06	1.17
	σ_{rd1}	5.28	5.28	5.28
	σ_{sd1}	3.73	3.15	2.86
ACI	v_{cout}	0.70	0.70	0.70
	V_{u2}	0.43	0.43	0.52
	v_n	2.17	2.17	2.17
	V_{u1}	1.34	1.31	1.38

In Table 3:

- τ_{rd3} and τ_{sd3} are the strength and acting stresses outside the shear reinforcement,
- τ_{rd2} and τ_{sd2} are the strength and acting stresses at the shear reinforcement region,
- τ_{rd1} and τ_{sd1} are the strength and acting stresses at the periphery of the column,
- σ_{rd3} and σ_{sd3} are the strength and acting stresses outside the shear reinforcement,
- σ_{rd2} and σ_{sd2} are the strength and acting stresses at the shear reinforcement region,
- σ_{rd1} and σ_{sd1} are the strength and acting stresses at the periphery of the column,
- v_n e V_{u1} are the strength and acting stresses at the shear reinforcement region,
- v_{cout} and V_{u2} are the strength and acting stresses outside the shear reinforcement.

Figure 2 shows the acting and strength stresses ratio in the slab-column connections and as it can be seen, the analyzed supports present good punching shear strength, since the acting stresses were smaller than the capacity. EUROCODE [9] was the standard that presented the highest shear stress ratios in all the supports studied.

The possibility of progressive collapse is always relevant when the acting and the strength stresses ratio are high, not to mention the possibility of an overload or errors being done at the construction phase, for example. The highest ratios of the acting over the resistant stresses were taken as potential failures possibilities and the behavior of the floor slab and the remaining connections was then examined following these failures.

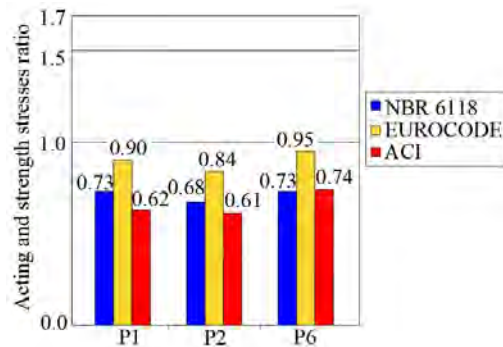


Figure 2. Acting and strength stresses ratio in the support.

3.1.2 Integrity reinforcement

Table 4 shows the integrity reinforcement designed according to the equations provided by the NBR 6118:2014 [10], GSA:2013 [17], CEB:2010 [8] and ACI 352:2011 [18] standards, basically considering the column reaction and the yield strength of the reinforcement.

Figure 3 shows a comparison between the amount of reinforcement found by the codes, with values being not so different, and ACI 352 [18] being surprisingly less conservative.

Table 4. Integrity reinforcement area.

Column	N_k (kN)	NBR 6118 (cm ²)	GSA (cm ²)	CEB (cm ²)	ACI (cm ²)
P1	177.10	7.33	10.81	8.23	6.46
P2	228.60	9.46	10.81	10.62	6.46
P6	290.50	12.03	10.81	13.50	6.46

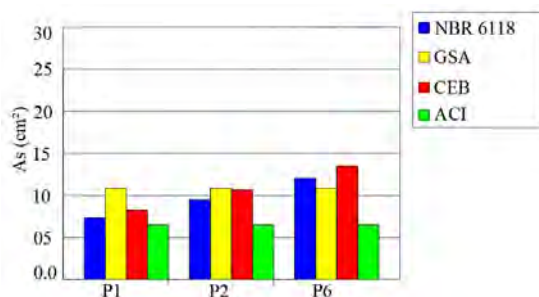


Figure 3. Comparison of reinforcement steel area.

3.1.3 Post punching shear pattern

After a punching shear failure at an internal slab-column connection, the possibility of a new punching failure at the neighboring connections was verified, considering zero or a partial residual strength at the damaged support. Table 5 shows the columns reactions when a punching failure is admitted at edge column P2.

Table 5. Reactions and bending moments of support after P2 punching shear.

Column	N_k (kN)	M_x (kNm)	M_y (kNm)	Column	N_k (kN)	M_x (kNm)	M_y (kNm)
P1	271.00	127.10	17.30	P7	267.80	7.30	1.90
P2	-	-	-	P8	235.70	19.00	0.90
P3	349.40	74.80	18.90	P9	172.10	11.30	20.90
P4	158.20	20.50	13.90	P10	207.90	4.30	5.70
P5	208.20	30.90	13.20	P11	223.40	4.50	12.20
P6	411.20	10.90	42.40	P12	178.90	22.60	23.70

Figure 4 shows the columns reactions changes for the neighbor’s connections following a punching shear failure at column P2, compared with the intact structure. Only the most affected columns connections are shown, together with column P12, far from column P2, for comparison.

As seen, with a total failure at P2 column connection a load increase of 53.0% is obtained at column P1, or an increase of 45.1% is obtained with a residual strength of 15% at column P2, stating the high probability of the occurrence of new failures in sequence, not to mention that the bending moments increased more than five times at P1 connection.

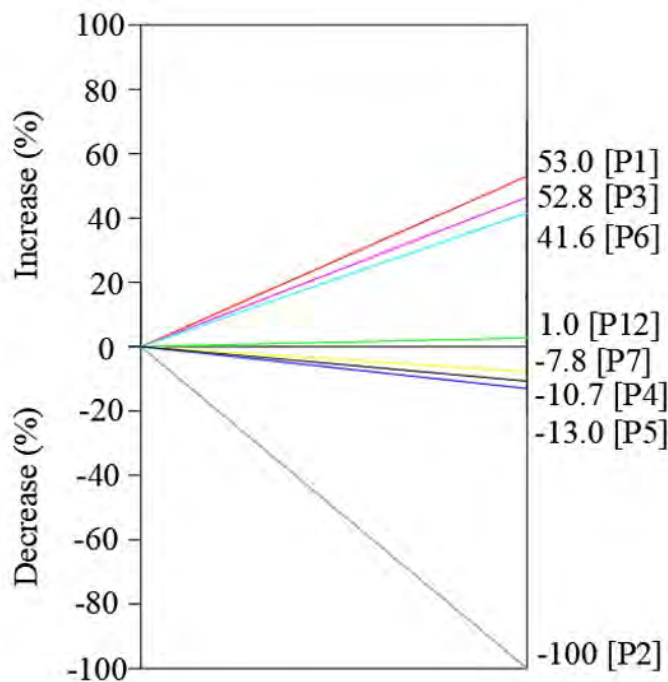


Figure 4. Variation of support reactions after failure at P2.

Integrity reinforcement at the failed slab-column connection can provide up to 60% residual strength, according to experimental research carried out by Melo [6], and by Lima [22] at the University of Brasília, allowing that failed connection can withstand more load and less load being spread to the other supports.

Big increases are always found at the “first neighbor line” supports close to a failed connection, as was seen at column connections P1 and P3 after failure at column connection P2. At a “second neighbor line” the load decrease, as seen at column connections P5 and P7. On the other hand, column connection P12, that is far from the failure has only a small increase in its load, as seen in Figure 4.

Table 6 shows the shear stresses for the internal slab-column connection P1, considering a zero or partial residual strength at the damaged connection, after a punching shear failure at connection P2.

The possibility of progressive collapse in the building would be avoided if the acting and strength stress ratio would be less than one, the defined limit, guaranteeing that the remaining strength is bigger than the actual acting load.

Table 6. Shear stresses in P1 after failure at P2.

Codes	Stress (MPa)	P1 No residual reaction in P2	P1 60% of residual reaction in P2
NBR 6118	τ_{rd3}	0.70	0.70
	τ_{sd3}	0.93	0.66
	τ_{rd2}	1.53	1.53
	τ_{sd2}	2.19	1.50
	τ_{rd1}	5.09	5.09
	τ_{sd1}	9.34	6.02
EUROCODE	σ_{rd3}	0.58	0.58
	σ_{sd3}	0.98	0.70
	σ_{rd2}	1.42	1.42
	σ_{sd2}	2.19	1.50
	σ_{rd1}	5.28	5.28
	σ_{sd1}	9.34	6.02
ACI	v_{cout}	0.70	0.70
	V_{u2}	0.79	0.58
	v_n	2.17	2.17
	V_{u1}	2.97	2.00

Figure 5 shows the acting and strength stresses ratios at the column P1, considering a residual strength of 0% or 60% at P2, aiming to verify the post-punching shear behavior of the analyzed structure.

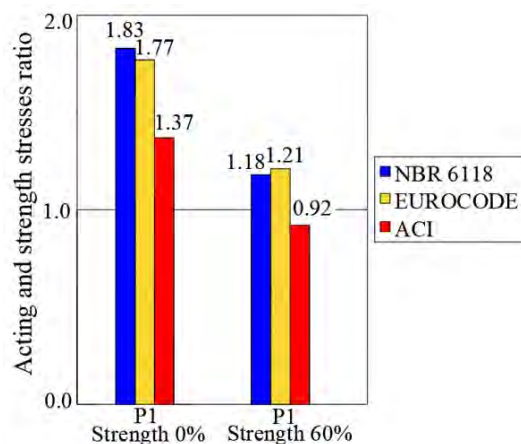


Figure 5. Shear stresses ratio in P1 for zero and for 60% of residual reaction in P2.

It is seen that according to NBR6118 [10] and EUROCODE [9] standards there is a great possibility of new punching shear failures in the structure, even with the presence of integrity reinforcement at P2, due to the large increase in reaction at P1.

3.1.4 Estimating the floor remaining capacity following a punching shear failure by the Yield Line Theory

The flexural capacity of the slab was determined after punching shear failure of a slab-column connection close to the edge (P2), without considering any residual strength. After the loss of support in the structure, the loads were redistributed to the columns, with an increase or decrease in reactions.

The Yield Line Method is applied for calculating the remaining capacity of the floor after a shear punching had occurred, taking in account all the well anchored flexural reinforcement according to the structural concrete requirements that crosses the supposed yield line rupture mechanisms and then can provide yielding resisting moment.

As seen in Figure 6, one possible yield line pattern is adopted after a punching shear had occurred in P2 connection, the Virtual Work Principle is used to calculate the remaining capacity of the floor by the Yield Line Method, assuming a virtual unitary displacement at the point “J”, in this case where the slab/column connection failed, and all the contributions of the hogging and sagging reinforcement is considered, provide it is well anchored and crosses the yield

lines. The volume of the deformed shape when the virtual unitary displacement (J) is applied is shown in Figure 7, considering the rotations of the floor.

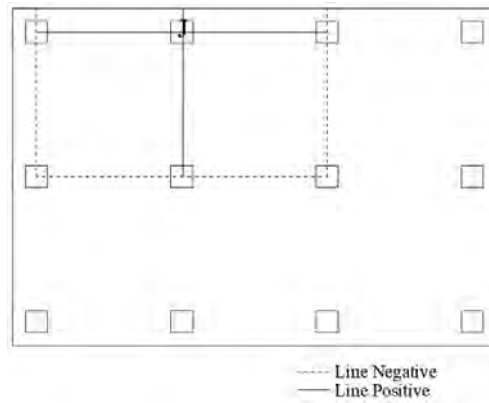


Figure 6. Positive and negative yield line configuration.

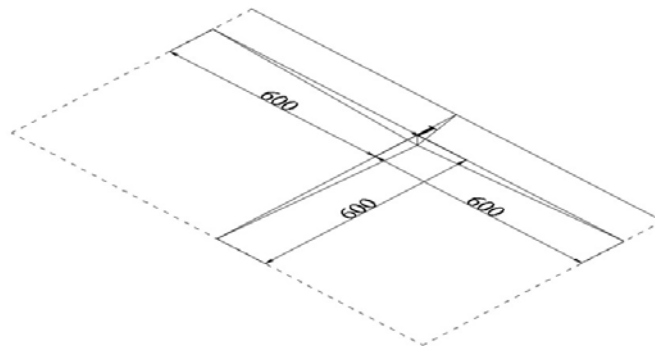


Figure 7. Deformation of a slab – Dimensions in cm.

Figures 8, 9, 10 and 11 show the positive and negative yielding resisting moments strengths of the floor slab, determined taking in account all the well anchored flexural reinforcement that crosses the assumed yield line pattern.

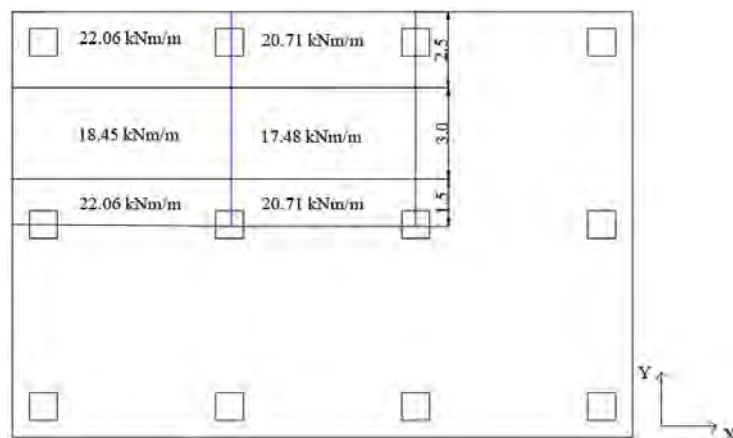


Figure 8. Positive moment strengths in the X direction – Dimensions in m.

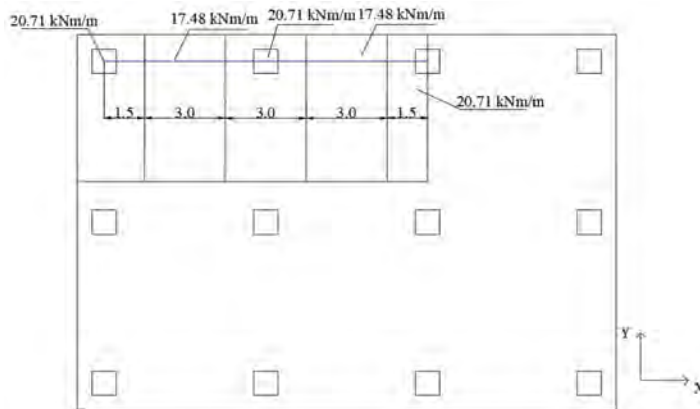


Figure 9. Positive moment strengths in the Y direction – Dimensions in m.

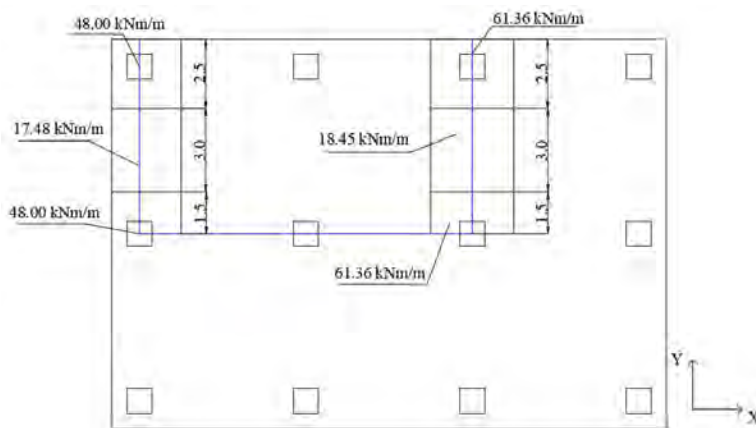


Figure 10. Negative moment strengths in the X direction – Dimensions in m.

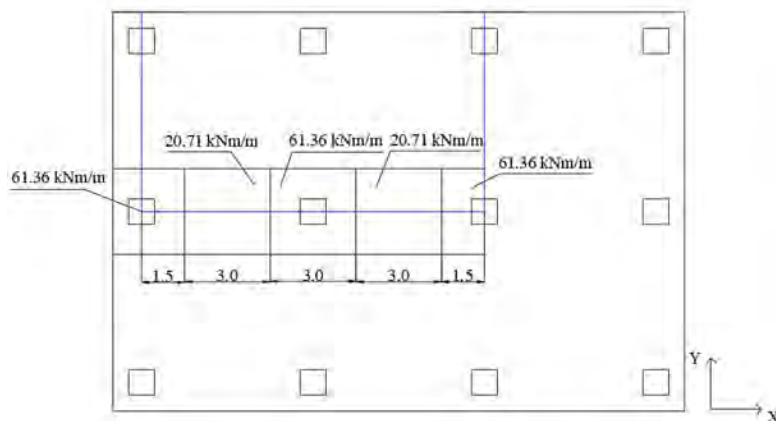


Figure 11. Negative moment strengths in the Y direction – Dimensions in m.

As seen the Yield Line Method can be calculated by the Virtual-Work Method considering the external work required by the load and the internal work used by the slab or floor to deform itself.

The external work required by a load applied uniformly on a slab can be determined by the product of the failure load and the volume of the displaced slab after the application of the virtual displacement. The internal work can be defined as the product of the strength moments and rotations in the slab [23].

The calculated collapse load (5.39 kN/m²) was 44% lower than the predicted actual load on the slab (9.58 kN/m²), after the loss of support P2, stating the real and big possibility of the occurrence of progressive collapse in the structure.

As Yield Line is a Superior Limit Method [23]–[25] other possible collapse mechanism could have been found with an even lower collapse load but there is no need for this search as the floor slab is already in a critical condition for the possibility of occurrence of a progressive collapse for the one yield line pattern investigated.

As was seen the Yield Line Method can be applied to verify the possibility of a progressive collapse following a punching shear failure at a connection. It should also be mentioned that for this analysis no residual strength at the damaged slab-column connection was considered. If integrity reinforcement at P2 was considered the situation would be less severe, as the collapse load would be higher.

3.2 Second Example

The studied building was designed in 2015 [26] and its post-punching shear behavior was analyzed using the software for structural design in reinforced concrete Eberick [2], using “Grid Analogy”, basically with plate elements connected to bars in two orthogonal directions presenting bending stiffness that can be adjusted.

The building structure has six floors, with a garage parking on the third floor formed by a 35 cm thick waffle slab and a ceiling height of 270 cm, two rigid cores formed by the stairs and elevator shaft, and floor openings for hydro-sanitary pipes. There is also a car access ramp at the left corner and presence beams connecting the columns at the periphery of the building.

The slab / column connections located at the third floor of the building were studied. Concrete with 30 MPa strength were adopted, and a cross-section of the ribbed slab and the floor plan of the structure are shown respectively in Figures 12 and 13.

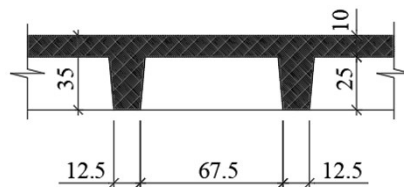


Figure 12. Section of the waffle slab – Dimensions in cm.

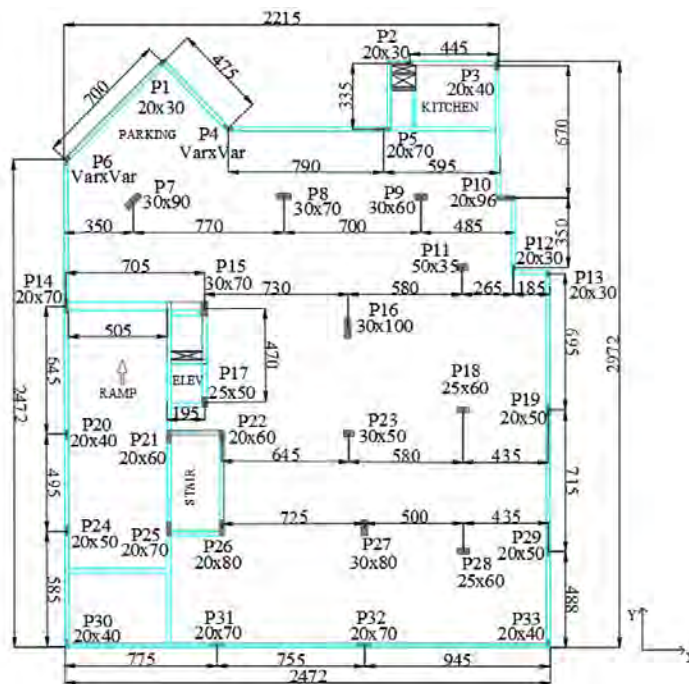


Figure 13. Floor plan of the parking – Dimensions in cm.

Horizontal forces from wind action were considered on the structure according to NBR 6123 [27], and Table 7 presents the gravity loads adopted at the structural design, according to NBR 6120 [21]. A live load of 5.0 kN/m² and a dead load of 6.02 kN/m² were used on the floor slab of the third floor.

Table 7. Load used.

Overview	Amount
Dead Load (distributed):	Load (kN/m ²)
Self-weight of slab	4.60
Cladding	1.23
Wall	0.19
Live Load:	Load (kN/m ²)
Load in parking building	5.00

3.2.1 Punching shear assessment

Punching shear was checked at three internal slab columns connections (P11, P23 and P27) of the intact structure, susceptible to punching shear failures, and according to the shear stresses obtained by the codes NBR 6118:2014 [10], EUROCODE 2:2004 [9] and ACI 318:2019 [16].

Table 8 shows all columns reactions and bending moments for the intact structure, calculated by the Eberick software [2]. Columns P11, P23 and P27 have respectively cross sections of 50 cm x 35 cm, 50 cm x 30 cm and 80 cm x 30 cm.

Table 8. Reactions and the moments of the support in the structure without damage.

Column	N_k (kN)	M_x (kNm)	M_y (kNm)	Column	N_k (kN)	M_x (kNm)	M_y (kNm)
P1	117.30	9.50	28.30	P18	465.70	3.50	30.10
P2	99.60	18.10	4.00	P19	220.40	0.30	14.10
P3	134.90	15.50	44.40	P20	82.90	5.40	41.30
P4	156.80	31.50	18.80	P21	128.10	7.50	35.90
P5	215.00	34.30	9.50	P22	193.00	10.20	39.10
P6	145.90	11.40	26.90	P23	415.70	1.30	57.30
P7	546.40	83.60	23.50	P24	163.40	11.30	65.20
P8	500.70	33.50	20.50	P25	240.30	13.60	102.60
P9	332.90	6.00	43.30	P26	317.90	9.00	29.20
P10	159.70	39.60	40.90	P27	530.00	25.70	107.30
P11	332.10	20.20	15.70	P28	424.30	3.40	33.90
P12	56.90	1.90	6.20	P29	186.40	4.40	36.20
P13	86.30	4.60	28.30	P30	153.60	27.80	40.90
P14	243.40	31.90	54.20	P31	278.30	59.40	0.60
P15	373.90	75.50	31.80	P32	255.40	48.40	1.40
P16	590.70	20.50	69.10	P33	131.00	35.30	19.70
P17	173.10	9.10	45.60	-	-	-	-

The top flexural reinforcement was 12.5 mm bars each ten centimeters and 16 mm bars each fifteen centimeters respectively for the x and y directions for column P11 connection, 12.5 mm bars each ten centimeters for the two directions for column P23 connection, and 16 mm bars each ten centimeters and 12.5 mm bars each ten centimeters respectively for the x and y directions for column P27 connection.

For the bottom flexural reinforcement was 10 mm bars each ten centimeters for the two directions for column P11 and P27 connections, and 10 mm bars each fifteen centimeters for the two directions for column P23 connection. For the ribs 12.5- or 16-mm bars were used at the bottom and 12.5 mm at the top at the two directions.

Shear reinforcement was present at all internal connections, designed by the NBR 6118 [10], in four layers, each with 4.36 cm² for the regions of columns P11 and P23, and with 4.98 cm² for the region of column P27, the first layer being 16 cm from the column and the others 24 cm apart.

Table 9 presents the acting and strength stress at the studied connections, according to the three codes presented, and Figure 14 presents the stress ratio for verifying the stability of the structure. It can be seen that the strength capacity is higher than the actual acting load for all three the studied columns regions, and the structure can be considered safe.

Connections at columns P11, P23 and P27 were chosen as are susceptible to punching shear failures even though P27 would be the most susceptible as seen in Figure 14.

Table 9. Shear stresses at the critical section.

Codes	Stress (MPa)	P11	P23	P27
NBR 6118	τ_{rd3}	0.52	0.51	0.56
	τ_{sd3}	0.15	0.19	0.24
	τ_{rd2}	0.61	0.61	0.65
	τ_{sd2}	0.31	0.40	0.52
	τ_{rd1}	5.09	5.09	5.09
	τ_{sd1}	1.29	2.00	1.99
	σ_{rd3}	0.48	0.48	0.52
	σ_{sd3}	0.16	0.20	0.26
EUROCODE	σ_{rd2}	0.52	0.52	0.55
	σ_{sd2}	0.31	0.40	0.52
	σ_{rd1}	5.28	5.28	5.28
	σ_{sd1}	1.29	2.00	1.99
ACI	v_{cout}	0.66	0.66	0.66
	V_{u2}	0.14	0.17	0.22
	v_n	1.17	1.18	1.17
	V_{u1}	0.43	0.58	0.69

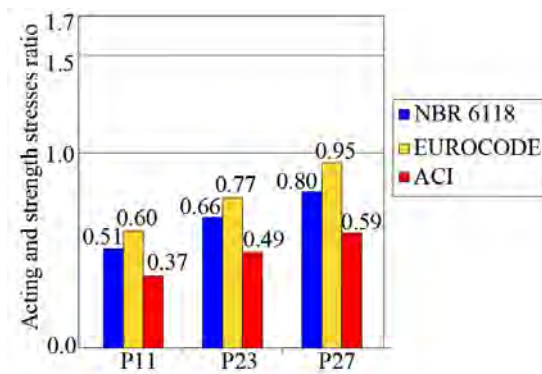


Figure 14. Acting and strength stresses ratio in support.

Estimations with NBR 6118 [10] and EUROCODE [9] are close, as the acting shear stresses are calculated in almost the same way, while the resisting shear stresses differs as the European code has a higher safety factor for the concrete strength and limits the top reinforcement ratio and the size effect.

3.2.2 Integrity reinforcement

The Table 10 shows the results obtained by the NBR 6118:2014 [10], GSA:2013 [17], CEB:2010 [8] and ACI 352:2011 [18] codes, for the integrity reinforcement steel areas. The most conservative standard was found, while Figure 15 shows a comparison of the reinforcement areas.

Table 10. Integrity reinforcement area.

Column	N_k (kN)	NBR 6118 (cm ²)	GSA (cm ²)	CEB (cm ²)	ACI (cm ²)
P11	332.10	13.75	25.55	15.43	5.62
P23	415.70	17.21	25.55	19.32	4.67
P27	530.00	21.94	25.55	24.63	5.77

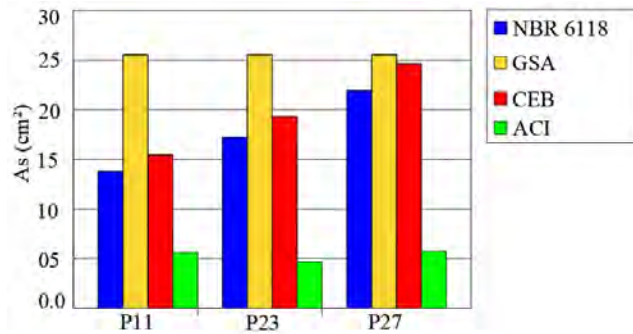


Figure 15. Comparison of reinforcement steel areas.

It can be seen that the GSA [17] standard is the most conservative in all cases, presenting the largest reinforcement areas against progressive collapse, leading to a possibly lower possibility of propagation of a collapse. For P11 it is observed that the GSA standard [17] has a steel area 86% larger than the Brazilian standard NBR 6118 [10], as the GSA [17] does not consider the support reactions in the calculation of the reinforcement, while for P27 the difference is small difference between GSA [17] and CEB [8].

3.2.3 Post punching shear pattern

The analysis of the post punching shear behavior of the slab studied was carried out considering as previous a total or partial loss of a slab-column connection after a punching shear failure, comparing the bending moments and column reactions, and checking the possibility of the damage being spread through other connections.

Table 11 shows changes in reaction and in bending moments when slab-column connection P23 is removed, and Figure 16 shows the internal connections with the highest variations in percentage.

Table 11. Reactions and moments of support after P23 punching shear.

Column	N_k (kN)	M_x (kNm)	M_y (kNm)	Column	N_k (kN)	M_x (kNm)	M_y (kNm)
P1	116.70	9.30	27.90	P17	182.30	7.20	50.10
P2	99.60	18.10	3.30	P18	520.00	3.20	27.60
P3	134.60	15.50	43.6	P19	210.10	0.20	18.20
P4	158.50	32.20	19.4	P20	82.40	5.70	46.60
P5	217.40	33.80	10.50	P21	117.10	7.90	38.10
P6	145.40	10.80	27.3	P22	220.10	8.50	35.10
P7	545.00	82.90	23.3	P23	-	-	-
P8	486.40	30.00	22.60	P24	164.50	12.10	63.50
P9	325.00	7.60	40.40	P25	242.60	16.00	99.70
P10	160.50	39.30	43.40	P26	334.60	10.40	36.80
P11	325.70	20.30	12.10	P27	714.30	34.70	105.40
P12	58.40	1.90	5.90	P28	415.00	1.90	41.00
P13	85.20	4.70	26.70	P29	185.00	4.20	38.30
P14	242.30	32.00	59.80	P30	155.40	28.10	43.00
P15	379.40	74.60	30.60	P31	273.40	54.20	0.50
P16	752.10	25.20	158.6	P32	245.60	55.70	1.20
-	-	-	-	P33	130.90	34.50	22.20

Column P23 was chosen to be removed to guarantee high loads at neighboring internal slab-column connections, more susceptible to punching shear failures, and avoiding the periphery columns with beams.

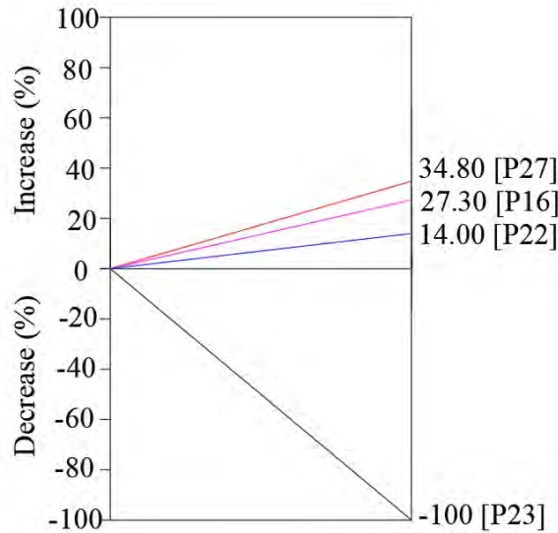


Figure 16. Variation of support reactions after failure at P23.

As seen in figure 16 the most loaded support following a failure at P23 is slab / column connection P27, presenting a 34.8% load increase in comparison with the intact structure, and is investigated.

Considering a residual strength of 15% in connection P23 the load increase in P27 drops to 29.6%, possibly still a high value that could contribute to spread the failure. With integrity reinforcement the residual strength could go up to 60%, reducing the load increase to 13.9% at P27, practically putting aside the possibility of progressive collapse with a 15% residual strength at connection P23 and the presence of the integrity reinforcement.

Table 12 shows the punching shear stresses in the region of slab column connection P27 when zero or 60% residual strength is considered for connection P23, and Figure 17 shows the comparison between the actual acting load and the strength capacity for these simulations.

It can be seen that the integrity reinforcement is effective in reducing the acting and strength stress ratio, preventing the possibility of a progressive collapse in the building, according to the NBR 6118 [10] and ACI 318 [16] standards.

Table 12. Shear stresses in P27 after failure at P23.

Codes	Stress (MPa)	P27 No residual reaction in P23	P27 60% of residual reaction in P23
NBR 6118	τ_{rd3}	0.56	0.56
	τ_{sd3}	0.32	0.27
	τ_{rd2}	0.65	0.65
	τ_{sd2}	0.67	0.58
	τ_{rd1}	5.09	5.09
	τ_{sd1}	2.45	2.18
	σ_{rd3}	0.52	0.52
	σ_{sd3}	0.34	0.29
EUROCODE	σ_{rd2}	0.55	0.55
	σ_{sd2}	0.66	0.58
	σ_{rd1}	5.28	5.28
	σ_{sd1}	2.45	2.18
	v_{cout}	0.66	0.66
ACI	V_{u2}	0.29	0.25
	v_n	1.17	1.17
	V_{u1}	0.88	0.77

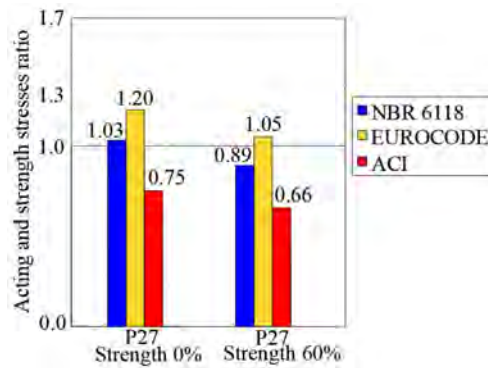


Figure 17. Shear stresses ratio in P27 for zero and for 60% of residual reaction in P23.

3.2.4 Predicting the floor remaining capacity following a punching shear failure by the Yield Line Theory

Assuming that there was a punching shear failure at P23, the flexural capacity of the slab was calculated and the possibility of a progressive collapse in the structure was checked, as the Yield Line Method is applied for calculating the remaining capacity of the floor after a punching shear had occurred, taking in account all the well anchored flexural reinforcement, according to the structural concrete requirements, that crosses the supposed yield line rupture mechanisms and then can provide yielding resisting moment. Yield lines were drawn considering that the collapse would be restricted around the damaged slab column region. Figure 18 presents a yield line pattern considering a possible slab collapse scenario, assuming negative lines connecting P16, P18, P27 and P22, and a positive line connecting P16, P23 and P27.

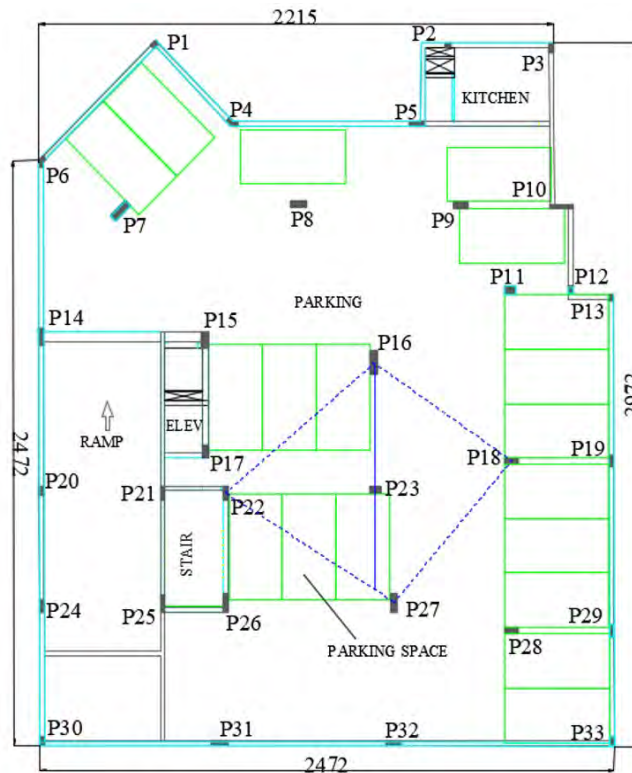


Figure 18. Positive and negative yield line configuration.

As seen in Figure 19, after a possible yield line pattern is adopted after a shear punching had occurred, the Virtual Work Principle is used to calculate the remaining capacity of the floor by the Yield Line Method, assuming a virtual

unitary displacement at the point “J”, in this case where the slab/column connection failed, and all the contributions of the hogging and sagging reinforcement is considered, provide it is well anchored and crosses the yield lines. The volume of the deformed shape when the virtual unitary displacement (J) is applied is shown in the figure, considering the rotations or deformations of the floor.

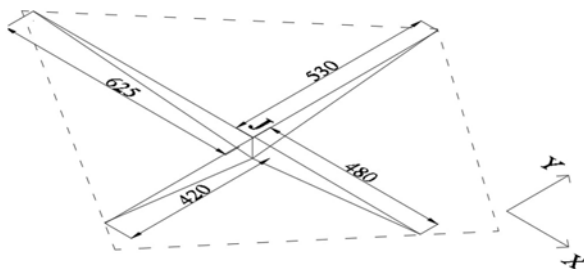


Figure 19. Deformations of slab – Dimensions in cm.

Figures 20, 21 and 22 show the positive and negative yielding resisting moments strengths of the floor slab, determined taking in account all the well anchored flexural reinforcement that crosses the assumed yield line pattern.

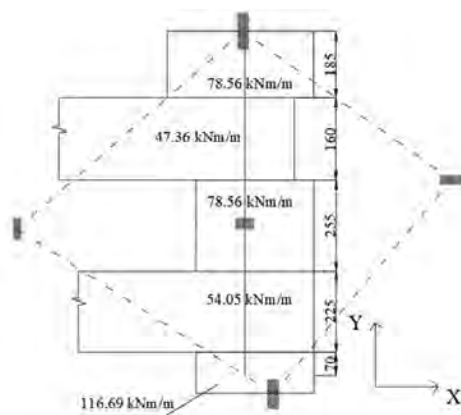


Figure 20. Positive moment strengths in the X direction – Dimensions in cm.

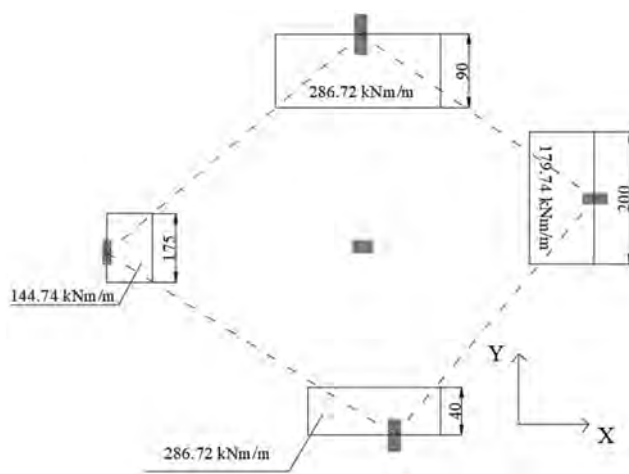


Figure 21. Negative moment strengths in the X direction – Dimensions in cm.

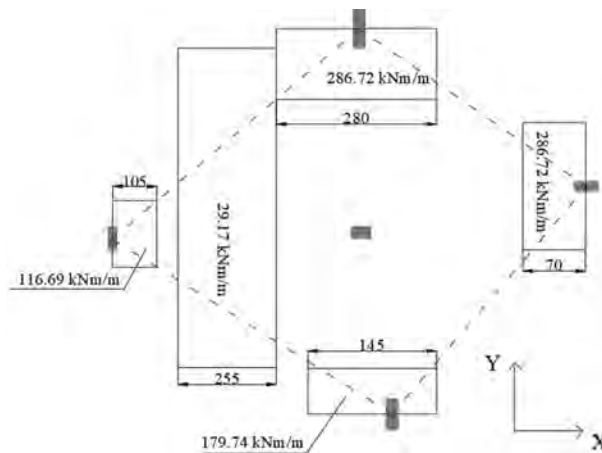


Figure 22. Negative moment strengths in the Y direction – Dimensions in cm.

As in the previous example the Virtual-Work Method was used to calculate the flexural remaining capacity of the floor and was estimated as 25.10 kN/m^2 , more than double of the actual acting load on the flat slab (11.02 kN/m^2), with practically no possibility of progressive collapse for this yield line pattern tested.

Having said that, as the Yield Line is a Superior Limit Method another yield line patterns should be tested before the possibility of a progressive collapse could have been disregarded.

As seen the Yield Line Method can be applied to verify the possibility of a progressive collapse following a punching shear failure at a connection.

4 CONCLUSIONS

The possibility of a second punching failure in sequence and of a progressive collapse following a column connection punching shear failure was investigated on a flat slab floor building with 20×14 meters in plan with three stories and twelve columns (Example 1) and on a waffle slab floor building with 25×30 meters in plan with six stories and thirty-three columns (Example 2).

Following a punching shear failure at the most loaded column connection, the remaining most loaded connection was checked for a punching shear failure, considering that the first failed column connection could hold zero or 60% of its original load, assuming that the connection could hold this amount of its original load when well designed and detailed integrity bottom reinforcement was installed at the column connection. The possibility of a progressive collapse at the slab floors after punching shear failures had occurred was then checked using the Yield Line Method [6], [7], [11], [22].

Regarding the possibility of a second punching shear failure in sequence, when there is no Integrity Reinforcement at the failed connection and it cannot hold any load, the three codes (ACI 318 [16], EUROCODE [9] and NBR 6118 [10]) indicate the possibility of a second punching shear failure in sequence for the first example, while only EUROCODE [9] and NBR 6118 [10] indicate this possibility for the second example. However, when Integrity Reinforcement well designed and detailed was present at the column connection only codes EUROCODE [9] and NBR 6118 [10] indicate the possibility a second punching shear failure in sequence for the first example, while only EUROCODE [9] indicates this possibility for the second example.

In respect to the occurrence of a Progressive Collapse of the floor slabs following the punching shear failure, investigated by the Yield Line Method and depending on the remaining capacity and the flexural resistance of the floors, it was shown that progressive collapse would have happen only for the first example, as the load applied would be about two times higher than the resistance of the floor. For the second example the resistance of the floor slab was more than double the applied load, securing it against the possibility of a progressive collapse.

As a general conclusion can be stated that slab column connections should be designed and detailed to prevent Progressive Collapse even when a punching shear failure had occurred in one of the connections. The post punching shear resistance of the top (hogging) bending reinforcement is low, but well anchored bottom bars going through the column (Integrity Reinforcement) can improve up to 60% the residual capacity of the connection [6], [7], [11], [22].

And that in flat slabs or plates the global behavior, the possibility of progressive collapse following a punching shear failure, and the remaining capacity of the floors depends on the *i*) post-punching resistance of the connection being punched; *ii*) post-punching resistance of the neighbors' connections; *iii*) flexural resistance of the slabs, and that it can be well estimated by the Yield Line Method.

ACKNOWLEDGEMENTS

The authors would like to thank the University of Brasilia, CAPES - Coordenação de Aperfeiçoamento de Pessoal de Nível Superior, CNPq - Conselho Nacional de Desenvolvimento Científico e Tecnológico, and FAP-DF - Fundação de Apoio à Pesquisa do Distrito Federal, Brazilian Research Development Agencies, for the support of this research.

REFERENCES

- [1] Computers and Structures, Inc., *Static and Dynamic Finite Element Analysis of Structure*, SAP2000 16, 2014.
- [2] Eberick, *Reinforced Concrete Structural Design Software*. AltoQi, 2022.
- [3] P. A. Martins, "Colapso progressivo em edifícios em laje cogumelo de concreto armado," M.S. thesis, UnB, Brasília, DF, 2003.
- [4] H. I. Longo, "Análise da estrutura para avaliação do colapso progressivo," in *VII CBPE Conference*, 2014, pp. 1-10.
- [5] H. Jaroslav, V. Aleksandar, and B. Viktor, "Failure analysis of collapsed parking garage building due to punching," *Eng. Fail. Anal.*, vol. 129, pp. 105712, Sep 2021, <http://dx.doi.org/10.1016/j.engfailanal.2021.105712>.
- [6] G. S. S. A. Melo, "Behavior of reinforced concrete flat slabs after local failure," Ph.D. dissertation, Polytech. Centr. London, London, 1990.
- [7] G. S. Melo and P. E. Regan, "Post-punching resistance of connections between flat slabs and interior columns," *Mag. Concr. Res.*, vol. 50, no. 4, pp. 319-327, Dec 1998, <http://dx.doi.org/10.1680/mac.1998.50.4.319>.
- [8] International Federation for Structural Concrete, *Model Code for Concrete Structures*, 2010.
- [9] European Committee for Standardization, *Design of Concrete Structures: General Rules and Rules for Buildings*, EUROCODE 2, 2004.
- [10] Associação Brasileira de Normas Técnicas, *Projeto de estruturas de concreto*, NBR 6118, 2014.
- [11] G. S. Melo and P. E. Regan, "Post-punching behavior of a waffle flat slab floor," in *Proc. 1st Int. Conf. Fract. Mech. Concr. Struct.*, 1992, <https://doi.org/10.1201/9781482286847>.
- [12] K. V. Udilovich, I. B. Shleykov, and M. V. Banchuzhnyy, "Design of flat-plate floors for progressive collapse using yield-line analysis," *Concr. Int.*, vol. 32, no. 7, pp. 1-8, Jul 2010. Accessed: Jun. 23, 2022. [Online]. Available: <https://www.concrete.org/publications/internationalconcreteabstractsportal/m/details/id/51663822>
- [13] M. Byfield, W. Mudalige, C. Morison, and E. Stoddart, "A review of progressive collapse research and regulations," *Proc. Inst. Civ. Eng., Struct. Build.*, vol. 167, no. 8, pp. 447-456, 2014, <http://dx.doi.org/10.1680/stbu.12.00023>.
- [14] J. Garzón-roca, J. Sagasetta, M. Buitrago, and J. M. Adam, "Dynamic punching assessment of edge columns after sudden corner column removal," *ACI Struct. J.*, vol. 118, no. 2, pp. 299-311, Mar 2021, <http://dx.doi.org/10.14359/51728195>.
- [15] S. A. E. Kakhki, A. Kheyroddin, and A. Mortezaei, "Evaluation of the progressive collapse of the reinforced concrete frames considering the soil-structure interaction: parametric study based on the sensitivity index," *Int. J. Concr. Struct. Mater.*, vol. 16, no. 38, pp. 1-24, 2022, <http://dx.doi.org/10.1186/s40069-022-00523-x>.
- [16] American Concrete Institute, *Building Code Requirements for Structural Concrete and Commentary*, ACI 318, 2019.
- [17] U.S. General Services Administration, *Alternate Path Analysis & Design Guidelines for Progressive Collapse Resistance*, 2013.
- [18] American Concrete Institute, *Guide for Design of Slab-Column Connections in Monolithic Concrete Structures Standards*, ACI 352, 2011.
- [19] R. A. Chaves, *Concreto Armado II – Lajes lisas e Lajes cogumelo*. Belo Horizonte: UFMG, 2011.
- [20] N. A. Silva, *Concreto Armado II – Especialização*. Belo Horizonte: UFMG, 2015.
- [21] Associação Brasileira de Normas Técnicas, *Cargas para o cálculo de estruturas de edificações*, NBR 6120, 1980.
- [22] A. F. Lima No., "Análise experimental na fase de pós-puncionamento de lajes cogumelo de concret," M.S. thesis, UnB, Brasília, DF, 2003
- [23] K. W. Johansen, *Linhas de Ruptura: teoria e prática*, 1ª ed. Curitiba: Editora LT, 1962.
- [24] J. D. Lima, A. T. Coelho, and V. Monteiro, *Manual de Betão Armado*, 5ª ed. Lisboa: Editora LNEC, 1980.
- [25] B. Balakrishnan and D. Menon, "Collapse load estimation of rectangular RC beam-slab systems: new insights," *ACI Struct. J.*, vol. 115, no. 5, pp. 1279-1294, 2018, <http://dx.doi.org/10.14359/51702246>.
- [26] E. M. Piancastelli, *Design of Reinforced Concrete Structure in DWG AutoCAD Software*, 2021.
- [27] Associação Brasileira de Normas Técnicas, *Forças Devidas ao Vento em Edificações*, ABNT NBR 6123, 1988.

Author contributions: The second author of this article was the supervisor of the research accomplished by the first author during his MSc Thesis.

Editors: Diogo Rodrigo Ribeiro, Guilherme Aris Parsekian.